NASA CONTRACTOR REPORT

NASA CR-154
C.1

NASA CR-1546

TWO GAS ATMOSPHERE SENSOR SYSTEM (MASS SPECTROMETER)

Phases IIa and IIb

Prepared by
THE PERKIN-ELMER CORPORATION
Pomona, Calif.
for Langley Research Center

NATIONAL AERONAUTICS AND SPACE ADMINISTRATION • WASHINGTON, D. C. • APRIL 1970

NASA CR-1546

TWO GAS ATMOSPHERE SENSOR SYSTEM

(MASS SPECTROMETER)

Phases IIa and IIb

1. Mass Spectrometer

Prepared under Contract No. NAS 1-6387 by
THE PERKIN-ELMER CORPORATION
Pomona, Calif.

for Langley Research Center

NATIONAL AERONAUTICS AND SPACE ADMINISTRATION

For sale by the Clearinghouse for Federal Scientific and Technical Information
Springfield, Virginia 22151 – CFSTI price $3.00

FOREWORD

This investigation was conducted by Perkin-Elmer Corporation, Aerospace Systems, Pomona, California during the period June 1966 through March 1969, under contract NAS 1-6387. This program of design, fabrication, and application followed an earlier study effort entitled, "Development of a Two-Gas Atmosphere Sensor System (Mass Spectrometer)," under NAS 1-5679.

As the projected duration of manned spacecraft missions has increased, a need to measure more accurately the parameters influencing man in his closed ecological system has evolved. In the early stages of the program it was necessary to monitor only the major atmospheric components. As man's exposure to these closed environments has increased, so has the complexity of his environment. The result of this evolution has been the need for the development of a front line atmospheric monitor capable of indicating the general condition of a spacecraft cabin atmosphere. It was the purpose of this program to develop an instrument capable of meeting the needs of present and future extended mission manned spacecraft.

The flight prototype hardware design described herein embodies inherent ruggedness, operational simplicity, reliability, minimum power requirements, optimum size and weight compatible with flight environments. The major requirements of NPC 200-2, 200-4, and 250-1 such as reliability analysis, certified soldering personnel and drawing change control were implemented.

The program was monitored by the Flight Instrumentation Division of the NASA Langley Research Center. Mr. A. L. Lindler, of the above Division, provided the monitoring of the reliability and quality assurance efforts. This work was conducted under the auspices of the Office of Advanced Research and Technology, NASA Headquarters, specifically under the Biotechnology and Human Research Division.

D. C. Popma
Technical Contract Monitor

Walton L. Jones, Director
Biotechnology and Human Research Division

ABSTRACT

Two Gas Atmosphere Sensor System (Mass Spectrometer)*

This report covers the two principal phases of an effort to design, fabricate, and test a mass spectrometer in a miniaturized, flight prototype configuration. The goal of this effort was a sensor capable of monitoring and providing control voltages proportional to the partial pressures of the four major constituents of a two gas atmosphere used on-board manned spacecraft: oxygen, nitrogen, carbon dioxide, and water vapor.

This report is divided into two parts: Phase IIa, the design of the sensor and the fabrication of an Engineering Test Model (ETM) to demonstrate the correctness of the overall sensor design; Phase IIb undertook the fabrication and acceptance testing of four sensors, and was subsequently modified to incorporate additional design, fabrication, and test efforts for a ball leak inlet system, a miniaturized ion pump, and the installation of one of the instruments on a 4-man, 60-day closed chamber test for monitoring and control of the atmosphere within the chamber.

This report covers the work performed on this contract, including the basis for the design, details of the modified reliability and quality assurance efforts, details of the fabrication and assembly, drawings of the components and electronic subsystems, and results of the acceptance testing accomplished.

* Phase I of this study has been published as NASA CR-66172.

TABLE OF CONTENTS

TABLE OF CONTENTS (Cont)

TABLE OF CONTENTS (Cont)

TABLE OF CONTENTS (Cont)

TABLE OF CONTENTS (Cont)

LIST OF ILLUSTRATIONS

LIST OF ILLUSTRATIONS (Cont)

LIST OF ILLUSTRATIONS (Cont)

LIST OF ILLUSTRATIONS (Cont)

LIST OF ILLUSTRATIONS (Cont)

LIST OF ILLUSTRATIONS (Cont)

LIST OF TABLES

LIST OF TABLES (Cont)

TWO GAS ATMOSPHERE SENSOR SYSTEM
(MASS SPECTROMETER)

PHASE IIa - FINAL REPORT

INTRODUCTION

STATEMENT OF THE PROBLEM

As man probes the unknowns of nature both in space and below the ocean surface, he is required to exist for more extended periods in enclosed environmental systems. As this occurs it becomes apparent that these systems must more closely approximate his natural environment if they are not to have physiologically deleterious effects. An area of principal concern is the maintenance of an atmosphere which is more tolerable for longer periods of time.

Past and present manned spacecraft have utilized pure oxygen atmospheres which minimize the problems of atmospheric control. Future space programs involving the Apollo spacecraft are being planned with mission durations from 45 to 120 days. For such periods it becomes prudent to consider a two gas system, either nitrogen-oxygen or helium-oxygen. Furthermore, the longer time period necessitates a tighter control on the principal products of human metabolism, carbon dioxide and water, and also makes feasible the use of an oxygen reclamation system to reduce the gas requirements.

The adaptation of existing atmosphere control systems to a two gas atmosphere presents the problem of sensing the two major constituents independently. In the past, a total pressure sensor was adequate whereas now a partial pressure analyzer is required. It is understood that present plans call for the use of nitrogen as the diluent gas. Therefore, a specific requirement was generated for a sensor system which can monitor the partial pressures of O_2, N_2, CO_2, and H_2O. This system must be compatible with typical operating environments and must present outputs which are suitable for input to existing types of atmosphere control devices and for telemetry or visual display.

THE SOLUTION OF THE PROBLEM

Preliminary investigations indicated that a mass spectrometer was in all probability the best suited instrument for this application. It was believed that the mass spectrometer offers several advantages over other possible sensor systems. First, it is an integrated approach to the problem allowing all of the required partial pressures to be measured on the same instrument. Therefore, a concentrated effort can be devoted to the development and improvement of a single-sensor technology. Second, the mass spectrometer is inherently fast, responding rapidly to sample changes. This will allow a tighter control of the atmosphere supply and replenishment systems to be maintained. Third, they have high accuracies allowing relative partial pressures of the major constituents to be determined with an accuracy on the order of 1% over the difficult

environmental conditions prevailing on typical space applications. Fourth, they can be made extremely rugged and operate equally well regardless of the prevailing conditions of gravitation, exposure to hard vacuu, or orientation. When sealed off, the instruments have a shelf life similar to an all metal vacuum tube that is limited only by the lifetime of electronic components. Fifth, a mass spectrometerinstrument gives a continuous direct detection of all partial pressures thus allowing direct integration into the control system without a complicated electronics interface. Each output signal is proportional to the partial pressure of a single constituent and therefore no non-linearities or cross-talk are introduced which must be compensated for electronically. Finally mass spectrometer systems are made up of components which may take on a variety of forms thereby assuring a high degree of compatibility with other control elements. At the same time all of these advantages apply to the monitoring of a wide variety of gases so that the instrument is readily adaptable to other atmospheres.

Functionally, a mass spectrometer can be viewed as a sophisticated electron tube which consists of a vacuum envelope, a filament for the emission of electrons, and various focusing and current collecting electrodes. In order to operate this 'tube' an appropriate set of electronics is required. One difference between this tube and other more conventional types is that since it must measure the surrounding environment it must have provisions for the introduction of a sample gas into the tube and since, like other vacuum tubes, a low internal pressure must be maintained at all times, a pumping system is utilized to remove the sample gas which has leaked into the system. With the vacuum tube analogy in mind, an operational description of the system is now to be given. A schematic representation of mass spectrometer operation is shown in Figure 1.

The sample gas is admitted to the mass spectrometer through the combination of a viscous flow pressure divider and a molecular leak. This reduces the gas pressure to a level compatible with the ion source operating pressure. Gas enters the ionizing chamber which is part of the ion source. The ion source supplies electrons from a hot wire filament through an electron gun to the ionizing region. Gas entering the ionizing chamber is ionized by electron bombardment and the resulting ions are accelerated out of the ionizing region through an ion focusing system and to an exit aperture. This exit aperture forms the 'object' of the magnetic sector analyzer. This consists of a uniform magnetic field which is generated by a permanent magnet, and a set of ion current collectors. A magnetic field permeates through the walls of the vacuum envelope in which the ions are travelling and causes them to bend in circular paths, the radii of which are dependent upon their mass-to-charge ratios. The ions are separated by this action and are then focused into collector buckets which are spaced out along the collector flange at distances proportioned to mass. There are collectors for each ion species of interest.

A vacuum envelope houses the ion source and the magnetic sector. It is typically a thin walled stainless steel housing which is electrically accessible through feedthroughs. Multiple pin headers introduce voltages from the ion source electronics and feeds them to the filaments and to the various focusing electrodes, while single pin feedthroughs transmit the ion currents from the

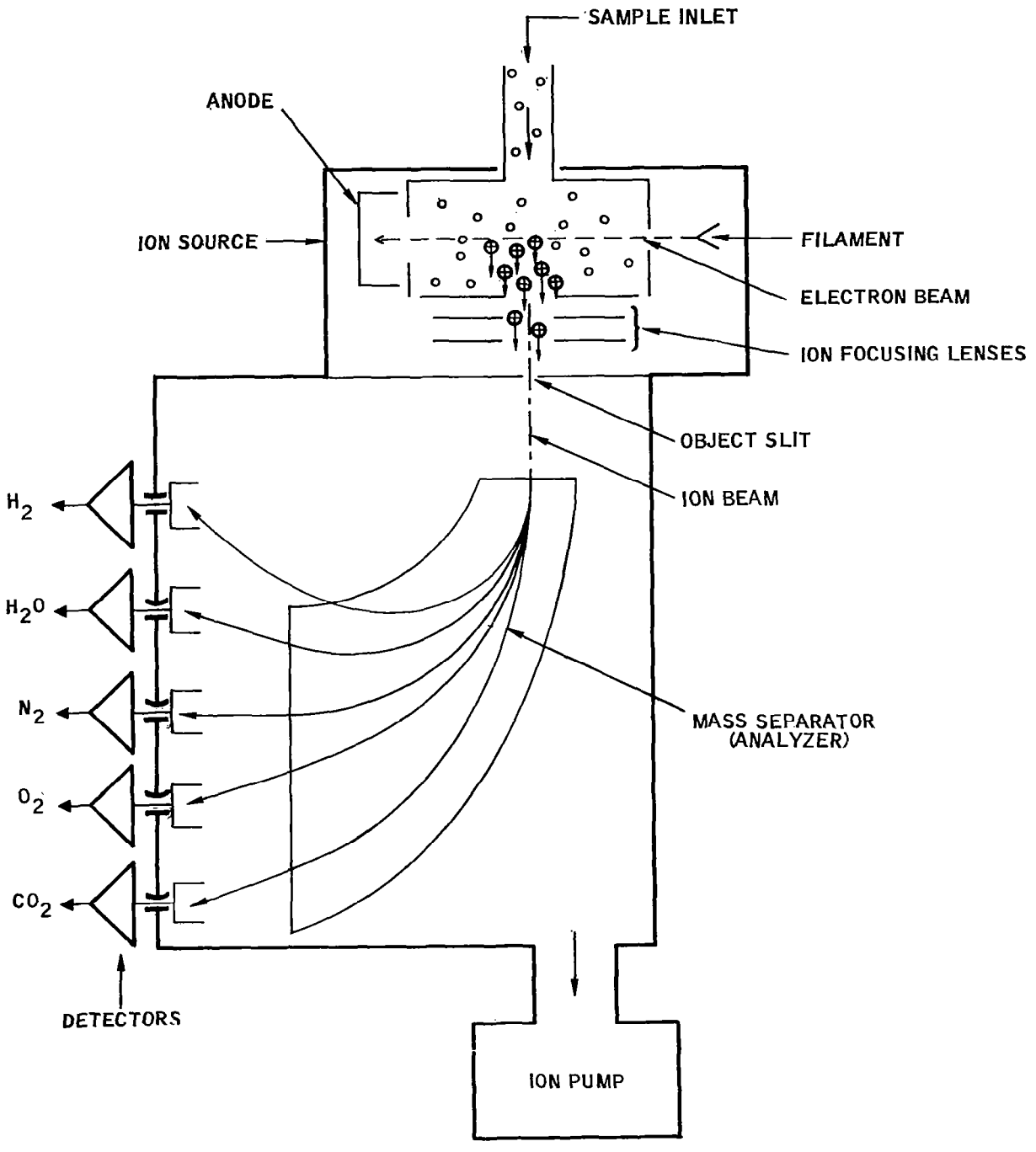

FIGURE 1
Mass Spectrometer Schematic

ion current collectors to electrometer amplifiers which amplify the small ion currents to the levels required for output.

The internal vacuum necessary for operation of the analyzer is maintained by some type of pumping system.

In addition to the electrometer amplifiers the support electronics consist of only three modules: the filament supply and emission regulator which senses the ionizing current and controls the filament current to keep it constant; the electrode bias supplies which provides the necessary voltages to the focusing electrodes; and the detector power supply which provides the B+ and B- voltages required for the electrometer amplifiers.

TASK DESCRIPTION

Under NASA Contract NAS1-5679, development of a Two-Gas Atmosphere Sensor System (Mass Spectrometer), Perkin-Elmer Aerospace Systems studied the use of a mass spectrometer sensor system to measure the partial pressures of oxygen, nitrogen, carbon dioxide and water vapor within a space vehicle cabin environment. The contract called for this sensor system to be compatible with the Apollo cabin environment (as well as possible extensions of the Apollo mission) and to be capable of presenting electrical voltage outputs which were suitable for input to existing types of atmosphere control devices as well as probable control systems on vehicles of longer duration, and for telemetry and visual display. The final report under this contract presented the results of this study, and recommended the use of a single-focusing magnetic sector type of mass spectrometer. This type of spectrometer was selected over the quadrupole mass filter type of spectrometer. The study included an examination of weight, electrical power requirements, complexity, and compatibility with system performance goals. A detailed analysis of this magnetic sector instrument led to a design, which was documented in the final report under this contract. The expected performance of this system was given, and no fundamental problems were anticipated in the attainment of these goals in the fabrication and testing of a flight-prototype instrument.

The present contract embodies Phases II(a) and II(b) of the study and developement program. The Phase II(a) program consisted of the following tasks: A preliminary design which led to a breadboard system. From the results of the analysis and testing of the breadboard system a redesign was carried out which led to the fabrication and test of an engineering test model. Due to the longer lead times involved in the design and fabrication of analyzer components there was only a breadboard phase for the electronics modules. The engineering test model has just begun testing which will continue during the month of May. At this time the design will be finalized and all drawings will be brought up to date. These drawings will be submitted to Langley Research Center along with a test plan for approval. When approval is obtained, Phase II(b) will be initiated. This phase consists of the manufacture, acceptance testing, and delivery of four (4) flight-prototype units to NASA Langley Research Center.

It is expected that the flight prototype hardware design will embody inherent ruggedness, operational simplicity, reliability, minimum power requirements, optimum size and weight compatible with flight environments. The units to be developed in this contract will not be required to undergo flight qualification, but should possess inherent characteristics which would be required if both

flight and reliability qualifications were to be imposed. The design approach which was followed was based upon the Reference System established during the Phase I conceptual design effort.

The major requirements of NPC 200-2, 200-4, and 250-1 such as reliability analysis, certified soldering personnel and drawing change control were implemented as agreed to with LRC.

For electronic subsystems, established reliability parts and components were used where possible, and in general, electronic parts were stressed to no more than 50 percent of rating. Electronic parts received 100 percent screening for known types of defects. The reliability and quality assurance effort for the development of the sensor system was flexible enough for the changes required by the developmental nature of the task, but they will assure that, for the deliverable items in Phase II(b), all major reliability and quality assurance requirements have been met. These efforts will provide assurance that, for possible future flight articles, the imposition of the full reliability and quality assurance provisions for manned flight will result in minimum discrepancies in the design and manufacturing procedures, and at the same time, the limited application of this technology will result in a delivered sensor that will show improved reliability and quality, without the expenditure of the time and effort that would be required if the sensor system were to be designed and constructed under the complete application of these documents.

This report describes the work which has been completed to date on the Phase II(a) portion of this development effort. This includes a detailed description of the design process and test results insofar as they have been obtained.

DESIGN REQUIREMENTS

The design requirements for this instrument were based upon an Apollo application. Therefore, two spacecraft models were established based upon an Apollo cabin environment. The pertinent numerical data relating to these models is given in Table 1. The proposed atmosphere which is to be monitored is a 50-50 N_2-O_2 mixture at about one-half atmosphere total pressure. The pertinent data on the atmosphere is given in Table 2. Based upon this information the performance goals for the mass spectrometer system were established during the early part of the Phase I work. These have undergone some slight revisions and the present performance goals are given in Table 3. These goals are to be attained with a minimum cost in terms of power, weight, and size.

TABLE 1

Spacecraft Models

	MODEL 1	MODEL 2
Type	Apollo Command Module, with or without the Lunar Excursion Module	Apollo Command Module, with dependent laboratory module
Volume	Apollo Command Module 138 ft^3. Lunar Excursion Module 180 ft^3	Apollo Command Module 138 ft^3. Laboratory Module 1500 ft^3
Power Penalty	Fixed - 450 #/KW Variable - 1.51 #/KW hour	Fixed - 500 #/KW Variable - 0.0 #/KW hour
Location of Sensor Unit	Apollo CM	Apollo CM
Operational Temperature Range	+40°F to + 90°F	+40°F to +90°F
Cabin Leakage Rate	0.3 pounds/hour	0.3 pounds/hour
Power	28 ±0.5 VDC	28 ±0.5 VDC

TABLE 2

Cabin Atmosphere Requirements

PARAMETER	NOMINAL DESIGN POINT
Total Pressure	362 ±11 mm H_g
O_2 Partial Pressure	181 ±5.5 mm H_g
N_2 Partial Pressure	Diluent, to provide total pressure
CO_2 Partial Pressure	<7.6 mm H_g; brief excursions to 15 mm H_g
H_2O Partial Pressure	5 to 16.5 mm H_g
Temperature	70° ±5°F
Minimum Detectible Partial Pressure Change on CO_2	±.38 mm H_g

Crew Safety Limits

PARAMETER	DEVIATION
O_2 Partial Pressure	140 to 200 mm H_g (ONE HOUR LIMIT)
CO_2 Partial Pressure	8 to 15 mm H_g (ONE HOUR LIMIT)

TABLE 3

Performance Goals

Monitored Species:	H_2O, N_2, O_2 and CO_2
Monitored Masses:	m/e 18, m/e 28, m/e 32 and m/e 44
Resolution:	Less than 1% contribution of m/e 17 to m/e 18
	Less than .5% contribution of m/e 28 to m/e 32 and vice versa
	Less than 1% contribution of m/e 40 to m/e 44
Detectible Limit:	0.2 torr on CO_2 and H_2O (10 MV at output)
	0.4 torr on O_2 and N_2 (5 MV at output)
Analyzer Sensitivity:	5×10^{-7} amperes/torr
Time Response:	
Detectors:	τ = 1 second
Sample Inlet Delay:	1.4 seconds
Accuracy:	±1% of the calibrated, nominal partial pressures for N_2 and O_2
	±2% of the calibrated nominal partial pressures for H_2O and CO_2
Sample Gas Loss:	Less than 0.5 pounds for 120 days
Linearity:	Maximum deviation from linear = 3% at 400 torr
Maximum Operating Pressure:	800 torr
Ion Source Pressure:	2×10^{-4} torr for 400 torr external pressure
Differential Pressure Ratio:	100:1
Output:	0 to -5 volts (linear)
Dynamic Range:	0-400 torr on N_2 and O_2
(0 to full scale)	0-20 torr on CO_2 and H_2O

DESIGN OF THE SYSTEM COMPONENTS

The Two Gas Atmoshpere Sensor System is composed of two basic subsystems; the analyzer subsystem and the electronics subsystem. These units are housed in a system package. Each of these subsystems is composed of several elements or modules. The analyzer subsystem elements are the sample inlet system, the ion source, the magnetic sector, and the pumping system. The electronics system modules are the filament power supply and emission regulator, the electrode bias power supply, the detector power supply, and the electrometer amplifier ion current detectors. In the Phase I study it was shown how these components are intimately interelated and that any design which attempts to approach an optimum configuration must consider all of the interfaces. The conceptual design was sufficient to establish the majority of these interface requirements so that in most instances the component designs could be carried out nearly independently. In a few cases the interfaces were modified and this was done as required. In order for a reader to have a thorough understanding of the evaluation and design of this instrument it is necessary to become familiar with the work carried out during the conceptual design phase.

ANALYZER SUBSYSTEM

The analyzer subsystem encompasses those areas of the instrument which are the most critical to the analytical process. These include sample transport and introduction, ionization, and resolution of the sample constuents. When supplied with suitable voltages the subsystem provides current outputs which contain all of the desired information that when amplified is placed in a form which is suitable for use by monitoring apparatus.

The design analysis has been detailed and adequate design margins have been allowed in the essential parameters because of the importance of the analyzer subsystem functions. These margins will not only ensure that the performance goals are obtained but additionally they will allow for flexibility in adapting the instrument to more specific applications through the use of trade offs. The true value of this can only become apparent as this program progresses.

MAGNETIC SECTOR

The function of the magnetic sector is to resolve the ions coming from the ion source according to their mass-to-charge ratios. During the conceptual design phase, the quadrupole and single focusing magnetic types of analyzers were investigated. It was found that the latter type possessed advantages in terms of a lower total effective weight and increased reliability and therefore it was selected for further investigation.

The single focusing magnetic sector analyzer operates on the principal that ions with differing momentums will follow circular trajectories through a normal magnetic field with radii which are proportional to their momentums. In this way ions with differing mass-to-charge ratios are dispersed. If the point from which the ions enter the analyzer (called the object slit) and the points at which the ions are collected are properly chosen with respect to the magnetic field, then the magnetic field will act as an ion optical lens which will focus the divergent beam of ions from the object slit to a small image width at the collector slit. The combined properties of focusing and dispersion allow ions of differing mass-to-charge ratios to be resolved.

In addition to achieving a prescribed resolution, the analyzer must meet the following requirements:

a. When operating with an ion source with known properties it must deliver a specified ion current to the ion current collectors. This property is known as the analyzer sensitivity and is described in terms of ion current per unit pressure.

b. The resolution and sensitivity must be accomplished under conditions of limited magnetic field density, magnet gap spacing and pole face area.

c. The location of the object and collector slits is limited by size constraints placed upon the analyzer.

Each of these requirements is related to the other and it is necessary to consider this interrelation in achieving an optimized design.

The requirements for the analyzer of the Two Gas Atmosphere Sensor System can be briefly stated as follows:

a. To have the following resolution at mass positions given:

m/e 18	$\Delta m/m = 1/18$
m/e 28	$\Delta m/m = 1/10$
m/e 32	$\Delta m/m = 1/10$
m/e 44	$\Delta m/m = 1/10$

In each case the required resolution implies that there will be no cross talk between masses which are separated by the given $\Delta m/m$ values.

b. The analyzer sensitivity must be greater than or equal to 5×10^{-7} amperes/torr.

c. The first two requirements must be achieved with a minimum size and weight.

As part of the conceptual design phase those parameters which affect the above requirements were analyzed. Figure 2 shows a schematic representation of the analyzer showing the important analyzer parameters. The analysis combined

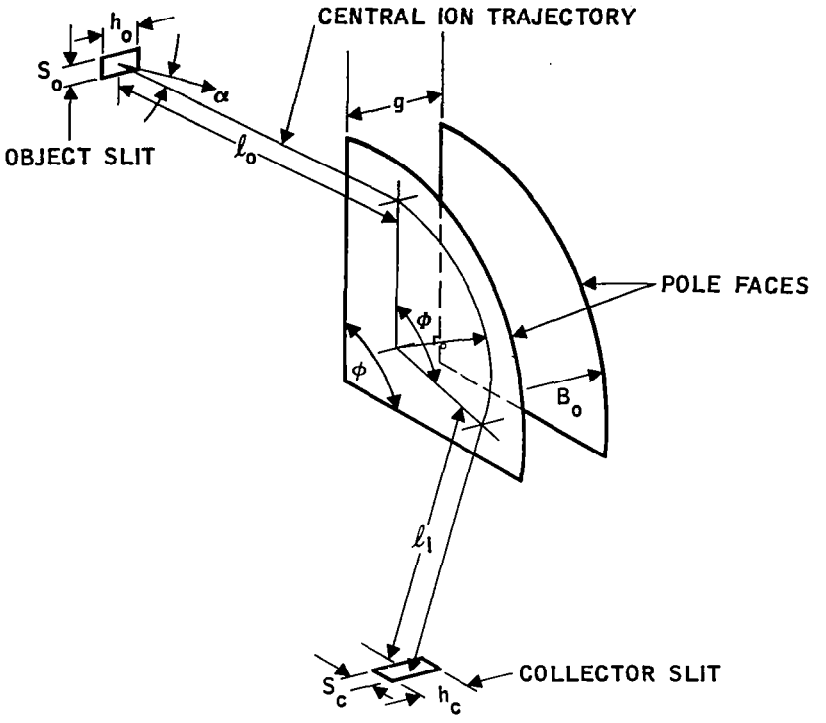

S_o = OBJECT SLIT WIDTH
h_o = OBJECT SLIT HEIGHT
ℓ_o = OBJECT DISTANCE
r_o = RADIUS OF CURVATURE OF ION TRAJECTORY
α = HALF ANGLE OF ION BEAM DIVERGENCE
ℓ_i = IMAGE DISTANCE
ϕ = MAGNETIC SECTOR APEX ANGLE
g = GAP SPACING
B_o = MAGNETIC FIELD FLUX DENSITY
S_c = COLLECTOR SLIT WIDTH
h_c = COLLECTOR SLIT HEIGHT
Φ = ION TRAJECTORY DEFLECTION ANGLE
V_i = ION INJECTION ENERGY

FIGURE 2
Single Focusing Magnetic Sector Parameters

the properties of the ion source and analyzer to achieve an optimized first order design. The results of this analysis are summarized below:

a. A 90° magnetic sector apex angle was shown to be the optimum configuration in terms of analyzer size vs. magnet weight trade off.

b. The use of multiple ion collectors for H_2O, N_2, O_2, and CO_2 was indicated as opposed to scanning with a single collector. This allows the reliazation of a simplified electronics system, and therefore maximum reliability.

c. The optimum analyzer and analyzer-ion source interface and optimum analyzer parameters were established. These are summarized in Table 4.

d. It was demonstrated that second order aberrations in the analyzer focal system were of small consequence in determining analyzer performance.

e. Ion beam widths at the collector slits were computed and compared with required values. They were shown to exceed the requirements in all cases.

TABLE 4

Optimum Analyzer Parameters
as Established in Phase I

S_o = 0.0307 cm
h_o = 0.0614 cm
ℓ_o = 2.86 cm
α = 0.4°
ϕ = 90°
g = 0.160 inch
B_o = 4000 gauss
V_I = 225 volts

Beginning with the information summarized above and in Table 4, the remaining task was to carry out the detailed analyzer design. The steps involved in this process are discussed in detail in the remainder of this section.

During the Phase I analysis it became apparent that it would not be necessary to have all of the ion current collectors at their optimum and focus positions because lower resolution may be accepted at the masses above m/e 18. This allows the collectors to be moved in toward the analyzer magnet, reducing the overall size of the instrument. While partial advantage was taken of this during the conceptual design phase, it was not exploited during the analysis of the 60° sector instrument nor was it fully utilized in the 90° sector case. Since the primary objection against the 60° sector instrument was its greater overall length, it seemed worthwhile to investigate the possibility of a shortened 60° sector instrument. The analysis is given in Appendix A Project Note #20.

The results are shown in Figures 3 and 4 where it is seen that the overall lengths for the 60° and 90° sector instruments are 8.89 and 13.32 cm respectively. This difference of length is significant in terms of overall package lengths, structural requirements, analyzer weight, and alignment. Therefore, it was decided to maintain the 90° configuration as determined in the conceptual design phase. With this established, the exact analyzer configuration was determined.

Fringe Field Effects and Focal Point Calculations

In order to carry out the detailed design it was necessary to take into account the effects of the fringe field of the magnet. This effect was not included in the Phase I analysis due to the added complexity and the fact that the effect of the fringe field is to shift the image points rather than having any great effect upon the aberrations. The primary effect of the fringe field is two fold. First, it bends the incoming ion beam before it reaches the actual magnet boundary. Second, it shifts the location of the effective magnet boundary so that it does not coincide with the actual magnet boundary. The result of the first alteration is to cause the incoming ion trajectories to cross the effective magnet boundary at a non-normal angle. This affects the focal properties of the magnetic field because trajectories with positive beam divergence angles ($+\alpha$) spend a different amount of time in the magnetic field than do those with negative beam divergence angles ($-\alpha$). In addition, the prebending of the trajectories rotates the positions of the collector slits. The effect of the second alteration is to reduce the value of the object length ℓ_o, which will require a new value of image lengths for a zero first order aberration. It should also be noted that similar effects occur at the exit boundary. In order to take these effects into account in the design it was necessary to have a suitable description of them in mathematical terms. This description involves the relation of the image space parameters, image length, exit angle, and image size, to the object space parameters of object length, beam divergence, entry angle, and object size.

The Johnson-Nier[1] equations which were used during the conceptual design phase are restricted in that they can only be applied to situations with normal entry and exit. These equations were developed primarily to show that a zero second order α aberration is obtainable. Since for this application it was shown that the second order α aberration was of little consequence, it is therefore possible to utilize a system of equations which yield only first order aberrations but which are generalized for the case of non-normal entry. Such a system of equations was developed by Von Richard Herzog[2]. These equations were carefully reviewed and a translated deviation is found in Appendix A Project Note #6.

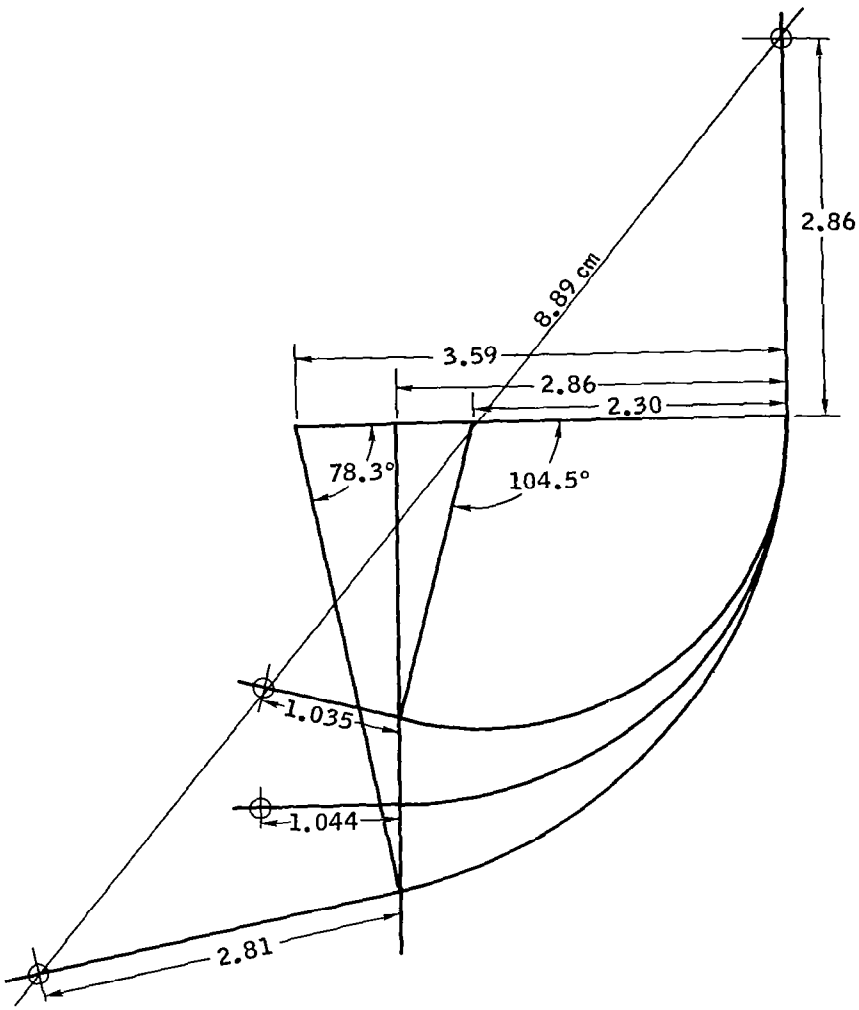

FIGURE 3
90° Magnetic Sector with Reduced Image Distances

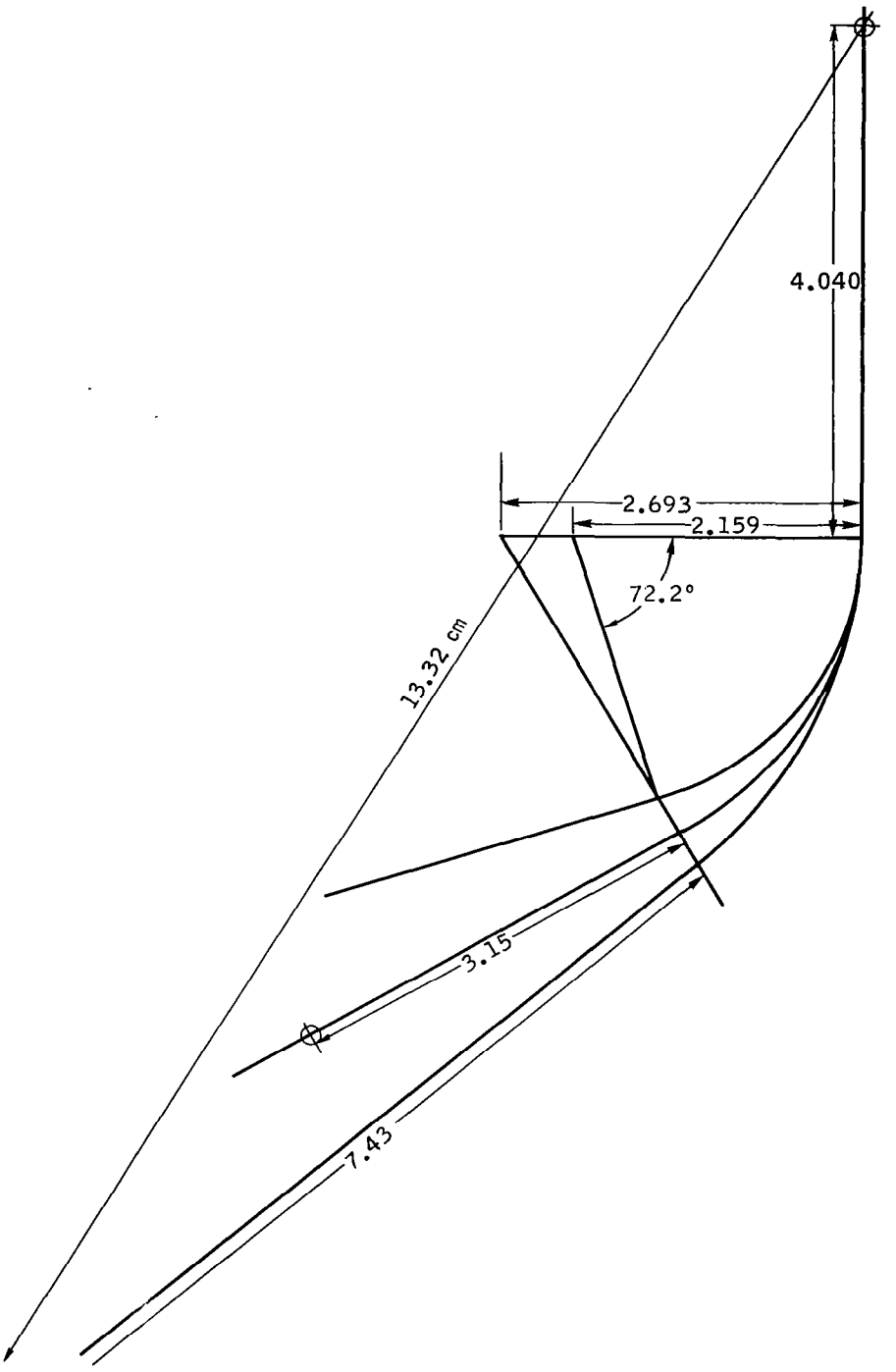

FIGURE 4
60° Magnetic Sector with Reduced Image Distances

The results of this derivation are an expression for the relationship between the object and image distances and an expression for the image width. The first equation is:

$$(l_o - g')\ (l_i - g'') = f^2 \qquad (1)$$

where

$$g' = \frac{r_o \cos \epsilon' \cos (\Phi - \epsilon'')}{\sin(\Phi - \epsilon' - \epsilon'')}$$

$$g'' = \frac{r_o \cos \epsilon'' \cos (\Phi - \epsilon')}{\sin (\Phi - \epsilon' - \epsilon'')}$$

$$f = \frac{r_o \cos \epsilon' \cos \epsilon''}{\sin (\Phi - \epsilon' - \epsilon'')}$$

The meanings of the parameters are given in Figure 5. In the figure it should be noted that all primed symbols are object space parameters while double primed symbols are image space parameters. If equation (1) is satisfied, then the image formed a distance ℓ_i from the exit magnet boundary will be free of first order α aberration and will therefore have a minimum width. The image width is found from the expression:

$$b'' = b' \left(\frac{g'' - \ell_i}{f}\right) + \delta \left\{ r_o\ (1 - \cos\Phi) + \ell_i\ [\sin\Phi + \tan \epsilon''\ (1 - \cos\Phi)] \right\} \qquad (2)$$

where

b' = distance of the aberrant trajectory from the optical axis at the object slit plane

b'' = distance of the aberrant trajectory from the optical axis in the image plane

$\delta = \beta + \gamma$

and $\gamma = \frac{\Delta m}{m}$ = mass differential between the ion taking the aberrant trajectory to the mass of the ion following the central trajectory.

$\beta = \frac{\Delta V}{V}$ = velocity differential between the ion taking the aberrant trajectory to the velocity of the ion following the central trajectory.

Care must be taken in computing an image width from equation (2) to insure that both positive and negative values of b' and β are included. It should be noted in equation (2) that b'' is independent of α and that it is equally dependent upon β and γ as would be predicted by the principal of operation.

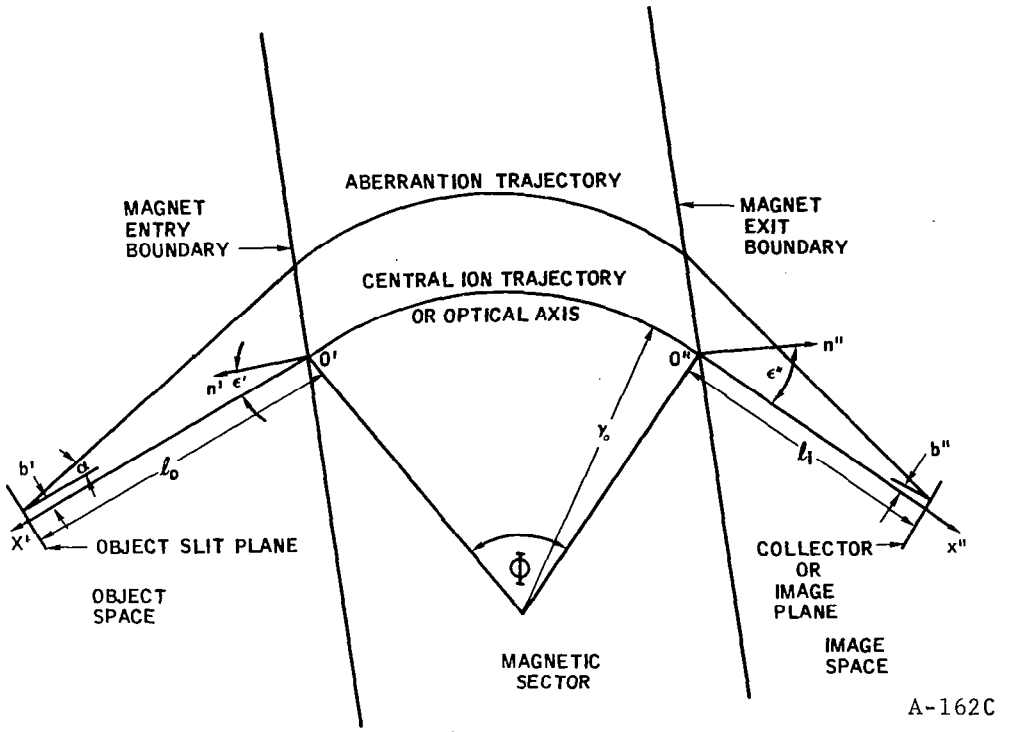

FIGURE 5
Relation Between Object and Image Distances

While the Herzog equations apply to the case of non-normal entry they do assume that the object and image spaces are magnetic field free and the magnetic sector has a constant flux density. Therefore, it was necessary to have a technique for describing the ion motion in the fringe fields and interfacing this information with Herzog equations. Several workers, including Bainbridge, Nier, and Coggeshall, have developed techniques which they claim satisfy these conditions. Their methods have been reviewed by Kerwin[3] and are found to be lacking. Kerwin has a recipe of his own which is somewhat more comprehensive and more consistent than the others and which agrees well with experimental results obtained by Barnard. Analysis of these methods showed that they were all somewhat lacking but that Kerwin's method did in fact appear to be superior. The method which was used is described in the following paragraphs.

Coggeshall has derived expressions for trajectory motions in a magnetic fringe field. This deviation appears in Appendix A Project Note #13. The pertinent results are repeated below:

$$\frac{dx}{dy} = \frac{\int h(y)dy}{\left(r_o^2 - \left[\int h(y)dy\right]^2\right)^{\frac{1}{2}}} \qquad (3)$$

and

$$x = \int_{o}^{y} \frac{\int h(y)dy}{\left(r_o^2 - \left[\int h(y)dy\right]^2\right)^{\frac{1}{2}}} \, dy \qquad (4)$$

The coordinates are described in Figure 6. The integrations are carried out from the object slit plane to a distance 1 gap width inside of the pole face boundary. This point is chosen since from this point on into the magnet, the density may be assumed to be uniform.

The effect of the fringe field was taken into account in two ways. First a theoretical magnet boundary was established which lies outside of the real magnet boundary and which was chosen in order to give the same degree of bending as the fringe does. A full strength magnetic field B_o was assumed to exist uniformally within the effective magnet boundaries. It was assumed that equal degrees of bending would correspond to similar focusing actions for neighboring trajectories and hence Herzog's equations may be applied from the effective boundaries. The expression for the distance between the real magnet boundard and the effective magnet boundary is derived in Project Note #21 of Appendix A and is stated as:

$$d = \int_{y_o}^{y_1} h(y)dy \; - 1 \qquad (5)$$

where d is in gap widths and:

y_1 = 1 gap width inside the real boundary

y_o = object slit plane

The use of the effective boundary alone does not assure an accurate design. The action of the fringe field over the full distance between the object slit and the magnet boundary causes a significant displacement which must be accounted for by the application of equation (4). The integration should be carried out between the object slit and the effective magnet boundary. While the proper choice of the upper limit on the integration was difficult to establish, it is believed that this choice is reasonable. These calculations must be made for m/e 18, m/e 28, m/e 32, and m/e 44.

Another point which must be considered is that the Herzog equations are dependent upon the entry angle ϵ'. Due to the prebending of the trajectories in the fringe field, non-zero values of ϵ' will exist. The question to be answered is, what degree of prebending should be cranked into the Herzog equations. It may be assumed at first glance that ϵ' should be computed at the effective boundary. Kerwin, however, chose to apply a value of ϵ' obtained by computation

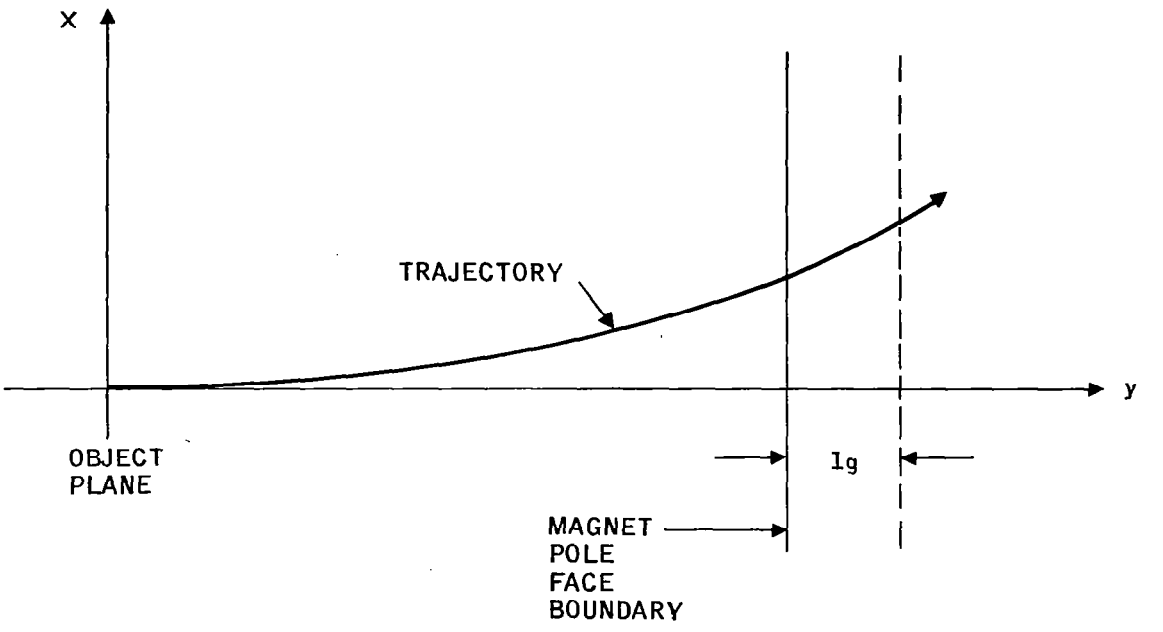

FIGURE 6
Trajectory Motions

with equation (3) all the way to the real magnet boundary. The resultant value was, however, applied at the effective magnet boundary. In this way, a larger deflection angle, ϵ', will be utilized. The justification for this is somewhat difficult, but it is supported by the fact that the results obtained in this way agree well with experimental data.

The difficulties encountered in the application of this scheme arise because it is being attempted to spacially separate deflection and focusing effects which occur simultaneously. Because of dissatisfaction with the methods which have been used in the past, some effort was expended to find a more exact technique. Initially the results were negative and therefore the method which is being described was utilized in the design. Somewhat later, a much improved method was developed and is given in Appendix A Project Note #14. This technique will be utilized during the analyzer test phase to verify the proper magnet and collector bucket locations.

In order to compute the effective boundary, the entry ϵ' and the displacement due to the fringe field, it was necessary to have fringe field data. Typically, data for a theoretical magnet with an infinite y dimension is used. This was not believed to be sufficiently accurate and, therefore, magnetic field data was taken on a magnet with a circular pole face and approximately the correct area to gap ratio. The results are plotted in Figure 7.

There was another effect of the fringe field which must be accounted for in the design. This is the effect known as z axis focusing. This arises due to the interaction of y component of the fringe field and the x component of the ion velocity. This is demonstrated in Figure 8. The analysis of this effect was carried out during the conceptual design phase. This analysis appears in Appendix H of the Phase I Final Report. The result is that the bending angle in the y-z plane is given by:

$$a'_z = \frac{z \tan \epsilon'}{r_o} \qquad (6)$$

where

z = the height of the trajectory above the central plane.

The significant thing to note at this point is that the deflection angle is inversely proportional to r_o. In the case at hand the most severe bending would occur for m/e 18. In order to minimize the z focusing effects of the fringe field, it was logical to tilt the entry magnet face at such an angle that the central ray for m/e 18 crosses the real magnet boundary at zero degrees to the normal vector. When this is done the most severe z focusing effect occurs on m/e 28 where ϵ' is equation (6) is the difference in the prebending angle between m/e 18 and m/e 28. The z axis focusing will be treated further at a later point in the discussion.

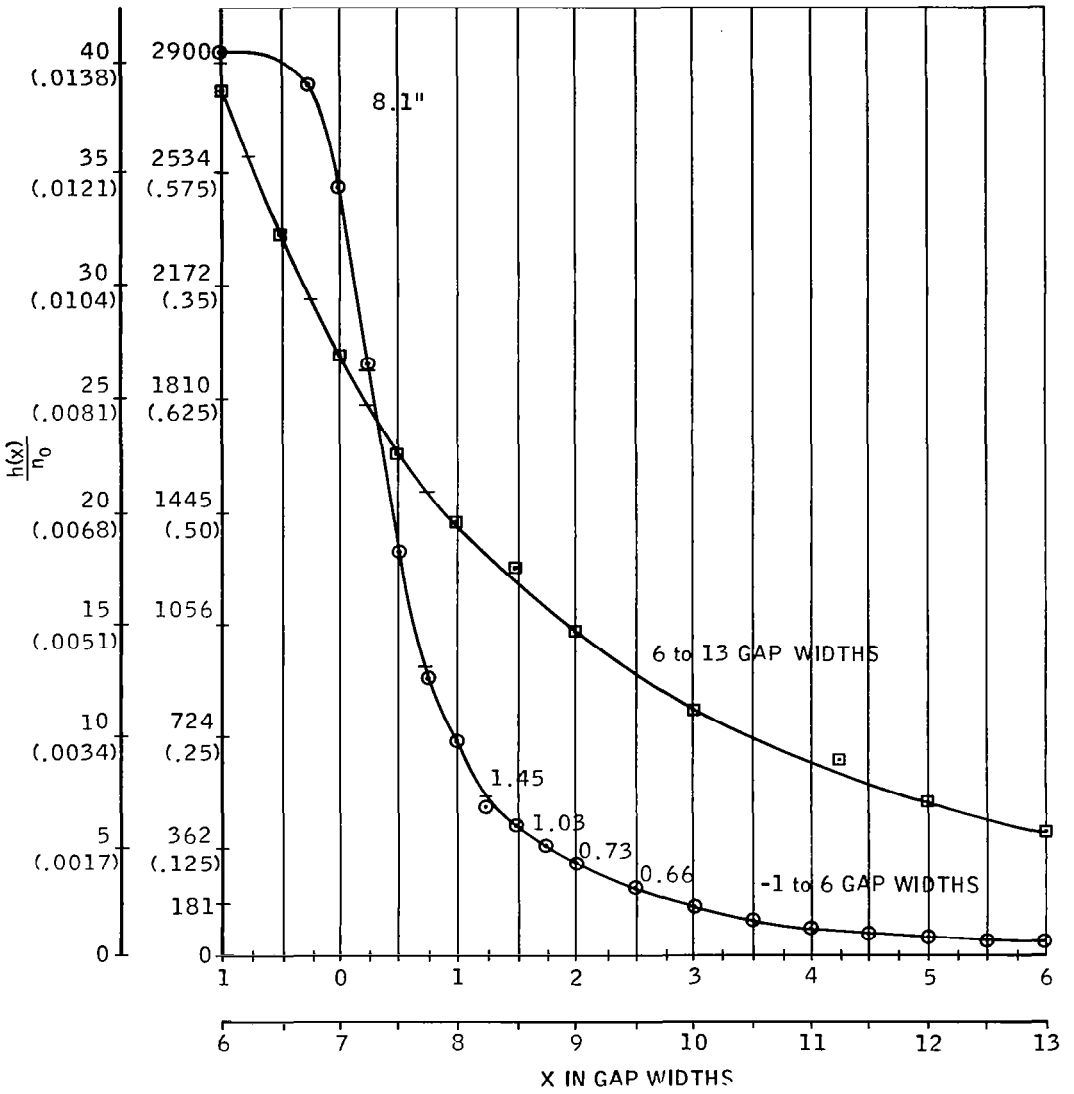

FIGURE 7
Fringe Fields of a Magnet Having Circular Pole Faces

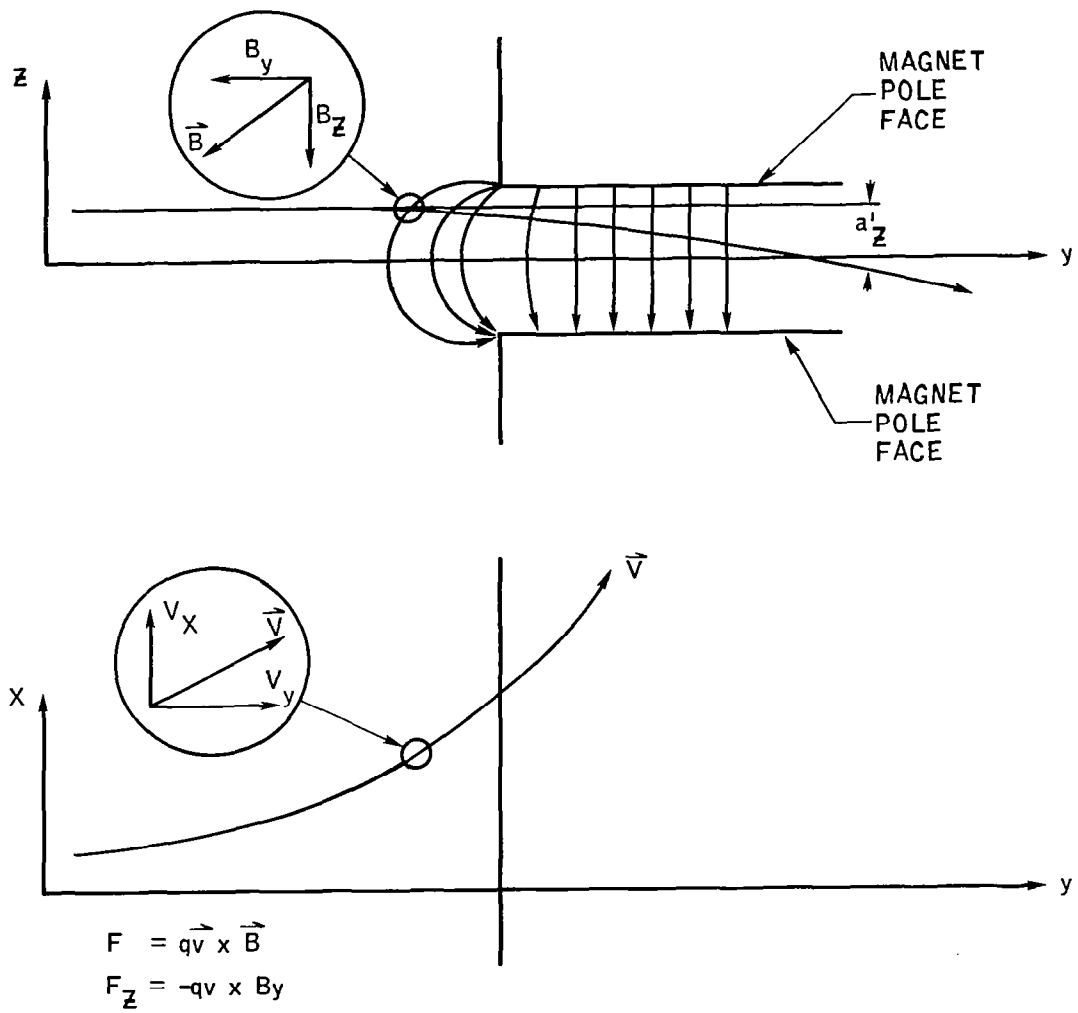

FIGURE 8
Z - Axis Foscusing

Having established that the magnet should be tilted as described above, it remains to describe the pole face geometry. As previously discussed, a 90° magnet apex angle represents an optimum choice for this application. Planar entry and exit boundaries were also selected rather than circular ones as done in some designs. The function of a circular pole face boundary is to allow for elimination of the second order α aberration. It was shown in the conceptual design phase that the contribution of this aberration to the ion beam width was very small and not necessary to include a second order correction in the design. The need for a second order correction is largely dependent upon the magnitude of the angles which come from the ion source. It is conceivable that the ion source sensitivity could be increased by allowing large α angles and then correct for this by a zero second order α design. However, in this application, the ion source configuration which was required prevented this because it was necessary to have symmetrical focusing about the ion source axis. This would imply large angles in the y - z plane which could not be tolerated by the analyzer.

At this point the entry conditions for the magnetic sector have been established. The travel of the ions through the pole face region itself must now be established. As stated earlier, the sector is to be a 90° type. In the initial design, optimization of a single mass was used which had a deflection angle equal to the magnet apex angle. In order to conform as closely as possible to this optimized configuration for a multiple collector design, it was decided to select one of the central masses for the 90° deflection. Mass 28 was selected since it is approximately the geometric mean between m/e 18 and m/e 44. The origin from which the magnet apex angle was swung was placed along the effective entrance boundary and a distance $r_o|_{m/e\ 28}$ from the point at which the m/e 28 ray crosses this boundary. The exit boundary for the magnet was established by swinging through 90° about this origin and defining this boundary as the m/e 28 theoretical exit boundary. The position of the theoretical exit boundary is mass dependent because it is a function of the integration of the leakage field from one gap width inside the real boundary to the image point where the ions are collected. Since the image distance varies with mass, the effective exit boundary will also vary. An iterative procedure is then required in the design.

With the magnet configuration established it was now possible to compute the angular relationships for each of the trajectories of interest. These supplied the necessary numbers for substitution into Herzog's equations from which the image lengths and beam widths were evolved. The detailed derivation of these relationships is given in Appendix A, Project Note #6. The significant relationships are given in Figure 9 and important relating equations are:

$$\Phi = \sin^{-1}\left(\frac{y_o}{r_o}\sin\phi - \frac{x_o}{r_o}\cos\phi\right) - \phi + \epsilon' \qquad (7)$$

and

$$\epsilon'' = \Phi - \phi - \epsilon' \qquad (8)$$

where r_o is for the mass of interest and x_o and y_o are defined in Figure 9.

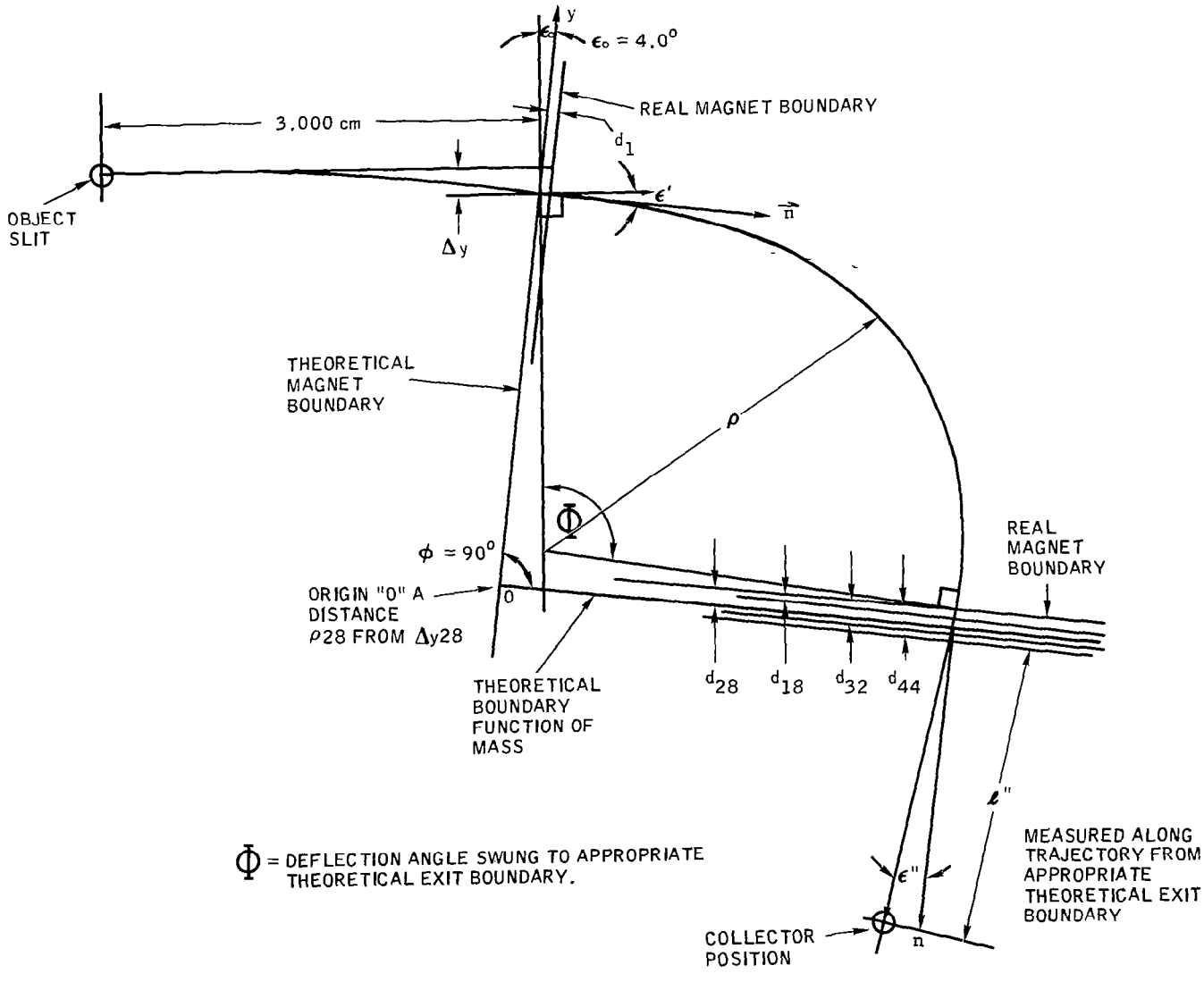

FIGURE 9

Analyzer Relations for Computation of Focal Points

The value of the exit angle ϵ'' which results from these calculations does not include the effects of post bending in the fringe field. Again an iterative procedure was used to arrive at exact values of ϵ''. Using initial values of ϵ'' from equations (7) and (8), the image lengths were computed from equation (1). Then using collector positions established by these lengths, equation (3) was applied to determine the amount of post bending in the fringe field. The effective exit boundary was then computed from equation (5). These two results were applied to equations (7), (8), and (1) to find new image distances. The iteration was then repeated in this way until convergence is obtained. The results of the entire operation are summarized in Table 5.

Beam Width Calculations

Having derived the image distances, the next step was to find the beam width at the image points. This was done with the aid of equation (2). In addition to the object magnification and the energy aberration, it was also believed that the image curvature aberration was important. During the conceptual design phase, an approximate expression was used for this aberration. It was felt that a more exact expression should be sought. Therefore, the original work by Berry[4] was studied. It is sufficient to state here the results of Berry's derivation:

$$\left[\delta^2 x\right]_{y_i} = M\left\{\frac{z_1^2}{2r_o} - z_1\beta\left[\frac{dx}{dy}\right]_{y_1} + \beta^2\,[x]_{y_1}\right\} - \left\{\frac{z_2^2}{2r_o} - z_2\beta\left[\frac{dx}{dy}\right]_{y_1} + \beta^2\,[x]_{y_1}\right\} \tag{9}$$

TABLE 5

Analyzer Parameters

	m/e 18	m/e 28	m/e 32	m/e 44
ℓ_o	3.000 cm	3.000 cm	3.000 cm	3.000 cm
y	0.063 cm	0.051 cm	0.047 cm	0.040 cm
ϵ'	0.0°	0.8°	1.0°	1.4°
r_o	2.291 cm	2.857 cm	3.055 cm	3.582 cm
d_{en}	0.435 cm	0.435 cm	0.435 cm	0.435 cm
d_{ex}	0.395 cm	0.434 cm	0.439 cm	0.448 cm
Φ	103.0°	90.8°	87.5°	80.2°
ϵ''	16.6°	3.5°	-0.1°	-8.2°
ℓ_i	1.220 cm	2.823 cm	3.435 cm	5.505 cm
y_o	0.516 cm	0.000 cm	-0.189	-0.700 cm

where

M = object magnification

z_1 = height of the aberrant ray above the central plane at a point one gap width inside the entrance boundary of the magnet

z_2 = height of the aberrant ray above the central plane when it is one gap width inside the exit boundary of the magnet

β = initial angle of the trajectory with respect to the central plane

$\left[\frac{dx}{dy}\right]_{y_1}$ = angular bending in central plane due to fringe field (equation 3)

$[x]_{y_1}$ = displacement in central plane due to fringe field (equation 4)

In the evaluation of equation (9), it should be noted that the magnification was negative and therefore the two terms in brackets were additive. It was decided to use a worst case value for the expression. This is given by:

$$\delta^2 x\Big|_{max} = -|M| \left\{ \frac{z_1^2}{2r_o} + \beta^2 [x]_{y_1} \right\} - \left\{ \frac{z_2^2}{2r_o} + \beta^2 [x]_{y_1} \right\} \tag{10}$$

The following worst case values were assumed for z_1, z_2, and β:

z_1 = 0.100 cm

z_2 = 0.125 cm

β = 2°

The correctness of the assumptions will be reviewed later. The evaluation of (10) led to values for $\delta^2 x|_{max}$ ranging from 0.004 cm for m/e 44 to 0.005 cm for m/e 18. These are somewhat smaller than the values which were obtained from the approximate expression during Phase I. A value of 0.005 cm was used in all cases. Having the expression for the image curvature aberration, it was then possible to compute the total image width. The expression for image width was obtained from equation (2) with the image curvature aberration added to it:

$$BW = S_o \left| \frac{g'' - \ell_i}{f} \right| + \frac{1}{2} \frac{\Delta V}{V_I} \left\{ r_o (1 - \cos\Phi) + \ell_i \left[\sin\Phi + \tan\epsilon'' (1 - \cos\Phi) \right] \right\} + [\delta x]_{max} \tag{11}$$

where $\Delta V/V_I$ is the total ion energy spread divided by the ion injection energy. Again with the use of equation (2), an expression was developed for the required beam width[5].

$$BW_R = r_o K \left(\frac{1}{2} \frac{\Delta m}{m} - \Psi\right) - 2\Delta Y \qquad (12)$$

where

$$K = (1 - \cos\Phi) + \frac{\ell_i}{r_o} \left[\sin\Phi + \tan\epsilon'' \ (1 - \cos\Phi)\right]$$

and

$\frac{\Delta m}{m}$ = resolution required

ΔY = collector misalignment = 0.005 cm

Ψ = variation accelerating potential = 0.0075

The results of the evaluation of these equations are shown in Table 6. The assumed energy aberration, $\Delta V/V_I$, was 3/225 which is the optimum value as obtained in Phase I. The tabulated results show that in all cases the actual beam widths are significantly less than the required values. Several comments are in order. First, the 0.010 cm allowed for "other" aberrations includes such things as all second order aberrations and aberrations due to misalignments. A detailed analysis of these was carried out in Phase I and they were found to be less than 0.010 in all cases. Second, the margin between actual and required beam widths has increased over the values obtained in the conceptual design phase. This is due to an increase in the dispersion of the magnetic sector caused by the fringe field, and the reduced image curvature aberration.

TABLE 6

Beam Width Data at Optimum Focal Points

	m/e 18	m/e 28	m/e 32	m/e 44
$M S_o$	0.024 cm	0.031 cm	0.033 cm	0.042 cm
$\frac{1}{2} \frac{\Delta V}{V} K_2 r_o$	0.030 cm	0.039 cm	0.042 cm	0.052 cm
$[\delta x]$	0.005 cm	0.005 cm	0.005 cm	0.005 cm
Other	0.010 cm	0.010 cm	0.010 cm	0.010 cm
BW	0.069 cm	0.085 cm	0.090 cm	0.109 cm
$\Delta m/m$	1/18	1/10	1/10	1/12
BW_R	0.090 cm	0.241 cm	0.260 cm	0.253 cm

Insofar as m/e 18 is concerned the increased margin led to greater stability margin and increased assurance of obtaining the required resolution. For the other masses, the margins are much greater than necessary and therefore the collectors can be moved in from the optimum focal points as described earlier.

Non-Optimum Focal Point Computations

In order to determine the amount that the collectors can be moved in the dependence of beam width on the distance from the exit edge of the magnet. This can be done by the use of the Herzog equations. An approximate technique was utilized in that the beam width at $\ell'' = 0$ (at the effective exit boundary) was computed and a linear variation of beam width versus position was assumed. This is nearly true. From Appendix A, Project Note #6 the following equation is found for beam width at the exit face:

$$Y'' = -r_o \alpha \sin\Phi + y_1 \frac{\cos(\Phi - \epsilon')}{\cos \epsilon'} + \delta r_o (1 - \cos\Phi) \qquad (13)$$

where Y'' is the variation from the central ray at the exit boundary. The beam width at the exit boundary is:

$$BW = S_o \left| \frac{\cos(\Phi - \epsilon')}{\cos \epsilon'} \right| + 2r_o \alpha \sin\Phi + \tfrac{1}{2} \frac{\Delta V}{V_I} r_o \{1 - \cos\Phi\} + A \qquad (14)$$

where A is the sum of the other aberrations. Furthermore, the required beam width changes with position in the image space. At the exit boundary the required beam width is:

$$BW_R = r_o (1 - \cos\Phi) (\tfrac{1}{2} \frac{\Delta m}{m} - \Psi) - 2\Delta Y \qquad (15)$$

The results of these equations are plotted on the left hand ordinate in Figure 10 and the data from Table 6 is tabulated on the righthand ordinate. In each case, the value of the "other" aberrations, A, was placed at a constant value of 0.020 cm. The mass of immediate interest is m/e 44 since its collector establishes one extremity of the magnetic sector dimensions. It is seen from Figure 10 that the collector can be moved in to 60% of its present distance and still have sufficient resolution. Allowing a little safety margin because of the linear approximation involved in this analysis it was decided to move in the m/e 44 collector position 1.5 cm from its zero α aberration point. This point is shown in Figure 10.

With the positions of the m/e 18 and m/e 44 collectors established, there is nothing to be gained by moving the m/e 28 and m/e 32 collectors in past the line joining the extreme collectors since all of the collectors will be mounted on a single, planar collector flange. It was then found that the resolution for m/e 28 and 32 is more than adequate. This is desirable since a high degree of accuracy is required on these peaks and requires that there be little or no cross talk.

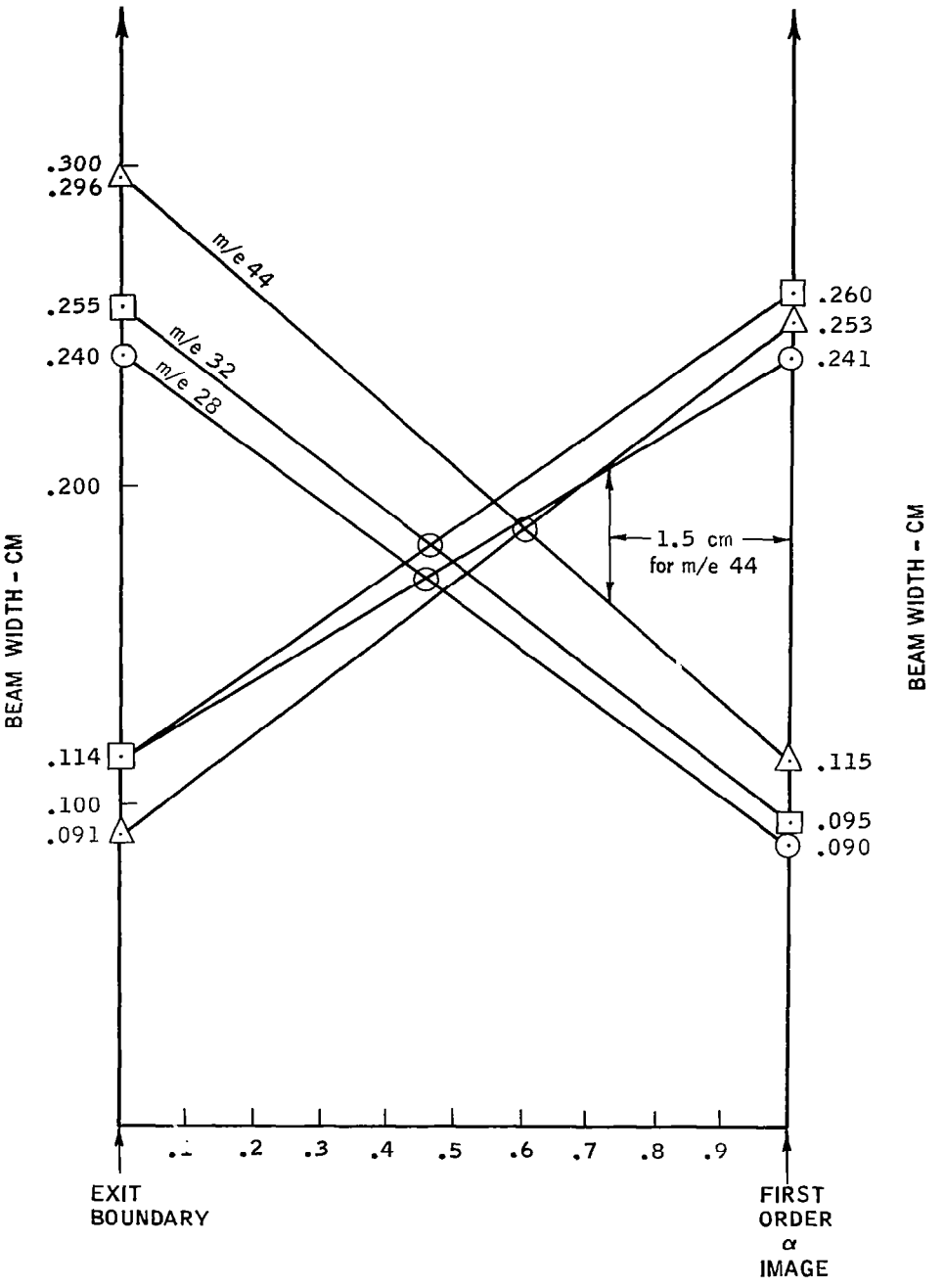

FIGURE 10
Beam Widths Vs Collector Position

The final configuration of the magnetic sector is shown in Figure 11.

The next step was to determine the collector slit widths. As indicated in the conceptional design phase this dimension should be equal to the dispersion. Consequently:

$$S_c = 1/2\ r_o \dot{K} \frac{m}{m} \tag{16}$$

where $\dot{K}$ is the same as in equation 12. The results of this calculation are presented in Table 7 along with the computed beam widths and collector distances, ℓ''.

The calculated beam width for m/e 18 is the same as determined previously since its position has not been changed. For the other beam widths the contributions due to the object magnification and energy aberration are determined from Herzog's equations with an α aberration included and 0.020 cm allowed for all other aberrations. Adequate safety margins are evident in all cases.

It must be realized that the calculations which have been carried out make certain assumptions about the configuration of the magnetic fringe field which may not in fact be valid. Perhaps one of the more significant of these is the assumption that there is no variation in the magnetic field in the direction parallel to the entrance and exit boundaries. In fact as one moves away from the boundaries the field will start to curve and variations will be experienced in these parallel directions. This effect is most significant on the m/e 18 and m/e 44 trajectories as they move away from the exit boundary of the magnet. In order to get an idea of the effects which this may cause the following analysis was performed. It was assumed that the field curvature was so severe that for m/e 18 and m/e 44 the exit angles ϵ'' were reduced to zero. (This of course is an over correction.) Then new values for ℓ_i were computed. They were found to be shorter by 0.241 cm for m/e 18 and 0.555 cm for m/e 44.

TABLE 7
Beam Widths, Required Beam, and Collector Widths at Reduced Image Distances

m/e	BW	BW_r	S_c*	ℓ''
18	0.069	0.090 cm	0.123 cm	1.220 cm = ℓ_i
28	0.114	0.214	0.263	2.225 cm
32	0.140	0.227	0.278	2.650 cm
44	0.158	0.209	0.268	4.005 cm

*Measured perpendicular to the beams.

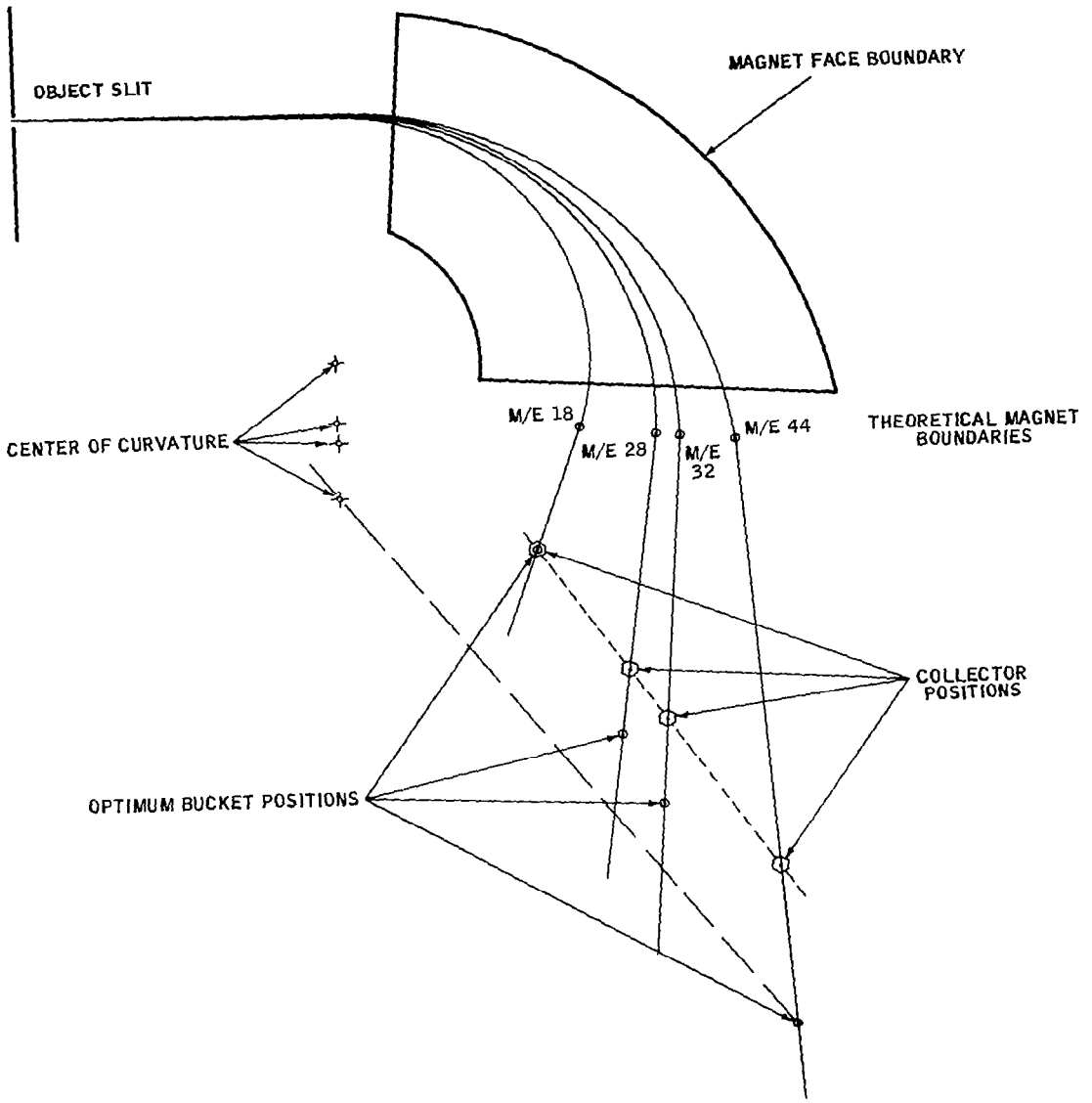

FIGURE 11
Magnet Focusing With Fringe Field Effect

These variations will be attenuated in the actual case, but it does indicate two things:

a. The safety margins which exist in the design may be necessary to obtain the required performance.

b. It would be desireable to have adjustable collector buckets so that the optimum focal points may be found.

With respect to point b, there are several good reasons to have moveable collector buckets. This would allow for compensation of the following effects:

a. Inaccuracies in the analysis

b. Variations in the magnetic field from the assumed configuration

c. Tolerance build up in the assembly

d. Errors in the fabrication of the analyzer.

The necessity for adjustable collectors is supported by the work of Lilly, Weismann, and Lowitz[6] which showed that the focal properties of a real system were significantly different than those of the theoretical system which supposedly models it.

Z-Axix Focusing

In order to insure that the output of the mass spectrometer will be nearly constant over some range of accelerating voltage it is necessary to design the instrument so that 100% of the ions leaving the ion source are collected by the appropriate m/e collectors. A design effort is therefore required in the y-z plane.

The y-z plane focusing is closely related to the ion source properties just as in the case of central plane focusing and some knowledge of the ion source properties is required. During the conceptual design phase it became apparent that a problem had developed regarding the requirement for low ion exit angles from the ion source. This came about due to the attempt to minimize the magnet gap spacing. During the computer optimization it was found that an α of 0.29° was necessary. By further analysis, an increase in the gap dimensions and going to an object imaging ion source it was found that a 0.4° angle could be tolerated. This solution was proposed at the conclusion of the conceptual design phase.

Further reflection during this phase of the work led to the realization that such small angles would be extremely difficult to obtain. The design of an object imaging ion source would require the use of an automatic trajectory plotter and many hours of trajectory plotting. Even with the aid of this equipment it was

possible that extreme difficulties could be encountered in achieving an operational design in a small ion source. Therefore, it was decided to seek an alternate solution.

On a previous instrument a z-axis focusing system was employed with success to contain the ions in tye y-z plane. It consisted of a set of three electrodes placed between the ion source and the magnetic sector. A schematic representation is shown in Figure 12. The electrodes form a two dimensional einzel lens which focus the ambient rays back toward the axis. There are three phases in the design of a z-axis focus system. First, the position of the lens and the required focal length must be determined including the z-axis focusing effects of the magnet. Second, the electrodes forming the lens system must be designed and the operating voltage determined. Finally, the effect of the z-axis focusing on the ion trajectories in the x-y plane must be ascertained.

In the Phase I optimization process a magnet gap width, g, of 0.400 cm was established. The analysis of the z-axis focusing problem demonstrated that a safer value would be 0.500 cm. It was further assumed that the envelope wall thickness, including depression due to external atmospheric pressure acting on the evacuated housing would be 0.100 cm. Finally, a safety margin of 0.050 cm was allowed at each inner wall surface. Then a trajectory length for an m/e 44 ion was laid out in a linear manner and the critical points along the paths were established. The envelope cross section was maintained at 0.500 cm for a distance of one cm past the exit magnet boundary at which point it was allowed to increase rapidly to a sufficient dimension so that the z restriction was no longer of importance. These factors are shown schematically in Figure 12.

The first part of the analysis was handled using a construction technique which is also shown in Figure 12. The position of the lens plane is established by making use of the fact that a trajectory which passes through the center of a thin lens will not be deflected. Since some ions must travel through the center of the lens the angle which they make with the axis must be reduced to an acceptable level by moving the lens plane away from the object slit. This procedure cannot be followed to extreme because diverging rays will travel too far from the axis before they are refocused thus causing them to be unacceptable. The maximum angle which an ion can have while passing through the center of the lens plane is also dependent upon the object slit height. It was found that in order to obtain an acceptable configuration that the height had to be reduced from 0.0614 cm as determined during Phase I to 0.050 cm. The position of the lens plane was determined to be 1.60 cm.

With the lens plane located the required focal length was next determined by constructing the paths of several trajectories through the lens system under different assumptions of initial angle, initial position and lens focal power. It was found that all combinations of angles up to 3° and initial positions from $-1/2\ h_o$ to $+1/2\ h_o$ could be accepted by a system with a focal length of 1.33 cm. This is shown in Figure 12.

The analysis thus far does not include the effects of z focusing of the magnet field. Using equation (6), which was given earlier, the bending angles are found at the entrance and exit faces of the magnet. Using ϵ'' and r_o values

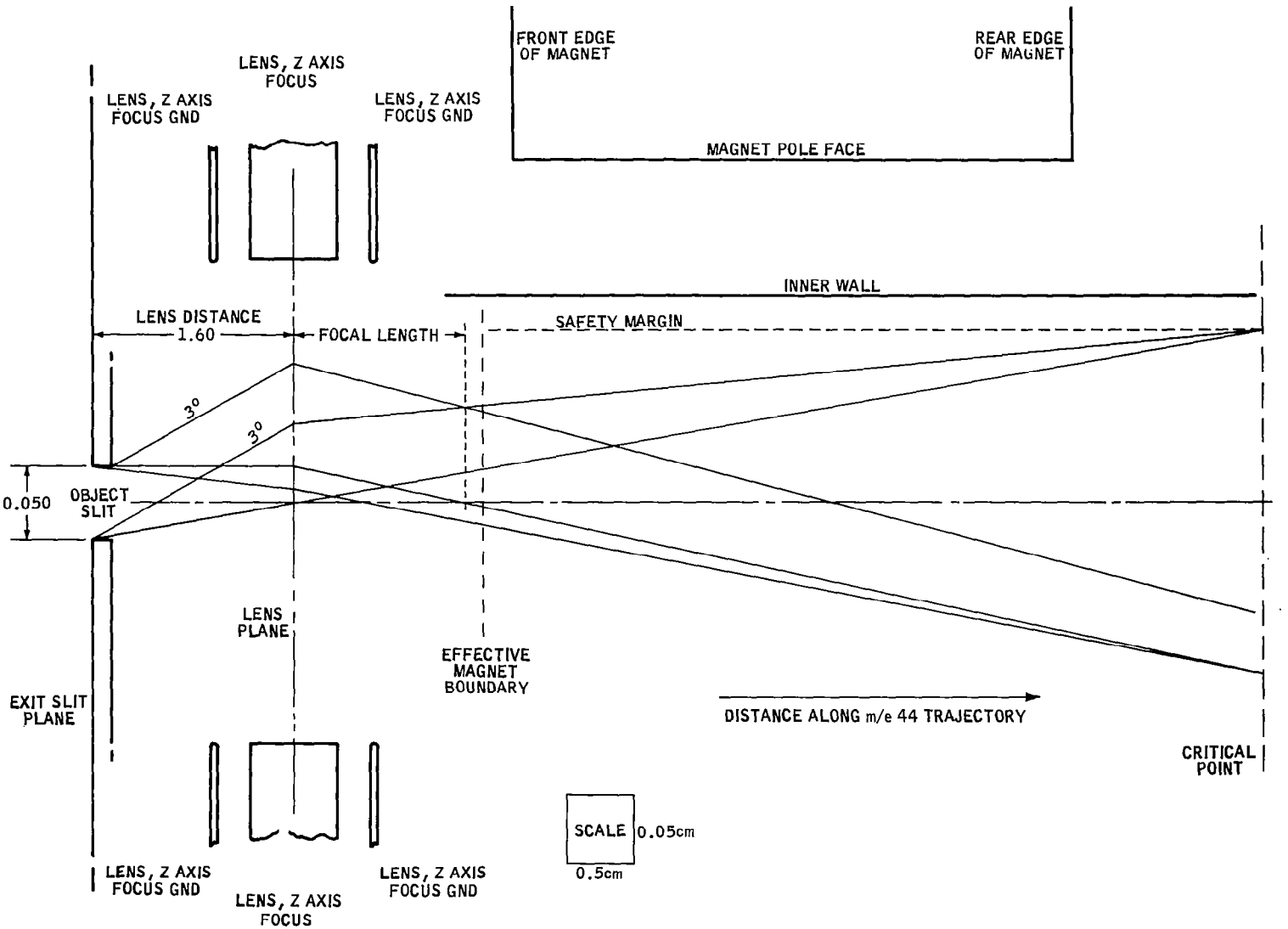

FIGURE 12
Z - Axis Design Schematic With Trajectory Construction

from Table 5 and z values from Figure 12 the angular deflection is calculated. In all uses the deflection at the entrance face is negligible. At the exit face the largest deflection is for m/e 18 and is 0.9° in the focusing direction. For m/e 28 and 32 the effects will be negligible. For m/e 44 the angle is 0.5° in the defocusing direction. This is acceptable.

The second step in the procedure is to design a lens system with the required focal length. Information was not available on a two dimensional Einzel lens and so it had to be generated. This was done with the aid of two computer programs. First, a proposed electrode design is established. The boundary shapes are punched on data cards and the cards areput into a computer program which solves LaPlace's equation by a relaxation technique. Figure 13 shows the output of the computer for the final electrode configuration with the axis at the far right. It was necessary to make several adjustments of the electrode thickness, spacing, potential and distance from the axis before a short enough focal length was obtained. The focal lengths were derived with the use of a trajectory plotting program. Appropriate initial conditions were given to several ion trajectories and their paths were computed. The result from these computations were graphed to determine the variation of focal length with lens spacing from the axis and changes in focal length with the initial positions of the trajectories. Based upon this information the final configuration was chosen.

The final step of the design was to verify that effects in the x-y plane are negligible. This is demonstrated in Appendix A, Project Note #15. Therefore the z-axis focus design is complete.

Having completed the z-axis focus design it was then possible to find the required collector width for the collectors. The worst case occurs at m/e 44. An approximate equation for the maximum beam distance in the z-direction from the axis at the collector is:

$$Z_{max} = Z_e + \ell'' \tan [a_z + a_z'] \qquad (17)$$

where

Z_e = height at exit boundary

ℓ'' = collector distance from exit boundary

a_z = maximum z-axis focus angle

a_z' = angle due to fringe field defocusing

Using appropriate values the result is:

$$Z_{max} = 0.265 \text{ cm}$$

A collector width of 0.250 inch (0.635 cm) was established giving a 25% safety factor.

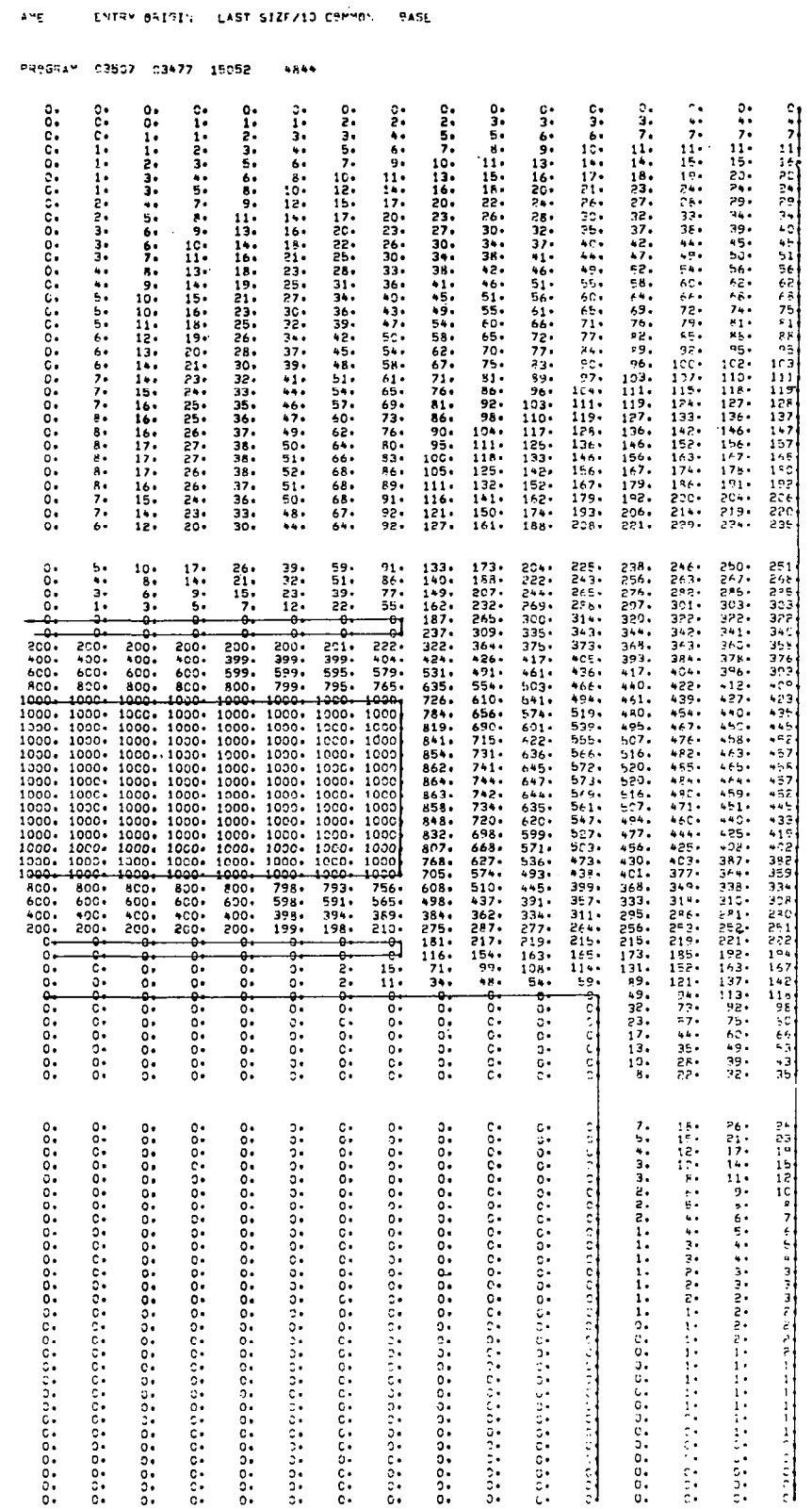

FIGURE 13
Z-Axis Focus Field

Analyzer Magnet Design

An important step in the analyzer design was the design of the permanent magnet which supplies the magnetic flux density for the magnetic sector operation. The design is significant in that the field configuration intimately affects the analyzer performance and the magnet weight is perhaps the single most important contributor to the overall package weight and every effort was made toward an optimum design. During the Phase I analysis it was shown that Alnico V was the best material which could be used for this task. A complete redesign was necessary due to a modified pole face area and additional constraints which were placed upon the magnet.

It was first necessary to establish the pole face configuration. It was decided to make a conservative magnet design which would conform as closely as possible to the ideal magnet field. For this reason the pole face area was made sufficiently large so that a uniform field would be assured over most of the trajectory. The entrance and exit faces were previously established. The other boundaries were placed two gap widths from the nearest trajectory. This should be a sufficient distance to assure a uniform field. This configuration is shown in Figure 11. By specifying the pole face configuration the area was computed and found to be 9.1 cm^2. The initial technical information applied to the magnet design is given in Table 8.

TABLE 8

Pole Face Area, A_g	9.1 cm^2
Gap Length, L_g	0.500 cm
Material	Alnico V
Maximum gap flux density, $B_g \Big\vert_{max}$	4500 gauss
Required flux density after stabilization, B_g	4000 ± 80 gauss
Reluctance Factor, f	1.2
Demagnitizing force, H_d	550 oersteds
Flux density at peak energy product, B_d	10,000 gauss

Several comments concerning the information in Table 8 are in order. First, the maximum gap flux density was specified to be greater than the required flux density so that the magnet could be stabilized by "knocking down" the field. A 7% reduction should be adequate but a larger value is desirable. Second, the reluctance factor, f, is defined as:

$$f = \frac{MMF}{MMF_g} + 1 \tag{18}$$

where

MMF = magnetomotive force required for soft iron pole faces and joints

MMF_g = magnetomotive force required for the air gap.

The parameters B_d and H_d are determined from a demagnetization curve for Alnico V and represent the maximum energy product point. Increasing B_d above this value would require a rapid increase in the amount of magnetic material used. Finally the tolerance placed upon B_g will keep the ion energy and ion source sensitivity in the required range.

Several other constraints were placed upon the magnet design:

a. Due to the altered analyzer shape the magnet yoke must extend around the high mass side of the analyzer envelope rather than the low mass side as anticipated in the conceptual design.

b. The yoke geometry must be such that the magnet can be moved in over the analyzer envelope and not have the two interface. A motion of 0.400" is specified and thus becomes the minimum dimension between the inner edge of the yoke and the envelope. The envelope will fold at the pole piece surface when the magnet is in the theoretical position.

c. The outer dimensions of the magnet are limited in order that the magnet will fit into the space provided for it. Initially, this limited the magnet width (perpendicular to the pole faces) to 2.00 inches.

d. Variations in the cross sectional area and shape from the pole faces to the yoke must be fairly gradual in order to minimize the leakage factor.

With this information an initial design was carried out using the following design equations[7]:

$$L_m = \frac{f H_g L_g}{H_d} \tag{19}$$

$$A_m = \frac{F B_g A_g}{B_d} \tag{20}$$

$$F = 1 + P_e/P_g \tag{21}$$

$$P_e = 1.24 \sqrt{S} \tag{22}$$

$$S = (1/2)C\, L_m + A_g \tag{23}$$

where

L_m = length of magnetic material
A_m = cross sectional area of magnetic material
F = leakage factor
P_e = leakage permeance
P_g = gap permeance
S = surface area of 1/2 of the magnetic material
C = perimeter of the pole face

The following values were obtained:

L_m = 4.909 cm

(A safety factor was added by letting L_m = 5 cm.)

A_g/L_g = 18.2
P_g = 19.5 (from Figure 28 of G.E. Manual)
S = 40.6 cm^2
P_e = 7.90
F = 1.405
A_m = 5.74 cm^2

Using these parameters as an initial guide and with the defined pole face configuration a magnet was designed. The cross sectional area at the midpoint of the yoke was set at 0.5 x 2.12 in^2 or about 6.8 cm^2 which is greater than required. When the constraints outlined above were applied it was found that the length of magnetic material was about 9.1 cm which is considerably greater than the specified value of 5.0 cm.

Two things can be done with this extra length. First, it can be utilized by placing ridges on the pole pieces in order to improve the uniformity of the flux density over the pole face area. This will increase the value of L_g and therefore the required value of L_m. The other thing which may be done is to utilize a soft magnetic material as a yoke to fill in part of the magnet circuit. A material such as Armco iron has a much higher permeability than does Alnico V so that a smaller yoke cross section can be utilized thereby saving weight.

Both of these methods were employed. Ridges 0.030 inch high were placed on the pole pieces. This actually amounted to dishing out the pole pieces so that at the edges the gap was 0.500 cm and in the center the gap was 0.660 cm. This also reduced the pole piece thickness in the center from 0.130 inch to 0.100 inch. The length of magnetic material required to sustain the required gap flux density was then computed. It came out to about 6.5 cm which left some magnetic circuit length to be filled in by Armco iron. After consulting with General Electric a new formula was applied to compute the leakage factor. The result was very close to F = 2.0. This value is exactly what the magnet designers at General Electric believed to be a reasonable value for a magnet of this size and shape. The area of the magnet was then computed to be 0.9 Ag. It should be pointed out that an iterative procedure must be followed in which A_m is computed with an assumed value of F and then F is computed using this value of A_m. Then A_m is recomputed and so forth. The effects of the yoke may be computed by using a modified form of equation (19):

$$H_d L_m = \frac{B_g L_g}{\mu_o} + \frac{B_y L_y}{\mu_y} \qquad (24)$$

where

B_y = flux density in the yoke

L_y = length of yoke

μ_y = permeability of yoke material

In this case it is assumed that other contributions to the reluctance factor are negligible (i.e. f = 1.0). For B_y = 16,000 gauss, L_y = 2.1 inches and μ_y = 700 (reasonable for Armco iron). It can be shown that the second term on the right of equation (24) is about 4% of the first term and therefore the value of the reluctance factor assumed earlier (f = 1.2) will be more than enough to account for the reluctance of the yoke. The area required for the yoke is found from:

$$A_y = \frac{B_d A_m}{B_y} \qquad (25)$$

For B_y = 14,000 gauss and the other parameters are before A = 0.91 in^2 which establishes the yoke thickness for a given yoke width.

The magnet design shown in Figure 14 was submitted to General Electric for their comment and they returned a slightly modified and more conservative design. The principal changes which were made were increasing the magnet height by 0.320" to increase the length of magnetic material and to allow a larger 'window' inside of the yoke (for the purpose of reducing leakage losses), and simplifying the shape of the Alnico V pieces so that they could be more readily fabricated. This created a variance between the magnet cross section and the pole face cross section at their interface but there was full assurance from General Electric that this would create no problems in the resulting field.

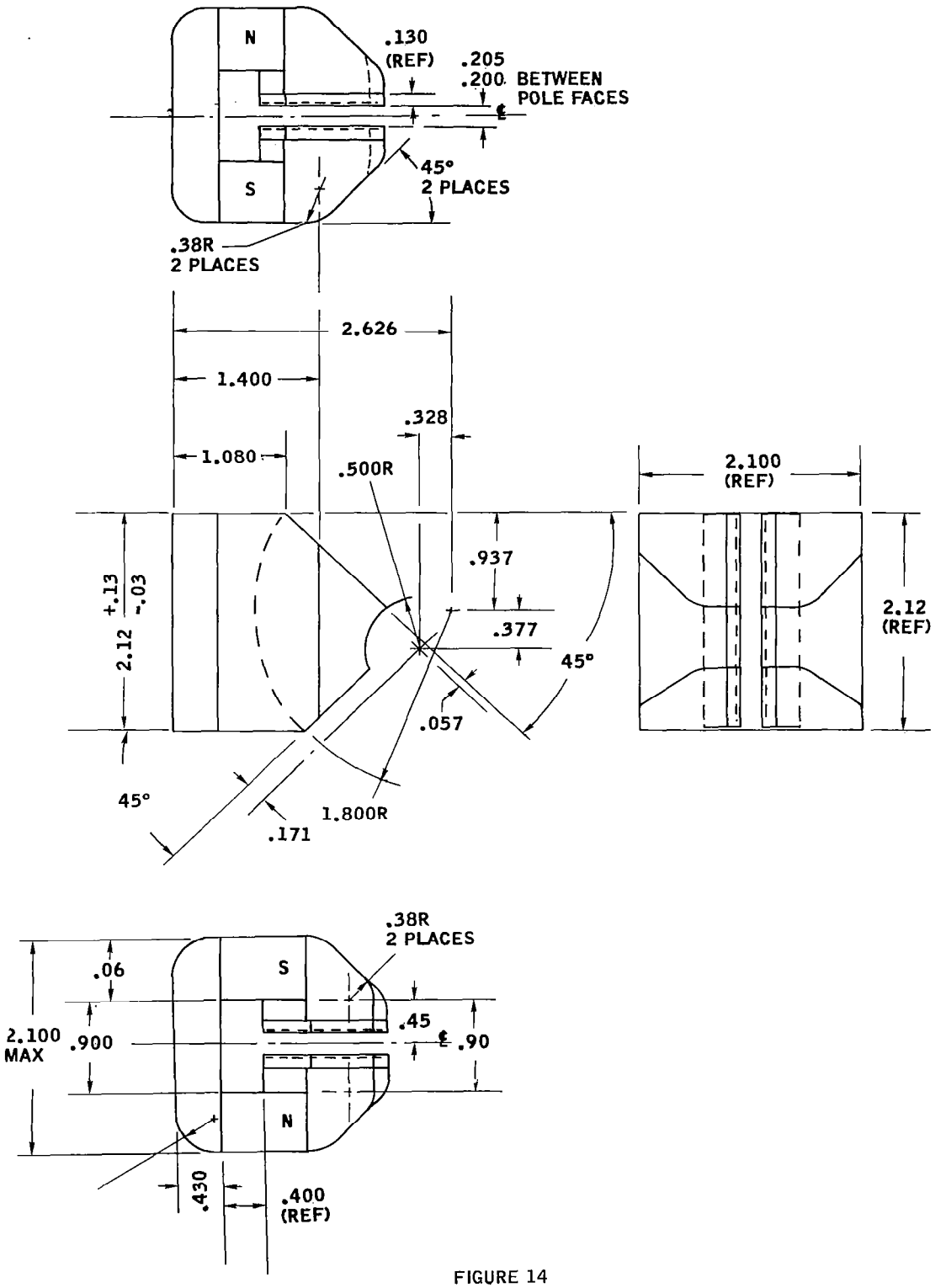

FIGURE 14
Initial Analyzer Magnet Design

The final magnet design is shown in Figure 15. One of these magnets has been fabricated and immediately after charging it was found to have a maximum flux density of 5200 gauss. When more careful measurements were made two days later the field was found to be about 4600 gauss. This is greater than the required value of 4400 gauss. The weight of the magnet is 1.74 pounds which is much greater than the estimated value of 0.9 pound given in the Phase I report. It is clear that a reduction in the weight can be achieved by a less conservative design. It is probable that the yoke can be made much smaller and the length of magnetic material can be reduced. The field strength was reduced to 4.1 kilogauss by application of an ac magnetic field. A preliminary field plot of the magnetic field indicated that flux density variations are no greater 5% over the region of interest.

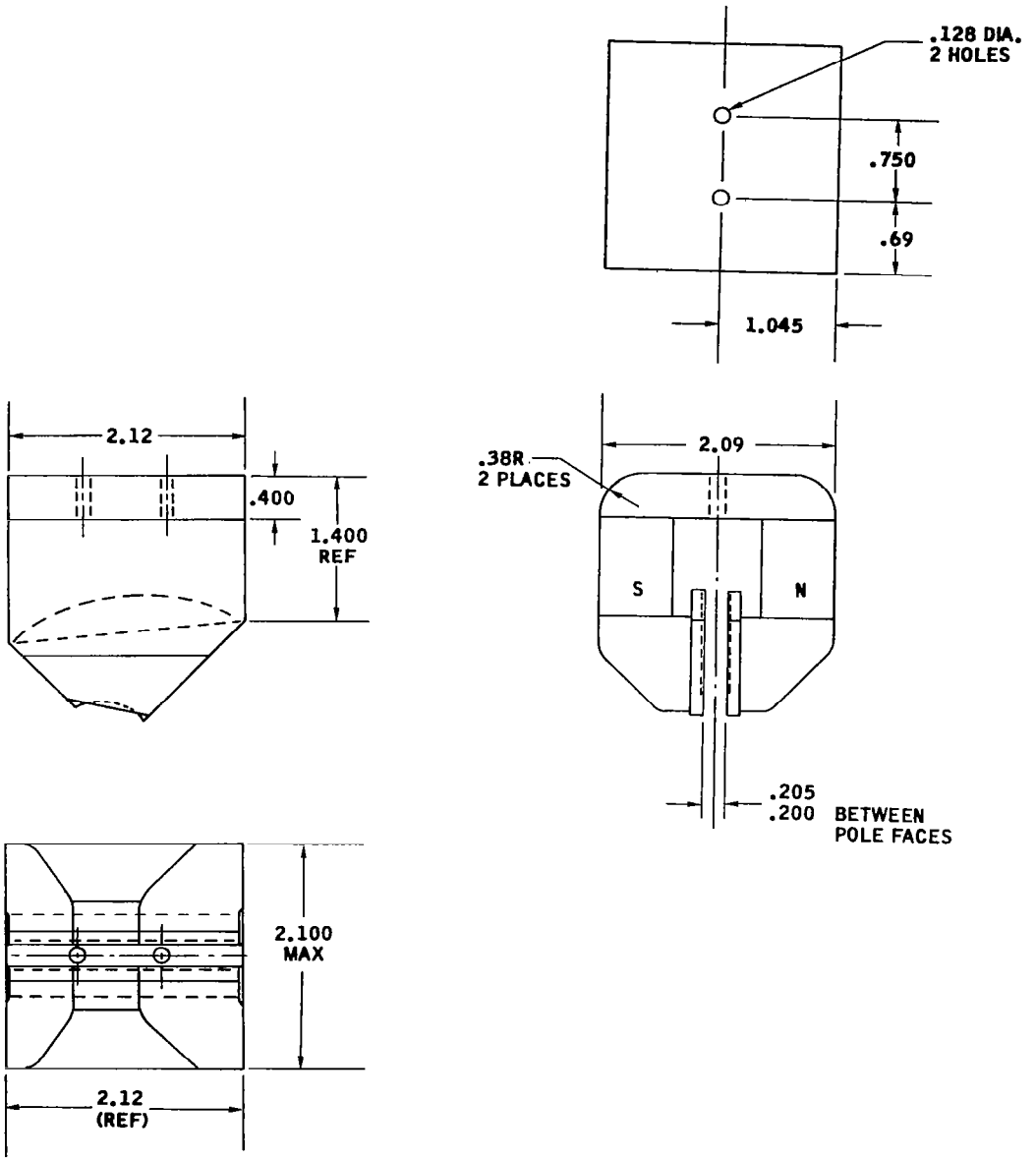

FIGURE 15
First Generation Magnet Design

ION SOURCE

Phase I Results

The ion source performs the important functions of ionizing the sample gas, focusing the resulting ions, and transmitting an ion beam with narrowly defined properties to the analyzer. The ion beam consists of a stream of positively charged particles, which are directly proportional to the admitted sample gas pressure. The mass resolving analyzer separates the ion beam by the mass-to-charge ratios of the ions. Consequently, each analyzer output is proportional to the partial pressures of their corresponding sample constituents. In performing its function, the ion source must not introduce appreciable distortion either by altering the composition of the sample gas or by causing a non-linearity in the ion current versus sample pressure relationship.

During the conceptual design phase, the following conclusions were reached relative to the ion source requirements for this instrument. These have been largely applied to the design efforts during this phase of the work:

a. A conventional electron bombardment ion source with a hot wire thermionic emitter as the electron source was the only type with sufficient development and sensitivity for this mission.

b. Since the filament is the least reliable component in the analyzer system a back-up filament should be incorporated in the design.

c. The most workable arrangement for a back-up filament is to have two electron guns and filament assemblies; both of which are capable of projecting electrons into a common ionizing region.

d. The configuration best suited for two electron guns is an orthogonal arrangement with the ions having the ionizing region at right angles to the two electron beams.

e. In order to sample distortion by filament interaction with the sample gas the filaments should be located in a region of lower pressure relative to the ionizing region. The pressure ratios should be 100:1.

f. In order to achieve the required differential pumping stated in e above the ion source conductance must be limited to 35 cc/sec and the pump which evacuates the analyzer must have a pumping speed of 4 liters/second.

g. Requirements were established for the magnetic sector interface. These are given in Table 9.

h. A schematic diagram of the selected configuration is shown in Figure 16.

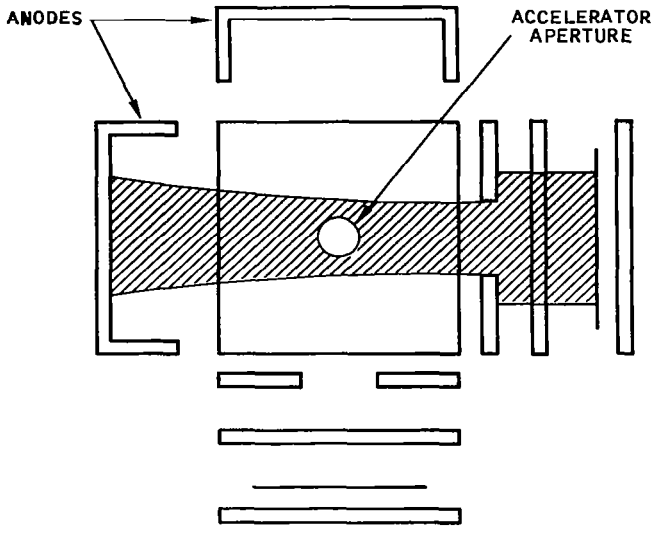

TOP VIEW

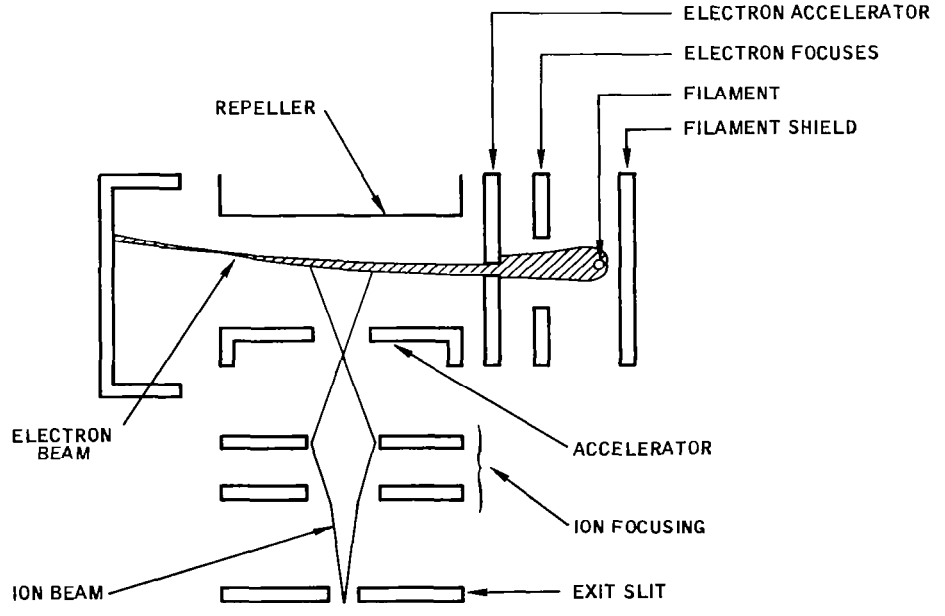

SIDE VIEW

FIGURE 16
Schematic Conceptual Ion Source Drawing

TABLE 9
Magnetic Sector Interface Parameters Established in Phase I

Parameter	Value
Sensitivity (N_2), S_{N_2}	5×10^{-7} amps/torr
Mean Ion Energy , V_I	225 volts
Ion Energy Spread, ΔV_I	±1.5 volts
Object Slit Width, S_o	0.0307 cm
Object Slit Height, h_o	0.0614 cm
Ion Beam Divergence, (half angle), α	0.4°
Maximum Ionizing Region Pressure	2×10^{-4} torr
Differential Pressure Ratio	100:1

OGO-F Ion Source Description

During the interim period between the conceptual design phase and the ETM design phase, Perkin-Elmer Aerospace designed and fabricated an ion source on NASA 5-9328 for the University of Michigan and Goddard Space Flight Center to be used on a quadrupole mass filter as part of an atmospheric composition experiment to be flown on the OGO-F polar orbiting satellite. This ion source met nearly all of the requirements stated above for the Two Gas Sensor ion source and therefore it was decided to adapt it for this application.

The OGO-F ion source is a dual filament ion source which employs two orthogonal electron guns. The ionizing region is formed by a rectangular box with dimensions 0.260" x 0.260" x 0.100". The top of the box is formed by the repeller electrode, the bottom by the accelerator electrode, two adjacent sides by the electron accelerator electrodes, and the remaining sides by the anodes. The electron accelerators form the last elements of the two electron guns.

The electron guns are formed by a straight wire filament and four electrodes. A filament shield is mounted behind the filament to depress the potential around the filament and thereby acts to focus the electrons and propel them toward the more positive area in the direction of the ionizing region. In front of the filament is a split electron focus electrode which assists in the focusing and which can deflect the electron beam to align it with the slot in the electron accelerator. The electron accelerator is the most positive electrode in the system and has a small, low conductance slot in it through which the electrons pass to the ionizing region. The electron beam passes through the ionizing region and is collected at the anode which is in the opposite face. The electron beam has sufficient energy that it can traverse the ionizing region while undergoing a minimum deflection due to the repeller-accelerator gradient.

Ions which are formed in the ionizing region are accelerated toward the accelerator by the repeller-accelerator voltage and a portion of them pass

through an aperture in the accelerator. They are then accelerated through an ion focusing system which is comprised of two ion focus electrodes, a baffle, and the object slit plate. The object slit plate contains the object slit which defines the dimensions of the ion beam for the analyzer. The object slit is also a low conductance aperture to maintain the differential pumping. The sample gas is admitted through a tube which is attached to the repeller. The surface of the repeller is a grid which allows the gas to enter the ionizing region while maintaining the appropriate potential at the surface.

A photograph of the OGO-F ion source is shown in Figure 17 showing the various electrodes layed out in an exploded view and the assembled ion source at the top. Starting at the bottom the electrodes in the center column are the nozzle (corresponding to the object slit plate in the Two Gas Sensor ion source), ion focus B, ion focus A, accelerator, and repeller block. The diagonal arrangement of electrodes starting at the lower right are the filament assembly with the filament shield mounted behind the filament, electron focus #1, electron focus #2, electron accelerator, repeller block, and anode. The repeller block forms the central portion of the assembly with the other electrodes mounting to it on ceramic and ruby insulators (which are not shown). Figure 18 shows the assembled ion source, viewed from the top with the repeller grid removed. This shows the ionizing region with accelerator and its aperture in the bottom and the electron accelerators with their slots for the electron beams shown on the two visible sides. A semi circular ridge is visible on the edge of the accelerator electrode. There is a corresponding ridge on the repeller. These ridges reduce the effect of the electron accelerator voltages upon the potential distribution in the ionizing region. A complete discussion of the design of the OGO-F ion source will be given in the final engineering report, on contract NAS 5-9328. A brief summary of the performance of the OGO-F ion source follows.

OGO-F Ion Source Test Results

Three of these ion sources have been fabricated and tested, without any filament failures to date. The filaments used in these ion sources are an alloy of 75% Tungsten and 25% Rhenium in a wire of 0.005 inch diameter. The testing of each unit involved approximately 100 hours with the ion source operating, and with the operation of each filament being about 50 hours.

The initial testing of the ion source was performed to analyze the electron transmission system from the filament of an electron gun to its respective anode. Figure 19 is a typical set of curves showing the peaked electron transmission to the anode out of a total electron emission current of 100 microamperes. The important observation of this plot is that to obtain the maximum

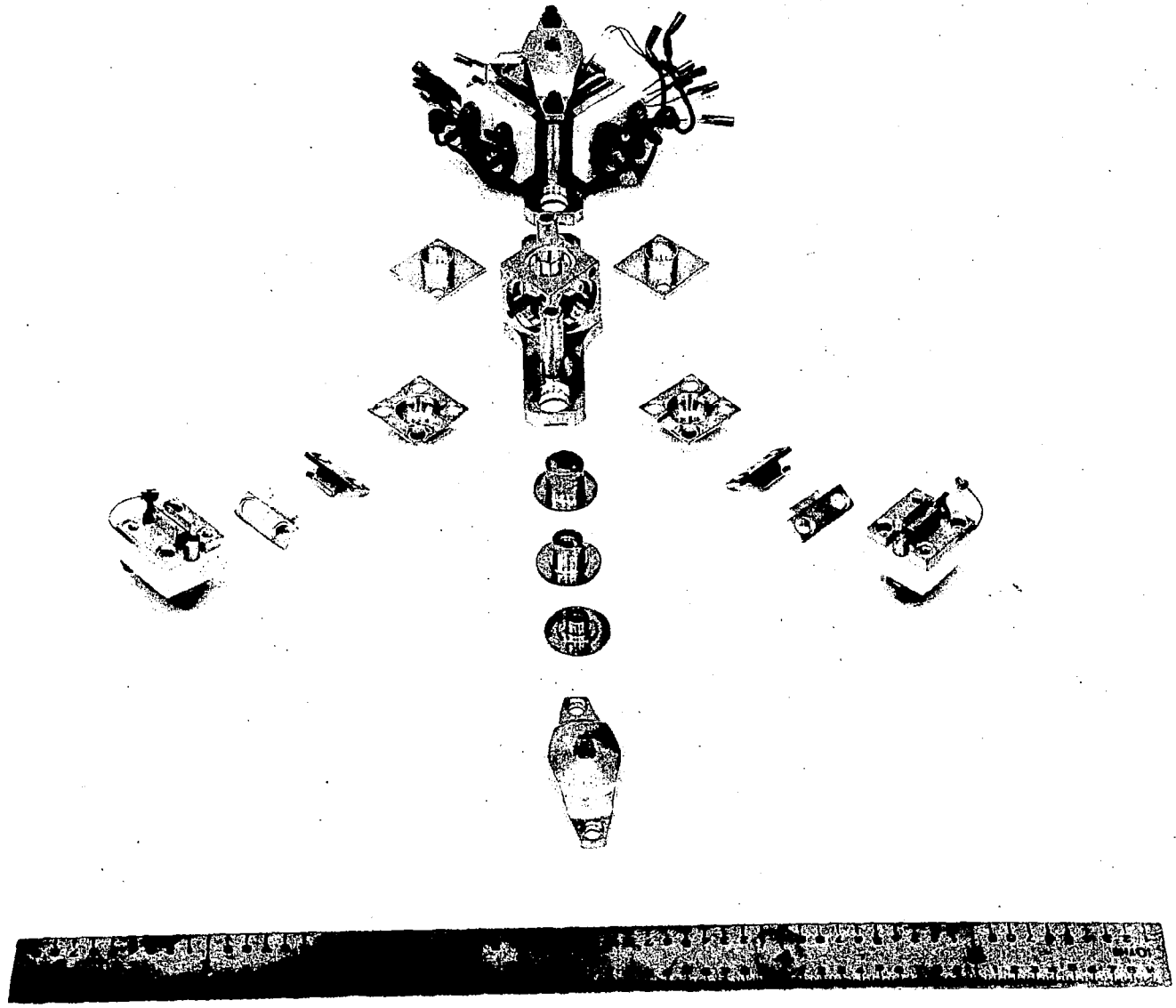

FIGURE 17
OGO-F Ion Source Assembly

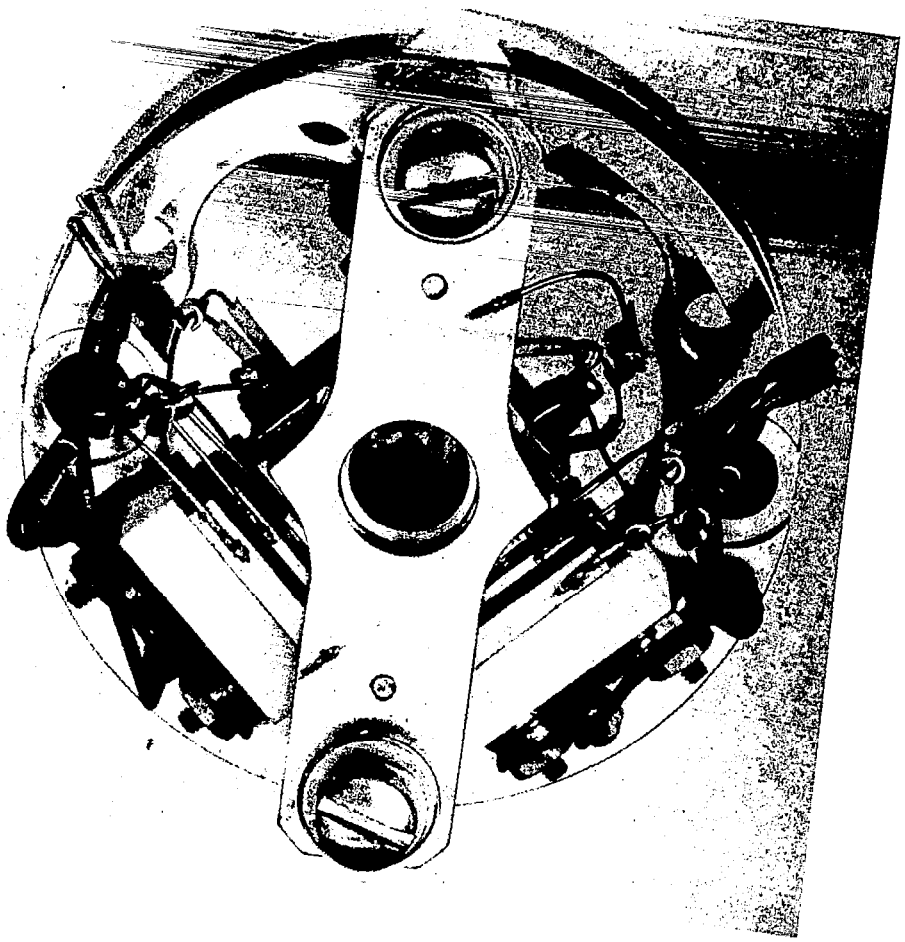

FIGURE 18
OGO-F Ion Source Showing the Ionizing Region

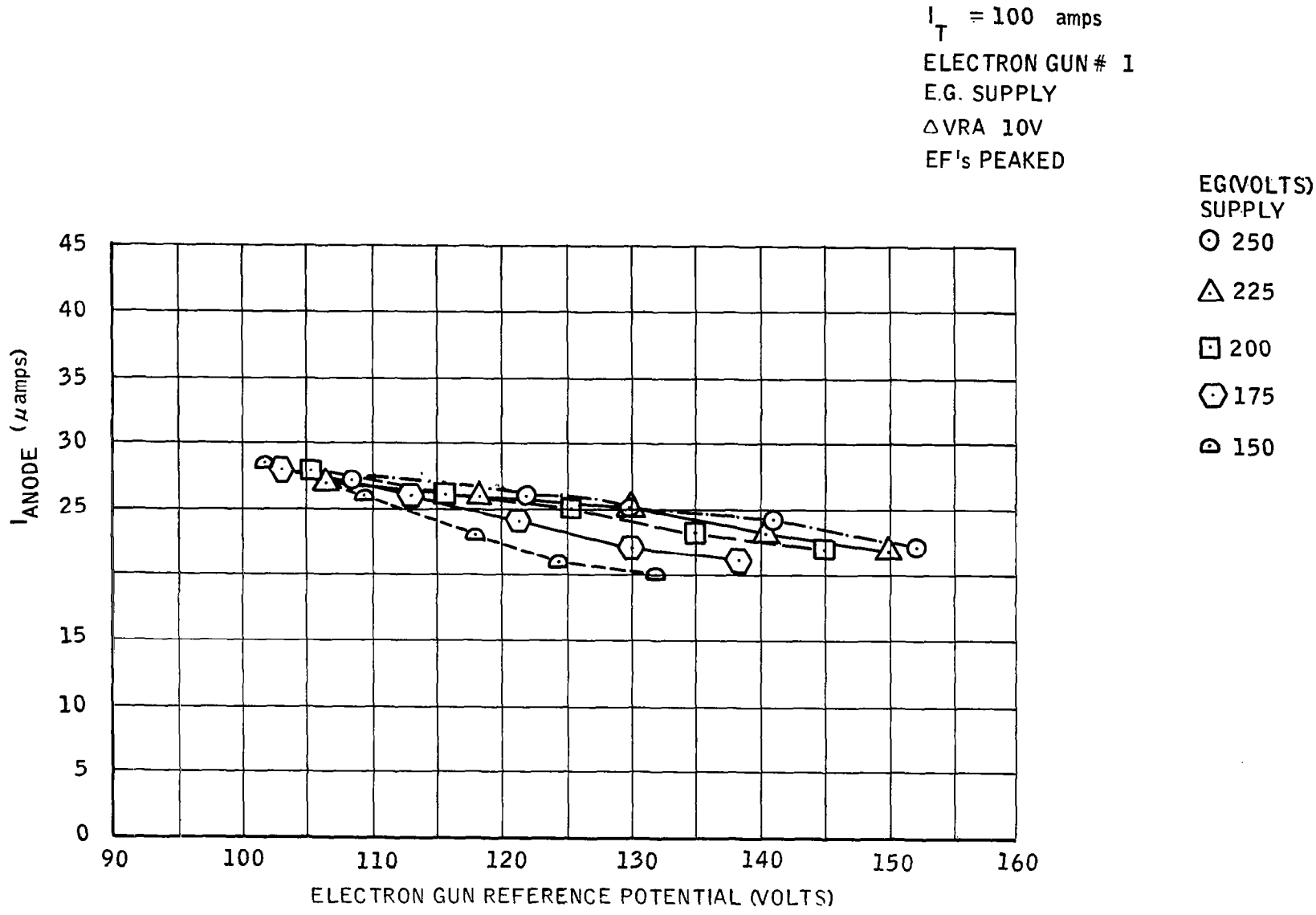

FIGURE 19
OGO-F Electron Gun Characteristics

electron transmission to the anode, the anode current appears to be nearly independent of the electron gun supply setting at the low values of the electron gun reference supply voltage. By lowering the electron gun supply setting, the potential of the electron accelerator is approaching the value of ion accelerator voltage. It thus appears that the electron accelerator potential can be operated at low values without sacrificing the transmission efficiency of the electron gun system. This is important in the OGO-F ion source as will be discussed later.

The distribution of the electron emission current and the potentials of the various ion source electrodes for a typical electron gun is recorded in Table 10.

This transmission efficiency is accomplished through the electron entrance aperture in the electron accelerator of which the dimensions are 0.060" wide by 0.010" high by 0.025" thick.

Testing of the ion focusing system of the dual filament ion sources is performed to optimize the ion output current, such that the maximum ion source sensitivity can be obtained. Figure 20 shows a typical family of curves varying the ion focus B electrode potential for different ion focus A voltages, at a set value of potential between the ion accelerator and the exit slit. The peak value at the right of the figure was chosen as the operating point due to differences between the operation of the two electron guns giving this point as the optimum compromise potentials. The ion source sensitivity when operating at this point is then calculated to be 8.35×10^{-7} amps/torr at an ionizing electron current of 35 microamperes.

The energy spread of the exiting ions from the source defines the thickness of the electron beam, and indicates what analyzer performance can be realized. Figure 21 shows a plot of the exiting ion current as a function of potential

TABLE 10

Electrode	I (Microamperes)	Potential (Volts)
Filament Shield	0	-150
Electron Focus A	2	-134
Electron Focus B	1	-136
Electron Accelerator	75	0
Repeller	.25	-39
Ion Accelerator	.1	-51
Anode	35	0
Side Electron Accelerator	2	0
Side Anode	2	0
Filament	--	-144

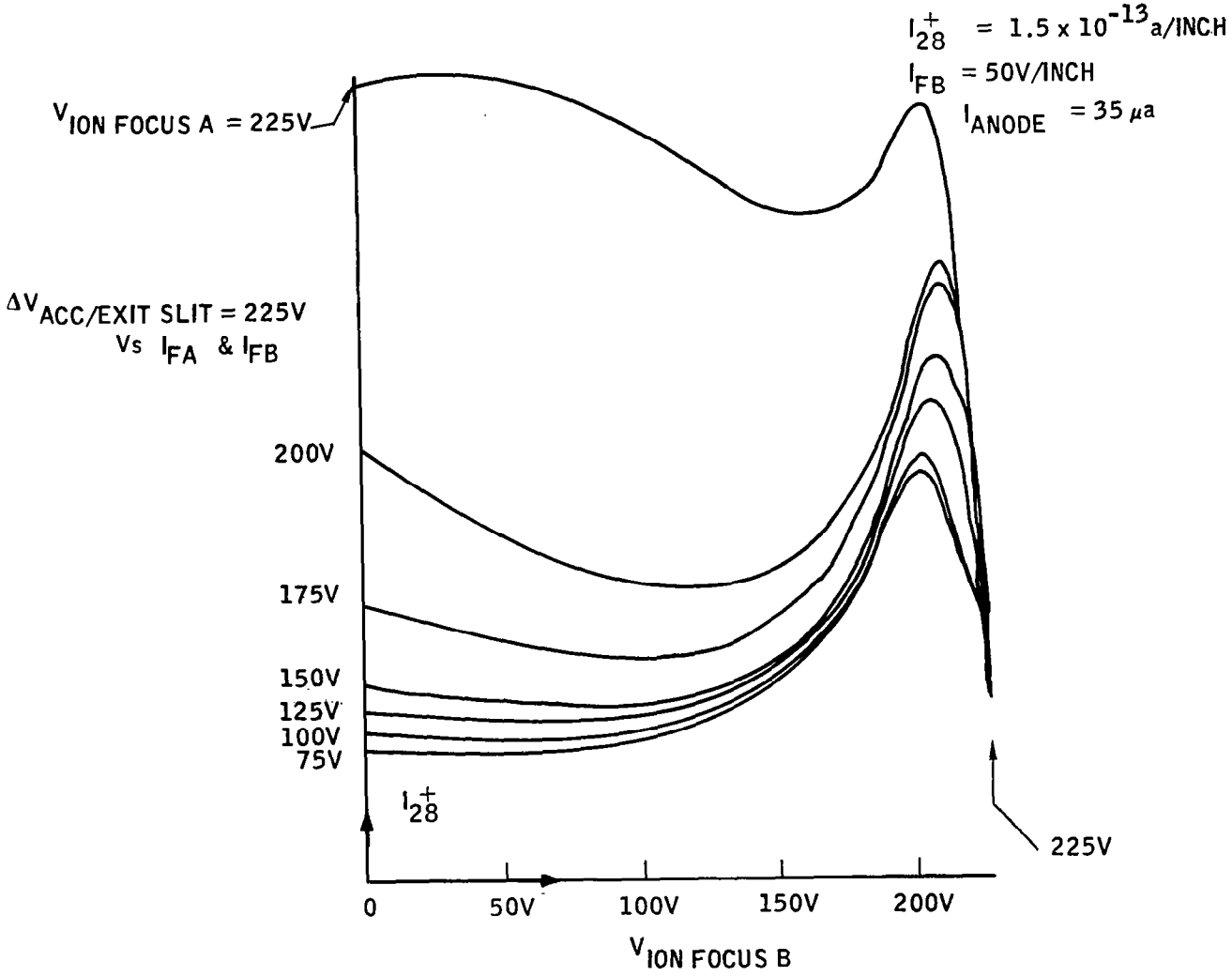

FIGURE 20

OGO - F Ion Focusing Characteristics

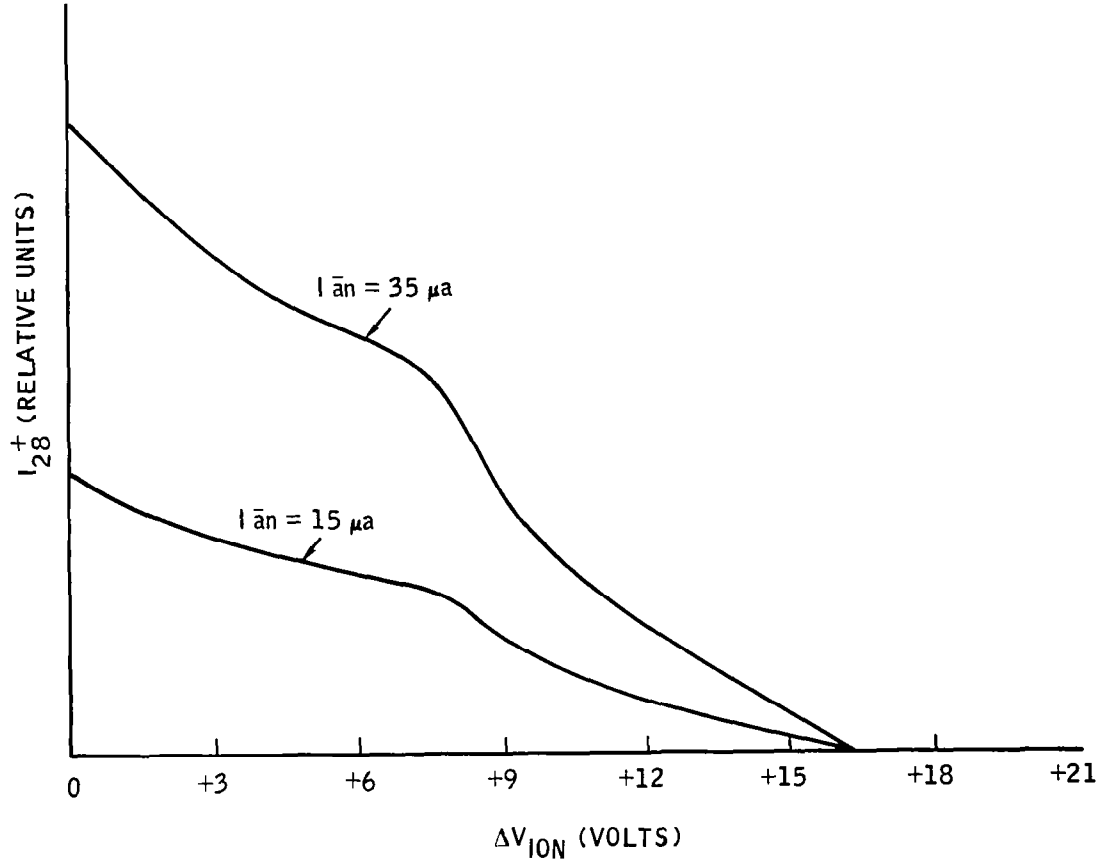

FIGURE 21
OGO - F Ion Energy Spread

where they are formed. It is seen that the energy spread of the ion beam is greater than the extraction potential between the repeller and accelerator. This is due to the influence of the electron accelerators and anodes within the ionizing region upon the space potential between the ion extraction electrodes. Consequently the extraction potential of the ions is not effectively being controlled by the potential across the repeller and accelerator electrodes. However, for mating with the quadrupole analyzer for the OGO-F mission, the ion energy spread was acceptable, and thus was not changed.

Ion source linearity testing was performed on the OGO-F dual filament ion sources. Figure 22 is a plot of the m/e 28 output current of the ion source as a function of the pressure in the ionizing region using a nitrogen sample. This curve indicates that the linearity of the source with nitrogen is linear up to about 1×10^{-4} torr. Higher pressures were not evaluated, since limitations occur above this point due to unstable operation of the vacuum pumping system, and the sample is admitted to the analyzer as well as the ion source since a differential pumping cannot be used with the designed system. Due to the absence of differential pumping, operation of the instrument with an oxygen sample was limited to low pressures because of instability of the electron guns when operating the analyzer at high partial pressures of oxygen. Without differential pumping, it was also necessary to monitor both the m/e 28 and 44 peaks due to sample distortion at the filament from conversion of oxygen to carbon monoxide and carbon dioxide. The output currents related to oxygen linearity with sample distortion can be expressed by

$$I^{+}_{32} = S_{O_2} P_{O_2} - S_{\text{converted CO}} P_{O_2} + S_{\text{converted CO}_2} P_{O_2}$$

$$I^{+}_{28} = S_{N_2} P_{N_2} + S_{\text{converted CO}} P_{O_2}$$

$$I^{+}_{44} = S_{CO_2} P_{CO_2} + S_{\text{converted CO}_2} P_{O_2}$$

When the data taken on the OGO-F ion sources is substituted into these equations the result is that the sensitivity of the source for the converted carbon monoxide and carbon dioxide by the filament operation is as follows:

$S_{\text{converted CO}}$ = 1.01% of the ion source sensitivity for an oxygen sample admitted to the source

$S_{\text{converted CO}_2}$ = 1.71% of the ion source sensitivity for an oxygen sample admitted to the source

This data is meaningful since it shows that for the ion source operation under a condition where differential pumping is not achieved, either the backstreaming of CO and CO_2 being generated at the filament into the ionizing region is small, or the generation of CO and CO_2 at the filament is very small when compared to the oxygen partial pressure admitted to the source.

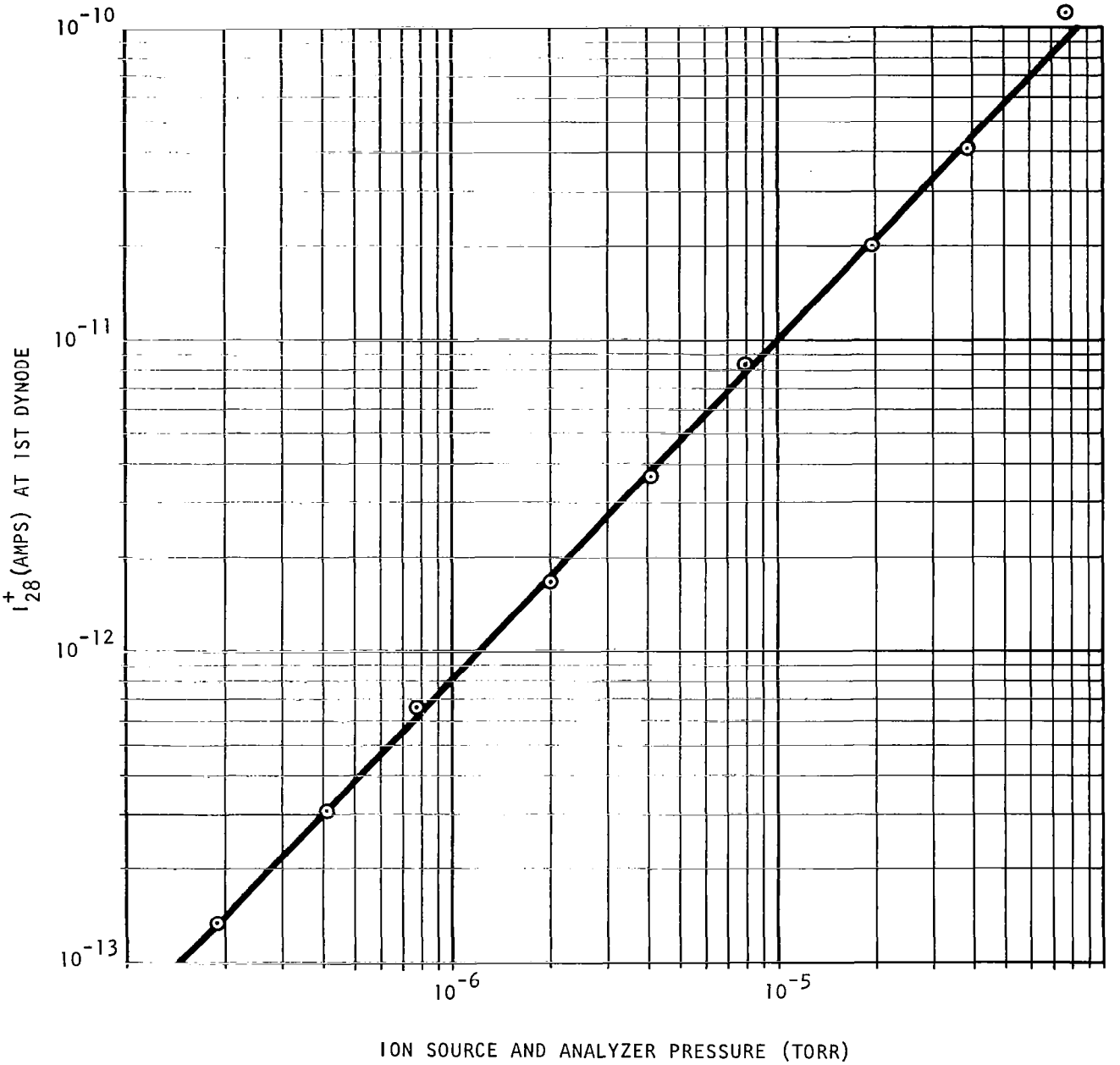

FIGURE 22
OGO-F Ion Source Linearity vs Pressure

Test data was also taken to determine the ion source linearity with respect to the electron current magnitude in the ionizing region. Figure 23 shows a plot of the ion output current, the total filament emission, and the current striking the electron accelerator as a function of the electron current reaching the anode. Also plotted is the filament current required by the 0.005 inch diameter filament to give the emission levels. This curve shows that the ion output current remains linear with the anode current over the operating range of emission required of the electron gun system. The transmission percentage of the total emission to the anode is seen to drop as the emission is increased, but the required range of emission to obtain an ion source sensitivity of 1 x 10^{-6} amps/torr is maintained, and the ion output remains linear with the emission level.

While stability of the operation of the electron guns and ion output has not been analyzed as a specific test, it has been seen that the repeatibility of the ion source operation has not varied throughout the testing of the analyzer section of the OGO-F mass spectrometers, such that retuning of the ion source was not required after the operating conditions were established in the source parameter testing.

Modifications of the Two Gas Sensor

Several modifications were required in order to adapt the OGO-F ion source for this application. These are discussed briefly below and expanded upon where necessary.

a. The ion exit aperture was modified to conform with requirements for the object slit dimensions as established by the analyzer requirements.

b. The accelerator and repeller electrodes were modified in order to alter the potential distribution in the ionizing region and reduce the ion energy spread.

c. The dimensions of the electron beam transmitting apertures in the electron accelerator electrodes were modified in order to reduce the ion source conductance.

d. The diameter of the filaments was reduced from 0.005" to 0.003" in order to reduce the power requirements of the mass spectrometer.

e. Modifications in the mechanical design were made in order to interface the ion source with the analyzer housing.

In addition to the modifications listed above it was also necessary to verify the operation of the ion source under the expected operating conditions. This was done for four parameters: sensitivity, ion beam divergence, non-linearity and sample distortion.

The sensitivity was verified by extrapolation of the experimental data taken on the OGO-F ion source. The sensitivity for N_2 of the OGO-F ion source is

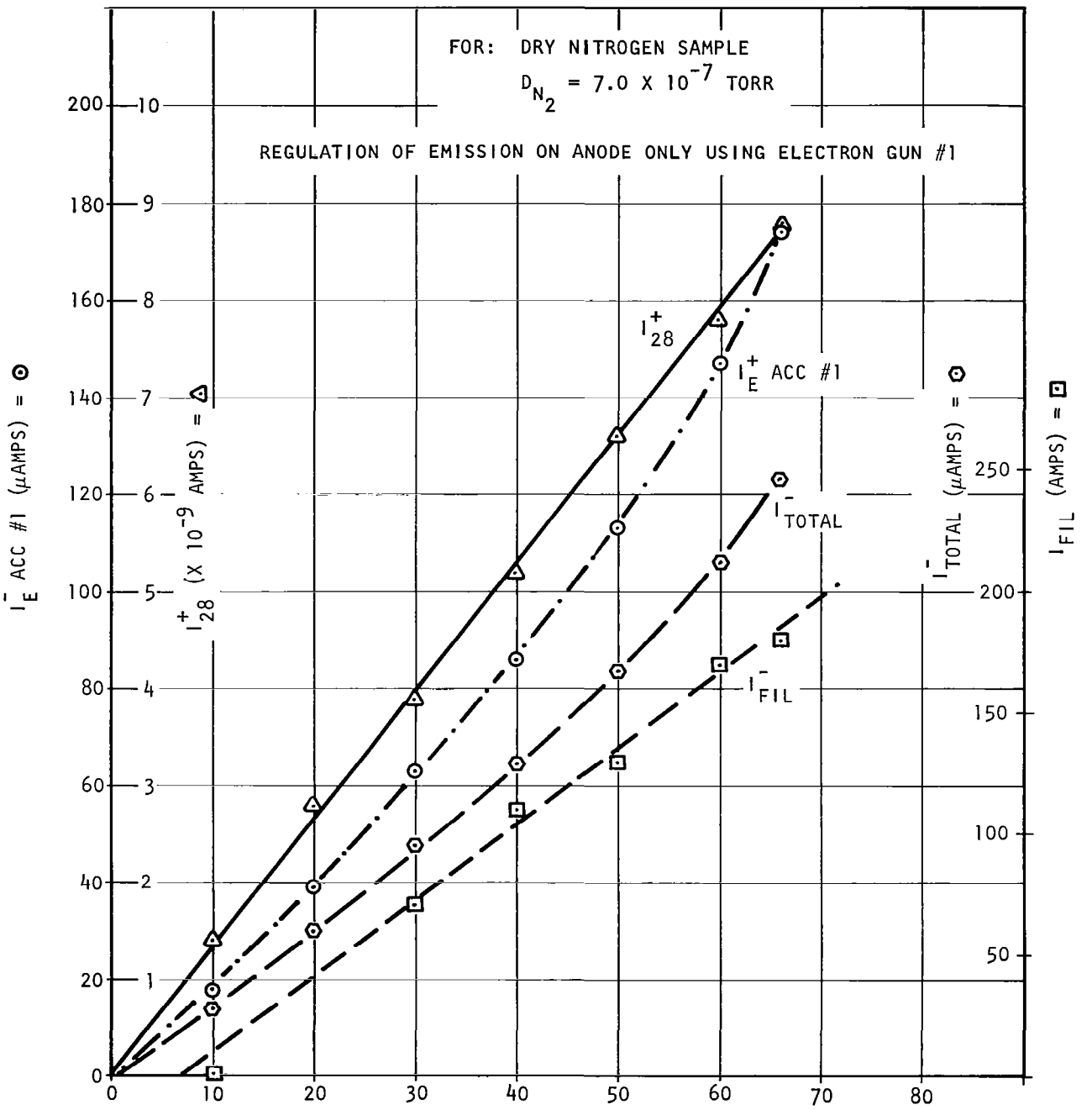

FIGURE 23
ELECTRON ACCELERATOR CURRENT, FILAMENT CURRENT, TOTAL EMISSION,
AND ION OUTPUT (m/e 28) VERSUS ANODE CURRENT

8.75×10^{-7} amps/torr for an ion energy of 225 volts and an ionizing emission current of 35 μA. The four factors which will alter this sensitivity for the modified ion source are:

a. The exit slit area is different.

b. The area from which ions are drawn is reduced.

c. Modification of the field curvature in the ionizing region will affect the ion focusing.

d. The reduced ion energy spread should reduce any chromatic aberration in the ion focusing system thereby increasing the ion transmission.

The first factor is readily taken into account by multiplying the OGO-F sensitivity by the ratio of the exit aperture areas. The only assumption involved here is that ion current density distribution is fairly uniform over the exit aperture area. This is a good assumption since the transmission efficiency of the OGO-F ion source is typically 6% and the distribution cannot fall off too rapidly. The second factor is more difficult to determine, but as a worst case, the sensitivity will be reduced in proportion to the reduction in the area from which the ions are drawn. This area is approximately one-fourth of the area for the OGO-F ion source. The final two factors will be of secondary importance and can be compensated for to some extent by adjustment of the potentials on the ion focus lenses. Then as a worst case sensitivity:

$$S = \frac{1}{4} \frac{A}{A_{OGO}} S_{OGO}$$

where $S_{OGO} = 8.35 \times 10^{-7}$ amps/torr at $V_I = 225V$.

$$A = h_o S_o = 238 \times 10^{-4} \text{ in}^2$$

$$A_{OGO} = \pi r_e^2 = 78.5 \times 10^{-4} \text{ in}^2$$

so that

$$S = 6.33 \times 10^{-7} \text{ amperes/torr}$$

This is a worst case value. It is expected that the sensitivity will be closer to 10^{-6} amps/torr, which is a factor of two greater than the required value.

There is no direct information on the ion beam divergence of the OGO-F ion source, however, it is possible to infer this information from the analyzer performance. Using theoretical equations developed for the quadrupole analyzer along with resolution and peak shape data it is found that the maximum ion source angle above which the concentration of ions is less than 1% is a little over 1°. This is actually a worst case value since it is known that several factors prevent the instrument from achieving theoretical performance. At the same time if the maximum theoretical OGO-F ion source sensitivity is computed assuming exit angles of 1° it is found that the value is a factor of two greater than the actual sensitivity, which lends additional weight to the argument that the angles are acceptably small.

The non-linearity of the ion source with pressure results from the effects of ion space change in the ionizing region. The analysis of this problem appears in Appendix A , Project Note 19. It shows that there will be about a 3% non-linearity at the maximum ion source pressure of 2 x 10^{-4} torr. The original estimate in Phase I was 2% but it is not believed that this small non-linearity will be of significance due to the limited dynamic range over which the samples are expected to vary.

In Phase I, the problem of sample distortion was discussed and it was shown how the maintenance of a pressure differential between the filament and the ionizing region could reduce this effect to a tolerable level. There was not sufficient information at that time to determine the magnitude of the sample distortion effects but the preceding data shows that with a differential pressure ratio of 100:1 the contribution to the m/e 28 and m/e 44 peaks due to the presence of the O_2 sample constituent is about 0.01% and 1% respectively. Since the minimum detectible pressure variations amount to 0.1% of the m/e 28 peak and 10% of the m/e 44 peak it is clear that no problem will exist due to sample distortion. In fact it is possible that the differential pumping requirements can be reduced, thereby reducing the pumping speed requirements. Having verified the basic ion source properties it is now possible to turn to the modifications which were made to the ion source and their effect upon the operation. These are covered in the order in which they were previously listed.

The requirement for a modified object slit is obvious from the analyzer calculations and its effect upon the ion source sensitivity has already been noted. The data presented on the OGO-F ion source indicated that the ion energy spread would be inacceptably large. The problem arises due to the penetration field from the electron accelerators and the modes, and the fact that ions are drawn from regions of the ionizing region which are subjected to this field. The present ion energy spread runs between 12 and 20 volts.

The following remedies appeared to offer promise:

a. Reduce the electron accelerator voltage to the lowest possible value consistent with acceptable electron gun operation. This will reduce the extent of the penetration field. The anode voltage would be reduced correspondingly.

b. Increase the height (and perhaps the thickness) of the ridges on the accelerator and the repeller which extend up in front of the electron accelerators. This will reduce the extent of the fringe field due to the electron accelerators. One problem which may arise when this is done is that the focusing action of the electron accelerator on the electron beam as it enters the ionizing region may be increased. This should be investigated by field plating. At the present time the transmission of the electron beam across the ionizing region is very good (only 1 microampere out of 36 microamperes to an electrode other than the receiving anode) so a certain amount of increased focusing may be tolerated.

c. The change in the ridges will cause an inbalance in the field distribution which could affect the electron beam and the ion focusing. In order to counter this the anode potential will have to be reduced.

This will necessitate a change in the power supply configuration. Originally the repeller was to be on a separate, regulated winding on the secondary of the electrode bias supply transformer in order to allow for the possibility of drawing electron current at this electrode. Testing thus far indicates that no current will be drawn at this point and therefore, by changing the voltage on this winding, it can be used as the anode voltage and the repeller can be moved to another point on the divider string. In this way the anode voltage can be placed at the necessary potential (different from the electron accelerator) to balance the penetration field in the ionizing region.

d. The size of the aperture in the accelerator electrode can be reduced, thereby reducing the area of the ionizing region from which ions are drawn. Ions will then be drawn primarily from the center of the ionizing region where the penetration field is the least. It should further be pointed out that the reduction of the penetration field may increase the ion source sensitivity by reducing the electron beam spreading and thereby increasing the density of the electron beam over the accelerator aperture. On the other hand, the reduced penetration field will change the field curvature in the ionizing region and thereby alter the ion focusing. This may cause a decrease in ion source sensitivity.

e. The final fix which may be tried is to reduce the potential of the side electrodes in the ionizing region in order to supress the penetration field. This may distort the ion focusing and thereby reduce the sensitivity. This will be investigated on the OGO-F instruments. If this appears to be desirable, it will necessitate some changes in the electronics. The side electrodes will have to be switched to alternate potentials and then switched back when the filaments are changed. This will require an additional relay to be operated in conjunction with the filament switch relay. This does not appear to present any severe problems.

Of the above remedies, b., c., and d. were incorporated into the design (c. being required because of the inclusion of b.); a. will be exploited during test, and e. remains as a good possibility in the event that a., b., c., and d. are insufficient.

The ridges on the accelerator and repeller were increased from dimensions of .010" wide by .020" high to .020" by .035". These values were selected based upon computer solutions of the potential distribution in the ionizing region and estimations of the expected ion energy spread as determined by the potential variations of those points from which ions are drawn. This is determined by tracing the trajectories of the electron beam through the ionizing region. Figures 24, 25, and 26 are computer field solutions and Figure 27 is a trajectory plot. The trajectories which were plotted represented the extreme dimensions (top and bottom) of the electron if it is assumed that all of the electrons enter the ionizing region normal to the electron accelerator aperture plane. This is probably not the case since there will be some beam divergence in the electron beam. The effect of the electron accelerator-accelerator-repeller interface is to create a focusing field for the electron beam so that

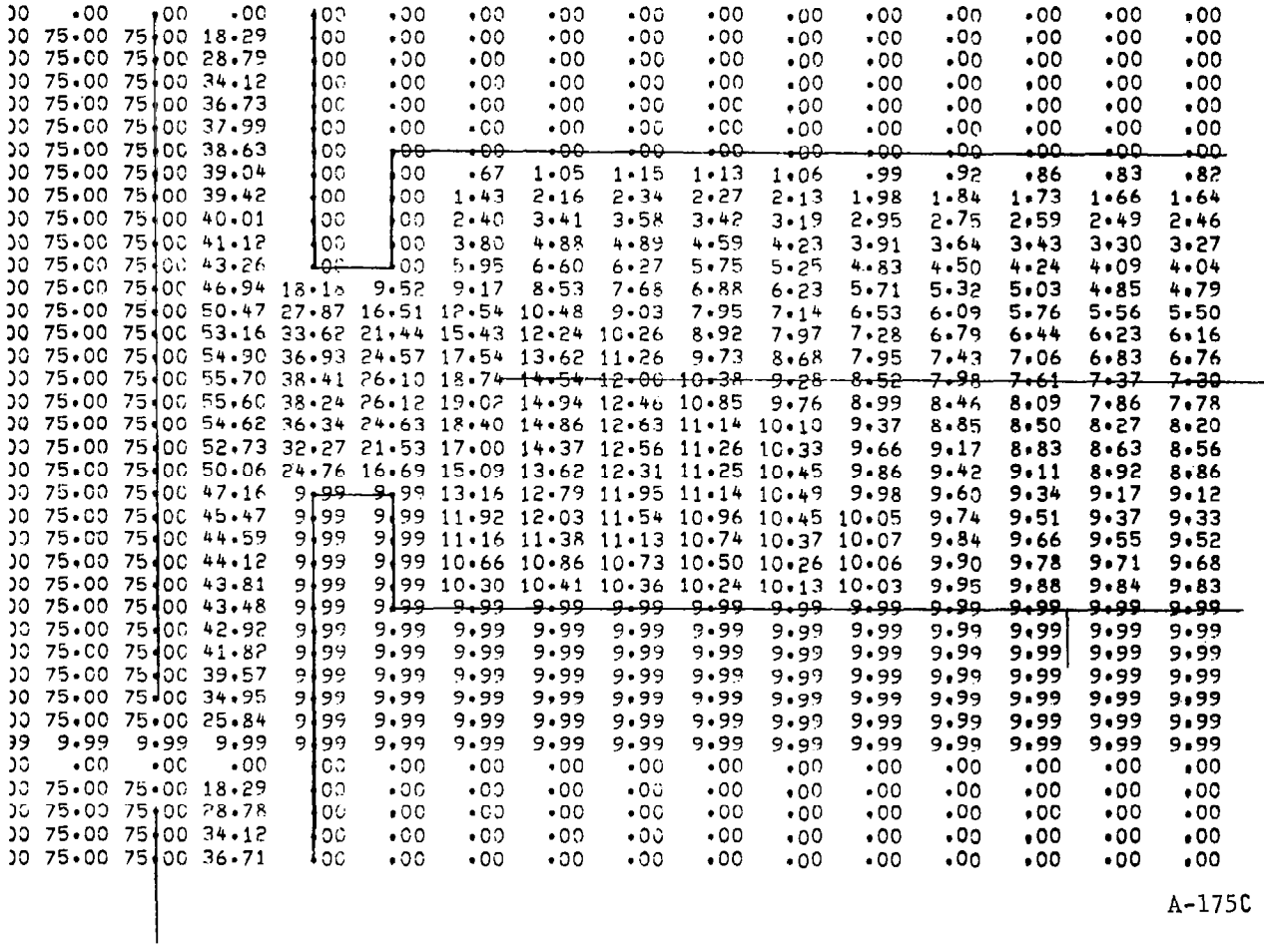

FIGURE 24

Potential Distribution of the Ionizing Region - Ridges .010" x .025"

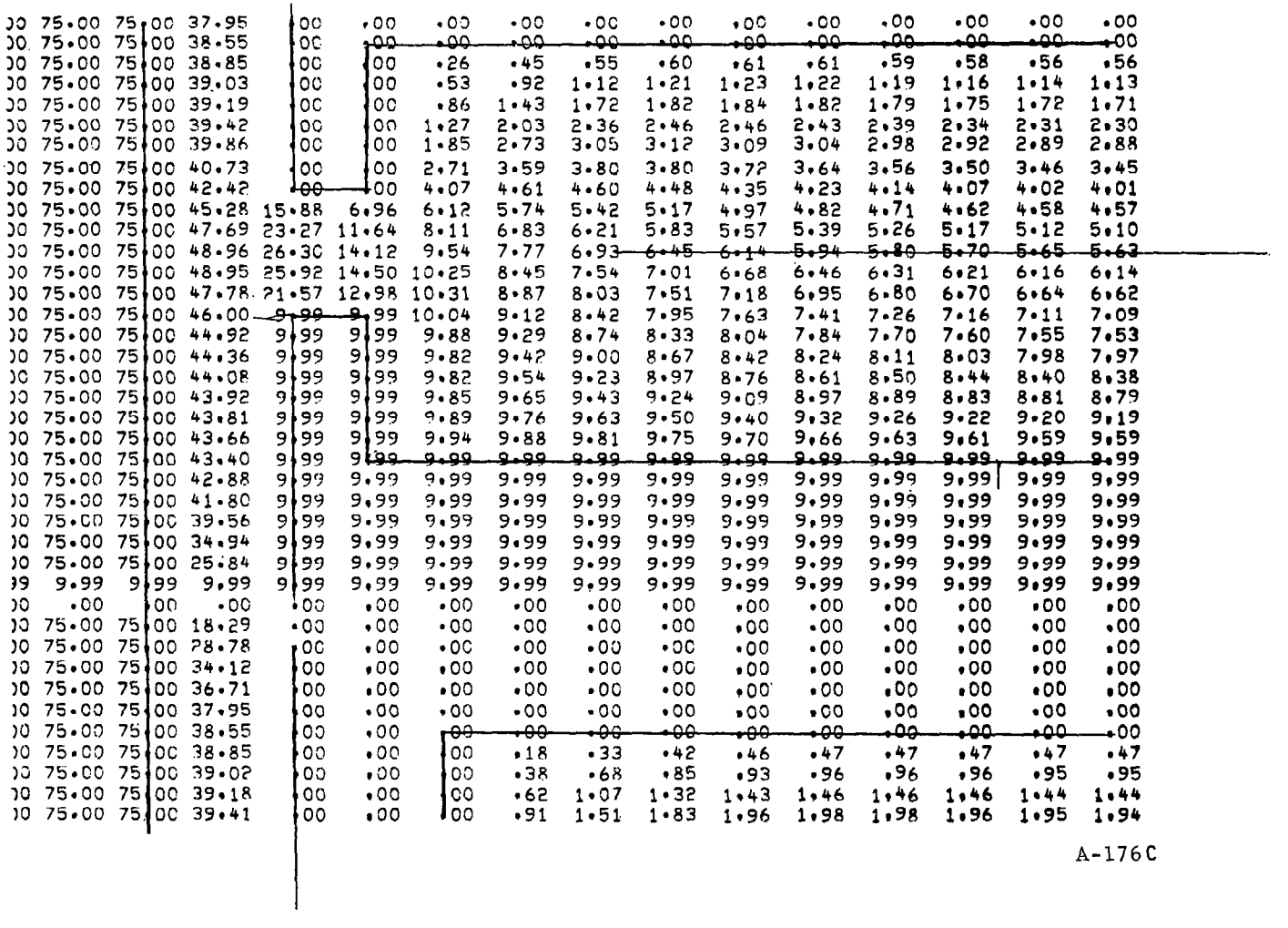

FIGURE 25
Potential Distribution of the Ionizing Region - Ridges .010" x .035"

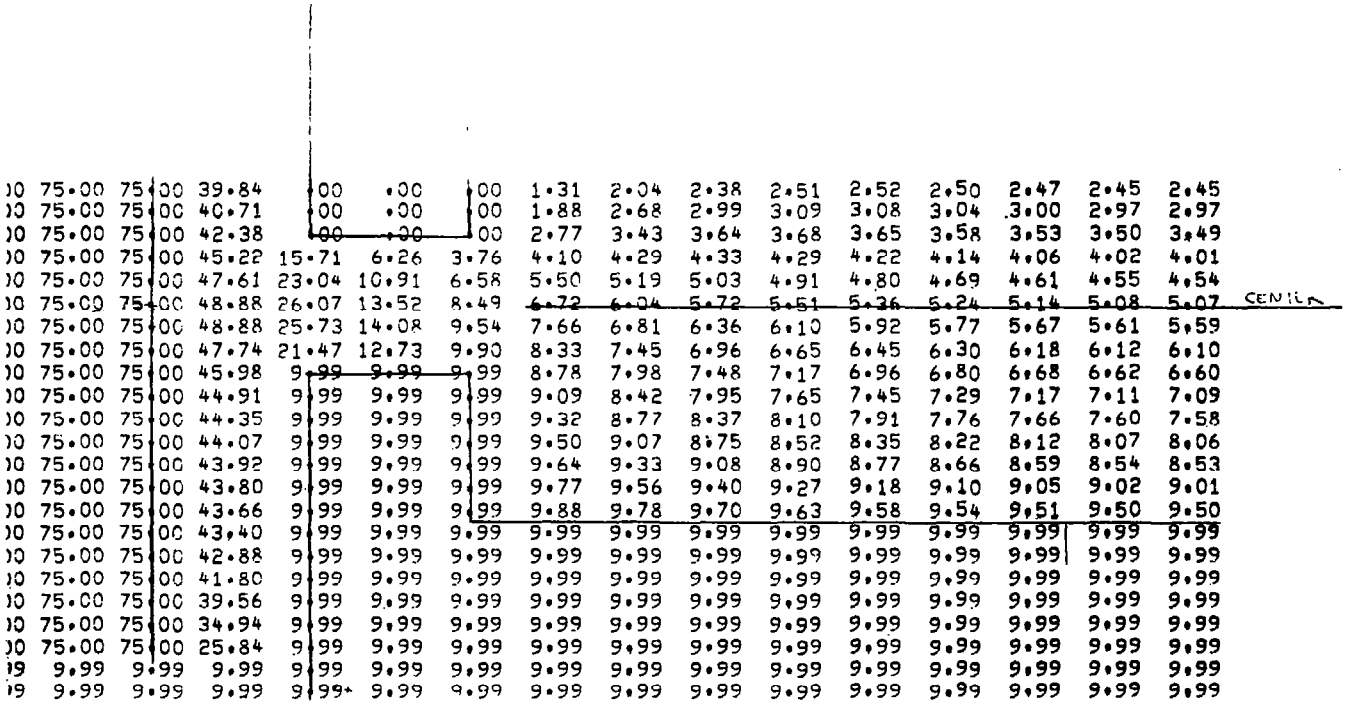

)0	75.00	75	00	39.84		00	.00	00	1.31	2.04	2.38	2.51	2.52	2.50	2.47	2.45	2.45
)0	75.00	75	00	40.71		00	.00	00	1.88	2.68	2.99	3.09	3.08	3.04	3.00	2.97	2.97
)0	75.00	75	00	42.38		00	.00	00	2.77	3.43	3.64	3.68	3.65	3.58	3.53	3.50	3.49
)0	75.00	75	00	45.22	15.71	6.26	3.76	4.10	4.29	4.33	4.29	4.22	4.14	4.06	4.02	4.01	
)0	75.00	75	00	47.61	23.04	10.91	6.58	5.50	5.19	5.03	4.91	4.80	4.69	4.61	4.55	4.54	
)0	75.00	75	00	48.88	26.07	13.52	8.49	6.72	6.04	5.72	5.51	5.36	5.24	5.14	5.08	5.07	CENTER
)0	75.00	75	00	48.88	25.73	14.08	9.54	7.66	6.81	6.36	6.10	5.92	5.77	5.67	5.61	5.59	
)0	75.00	75	00	47.74	21.47	12.73	9.90	8.33	7.45	6.96	6.65	6.45	6.30	6.18	6.12	6.10	
)0	75.00	75	00	45.98	9.99	9.99	9.99	8.78	7.98	7.48	7.17	6.96	6.80	6.68	6.62	6.60	
)0	75.00	75	00	44.91	9.99	9.99	9.99	9.09	8.42	7.95	7.65	7.45	7.29	7.17	7.11	7.09	
)0	75.00	75	00	44.35	9.99	9.99	9.99	9.32	8.77	8.37	8.10	7.91	7.76	7.66	7.60	7.58	
)0	75.00	75	00	44.07	9.99	9.99	9.99	9.50	9.07	8.75	8.52	8.35	8.22	8.12	8.07	8.06	
)0	75.00	75	00	43.92	9.99	9.99	9.99	9.64	9.33	9.08	8.90	8.77	8.66	8.59	8.54	8.53	
)0	75.00	75	00	43.80	9.99	9.99	9.99	9.77	9.56	9.40	9.27	9.18	9.10	9.05	9.02	9.01	
)0	75.00	75	00	43.66	9.99	9.99	9.99	9.88	9.78	9.70	9.63	9.58	9.54	9.51	9.50	9.50	
)0	75.00	75	00	43.40	9.99	9.99	9.99	9.99	9.99	9.99	9.99	9.99	9.99	9.99	9.99	9.99	
)0	75.00	75	00	42.88	9.99	9.99	9.99	9.99	9.99	9.99	9.99	9.99	9.99	9.99	9.99	9.99	
)0	75.00	75	00	41.80	9.99	9.99	9.99	9.99	9.99	9.99	9.99	9.99	9.99	9.99	9.99	9.99	
)0	75.00	75	00	39.56	9.99	9.99	9.99	9.99	9.99	9.99	9.99	9.99	9.99	9.99	9.99	9.99	
)0	75.00	75	00	34.94	9.99	9.99	9.99	9.99	9.99	9.99	9.99	9.99	9.99	9.99	9.99	9.99	
)0	75.00	75	00	25.84	9.99	9.99	9.99	9.99	9.99	9.99	9.99	9.99	9.99	9.99	9.99	9.99	
)9	9.99	9.99	9.99	9.99	9.99	9.99	9.99	9.99	9.99	9.99	9.99	9.99	9.99	9.99	9.99	9.99	
)9	9.99	9.99	9.99	9.99	9.99	9.99	9.99	9.99	9.99	9.99	9.99	9.99	9.99	9.99	9.99	9.99	

A-177C

FIGURE 26

Potential Distribution of the Ionizing Region - Ridges .020" x .035"

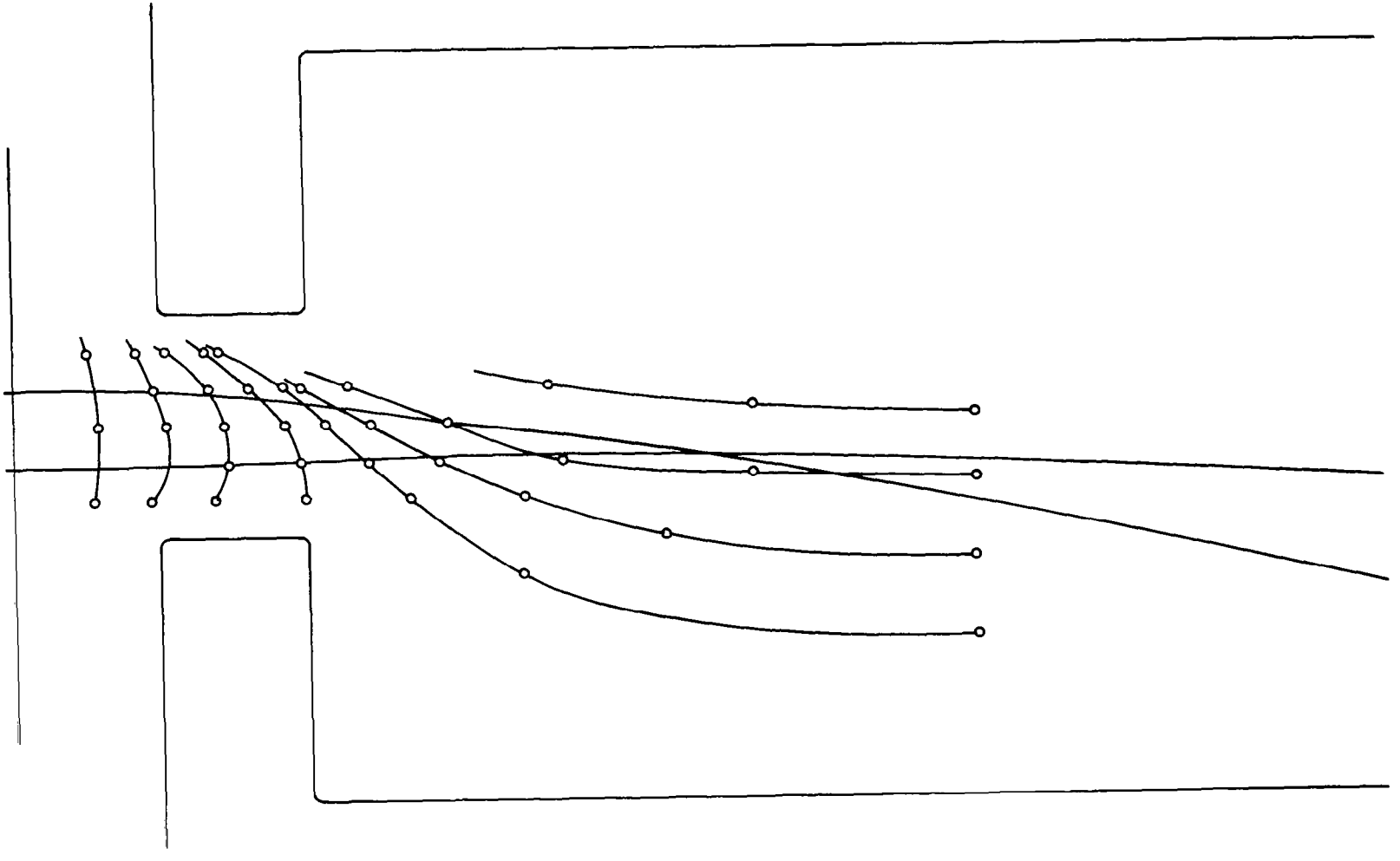

FIGURE 27
Electron Beam Trajectory Plot

the beam divergence can be counteracted. The reduction of the electron accelerator potential, as required to reduce the penetration field into the ionizing region, will reduce this focusing effect and this may lead to greater electron beam spreading. A compromise setting may be necessary. As shown in Figure 27 the deflection of the electron beam due to the 10 volt difference between the repeller and the accelerator is tolerable. Another effect upon the electron beam is space charge. If a ribbon beam is assumed then:

$$y = y_o + \frac{I}{V^{3/2}} \quad \frac{z^2}{4k} \quad \text{inches}$$

$$k = 10.4 \times 10^{-6} \text{ amps/volt}^{3/2}$$

I = beam current/unit length (amps/inch)

V = electron beam energy (volts)

For this problem

$$y_o = 0.005,$$

$$I = \frac{25 \times 10^{-6} \text{ amps}}{.040"} \approx 6.25 \times 10^{-4}$$

$$V = 100 \text{ volts},$$

$$z = .260"$$

The result is $y \approx 0.015"$ which represents the half beam thickness at the anode if there were no focusing effects. Actually the space charge effects will tend to lengthen the distance to the cross-over point shown in Figure 27, and it is likely that the net effect of the space charge will be to reduce the electron beam spread. The accelerator aperture was reduced from 0.020" diameter to 0.022" diameter as suggested in remedy d.

The change in the electron accelerator dimensions was determined by conductance calculations. The electron accelerator aperture is a tapered rectangular duct and therefore equations had to be developed for the conductances. The same equations were applied to the ion exit aperture. The development of the equations and tabulated values are given in Appendix A, Project Note 16 .

Having established the dimensions of the electron accelerator aperture it is worthwhile to consider the transmission efficiency of the electron gun. On the OGO-F ion source the maximum transmission efficiency for electrons through a duct with a minimum cross-section of 0.060" x 0.010" was 35%. Typically, however, when final operation was obtained the value was closer to 30%. With the aperture width reduced to 0.040" the transmission efficiency will be reduced to about 20%. This will not affect the ion source sensitivity since the controlling parameter is ionizing current per unit width, provided that the beam width is sufficient to provide ions over the entire accelerator aperture and that the field curvature does not draw ions from an area greater than the accelerator aperture. These conditions are satisfied in this ion source.

At this point in the analysis it was possible to establish the interface between the ion source and the support electronics. These values are given in Table 11. The regulations and ripples are only specified at those points which are at the top of a supply. The other electrodes should experience the values corresponding to the supply which they are on. A schematic diagram of the voltage divider system is shown in Figure 47. The other electronics interface information is given in the discussion of the electronics modules.

Finally, a cross-section drawing of the ion source is shown in Figure 28, and photographs of the assembly with z-axis focus electrodes are shown in Figures 29 and 30. Details of the mechanical design are given in the Mechanical Design and Packaging Section.

TABLE 11

Electronics Interface Specifications

	Electrode	Voltage Max	Voltage Nom	Voltage Min	Set Range	Regulation	Ripple P-P	Current (a)	Remarks *
1.	Repeller	15*	10*	5*			1%		W/R Accelerator
2.	Accelerator	240*	225*	200*					For B = 4400, 4000, 3800 gauss
3.	Ion Focus A	0*	0*	-50*					W/R Accelerator
4.	Ion Focus B	0*							W/R Accelerator
5.	Exit Slit	0*	0*	0*					Grounded
6.	z-Axis Focus 1	0*		-100*					W/R Accelerator
7.	z-Axis Focus 2	0*		-100*					W/R Accelerator
8.	Electron Accelerator	50*	25*	0*		±1%		30-300	W/R Accelerator
9.	Electron Focus A	30*	15*	0*				0-1	W/R Filament Reference
10.	Electron Focus B	30*	15*	0*				0-1	W/R Filament Reference
11.	Filament Reference	-90*	-100*	-110*		±0.25%		50-350	W/R Accelerator
12.	Filament Shield	0*	-10*	-15*				0	W/R Filament Reference
13.	Anode	50*	20*	0*		±0.25%	1%	20-50	W/R Accelerator

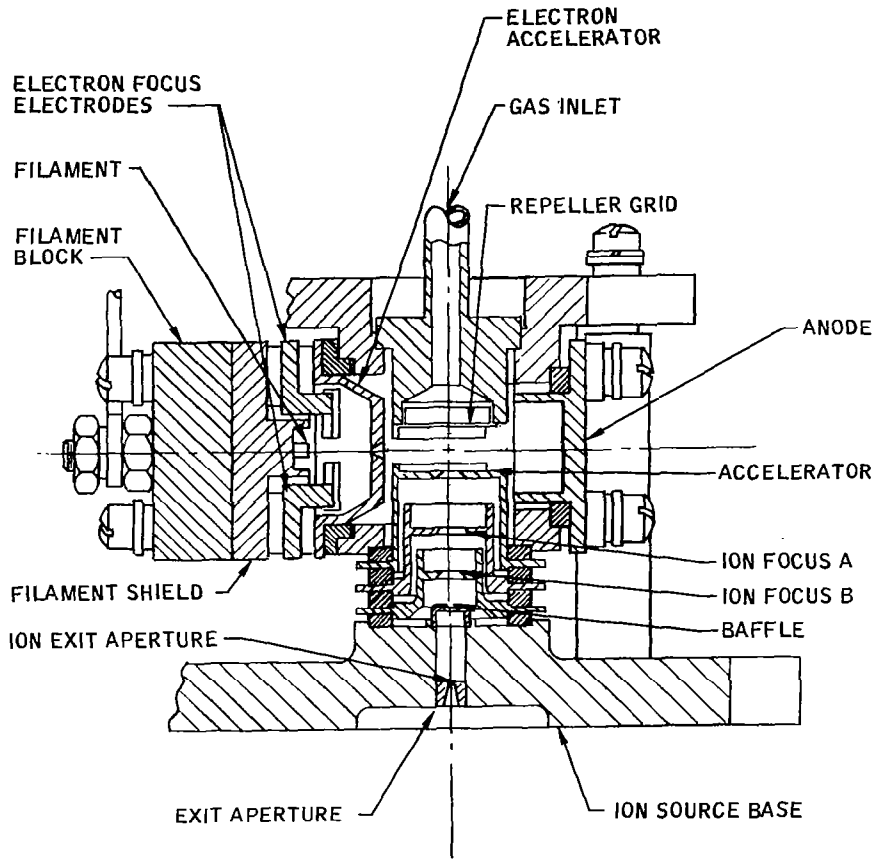

FIGURE 28
Ion Source Assembly

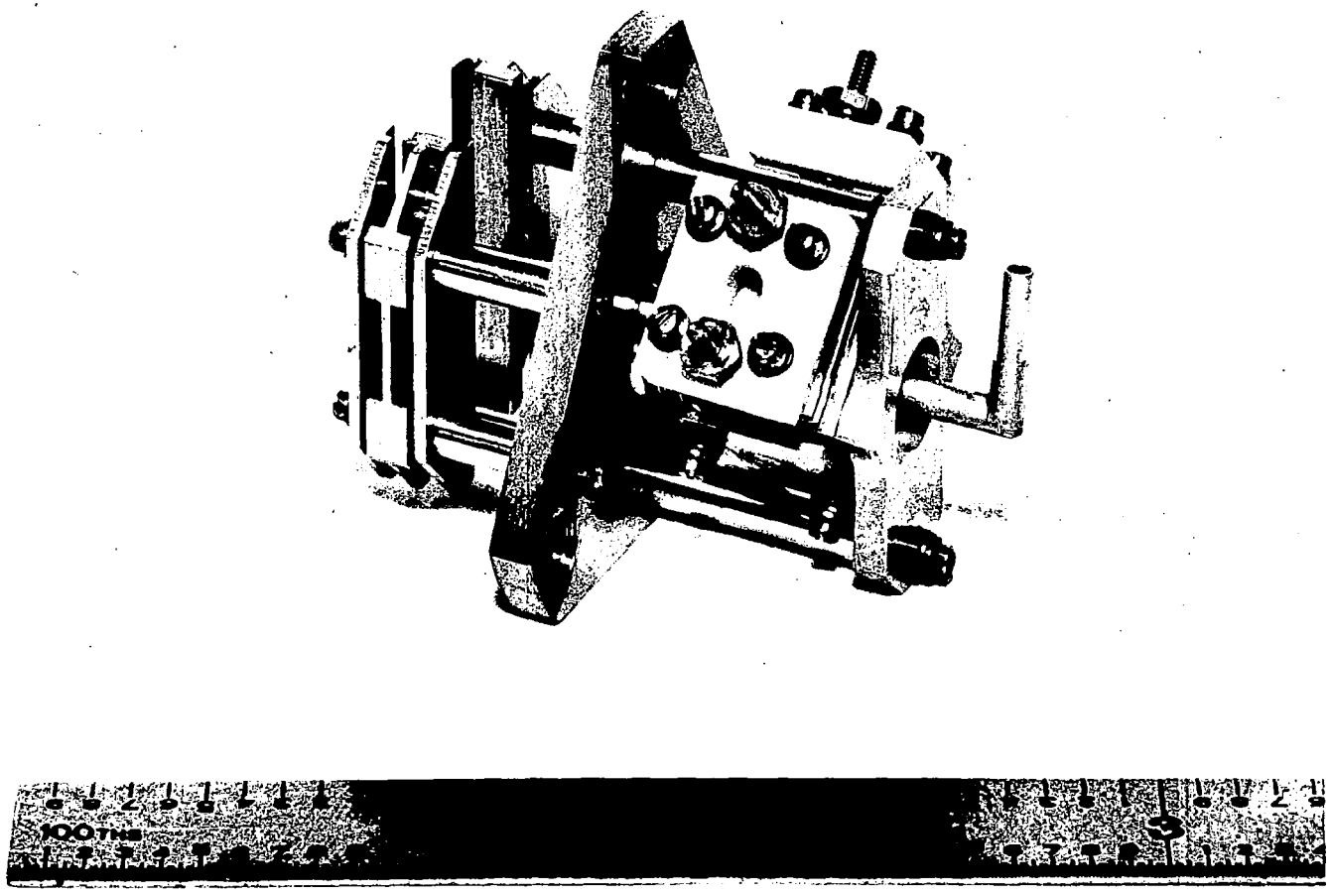

FIGURE 29
Two Gas Sensor Ion Source

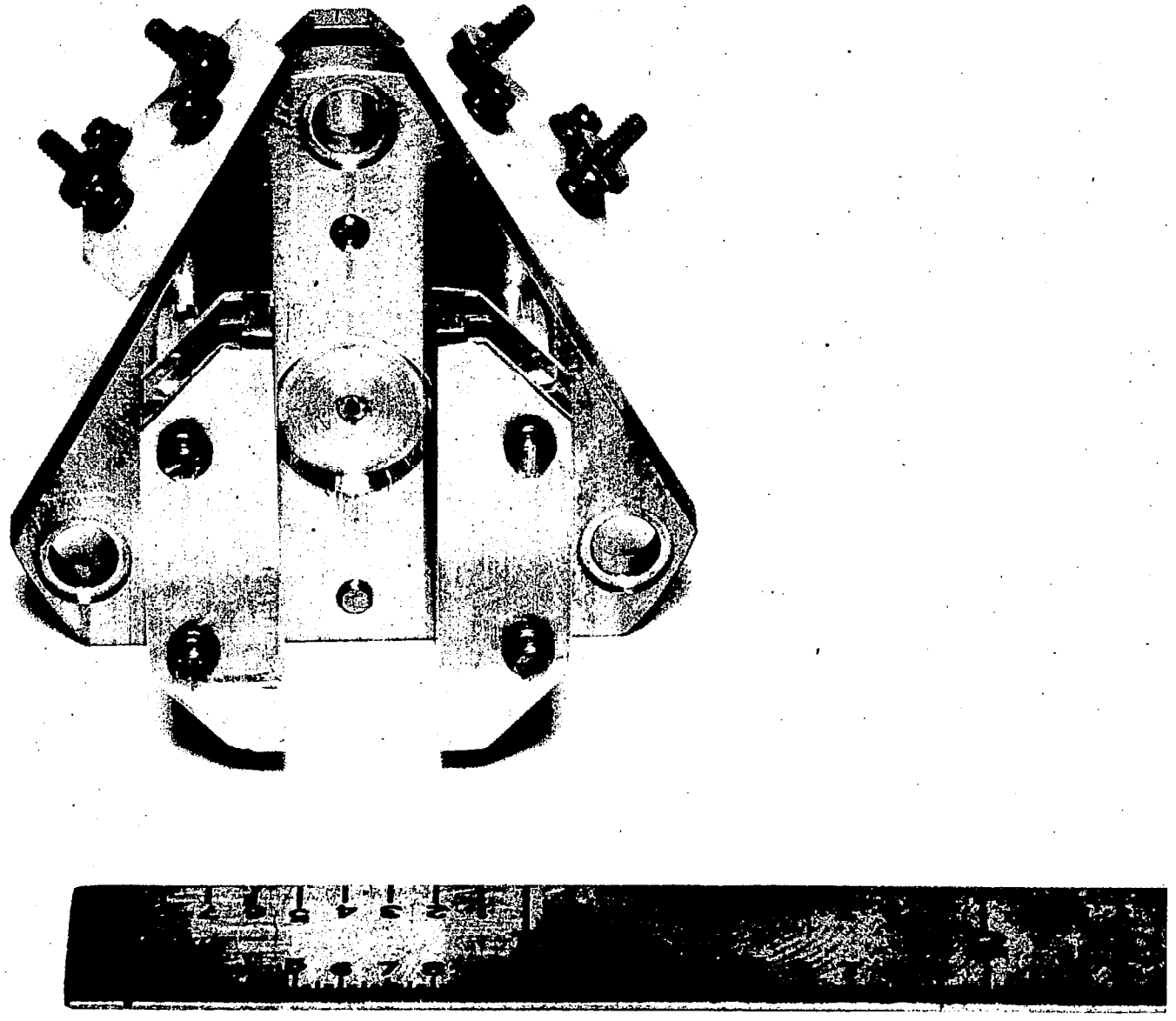

FIGURE 30
Two Gas Sensor Ion Source Showing Object Slit

SAMPLE INLET AND PUMPING SYSTEMS

Atmospheric Sampling System

The upper pressure limitation of the cabin atmosphere is designed at 400 torr, and the maximum designed ion source pressure is 2×10^{-4} torr. Therefore, a pressure dividing network was required which will not distort the gas mixture, such that the partial pressures of the sample admitted to the ionizing region remain directly proportional to the sample constituents of the cabin atmosphere at the point where the sampling takes place. A detailed analysis of various methods of gas transport systems was performed in the conceptual design study report on the first phase of this contract. The conclusions of that analysis indicated that the recommended transport method be composed of a viscous flow channel utilizing a capillary line to an intermediate sampling point from which a molecular flow leak will extract a portion of the sample into the ionizing region of the mass spectrometer.

A principle of operation has been studied and analyzed by C. F. Robinson[8] whereby the sample flow remains continuous from the pressure of sample atmosphere to a first vacuum system while maintaining the gas composition relatively constant. At an appropriate point along the flow line, i.e., where the pressure is compatible with the design, a small portion of the gas is sampled through an aperture by molecular flow into the mass spectrometer, and then to a second vacuum system.

In principle, the extreme range of pressure division can be achieved since the viscous flow and the molecular flow regions are each a pressure dividing system. However, two difficulties may arise. First, the velocities of flow can reach the speed of sound which leads to a breakdown of the defined operating conditions and to changes in the mixture.

Secondly, large degrees of pressure drops will cause separation of the various species in the mixture owing to the premature changes from viscous flow to molecular flow.

To overcome the difficulties stated above, two types of tapered flow lines are considered, the constant velocity line, and the constant diameter to mean-free-path ratio (D/λ) line. The constant velocity line allows one to maintain the velocity at some prescribed fraction of the speed of sound (in the neighborhood of 0.01 to 0.2 times); first, so that turbulent flow is avoided and secondly, so that sonic separation of the composite materials does not take place. The constant D/λ line allows one to maintain a large and constant D/λ as the pressure drops along the line. The degree of viscous flow remains the same and separation of the viscous species in the mixture is avoided. The derivation of the governing equations and detail calculations are shown in Appendix A, Project Note Number 17.

The final inlet and pump out line system includes the following combinations of flow lines. A constant diameter line is used at the entrance to get the velocity to a desired value quickly; a constant velocity section is used for the bulk of transport and particularly through the intermediate sampling point. (A small portion of sample goes into the ion source through an aperture.) A constant D/λ section is used after the sampling point where transport speed is not important but chiefly to avoid the flow separation that can be reflected upstream to the sample point; and finally, the line is terminated in a critical orifice in order to maintain bulk flow without separation of the sample components.

The parameters to which the atmospheric sampling system must interface are defined by the external environment of the cabin, the design parameters which optimize the mass spectrometer, and the available pumping system. The maximum expected cabin pressure is chosen to be 400 torr and the maximum ion source pressure is designed at 2×10^{-4} torr, as stated previously. A two meter capillary line, being a combination of a constant diameter line and a constant velocity line, was chosen as a compromise in order to obtain a proper time response, and still maintain the ability to sample the cabin atmosphere from a variety of positions, if necessary.

The maximum gas flow rate was then set at 10 torr-cc/second. This flow rate corresponds to an extended weight of the atmosphere of .37 pound of gas, .17 pound of N_2 and .20 pound of O_2, over the 120-day mission. It is felt, however, that this additional weight of sample gas required for operation of the instrument should not be included in the weight of the package, since the expected cabin leakage rate is specified at 0.3 pounds per hour which corresponds to an extra payload weight of 864 pounds for a 120-day mission. Thus, it is believed that due to the uncertainties in the cabin leakage rate, the addition of .043% of the extra gas payload expected is of no consequence.

The delay time associated with the gas transport system is calculated to be 1.53 seconds. This means that a change in the atmospheric constituents of the cabin will be reflected in the ion source after a delay period of this value. An approximate calculation performed in the study phase of this contract indicated that the response time of the cabin would be about 15 seconds, so that the additional delay time imposed by the sampling system becomes small compared to that of the cabin. Due to the condensible nature of water vapor, the delay time associated with the measurement of this mass will necessarily be considerably larger than that determined for the other gases, due to condensation on the walls of the capillary until equilibrium has occurred. This may not be too important, since the rate of change of the amount of water vapor is very small compared to the other masses of interest, and the importance of the accurate measurement of this quantity is not nearly as significant as that of the others. If more accurate knowledge is required with a faster time response, there are two possible solutions which could overcome this difficulty. First, direct heating of the capillary and inlet system can be applied. This solution reduces the amount of condensation occurring at the walls, and consequently equilibrium is established faster along the walls of the system. The disadvantage to operation of the system in this manner is imposed by the additional power required to heat the inlet system. The second solution involves the possibility of obtaining a capillary line of Teflon, since it is known that

this material does not condense water vapor as readily as a metal line, and thus the flow time associated with the water vapor can be substantially reduced. This solution would require further analysis to determine its potential improvement and its effects upon the other system variables and parameters.

For the simplification of manufacturing, the tapers are replaced approximately by using constant diameter segments. Previous experience has shown that the result should be very close to the real tapered line. Figures 31 and 32 give the dimensions of the truely tapered lines, and the approximately stepped lines respectively.

Pumping System

A pumping system is required in order to maintain the necessary interval vacuum within the mass spectrometer against the incoming sample flow to be analyzed. According to the previous calculations in the Ion Source, a pumping speed of four liters/second is required to obtain a differential pumping factor of 100 at the ion source. This will reduce the filament interaction with the sample to an acceptable level. Conclusions from the analysis performed in the Phase I study show that the most desirable pumping system utilizes outer space to maintain the necessary interval vacuum within the analyzer.

In Phase I it was assumed that interfacing the sensor system with the spacecraft to utilize outer space as a pump would require approximately an eighteen inch long pump out line. It was found that a 1-1/8 inch ID tube of this length will give a gas conductance of 3.94 liters/second which is approximately the necessary pumping speed. The weight associated with a stainless steel tube of these proportions, having a wall thickness of 1/32 inch, is 0.47 pound, however, an aluminum line is being considered for this interface which would reduce this weight to about 0.16 pound.

A second pump out line connected to the by-pass line of the inlet system is also required, situated in such a manner that the pump out of the gas could not enter into the pump out tube of the mass spectrometer. The additional weight of this line, as determined in the Phase I study, was estimated as 0.2 pound.

At the surface of the spacecraft, it is then necessary to utilize an effective means of sealing the pump out tube so that the instrument's internal vacuum can be maintained during launch, and contamination of walls of the pumping system is avoided. Another necessity is to enable a means of connecting a vacuum pump to the system for preflight checkout of the instrument operation. This last requirement would be most easily satisfied by applying the checkout vacuum system to the external side of the spacecraft, rather than within the cabin where the space available for ground checkout equipment is severely limited. The means of obtaining both a vacuum seal and a connection to the preflight checkout equipment has been investigated resulting in the following three methods:

a. A vacuum valve system

b. A rupture disc system

c. A breakaway hat

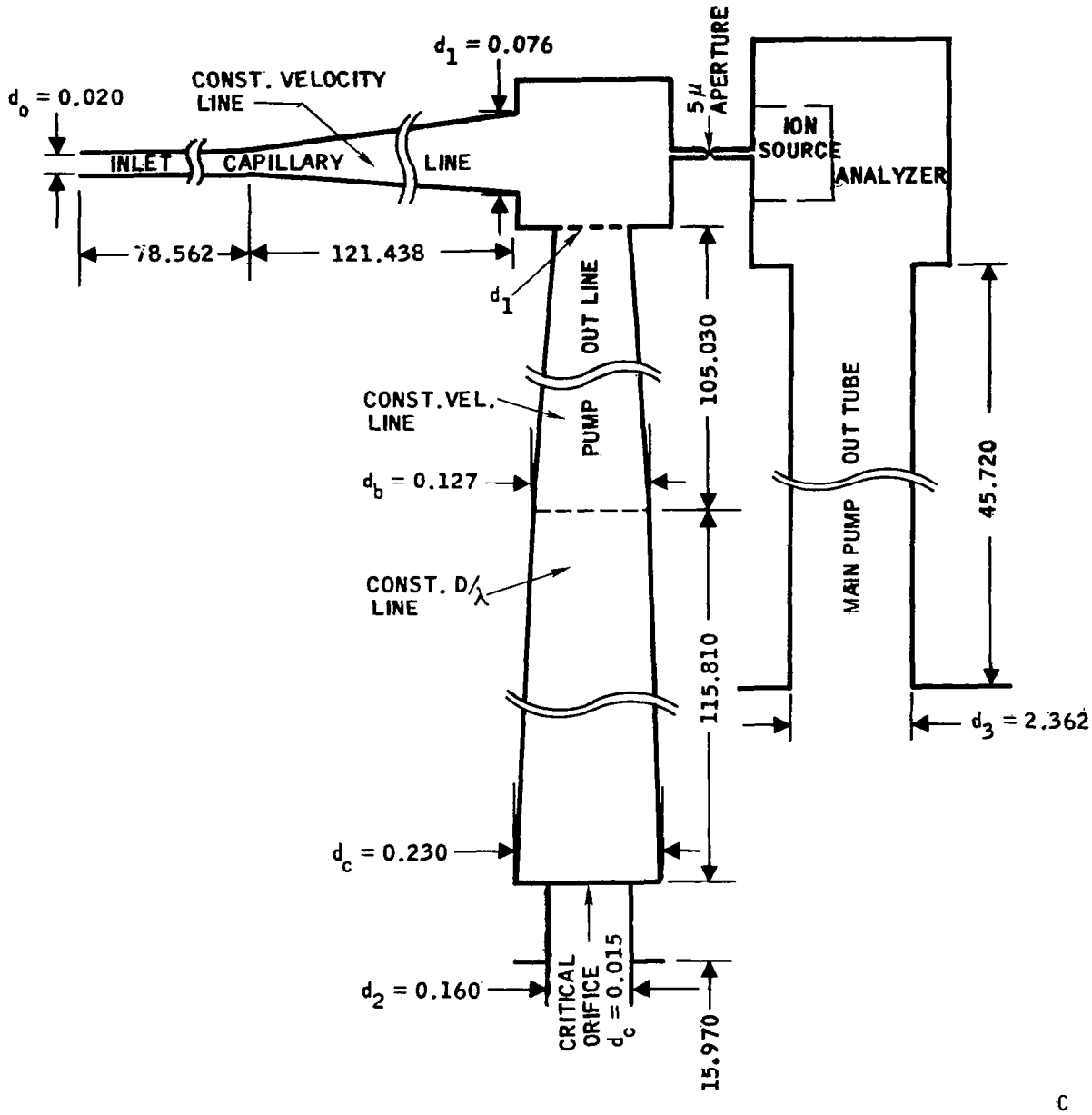

FIGURE 31
Two Gas Atmosphere Sensor System
Inlet and Pump Out Lines System

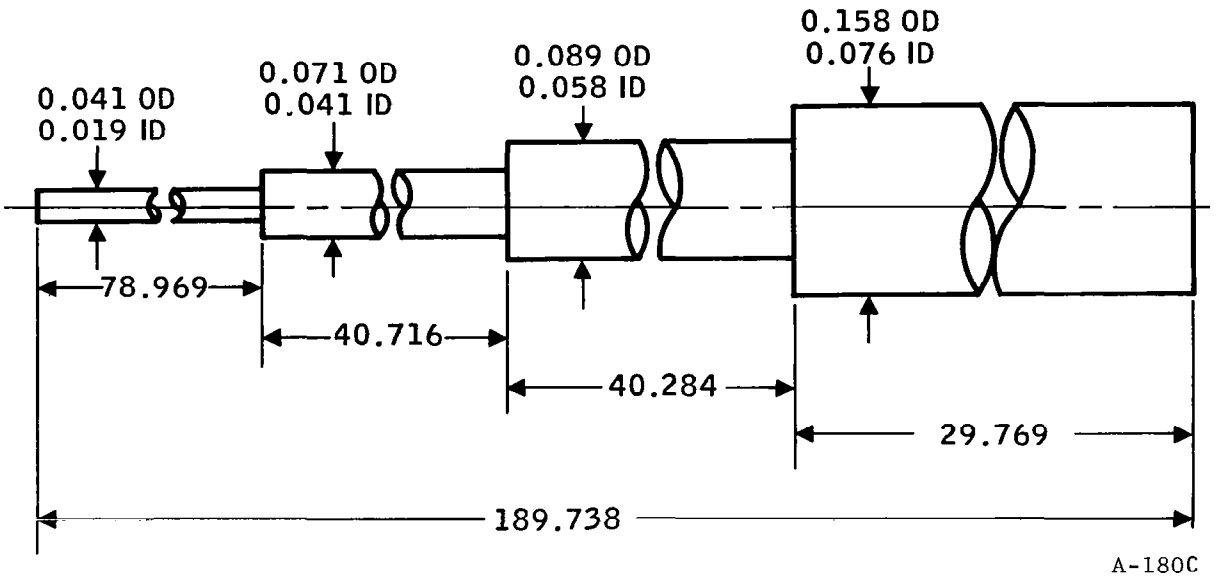

FIGURE 32
Inlet Capillary Line Design

The use of a vacuum valve at the spacecraft surface provides a solution with the capability of opening or sealing the sensor system at any time, either in-flight or during ground checkout. The valve would thus require an extension handle from its position into the spacecraft interior so that manual operation of the valve mechanism could be accomplished by the astronauts. A second valve and extension handle would also be required for the sample pump out system. The positioning of the valves of the spacecraft surface is to keep the inner surface walls of the pump out lines clean during launch such that the pump down time of the instrument upon achieving orbit would not be extended due to excessive outgassing of the wall surfaces. The capability of sealing the system during flight is not a necessary requirement, since the system would be operating continuously once orbit had been achieved, and during launch or re-entry, the astronauts would be operating on their suit loops.

Thus the only time the system need remain sealed would be during launch. The disadvantage to the valve arrangement is the fact that to obtain small light-weight high vacuum valves having high gas conductances, the reliability of the sealing mechanism is generally compromised. Also, the manual operation required of the astronauts may be unacceptable, and while solenoid valves could be investigated, the weight of a solenoid operated valve, such that reliability in the seal is assured, tends to exclude this area.

Rupture discs were examined for their application to a described pump out system. These discs would be placed at the free space end of the pump out tube, and require a positive internal pressure in the pumped area to rupture the seal. Consequently, a means of establishing a positive interval pressure is required, such as a pressurized vessel of an inert gas connected by valves to the sample and sensor pump out tubes. After rupture is achieved, the system must then be evacuated of the gas used for pressurization before the sensor system could be activated. A secondary problem involves the method by which the pump out lines would be sealed under vacuum following preflight checkout. At present, this is being examined, however, the necessary complexity of the system appears to rule out this type of sealing mechanism.

A breakaway hat shows the most promise for obtaining a vacuum tight seal and yet allowing preflight checkout to be carried out in the most effective manner. A breakaway hat consists of a metal cover hat separated from a base by a ceramic ring and joined by two ceramic-to-metal seals. Once orbit is obtained, Teflon sealed pyrotechnic chisels break the ceramic, and springs eject the hat and break off mechanism. These devices have been proven as a satisfactory solution in this type of application on previous unmanned satellites and rocket vehicles. A current design, presently being used on a quadruple mass spectrometer for analysis of the upper earth's atmosphere from the OGO-F satellite, is shown in Figure 33, reproduced with the permission of the University of Michigan[9]. This particular design can be adapted directly to the Two Gas Sensor System, having outer and inner dimensions that require almost no redesign, and a total weight of 0.69 pound, including the squib firing mechanism. Designs similar to this one, in larger sizes, have also been flown on mass spectrometers on Explorers 17 and 32, and various sub-orbital rocket payloads, without any failures in their operation. While two squibs are utilized, the second is a

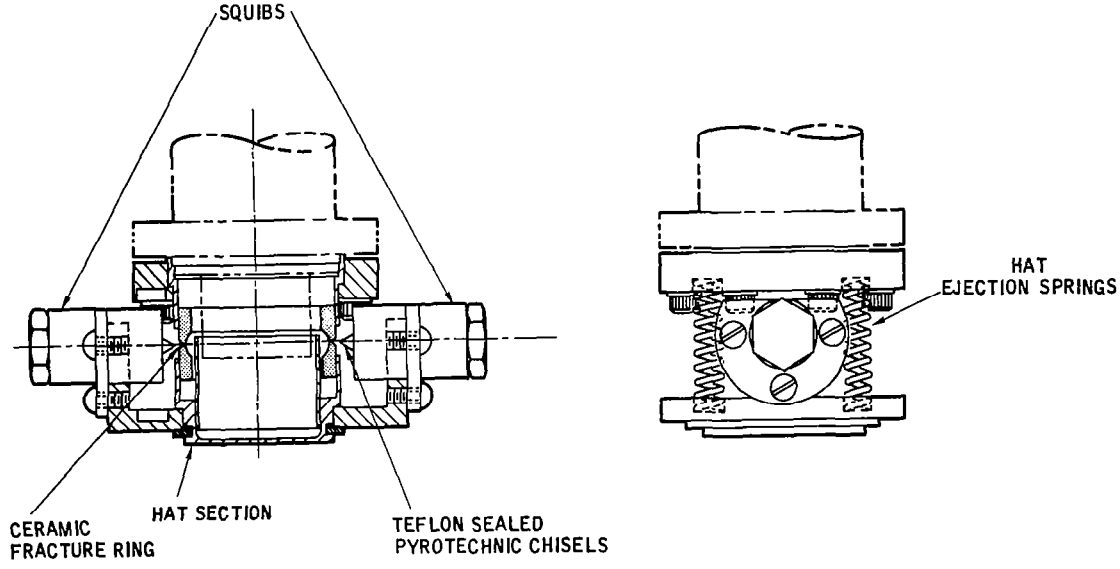

FIGURE 33
Breakaway Hat

redundant unit, one being sufficient to fracture the ceramic and eject the hat section. The use of a breakaway hat also simplifies the pump out interface of the sample bypass line. As shown in Figure 34, the bypass tube would enter into the main pump out tube and run down to the opening and slightly past the orifice of the fractured ceramic.

In this arrangement, gas evolving from the sample bypass line could not re-enter into the mass spectrometer pump out line. This solution thus requires only one interface through the outer skin of the cabin, simplifying the interfacing demands. Preflight checkout would be accomplished by attaching a vacuum system to a copper pinch-off tube brazed into the breakaway hat, and just before launch, the pinch-off tube sealed and the vacuum system removed. Utilizing a 3/8 inch ID pinch-off tube which is three inches long would limit the pumping speed to about 1.2 liters/second during the checkout phase. This would raise the analyzer pressure during ground checkout to about 6.7×10^{-6} torr for an ion source pressure of 2×10^{-4} torr (thus lowering the differential pumping), however, data taken on the previously built OGO-F ion sources indicates that the electron gun characteristics do not change at this level, and in fact, at higher pressure stability of the source operation has been maintained.

On the basis of the analysis above, it is therefore recommended that the breakaway hat be utilized as the sealing mechanism for the pumping system, which gives simplicity and reliability to both the maintenance of the interval vacuum of the sensor system, and the interfacing demand upon the spacecraft.

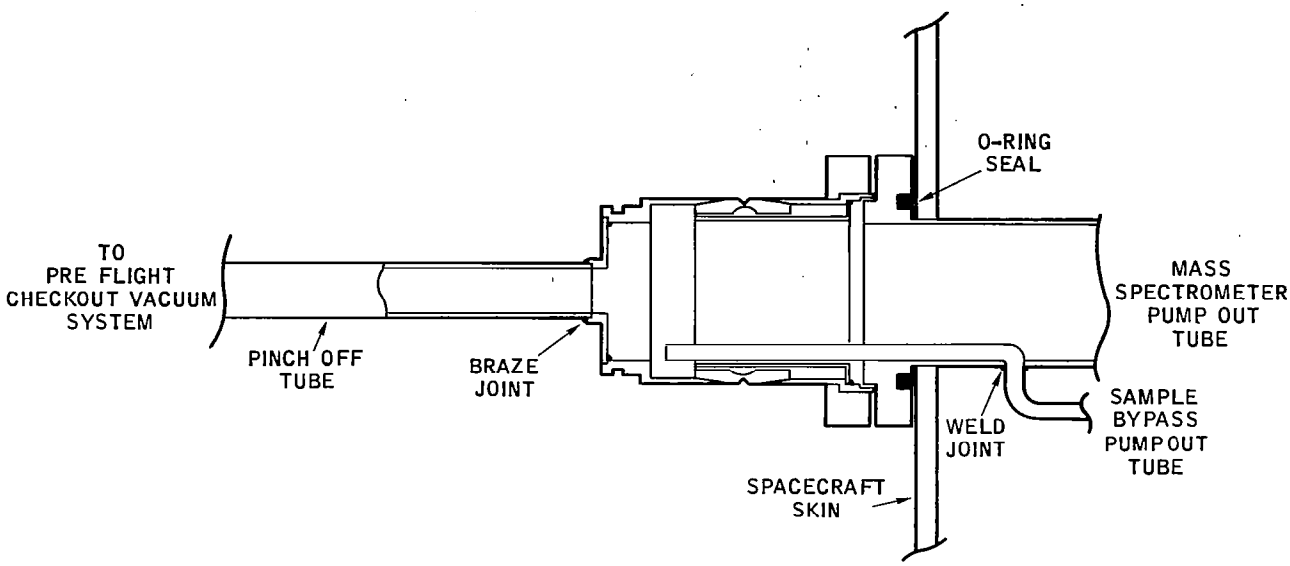

FIGURE 34
Conceptual Application of Breakaway Hat

SENSOR SYSTEM SUPPORT ELECTRONICS SUBSYSTEM

SUBSYSTEM DESCRIPTION

The sensor system support electronics subsystem consists of four modules which provide the electrical functions necessary for the operation of the complete Two Gas Atmosphere Sensor System. The four functions are:

a. Provide a controlled amount of power to the filament so that constant electron emission is maintained.

b. Provide the proper potentials to guide the electron beam within the electron gun.

c. Provide the necessary potentials to maintain the ion beam on its proper course.

d. Condition the ion beam signals so that they are useable by a monitoring system and/or a servomechanism control system.

A block diagram of the support electronics is shown in Figure 35. The pertinent parts of the analyzer are also shown (within the dashed lines). A brief description of each module's function will serve as an introduction to more thorough descriptions in the following sections.

Filament Supply and Emission Regulator

This module is a power supply that provides ac power to the filament located within the analyzer housing. The supplied power is controlled by a feedback loop

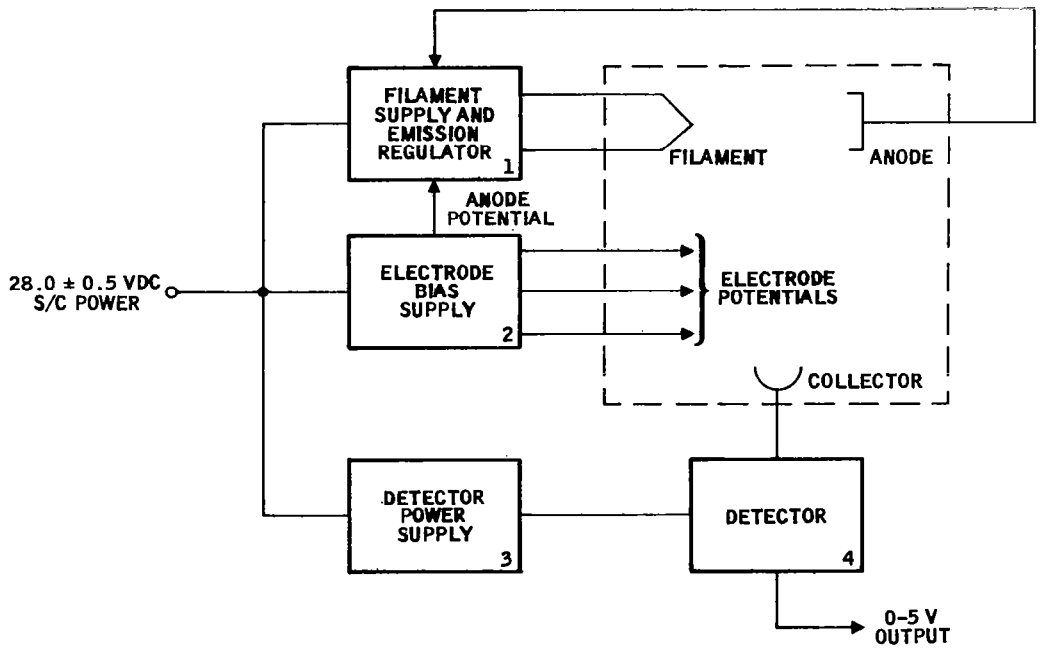

FIGURE 35
Sensor System Support Electronics

so that a preset amount of current flows between the anode and the filament despite changes in the environment. System considerations also require this module to be floated above ground potential by an amount determined by the anode potential.

Electrode Bias Supply

The electrode bias supply module consists of two regulated power supplies that provide the stable voltages required by the analyzer electrodes. It also provides the potential necessary to bias the filament supply and emission regulator module at the proper point for correct system operation.

Detector Power Supply

This module produces the positive and negative voltages required by the detectors. The supply has extremely low noise and drift so that it does not contribute any appreciable deviations to the output of the detectors.

Detectors

The sensor system utilizes four detectors, one for each of the gasses being measured. The detectors amplify the minute ion currents developed in the system to the level required by monitoring units and/or servomechanism control systems. The output varies between zero and five volts proportional to the number of ions reaching the collector.

Design Summary

The three power supply modules operate from a 28 Vdc source and are isolated from the source common by a shielded transformer. The DC/DC converter in the filament supply and emission regulator drives the DC/DC converters in the electrode bias supply so that they all operate at the same frequency and may have their switching transients more readily suppressed.

The modules are constructed of standard discrete electronic components mounted on printed circuit boards. The boards then plug into the mainframe of the system. Each power supply module consists of two open boards while each detector is a single board enclosed in an aluminum case. All the boards are conformally coated to seal out moisture and other detrimental pollutants from the environment. Adjustment controls and test points are provided when required for system set-up and maintenance.

Phase II consisted of designing the circuits and meeting the goals proposed in the Phase I study, as well as constructing an electronics subsystem breadboard and a complete engineering test model. The Phase II design effort closely followed the concepts presented in the Phase I report. There were two exceptions:

a. The electrode bias supply as originally proposed had its regulators on the primary side of the transformers but because of advancements in semiconductor technology, the final design placed the regulators on the secondary side where they could provide better performance.

b. The preferred parts list of the Phase I report was expanded to include recently developed electronic components and thus give the design engineer greater flexibility in circuit design.

During the design effort, emphasis was placed on producing electronics circuits that would provide the best possible system performance while keeping the overall system highly reliable. These goals were implemented by thorough worst-case design analyses of each circuit plus confirmation of the predicted performance by breadboard testing and testing of the complete test model. Three secondary goals were also given consideration during the design phase. A significant effort was made to reduce the weight and volume of the system by packaging the modules so that they would fit around the analyzer housing and take advantage of the open spaces created by the peculiar shape of the instrument. Also, the support electronics were designed to minimize power consumption by making trade-offs between the various types of circuits available to perform each system function.

The engineering test model has demonstrated that the goals established in Phase I have been bettered in each case. The proposed power consumption was 4.88 watts but the subsystem tests have indicated that total power consumption may be as low as 3.5 watts The nominal power consumption of each module is:

a.	Filament Supply and Emission Regulator	2600 mW	(Including Filament Power)
b.	Electrode Bias Supply	550 mW	
c.	Detector Power Supply	150 mW	
d.	Detector (each)	100 mW	

The weight of the electronic subsystem was estimated at 2.5 pounds in the Phase I study but the actual weight of the modules and their associated hardware is approximately 2.0 pounds, apportioned as follows:

a.	Filament Supply and Emission Regulator	10.0 ounces
b.	Electrode Bias Supply	8.0 ounces
c.	Detector Power Supply	4.0 ounces
d.	Detector (each)	2.0 ounces
e.	Miscellaneous Hardware	2.0 ounces

The volumetric goal of Phase I was 93 cubic inches and the actual subsystem volume is 80 cubic inches, with each module contributing the following:

a.	Filament Supply and Emission Regulator	26 cubic inches
b.	Electrode Bias Supply	22 cubic inches
c.	Detector Power Supply	12 cubic inches
d.	Detector (each)	5 cubic inches

The study made in Phase I coupled with the design effort of Phase II has culminated in a support electronics subsystem that not only meets its major goals of performance and reliability but also betters its minor goals of low power consumption, small size, and minimum weight.

FILAMENT SUPPLY AND EMISSION REGULATOR

The filament supply and emission regulator is a special purpose power supply whose function is to maintain emission current at a constant value. It is a closed loop system which samples the emission current (microampere magnitudes) and adjusts the power (watt magnitudes) to the electron gun filament so that the emission current remains constant.

Specifications

a. Output Requirements:

Parameter	Min.	Max.	Units
Voltage		2.0	V Peak
Current	0.5	2.0	Amps Average
Regulation		0.5%	
Dynamic Range of Emission Regulator	50	200	μA

b. Input Requirements:

Parameter	Min.	Max.	Units
Voltage	27.5	28.5	Vdc
Current		120	mA
Ripple & Noise		0.5	Vp-p
Transients		52	V (100 μsec)

c. Other Requirements:

Temperature Range 0°C - 35°C

Circuit Description

The filament supply and emission regulator maintains a constant emission current by controlling the ac power supplied to the filament. A block diagram of this system is shown in Figure 36. Basic operation of the system is as follows: The inverter produces 3.5 KHz, 35 volt square waves which are supplied the 20 Vdc regulator, the output amplifier, and as synchronization pulses to the voltage controlled oscillator (VCO). The error amplifier monitors a voltage proportional to the emission current level, compares it to a reference voltage, and amplifies the difference between the two voltages. The amplified difference voltage is supplied to the input of the VCO. The VCO is reset each time the squarewave sync signal changes polarity. After being reset, the VCO delays a finite time interval and then produces a pulse. The length of the time delay is determined by the magnitude of the error amplifier output voltage. Each VCO output pulse turns the output switching amplifier on. It then remains on until the square wave voltage from the inverter changes polarity. The overall effect is that the output switching amplifier passes only a portion of the squarewave. The percentage of the squarewave passed is determined by the amount of power required by the filament to produce the desired magnitude of emission current.

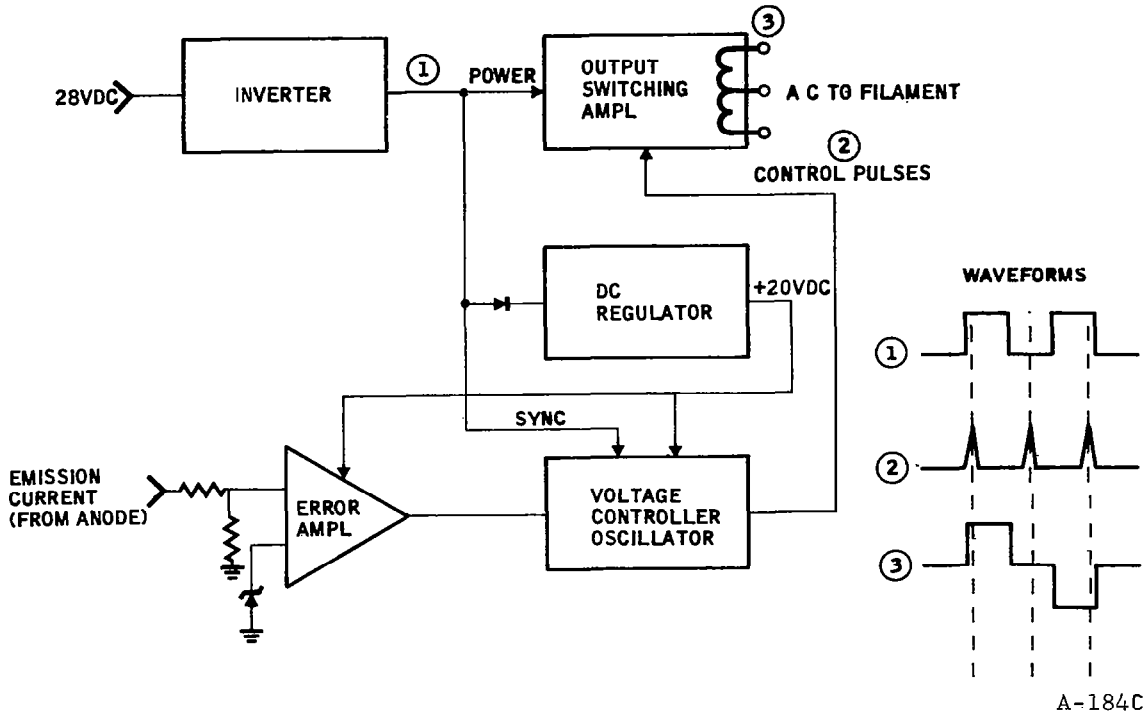

FIGURE 36
Filament Supply and Emission Regulator

The purpose of the inverter is to produce 3.5 KHz, 35 volt squarewaves. The inverter consists of transistors Q201 and Q202 (see Figure 37) and associated circuitry. Switching of the inverter transistors is accomplished by saturation of the core of transformer T204. Transformer T201 operates in a linear (non-saturating) mode. T201 is a power transformer and steps the voltage up from approximately 28 volts to 35 volts. T201 also provides isolation between the emission regulator and output circuitry and the 28 volt power line. Inductance L201 and capacitors C210, 211, 215 and 216 form a low pass filter whose purpose is to keep the inverter switching noise off of the 28 volt power line. Diodes CR201 and CR202 help to reduce voltage transients during switching.

The purpose of the 20 Vdc regulator is to provide regulation of the supply voltage used by the error amplifier and VCO. This regulator (see Figure 38) is a series type consisting of Q205 and Q206 and associated circuitry. The DC input voltage to the regulator is provided by rectifiers CR203 and CR204. Diode CR205 is the reference diode. Transistor Q205 is the series pass transistor and Q206 a difference amplifier. Regulation is accomplished by feeding back a portion of the output voltage to the base of Q206 via R211, R212, and R213. This voltage is compared with the reference voltage across CR205. The difference voltage is amplified by Q206 and Q205 and thus used to adjust the output voltage to a level which minimizes the error voltage.

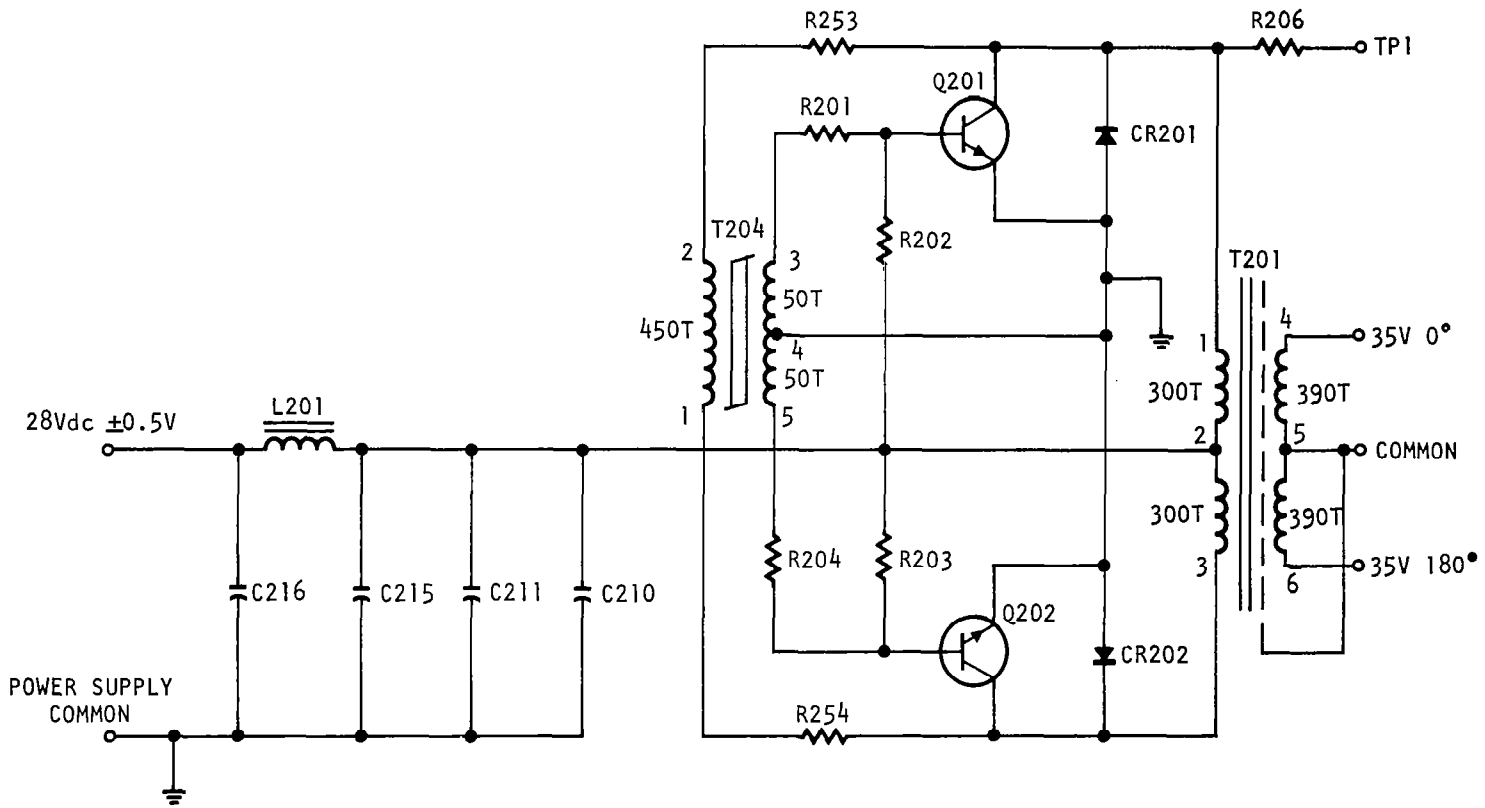

FIGURE 37
DC/AC Inverter

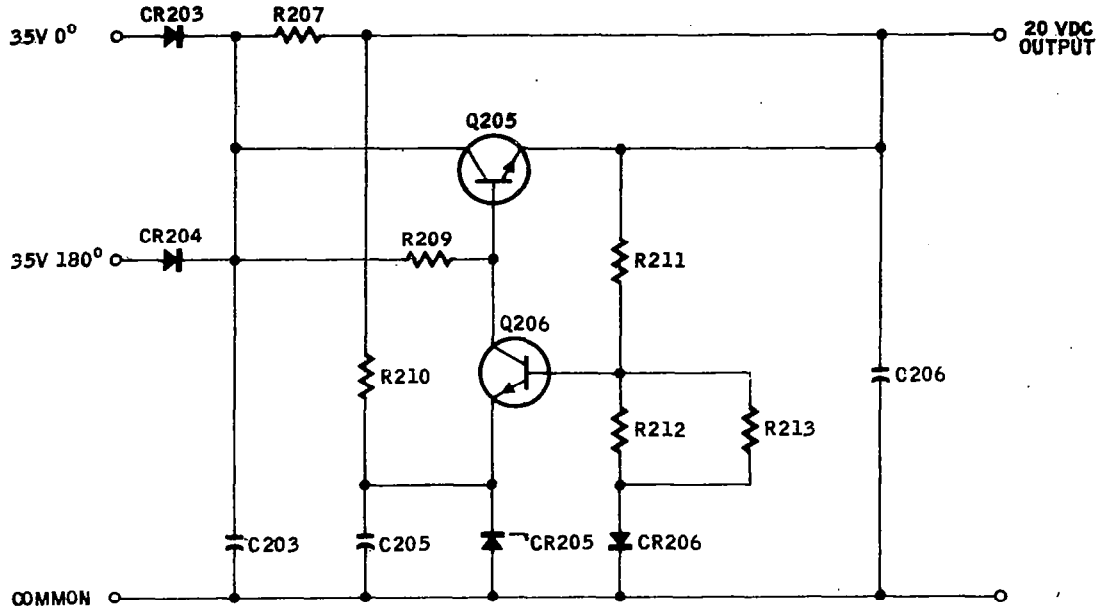

FIGURE 38
20 VDC Regulator

The purpose of the error amplifier, shown in Figure 39, is to compare a voltage proportional to the emission current to a reference voltage and to amplify the difference voltage. The error amplifier consists of transistors Q207, Q208, and Q209. Q209 is a differential amplifier. It consists of a matched pair of NPN transistors contained in a single can for thermal tracking. Diode CR207 provides a temperature stable reference voltage for the amplifier. Diode CR210 provides a stable bias voltage for the base of Q209B. Transistors Q207 and Q208 amplify the output of Q209 and condition the amplifier error signal for operation of the VCO.

The voltage controlled oscillator (VCO) converts the error information contained in the error amplifier output voltage into equivalent pulse repetition frequency information. The VCO is shown in Figure 40. The VCO consists of transistors Q210, Q211, and Q212 and associated circuitry. Q212 is a unijunction transistor which operates as a relaxation oscillator. Capacitor C220 is the oscillator timing capacitor. Charge current for C220 is supplied by R247. The unijunction will "fire" and deliver a pulse to T203 each time the voltage across C220 charges to a specific level (approximately 13 volts). Q211 controls the net amount of charging current that charges the timing capacitor. The value of the collector current of Q211 is proportional to the magnitude of the error amplifier output voltage. Since this current subtracts from the charge current through R247, the charge time of C220 and thus the relaxation oscillator frequency is inversely proportional to the error amplifier output voltage. The purpose of transistor Q210 is to synchronize the VCO by discharging capacitor C220 each time the

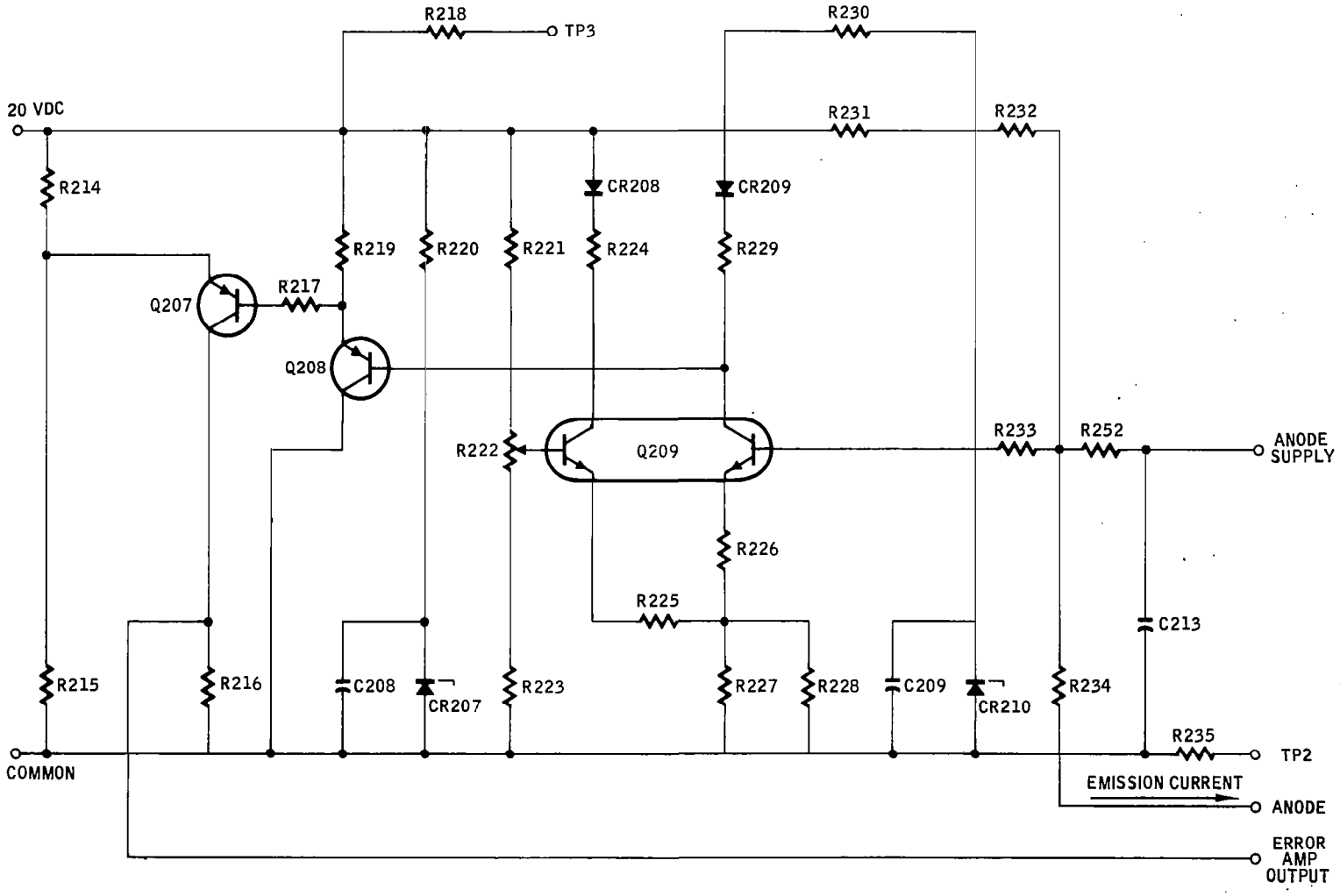

FIGURE 39
Error Amplifier

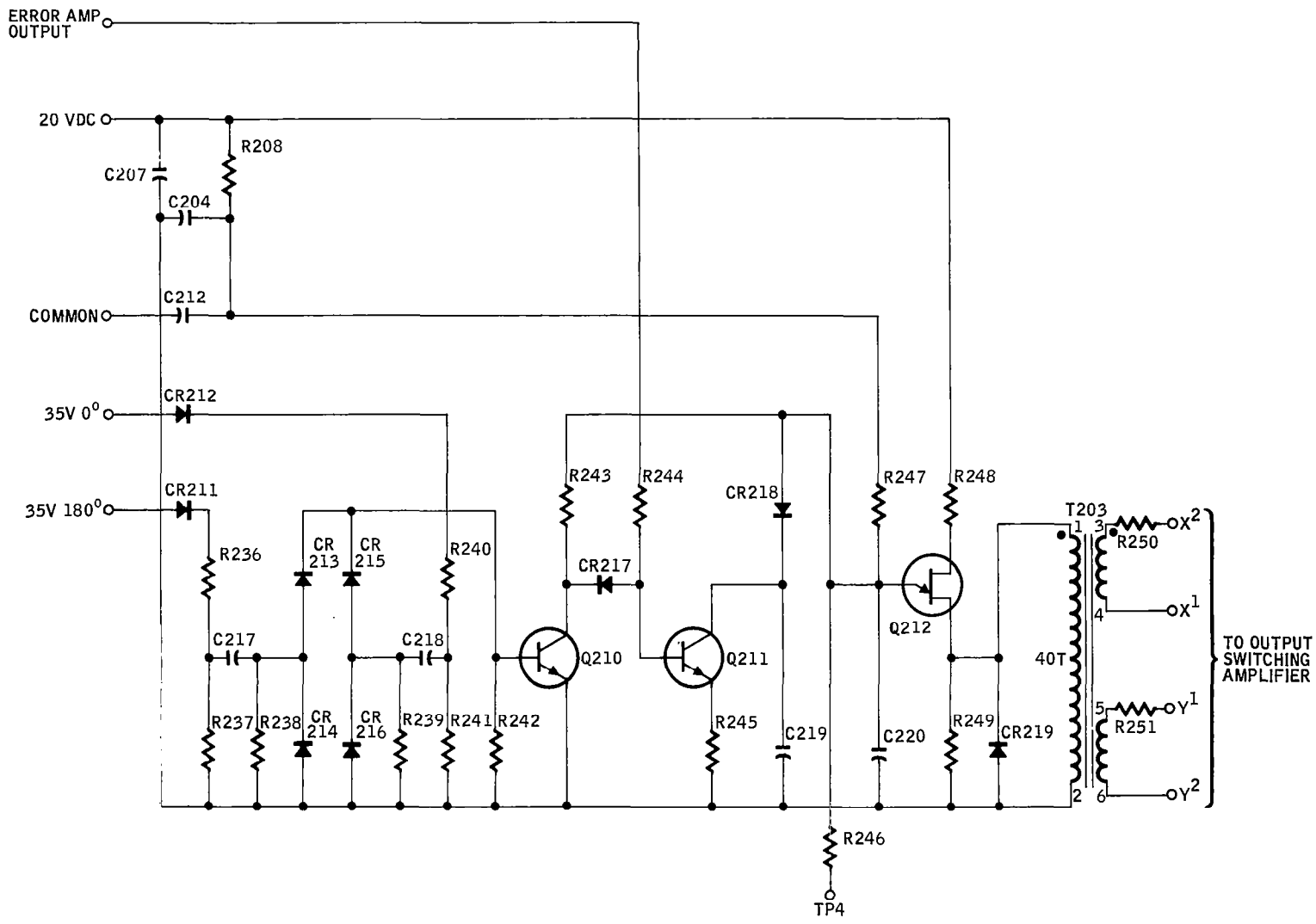

FIGURE 40
Voltage Controlled Oscillator

squarewave sync signal changes polarity. The squarewave sync signal is full wave rectified and differentiated by dual differentiating networks R236 - C217 and R240 - C218. The resulting differintiated pulses turn Q210 on momentarily at the beginning of each half cycle of the squarewave, thus discharging C220 and resetting the start of the C220 charge cycle. The error amplifier output determines how much current Q211 will pass and therefore how soon Q212 will produce an output pulse after synchronization has occurred.

The purpose of the output switching amplifier is to supply ac power to the filament. The output switching amplifier is shown in Figure 41. The output switching amplifier consists of silicon controlled rectifiers (SCR's) Q203 and Q204 and their associated circuitry. The output pulses of the VCO are coupled to the gates of Q203 and Q204 by transformer T203. Each pulse turns on the SCR which has proper polarity of voltage from anode to cathode. The SCR stays on until the squarewave changes polarity. When the SCR's turn on, they couple the 35 volt squarewave to the primary of step-down transformer T202 and hence to the filament. Capacitors C201 and C204 reduce the rise time of the SCR anode waveform and thereby remove the possibility of SCR turn-on due to fast squarewave rise time.

Derivation of Equations and Worst Case Analysis

The equations which define the filament supply and emission regulator consist of:

a. Minimum base current requirements for the converter switching transistors.

b. Wire size determination for transformer design.

c. Determination of the minimum number of turns on the filament power transformer primary.

d. Determination of power stress of all resistors.

e. Determination of power stress on all semiconductors.

The results of the analyses show that the components used are adequate to perform their function and also show which components need special packaging consideration.

Test Procedures

The purpose of the breadboard test is to verify the regulation of the emission current with line, load and temperature variations.

a. Test Set-Up

The test set-up is shown in Figure 42.

b. Test Conditions

1. The line voltage is varied from 27.5 to 28.5 Vdc in 0.5 V steps.

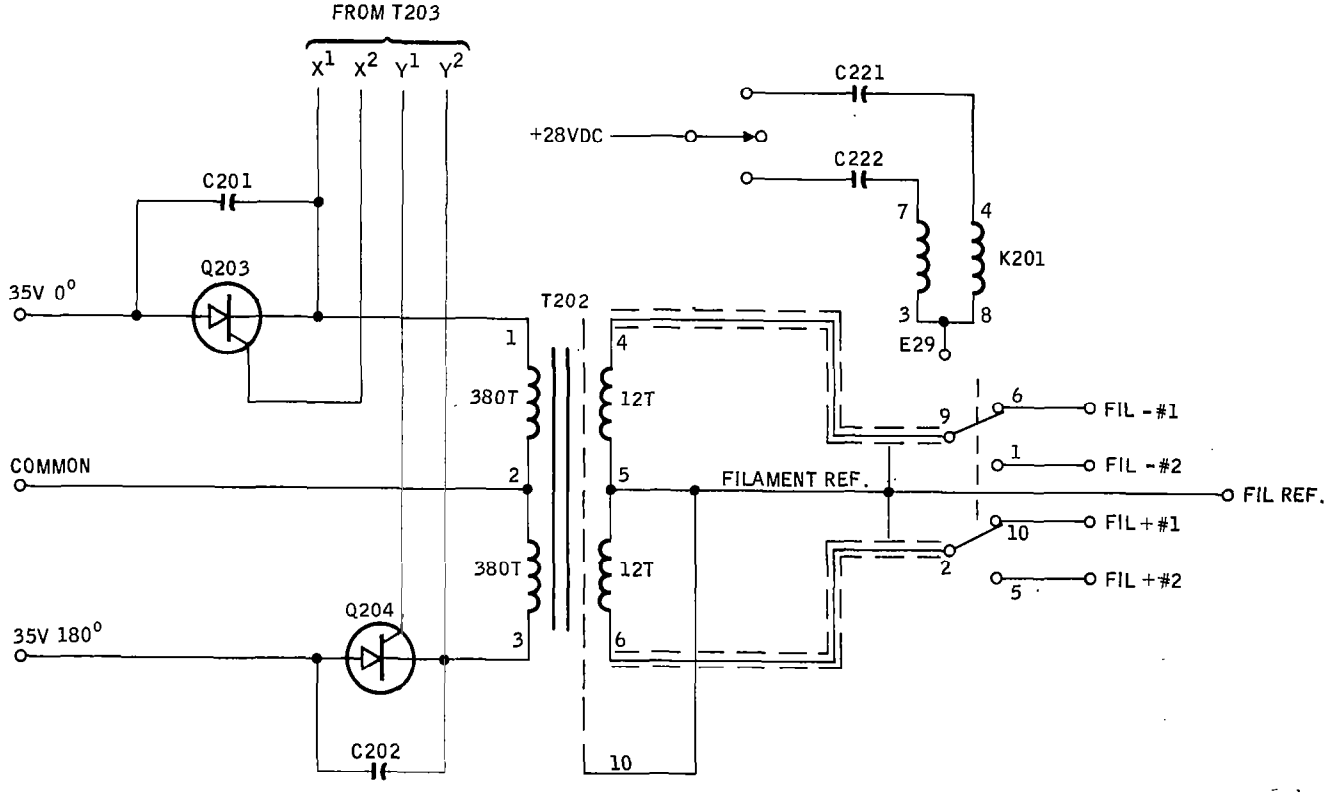

FIGURE 41
Output Switching Amplifier

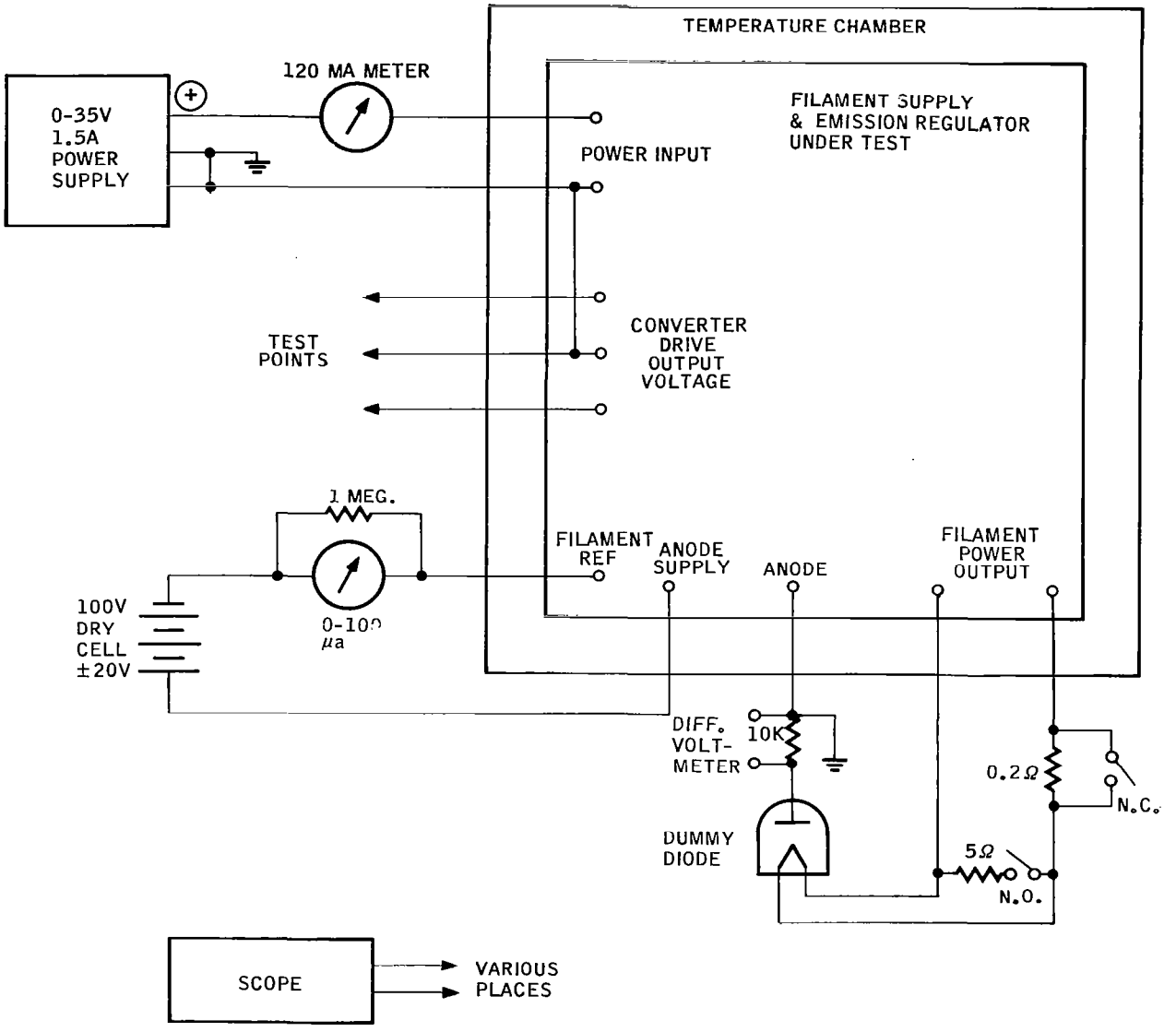

FIGURE 42
Test Schematic

2. The load consists of a 0.2 ohm resistor which can be inserted in series with the filament and a 5 ohm resistor which can be placed in parallel.

3. The test temperatures are 0°C, 25°C and 40°C.

c. Resistor Selection

There are five "Select at Test" resistors. They are: R254, R213, R220, R228, and R230.

The function of each is as follows:

1. R254 is used to set the DC/AC inverter nominal frequency at approximately 3.5 KHz.

2. R213 is used to set the output voltage of the series regulator at 20 Vdc ±100 mV.

3. R220 is used to adjust the current through CR205, a 6.4 V reference diode, to 1 mA.

4. R228 is used to balance the current in each half of the differential amplifier (Q209).

5. R230 is used to adjust the current through CR210, a 9.1 Volt reference diode to 1 mA. This resistor should be chosen when the desired anode current is flowing.

Temperature variations may produce a small change in anode current. By adjusting R220, R228, and R230 in combination, this change in current can be minimized.

Test Results

The test data sheet (see Tables 12 and 13) was developed for environmental testing of the filament supply and emission regulator.

Raw data was recorded on this sheet, and the curves of Figure 43 were drawn to show effects of line, load, and temperature variations.

On the data sheet, the left hand column (temperature) records the test temperature. The next two columns, respectively E_{in} and I_{em} or ΔI_{em}, record the effects of line variations. Emission current is recorded at normal line voltage (28VDC) and variations in emission current are recorded due to +1/2 and -1/2 volt line variations.

The fourth column (Shunt Load, ΔI_{em}, Load In) records the change in emission current when the five ohm shunt load is placed across the filament, the fifth column (Series Load, ΔI_{em} Load In) records the change in emission current when the 0.2K resistor is added in series with the filaments.

The sixth column (20 V) is not necessary for final tests, and was used in earlier breadboard testing to obtain data on the stability of the +20 volt regulator.

The seventh column (I_{BB}) records power supply input current under several conditions.

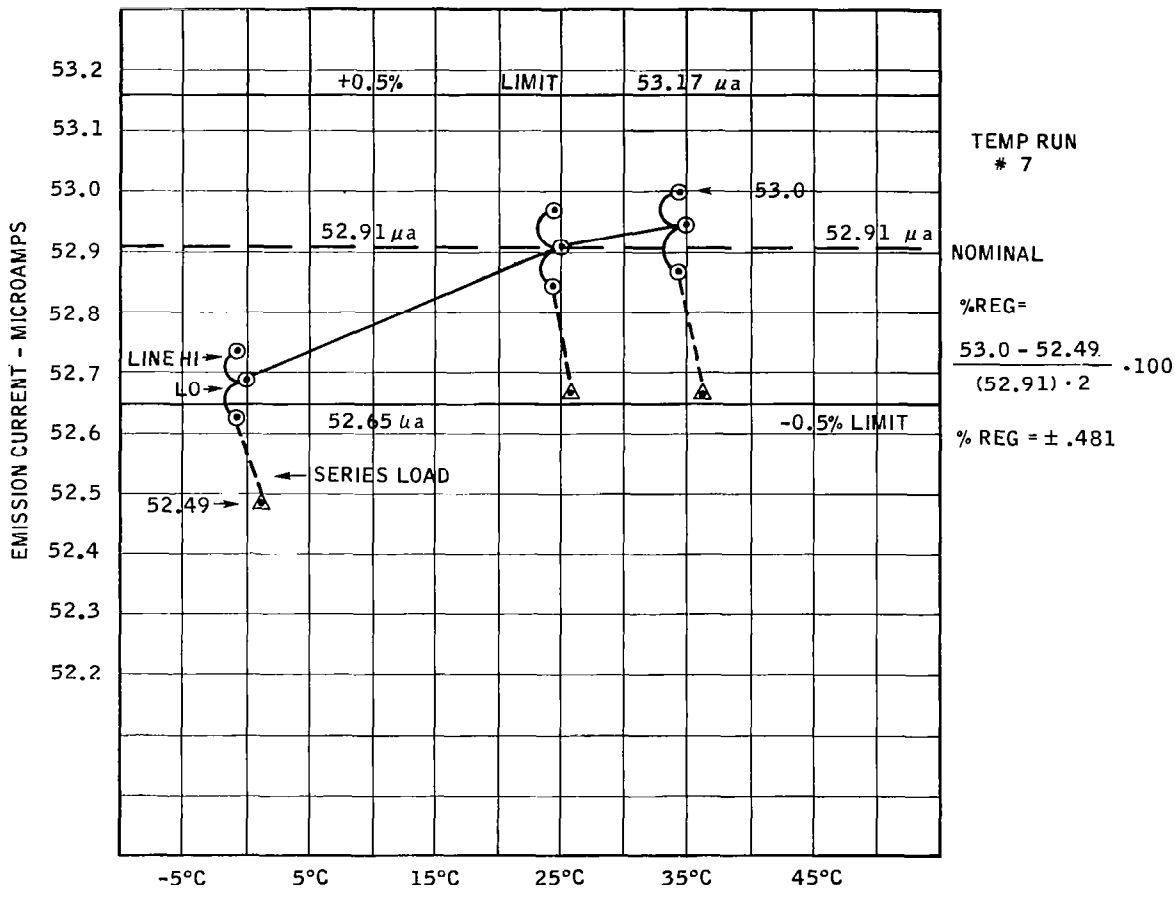

FIGURE 43
Test Results (50 μA Emission Current)

The last column (Comments) on the test sheet is for any comments that may be important.

In order to measure emission current accurately, a differntial voltmeter (John Fluke, Model 801) was used to measure the voltage drop across a 10 K resistor. The current through the 10 K resistor was the emission current of the diode. This set up gave a sensitivity of 10^4 V per amp, or 10 MV/μA. The most sensitive scale on the differential voltmeter is 10 MV full scale, or 1 μA full scale, with minor divisions equal to .02 μA, or 20 nano-amps.

This method allows measurements of small variations of emission current ($\approx$20nA) at all expected levels of total emission (5 μA to 200 μA).

The test data tabulated in Tables 12 and 13 indicate that the filament supply and emission regulator meets the requirements of Test Procedures.

TABLE 12

Test Data

TEMPERATURE	Line E_{in}	Reg. I_{em} or * ΔI_{em}	Load Shunt ΔI_{em} Load In (NA)	Reg. Series ΔI_{em} Load In (NA)	20 V (VDC)	I_{BB} (MA)	COMMENTS
	+0.5V	*60 NA	-40	-210			
75°F	Norm.	103.53 UA	-40	-300			12:35
	-0.5V	*60 NA	-45	-360			
	+0.5V	*45 NA	-30	-200			
32°F	Norm.	103.43 UA	-40	-220		85 Normal Load	
	-0.5V	*80 NA	-35	-320		99 Shunt Load 91 Series Load	I_{BB} 6 MA too high throughout
	+0.5V	*50 NA	-40	-290			
105°F	Norm.	103.64 UA	-50	-310			
	-0.5V	*80 NA	-50	-390			

TABLE 13

Test Data

TEMPERATURE	Line E_{in}	Reg I_{em} or $*\Delta I_{em}$	Shunt Load ΔI_{em} Load In (NA)	Series Load ΔI_{em} Load In (NA)	20 V (VDC)	I_{BB} (MA)	COMMENTS
	+.5V Hi	*50 NA	-20	-150			
30°F	Normal (28 VDC)	52.69 UA	-20	-140	20.056	80 Normal Load	11:40
	-.5V Lo	*60 NA	-20	-140		93 Shunt Load	
						87 Series Load	
	+.5V Hi	*50 NA	-30	-170			
105°F	Normal	52.95 UA	-35	-185	20.002	82 Normal Load	12:10
	-.5V Lo	*80 NA	-35	-200		95 Shunt Load	
						88 Series Load	
	+.5V	*60 NA	-30	-160			
75°F	Normal	52.91 UA	-30	-170	20.024	81 Normal Load	
	-.5V	*60 NA	-25	-180		93 Shunt Load	I_{BB} Reading 6 MA high throughout
						87 Series Load	

ELECTRODE BIAS SUPPLY

The electrode bias supply (Figure 44) consists of two DC/DC converters, two series regulators, and a resistive voltage divider string. Its function is to provide the potentials required by the analyzer electrodes.

The converters (Figure 45) are driven by a signal from the filament supply so that the operating frequency of both modules are synchronized. Each transformer has multiple windings and several windings have multiple taps; in this way, a wide range of output voltages is obtained and the operation of the module is highly flexible.

The series Regulators (Figure 46) are adjustable from approximately 5 to 50 volts. The output of an unregulated winding is placed in series with the regulator and a sample of the total voltage is sensed by the regulator feedback loop. This produces a regulated voltage that is much greater than the regulator alone is capable of providing.

The resistive divider string (Figure 47) makes a large number of adjustable voltage taps available for the analyzer electrodes. Under normal operating conditions, the electrodes that are connected to the string do not draw current so that the high source impedance of the divider is not a disadvantage.

Specifications

a. Output Requirements:

Low supply	
Voltage	225 Vdc maximum
Current	1.0 mA maximum
Ripple and noise	1.0 Vp-p
Regulation	±0.1%
High supply	
Anode potential	
Voltage	165 Vdc maximum
Current	1.0 mA maximum
Ripple and noise	1.0 Vp-p
Regulation	±0.1%
Electron accelerator	
Voltage	60 Vdc maximum
Current	1.0 mA maximum
Ripple and noise	1.0 Vp-p
Regulation	±1%

b. Input Requirements:

Parameter	Min.	Max.	Units
Voltage	27.5	28.5	Vdc
Current		25.0	mA
Ripple and noise		0.5	Vp-p
Transients		52	V (100 μsec)

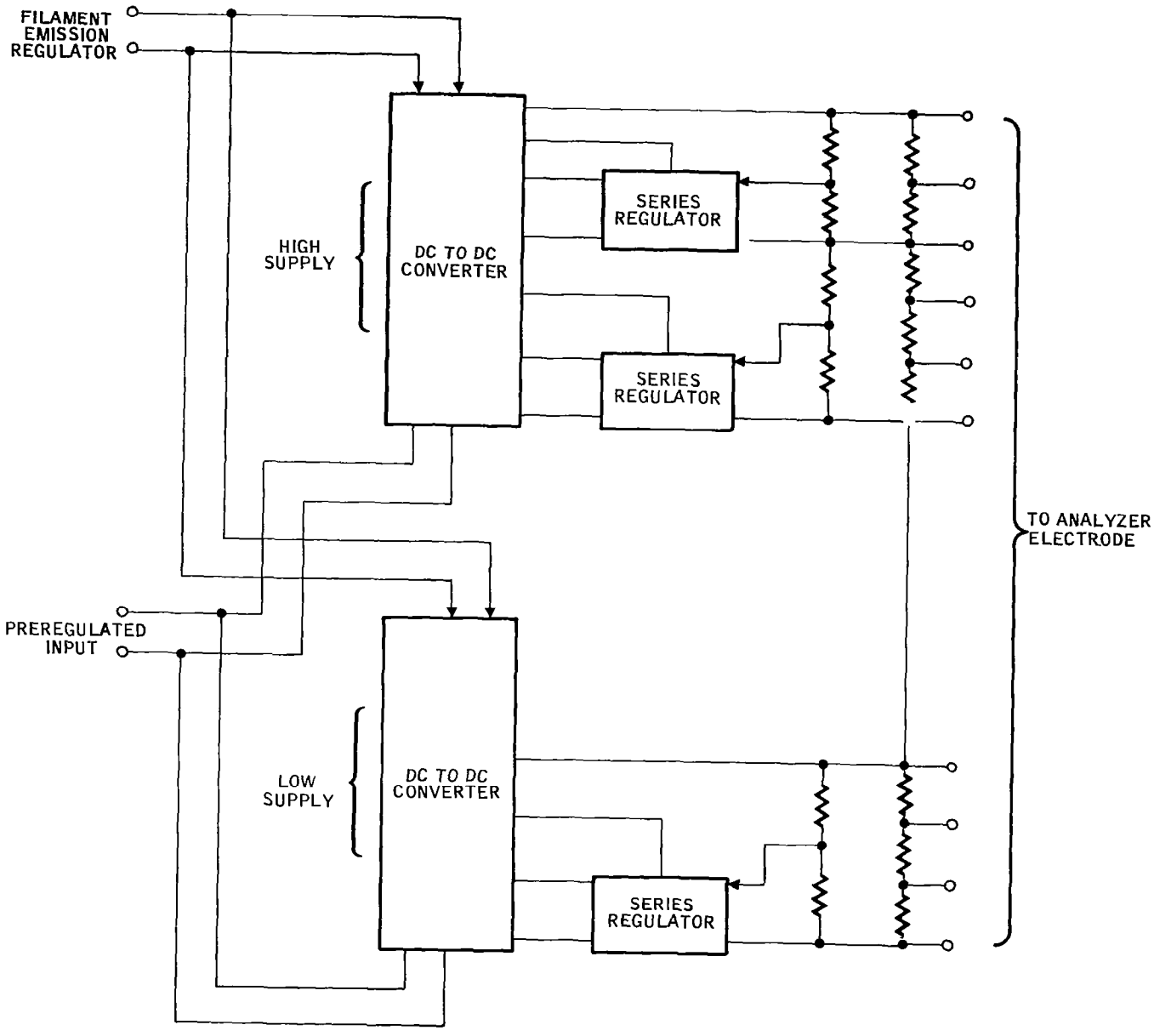

FIGURE 44
Electrode Bias Supply Block Diagram

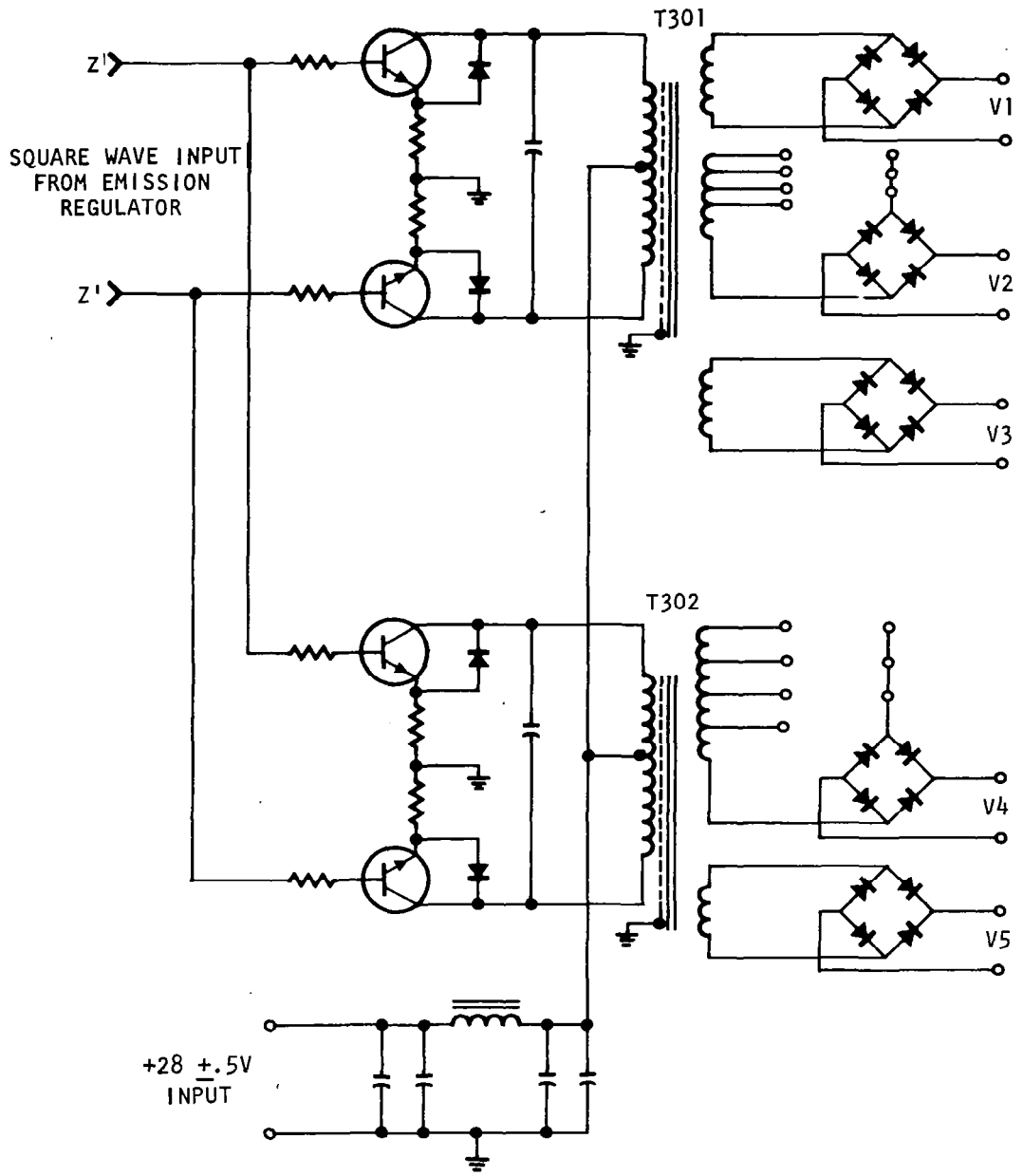

FIGURE 45
DC/DC Converters

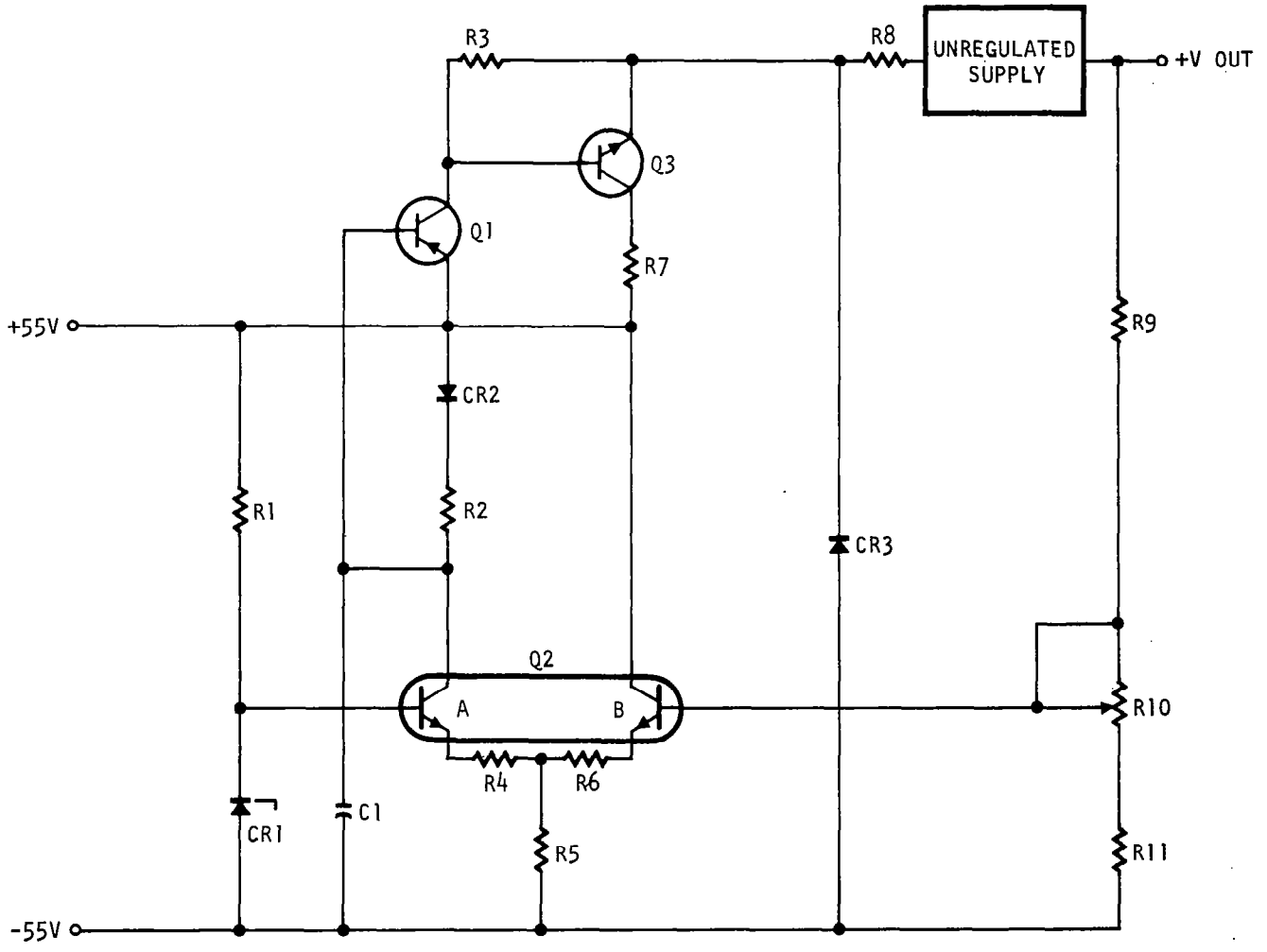

FIGURE 46
Series Regulator

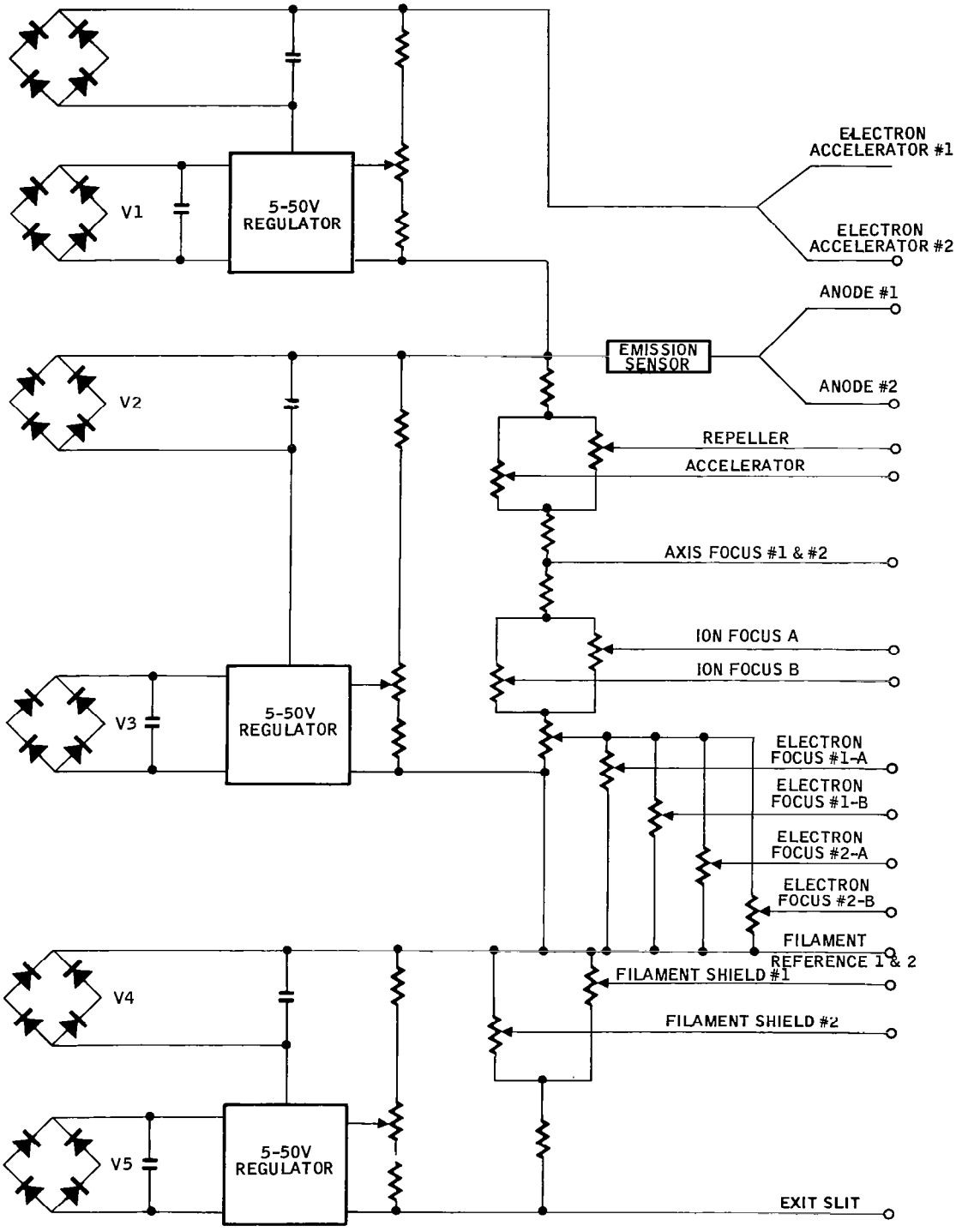

FIGURE 47
Resistive Divider String

c. Other Requirements:

Parameter	Min.	Max.	Units
Temperature	0.0	35	C

Circuit Description

a. DC/DC Converters:

The two DC/DC converters are identical and the following circuit description will apply to both. (See Figure 45) The electrode bias supply utilizes a driven DC to DC converter. A drive signal in the form of a squarewave is obtained from the filament supply. The drive signal switches the transistors OFF and ON out of phase, and this action produces the AC signal necessary for transformer action. The output of the transformer is a squarewave which is rectified by bridge rectifiers. Each transformer has several windings and taps so that a range of voltages is obtained.

b. Series Regulators:

The two series regulators are identical and the following description applies to both. (See Figure 46) The series regulator may be considered as an operational amplifier with a differential input. One input is the base of Q2A and the other is the base of Q2B. The output is taken from the emitter of Q3. The temperature-compensated reference diode, CR1, establishes a fixed voltage at the noninverting input (base of Q2A) and the feedback voltage divider (R9, R10, and R11) presents a portion of the output at the inverting input (base of Q2B). Any difference appearing between the two inputs results in an adjustment in the output that brings the voltage difference between the two bases back to zero. Therefore, the output is held constant at a value determined by the reference voltage and the setting of R10. The functions of some of the pertinent components are as follows:

1. Diode CR2 is used for temperature compensation of the base-emitter voltage drop of transistor Q1 so that the current through resistor R2 remains constant. With the current through R2 constant with temperature, the temperature stability of the differential amplifier is enhanced.

2. Resistors R4 and R6 may be used to control the gain of the differential amplifier and thus ensure high frequency stability.

3. Resistor R7 limits the current through Q3 in case of a short-circuited output and protects the transistor.

4. Capacitor C1 is used to prevent noise spikes that might appear at the base of Q1 from interfering with circuit operation.

5. Diode CR3 is used to shunt the regulator portion of the circuit if the total output of the supply is shorted. Such a condition places the unregulated supply across the regulator with a reversed polarity. The diode then conducts and prevents damage to the regulator components.

6. Resistor R8 limits the current through CR3 if the output is shorted as described above.

c. Resistive Voltage Divider:

The resistive divider string consists of several potentiometers and fixed resistors connected in a series-parallel combination that provides the proper potentials to the electrodes of the analyzer. The string is made up of wire wound resistors with excellent temperature characteristics (±20 ppm) so that the electrode potentials will not be affected by temperature to any significant extent.

Derivation of Equations and Worst Case Analysis

The electrode bias supply may be considered as an operational amplifier as illustrated in Figure 48. The amplifier is used differentially so that any change in V_O, the output voltage, is sampled by the feedback network, R9, R10, and R11. The sample voltage, V_S, appears at the inverting input 1 where it is compared to the reference voltage, V_{REF}, applied to input 2. Any difference between the two voltages, V_S and V_{REF}, is amplified and the output is driven in the direction that will change V_S and make the voltage differerence at the inputs zero (ideally).

Inspection of Figure 48 reveals that the output voltage is dependent only on the reference voltage and the ratio of the feedback resistors. However, the equations shown are based on two ideal factors - zero offset voltage and zero offset current at the inputs.

Changes in the output voltage due to age and environment can be related to the above four factors as shown in the first four equations listed below. The total worst case deviation may then be calculated by using the fifth equation.

a. Equations

1. Change in V_o due to change in V_{REF}

2. Change in V_o due to change in feedback resistors

3. Change in V_o due to change in offset voltage

4. Change in V_o due to change in offset current

5. Total worst case deviation of the output voltage

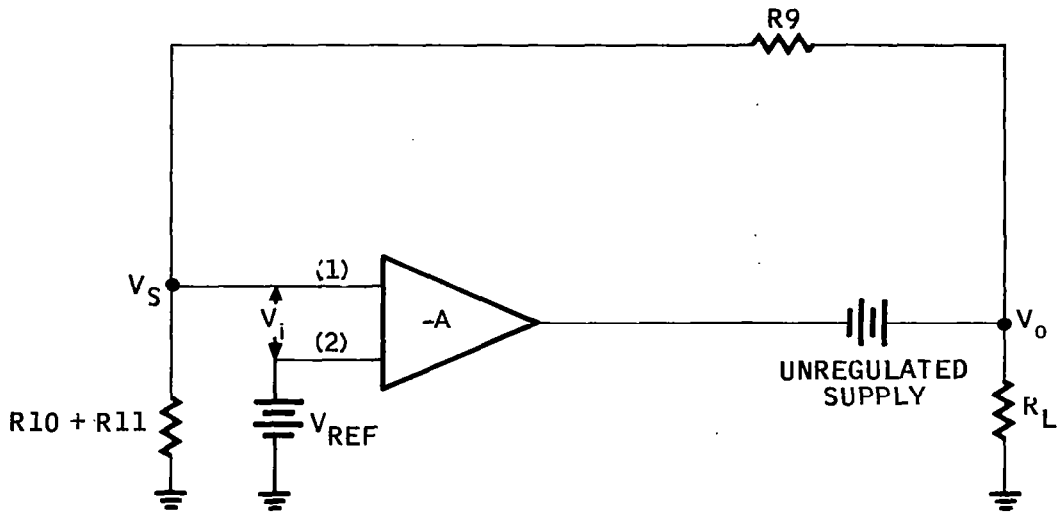

(1) $$\frac{V_i + V_{REF}}{R10 + R11} = \frac{V_o - (V_i + V_{REF})}{R9}$$

(2) $$V_o = -AV_i$$

(3) $$V_i = \frac{-V_o}{A}$$

IF A IS VERY LARGE

$$V_i \approx 0$$

THEREFORE EQUATION (1) IS

(4) $$\frac{V_{REF}}{R10 + R11} = \frac{V_o - V_{REF}}{R9}$$

(5) $$\frac{V_o - V_{REF}}{V_{REF}} = \frac{R9}{R10 + R11}$$

(6) $$\frac{V_o}{V_{REF}} - 1 = \frac{R9}{R10 + R11}$$

(7) $$\frac{V_o}{V_{REF}} = \frac{R9}{R10 + R11} + 1$$

(8) $$V_o = V_{REF}\left(\frac{R9}{R10+R11} + 1\right)$$

FIGURE 48
Electrode Bias Supply Analysis

b. Results

The results of the worst case analysis show that the maximum deviation of the output voltage due to age and environment will not exceed 1% of the total voltage.

Test Procedures

The purpose of the test procedures was to verify the results of the worst case analysis and to show that no problem areas had been neglected.

The following test procedure was performed on the breadboard circuitry and the engineering test model. The results of the tests on the engineering test model are presented in Table 14.

The results of the testing showed that the analysis was correct and that the module met all specifications.

a. Electrode Bias Supply Test Procedure

The purpose of this test was to establish the operational characteristics of the electrode bias supply under temperature, supply voltage, and loading variations.

b. Test Equipment

1. DVM - HP 3460A or equivalent
2. Ammeter - 0 to 500 mAdc
3. System Power Supply (27.50, 28.00, 28.50 Vdc ±0.05V)
4. External converter drive circuit
5. Scope
6. Load resistors
7. Temperature chamber

c. Test Procedure

1. Make all connections as shown in Figure 49.
2. Adjust the filament reference voltage (with respect to common) to 115.0 volts. Adjust the anode with respect to filament reference voltage to 115.0 volts.
3. Set the temperature to 50°C and allow it to stabilize for one half hour. Set the supply voltage to 27.5 Vdc. Measure and record in Table 14.

(a) Filament reference with respect to common voltage

TABLE 14

Engineering Test Model Results

	Temperature	50°C			25°C			0°C		
	Load \ V_{in}	27.5	28.0	28.5	27.5	28.0	28.5	27.5	28.0	28.5
Filament Reference voltage W/R to Common	Nominal	115.002	115.024	115.042	115.071	115.089	115.107	115.208	115.226	115.242
	Full	115.001	15.012	15.032	115.062	115.081	115.099	115.194	115.213	115.231
Anode voltage W/R to Filament Reference	Nominal	115.054	115.073	115.090	115.049	115.064	115.087	115.052	115.082	115.101
	Full	115.051	115.070	115.085	115.042	115.061	115.080	115.047	115.075	115.096
Electron Accelerator voltage W/R to Anode	Nominal	63.542	64.725	65.898	63.418	64.602	65.775	63.298	64.482	65.656
	Full									

NOTE: Filament Reference Regulator was not adjusted for best temperature compensation.

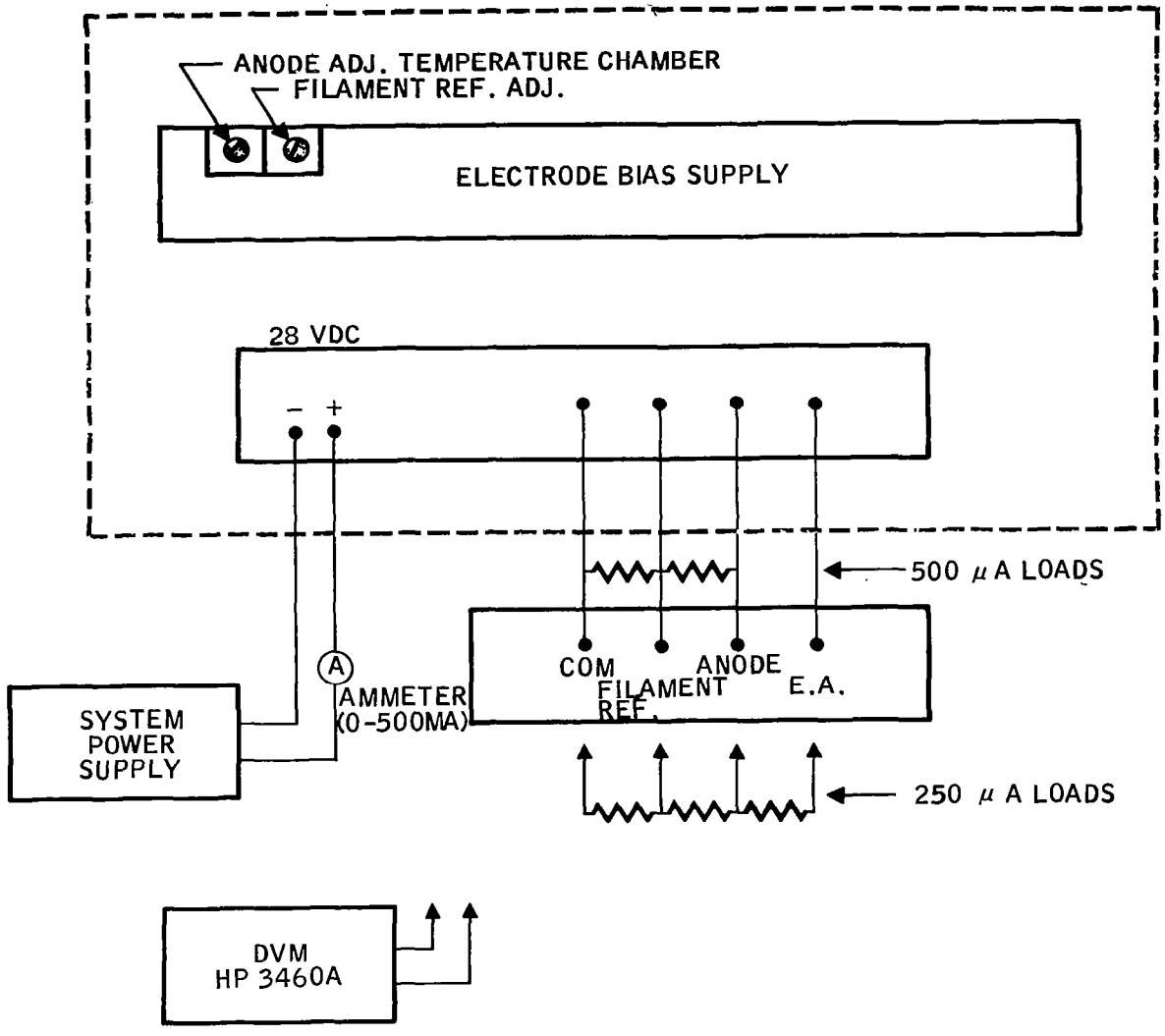

FIGURE 49
Test Schematic

(b) Anode with respect to filament reference voltage

(c) Electron accelerator voltage with respect to the anode voltage under the nominal 500 μA load and the additional load of 250 μA.

Repeat for supply voltages of 27.5 and 28.5 Vdc.

4. Set the temperature to 25°C and allow it to stabilize for one half hour.

Repeat procedure c.3.

5. Set the temperature to 0°C and allow it to stabilize for one half hour.

Repeat procedure c.3.

DETECTOR POWER SUPPLY

The detector power supply consists of a free running DC/DC converter and two series regulators to deliver +10 Vdc and -10 Vdc at 0.1% regulation to the four detectors.

Specifications

a. Output Requirements:

Parameter	Minimum	Maximum	Units
Voltage	+9.990	+10.010	Vdc
	-9.990	-10.010	Vdc
Current		20.0	mA
Regulation		0.1	%
Ripple & Noise		20.0	MVp-p

b. Input Requirements:

Parameter	Minimum	Maximum	Units
Voltage	27.5	28.5	Vdc
Current		25.0	mA
Ripple & Noise		0.5	Vp-p
Transients		52.0	V(100μsec)

c. Other Requirements:

Short Circuit Protected
Temperature 0°C to 35°C

Series Regulator

The ±10 Vdc series regulators are modifications of Perkin-Elmer Aerospace Systems standard regulator designs used in previous projects that have proven to be reliable, stable, and precise.

The schematics of the +10 Vdc regulator and the -10 Vdc regulator are shown in Figures 50 and 51 respectively. The parameter configurations and values of respective resistors in the two regulators are identical. The only differences are the reversal of diode polarities and the exchange of NPN transistors with PNP transistors. The detailed circuit description will simultaneously pertain to Figures 50 and 51, although reference designations of Figure 50 will be used.

The 10 Vdc series regulator basically consists of a reference voltage source (CR401), a differential amplifier (Q401 and Q402), two stages of current gain (Q403 and Q404), and a series pass (or power) amplifier (Q405).

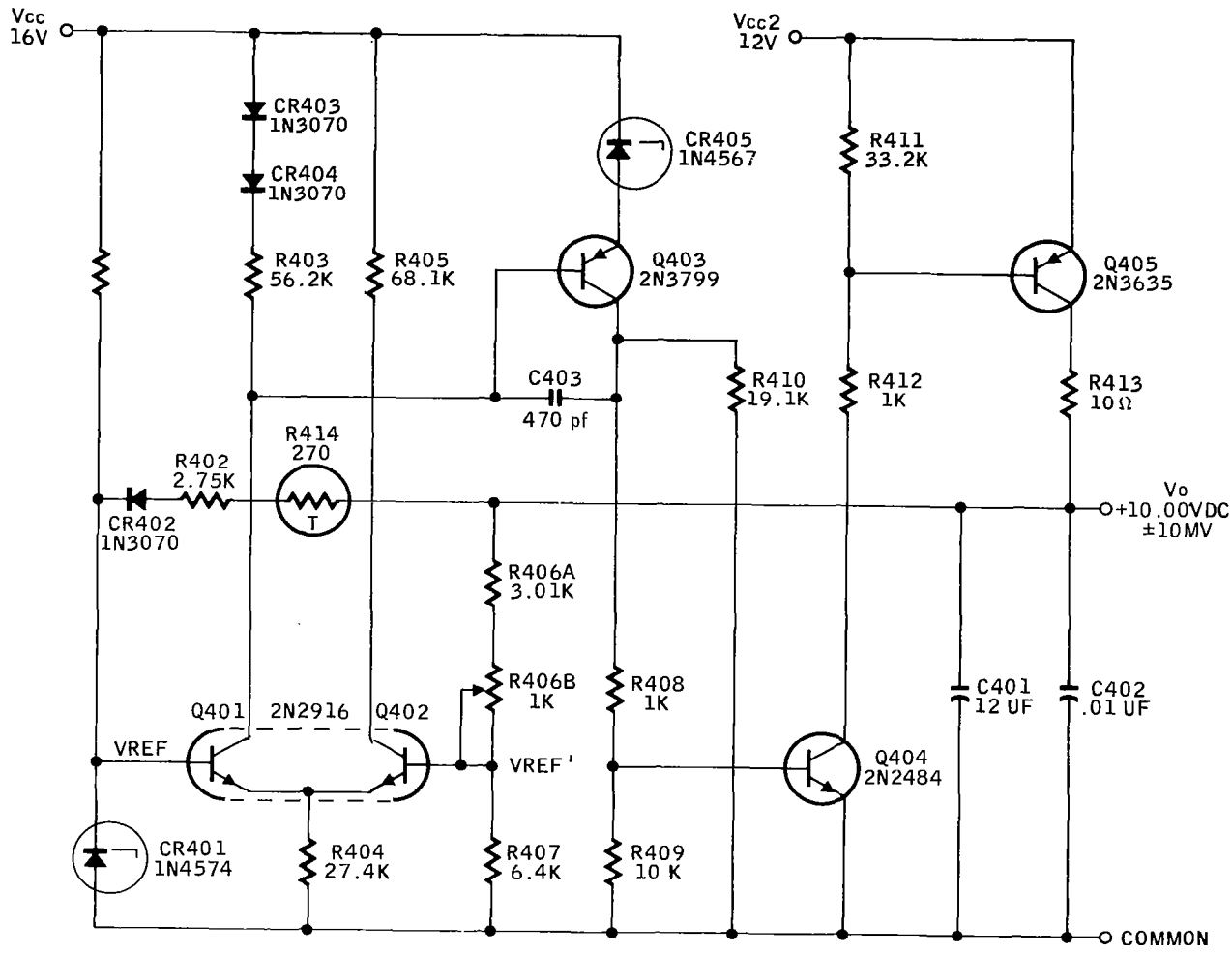

FIGURE 50
+10 VDC Regulator

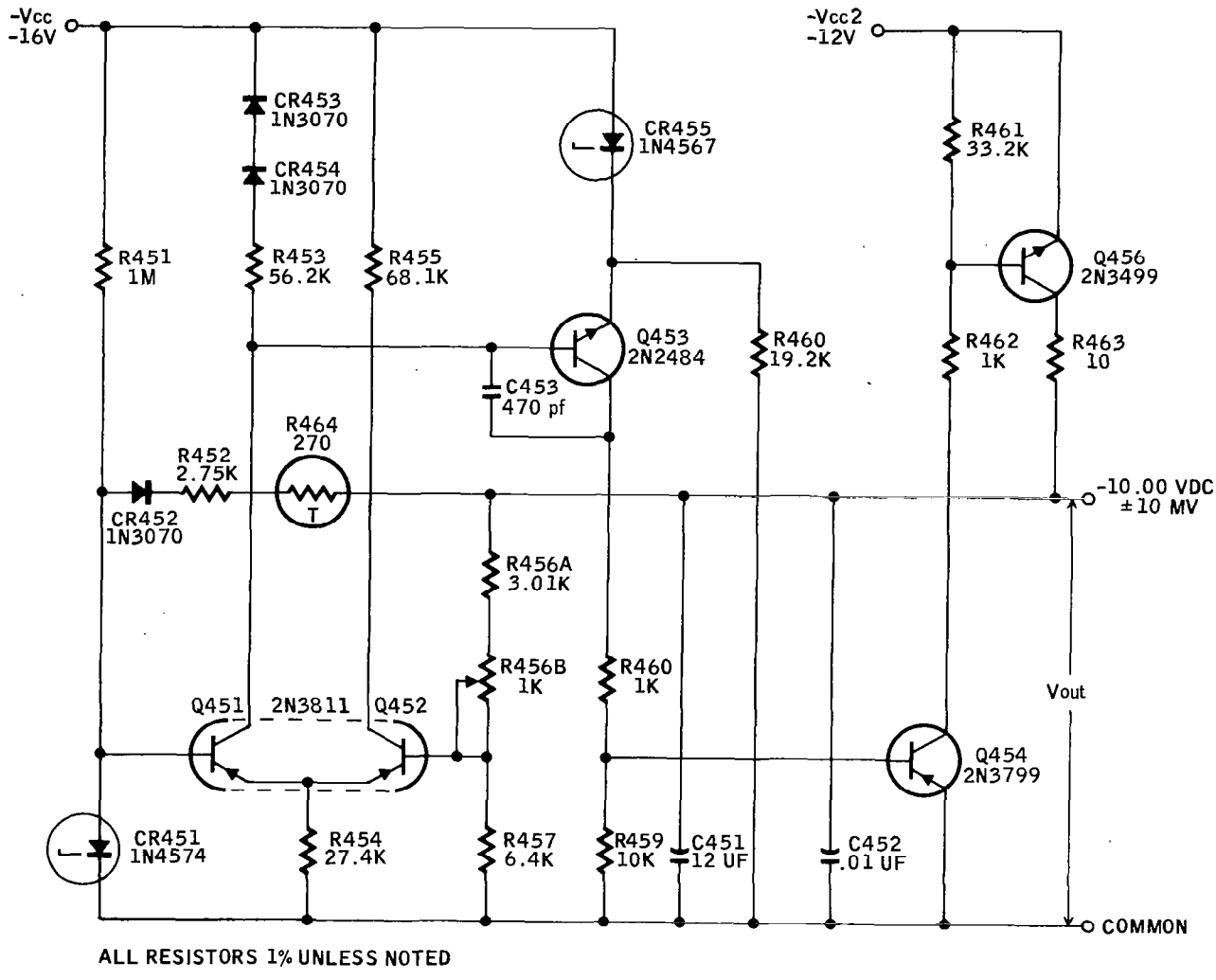

FIGURE 51
-10 VDC Regulator

Under normal operating conditions, with 10 volts output voltage, the reference diode, CR401, receives a stable bias current (via R402, R414, and CR402) from the regulated output voltage. However, upon initial turn-on, the output voltage is zero. Under this condition, a starting current is supplied to the base of Q401 through R401. This current is amplified and applied to capacitors C401 and C402, and to the output load. When the voltage across C401 and C402 increases sufficiently to forward bias CR402, the output voltage quickly rises to 10 volts due to the increased supply of reference diode bias current. As the output voltage approaches 10 volts, Q402 begins to conduct and the output voltage stabilizes as the differential amplifier input voltage approaches zero. Temperature sensitivity of the reference diode current is reduced by use of sensistor R414 to compensate for changes in forward voltage drop of diode CR402. Overall reference voltage stability is insured by using a temperature compensated reference diode (±0.0005%/°C) for CR401 and by the highly stable reference diode bias scheme.

The differential amplifier (Q401 and Q402) senses a portion of the output voltage dropped across R407 and compares this voltage with the reference diode voltage. When these voltages are nearly equal, the differential amplifier is nearly balanced and the current supplied to current amplifier Q403 is just sufficient to maintain the output at 10 volts. If the output voltage attempts to change, an error signal between the reference voltage and the voltage across R402 will exist. This error will be amplified and the output voltage automatically adjusted to minimize the error. Temperature stability of the differential amplifier is insured by using a matched pair of transistors in a common case for thermal tracking and by maintaining the amplifiers at nearly identical operating points. The collector current of Q401 is held constant by the constant voltage drop across R403. The values of resistors R403 and R404 are selected so that under normal operating conditions, the current through R404 is twice that through R403. The voltage across R404 is held constant by the reference diode (CR401) voltage and the relatively constant base to emitter voltage drop of Q401. Temperature coefficients of the base to emitter voltage drops of Q401 and Q403 are compensated for by the nearly equivalent temperature coefficients of the forward voltage drops of CR403 and CR404. Since the collector current of Q401 and the sum of the Q401 and Q402 emitter currents flowing through R404 are held constant, the collector current of Q402 must also be constant. Therefore, the differential amplifier transistors Q401 and Q402 are operated at nearly identical operating points.

Transistors Q403 and Q404 act as high gain current amplifiers. Capacitor C403 reduces the high frequency voltage gain of the amplifier and helps to prevent the regulator from oscillating. Transistor Q405 acts as the series pass amplifier. The supply voltage for Q405 is 12 volts rather than 16 volts to minimize the power loss in this transistor. R413 is placed in the collector circuit of Q405 to limit the surge current to capacitor C401 during turn-on.

DC/DC Converter

The DC/DC converter schematic is shown in Figure 52. The converter is an astable multivibrator utilizing transformer feedback to accomplish toggling. Starting current is fed to both Q406 and Q407 bases via Q415. The innate

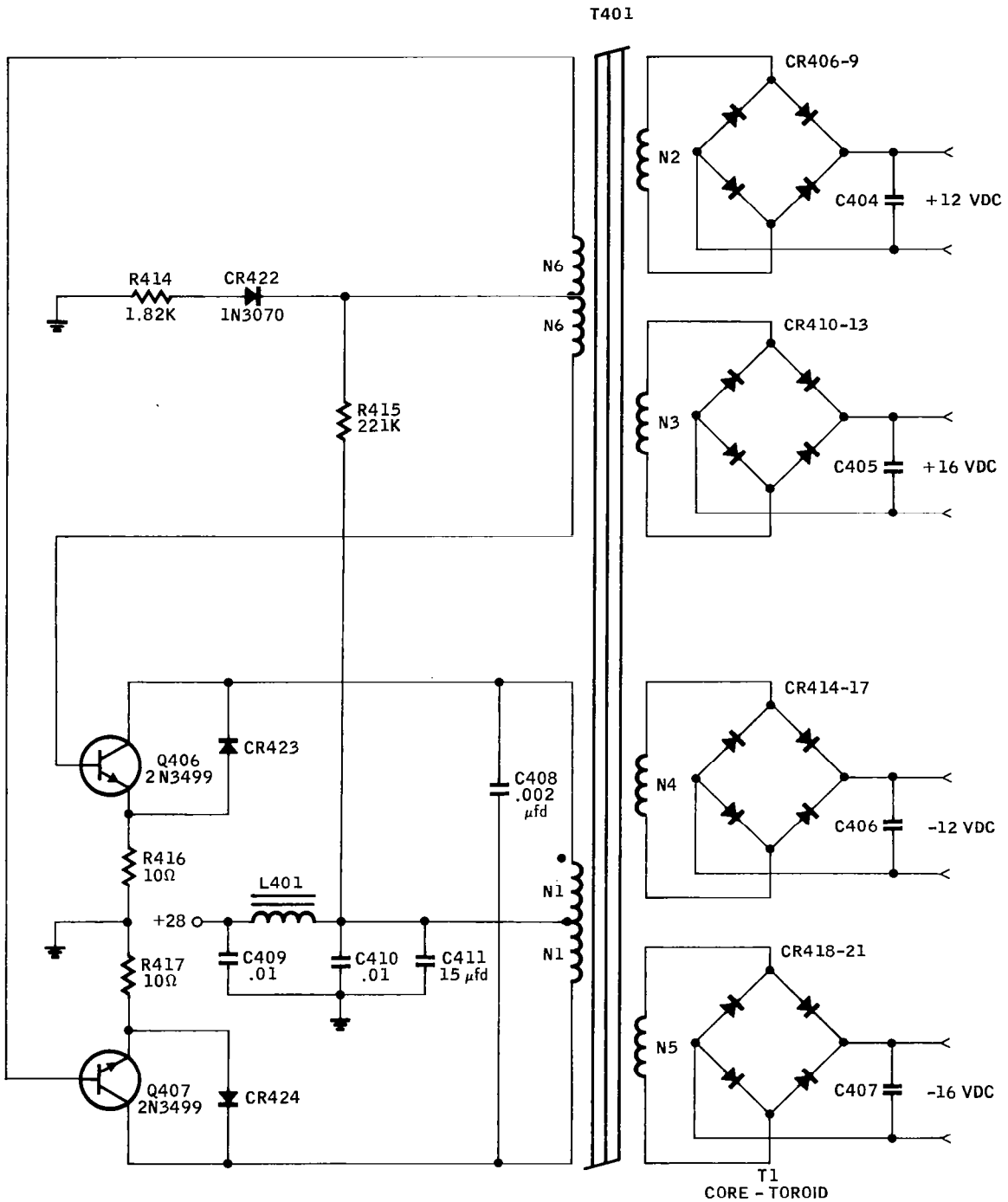

FIGURE 52
DC/DC Converter

unbalance of the transistors will cause one of the transistors to turn ON faster than the other. This results in negative feedback to the slower transistor and positive feedback to the faster transistor to start the toggle action. The faster transistor will turn ON due to the voltage V_{N6} and the starting current providing base drive. The multivibrator will toggle when the transistor turning ON saturates the core. At the point of saturation, the impedance of the square hysteresis loop core approaches zero very rapidly. When this occurs, two processes take place:

a. The emitter current increases suddenly, raising the emitter voltage due to the voltage drop across R416 or R417. (This provides degenerative feedback which helps to turn the transistor OFF)

b. When the core saturates, the change of flux ($d\phi/dt$) becomes zero. Therefore, the voltage V_{N6} goes to zero ($E = N\ d\phi/dt$), turning OFF the transistor.

The OFF transistor will be turned ON by the inductive energy stored in the collapsing field when the ON transistor turns OFF. This energy produces base current for the new on transistor via R414 and the voltage V_{N6}.

The above process repeats, generating a square wave signal equal to twice the supply voltage at each OFF collector, at a frequency, determined by N1, Vcc, and the flux of the core.

Due to the lag in time between a transistor turning OFF and the other one turning ON, noise voltage spikes are generated. The diodes CR423 and CR424, and the capacitor C408 eliminate most of this noise.

L401 is a filter inductor used to keep the current surges generated during transformer saturation from generating noise back into the system power supply.

Derivation of Equations and Worst Case Analysis

The equations which define the regulators of Figures 50 and 51 consist of:

a. DC Bias Equations
b. Differential Balance Error
c. Differential Temperature Error
d. Reference Error
e. Differential Stage Gain Error
f. Feedback Resistor Error
g. Regulation Error

The equations which define the DC/DC converter of Figure 52 consist of:

a. Base Drive Analysis
b. Starting Circuit Analysis
c. Frequency Deviation Analysis
d. Input Filter

A complete power analysis of the detector supply consists of the following individual analyses:

a. Subsystem Power

1. Regulator Power
2. Bridge Network Power
3. Transformer Power
4. Multivibrator Power
5. Total System Power

b. Component Power Stress

1. Resistors
2. Transistors
3. Diodes

c. Subsystem % Efficiency

1. Regulator Efficiency
2. Converter Efficiency
3. Total System Efficiency

Test Procedures

The purpose of the breadboard test performed on the ±10 Vdc regulators was to empirically verify stability and regulation.

a. Stability

The ±10 Vdc regulators consist of a cascade of four amplifiers whose open loop gain is greater than 100 db. To obtain bode plots of devices with such high gain magnitudes requires extremely fine low-level biasing and signal sources. 60 cycle isolation must also be in order of -100 db. Because of this, it was very difficult to acquire valid response and phase shift data.

To confirm the fact that the breadboards were stable, high gain components were selected and used and special tests were run. These tests consisted of closed loop operation (regulating) with no load, and at higher than the specified elevated temperature (+70°C). The results of these tests confirmed that the regulators were stable with the addition of the capacitors (C401, C402, and C403) shown in Figure 50 and their equivalents in Figure 51.

b. Regulation

Extensive regulation data was compiled from the schematics shown in Figures 50, 51, and 52. The test setup used to compile the regulation data is shown in Figure 53.

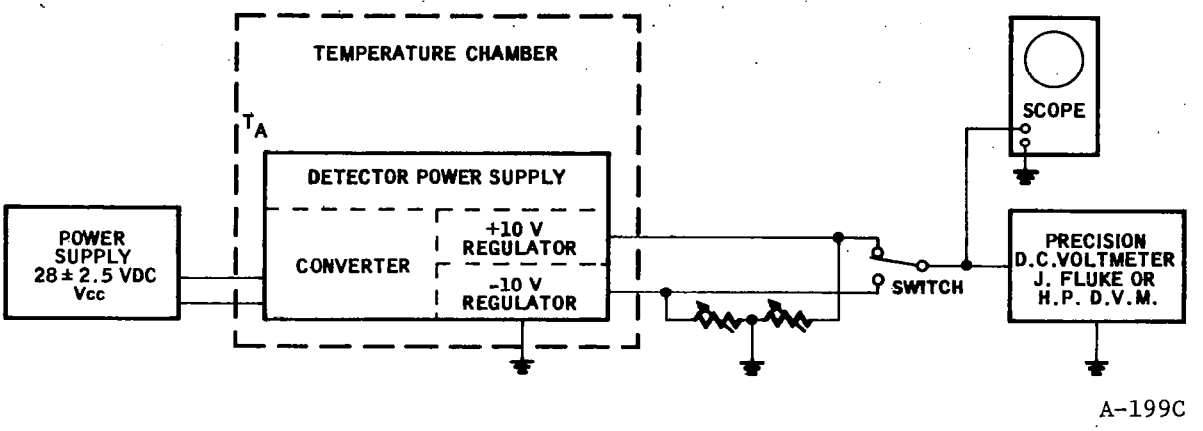

FIGURE 53
Test Setup, Detector Supply

The test procedure consisted of setting T_A at +35°C, +25°C, or 0°C. At each setting of T_A, the variables Vcc and load were varied.

The output voltage V_O of each regulator was monitored with an oscilloscope with a one mV/cm plug-in, and a precision dc voltmeter (John Fluke or Hewlett Packard DVM). The scope checked for stability and noise. The precision dc voltmeter measured the dc output voltage V_O.

Test Results

a. There were no detectable oscillations using the compensating capacitors shown in the schematics.

b. The noise level was 0.5 mV, which is well within the specification.

c. The regulation data is compiled in Tables 15 and 16.

TABLE 15
+10 Volt Regulator

T_A (°C)	I_L (MA)	V_{out} (VDC)		
		27.5 VDC INPUT	28.0 VDC INPUT	28.5 VDC INPUT
0	0	9.998	9.998	9.998
	14	9.997	9.997	9.997
+25	0	9.999	9.999	9.999
	14	9.998	9.998	9.998
+50	0	10.000	10.000	10.000
	14	9.998	9.998	9.998

TABLE 16
-10 Volt Regulator

T_A (°C)	I_L (MA)	V_{out} (VDC)		
		27.5 VDC INPUT	28.0 VDC INPUT	28.5 VDC INPUT
0	0	10.010	10.010	10.010
	16	10.008	10.008	10.008
+25	0	10.011	10.011	10.011
	16	10.009	10.009	10.009
+50	0	10.012	10.012	10.012
	16	10.011	10.011	10.011

DETECTORS

The detectors are all solid-state electrometer amplifiers capable of amplifying the minute ion currents to the required output level. There are two types, each with the sensitivity required by two of the four atmospheric components (C_2O and H_2O or N_2 and O_2).

Specifications

a. Performance Standards:

Minimum Detectable Signal	5×10^{-14} amperes
Noise and Drift	10 mV or less
Response	
H_2O and CO_2	1 second
O_2 and N_2	0.2 second
Operating Temperature	0 to 35°C

b. Interface Requirements:

Input

Voltage	+10.00 ± 0.01Vdc -10.00 ± 0.01Vdc
Current	5MA maximum (each)
Ripple and Noise	10MV p-p or better
Regulation	±0.1% or better

Output

Voltage	0 to 5 V linearly proportional to input current
Current	500 μA maximum
Load Resistance	10K ohms minimum

Circuit Description

Figure 54 is a schematic diagram of the detector. The first stage of the detector is the MOS-FET version of the cascode amplifier. This configuration was chosen because of its extremely small feedback capacitance and low noise properties. The overall feedback capacitance is equivalent to the feedback capacitance of a single device divided by the amplification factor of that device. The noise properties of the cascode combination are approximately that of a single device. This is because the noise contributed by the upper common-gate MOS-FET is significantly reduced by the degeneration caused by its source resistance, which is the dynamic drain resistance of the lower common-source MOS-FET. The dc temperature stability has been optimized by operating at a current equivalent to the 0-TC (zero-temperature coefficient) current of the dual MOS-FET. Since the 0-TC current is different for each particular unit, individual first-stage compensation will be required for each amplifier produced. This will consist of the

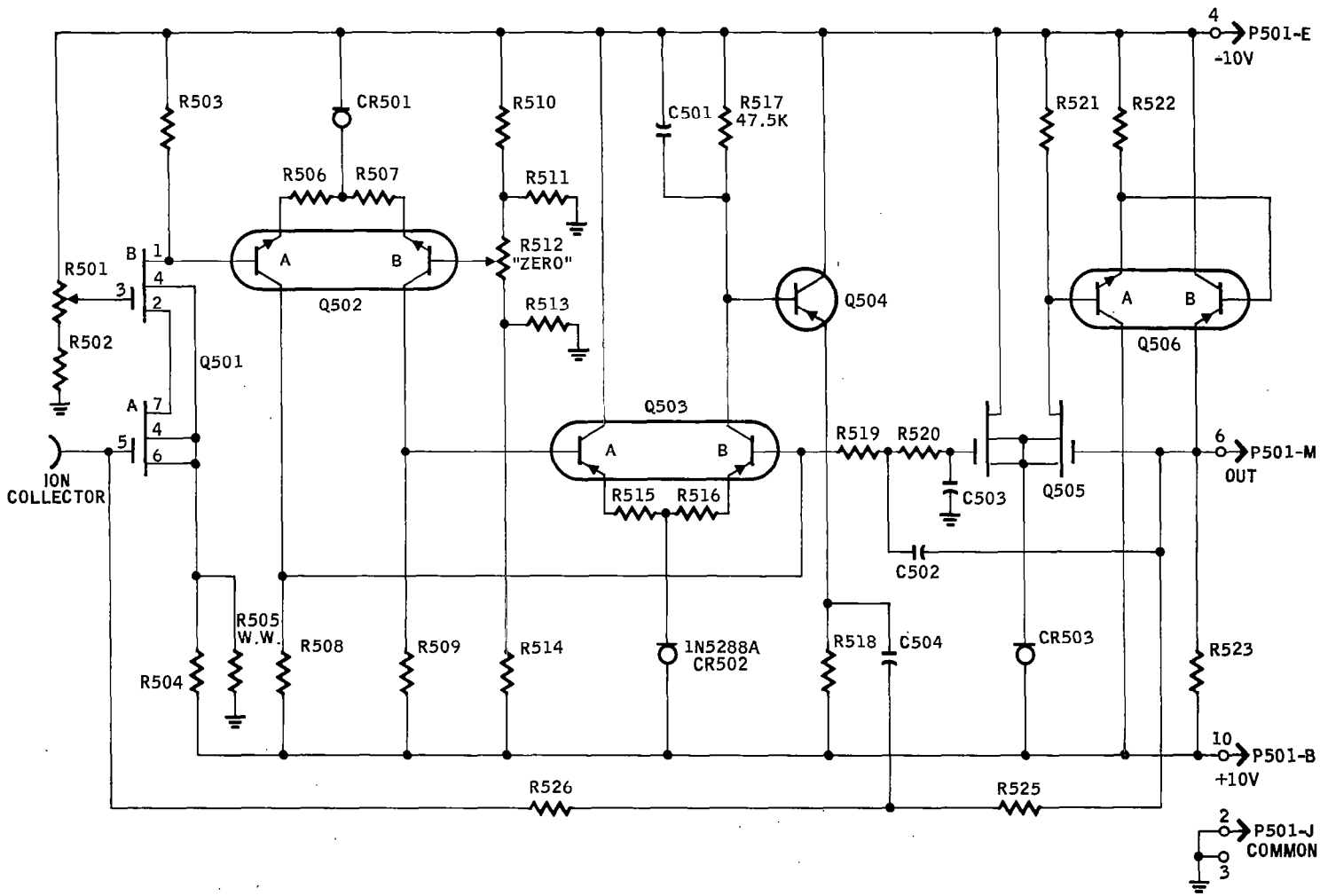

FIGURE 54
Detector Schematic

selection of R503, 4 and 5 for proper voltage drops with the 0-TC drain current. The first-stage current will then be adjusted, during set-up, by varying R501 until the drain current produces the required voltage drop across the drain load resistor, R503.

The second stage is a conventional differential amplifier chosen for its low dc drift characteristics. With this type of circuit, common mode voltage variations cause no output variation. The temperature effects of the current source, CR501, the two identical emitter resistors, R506-7, and the two identical collector resistors, R508-9, can thus be neglected. In an effort to minimize differential changes, a dual transistor, type 2N4044 was used. It has very good differential V_{BE}, and I_B matching, and DC drift specifications. The stage voltage gain has been designed to be approximately 20. A "Zero" control has been incorporated in this stage to provide a method of zeroing the entire electrometer.

The third stage consists of a similar differential amplifier using the PNP dual transistor, 2N3811 (Q503). It has a single-ended output and a design voltage gain of about 20. The major cause of output dc voltage variations with temperature are differential V_{BE} and I_B variations of Q503 and variations in the limiting current of CR502. Through proper component choices, these drift errors are minimal and their effect is insignificant under closed loop conditions. A capacitor, C501, is placed across the load resistor, R517, to roll off the amplifier internally beyond about 6 KHz. This prevents oscillations due to stray coupling between the high-gain stages.

The fourth stage is a simple emitter follower designed for a reasonably low output impedance (573 ohms worst case). Its purpose is to drive both the active filter and the high pass network which couple to the feedback resistor R526.

The fifth stage (Q505, 6) is an active low-pass filter. This represents the best approach, in this case, for compensating the entire amplifier for the desired response time. The low pass combinations, R519 and C502, and R520 and C503, determine the filter rise time. They have been selected to give a damping ratio of approximately 0.7. The first part of the filter stage consists of a differential amplifier using a dual MOS-FET, Q505. This is followed by two cascaded complementary emitter-followers using a dual transistor, Q506, connected to supply negative feedback to Q505. This negative feedback results in a number of advantageous characteristics. Output variations due to power supply changes, composite V_{BE} drift of the complementary emitter follower, and changes in the current source CR503, are all reduced by a factor of the differential amplifier open loop gain.

Since the active filter attenuates frequencies beyond f_c, closing the loop from the electrometer output to the input through R526, causes insufficient cancellation of internally generated noise beyond f_c. Therefore, the high-pass network C504-R525 has been added to bypass the output noise and signal beyond f_c around the active filter to the input. Thus the feedback resistor is driven from the active filter for low frequencies and from the stage preceding the active filter for high frequencies.

Derivation of Equations and Worst Case Analysis

Figure 55 is an aid for deriving the active filter dc drift equations.

Test Procedures and Test Results

a. Detector Set-Up Procedure

Allow a one hour warm up before making any adjustments. Then short the detector input to ground and adjust R501 until the voltage from Q501B, Pin 1 to ground is 0.000 volt. Next, with no signal applied, adjust R512 until the output voltage of the detector amplifier is 0.000 volt. This completes the required set up adjustments.

b. Detector Check Out

1. Signal Rise Time

Test Procedure:

Feed a 0.2 Hz triangular signal through a small air gap (about 1/50 inch) to the input of the electrometer. Connect a chart recorder or scope to the output and adjust its controls for 0.2 volts/DIV vertical and 1.0 second/DIV horizontal. Adjust the amplitude of the input signal until a presentation similar to Figure 56 is obtained. The rise time is defined as the time for the signal to rise from 0% to 90%.

Results:

Figure 56 also shows the results of this test. This amplifier was designed to have a rise time of approximately one second; the test results show a rise time of 1.1 seconds.

2. Output Noise Level

Set up the detector with the input open and shielded. Connect a chart recorder or scope (set to 1 MV/DIV vertical and 10 second/DIV horizontal) to the output.

Results:

Typical results of the one second rise time detector are shown in Figure 57 and of the 0.2 second rise time detector in Figure 58.

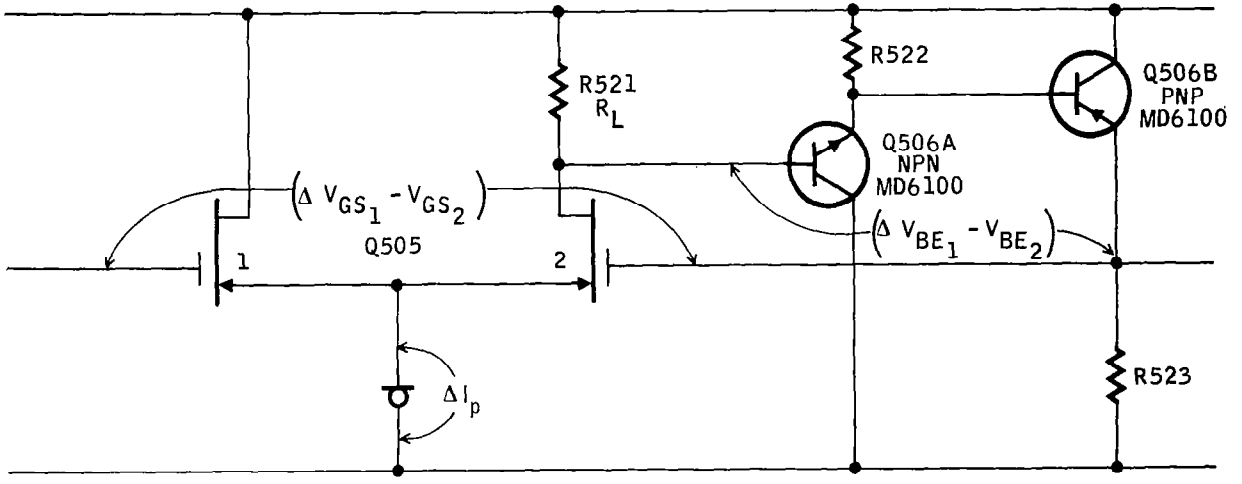

FIGURE 55
Active Filter

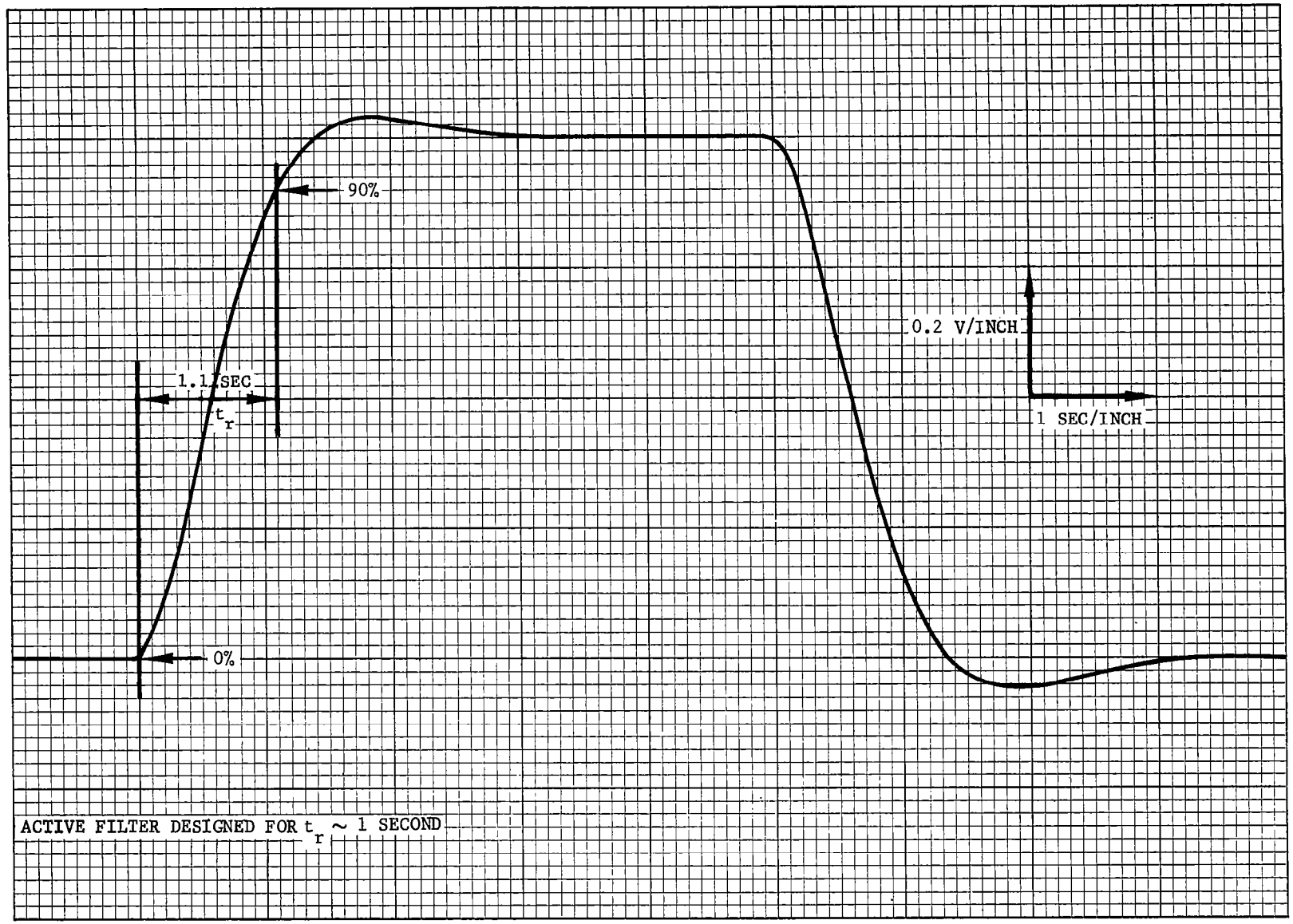

FIGURE 56
Signal Rise Time Test

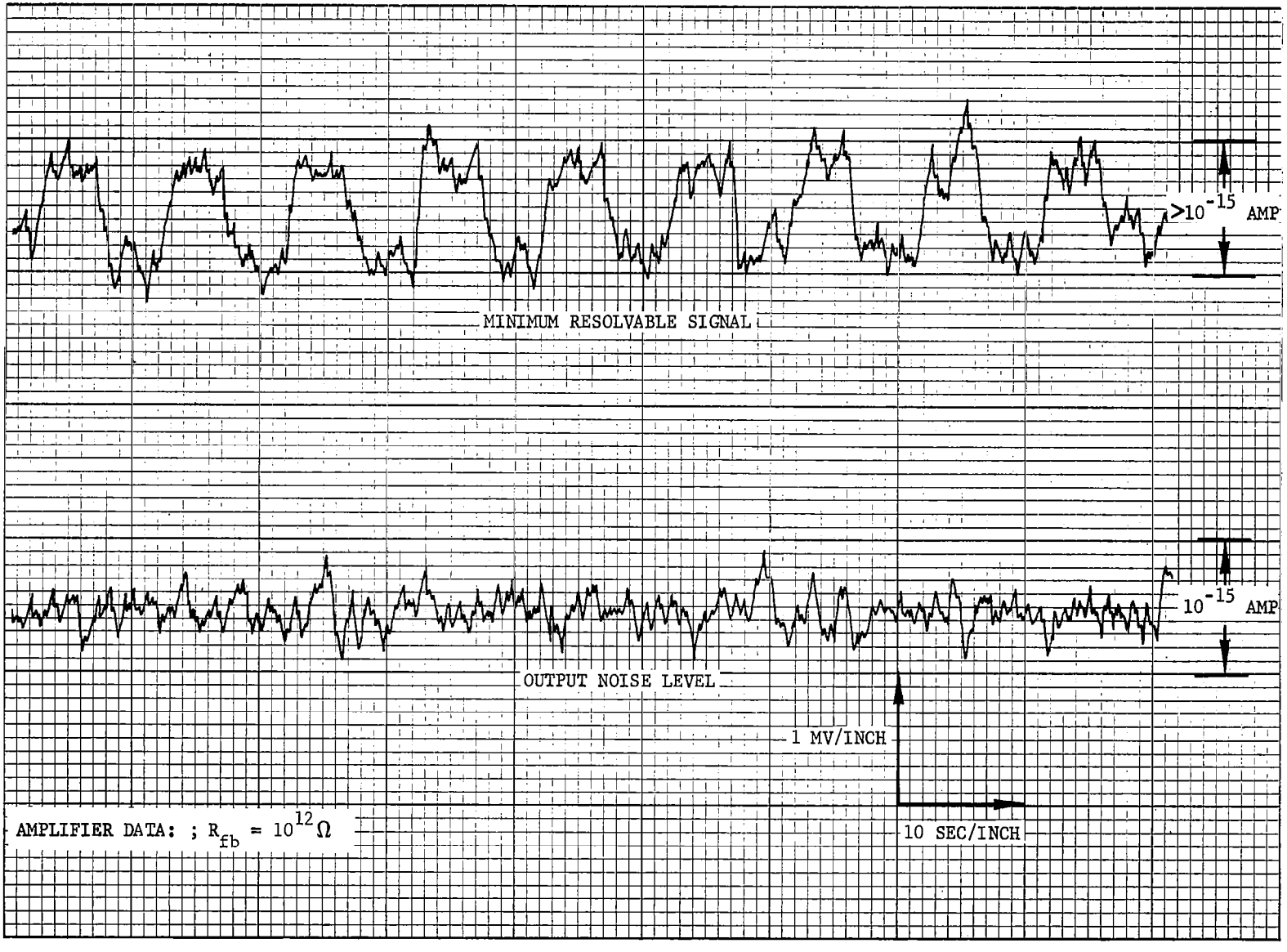

FIGURE 57
$t_r \sim 1$ Second (0-90%)

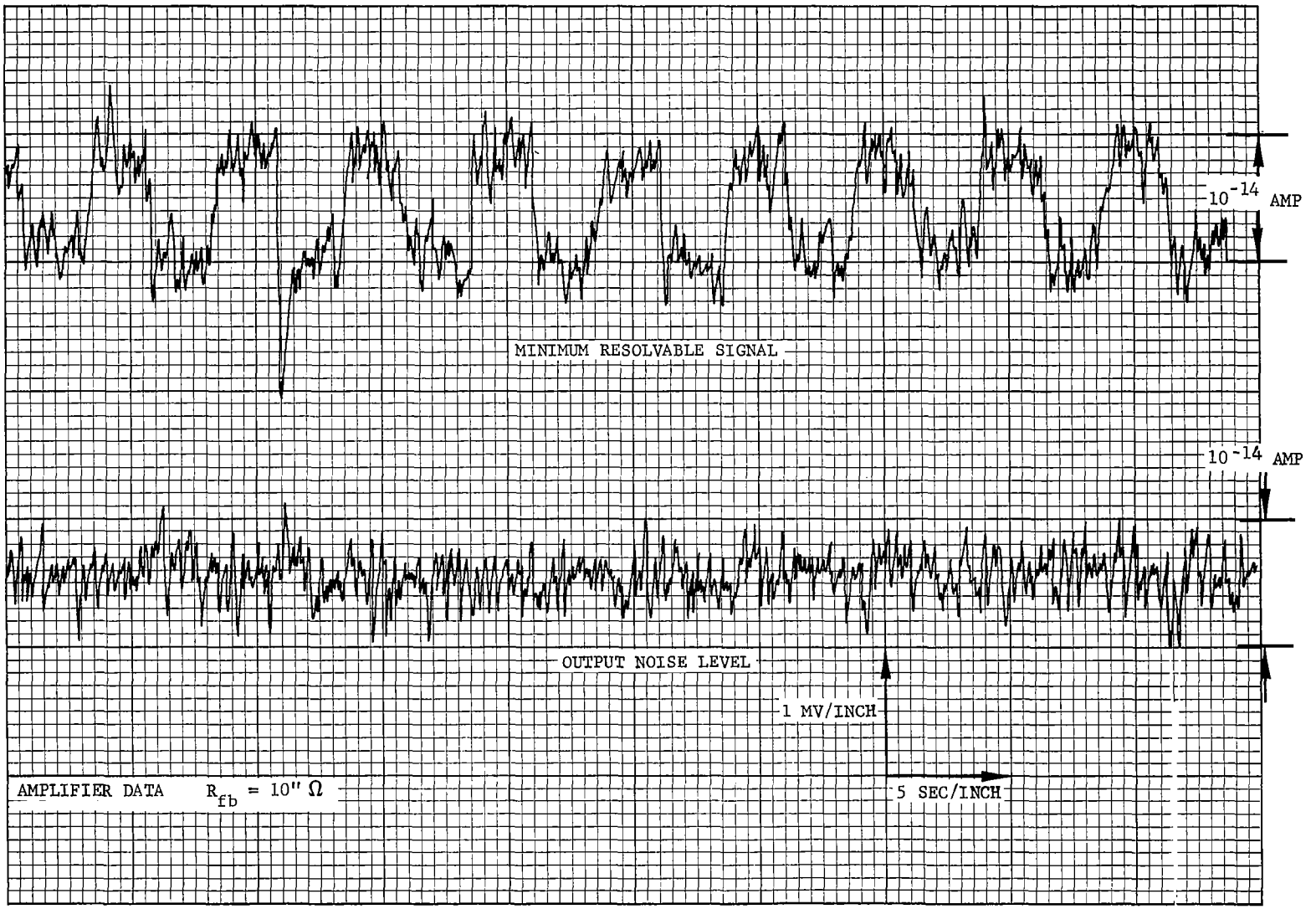

FIGURE 58
$t_r \sim 0.2$ Second

3. Temperature Drift

Test Procedure:

The detector and its power supplies are checked together over temperature. Place the ±10 volt regulated supplies and the detector amplifier in an environmental oven. Apply 28 volts DC to the ±10 volt regulated supplies; monitor the detector output with a digital millivolt meter. First with the system at room temperature, allow the system to stabilize for at least one hour. Adjust the zero control, R512, for 0.000 volt at the detector output. Set the oven to 35°C and allow one half hour stabilization period. When it reaches temperature, record the output voltage reading. Then readjust the oven to 0°C and allow the system to stabilize at that temperature for one half hour. Record the output voltage reading at this temperature. The detector can be checked alone using the same procedure except removing the ±10.000 volt regulated supplies from the oven.

Results:

Typical test results are:

	0°C	35°C	NET CHANGE	MAXIMUM ALLOWABLE
DETECTORS AND POWER SUPPLY	-0.004V	+0.002V	6mV	20 mV
DETECTORS ALONE	0.000V	-0.005V	5mV	10mV

Component Parameter Requirements

The following component is not to be checked in incoming inspection:

Q501 - General Instruction MEM551
Q505 - General Instruction MEM551

Do check CR501, CR502, CR503 for:

I_p = 0.40 mA ±5%

DERATING RULES

General

This section contains the basic design characteristics for each of the component types used in the Two Gas Atmosphere Sensor System (Support Electronics). It shows the most commonly used end-of-life specification factors for transistors diodes, capacitors, and resistors. These derated parameter values are to be used in all worst-case analyses, with the appropriate section of this document referenced in each analysis. Since this document covers only the most commonly used parameters, of the most commonly used components, the designer will occasionally be required to do his own derating. When doing so, the designed must then define in his analysis the method by which he arrived at his derated parameter.

The minimum system ambient temperature is 0°C although the maximum system ambient temperature is specified at +35°C, ratings are given at +50°C to allow for local heating. If any component is found to dissipate twenty milliwatts or more for any two second period, additional derating is required for that part. Those parts which dissipate more than ten milliwatts should be identified, as they may require special layout.

More detailed guidelines on allowable stress levels in all types of components can be found in MIL-HDBK-217, "Reliability Stress and Failure Rate Data for Electronic Equipment". This handbook should not be taken literally with respect to specific failure rates, but should serve as a guide in judging reasonable stresses.

Component Type Discussion

a. Resistors

All of the resistors to be used in the mass spectrometer exhibit changes due to temperature and aging. The value of stress in Table 17 applies only to the power rating of the resistor. Any resistor which develops more than 20 milliwatts of power should be packaged, with care, since about 80% of the heat is conducted through the leads.

The maximum peak voltage impressed across a resistor should not exceed 80% of its maximum rated value.

The preferred values listed in Table 18 should be adhered to, if possible, to minimize the project parts inventory.

Resistors are of the following types:

1. Metal Film - These resistors will be used in the majority of circuits in the system. Their accuracy and stability provide a reasonably tight control over circuit operation. RN55 and RN60 styles will be used. The RN55 is a 1/8 watt resistor with a maximum rated voltage of 200 volts. The RN60 is a 1/4 watt resistor with a maximum rated voltage of 250 volts.

TABLE 17
Resistor Derating Factors

Resistor Type	Manufacturer and Type	Parameter	Purchase Tolerance	Temperature +50°C	Temperature 0°C	Aging	Total Tolerances	(1) Power Stress
Metal Film (RN-55 & RN-60 Equivalents)	Electra MF4C, MF52C (MIL-R-10509C) Pyrofilm PME55		±1%	+100 PPM or A/R	-100 PPM or A/R	±1%	±3%	X0.4
Wire Wound	Genistron GHS (MIL-R-93B)		±0.05% or A/R	+10 PPM	-10 PPM	±.05	±.08%	X0.4
	CAL-R M-10		±1% or A/R	+10 PPM	-10 PPM	±.05	±1.1%	X0.4

NOTE: (1) Power Stress should not exceed 0.4 of the rated value.

The overall derated tolerance on these parts is ±3%. More information can be found in MIL-R-10509C and MIL-HDBK-217, as well as on the Electra MF Series or SHRM 1/8 series data sheets.

2. Wire Wound - These resistors should be used only where a precision of better than ±3% is required, or where resistor dissipation will exceed 100 milliwatts. In the first case, units are available to purchase tolerances of ±0.005%, but tolerances better than ±1.0% should not be specified for resistors used in power applications. The GHS series of Genistron or M-10 series of CAL-R resistors will be used for all wire wound applications.

3. Potentiometers - In special cases where it becomes absolutely necessary to use an adjustable resistor, the Bourns Model 3250 or 3260 Trimpot is the standard component. Derating shall be done by the individual design engineer.

b. Capacitors

All types change with temperature and age. Among the parameters the designer should pay particular attention to are: 1) capacitance (this can vary with frequency, voltage, and temperature); 2) dissipation factor; and 3) breakdown voltage. The allowable stress level indicated on the derating sheets refers to applied voltage. (See Table 19.)

TABLE 18
Preferred Component Values
(Resistors)

1% Metal Film

10.0*	100*	1.0 K*	10.0 K*	100.0 K*
11.0	110	1.1 K	11.1 K	110.0 K
12.1*	121*	1.21 K*	12.1 K*	121.0 K*
13.0	130	1.3 K	13.0 K	130.0 K
15.0*	150*	1.5 K*	15.0 K*	150.0 K*
16,2	162	1.62 K	16.2 K	162.0 K
18.2*	182*	1.82 K*	18.2 K*	182.0 K*
20.0	200	2.0 K	20.0 K	200.0 K
22.1*	221*	2.21 K*	22.1 K*	221.0 K*
24.3	243	2.43 K	24.3 K	243.0 K
27.4*	274*	2.74 K*	27.4 K*	274.0 K*
30.1	301	3.01 K	30.1 K	301.0 K
33.2*	332*	3.32 K*	33.2 K*	332.0 K*
36.5	365	3.65 K	36.5 K	365.0 K
39.2*	392*	3.92 K*	39.2 K*	392.0 K*
43.2	432	4.32 K	43.2 K	432.0 K
47.5*	475*	4.75 K*	47.5 K*	475.0 K*
51.1	511	5.11 K	51.1 K	511.0 K
56.2*	562*	5.62 K*	56.2 K*	562.0 K*
61.9	619	6.19 K	61.9 K	619.0 K
68.1*	681*	6.81 K*	68.1 K*	681.0 K*
75.0	750	7.5 K	75.0 K	750.0 K
82.5*	825*	8.25 K*	82.5 K*	825.0 K*
90.9	909	9.09 K	90.9 K	909.0 K
				1.00 M*

*Preferred Values

TABLE 19
Capacitor Derating Factors

Capacitor Type	Manufacturer and Type	Parameter	Purchase Tolerance	Temperature +50°C	Temperature -30°C	Aging	Total Tolerance	Stress (1) Hi	Stress (1) Lo
Ceramic (330 to 1000 PF)	Vitramon VK Series, CK05, 06 (MIL-C-11015B)	Capacitance	±10%	-6%	±3%	±5%	±25%	X0.8	
Ceramic (.01 to 10 MF)	USCC C-12 Series (MIL-C-11015B)	Capacitance	±5%	-2%	+2%	±5%	±12%	X0.8	
Mylar (5000 to 0.5 MF)	Elpac Z Series	Capacitance	±5%	+5% -0%	°0% -5%	±5%	±15%	X0.8	
Tantalum (0.1 to 50 MF)	Kemet J Series CS12, 13 (MIL-C-26655B)	Capacitance	±10%	±4%	±6%	±5%	±25%	X0.8	
		Dissipation Factor		±20%	±20%	±20%	±60%	-	
		Leakage		+100%	-	+25%	+125%	-	

NOTE: (1) Stress rating applies to applied peak voltage

Capacitors are utilized in increasing value groups according to type, as follows:

1. Ceramic - The ceramic capacitor offers the smallest size for its capacitance, but it does experience a comparatively large change in value with temperature. Dissipation Factor also changes with frequency and temperature. Vitramon VK series (CK05 and CK06) or the USCC C12 series will be used.

2. Mylar - Characterized by their extremely high leakage resistance, they do present a problem as the result of their comparatively large size. The voltage stress limit of .8 of rated voltage should be observed for reliability. Elpac Z series will be used.

3. Tantalum - For filtering applications above 100 KHz (or less for the 5-50 F sizes), the tantalum capacitor must be by-passed by a ceramic or mylar capacitor. The Kemet J series (Polar Solid Tantalum) will be purchased at a tolerance of ±10%. These capacitors meet the requirements of styles CS12 and CS13 of MIL-C-26655B.

   The preferred component values, listed in Table 20, are what the name implies. If the designer tries as much as possible to adhere to these values it will reduce the total project parts ordering.

c. Diodes

Several types of diodes are used in the mass spectrometer. These are the 1N3070, 1N5288A, and the 1N4565 to 1N4774 reference series, FCT 1035 reference and 1N3287 stabistor. The 1N3070 is a high speed, high conductance planar diode with moderate current capabilities (300 mA). It will be used wherever feasible. The derated parameters are forward voltage and leakage current. The derating curves appear in Figures 59 through 61. The reverse voltage applied should not exceed 80% of the PRV.

The 1N5288A is a constant current source diode. It provides a current of 0.4 mA ±5% and has an approximate zero temperature coefficient. The design engineer using it will derate the device.

The 1N4565 to 1N4774 is a temperature-compensated reference diode series. They are used where stable reference voltages are necessary. The design engineer using it will derate the device.

The FCT 1035 is an ultrastable reference diode which operates with 100 mA of current flow. The device will be derated by the design engineer using it.

The 1N3287 is a stabistor and is used to temperature compensate the base-emitter junction of a transistor.

d. Transistors

Eight types of silicon transistors are used in the support electronics. These are the 2N2484, 2N3799, 2N3499, 2N3635, 2N3811, 2N4044, 2N2916, MD6100 and the 2N2891. In addition a dual MOS FET type MEM551 is used.

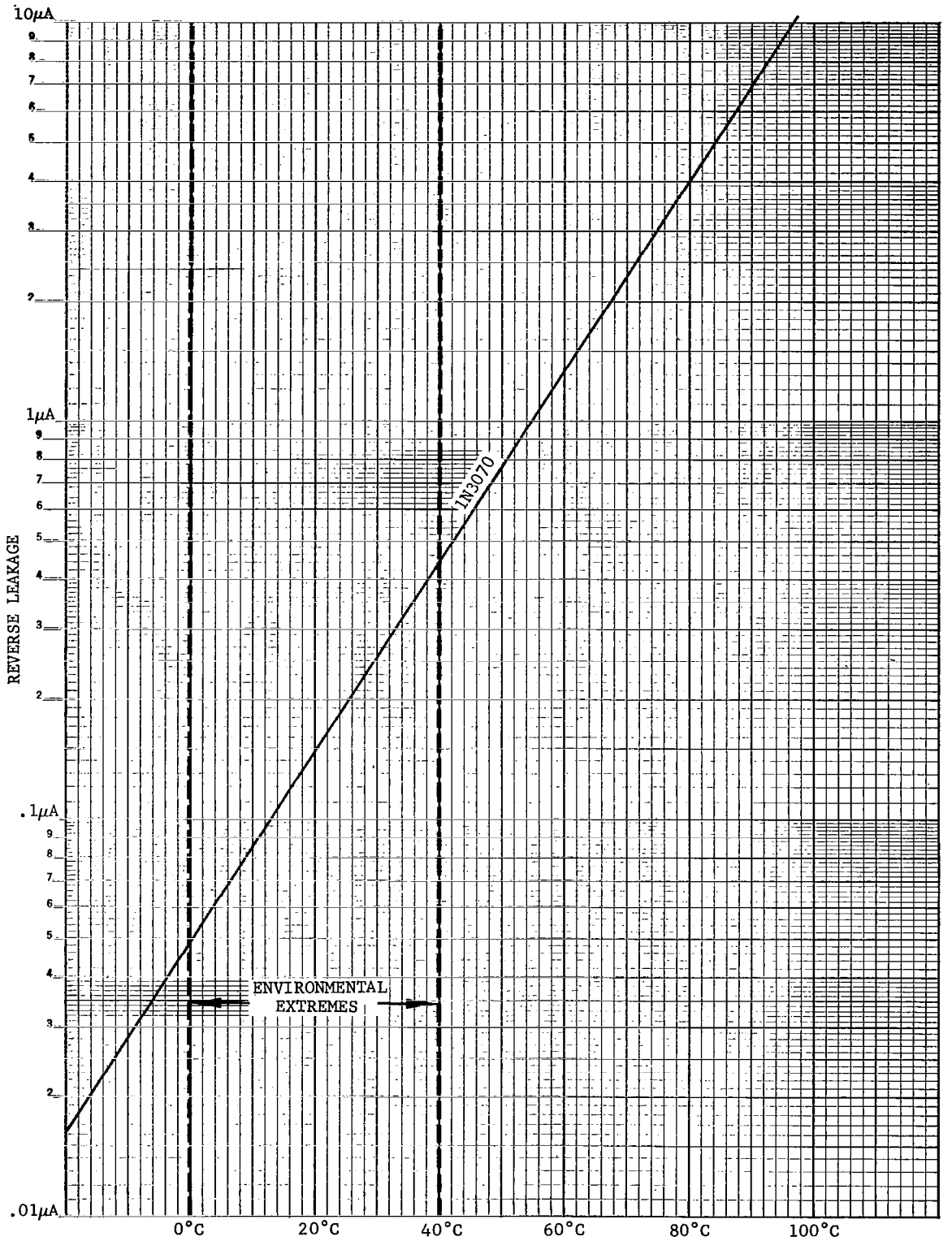

FIGURE 59
End of Life Diode Leakage

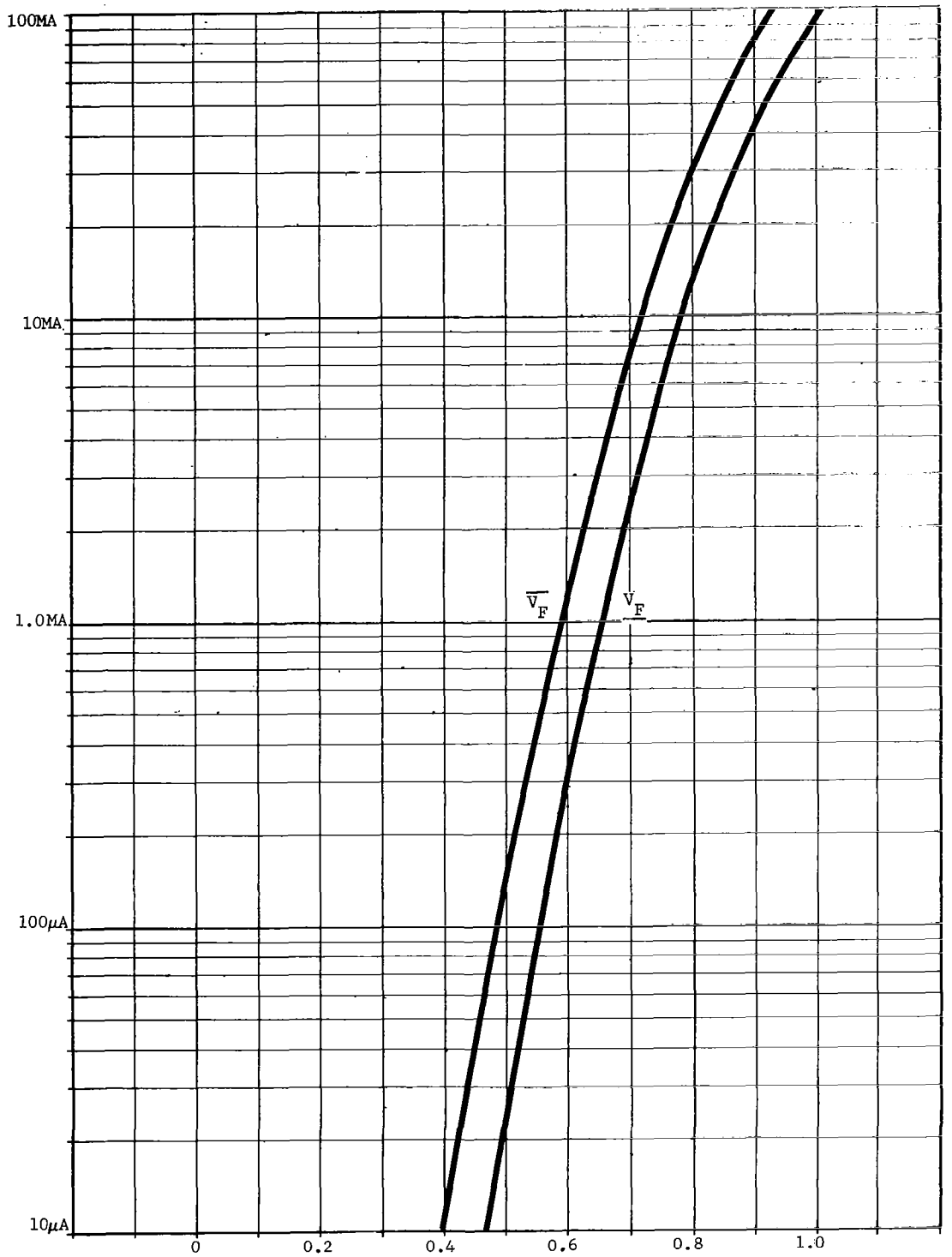

FIGURE 60
End of Life Forward Voltage Characteristics
of the 1N3070 Diode ($0^{o}C$)

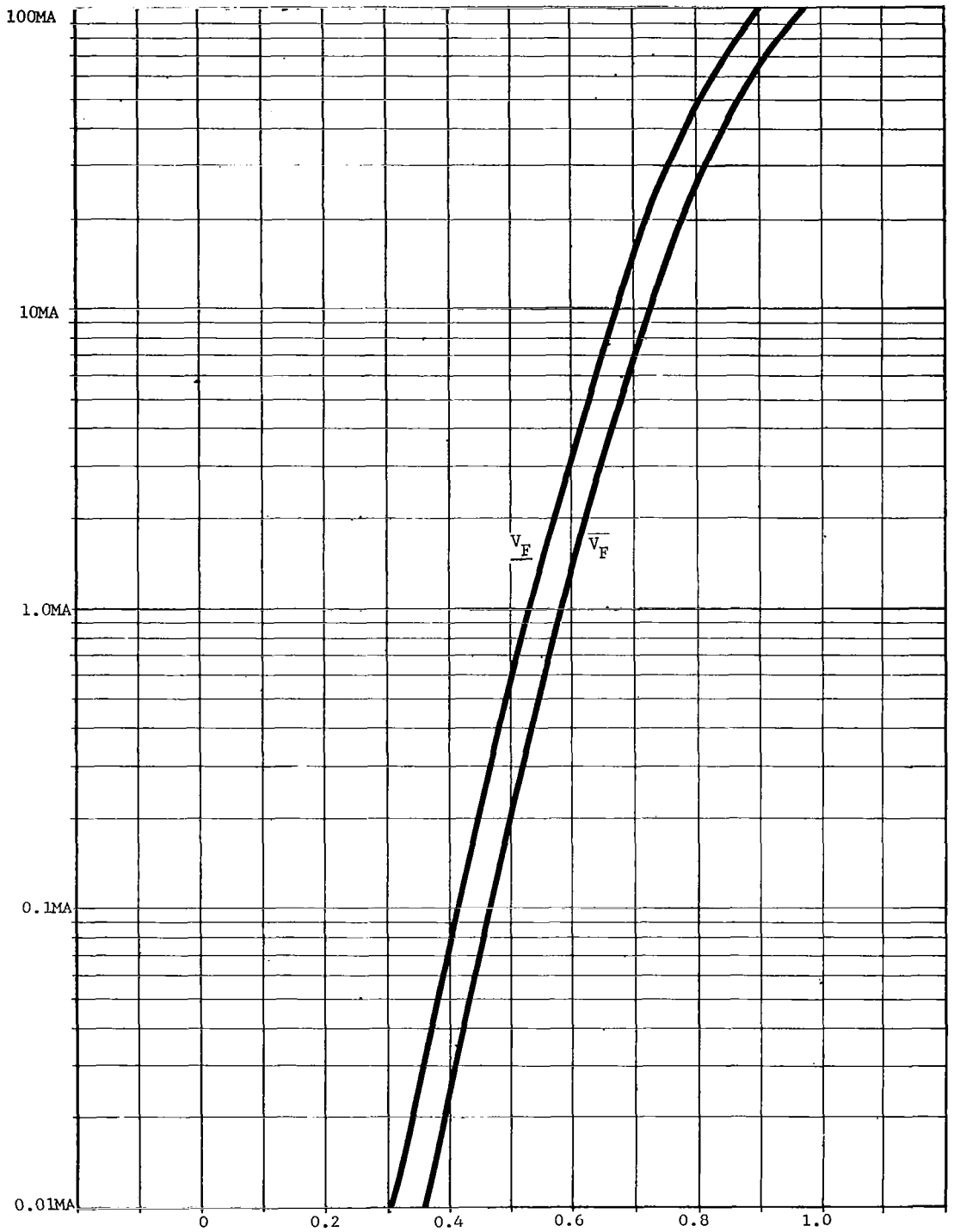

FIGURE 61
End of Life Forward Voltage Characteristics
of the 1N3070 Diode (35°C)

TABLE 20

Preferred Component Values
(Capacitor)

a. Ceramic (PF) ±10% Purchase Tolerance

330	1500	7500
470	2200	10000
750	3300	
1000	4700	

b. Mylar (MF) ±5% Purchase Tolerance

0.005	(.0047)	0.033		0.22	
0.007	(.0068)	0.05	(.047)	0.33	
0.01		0.075	(.068)	0.5	(0.47)
0.022		0.10			

c. Tantalum (MF) ±10% Purchase Tolerance

0.10		2.2		33.0	
0.22		3.3		50.0	(47.0)
0.33		5.0	(4.7)		
0.50	(0.47)	7.5	(6.8)		
0.75	(0.68)	10.0			
1.0		22.0			

The 2N2484 (NPN) and the 2N3799 (PNP) are used as low level amplifiers and switches in the Support Electronics. They exhibit high gain characteristics at very low current levels.

The 2N3499 (NPN), the 2N2891 (NPN), and the 2N3635 (PNP) are used in the Support Electronics as high level amplifiers and switches. They exhibit good current capability with moderate switching speeds, and they have a high breakdown voltage rating.

The 2N3811 (dual PNP), 2N2916 (dual NPN), and 2N4044 (dual NPN) are matched pairs of high gain transistors used in differential amplifiers. The MD6100 is a dual complementary transistor used in low level amplifiers. It is similar to the 2N2484 (NPN) and the 2N3799 (PNP).

The most important factor in maintaining reliable transistor operation is power dissipation. For this reason, the power dissipation of devices used in this design shall be derated to 50 percent of the manufacturer's maximum rating at the operating temperature. Any transistor dissipating more than 10 milliwatts should be given special consideration both for the affect of heating on the unit itself and the affect of its heating on surrounding components.

The derated values of I_{CBO}, h_{FE}, SF_{CE}, and SV_{BE} are given in Figures 62 through 69, which include the effects of temperature and age. In the following section, both the derating rules used for the curves and the other parameters are explained. Derating for parameters other than those given in Table 21 is the responsibility of the individual design engineer.

h_{FE} - The transistor minimum gain is established at 0°C from the minimum value specified at 25°C in the manufacturer's data sheets. The derating factor for the temperature is 0.85. Another derating factor of 0.8 is applied at all temperatures to account for the effects of age. The total derating at 0°C is, therefore, 0.7 times the initial minimum value at 25°C.

I_{CBO} - Transistor leakage currents have been derated by the same factors as diode leakage currents; a factor of 2 times the maximum specified current for age. Leakage currents between 25°C and 100°C have been derived by interpolating the data given at these two temperatures.

SV_{CE} - Collector saturation voltage curves are established at forced betas of ten, and are derived from the maximum values stated on the manufacturer's specification sheet.

SV_{BE} - Maximum base-emitter saturation voltages are established at current gains of ten, and derived from the maximum values given on the manufacturer's specification sheets. For the sake of simplicity, voltage levels below the minimum collector current at which the data was specified have been considered constant.

$V_{BE_{OFF}}$ - At a junction temperature of 60°C any transistor can have its base-emitter diode forward biased by as much as 0.3 volts and the resulting emitter current will not exceed I_{CBO} plus 5 MA.

Q_S (Stored Charge) - When a transistor is used in the switching mode, stored charge plays a primary role in determining the turn-off time. The maximum value of stored charge is a function of collector current, base current, and temperature. The maximum value determined for a given operating condition at 25°C should be multiplied by a factor of
at a temperature of 50°C, and by an additional factor of
at all temperatures for the effect of age. Stored charge is not related to junction capacitance, which is an additional separate factor.

Breakdown Voltage - No transistor should have a collector-emitter bias voltage greater than 80% of BV_{CEO}.

Collector Current - No transistor should have a collector current greater than 50% of its maximum rated value.

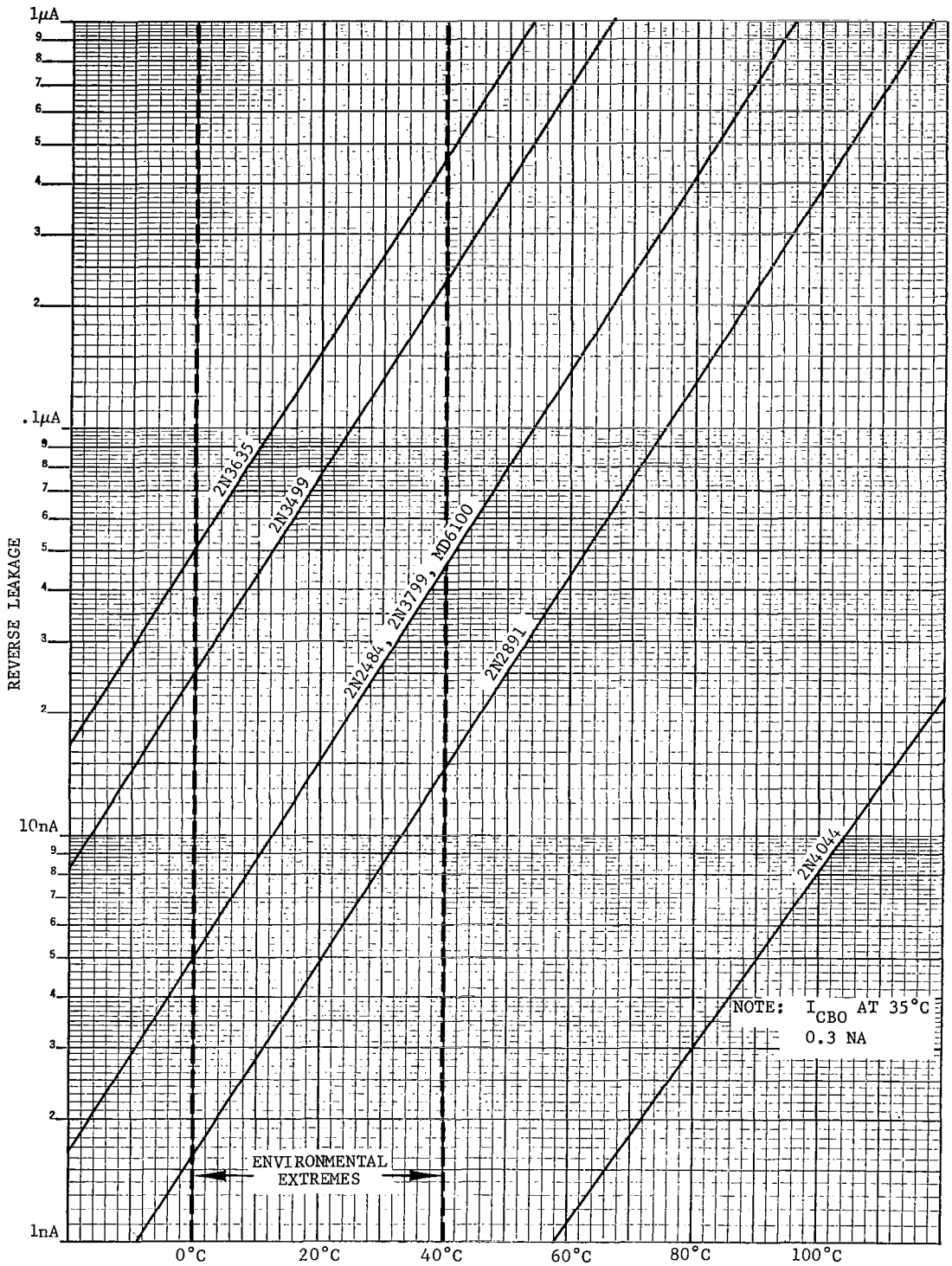

FIGURE 62
End of Life Transistor Leakage (I_{CBO})

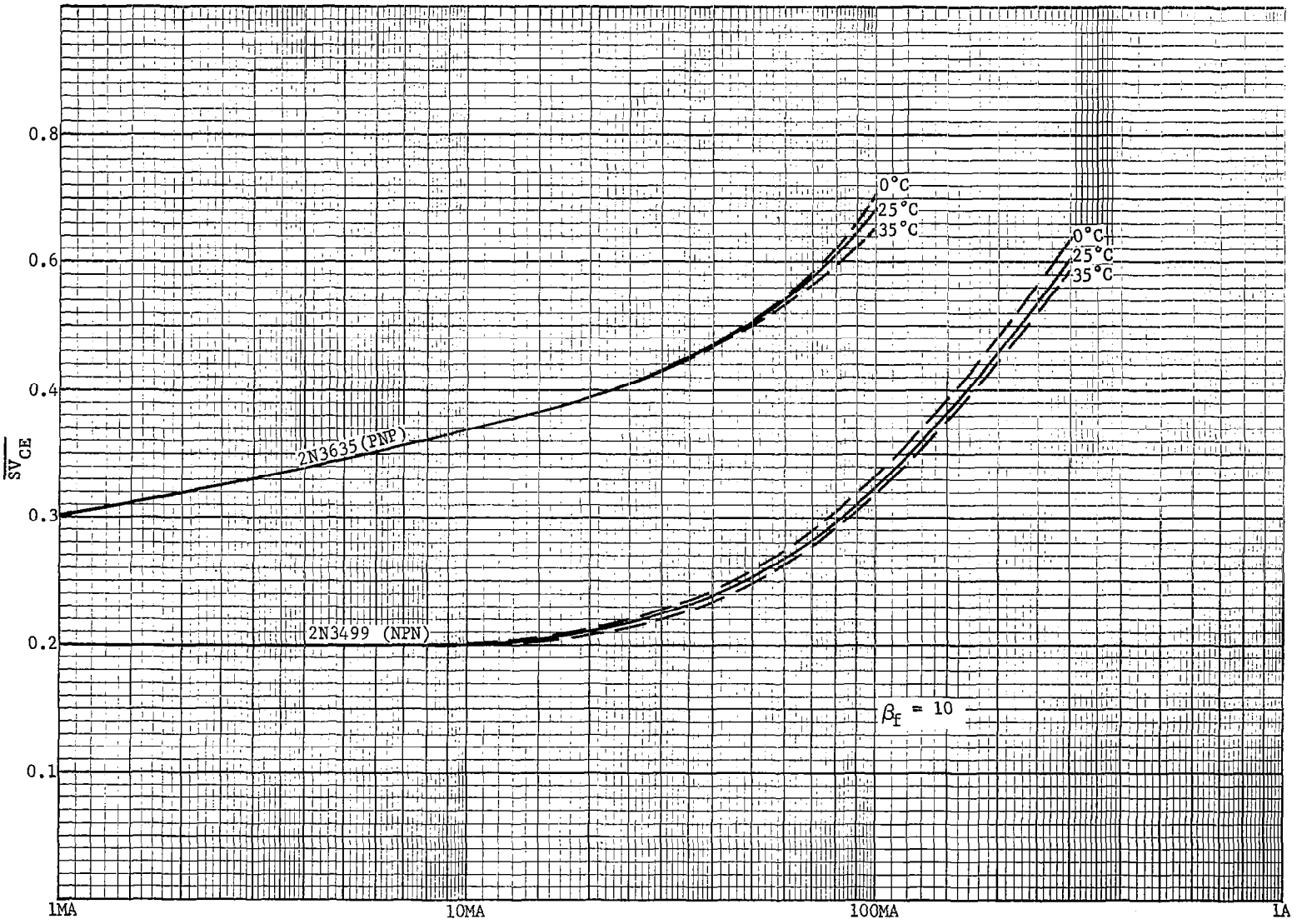

FIGURE 63
$\overline{SV_{CE}}$ Characteristics

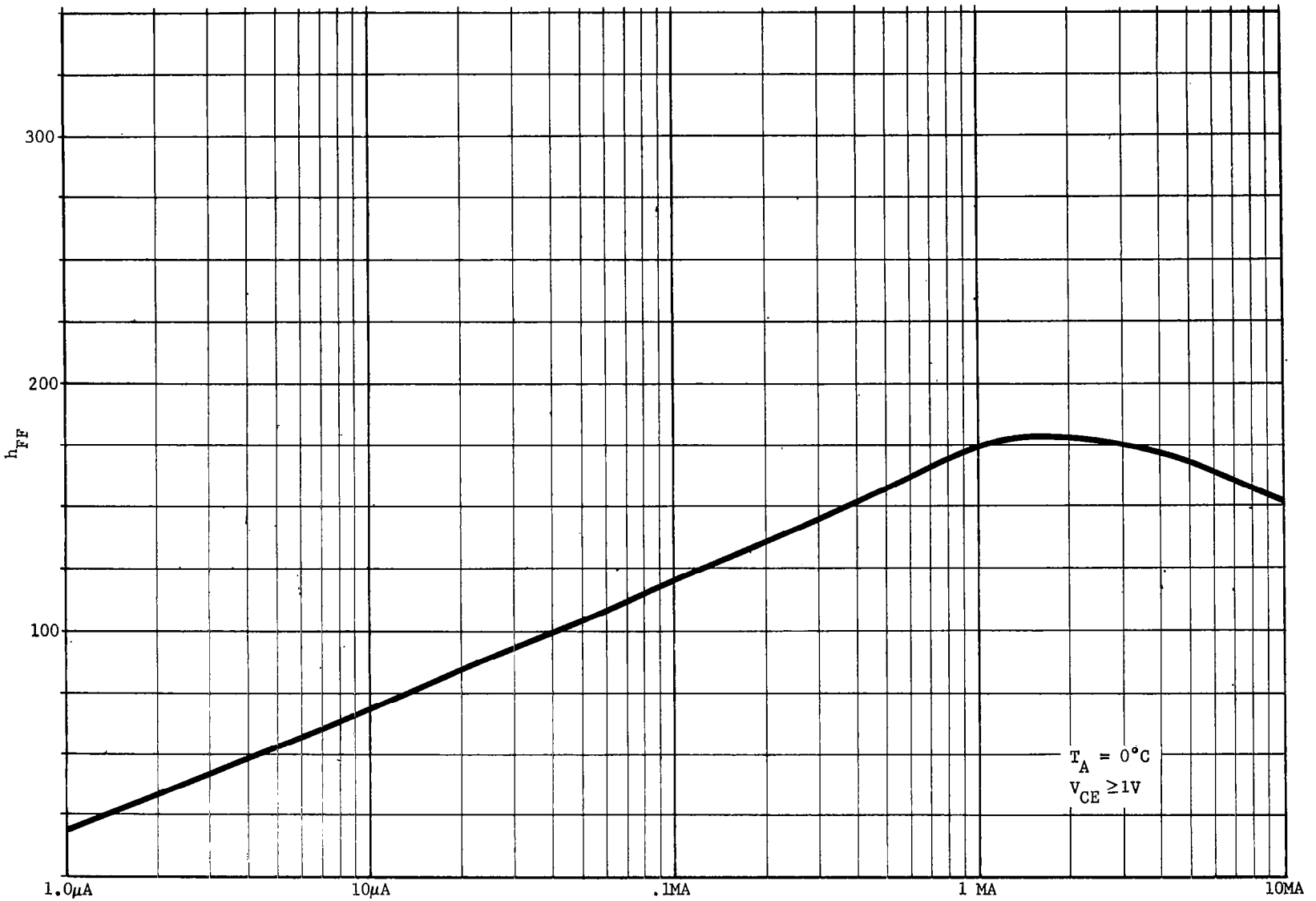

FIGURE 64
End of Life h_{FE} Characteristics of the
2N2484 (NPN Silicon)

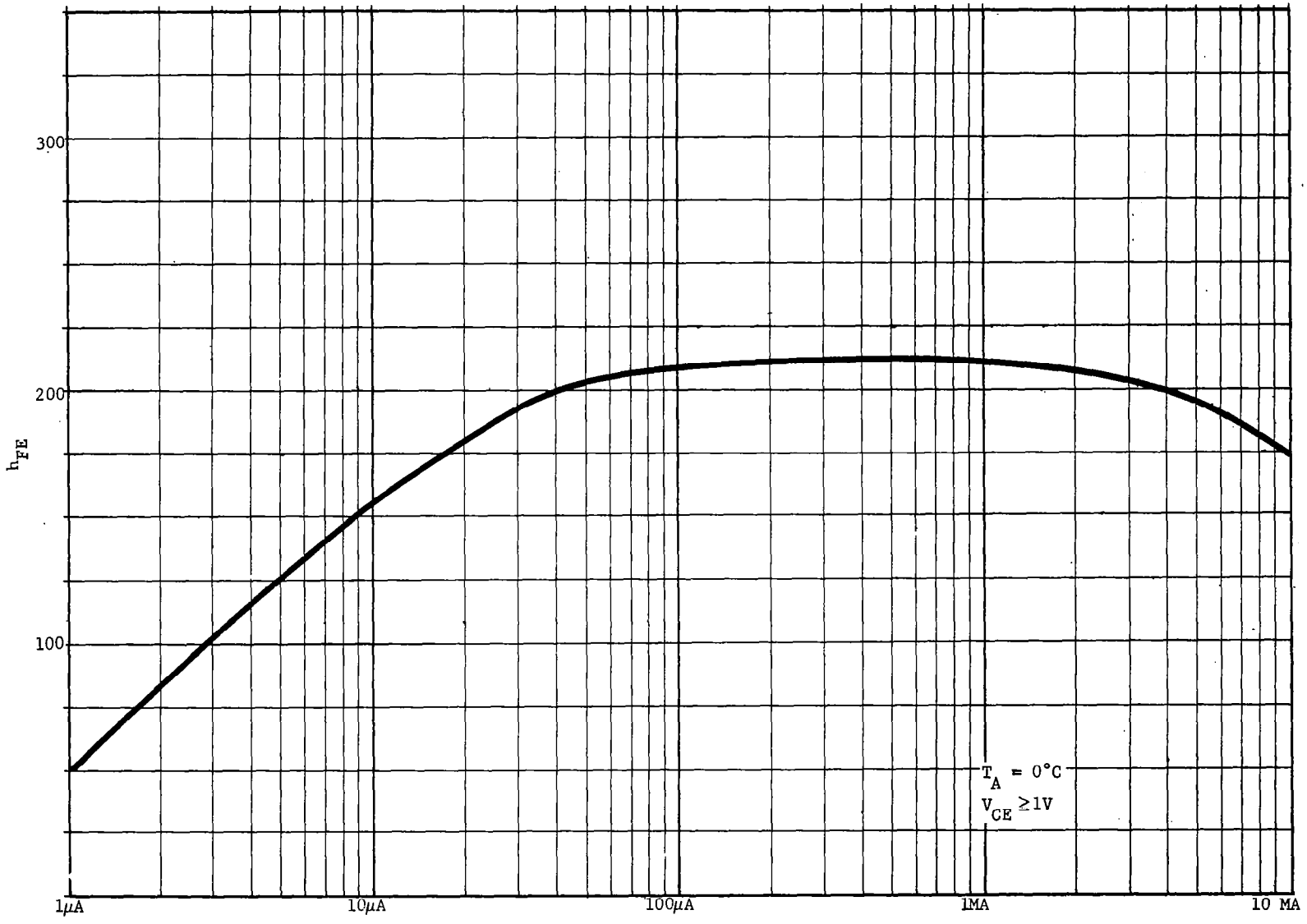

FIGURE 65
End of Life h_{FE} Characteristics of the
2N3799 (PNP Silicon)

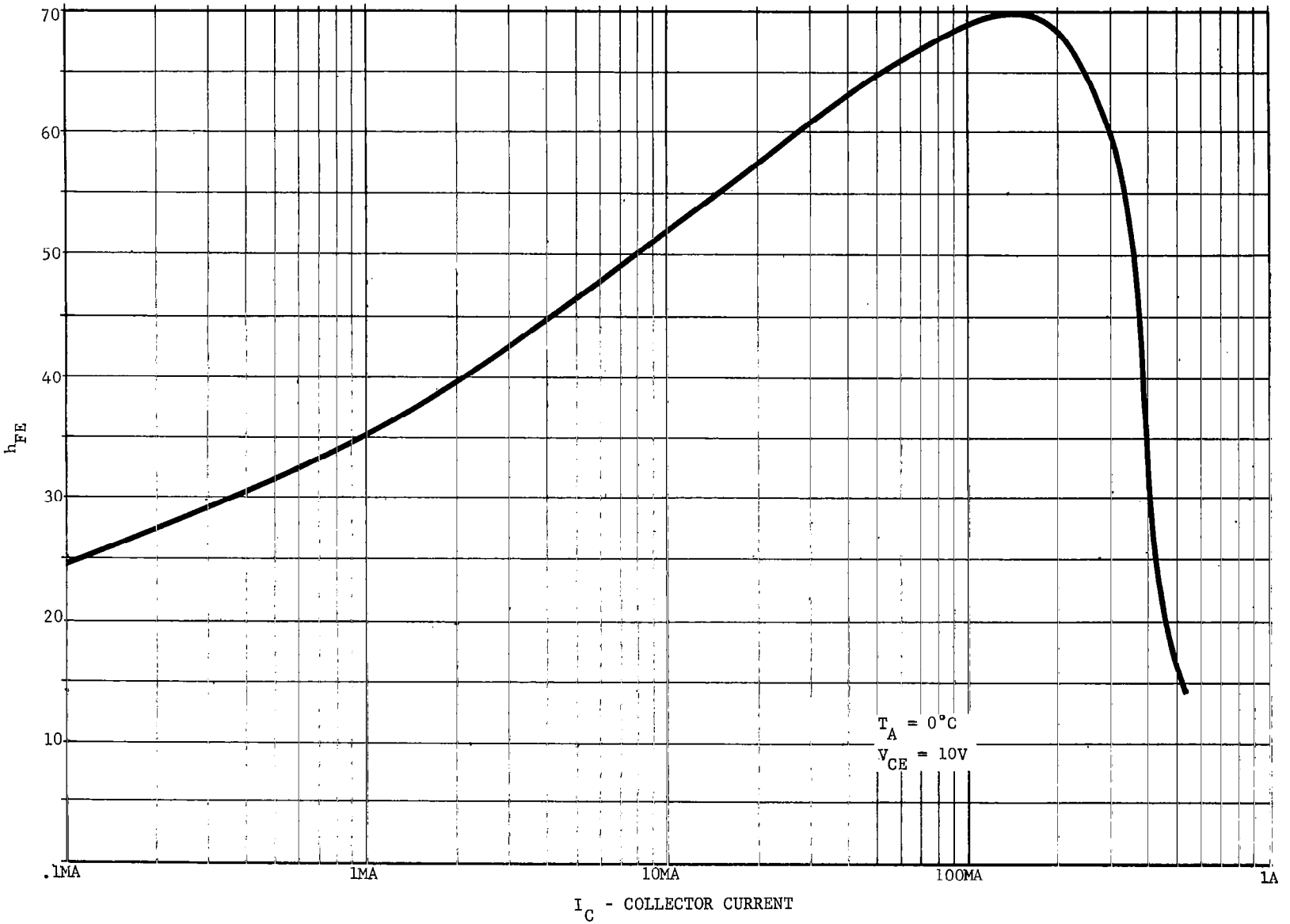

FIGURE 66
End of Life h_{FE} Characteristics of the 2N3499

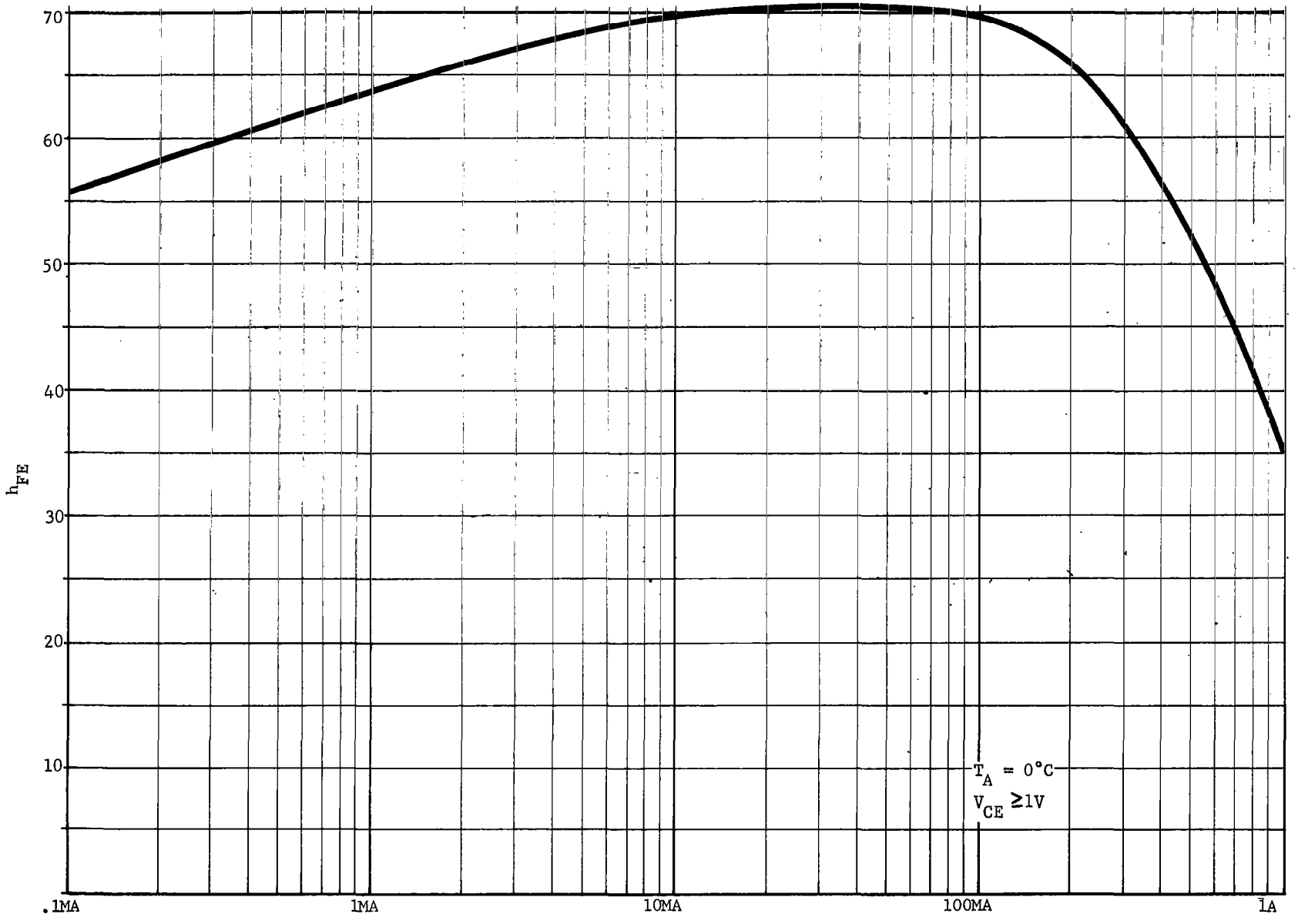

FIGURE 67
End of Life h_{FE} Characteristics of the
2N3635 (PNP Silicon)

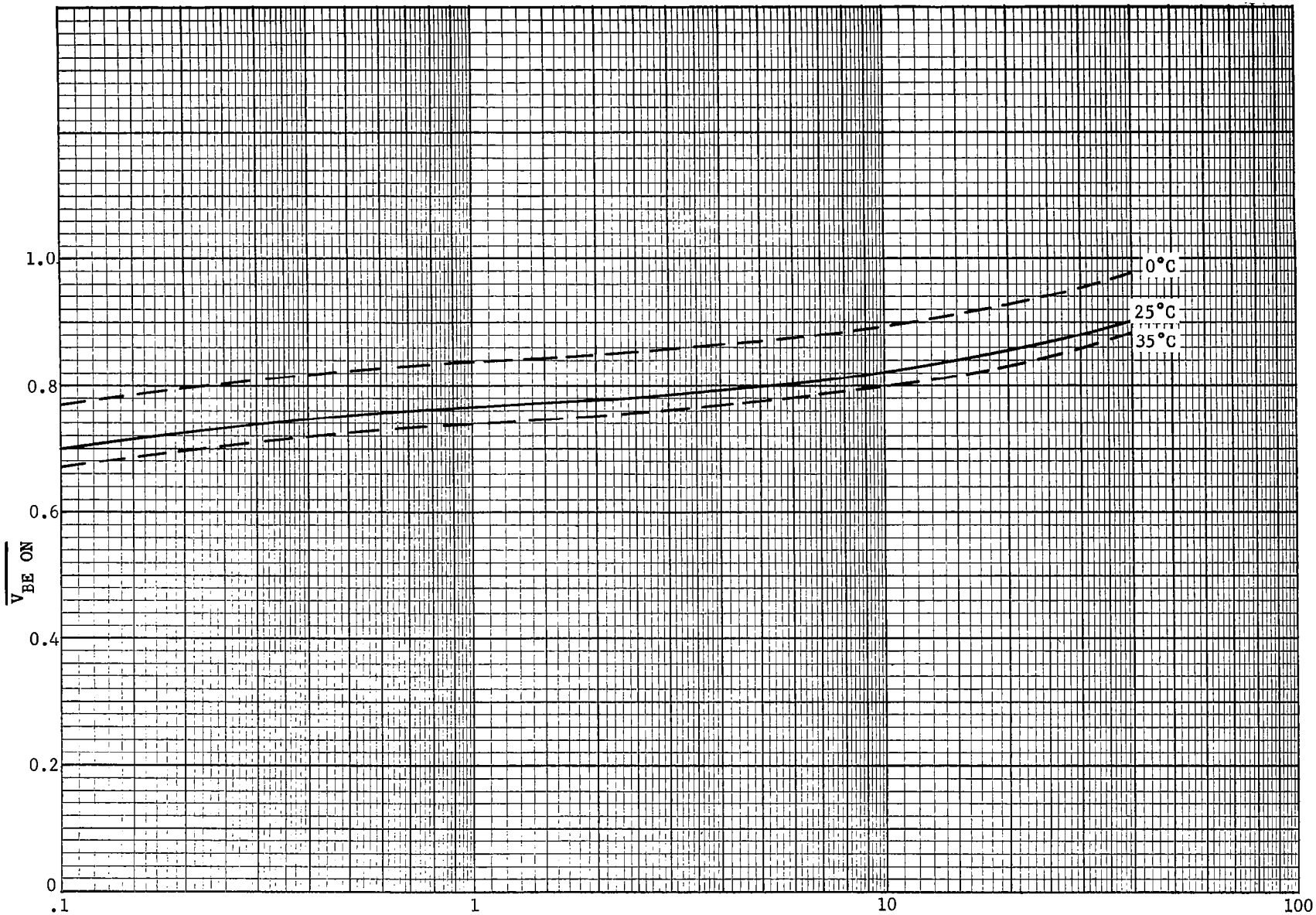

FIGURE 68

End of Life $\overline{V_{BE\ ON}}$ Characteristics of the
2N2484, 2N3799 Transistors (NPN Silicon)(PNP Silicon)

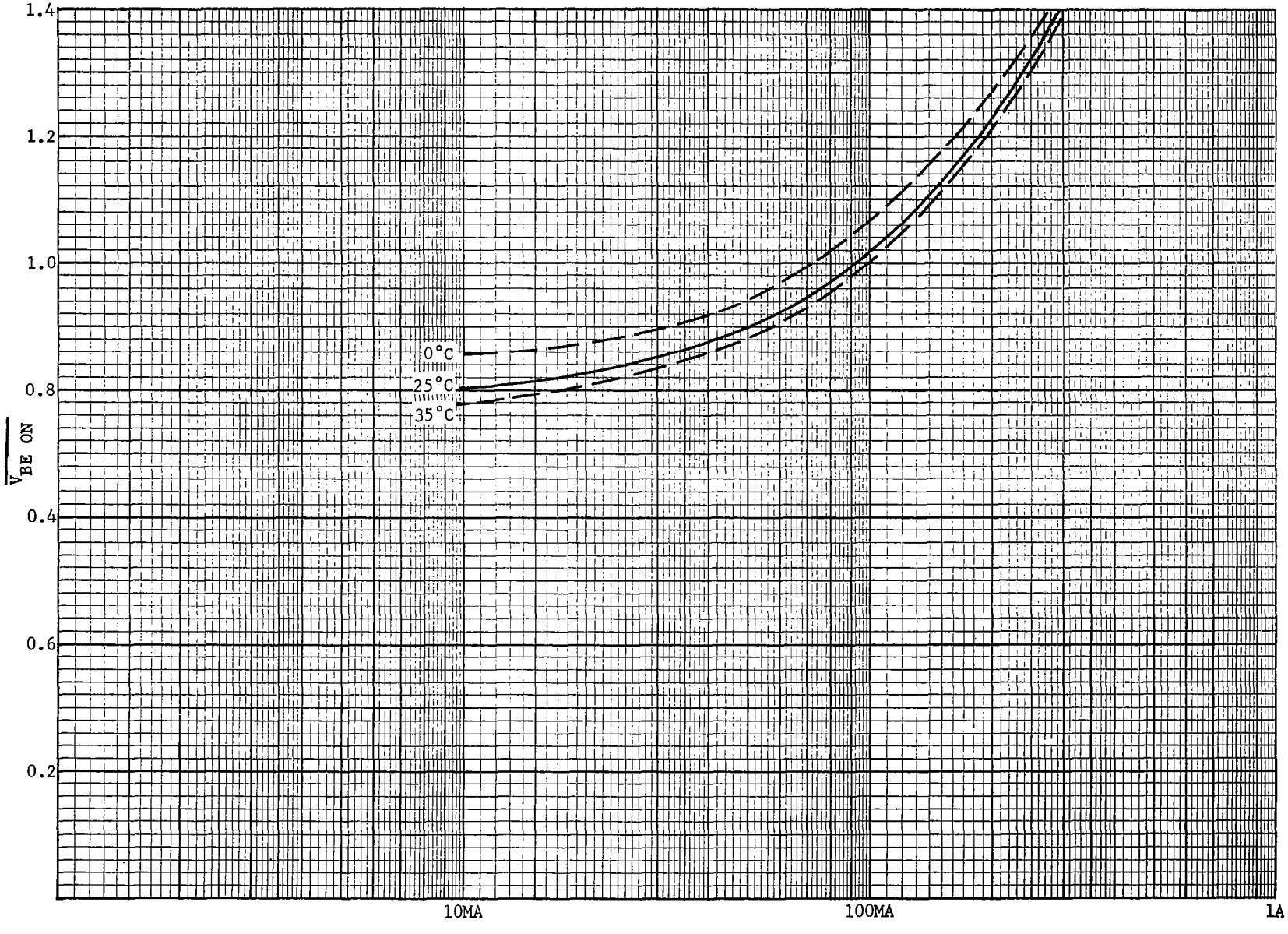

FIGURE 69

End of Life $\overline{V_{BE\ ON}}$ Characteristics of the

2N3499, 2N3635 Transistors (NPN Silicon)(PNP Silicon)

TABLE 21

Transistor Derating Factors

Transistor Type	Manufacturer and Type	Parameter	Purchase Tolerance	Temperature 50°C	Temperature 0°C	Aging	Total Tolerance
Low Level	Motorola MD6100	Beta	PER	-	X.85	X.8	X.7
	2N3799(PNP) Fairchild 2N2484(NPN)	$\overline{I_{CBO}}$	SPEC	See curves		-	X.2
	Union Carbide 2N4044	$\overline{V_{CE\ SAT}}$		See curves		-	(1)
High Level	Motorola 2N3635(PNP) 2N3499(NPN)	$\overline{V_{BE\ SAT}}$		See curves		-	-
	Fairchild 2N2891						

Notes:

(1) The collector saturation voltage is assumed to be 0.7 volts for worst-case calculations; the voltage will vary according to application.

MECHANICAL DESIGN AND PACKAGING

The mechanical design and packaging considerations involve five principal mechanical design areas:

a. Ion Source Assembly

b. Collector Assembly

c. Analyzer Envelope and Interfacing

d. Analyzer Magnet & Support Structure

e. System Package

The electronic modules are not specified in the above light since the mechanical design in this area is limited primarily to printed circuit board layout. In general the design goal for these modules was to provide the necessary mechanical functions and rigidity in harmony with the functional requirements with a minimum required weight. Generally speaking the design follows the recommendations.

The configuration of the analyzer envelope was determined by the object slit, analyzer magnet, and collector positions as calculated by the magnetic sector design. The analyzer housing provides a vacuum tight chamber which houses the ion source and collector assemblies and which interfaces with the inlet system. The housing was fabricated in a cylindrical ion source housing and a curved section with two flat side walls to house the collector assembly. The two sections were joined by inert arc welding and one flat face of the second section was sealed by low temperature electron beam welding to minimize stresses and warpage. The total assembly was then stress relieved and then final machining of critical surfaces was completed to proper tolerances. The housing material is 304 stainless steel which was selected because it has good vacuum properties, is non-magnetic, and is weldable. In order to eliminate the need for heavy flanges the envelope is entirely welded at the final assembly after test. These welds occur at the collector flange and at the end of the ion source housing. The collector flange weld is very critical because it must be assured that the welding process will cause no movement of the collector buckets. A test collector flange and mating part were fabricated and welded to evaluate this problem. Weld reliefs were machined into both parts and both parts were heat sinked. Distortion was checked along the length of the collector flange and found to be no greater than 0.0003". Voltages are introduced to the ion source by the use of three nine pin feed throughs. A new design was utilized to minimize heating of the glass to metal seals when the headers are welded into the housing. New single pin headers were also designed which were needed to bring the collected ion currents out to the electrometers. These headers must have a pin to body resistance of about 1×10^{13} ohms. Under dry conditions this is achieved, but in the presence of moisture the resistance drops rapidly. Experimentation with desicants and/or surface coatings will be required to keep the resistance up. The entire housing, when sealed, should be bakeable to over 300°C so that the instrument can be outgassed. The headers are generally a weak point in this process, however, samples of these units were welded in tubes and baked out

successfully. A photograph of the analyzer is shown in Figure 70. The pump out tube is part of the end cap which welds into the ion source housing.

The analyzer magnet is a five piece assembly consisting of two Armco iron pole pieces, two Alnico V magnet arms, and an Armco iron yoke. The magnet arms were the most difficult parts to fabricate. The small quantity requirements and short delivery time made it possible to have the pieces cast in the final shape as it is usually done. Therefore, raw billets were purchased and the magnets were cut and ground to shape. Initial attempts at cutting the material were futile and finally electron discharge machining was used for the fabrication process. Once the parts are cut they must be heat treated and then have the critical dimensions ground. Finally, the pieces are cemented together and the magnet is charged. To assist in the charging process a three piece shunt and keeper assembly was fabricated so that the entire volume between the pole pieces, including the dished out regions can be filled with material. If an over charge results the field strength is reduced by the application of an ac current in the charging coil.

The ion source is a modified version of the one used in an instrument for the OGO-F satellite. This source was described previously. The nozzle on the OGO-F ion source was replaced by an object slit plate which also became the mounting plate for the ion source and the z-axis focus lens assembly. This permits the ion source to be completely assembled and then aligned under a traveling microscope before installation in the analyzer housing. The fabrication of the object slit in the mounting plate was a difficult task due to the small dimensions, 0.012" by 0.020" with a thickness of 0.050" and a 5° taper requirement on the walls. Electron discharge machining was again used. All of the ion source parts are gold plated to minimize secondary emission and surface interaction problems. The construction embodies locating counterbores throughout to obtain location of the electron guns, and the ion focusing system. The filaments, which are 0.003" diameter 75-25 tungstem-rhenium alloy wires are mounted on filament posts with one end mounted to a thin strip of similar ribbon material which is best to form a tension spring. This is required to hold the filaments in position when they expand due to thermal expansion when they are in operation. The similarity of operation seen in the OGO-F units thus far indicates that adequate repeatability in the fabrication can be readily achieved. The z-axis focus assembly is a split assembly which will allow the ion beam to be deflected in the event of misalignment.

The collector assembly consists of three movable frames (m/e 18, m/e 28 and 32, and m/e 44) that mount on the collector flange and to which the ion collectors are attached. Each of the frames can be moved ±0.075" about the theoretical position along the flange. In addition, the collectors and their shields can be moved up or down 0.100 inches on the frames parallel to the ion paths. The necessary isolation between the buckets and the shields is obtained by using ruby washers. Wires attach from the collectors to the feed through pins in the collector flange. The assembly drawing of the collector assembly is shown in Figure 71. After the collectors have been properly positioned then shim stock is spot welded on the sides and on the top between the collectors to shield the feed through pins and connections so that stray ions will not be registered.

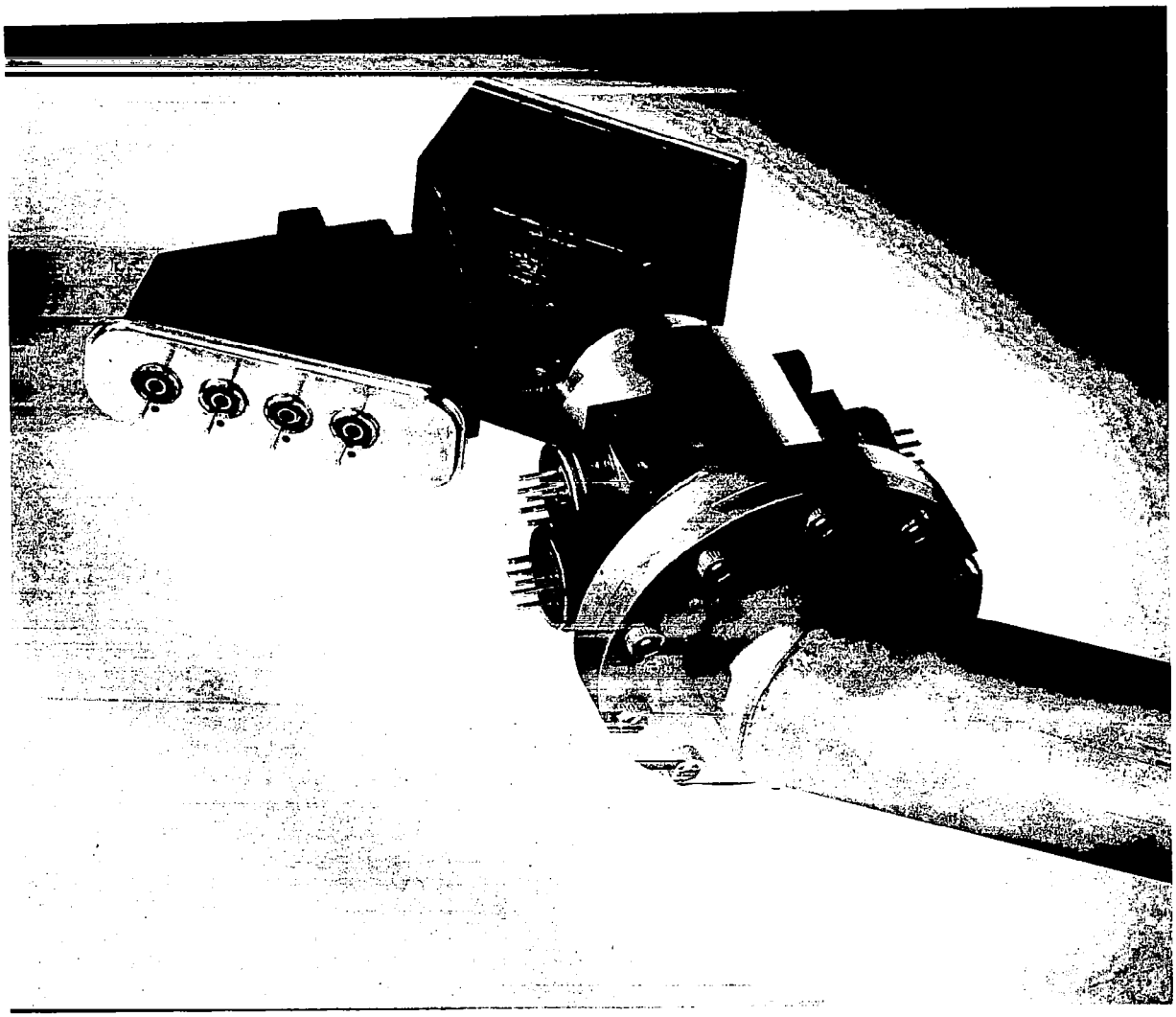

FIGURE 70
Two Gas Sensor Mass Spectrometer Analyzer

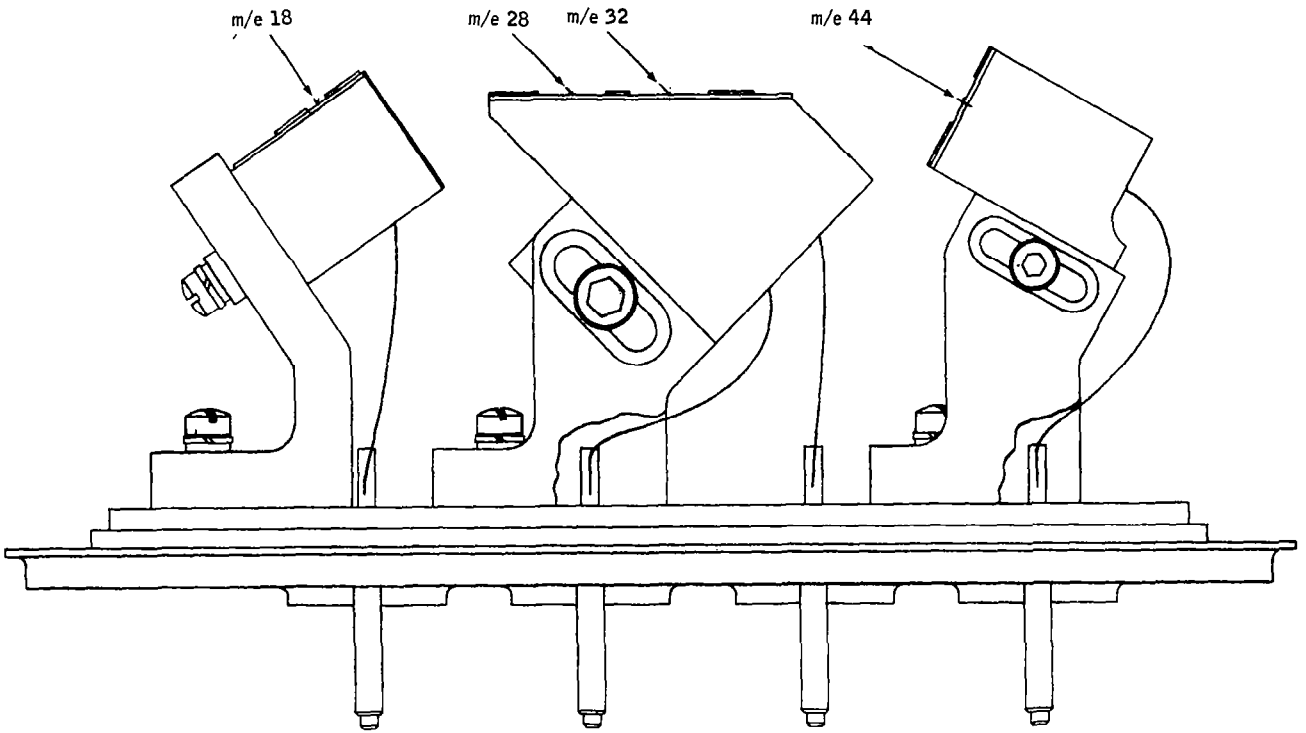

FIGURE 71
Collector Flange Assembly

The system packaging has undergone several changes from the conceptual design phase. First, the analyzer was layed down on its back so that the greatest dimension of the package is no longer than its height. This was permitted by placing the pump out tube in the end cap and by dropping the requirement that the electrometer amplifiers be accessable at the front of the package for replacement. This requirement was dropped because it was not believed that the redundancy introduced by allowing interchangeability of electrometers would make a significant improvement in the overall reliability. The second change of importance was to place some of the electronics on each side of the analyzer, thereby making better utilization of the available space. In this way the volume requirements were reduced from 244 in^3 to 167 in^3. The mounting of the electronic modules was similar to the method originally proposed. The electrometer amplifier detectors are plugged onto locating pins on the collector flange and their input-output connectors are held in place by the lid of the box. The other modules amount to the sides of the box on standoffs and also plug into connectors which are located on the bottom of the box. All of the intermodule wiring is hand wired on the bottom of the box.

The box itself is fabricated of 6061-T4 aluminum. The sides and lid of 0.031" thick and the bottom is 0.063" thick. While the tensile strength of this type of aluminum is not as high as some others, the mechanical stress calculations showed that there is no problem with this material. There is also difficulty in obtaining some of the stronger types. The box was fabricated by bending a single side piece to form the walls, welding it in the back and then electron beam welding it in the back and then electron beam welding it to the base. The box is mounted to a flat horizontal surface with four #6 bolts through four pads, two on each side of the box. The pads are integral with the bottom of the box and are braced to the sides.

The analyzer envelope mounts in between the electronic modules and is bolted to the front and back of the box. An adjustable magnet bracket holds the magnet and ties into the analyzer housing at two points and into the bottom of the box. It also acts as a stiffener for the bottom of the box. The present structure has been shown to have too low a resonant frequency and therefore once the testing has shown the limits which can be placed upon the magnet motion a more rigid structure will be designed.

The system package is not presently designed as a hermetically sealed container or with RFI gasketing. These requirements may ultimately be imposed and if they are the necessary adaptations may be readily accomplished. It should further be noted that if structural improvements are required in the package there is room for the inclusion of braces and stiffeners between the modules. There is also adequate room for the addition of other electronic functions should this become desirable.

The drawings of the ETM package are shown in Figures 72 and 73. They show many features of the packaging which have been discussed. In addition one of the views shows the front face of the package with the functional controls. The other view shows the back of the package with the pump out tube, the capillary inlet and bypass lines, and a cover plate which is required in order to make attachment to one of the analyzer headers.

The mechanical analyses which were carried out in support of the mechanical design and packaging are presented in Appendix A .

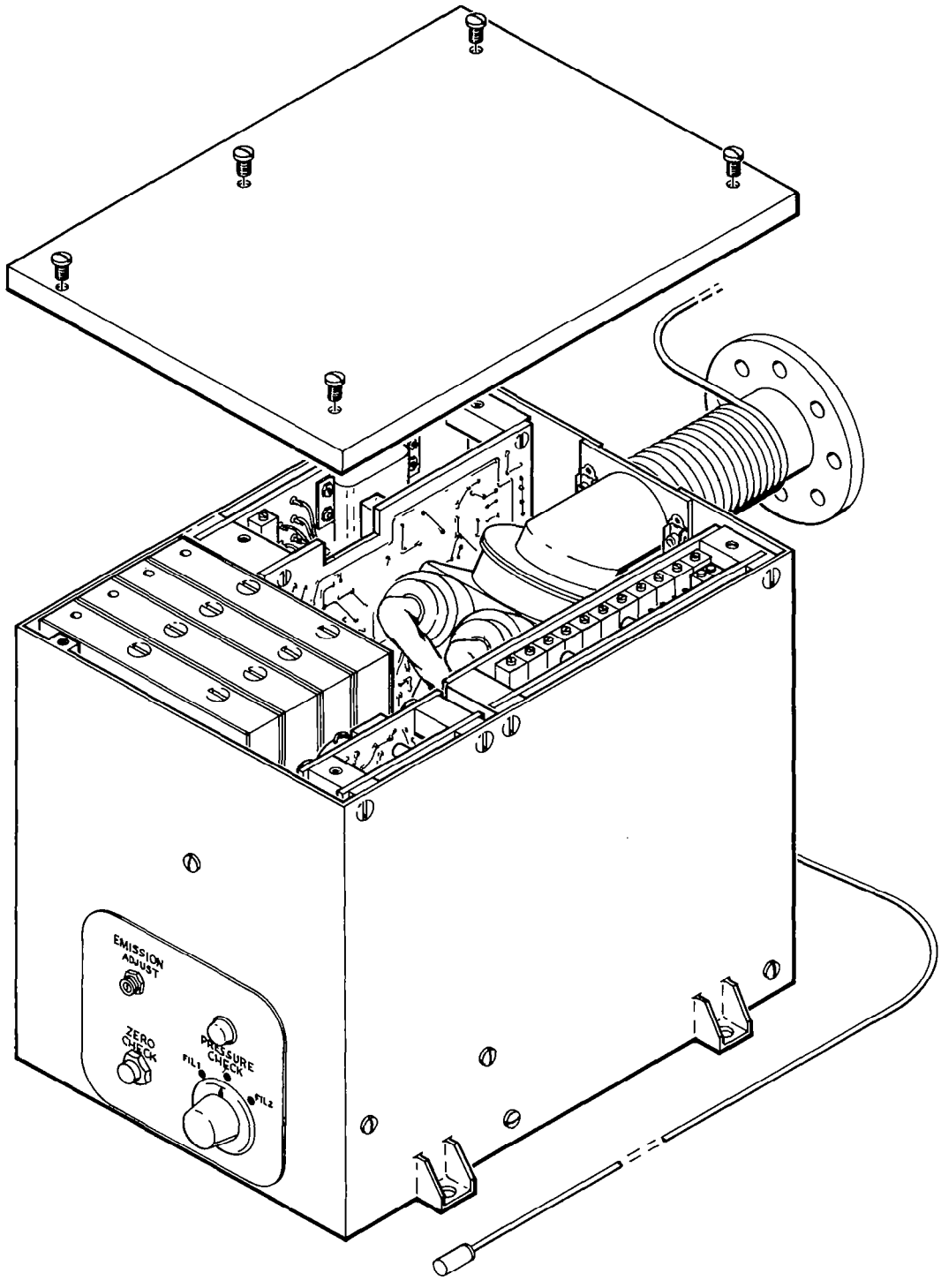

FIGURE 72
System Package - Front View

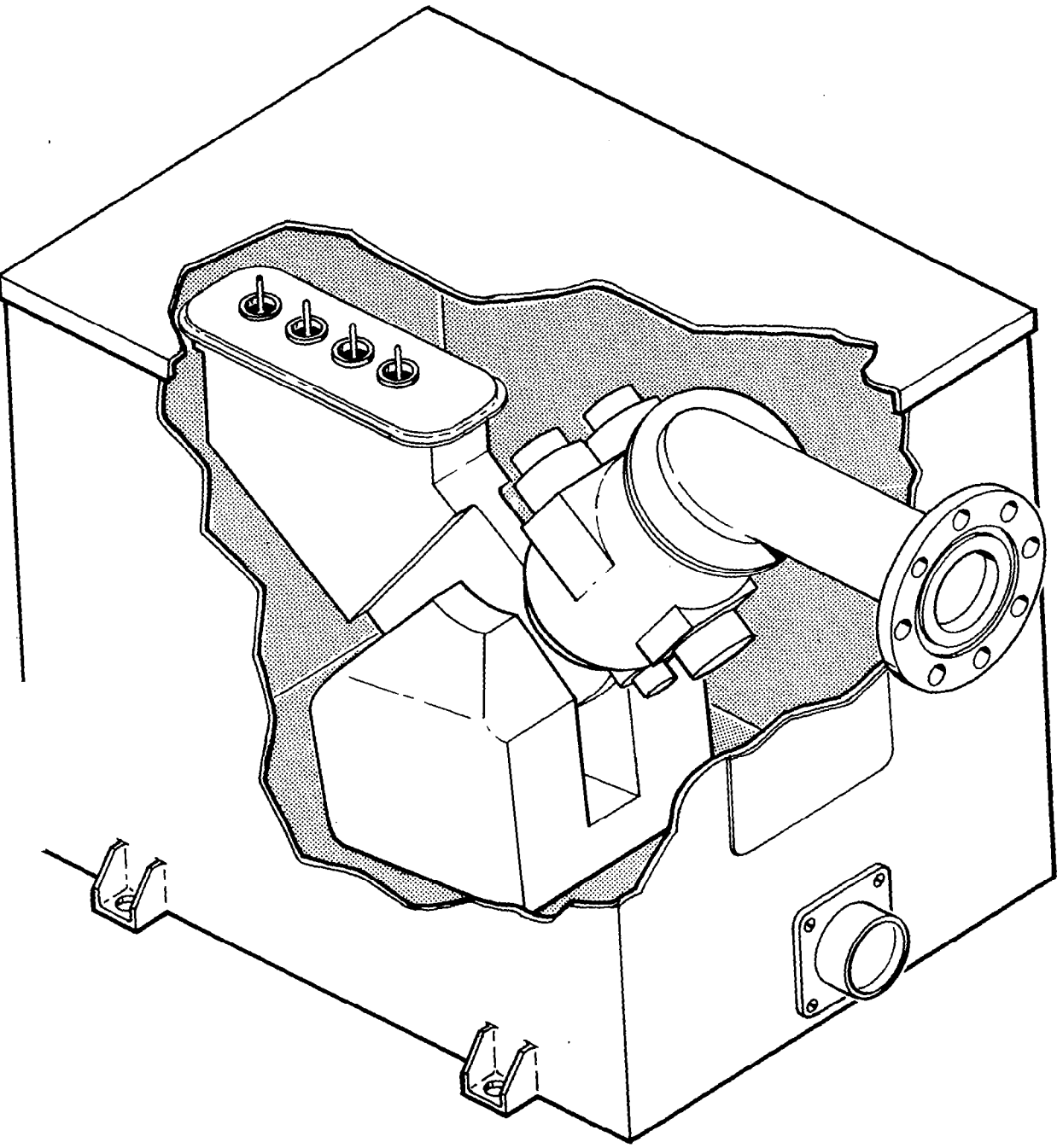

FIGURE 73
System Package - Rear View

EMITTER STUDY

The reliability and performance of the two gas atmosphere sensor system is a function of each component's stresses and characteristics in the environment to which it must be subjected. Consequently, the parameters of the components used within the system, i.e. electronics, materials, etc., must be understood in order to evaluate and design the completed system to the goals to be achieved. Failure of any one component can destroy the instrument operation, such that it becomes imperative to understand all the necessary component characteristics before the design finalization of an optimized system can be achieved.

The area in which the greatest lack of knowledge occurs within the sensor system is the effects created by the emitter, and what effects are imposed upon it by the environment to which it will be subjected. For these reasons, and to obtain the lifetime reliability, the redundancy inherent in the dual-filament ion source was deemed necessary.

The Phase I study examined the necessary data to evaluate the know performance characteristics of the various emitters presently being used, and the present work entails testing and analyzing their performance under conditions approximating the working conditions imposed by the analyzer system. From the conclusions of the Phase I report, and further examination, the following materials were selected for investigation:

a. Tungsten-Rhenium alloy (75%W - 25%Re and 97%W - 3% Re)

b. Thoriated Tungsten Rhenium (74%W - 24%Re - 2%ThO_4)

c. Rhenium coated Tungsten

d. Iridium

e. Thoriated Iridium

f. Rhenium

g. Tantalum

To reduce the instrument's power requirement, a 0.003 inch diameter wire has been selected (or a comparable cross-sectional area) for evaluation of the above materials. However, difficulties in procurement of a few of these materials has led to their exclusion from the test program, namely, thoriated iridium which can only be obtained in 0.007 inch minimum diameters has been eliminated, since it is felt that the power reduction due to thoriating the base metal would not compensate for the factor of 5.4 increase in the cross-sectional area, and rhenium has been excluded because of surface irregularities and poor consistency which are apparent along the wire length which leads to short lifetimes. However, since rhenium has indicated a high resistance to corrosion and embrittlement in the presence of water and

hydrocarbons, it has been decided to investigate the possibility of utilizing it in a ribbon form which is available in higher quality and consistency, and would have the desired cross-sectional area when cut in strips having dimensions 0.0012 inch thick by 0.006 inch wide.

The present investigation is being carried out to determine the following filament characteristics:

a. Comparative work function determination

b. Sample distortion by reactivity of the emitter

c. Change in work function due to specific gases present

d. Mechanical properties

e. Filament life testing

Comparison of the material work functions is accomplished by analysis of the filament efficiencies under similar conditions. Thus, results plotting the filament emission versus the power required for identical filament assemblies will give the necessary relative operational parameters for the comparisons to be made.

Sample distortion can be created by the filament by chemical reactions of the gases present with each other or with other materials present at the hot surface of the emitter. Analysis of these effects can be accomplished utilizing a residual gas mass spectrometer to obtain a spectra of a sample gas admitted to the system, and comparing it to spectras obtained with the various filaments operating. The particular sample gas reactivities of interest for the sample distortion analysis are believed to be due to the presence of oxygen and water vapor in the system, and thus the major testing in this area will involve samples of these two offenders.

At the same time that the sample distortion measurements are taken, it will also be convenient to examine the effects of the samples upon the work function of the emitters, i.e., the change in the efficiency of the emission with respect to the power required as the sample environment is changed.

Examination of the mechanical properties will be carried out to investigate the adaptability of the wires to the assemblies and materials to which they must interface. Further observations will require an analysis of the work hardening and embrittlement created by operation at emission temperatures, and evaluation of repeatibility of positioning as a function of the thermal shock and possible sagging characteristics.

From the results of the above analyses, it is expected that three filaments of each of three different materials, which compromisingly are judged to have the best operational characteristics, will be subjected to life testing. The life test program will involve operation of the filaments over a period of 4000 hours, recording at specified time intervals the operational characteristics of each emitter. One of the three materials will be the 75% tungsten - 25% rhenium wire since this is the material presently being used in the engineering test model (ETM) and thus the comparison of the operation of the other two materials can be extrapolated to the type of response they would present when mounted in an electron gun assembly.

The test setup by which the above testing program will be accomplished consists of a vacuum system with a 15 liter/second ion pump. Sample introduction is obtained with the use of a variable leak valve, by which stable pressures are maintained, and analysis of partial pressures present within the system is done by a residual gas analyzer manufactured by Consolidated Electrodynamics Corporation. A photograph of the testing station is shown in Figure 74. Filament assemblies, identical to those used in the ion source of the ETM are mounted to the vacuum system in a test fixture which was designed to hold up to nine different emitters. Shielding each filament from the others are 9 separate anodes, such that all nine filaments can be operated at the same time if desired. The filament control unit is designed to operate all nine test diodes within the test fixture individually or in any combination. Emission regulators are not utilized in this system, since measurement data will be taken directly on the control unit as the investigation takes place, so a power supply capable of delivering about 10 amperes at 5 volts is used for the filament power of all 9 assemblies. During the life testing, slight drift in the emission will not be important, since the filaments will be adjusted to the operating emission levels prior to measurements of their current and voltage requirements. The test program previously outlined will be conducted utilizing this fixture, from which all the defined tests can be accomplished. During the life testing, it is assumed that an ion sample will be admitted with the appropriate partial pressures of nitrogen and oxygen, and at a level corresponding to the maximum analyzer pressure for which the two gas sensor system is designed.

The results of the study program to date have involved completion of the design, and the delivery of the components necessary for the testing of the filament materials. The filament materials have also been obtained, with the exception of the rhenium coated tungsten which is presently having the rhenium being put on a 0.002 inch diameter wire to bring it up to the 0.003 inch filament diameter. The thoriated tungsten rhenium wire requires a carburization of the material in order to increase the filament efficiency, and reduce both the evaporation rate of thorium and the sensitivity of poisioning by oxygen. Carburization of this material has been performed, with the results of the filament efficiency versus the percentage of carburization shown in Figure 75. Here, the percent of carburization is defined as the percentage change in the filament current for a given operating temperature.

Checkout of the residual gas analyzer and the associated vacuum and testing equipment has been completed, and the filament assemblies are presently being placed in the test fixture for analysis of the emitter characteristics, pending receipt of the rhenium coated tungsten wire. The rhenium ribbon filament manufacturing processing is examined for methods to obtain the required cross-sectional dimensions, and while failure to cut the material by mechanical means has occurred, other processes such as photo-etching or chemical milling may prove worthwhile.

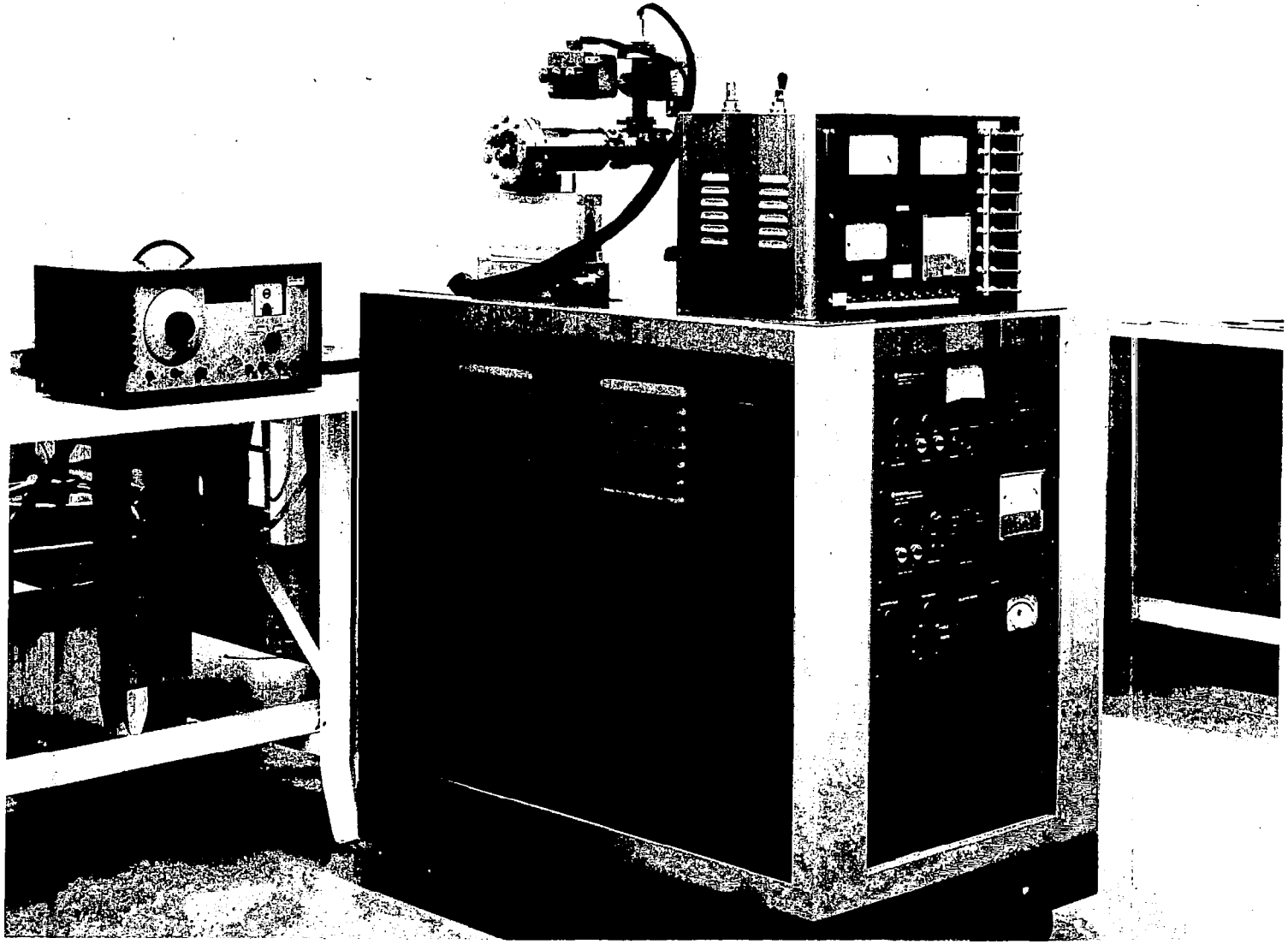

FIGURE 74
Vacuum Test Station

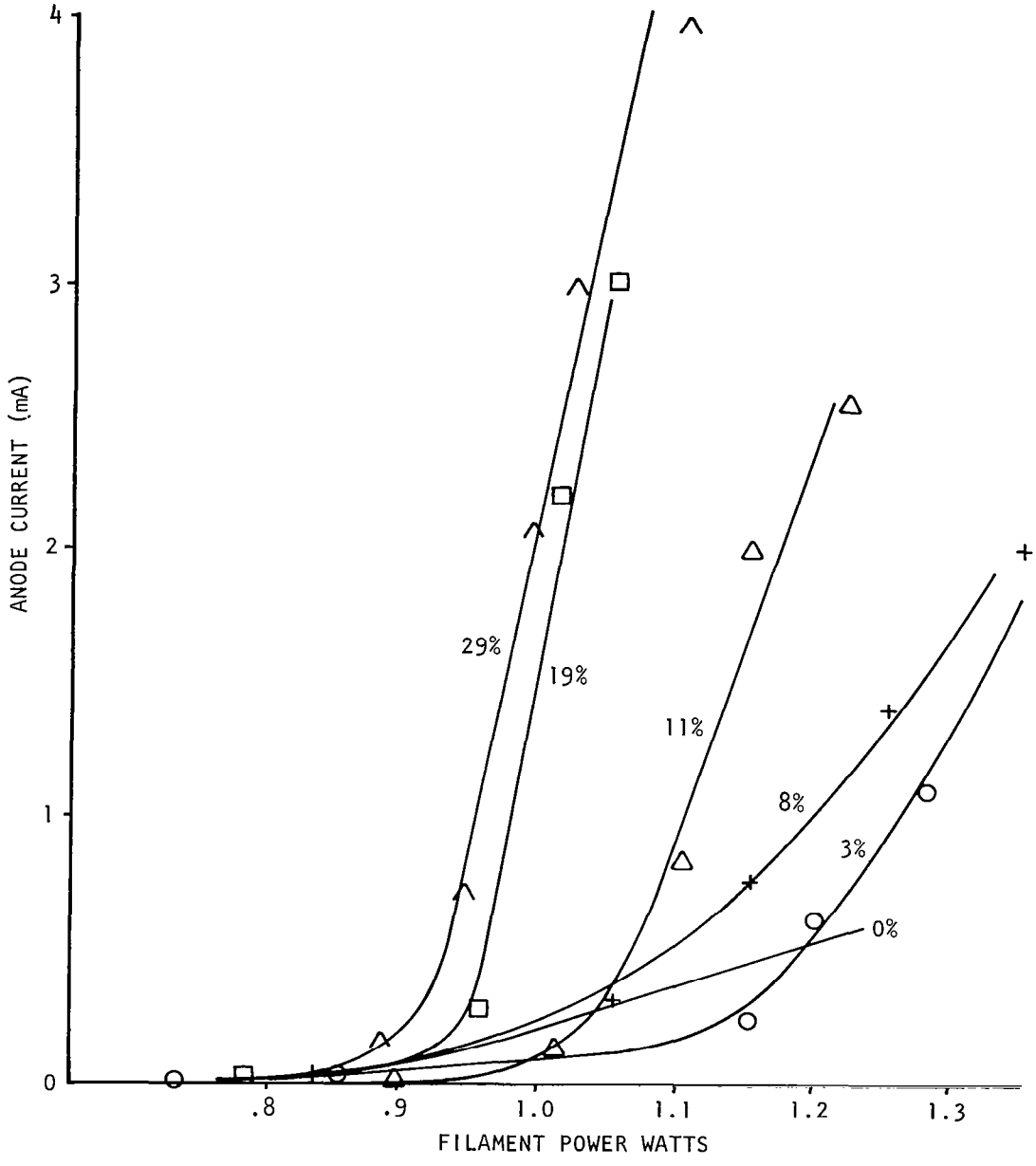

FIGURE 75
ANODE CURRENT VS FILAMENT POWER FOR WRETHO (74-24-2) FIL.
FOR DIFFERENT AMOUNTS OF CARBONIZATION

TEST PROGRAM

The verification of the Two Gas Sensor design will be carried out in a thorough test program. This program will also be the forerunner of the acceptance test program to be used in Phase II(b) for the flight prototype units. There are several phases of testing which will be briefly discussed below.

ANALYZER TEST

The analyzer test program consists of a detailed set of tests designed to examine all of the analyzer characteristics. The tests are set up in such a way that each of the functions which contributes to the analyzer operation is studied independently or as nearly as possible. Since there has been no 'breadboard' phase in the analyzer development, as in the case of the electronics modules, the tests conducted on the ETM must serve a dual purpose. A list of the principal steps in the analyzer test procedure is given below:

1. The analyzer is carefully inspected during assembly and all alignments are recorded.

2. The assembled analyzer tube is leak checked, checked for shorts, and pumped down on a laboratory support vacuum system.

3. The ion source filaments are turned on in a standard operating mode for outgassing and warmup to assure maximum life. Operating characteristics are recorded, including current and voltage.

4. The instrument is subjected to a bakeout to obtain maximum cleanliness and to minimize any possibility of contamination.

5. Each electron gun is tested with a variety of voltages and emission current levels to find the maximum transmission efficiency for electrons to the anode of the ion source.

6. The analyzer magnet is put in place and its effect upon the electron gun operation is checked. Then the necessary magnetic shielding is put into place.

7. A mass scan is then obtained on a convenient collector and the ion current is then monitored to tune up the ion source.

8. The ion focusing electrodes are tuned for maximum ion source output.

9. The side electrodes in the ionizing region are tuned for maximum ion current output. This corresponds to centering the electron beam in the ionizing region.

10. The ion source sensitivity $\Delta I^+/\Delta p$ is measured using a nitrogen sample, and monitoring the I^+_{28} output.

11. The z-axis focus electrodes are tuned. This should be done on m/e 18, m/e 28 and m/e 44.

12. The analyzer is tuned for maximum resolution at each mass position by adjusting the magnet position in two directions of translation, and rotation. Successive mass scans are made to determine the resolution and peak shape.

13. The alignment of the collectors is checked to see that the masses of interest fall into their respective collectors at the same ion energy. Tolerance to ion energy variation is also measured.

14. At this point if adequate operation is not being obtained two alternative actions may be taken:

    (a) The ion energy spread may be checked by placing a collector bucket in place of the z-axis focus electrodes and this can be used to measure the ion energy spread by biasing the ion source negative. An excessive ion energy spread will cause poor resolution. If the spread is excessive, the electron accelerator repeller, and anode potentials may have to be reduced.

    (b) The analyzer magnet may be mapped in the central plane including the fringe field. Then trajectories may be plotted through the field to determine the α focus points. The ion current collectors can then be positioned as indicated.

    The previous steps should then be repeated.

15. Sample distortion effects are examined by the introduction of an O_2 sample and measuring the variations in the outputs of all current collectors.

16. The capillary inlet and bypass line is checked out to determine if the proper pressure division is obtained. Linearity is also examined.

17. The capillary line is mounted on the analyzer tube and the analyzer is operated to determine if the proper ion source pressure is being obtained. The ion source output is measured and the ion source pressure is computed to find the differential pressure.

18. The analyzer linearity is checked as the input pressure is varied from 0 to 400 torr.

19. The effects of sample interaction are examined to show that they are reduced by differential pumping.

20. The time delay of the capillary line is checked.

21. The analyzer is allowed to run in a continuous mode to check stability.

22. The final operating voltages for the analyzer are measured so that the voltage divider string for the electrode bias supply can be built.

23. The filaments are operated in the standard check mode to check for aging effects.

24. When the analyzer operation has been thoroughly checked and it is operating successfully, the test flanges are removed and the collector flange and pump out tube are welded in place. The instrument is then rechecked briefly.

The ETM analyzer has only been in test for a short time and therefore only preliminary results have been obtained. An electron gun transmission efficiency of 17% has been obtained which agrees well with the expected value in view of the fact that the electron accelerator aperture is undersized. The ion source sensitivity has been measured at 5.2×10^{-7} amperes/torr which is just above the design value. Some samples of the mass spectra obtained are shown in Figures 76 through 80. It can be seen that adequate resolution is being obtained between m/e 28-32 and m/e 17-18. The masses all appear in their respective collectors at the same scan potential. Figure 81 shows the width of the m/e 28 peak in terms of scan potential. Figure 81 shows the width of the m/e 28 peak in terms of scan voltage. It is seen that the allowable variation in ion energy is almost ±4%. In the case of m/e 18, the allowable variation is about ±1.2% which is also better than necessary.

ELECTRONICS MODULE TEST

Each of the electronics modules is tested after assembly. The procedures used in the testing of these modules and the test results are given in Section 2.2.

ELECTRONICS SUBSYSTEM TEST

Once the module tests have been completed, the modules are integrated into the electronics subsystem with the appropriate interwiring. The outputs of each module are rechecked using similar procedures as in the module checkout to insure that the modules do not have interferences. The entire electronics subsystem is then temperature tested. The voltage divider is designed from the information supplied from the analyzer test. The divider is assembled and tested as part of the electrode bias supply.

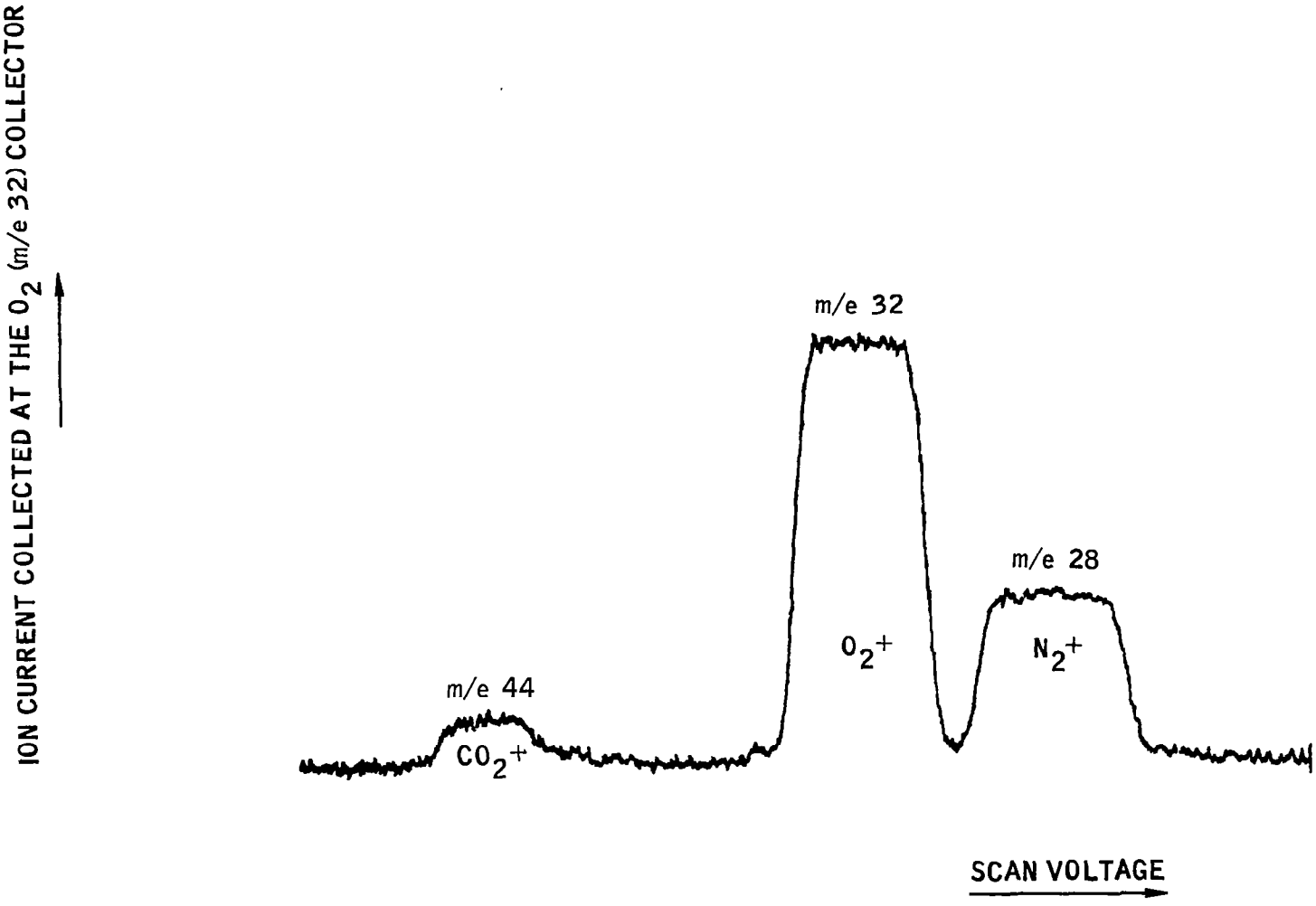

FIGURE 76
MASS SPECTRUM AT THE O_2 COLLECTOR

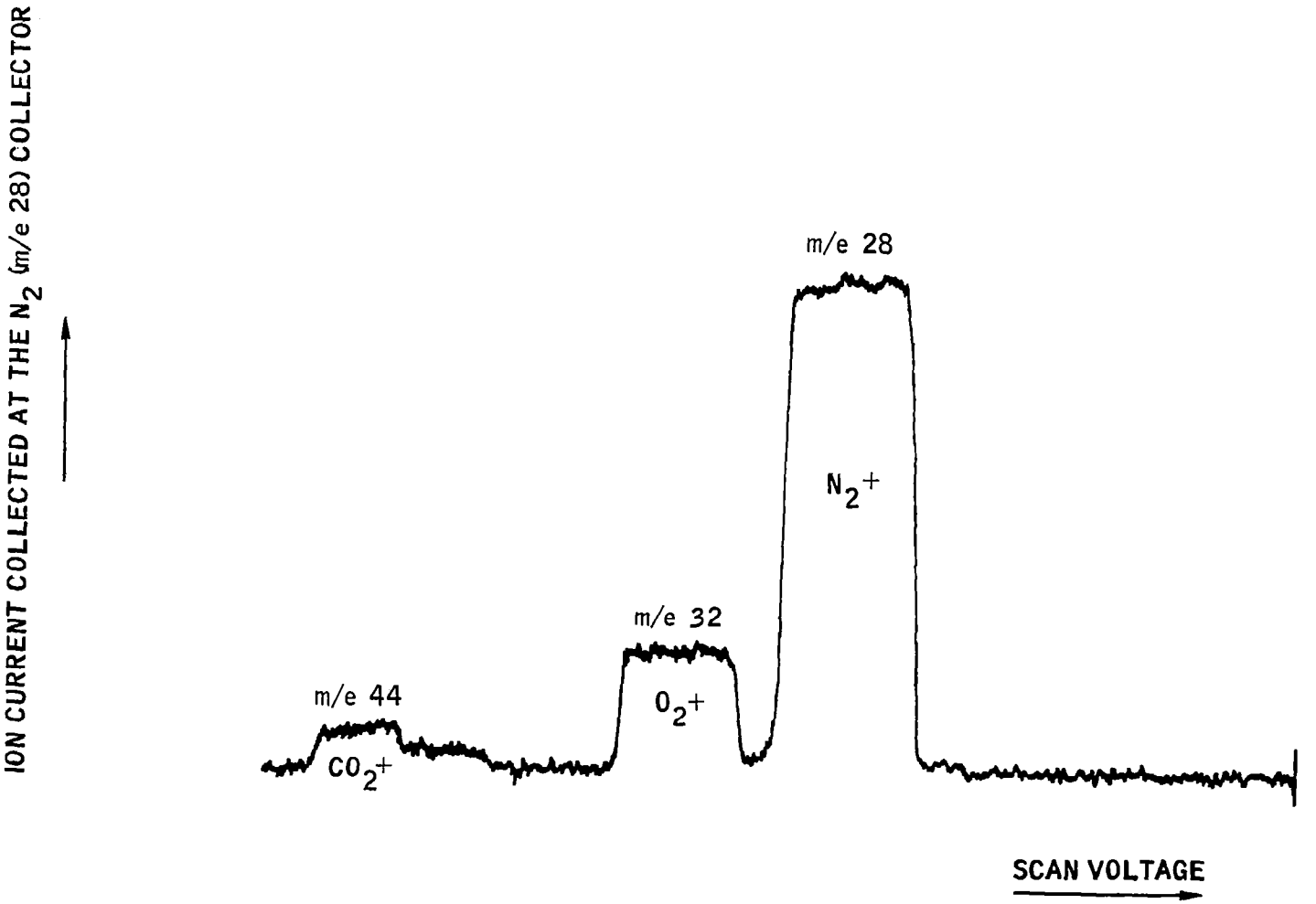

FIGURE 77
MASS SPECTRUM AT THE N_2 COLLECTOR

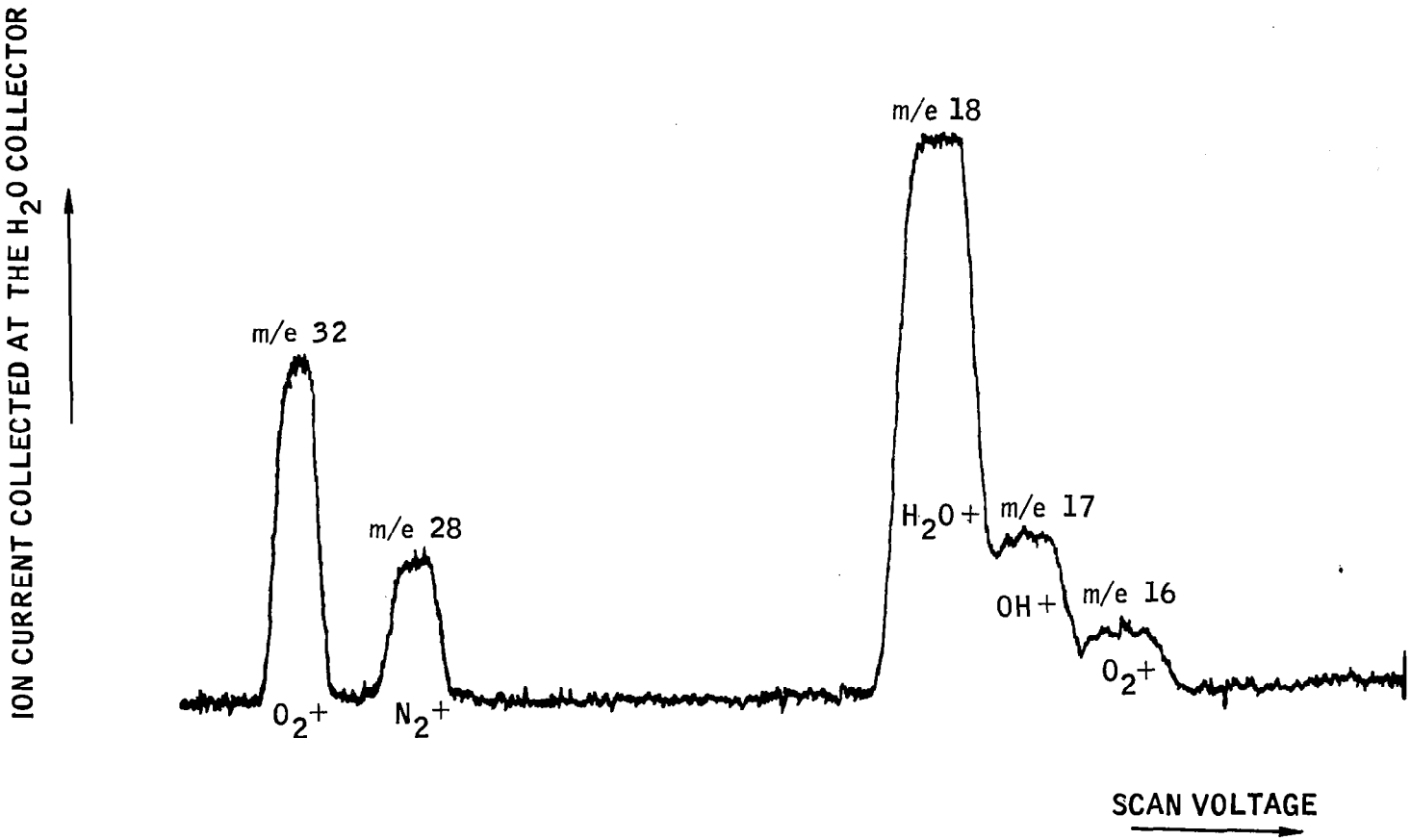

FIGURE 78
MASS SPECTRUM AT THE H_2O COLLECTOR

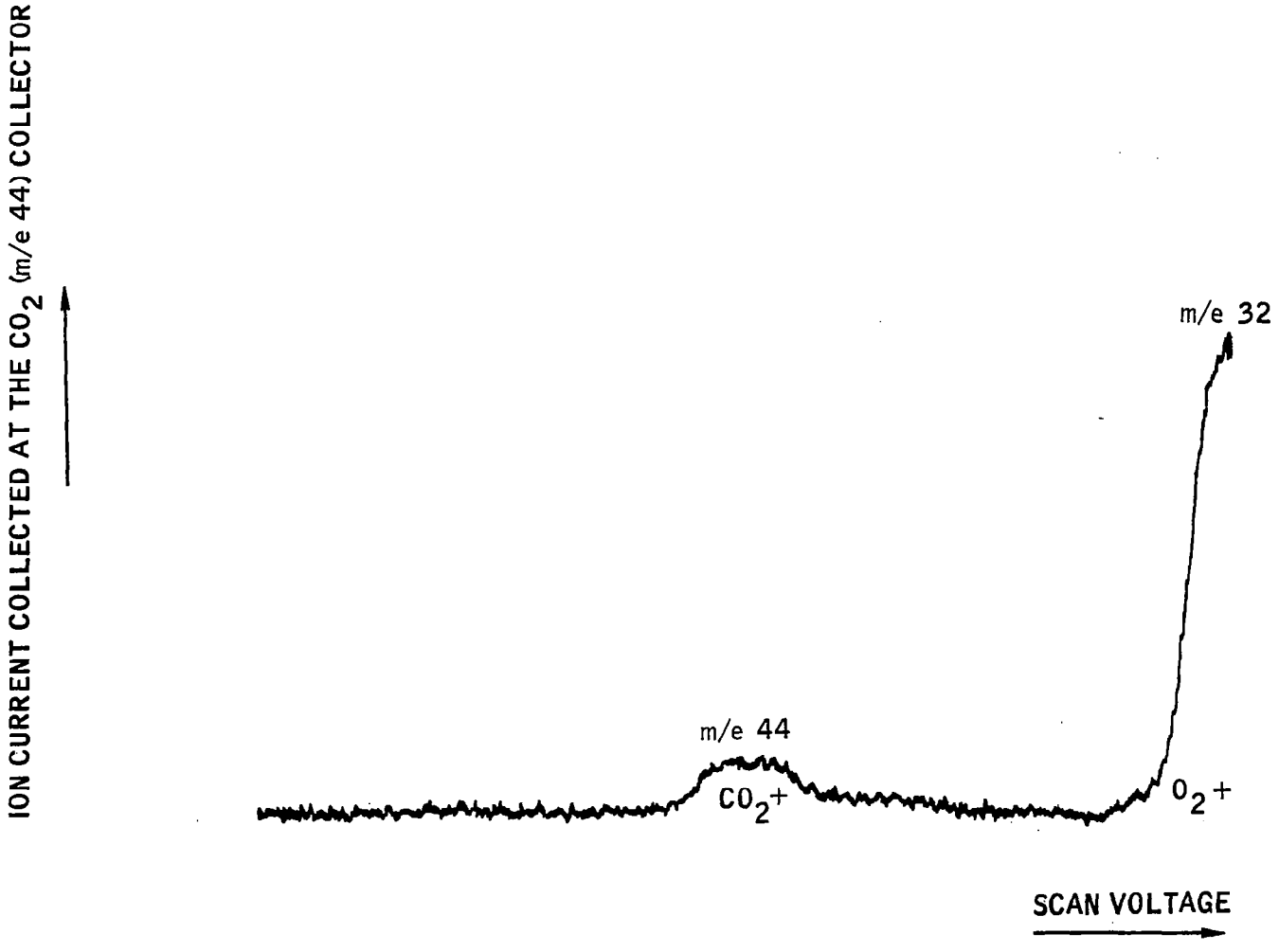

FIGURE 79
MASS SPECTRUM AT THE CO_2 COLLECTOR

ALLOWABLE V_I VARIATION FOR

I^+_{28} IN m/e 28 COLLECTOR

$P = 3.0 \times 10^{-6}$ TORR

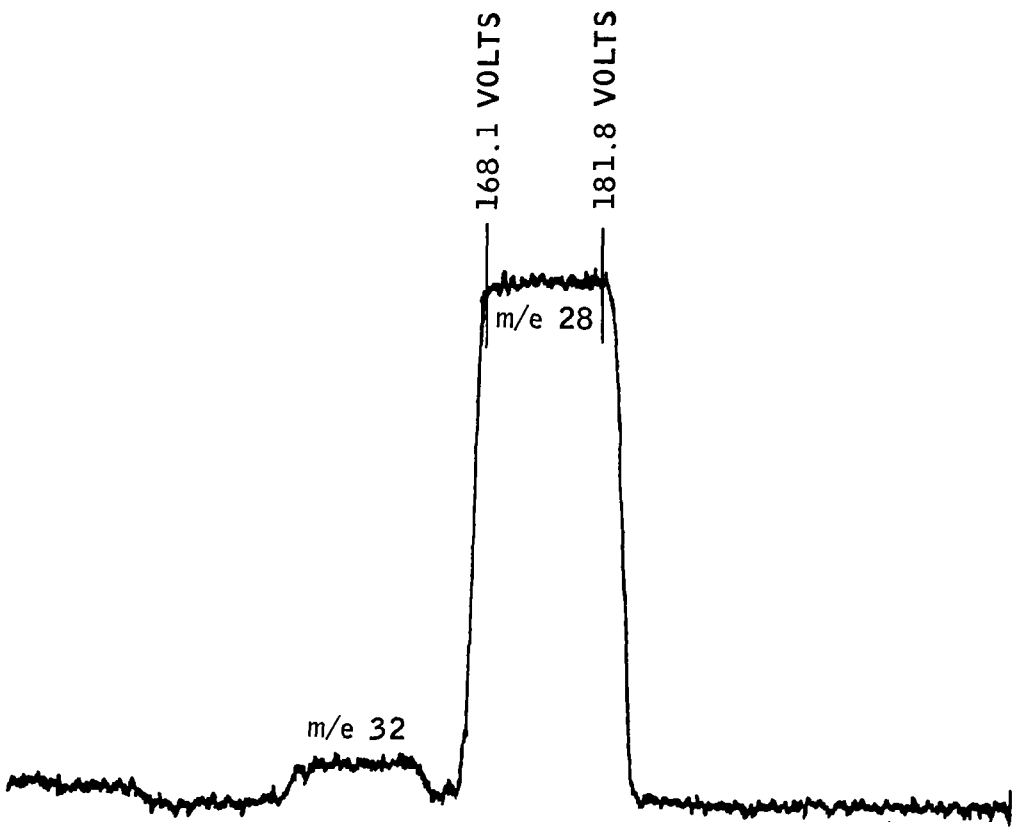

FIGURE 80

SYSTEM TEST

Once the analyzer and the electronics subsystems have been properly tested they are integrated to form the complete system. The integration is performed module by module. A preliminary integration has been performed and it went very smoothly. No incompatibilities are apparent.

Once the complete system is integrated it is tested for those parameters which specify the overall instrument performance. These are minimum detectible signals, full scale outputs, linearity, crosstalk, time response, accuracy, and variations with temperature.

ENGINEERING TEST MODEL

The detailed analysis presented in previously has led to the design of a Two Gas Atmosphere Sensor System. This engineering test model is presently undergoing evaluation which will lead to the finalization of a design for the four flight prototype units to be delivered in Phase II(b) of this contract. Since the ETM and the updated drawings are the end products of the Phase II(a) effort, it is difficult to give a detailed discussion of the instrument as it is now envisioned. The following discussion includes: a summary description; discussions of operational characteristics, power, weight and size requirements; environmental compatability, reliability, maintainability, and calibration; its improvement potential, and adaptability for helium buffer gas.

DESCRIPTION

The engineering test model Two Gas Atmosphere Sensor System consists of a small single focusing 90° magnetic sector-type mass spectrometer. Ions are supplied to the analyzer from a non-magnetic dual electron gun, high differential pumping ion source with a parallel electrode ionizing region, and a thermal imaging type of ion focusing. The ionizing beam of electrons is obtained from one of two 0.003-inch diameter tungsten-rhenium alloy wire filaments. The object slit plate of the ion source also forms the mounting plate for the ion source components on one side and the z-axis focus lens elements on the other side. This assembly is mounted in a thin-walled housing which is an integral part of the analyzer envelope and collector flange assembly. The mass resolution is accomplished by the action of the magnetic field (from an Alnico V permanent magnet) as the ions pass through the envelope section of the analyzers. The four gases of interest are separated and collected in separate adjustable ion collectors which are mounted on the collector flange. These gases are H_2O, N_2, O_2, and CO_2 which correspond to ion mass-to-charge ratios of m/e 18, m/e 28, m/e 32 and m/e 44.

The cabin atmosphere will be admitted to the ion source through a viscous pressure divider inlet system. This consists of a single two meter capillary line, a pump out line, with a platinum aperture molecular leak at their conjuncture. This system can sample at various points in the cabin or be attached to a suit loop or calibration source.

The internal vacuum necessary for operation of the analyzer will be maintained by pumping to outer space through a pump out tube.

During preflight and launch periods, the analyzer will be maintained in a sealed off condition by the action of a break off device which will be opened once the appropriate altitude has been attained.

Each of the collected ion currents will be amplified to the required output level by an all solid-state electrometer amplifier. Each amplifier is set for the sensitivity commensurate with the expected sample range of that atmospheric component.

These amplifiers have a high input impedance and utilize 100% current feedback to obtain an output which is essentially independent of any active devices which is equal to the input current multiplied by the feedback resistance.

In addition to the four ion current amplifiers the sensor system support electronics subsystem consists of three modules which provide the electronic functions necessary for the operation of the analyzer. First, there is a filament supply and emission regulator which supplies an ac voltage to the filament. This is a closed loop control system which senses on the ionizing current collected at the anode of the ion source and uses this feedback current to control the filament current so that the ionizing current remains constant. System considerations also require that this module be floated above ground at the anode potential. An inverter is used for this and its pulse width modulated output drives the filament.

The electrode bias supply provides the voltages to the various focusing electrodes in the ion source. It consists of a single inverter with a multiple winding output. Series voltage regulators operate off of two of the rectified outputs and these are used to compensate for variations in two of the other outputs. The result is three stacked high voltage outputs two of which are regulated and the third which is unregulated. These outputs are loaded by a voltage divider resistance network with potentiometers which are cabled to the ion source headers.

The detector power supply consists of a single free running inverter which drives B^+ and B^- series regulators. These regulators operate using a common zener diode reference and supply +10 and -10 volts to the detectors. A block diagram of the support electronics system is shown in Figure 35.

PERFORMANCE

The performance goals for the Two Gas Sensor System were given in Table 3. The design calculations indicate that these goals can be achieved, but it remains to complete testing of the ETM before they can be verified. Preliminary analyzer tests indicate that the analyzer sensitivity and resolution goals will be met. The electronics testing indicates that all of the requirements for the electronics have been met including the detector time response.

DEMAND FACTORS

The power, weight and size estimates for the ETM are given in the following paragraphs. In some cases the weight breakdown relies upon estimated values, because actual weights were not yet obtainable.

ETM SYSTEM POWER

The power requirements for the ETM electronics are 3.7 watts and a breakdown is given in Table 22. These values were obtained using a dummy diode in place of the actual filament so they may be subject to slight variations.

TABLE 22
ETM System Power

a.	Filament Supply and Emission Regulator	2600 mW (including filament power)
b.	Electrode Bias Supply	550 mW
c.	Detector Power Supply	150 mW
d.	Detector (each)	100 mW x 4
	Total	3.700 watts

ETM SYSTEM WEIGHT

The weight of the completed ETM system package is estimated to be 6.49 pounds and the support equipment will be 1.70 pounds as shown in Table 23. These numbers are largely based upon actual weights with some computed weights and a few estimates. It should be noted that these values are a total of 0.56 pounds less than the values estimated on the Phase I study.

ETM SYSTEM SIZE

The dimension of the ETM are 6.425 inches long by 4.750 inches wide by 5.485 inches high. This does not include the 0.031 inch metal thickness of the top which will increase all dimensions slightly.

It also does not include the mounting feet which protrude an additional 0.31 inch on each side of the box. The length dimension is increased by the control function switches or the front of the box, and the vacuum and electrical connections on the rear of the box.

The volume based upon the basic dimensions as given above is 167 cubic inches. This compares favorably with the estimated volume of 225 cubic inches given at the conclusion of Phase I.

TABLE 23
Reference System Weight Distribution

Reference System	Pounds
Analyzer Tube (Includes pump out tube and including flange) (Actual)	1.0
Analyzer Magnet (Actual)	1.74
Magnetic Shielding (Calculated)	0.3
System Package (includes connector and control switches) (Actual)	0.8
Magnet Mounting and Connector Mounting Hardware and System Wiring (Estimated)	0.25
Electronics Modules	2.0
Potting (Conformal coating) (Estimated)	0.1
Capillary Inlet Line (2 meters long) (Estimated)	0.1
Mating Flanges and Swagelok Fitting for Pump Tubes (Estimated)	0.20
Total Pounds	6.49

Supporting Equipment	Pounds
1-1/8 inches I.D. x 18 inches long x 0.031 inch Wall Pump Out Tube (aluminum, with two mating flanges) (Computed)	0.35
Breakaway Hat to Seal Pump Out line (Actual)	0.75
Valve and Pump Out Line for Sample System (Estimated)	0.2
Calibration Bottle (Flight Weight) (Estimated)	0.4
Total Pounds	1.70

INTERFACE REQUIREMENTS

The following is a list of interface requirements for the ETM sensor system.

INPUT POWER

The input power is assumed to be 28 ± 1/2 Vdc with a power ground. It is recognized that power supply voltages generally are not clean but have ac components. When specifications covering this area become available, specific recommendations can be made. Filtering has been provided on all 28 volt inputs to the various electronic modules.

INPUT COMMANDS

The sensor system is turned on and off by a remote command which supplies or cuts off the 28-volt power. There are no provisions for an on-off command to be received directly by the sensor. A manual push button switch is provided to place the instrument in a zero check mode. A rotary switch is provided for switching between one filament and another, and to check the internal pressure. Both switches are mounted in the front cover.

SAMPLE INLET

A single flexible two meter capillary line accepts the sample gas. This line is filtered and has a termination compatible with the calibration bottle.

OUTPUTS

There are four system outputs; one corresponding to each of the sampled gases. All outputs are 0 to -5 V with an output impedance of 500 ohms in the operating frequency range. There is also a signal ground connection.

ELECTRICAL CONNECTIONS

The input power and output signals are supplied through a connector located at the base of the rear panel.

VACUUM CONNECTIONS

The analyzer pump out tube is approximately one inch in diameter and projects through the rear of the package. It connects to the pump out line with flanges and an O-ring seal. (For laboratory test, a vacuum system can be mounted at this point.) A second pump out line of smaller diameter (1/4 inch) also projects through the rear of the package. Connection to this line is made with a Swagelok type fitting.

ACCESS

Access to the sensor system components is provided by a lid which covers the top of the box. This is held down by six screws. There is no gasketing, either hermetic or RFI but modifications to include this can be readily made. It is not intended that there be any access to the system once it is installed in the spacecraft.

ADJUSTMENTS

An external adjustment in the form of a potentiometer is provided for the ionizing current level. This is located in the front of the box and is used to adjust the output for recalibration. Other adjustments are located within the package but these are not intended for use in flight.

MOUNTING

The sensor system package is provided with clearance holes for four screws which mount the package to a flat surface. The required surface area is about 30 square inches.

ENVIRONMENTAL COMPATIBILITY

The reference system is designed to meet the performance parameters given in Section 5.3 under the following environmental conditions:

OPERATING TEMPERATURE RANGE

40°F to 90°F

VIBRATION

The sensor system will function normally after passing through an Apollo launch vibration profile. Operation is not intended during launch or re-entry of the spacecraft.

EXTERNAL PRESSURE

The instrument can only be operated at altitudes where the ambient pressure is less than 5 x 10-6 torr.

LEAKAGE RATE

The rate of gas loss due to the sample inlet system is less than 0.00015 pounds/hour or 0.1% of the total cabin leakage rate.

ZERO GRAVITY OPERATION

There is no problem in operating the sensor system in a zero environment, since its operation is in no way affected by gravitational fields.

EXPOSURE TO HARD VACUUM

Exposure to hard vacuum will not affect any of the sensor system components.

SHELF LIFE

The shelf life of the sensor system is limited only by degradation of electronic components. The analyzer tube should preferably be pumped in order to keep it clean, but it can be kept in a "pinched off" condition for long periods of time with no harmful effects.

ACCURACY

The accuracy of the two gas atmosphere sensor system is controlled by several factors. A brief summary of sources of errors is given below:

a. Inlet line memory effects (small except in the case of water).

b. Ion source temperature dependences (ionization sensitivity and ion focusing).

c. Feedback resistor temperature coefficient (compensatable).

d. Changes in the sample distortion due to filament interaction. (Relatively long term and therefore minimized by calibration; also reduced by differential pumping and the constant nature of the sample.) Stability of emission characteristics and mechanical stability of the filament could cause variations.

e. Detector zero drift (very small and capable of adjustment).

f. Variations ionizing current (controlled by the emission regulator).

g. Variations in electron beam position due to surface contamination and charging.

h. Variations in the ion source sensitivity due to voltage variations (controlled by power supply voltage regulation).

i. Variations in the magnet field strength causing drift off the peak

Examining these sources of error leads to the following conclusions:

a. Variations due to ambient temperature changes will not be of major significance, due to the relatively small temperature range and partial compensation of different effects. Total instrument compensation for temperature should be possible once the ETM system has been tested.

b. Variations due to voltage instability can be minimized to the necessary levels by power supply design. Present indications are that regulations are sufficient to eliminate voltage variations as a significant source of error.

c. The error due to emission level variation is probably the most significant contributor with a present value of about ±0.5%.

d. Present information on filament interaction indicates that the differential pumping should eliminate sample interaction as a source of error.

e. The magnet stability is high because its field strength is reduced from maximum. Also the over design in terms of resolution will give a wide tolerance to magnet variations. If these occur it will effect m/e 18 first. This would not be too serious.

f. The filament study should indicate the best filament material for stability. Mechanical variations have not been indicated thus far in this type of filament mounting. Again these should be long term, and therefore calibratable.

g. Surface contamination and charging effects should be eliminated by following through cleaning practices including high temperature bakeouts of the assemblies prior to installation. Total analyzer bakeouts should also be used.

RELIABILITY

The design of a high reliability instrument has to be considered as a primary goal for this task. Several techniques have been applied to insure a design of maximum reliability. First, basic design simplicity has been a primary goal. The choice of the magnetic sector analyzer over the quadrupole analyzer leads to a great reduction in the amount of support electronics which the analyzer required. Second, an effort was made to minimize the number of components in series with the output. This was implemented by going to multiple output channels as opposed to single collector and detector. This reduced the complexity of the electrode bias supply (non-scanning) and eliminated the need for a logic circuit or multiple ranges on the detectors. Third, safety margins were applied throughout the design analysis which allow degradation in performance, with a serious effect upon the essential content of the output information. Fourth, redundancy was applied in the ion source design by the use of dual filaments and electron guns. Fifth, filament life testing being carried out in a parallel program may lead to the selection of an improved material. Sixth, all electronic components were subjected to at least a 50% derating of their critical parameters. The derating rules are discussed in detail in Section Seventh, all circuits were worst case analyzed to show that they will function within tolerance over expected component variations and aging. And finally almost all of the electronic components which have been used in the ETM system have high reliability counterparts which can be substituted when flight qualifiable units are required.

It must be pointed out that thus far in this program a specific reliability goal has not been set for the Two Gas Sensor System. It has been specified that the maximum mission duration is 120 days but no probability of success has been specified for this time interval (or the inverse, a mean time between failure). While components have been derated this derating must be considered to be somewhat arbitrary until such time as a reliability goal has been established. It can be stated, however, that there do not appear to be any fundamental limitations in obtaining any required MTBF.

MAINTAINABILITY AND CALIBRATION

The ETM sensor system is designed such that only the following minimal maintenance functions will be necessary in flight:

a. Checking the zero by throwing the zero check switch. It is not expected that the gear will drift out of the allowable range .

b. Calibration of the instrument by attachment of the calibration sample source to the capillary input and adjusting the emission current set. This should be required once every one or two days and will take approximately one minute.

c. Switching the filament if one of them burns out. This is accomplished by a rotary switch mounted on the front cover. During this process the analyzer pressure may also be checked at an intermediate switch position.

d. When the sensor system is first required to operate the break off device must be fired so that the analyzer may be pumped down. Once this occurs within a few minutes then the capillary line may be opened up and the instrument turned on. This sequence is readily accomplished and only occurs once.

IMPROVEMENT POTENTIAL

The design of the ETM Sensor System has been carried out in a detailed manner and in many instances conservative design practices have been followed. Until the ETM has undergone a complete system test it will not be possible to determine if the resulting instrumentation has realized all of these safety margins so that the performance will exceed the specified goals. Several possibilities for improvement presently appear possible and these are briefly discussed below:

a. The present analyzer resolution appears to be exceeding the design values and this excess could be traded for increased sensitivity which would be useful in the event of difficulties in other areas.

b. The filament study may lead to the selection of an improved emitter with better life characteristics, lower power requirements, or improved stability.

c. The information obtained on the OGO-F ion source indicates that the differential pumping requirements might be reduced without causing an accuracy problem. This would allow the pumping speed requirements to be diminished which is reflected in a smaller pump out line. This might be especially important if it were decided to go to an ion pump.

d. The present analyzer magnet is conservatively designed and it is believed that a few tenths of a pound might be shaved off its weight without significantly affecting the analyzer performance.

e. The possibility still remains to go to a direct molecular leak which would eliminate the capillary and bypass lines and their fittings.

f. By going to welded wire circuitry in all of the electronics it would be possible to substantially reduce the volume of the electronics which could save a significant amount in packaging weight.

ADAPTION FOR A HELIUM BUFFER GAS

There has been a great deal of discussion concerning the use of helium as the buffer gas rather than nitrogen as is presently contemplated. Should this become a reality it is important that the Two Gas Sensor be adaptable to this gas.

There are no fundamental differences in the monitoring of helium and nitrogen. Some of the numbers which are applied to the design analysis would be changed and this would require some design changes. The areas which would have to be reinvestigated are briefly discussed below.

a. The sample inlet line will have to be reanalyzed because of the differences in the viscosity and mass of helium relative to nitrogen. This might require slight dimensional changes in the capillary line or affect the delay time or sample flow.

b. Helium has a lower ionization efficiency than nitrogen so that the ion source sensitivity for helium will be about one fifth of the value for nitrogen. This implies that the value of the feedback resistor in the helium ion current detector must be 5 inches by 10 inches ohms rather than 1 inch by 10 inches ohms for nitrogen. The minimum detectible partial pressure should still meet the required level since although the noise will be somewhat increased with the larger resistor it is presently at least a factor of ten below the specified value.

c. It is also possible that a small amount of mass discrimination would be present with helium because of its smaller mass. This may be compensated for by enlarging the size of the accelerator aperture to form a larger object size for the ion focusing system. This should in turn allow an increase in the image area so that a small deflection of the helium ion beam will not cause an appreciably reduced sensitivity.

d. Helium has a smaller radius of curvature in a magnetic field than nitrogen and therefore the m/e 4 collector must be mounted on the collector flange and the m/e 28 collector deleted. In order to locate the m/e 4 collector at its appropriate place, the m/e 18 collector mounting arrangement must be modified to make room for it or it may be necessary to alter the envelop and collector flange to allow for the positioning of the m/e 4 collector closer to the ion source. The resolution required at m/e 4 is very low so that the positioning of the collector will not have to be precise and detailed focal point and beam width calculations will not be required.

e. Finally, the z-axis focusing effects at the magnet boundaries will be greater for helium than the other ion species and some compensation will be required either with the z-axis focus lens or by tilting the entry face of the magnet.

None of these changes represent significant modifications to the instrument and they could be readily accomplished.

CONCLUSION

This report presents the results which have been obtained in the second phase of the development of a Mass Spectrometer Two Gas Atmosphere Sensor System. This instrument was designed based upon a reference sensor system which resulted from the Phase I study. An Engineering Test Model (ETM) has been fabricated and assembled and is presently undergoing test. Some of the design goals have already been verified, and it is expected that all of them will be verified by the end of the test and evaluation program. At the same time the power, weight, and size requirements have been reduced from the Phase I estimates. At the conclusion of ETM testing the necessary design modifications will be completed, the manufacturing drawings will be brought up to date and submitted to Langley Research Center for approval before beginning the fabrication of the flight prototype units.

The results of the design, fabrication, and initial testing indicate that this instrumentation represents a sound approach to monitoring a two gas atmosphere in a capsule environment. It embodies reliability through its inherent simplicity, conservative design, worst case analysis, and component derating. Its performance will exceed the mission requirements which are likely to be imposed, and the power, weight, and size demands are well within the limits for this application.

TWO GAS ATMOSPHERE SENSOR SYSTEM
(MASS SPECTROMETER)

PHASE IIb - FINAL REPORT

INTRODUCTION

The aim of this program was to develop a system capable of monitoring oxygen, nitrogen, carbon dioxide and water vapor in a closed spacecraft cabin atmosphere. It was assumed that such a sensor would form an integral part of the atmosphere control loop. The first phase of this program under contract NAS 1-5679 was a study directed toward the selection of the mass spectrometer type and configuration most suited for the task. A single focusing 90° magnetic sector instrument was selected based upon a computer optimization. The ion source, the support electronics and the sample inlet system were also thoroughly analyzed and the preliminary configurations established. This effort culminated in a final report which was completed in March of 1966.

Later that same year contract NAS 1-6387 was awarded for the second phase of the program. This covered the design, fabrication and test of an Engineering Test Model (ETM) and the fabrication and test of four flight prototype units. The first part of this effort designated as Phase IIa covered the development and test of the ETM. The ETM was successfully demonstrated at Langley Research Center in April 1967. The Phase IIa final report was submitted at this time. This document covered in detail the design of the Two Gas Atmosphere Sensor System. After the Langley demonstration the ETM was returned to Aerospace Systems where it underwent further testing. A go-ahead was then received from Langley Research Center for the production of the flight prototype instruments. The part of the program described in this report was designated Phase IIb.

The phased program described above has been very successful. The ETM and preflight prototype units have been tested and shown to be functional as a monitor for oxygen, nitrogen, water and carbon dioxide. Design goals have been met in most areas and in particular with respect to sensitivity and resolution of the instrument. The ETM was upgraded to flight prototype status and tested on the McDonnell Douglas Space Cabin Simulator for a period of 60 days. This test demonstrated that the instrument could function reliably for an extended period of time. While there is some discussion of the preparation of the ETM for this test, the results will be covered in a separate report. The instrument was placed in control of the oxygen and nitrogen partial pressures during the test and functioned in this capacity until its completion. The two gas sensor demonstrated the ability to act as the primary atmosphere monitor and to measure the principal constituents with sufficient accuracy for control purposes.

The successful performance of this instrument is reflected in the fact that new programs are being initiated to apply the basic two gas sensor in other areas. These include the analysis of total hydrocarbons, monitoring helium and argon in addition to the existing species, and as a rapid rate metabolic sensor. It

is evident that the flexibility of this instrument in addition to its desirable analytical properties are likely to lead to its application in several critical life support areas.

In addition to the development of the instrument several study programs have also been conducted. The first of these was a filament material investigation. This was believed to be desirable based upon the criticality of the filaments in the ion source. The results of this investigation are included as part of this final report. Three other study programs are now in process. These cover the development of a small ion pump; the development of a rough ball leak; and the investigation of the stability of the analyzer magnet. Reports on these efforts will be submitted at their conclusion.

The next phase of the development of the Two Gas Atmosphere Sensor System will be directed toward the upgrading of the present flight prototype configuration to a flight qualifiable level. At this point the instrument would be available for service on flight programs.

INSTRUMENT DESCRIPTION

A description of the Two Gas Atmosphere Sensor System was presented in the Phase IIa Final Report. In the following paragraphs a description of the flight prototype system will be given. The description is accompanied by a more up to date set of photographs. The Two Gas Atmosphere Sensor System is a single focusing 90° magnetic sector mass spectrometer. The central part of the instrument is the mass spectrometer analyzer commonly referred to as the 'tube'. A photograph of the analyzer tube and analyzer magnet is shown in Figure 81. The analyzer tube is composed of the following components. The first is the vacuum envelope in which the functional elements of the tube are housed. At one end of the vacuum envelope a pump out tube is attached. The one shown in the photograph is a laboratory support apparatus and is replaced by a smaller welded-on pumpout tube in the flight instrument. A collector flange is welded to the other end of the vacuum envelope. There are three nine-pin headers mounted in the walls of the vacuum envelope through which voltages are supplied to the ion source. The ion source performs the function of ionizing the gas to be monitored and focusing a beam of ions which is directed toward the magnetic sector region. In passing through the magnetic field the ions are dispersed according to their mass to charge ratios and fall into collectors mounted in a collector assembly mounted on the collector flange. The ion currents corresponding to oxygen, nitrogen, carbon dioxide and water vapor then pass through single pin feedthroughs in the collector flange and are measured by electrometer amplifier detectors.

The analyzer magnet shown in detail in Figure 82 is a permanent magnet utilizing two shaped pieces of Alnico V to obtain the magnet charge. These are coupled together with an Armco iron yoke and faced off with two Armco iron pole pieces. The pole pieces are utilized to obtain a uniform magnetic field in the magnet gap. The yoke is utilized to complete the magnetic circuit with the least required weight. Also shown in the photograph are a keeper used when the magnet is in storage and a special charging keeper, used when charging the magnet to ensure a uniform field.

The ion source is shown in Figures 83 and 84. It is an electron bombardment type which utilizes a hot wire filament to obtain electron emission. The electrons bombard the gas sample entering the ion source and form the ions. This ion source has two filament and electron gun subassemblies for purposes of redundancy. Gas from the sample inlet system enters the ion source through the ceramic tubulation and right angle bend shown at the top of the photograph. It then enters the ionizing region. One of the electron gun subassemblies has been removed in Figure 83 so that the ionizing region is visible. The ionizing region is bounded by repeller and accelerator electrodes at the top and bottom, by the two electron guns on two walls and by two collecting anodes on the other

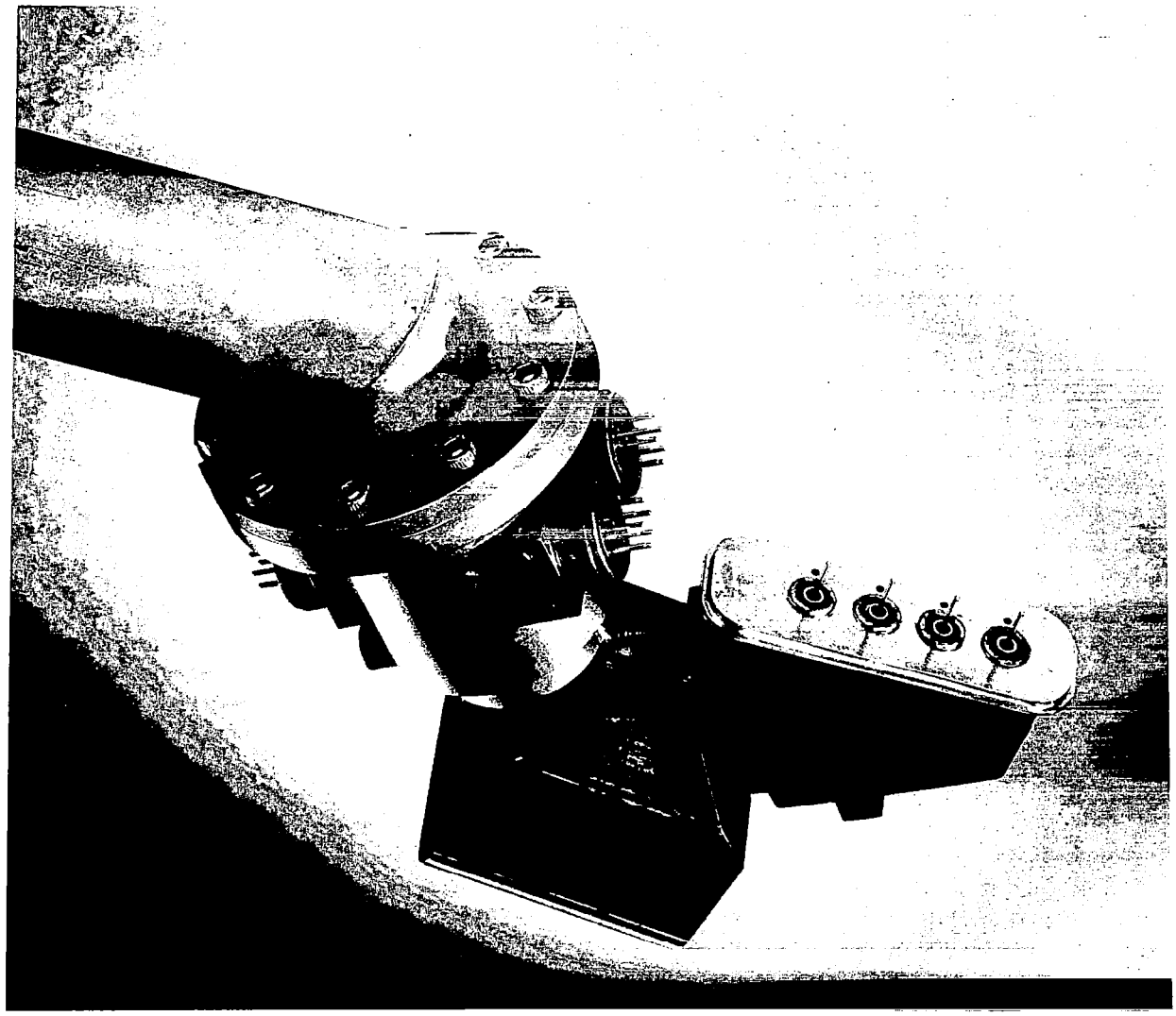

FIGURE 81
Analyzer Tube and Magnet

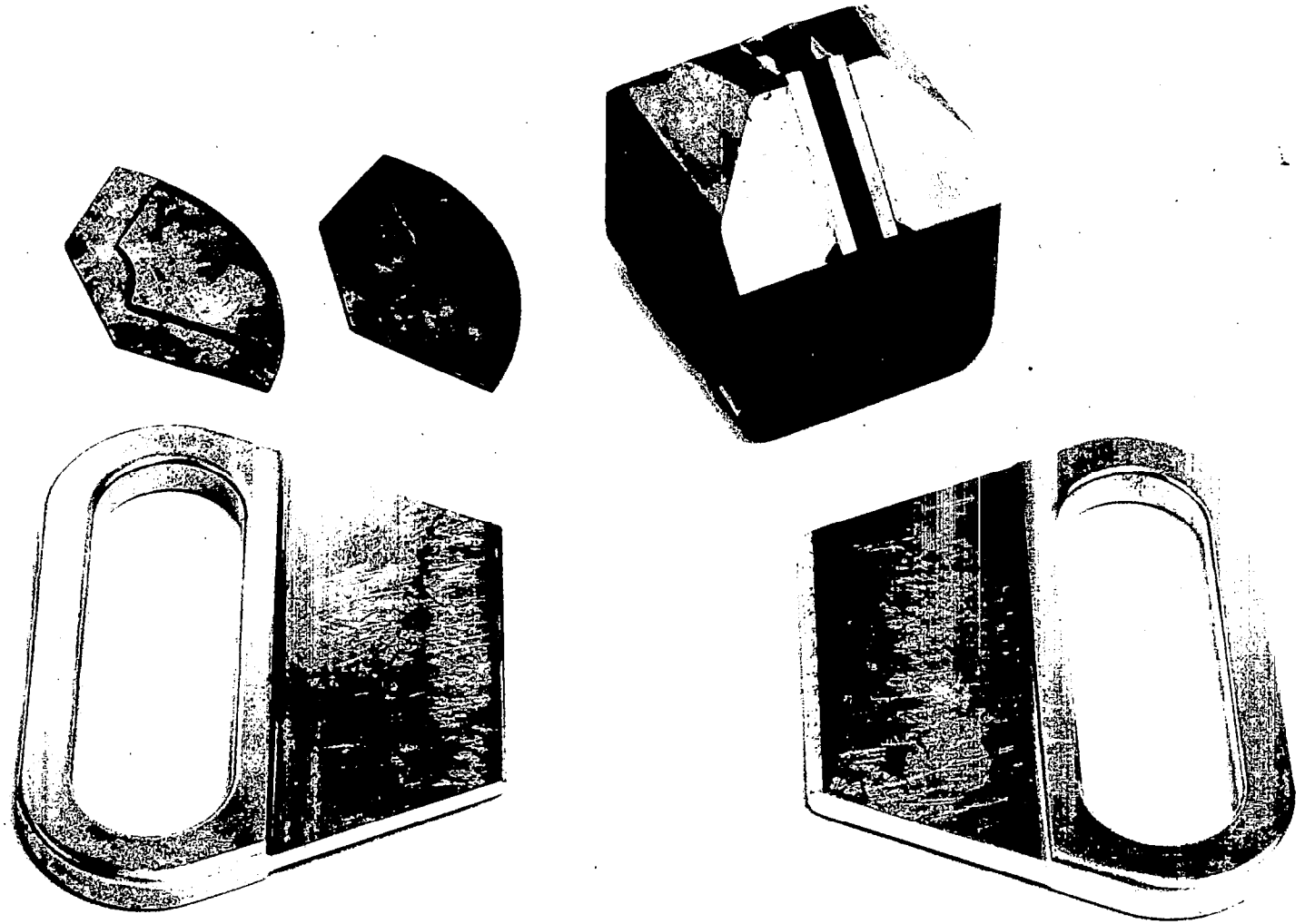

FIGURE 82
Analyzer Magnet

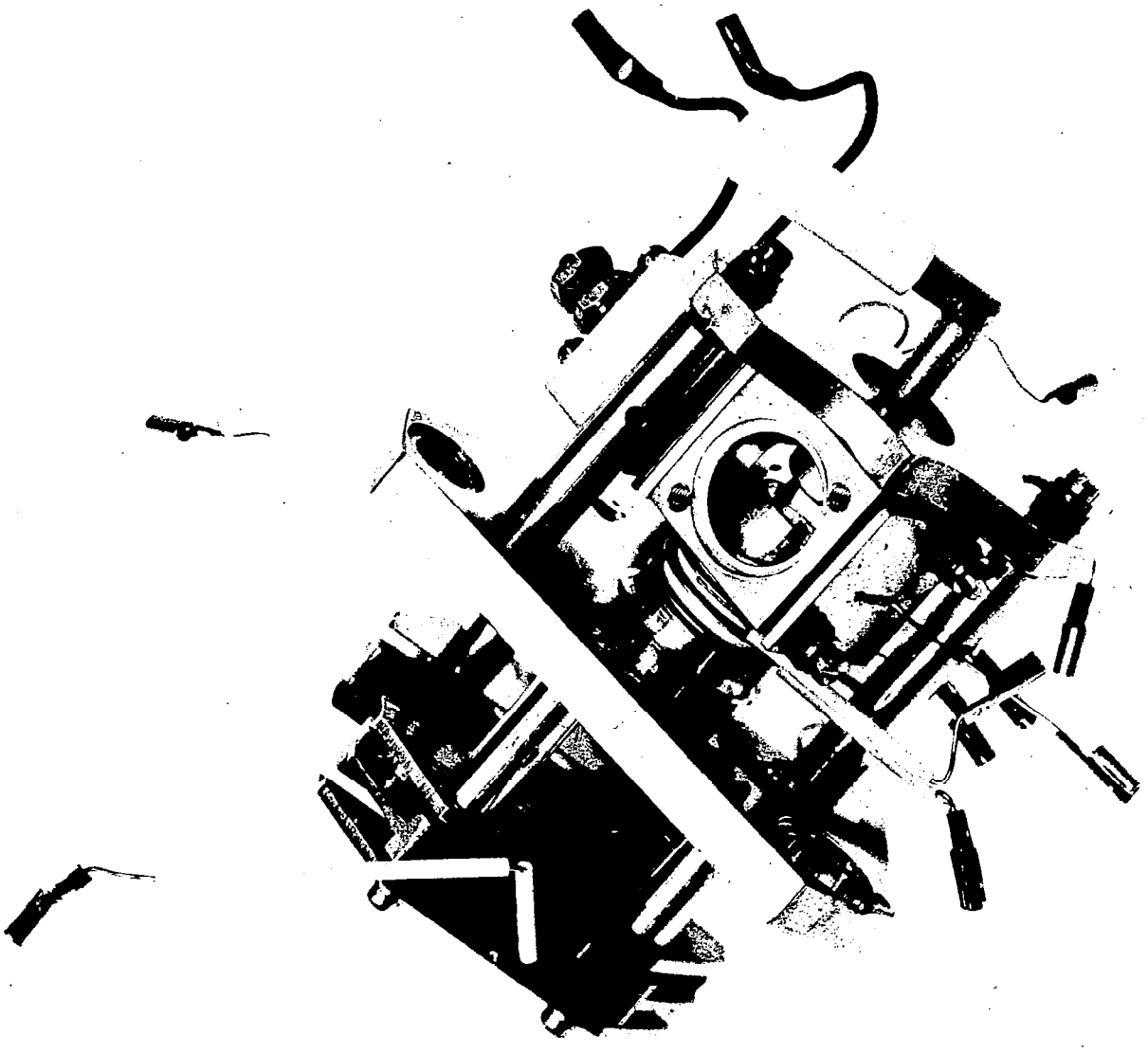

FIGURE 83
Dual Filament Ion Source

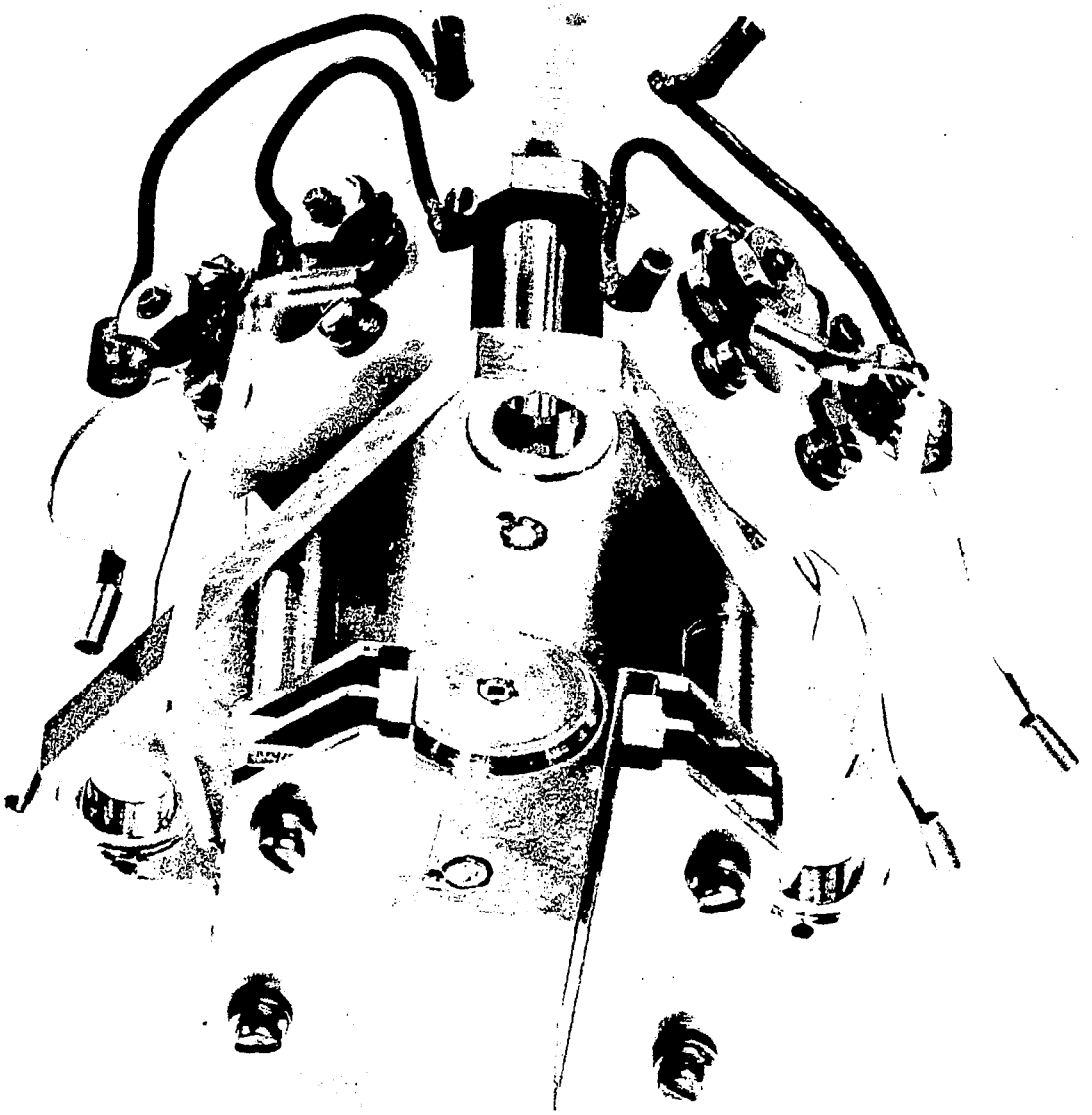

FIGURE 84
Dual Filament Ion Source

walls. Electrons from one of the guns enter the ionizing region through a tapered slot which is visible in the photograph. The beam travels across the ionizing region where it is collected by the anode on the opposite wall. The ions formed are extraced from the ionizing region by the repeller and accelerator electrodes and travel through ion focusing system leaving the ion source through the ion source exit aperture in the ion source base. This exit aperture, again a tapered channel, is shown in Figure 84. This figure also clearly shows the two ceramic filament blocks on which the filament posts are mounted. The large diameter leads attached to the block are the leads through which the filament current is passed. Also visible in both photographs is the Z-axis focusing assembly at the end of the ion source. This is used to constrain the ion beam prior to its entry into the analyzer.

An exploded view of the dual filament ion source is shown in Figure 85. The gas entry tube is shown at the top of the photograph. Just below this is the central structural element to which the electron guns anodes and ion focusing assemblies are mounted. To the right and left of this piece are shown the pieces of the electron gun assemblies. The elements of the ion focusing system are shown in a vertical line extending down to the source base and the elements of the Z-axis focusing system are shown to either side of the source. The components of the ion source are fabricated of non-magnetic stainless steel. The electrodes are separated by ceramic or ruby insulators. Electrical connections are made to the electrodes by means of nichrome lead wires which are spot welded to the electrodes. The other end of the lead wires are attached to the nine-pin headers in the vacuum envelope. The ion source has been carefully designed to eliminate electrical shorts and together with dual electron gun has proven to be a highly reliable unit.

The ions leaving the source are dispersed in the magnetic field of the magnetic sector. They enter the collectors mounted on the collector assembly shown in Figure 86. The bucket assembly shown at the left is for m/e 18, the center one is for m/e 28 and m/e 32 and the one at the far right is for m/e 44. The collector subassemblies are on adjustable mountings. They may be adjusted either along the ion beam or along the collector flange. The first of these adjustments is used to facilitate optimization of the resolution of the instrument. The second one is used to align the collectors so that all of the ions to be monitored are simultaneously collected. The collectors are mounted inside grounded shield assemblies and are connected to the feedthrough pins by lead wires as shown in the photograph. After the collectors have been properly positioned as determined by test additional shielding is added to the collector assembly to prevent stray ion current from connecting pins and collectors. During tests the collector flange to which the assemblies are mounted is clamped to the analyzer vacuum envelope by means of clamping flanges. After final collector alignment the clamp flanges are removed and the collector flange is welded to the vacuum envelope. A weld relief for this purpose is shown in the figure.

The gas to be sampled enters the mass spectrometer through a capillary divider inlet system. The capillary line consists of a series of joined stainless steel tubing ranging in diameter from 0.0075 inch to 0.030 inch with a total length of 187.5 inches for an inlet pressure of 0.5 atmosphere. The capillary line is

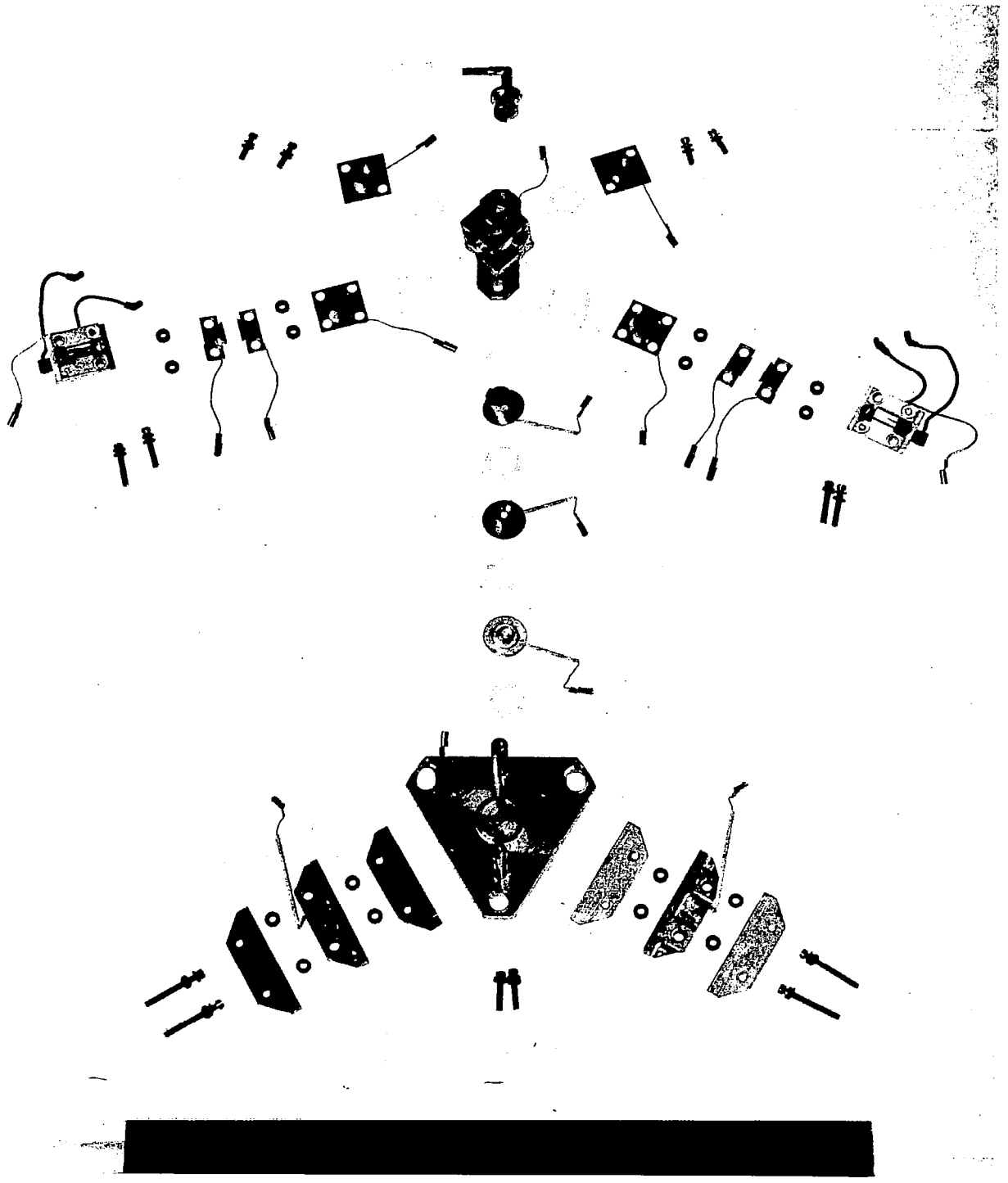

FIGURE 85
Exploded View - Dual Filament Ion Source

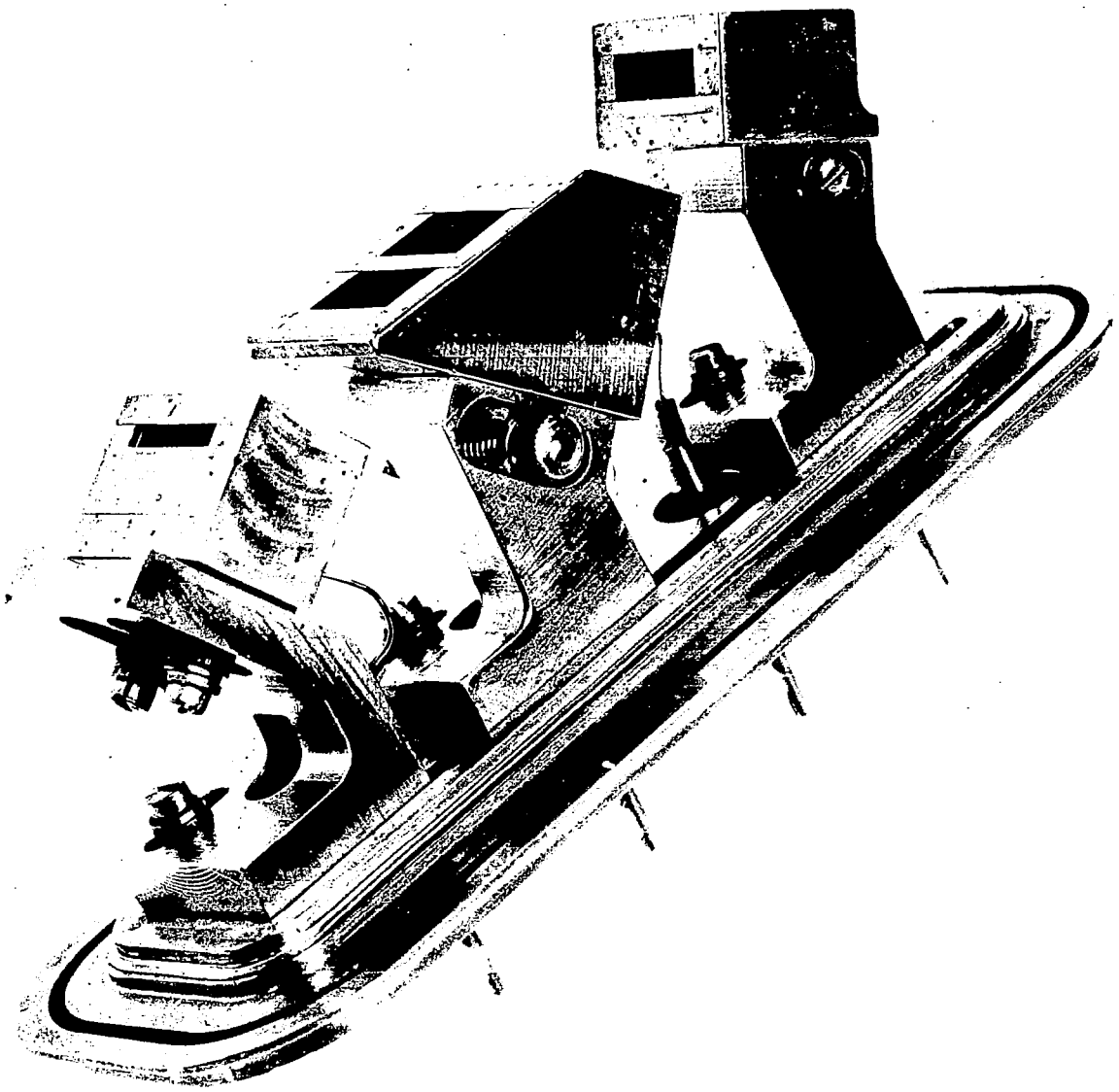

FIGURE 86
Collector Assembly

followed by a bypass line of similar construction, with a shorter length and larger diameter. These diameters are adjusted to maintain viscous flow through the inlet system. The two lines are joined at a manifold (see Figure 87) which houses a molecular leak. The molecular leak is a five micron diameter hole in a 0.080 diameter platinum disc secured in the manifold with a gold gasket seal. A portion of the gas flowing through the capillary divider system passes through the molecular leak and enters a tubular connection joining the ionizing region of the ion source as shown in Figure 83. The lower end of the bypass line is connected to a vacuum system vented to outer space. The manifold assembly is attached to the vacuum envelope and sealed with a gold wire gasket to prevent leaks from the atmosphere directly into the analyzer.

A ball leak is under development that will allow direct molecular flow of a gas sample into a mass spectrometer from an environment greater than 1/2 atmosphere. Its principal advancement is that the gas flow is in the molecular region; this allows the gas conductance to be independent of the total pressure, the gas viscosity and mixture composition. Each gas partial pressure causes an independent flow through the leak providing the optimum sampling mode for a mass spectrometer inlet system. The nominal gas conductance is about 10^{-5} cc/sec. and can be varied over an estimated range of three decades by increasing contact pressure of the ball against a knife edge orifice. The implementation of the leak will eliminate the capillary line and the need for auxiliary pumping.

This leak is designed to be very small and low in mass, reducing the amount of heater power necessary for stabilized temperature application. The diameter is about 3/8 inch and the length is about 1 inch. A sintered stainless filter is used to prevent small particles, that may be present in the gas sample, from plugging the leak.

A second generation leak has been fabricated and test results are available in final report of the ball inlet leak.

The analyzer tube is operated by a set of support electronics consisting of four circuit functions which are discussed below. The first electronic module is a filament supply and emission regulator shown in Figure 88. The two printed circuit boards comprising this module are shown at the bottom of the photograph and at the top they are shown in assembled condition. This circuit receives 28 volt input power and converts it to an ac voltage by means of a power inverter. The secondary winding of the inverter transformer is floated at the potential of the ion source anode. The electronic emission current collected at the anode of the ion source is fed to the emission regulator circuit where it is amplified to control the pulse width of the voltage supplied by the inverter. This voltage drives the filament transformer, the secondary of which drives the filament and is floated at the filament potential.

A second circuit is the electrode diode supply shown in Figure 89. This supply consists of a single inverter which drives two regulated secondary windings. The regulated points supply low impedance pass to ground for the filament reference potential to the electron accelerator. This supply drives an electrode bias string which is mounted on the potential divider board shown on the bottom

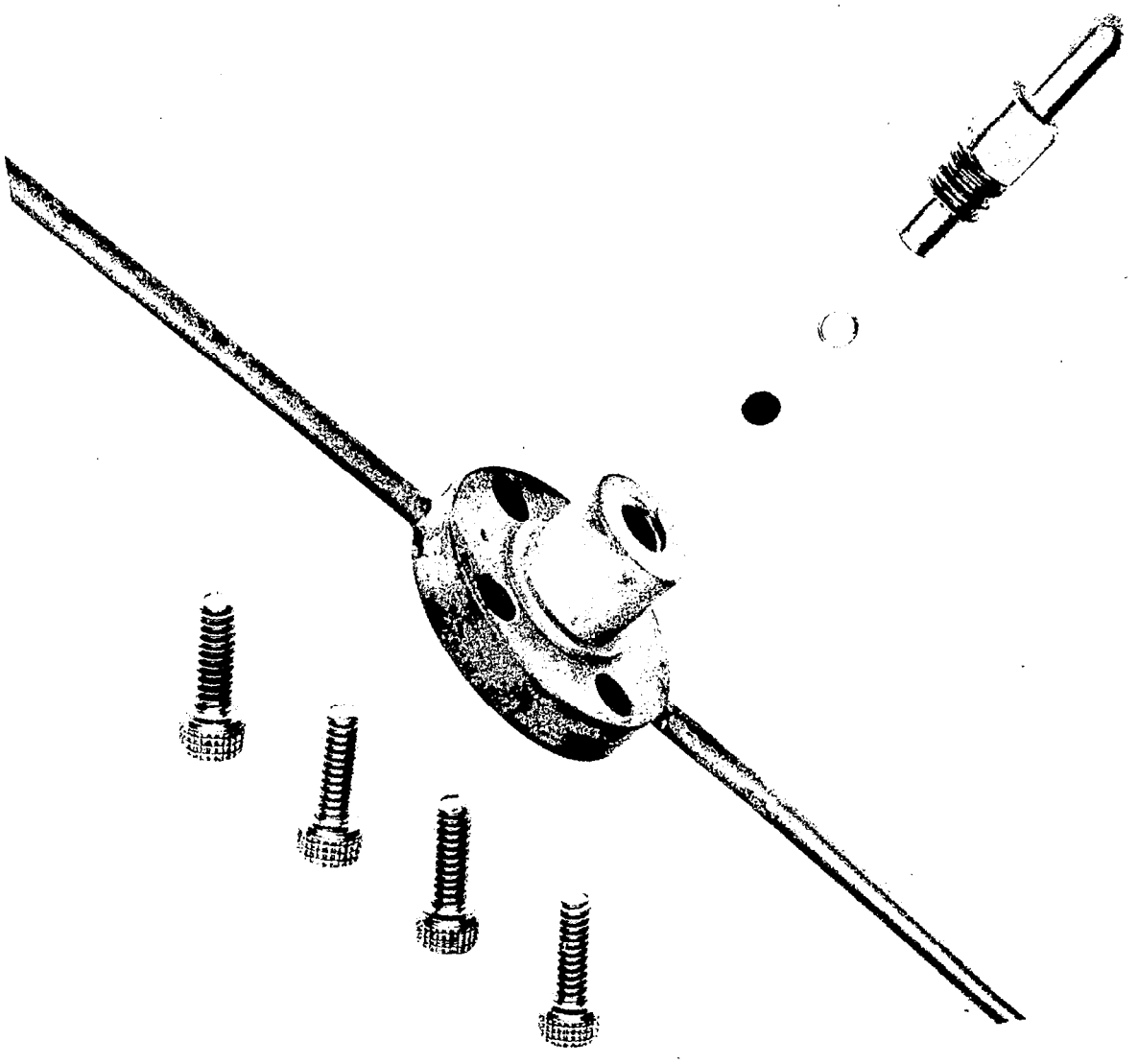

FIGURE 87
Inlet Leak Assembly

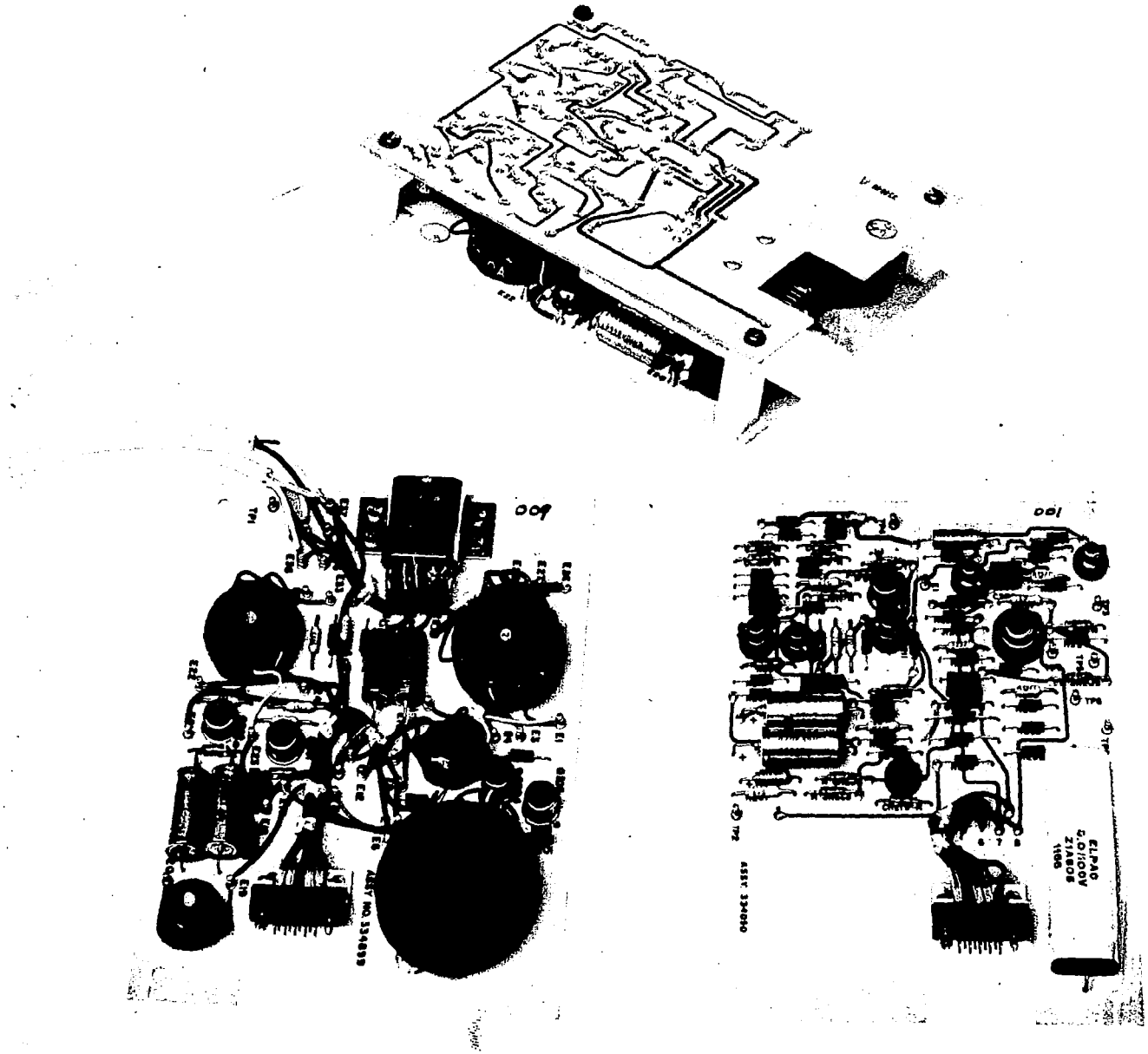

FIGURE 88
Filament Supply and Emission Regulator

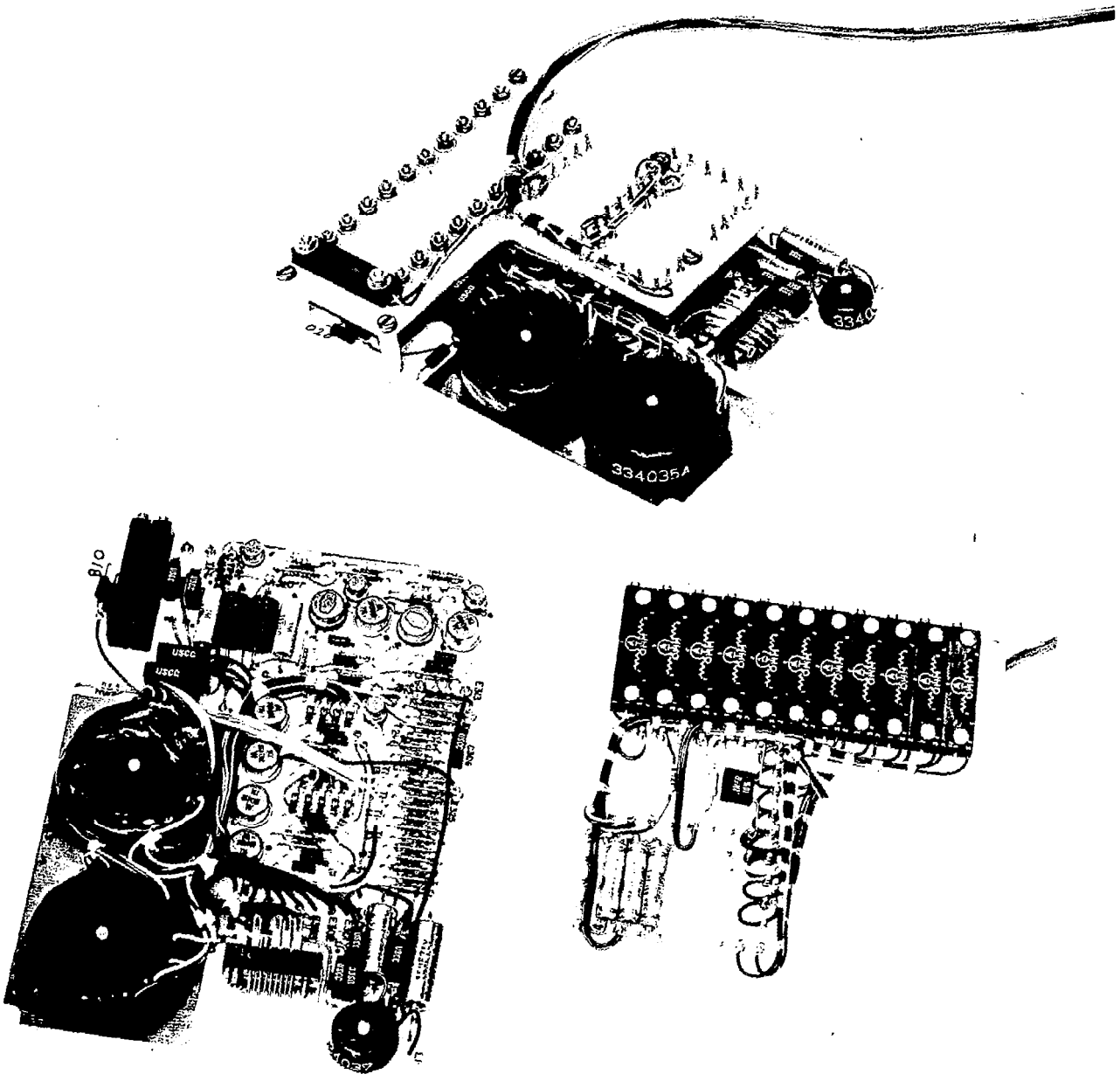

FIGURE 89
Electrode Bias Supply

right of the figure. Voltages from this divider string pass through the nine-pin headers into a vacuum envelope containing the ion source. The pot board also contains a zero check relay which is used to switch potential on one of the Z-axis focus electrodes to ground thereby deflecting the ion beam so that it cannot reach the collectors.

The third circuit required for support of the analyzer is the detector power supply shown in Figure 90. This circuit is actually a dual power supply giving a highly regulated ± 10 volts for the electrometer amplifiers. Again the boards are shown in their disassembled and assembled conditions.

The ion currents arriving at the collectors of the analyzer are amplified by electrometer amplifier detectors. One of these is shown in Figure 91. The circuit consists primarily of a high gain dc amplifier followed by an active filter with 100 percent feedback around these circuits through a 10^{11} or 10^{12} ohm resistor. The input device to the dc amplifier is a high impedance MOS-FET semiconductor device having inherently low leakage. Although this circuit can amplify currents of the order of 10^{-15} amperes to detectible levels it is comprised of only 36 electronic components. (Current specifications require only that a 5×10^{-14} ampere level be detectible.) In fact it is worthwhile noting that throughout the electronic system the inherent simplicity of the electronic equipment and of the circuit designs has led to high reliability. Four electrometer amplifier detectors are used; one for each of the constituents to be monitored. The entire electronics support system requires only 3.5 watts during full operation.

The mass spectrometer system is mounted in an anodized aluminum sheet metal box as shown in Figure 92. The dimensions of the enclosure are 5-1/2 x 4-3/4 x 6-1/2 inches. A set of controls are visible on the front panel of the enclosure. These consist of an emission adjust to set the overall gain of the instrument; a zero check to allow the zeros of the detectors to be monitored; and a filament switch which switches from one filament to the other with an intermediate pressure position. The pressure check system has not been incorporated into the system but plans for this are in process. Figure 93 shows a rear view of the sensor system enclosure. Shown here is the pumpout tube through which the analyzer envelope is evacuated. Also shown is the input-output connector and a bulkhead fitting for the capillary line. A cover plate is also visible which is necessary to gain access to one of the nine-pin headers.

In Figure 94 the sensor system is shown along side a display unit which shows the various modules and subsystems in their proper locations in the enclosure. Electronics modules are located on either side of the analyzer tube with the electrometer amplifiers plugged onto the collector flange pin. The see-through model is somewhat larger than the final flight package due to the flange on the ion source end of the analyzer housing which has not yet been removed.

While the original Two Gas Atmosphere Sensor System was designed to be evacuated to outer space it was felt that there would be certain advantages to a completely self contained system. Therefore a program was initiated to develop a minimum power and minimum weight ion pump.

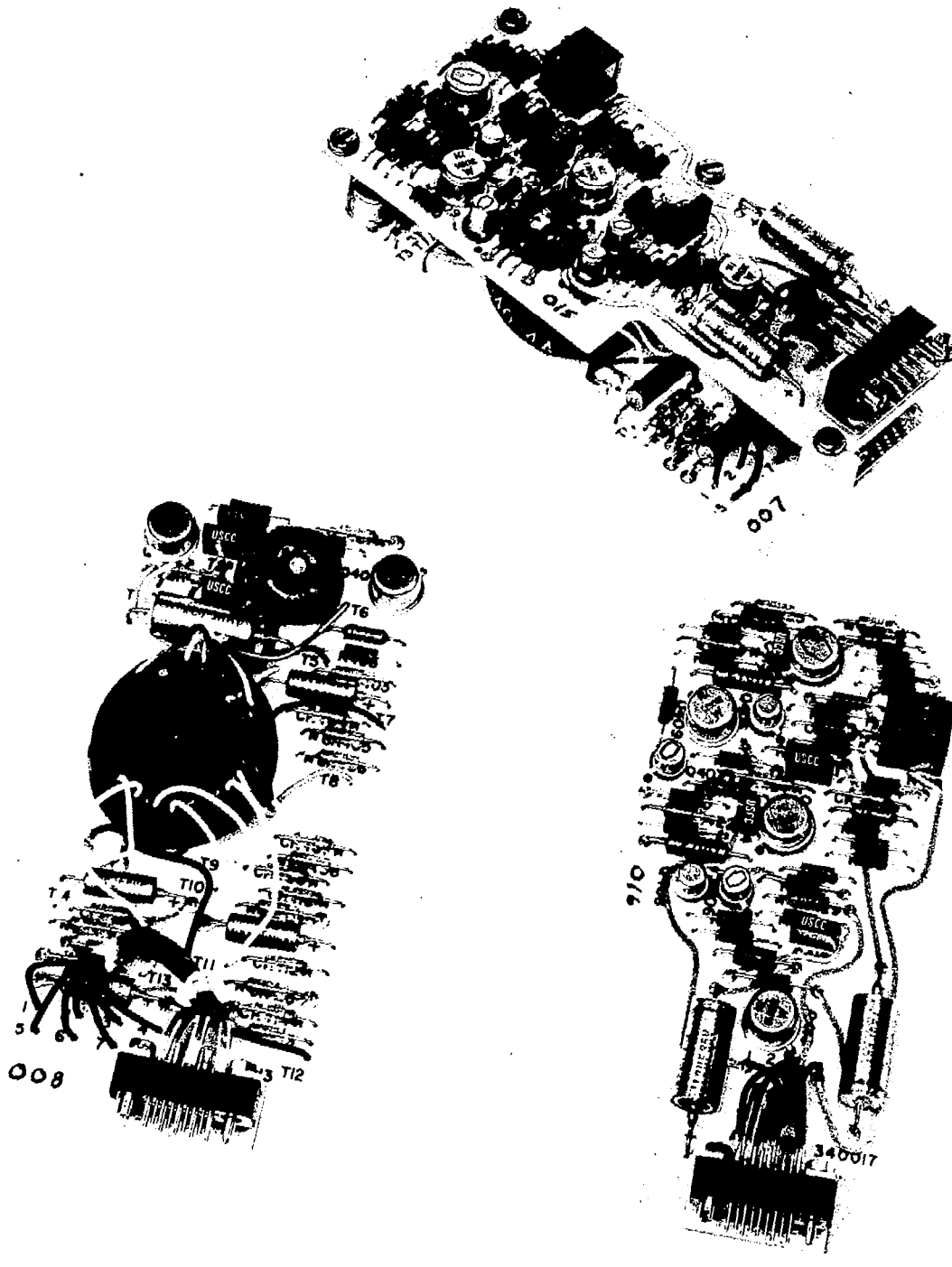

FIGURE 90
Detector Power Supply

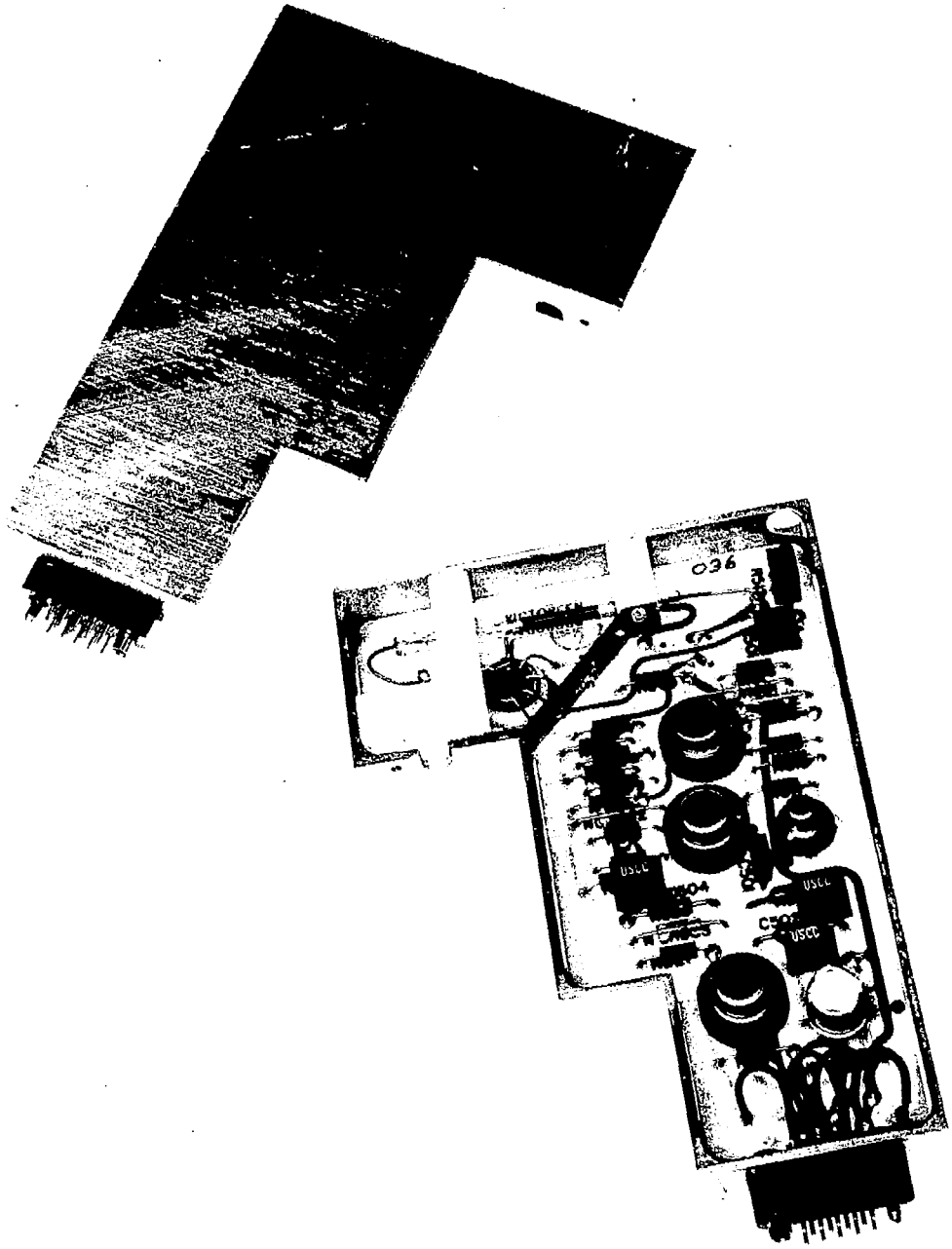

FIGURE 91
Electrometer Amplifier Detector

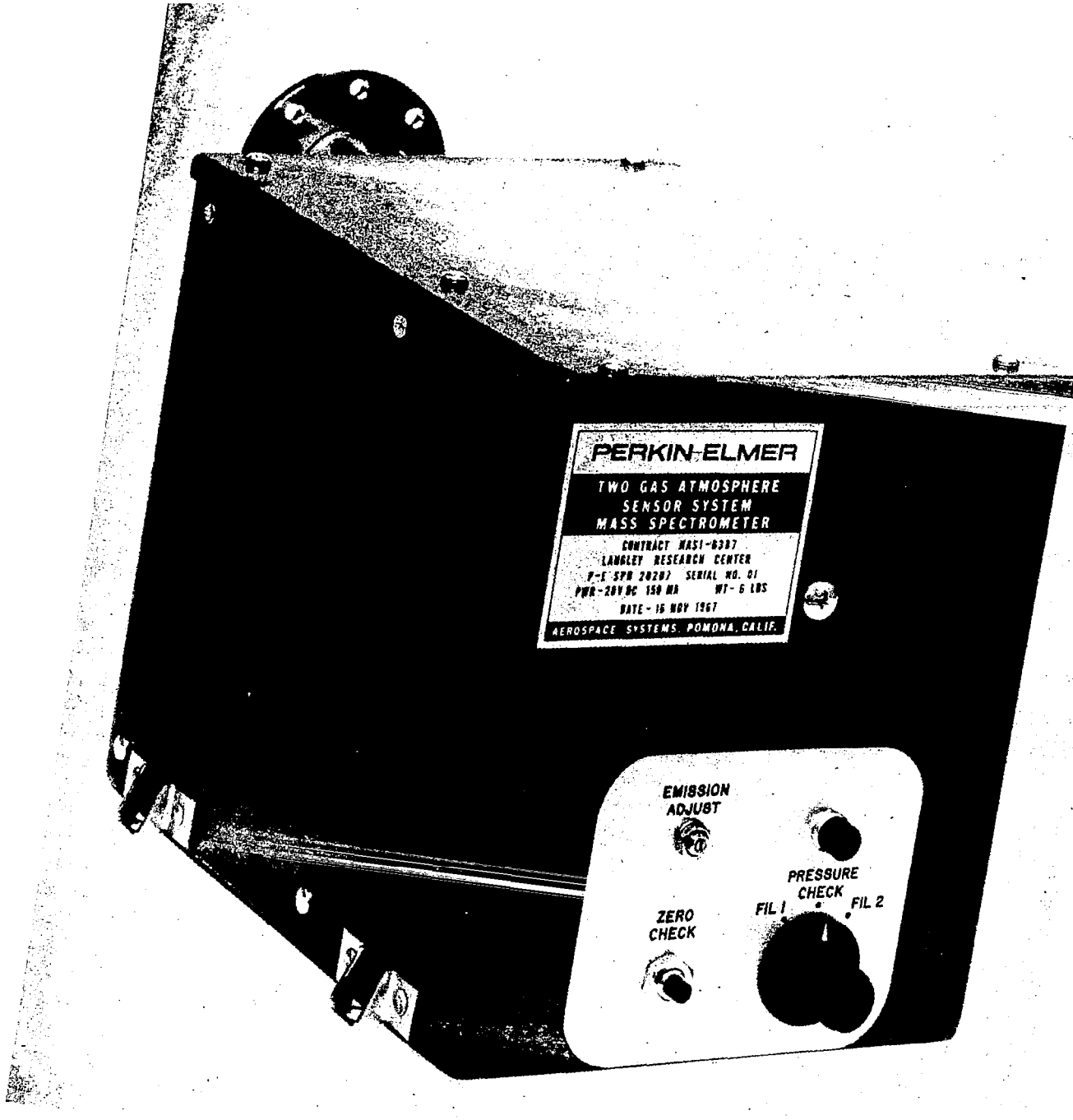

FIGURE 92
Two Gas Atmosphere Sensor System (Front View)

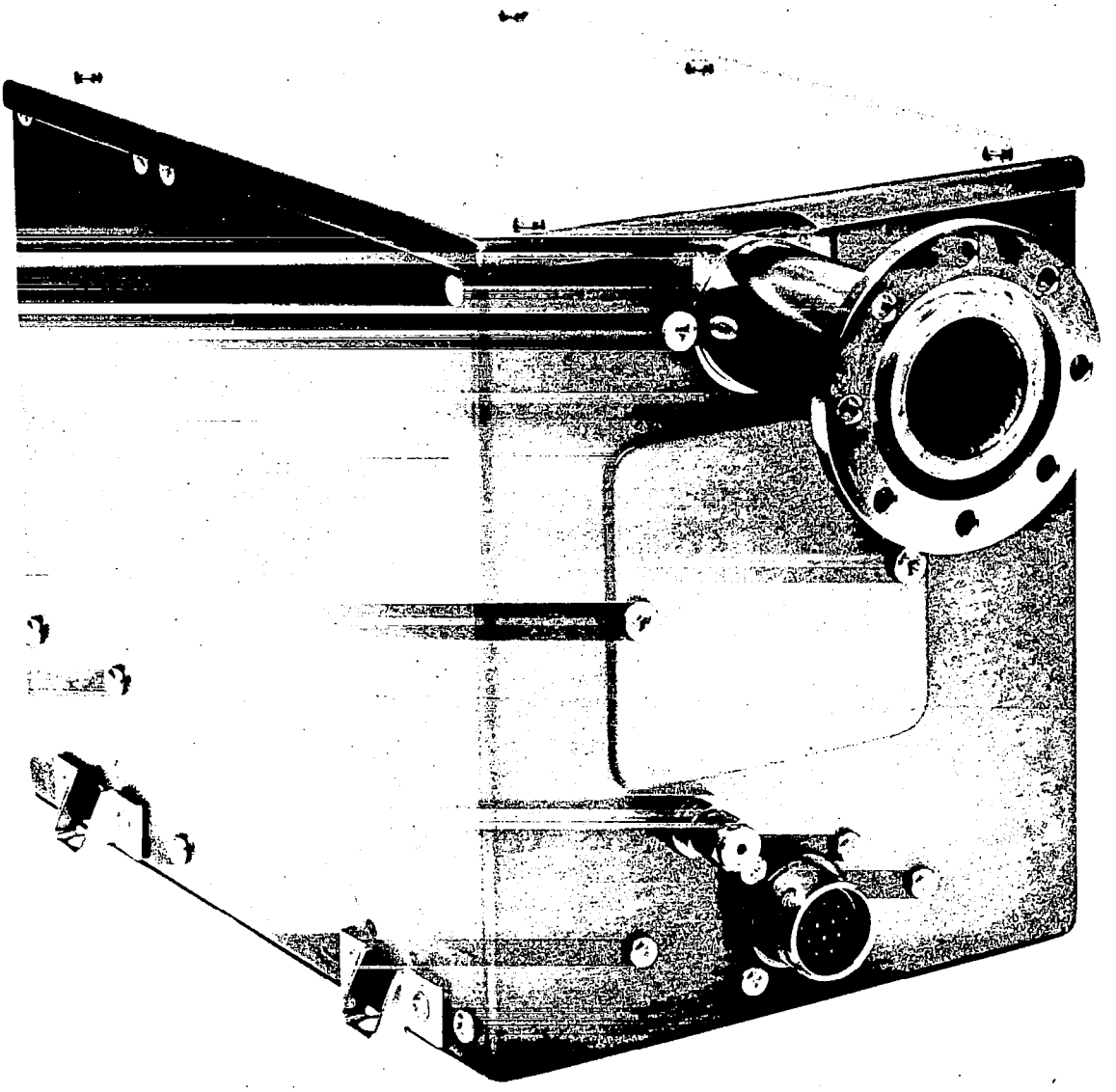

FIGURE 93
Two Gas Atmosphere Sensor System (Rear View)

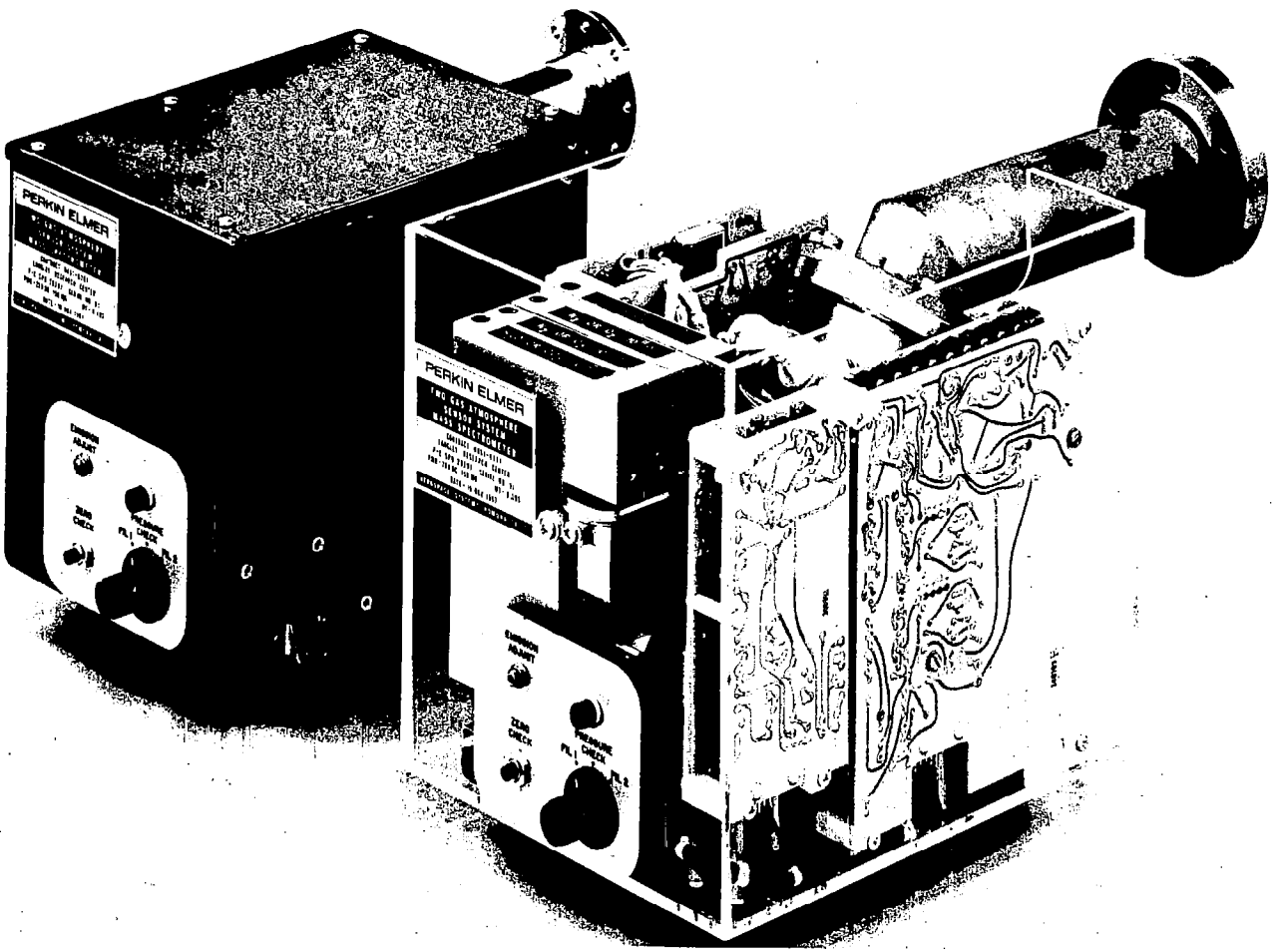

FIGURE 94
Two Gas Atmosphere Sensor System and Display Unit

Specifications for the Two Gas Atmosphere Sensor System are given in Table 24.

TABLE 24
Two Gas Atmosphere Sensor System Specifications

MONITORED SPECIES:	H_2O, N_2, O_2 and CO_2 (can be modified for He, A, CH_3^+, total hydrocarbons, etc.)
MONITORED MASSES:	m/e 18, m/e 28, m/e 32, and m/e 44 (can be modified for other m/e ratios in the range m/e 4 to m/e 44)
RESOLUTION:	Less than 1% contribution of m/e 17 to m/e 18 with equal sized peaks. Less than 0.5% contribution of m/e 28 to m/e 32 and visa versa with equal sized peaks. Less than 10% contribution of m/e 40 to m/e 44 and visa versa with equal sized peaks. (The higher m/e collectors are not at their optimum positions.)
DETECTIBLE LIMIT: (in 400 torr atmosphere)	0.1 torr on CO_2 and H_2O (500 ppm) (10 mv at output) 0.2 torr on O_2 and N_2 (0.1%) (5 mv at output)
ANALYZER SENSITIVITY:	1×10^{-6} amperes/torr. This can be increased by raising the emission level.
TIME RESPONSE:	
DETECTORS -	τ = 1 sec 0 to 90 percent
CAPILLARY LINE -	Delay time: 2 sec. (only achievable with original line which gives too high a pressure. Inlet system modifications may allow this to be achieved with proper pressure.) The implementation of the ball leak has given an inlet system time response of 0.02 seconds.
ACCURACY:	Based on calibration data, the instrument appears to be capable of better than $\pm$2% accuracy on N_2 and O_2 for periods of 30 days. The unit tested was not in its final condition (i.e., no potting and not fully temperature compensated). With calibration this accuracy can be extended over the life of the instrument. For CO_2 the accuracy is better than $\pm$5% for 20 days, and better for shorter periods. No data yet on H_2O.

TABLE 24 (Continued)

SAMPLE GAS LOSS:	Less than 0.5 pounds for 120 days.
LINEARITY:	Design goal - Maximum deviation from linearity $\leq$ 3% at 400 torr sample inlet. Due to an excess ion source pressure condition this goal has not been met consistently but is achievable.
MAXIMUM OPERATING PRESSURE:	For a 400 torr capillary: $>$1 atmosphere up to several atmospheres with capillary modifications or the ball leak.
ION SOURCE PRESSURE:	Design goal - 2×10^{-4} torr for 400 torr external pressure has been achieved by use of the ball leak or with an inlet line modification.
DIFFERENTIAL PRESSURE RATIO:	100:1 (Ion source pressure to analyze pressure ratio.)
OUTPUTS:	Four simultaneous, linear 0 to -5 volts dc.
DYNAMIC RANGE:	0.2 to 400 torr for N_2 and O_2. 0.1 to 20 torr for H_2O and CO_2.
POWER:	$<$ 3.5 watts
WEIGHT:	$<$ 7 pounds
SIZE:	$\backsim$ 0.12 ft.^{3}
OPERATING TEMPERATURE RANGE:	40 to 90°F
VIBRATION & SHOCK:	Designed to be Apollo compatible.
WARM UP:	$<$ 30 minutes for full source temperature stabilization. Can be reduced by the use of an ion source heater.
EXPECTED OPERATING LIFE:	The limiting factor is filament life. Sixty days of continuous operation without filament failure has been achieved. A discussion of an emitter study is contained in Section 10 of this report.

ETM TESTING AND MODIFICATION

The following is a discussion of the more significant results of the tests held at Aerospace Systems and the changes which were made to the sensor system as a result of these tests.

ION SOURCE MAGNETIC SHIELDING

During the design phase of this program it was recognized that magnetic shielding would be required around the ion source, in order that the ionizing electron beam would not be deflected from its desired path, due to the fringe field from the analyzer magnet. Estimates had been made of the amount of shielding required. However, it was decided to wait until the test phase to add the shielding to the system. This was done shortly after the ion source test was started. A double shield of Netic and Conetic material each 1/32 inch thick was employed. The shield had three parts. The first was a bottom section which fit at the bottom of the ion source housing and had a cutout for the end section of the analyzer envelope. The other two parts fit together to surround the cylindrical walls of the ion source housing. The first shields which were built were not very effective shielding source. It was found that this was due to the split in the two piece section of the shielding which was in such a position as to prevent the effective shunting of the magnetic flux around the source. The shields were modified to place the splits in a different position and effective shielding was obtained. These shields were used throughout the remainder of the ETM test program.

A drawing was made for a set of flight prototype shields similar to the ETM shields, however, the bottom section of the shielding was formed as a part of one of the side sections. This was done in order to reduce the number of pieces in the shield assembly and to facilitate the mounting of the shields. When testing of the prototype units was begun it was found that this new shield did not seem to give effective shielding. The shield assembly was examined by placing it in its normal operating position with respect to an analyzer magnet and measuring the region inside the shield with a gauss meter probe. It was found that the shield gave almost no reduction in the flux level in the vicinity of the ion source. It was determined that this resulted from the bottom section of the shields aiding in transmitting the magnetic flux toward the ionizing region. The shields were therefore modified to return to the original ETM configuration with a separate bottom section. At this point it was determined that a single 1/16 inch thickness of cold rolled steel was more effective in shielding the ion source than was the double thickness of Netic and Conetic material. Therefore, the final flight prototype ion source shield is a three piece assembly using a single thickness of cold rolled steel.

STABILITY

During the ETM testing a problem developed with the stability of the mass spectrometer output. Severe and rapid fluxuations of the ion current output were noted. An extensive series of tests were conducted to determine the source of this problem. Attempts were made to correlate the variations with all other parameters. It was finally determined that the instability appeared to be in the ion source output and was not correlated with variations in the sample inlet or in the emission system. After disassembly of the instrument it appeared that the problem was perhaps due to inadequate cleaning. This prompted a thorough investigation of cleaning procedures. As a result of this investigation, major improvements were made in the cleaning procedures and facilities. An improved cleaning procedure with logical sequencing was developed based upon the use of Freon TF as the primary cleaning agent. In the past all precision assembly and cleaning was done in one room. In the new procedure one room was allocated for initial assembly and precision machining and fitting, the second room was for preliminary cleaning steps and a third room was used for final cleaning and final assembly. The final cleaning room incorporated a laminar flow bench on which all assembly was to be done. After reassembling the instrument under these new more rigid conditions the instrument was found to perform satisfactorily and no re-occurrence of this difficulty was noted, either on the ETM or the four flight prototype units.

One of the tests performed during the examination of the stability showed that approximately 50 percent of the ion current striking the exit plane of the ion point is transmitted to the analyzer. This is a much larger percentage than was originally anticipated. Normally approximately 10 percent of the ion current or less is transmitted. At the time it was believed that this might also be a source of some of the instability and therefore, the baffle preceding the exit aperture was tabbed down from 0.020 inch x 0.012 inch to a 0.012 inch square. The sensitivity of the ETM was sufficiently high so that the loss in the ion current transmitted in the analyzer could be tolerated. Since it was subsequently shown that the problem was due to cleaning rather than the size of the exit aperture, this change was not made on the flight prototype units. It is not anticipated at the present time that the baffle will be tabbed down on any succeeding units.

INLET SYSTEM TESTING

Before mounting the capillary divider on the mass spectrometer it was tested to see if the desired pressure was obtained at the manifold. It was found that, although the design pressure at the manifold was to be 13.4 torr, the actual pressure obtained was 26.6 torr with an inlet pressure of 400 torr. Since this would cause the pressure in the ion source to be twice the design value, it was necessary to modify the capillary line. The initial section of capillary line which is 0.006 inch in inside diameter was lengthened gradually from its original value of 33 inches to 75 inches at which length the manifold pressure was reduced to approximately 15 torr. At this point it was decided that the slight overpressure could be tolerated. Calculations were performed which explained the reason for the required added length. The initial design calculations had assumed a tapered line in order to obtain constant velocity flow and thereby stay below critical flow. The actual line however was an approximation of a tapered line using 4 sections of enlarged diameter. When the actual

system which was fabricated was recalculated it was found that this was not a very good approximation to the tapered line and that the added length was required in order to achieve the proper pressure at the manifold.

This phase of the test program was complicated further by difficulties in obtaining repeatable measurements of the manifold pressure. It was believed that this was due to partial plugging of the capillary line. Originally the sections of the line were soldered together. Two changes were made for the flight prototype capillary lines. First, the lines were brazed together rather than soft soldering. It was believed that this would lessen the liklihood of plugging the line since solder or flux could be responsible for the plugged capillary line and the flow of the braze and the flux are more readily controlled during the brazing process than are the counterparts in the soldering process. The second improvement was in the cleaning procedures for the capillary line. A test apparatus was built which allowed cleaning solution to be injected through the line at a high pressure. It was found that the conductance of ether through the line was much higher than it was for Freon and therefore, ether was used as the cleaning agent. Another problem encountered with the capillary lines was that when first applied to the mass spectrometer system the lines frequently plugged. This was due to oil which entered the line from the bypass end. This situation was later rectified by the addition of a molecular sieve trap in the pumping line. This only partially solved the problem. Although a charcoal trap was used in the sample inlet system, oil from the system roughing pump continued to enter the capillary line. This was corrected by the addition of a second molecular sieve trap. This experience showed that the Millipore paper filters did not adequately stop oil vapors. Subsequent tests have indicated that during normal operation the lines will remain open.

After capillary line tests the platinum aperture leak was inserted in the manifold and the leak assembly was mounted to the analyzer. Great difficulty was encountered in properly mounting the platinum aperture in the manifold assembly. This led to excessive pressure in the analyzer due to leaks around the platinum aperture. After several attempts an aperture was successfully mounted and pressure levels closer to the expected values were obtained. When the instrument was operated it was determined that the ion source pressure was still higher than the design value of 2×10^{-4} torr. For sometime it was believed that this was possibly due to improper seating of the platinum aperture. Later tests however conducted on the ETM when it was being prepared for the test at McDonnell Douglas indicated that the problem was in the apertures themselves. There was inadequate data at the time of the ETM test to resolve this problem and therefore the flight prototype units used the original platinum apertures. In general their pressures were somewhat excessive. This situation can be rectified either by a new design for the inlet leak or by a longer capillary line.

ANALYZER MAGNET STABILITY

The original ETM analyzer magnet was a five piece assembly which was held together by epoxy. The magnet was wrapped with a coil of wire at Aerospace Systems and taken to an outside vendor for charging. It was found that in

handling the magnets back at Aerospace Systems that the flux level did not appear to be stable but would drop with time. While this problem did not seem to be too detrimental to the ETM testing it was more severe once testing of the flight prototype units began. Attempts to stabilize the magnet by shock treatment proved unsuccessful. While this technique had been useful in stabilizing earlier magnet designs it seemed to continually reduce the field of these magnet assemblies. Continued experimentation with the shock treatment led to another problem. The magnet assemblies were occasionally broken since the epoxy was not a sufficiently strong binding material to withstand the shock.

At this point several steps were taken. One of the magnets was sent to General Electric for analysis of the Alnico V material. Conversations with the people at General Electric indicated that one of the problems might be the joining process which would not give adequate mechanical stability. General Electric recommended that the pieces of the magnet assembly be soldered together. Various soldering techniques were investigated and a procedure for joining the magnet pieces was established. General Electric reported that the magnet material furnished by Aerospace Systems seemed to be normal in every respect. While discussing this it was brought out that magnetically soft material had been used to strike the magnet during the shock treatments. General Electric felt that this was very likely to be the problem. General Electric indicated that striking the surface of a permanent magnet with a magnetic material will cause a small additional pole to be created at the point of impact, which will effect the gap flux density. General Electric felt that great caution should be taken against striking the surface with the magnetic material and that when conducting any further shock treatments a rubber mallet should be used. It was then realized that during the handling of the ion source magnetic shields the bottom shield often slipped down and struck the magnet and it was reasoned that perhaps this caused a drop in the flux density. A coating material for the magnets was then obtained and all magnets from that point on were coated with approximately 1/8 inch thick protective resiliant coating. At the same time steps were taken to purchase a magnet charger and magnet treater so that Aerospace Systems would have more control over the processing of the magnets. In the past the magnets were charged out of the plant and this gave Aerospace Systems much less control over the process and did not afford an opportunity to learn about the elements in the charging technique which might lead to magnet stability.

At this point it was decided that additional study would be required in this area. As a result of a proposal sent to Langley Research Center a study contract is now underway to fabricate two magnets with improved design and to investigate means for stabilizing them. It is believed that this program will lead to stable magnet design and that this will no longer be a problem with the analyzer. Results of this study will be reported upon its completion.

SUPPORT ELECTRONICS

The changes in the system support electronics as the result of tests have been very minimal. The most significant of these is in the electrode bias supply. Originally it had been assumed that the anode and electronic accelerator electrodes both of which receive an appreciable electron beam current would be operated at the same potential. This would allow them to be placed at the same

point on the electrode bias divider string. In fact this point was to be the top of the divider string so that there would be a low impedance through the power supply back to the filament reference. Tests conducted on a similar ion source on another program have shown that there might be some difficulty with the ion energy spread of the source. Steps taken to correct this difficulty required the increasing of the size of the ridges of the repeller and accelerator electordes thereby isolating the potential of the electron accelerator electrode from the ionizing region to a greater degree. When this was done however it was found that in order to obtain a balanced flow of electrons across the center of the ionizing region that the electron accelerator potential had to be operated above the anode potential. Unfortunately there was no low impedance point below the electron accelerator potential through which the anode current could be returned to the filament reference. It was determined however, that since the current arriving at the anode is controlled by the emission regulator and held constant that this current injected into the divider string would not cause variations in the electrode voltages during operation. Therefore, the anodes of the ion source were connected by a potentiometer to the divider string at a point below the electron accelerator potential. No problem from this source has been apparent, however, it is believed, in the interest of good design that a future electrode bias supply should have a provision for a low impedance point for the attachment of the anodes.

The ETM did not have provisions for deflecting the ion beam so that the instrument could be put in a zero check mode for checking the detector zeros. This provision was added on the flight prototype units by placing a relay on the bias board. When this relay was actuated by pressing the button on the front of the box, one of the Z-axis focus electrodes was switched from its normal potential, which is approximately at the accelerator level, to ground. This caused the ion beam to be deflected as it passes through the Z-axis focusing section and strike the sidewall of the analyzer rather than be conducted all the way to the ion current collectors. A modification was made in the filament switch circuit which allowed rapid switching from one filament to the other.

Although not a design change there is another point worth noting. In preparing the electrode bias divider string it is necessary to tailor each divider for the analyzer tube with which it is to be mated. This is not uncommon in mass spectrometers, and is due to small variations in the alignment of the of the ion source lens system. While it might be possible to increase the tightness of tolerances on the piece parts this would be unduly expensive and is not necessary if the matching process is performed on the divider string. Since there is a fair degree of flexibility within the divider it is believed that by examining data from the four flight prototype units it may be possible to develop a universal divider string which will allow the appropriate potentials to be obtained for any analyzer tube simply by adjustment of potentiometers. Otherwise the integrating of the electronics and the analyzer tube is a routine task and has been readily accomplished on all instruments.

Additional testing of the ETM system was also carried out in preparation for the test program with the McDonnell Douglas Space Cabin Simulator. This testing is described in the test report for that effort.

EMITTER STUDY

The initial effort on the emitter study is described in the Phase II(a) Report. In summary the study was directed toward the determination for various materials of the following filament characteristics:

a. Comparative work function.

b. Sample distortion by reaction with the emitter.

c. Change in work function due to specific gases present.

d. Mechanical properties.

e. Filament life.

This program investigated these properties of the filament materials and provided the necessary information for the future choice of emitter materials for the Two Gas Atmosphere Sensor System. The experimental program was structured to give primarily relative information rather than quantitative data on filament life or other parameters.

MATERIAL SELECTION AND TEST SETUP

The Phase II(a) Report listed the following materials to be investigated:

a. Tungsten-Rhenium Alloy

b. Thoriated Tungsten Rhenium

c. Rhenium Coated Tungsten

d. Iridium

e. Thoriated Iridium

f. Rhenium

g. Tantalum

It was found that Thoriated Iridium, Rhenium and Rhenium Coated Tungsten materials were not available in the three mil diameter wire size and were thus omitted. It was believed that any larger diameter would require too much power for sustained emission.

A special test fixture was designed and built to simultaneously test nine filaments under the same conditions. This setup was designed for total emission collection. The filaments were thus operated in a diode-type configuration

whereby all the emission from an individual filament was collected. In the two gas sensor, however, it is known that the electron gun design imposes restricting electric fields around the filament such that the total emission observed is less than that coming off the filament surface. This is due to the return of some emitted electrons to the filament. Consequently, the filament in the two gas sensor will run slightly hotter than those in the study diodes. However, for the comparative purposes of this study program, the diode configuration used is sufficient for the evaluation study. Furthermore no emission regulators were used due to the prohibitive cost for nine units. Instead the nine filaments were driven in parallel from a single power supply and a parallel load potentiometer was adjusted to vary the filament current and thereby give the proper emission level. Each diode was separately monitored and precautions were taken to avoid measurement error by using the same monitoring devices for each test setup. The filament voltage measurements were made directly at the feed-through pins on the test chamber. This was done with the voltage measurement leads soldered directly to the header pins. This was necessary to eliminate error caused by long-term resistance buildup at the connector interface which is inherent at these current levels.

All life testing was done with an environmental atmosphere of water-saturated air at a pressure of 5.0×10^{-6} torr, thus giving partial pressures of water of about 1.5×10^{-7} torr and oxygen about 1.1×10^{-6} torr. This approximates the environmental exposure which the filaments in the two gas sensor will have.

In the past it has been seen that filament life expectancy and general mechanical stability has been increased by slowly raising the filament power to the operational level over a period of at least 1/2 hour. This burn-in serves to gradually outgas the filament and relieve any mechanical stresses incurred in the fabrication processes. During such burn-in the vacuum system pressure is kept below 5.0×10^{-7} torr by controlling the temperature of the filament.

PREPARATION AND INVESTIGATION OF THORIA ALLOY FILAMENT

Carburization was done utilizing information on work done by Jolly[12]. Percent carburization, throughout this paper, is referred to as the percent current change at 2000°K from before and after carburization. The following technique was employed. Consider the useful emitting area of the .300 inch long by .003 inch diameter wire to be about .009 cm^2 and carburization was done at approximately 100 microamps of total emission. Then by Figure 95 the filament temperature was approximately 2100°K. By monitoring the filament current at the beginning of carburization and correlating this with Figure 96 for the proper percent of carburization, the change in filament current required for various carburization levels can be determined. Carburization was done by exposing the operating filament to xylene vapor at approximately one micron total pressure until the proper filament current drop occurred. Again considering the work done by Jolly[12], it was decided that carburization levels of 10, 20, and 30 percent would be done on the three thoriated tungsten rhenium filaments under test. Although it was fairly apparent that thirty percent would yield a filament of too fragile a nature, it was felt that the experimental data would have value. The twenty percent carburized filament should have the resilience to withstand flight acceleration and vibrational forces while providing a significant power advantage.

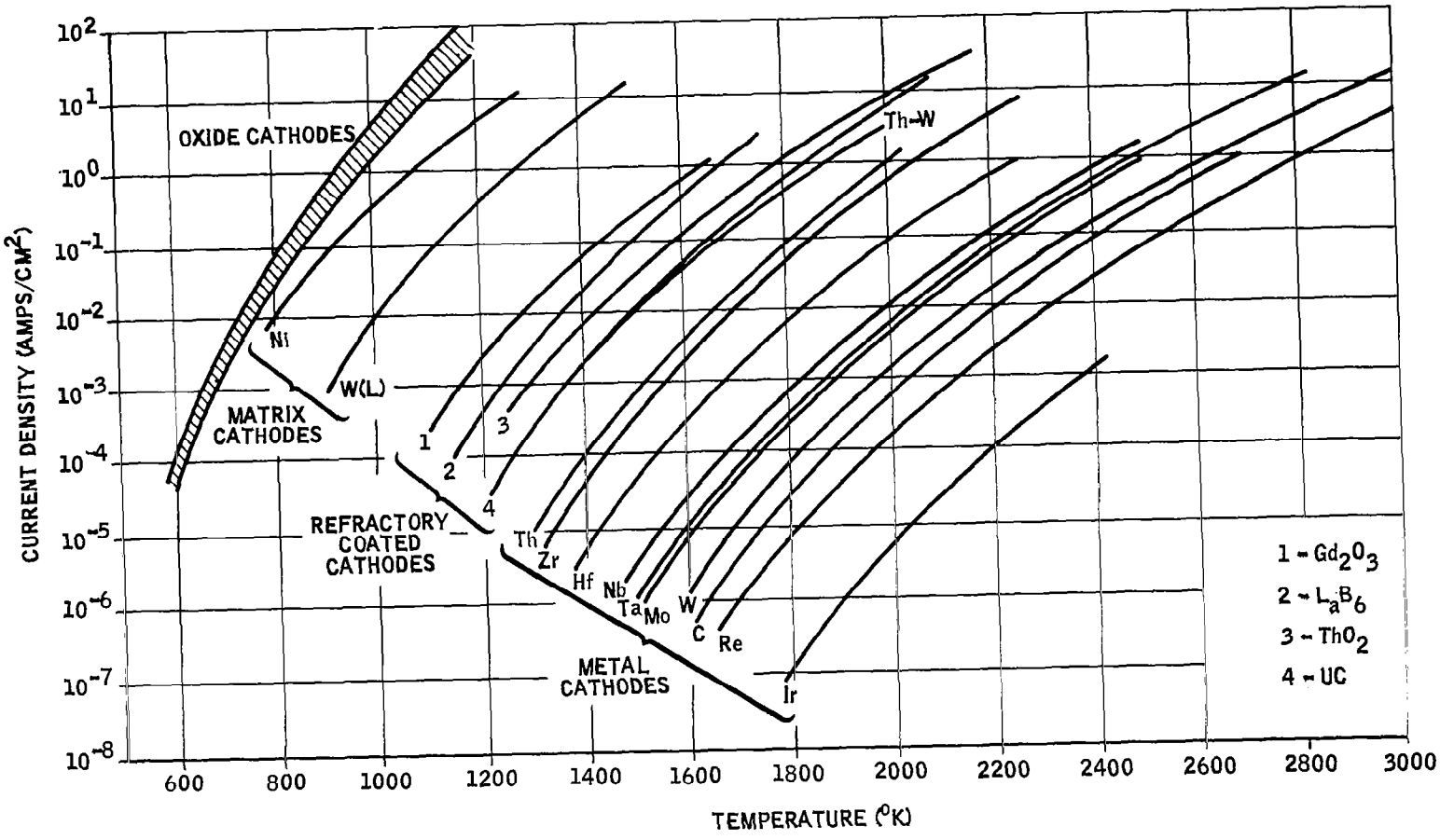

FIGURE 95
EMISSION CHARACTERISTICS OF VARIOUS THERMIONIC CATHODES

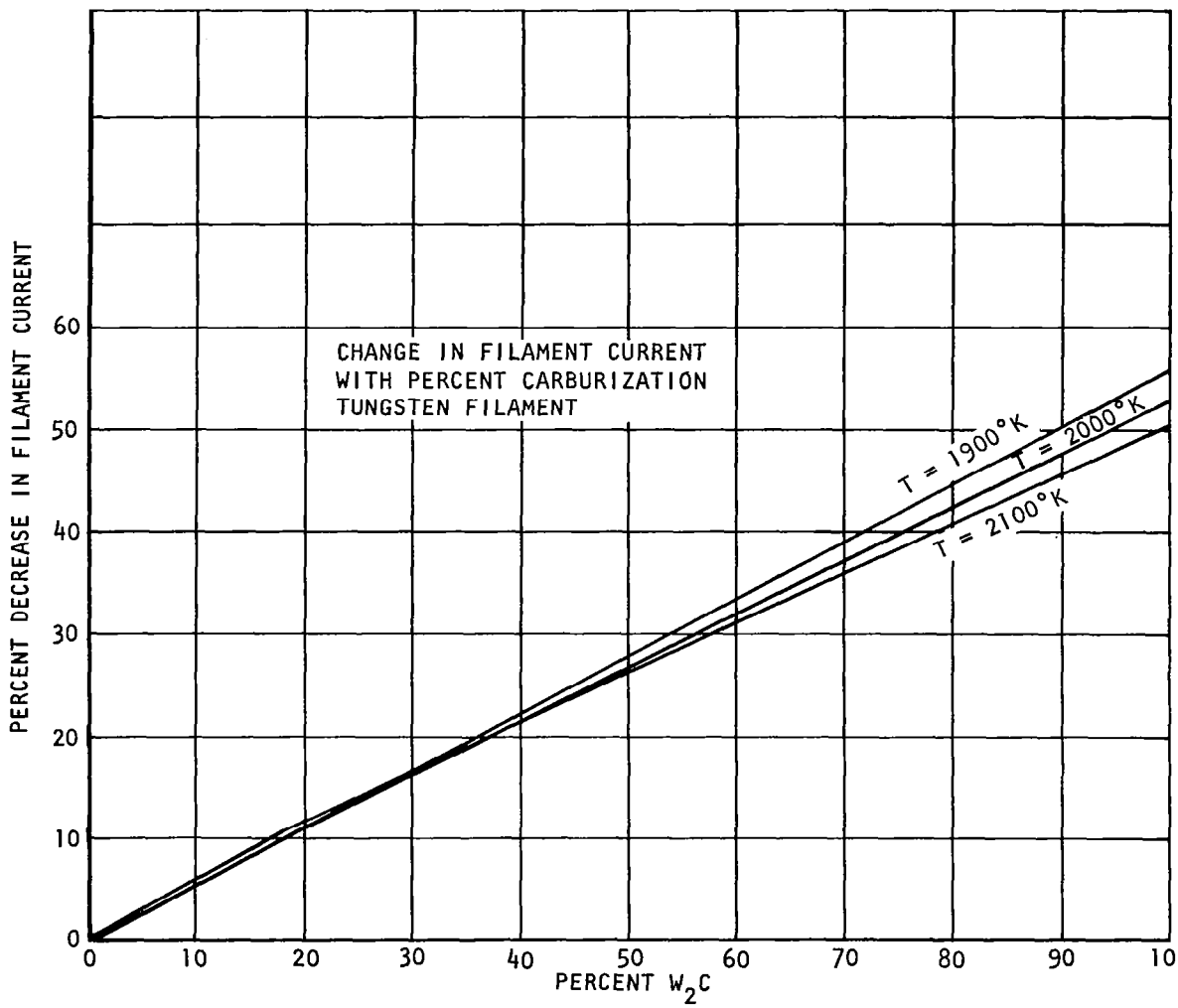
CHANGE IN FILAMENT CURRENT
WITH PERCENT CARBURIZATION
TUNGSTEN FILAMENT
T = 1900°K
T = 2000°K
T = 2100°K
PERCENT DECREASE IN FILAMENT CURRENT
PERCENT W_2C
0
10
20
30
40
50
60
70
80
90
100

FIGURE 96

Poisoning of thoriated tungsten rhenium is caused by exposure at operating temperature to oxygen, water vapor or carbon dioxide. Poisoning occurs as a function of the partial pressure of either or all of these constituents and manifests itself as a drop in emission once a critical pressure has been reached.

There is some observed resistance of thoriated cathodes to poisoning by oxidizing gases. However, once a certain critical pressure is exceeded poisoning commences and becomes rapid with further small increases in pressure. For a fully carburized cathode at 2000°K the critical partial pressures are as follows:

a. O_2, 1×10^{-5} torr

b. CO_2, 2.5×10^{-5} torr

c. H_2O, 6×10^{-6} torr

Poisoning decarburizes the surface and these critical pressures decrease. For a cathode whose immediate surface has been decarburized, the pressures are about a quarter of those with the fully carburized surface[13]. This dependence upon pressure is due to a relation between the reaction rates for these sample constituents with carbon or the filament and the reaction rate of thoria along with the diffusion of the thorium to the filament surface.

Above this critical pressure emission decreases occur more rapidly as can be seen in Figure 97[13]. It was anticipated that the operating pressure on the two gas sensor would be sufficiently low that poisoning would not occur.

The filament may be reactivated by operation at high temperature and low pressure for a period of time. It has been found by Jenkins and Trodden[13] that the filament resistance to poisoning decreases with the number of times it has been poisoned. (See Figure 98.)

While the literature concerning this type of filament was not too encouraging, it was felt that there was insufficient test data available with the operational parameters of this application to rule them out. If successful, this material would represent a substantial power advantage over the alternate materials.

With the environmental conditions stated previously, poisoning occurred within the first few days of operation and thus negated the power advantage gained after carburization. This poisoning occurred with such rapidity that no useful operation could be obtained due to instability. After the sixth day of operation all power advantage and thus surface carburization was lost. Because of this and also the accompanying probable large sample distortion which would be incurred, it was not felt that, for the intended application, there was sufficient justification for further consideration of this material. It is recognized, however, that perhaps more experience and better methods of carburizing could produce a more acceptable filament.

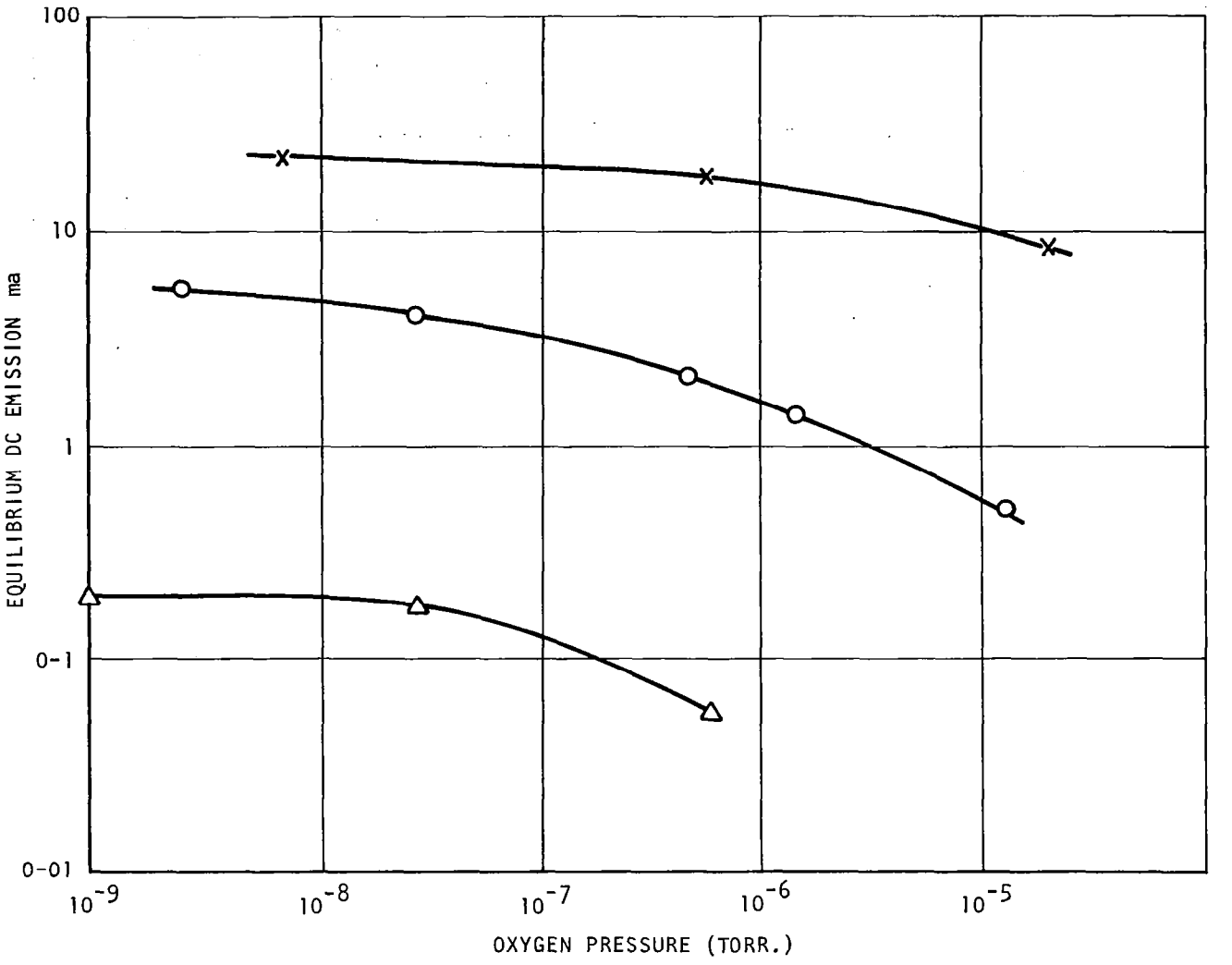

POISONING OF D.C. EMISSION FROM A THORIA-COATED TUNGSTEN FILAMENT BY OXYGEN.

X FILAMENT TEMPERATURE 1800°K;

O FILAMENT TEMPERATURE 1700°K

△ FILAMENT TEMPERATURE 1600°K.

FIGURE 97

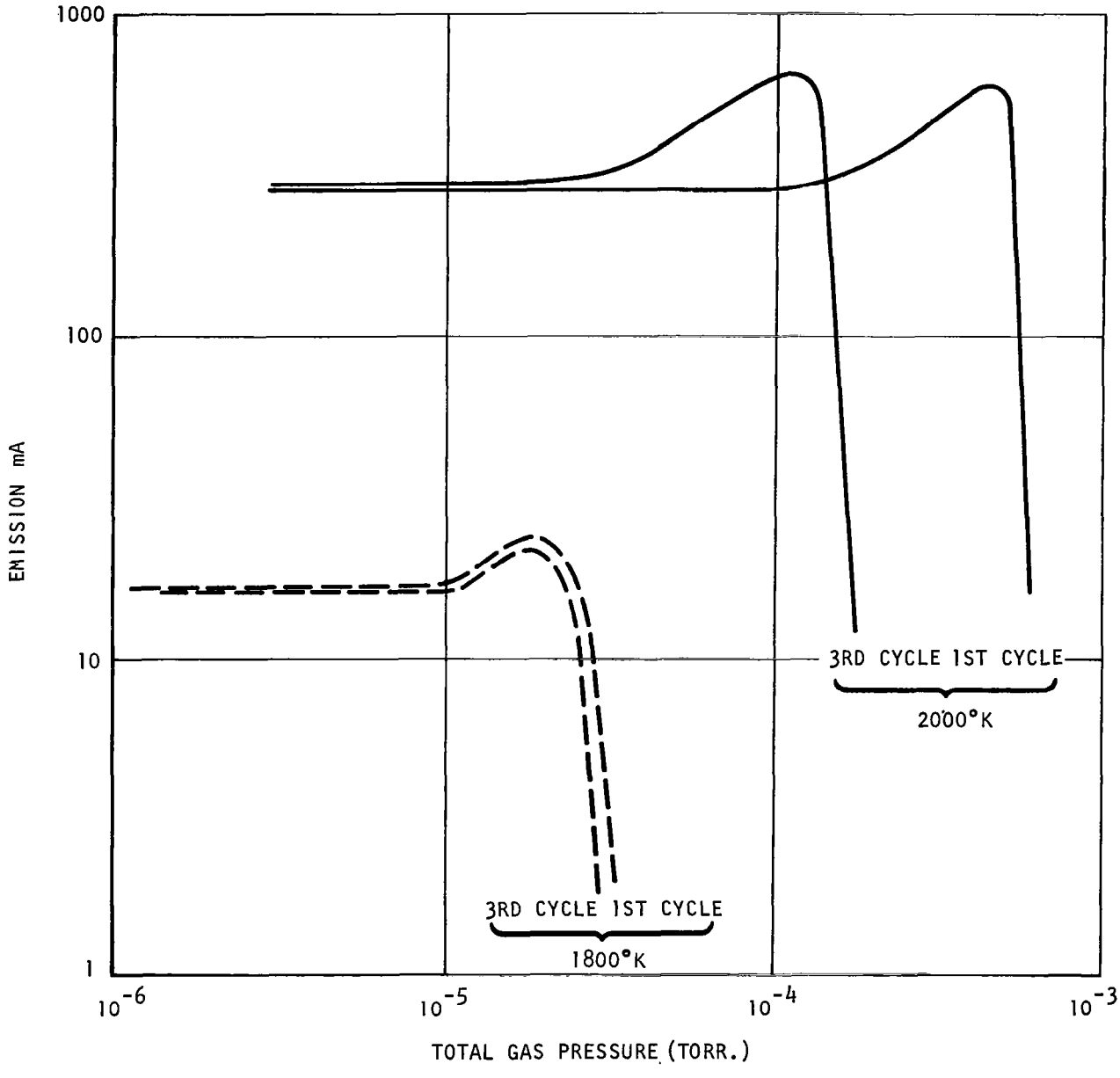

FIGURE 98

TYPICAL EMISSION-PRESSURE CURVES FOR A FULLY CARBURIZED CATHODE DURING OXYGEN POISONING.

WORK FUNCTION COMPARISON

Comparison of the material work functions was accomplished by analysis of the filament efficiencies of the various materials under identical environmental conditions. This was done by plotting emission versus the power required for identical filament assemblies. This plot can be seen in Figure 99.

While three filaments were tested for both the 75% W 25% Re and the 97% W 3% Re materials, each filament of the same materials was sufficiently close in its emission characteristics that only one plot is shown for each of these materials. Figure 99 shows that prior to poisoning a significant power advantage could be gained by using thoriated tungsten rhenium and that the 30% carbonized thoria alloy material had the lowest work function. Tantalum also had a low work function. However, tantalum wire of this diameter was found to have a useful life of only a few days. There seems to be some inconsistency between Figures 95 and 99 regarding tantalum. This may be symptomatic of anomalies in the fabrication processes due to the small wire diameter which could produce extreme hot spots. Iridium as an emitter of this diameter was also found to be impractical because the life expectancy of this material was only about 15 minutes.

SAMPLE DISTORTION BY REACTIONS WITH THE EMITTER

Sample distortion can be caused by the chemical reaction of the gases present at the filament with each other or with the materials present at the hot surface of the emitter. An analysis of these effects was made utilizing a residual gas mass spectrometer to obtain a spectra of a sample gas admitted to the system and comparing it to spectra obtained with various operating filaments. The reactions of the sample gas of interest for the sample distortion analysis are believed to be due to the presence of oxygen and water vapor in the system. The pertinent reactions are:

$$O_2 + 2W_2C \text{ ----- } 2CO + 2W_2$$

$$O_2 + W_2C \text{ ----- } CO_2 + W_2$$

$$H_2O + W_2O \text{ ----- } CO + 2H + W_2$$

The formation of CO and CO_2 cause a distortion in the measurement of N_2 (both CO and N_2 fall at m/e 28) and the CO_2 sample. Also the conversion of O_2 distorts its own measurement. These effects are reduced by the use of differential pumping. This required the use of a larger pump. The poisoning of the carburized thoriated tungsten rhenium filaments also results from these interactions.

To gain comparative data on these reactions was somewhat hindered because of the large overall volume of the vacuum system. This meant that the reactions which occurred created very small changes in the CO and CO_2 percentages and approached the detectable limit of the measuring apparatus. Plots of this data may be seen in Figures 100 through 105. The data is somewhat inconclusive however.

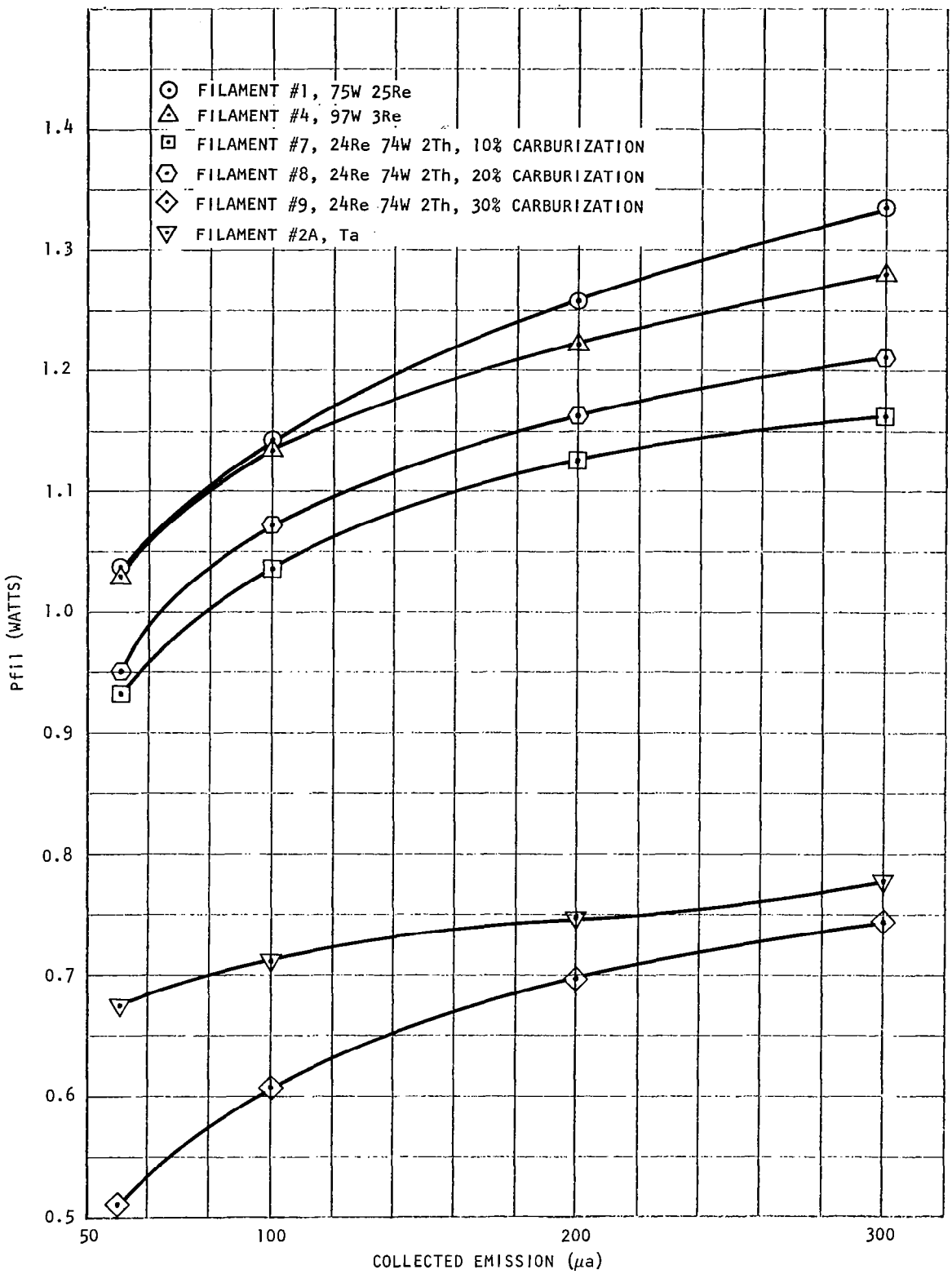
FILAMENT #1, 75W 25Re
FILAMENT #4, 97W 3Re
FILAMENT #7, 24Re 74W 2Th, 10% CARBURIZATION
FILAMENT #8, 24Re 74W 2Th, 20% CARBURIZATION
FILAMENT #9, 24Re 74W 2Th, 30% CARBURIZATION
FILAMENT #2A, Ta
Pfil (WATTS)
1.4
1.3
1.2
1.1
1.0
0.9
0.8
0.7
0.6
0.5
50
100
200
300
COLLECTED EMISSION (μa)

FIGURE 99

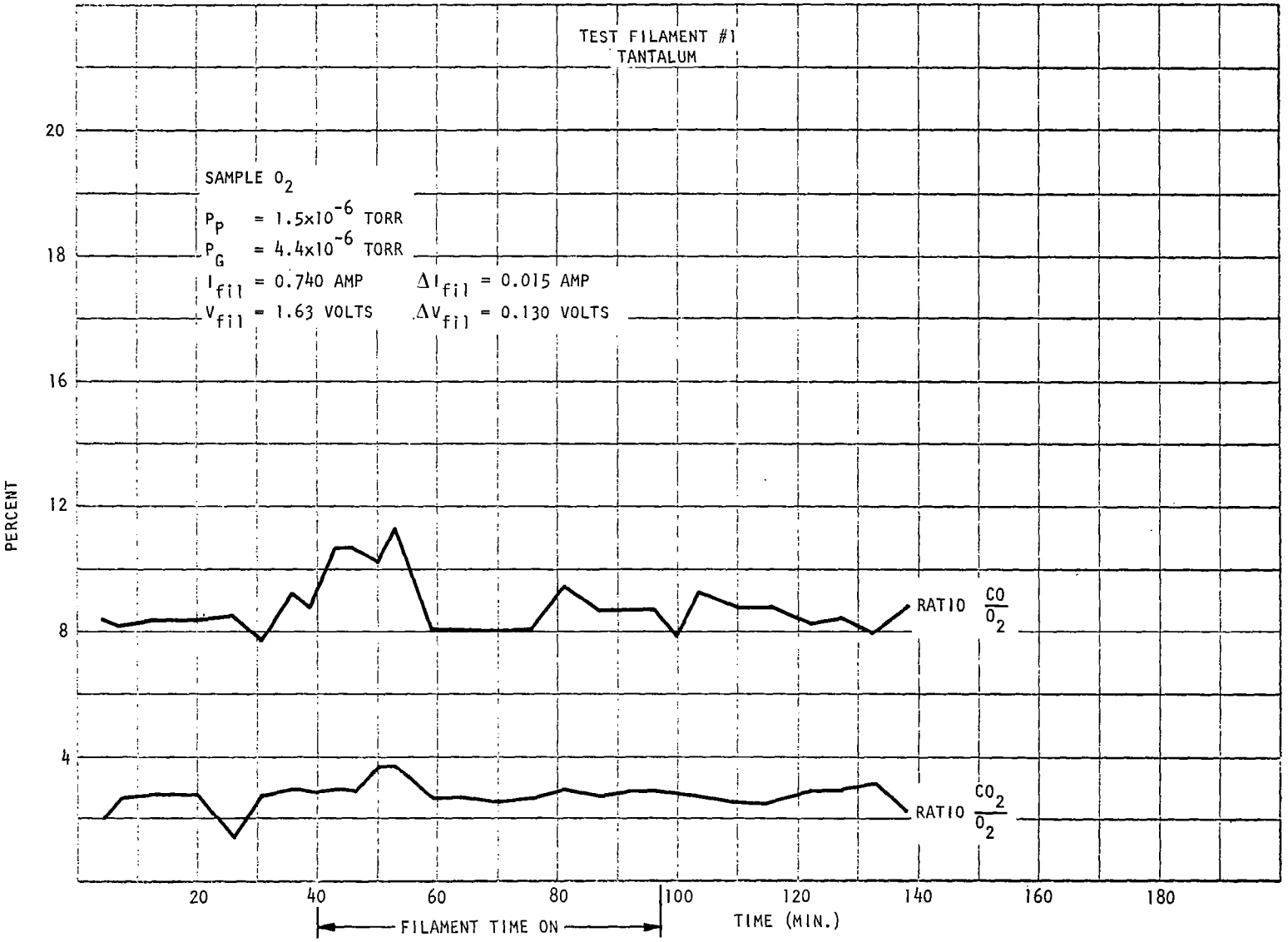

FIGURE 100

RATIO OF $\frac{CO}{O_2}$ AND $\frac{CO_2}{O_2}$ VS. TIME

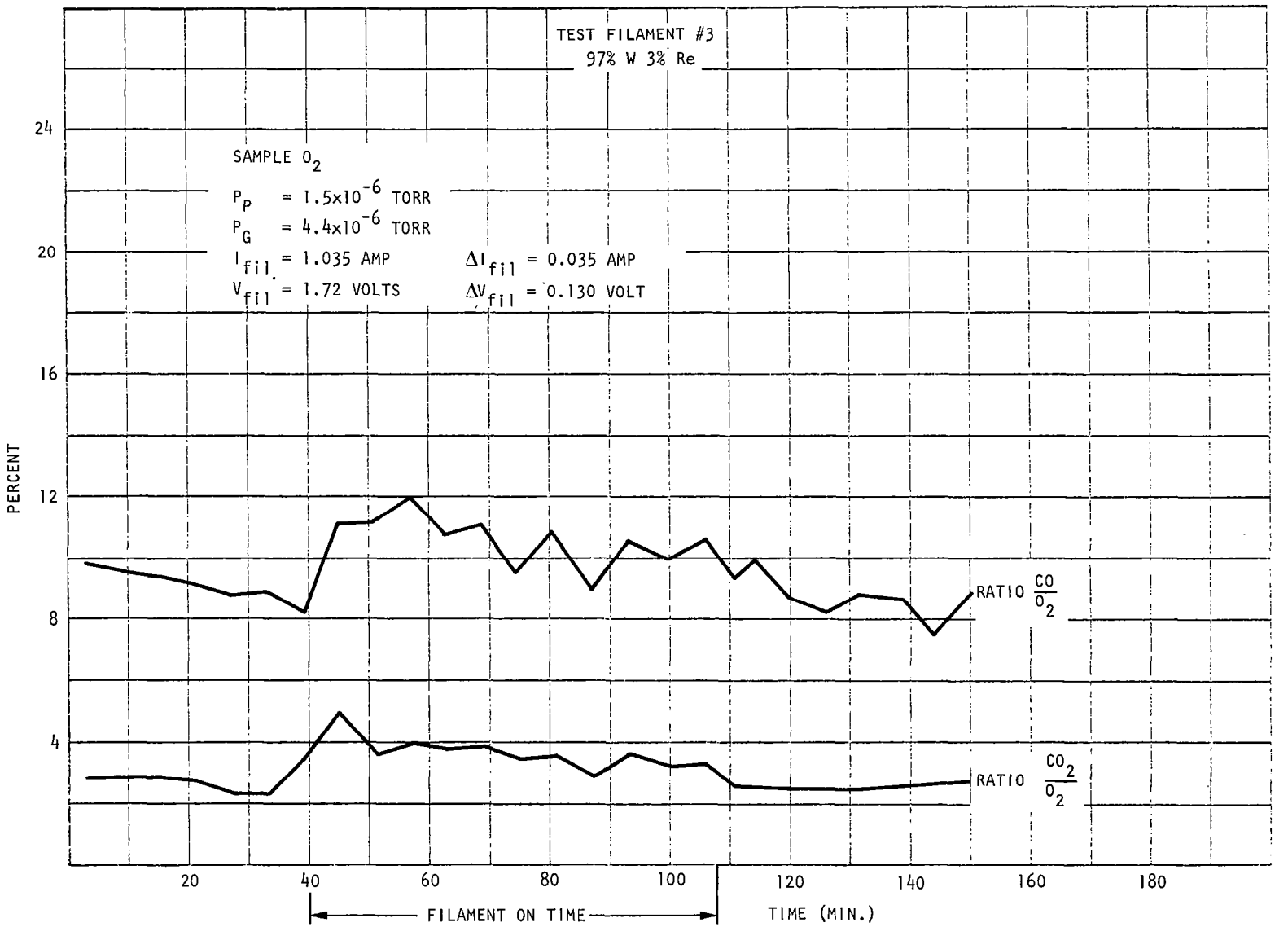

FIGURE 101

RATIO OF $\frac{CO}{O_2}$ AND $\frac{CO_2}{O_2}$ VS. TIME

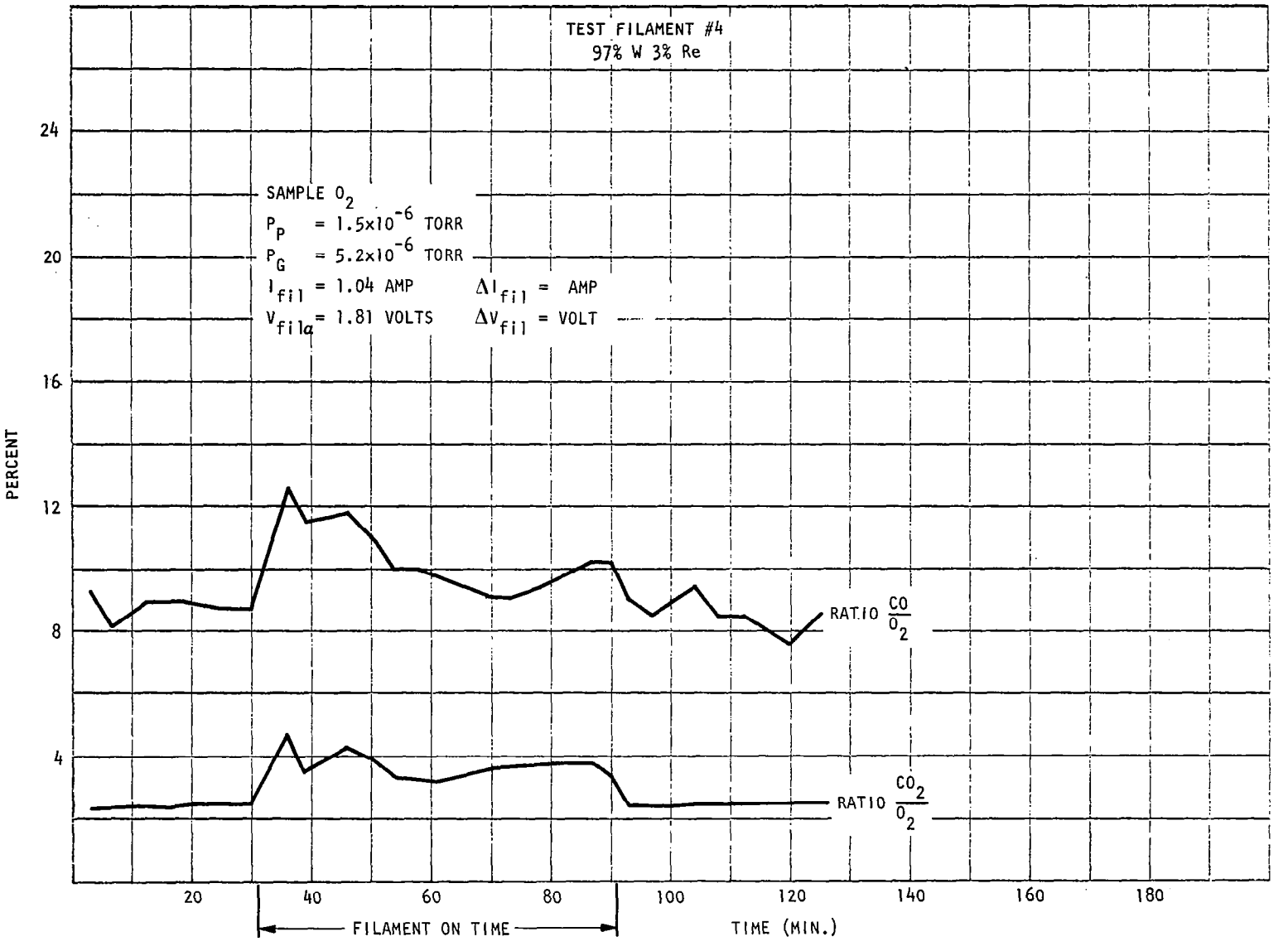

FIGURE 102

RATIO OF $\frac{CO}{O_2}$ AND $\frac{CO_2}{O_2}$ VS TIME

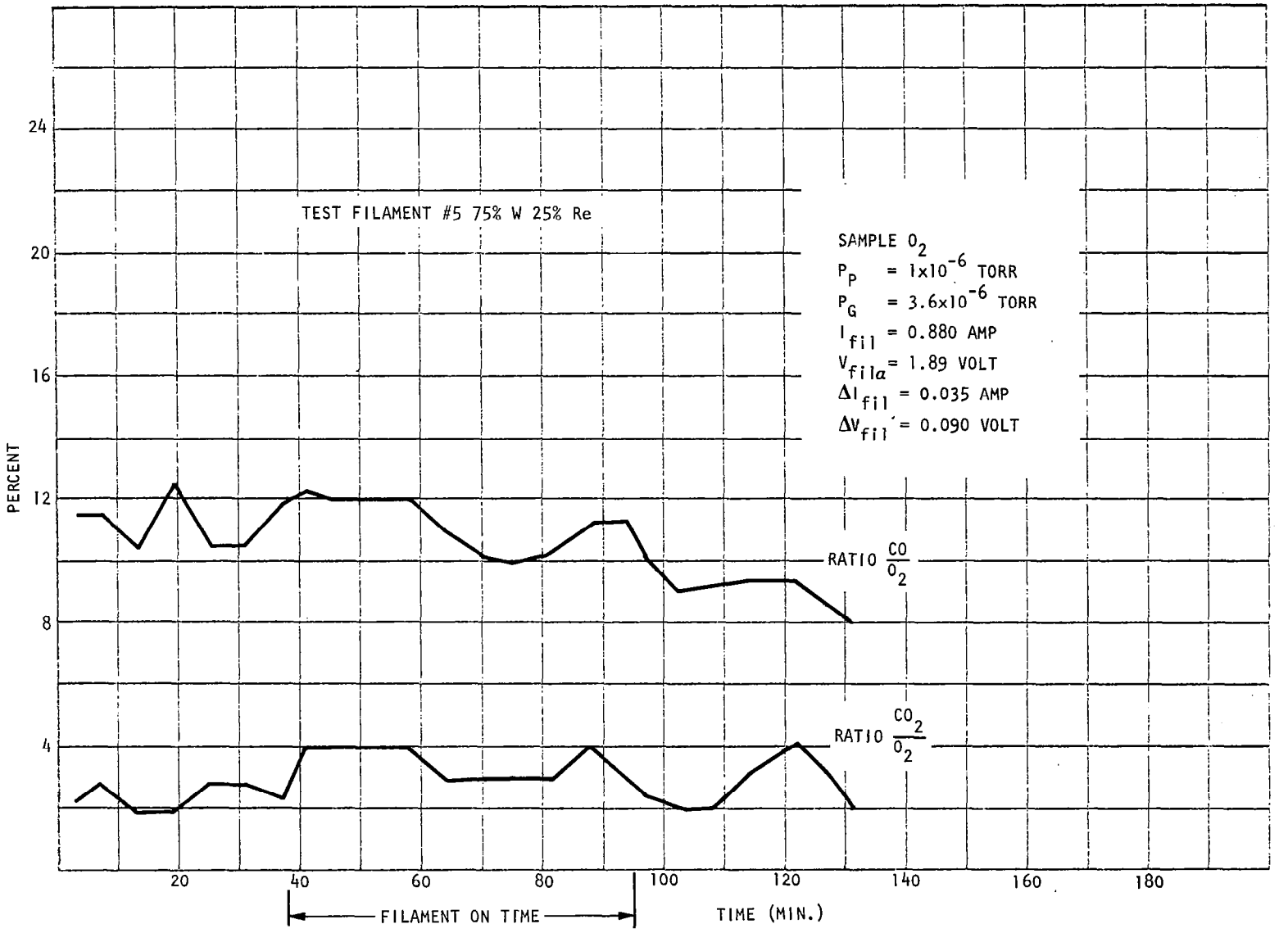

FIGURE 103

RATIO OF $\frac{CO}{O_2}$ AND $\frac{CO_2}{O_2}$ VS. TIME

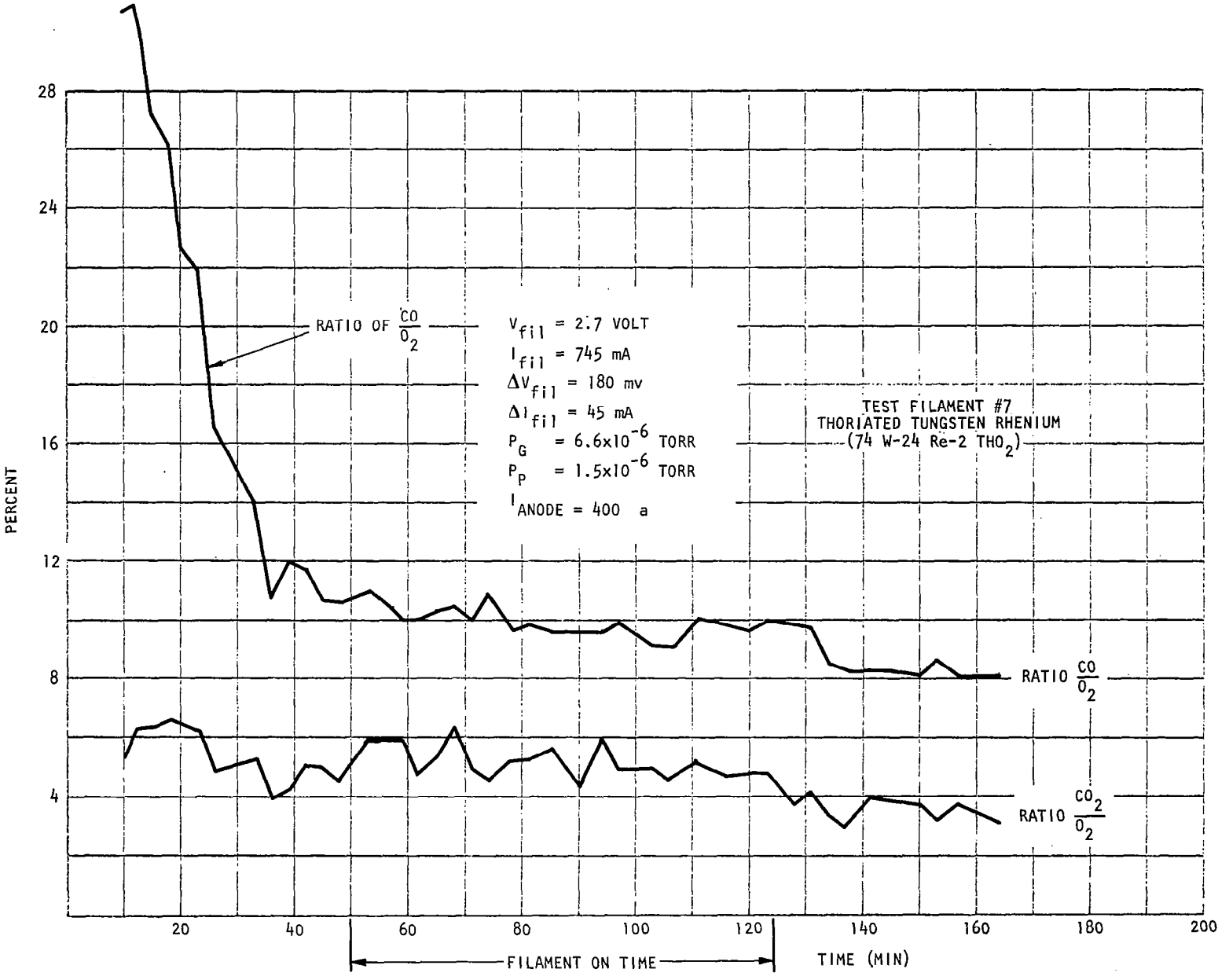

FIGURE 104

RATIO OF $\frac{CO}{O_2}$ AND $\frac{CO_2}{O_2}$ VS. TIME

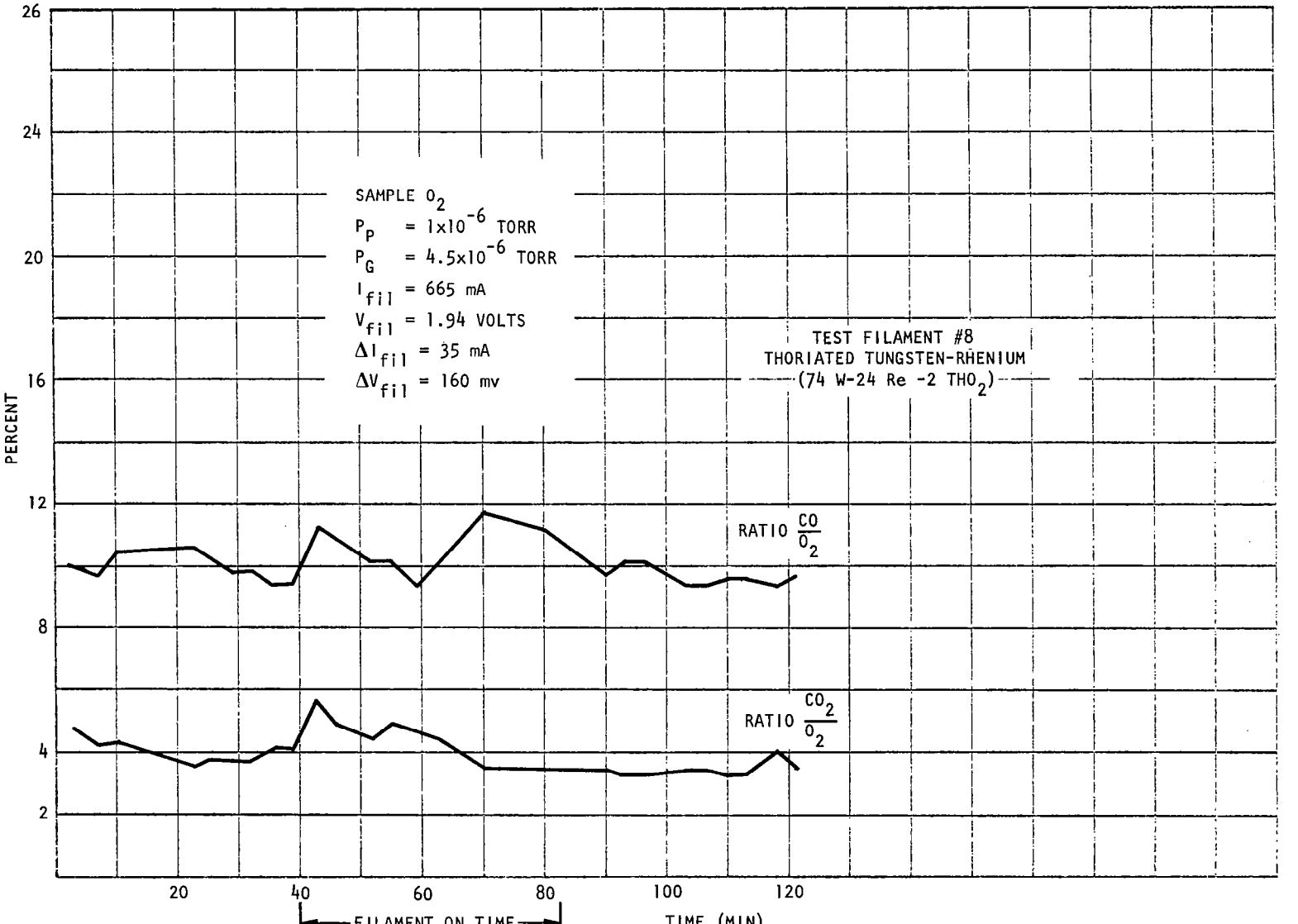

FIGURE 105

RATIO OF $\frac{CO}{O_2}$ AND $\frac{CO_2}{O_2}$ VS. TIME

CHANGES IN WORK FUNCTION DUE TO SPECIFIC GAS ENVIRONMENTS

This test was not conducted in the manner originally stated by the intended program. However, at a pressure of 5.0×10^{-6} torr and with an H_2O saturated air sample gas, the power requirements of all the filament materials was plotted over the test period of 192 days. This data shows that generally the power requirement for a given emission remained the same. At the same time however, filament resistance was changing. The resistance change was for the most part due to the reduction of the filament diameter and therefore the emitting surface area. Thus, while the power remained the same, the filament temperature increased in order to maintain the same overall emission from the reduced emitting area. This effect accelerates the filament deterioration but is still a very long-term process. It is felt that these long-term changes were affected only slightly due to the surface work function changes in the test atmosphere. This is not to say that the environmental atmosphere does not strongly contribute to the shortening of filament life. Increased power is required to obtain the same emission levels as the pressure increases. This is, in this case, not due to mean-free-path limitations but rather to greater heat transfer and filament work function changes. However, this area has not been explored to derive a definitive conclusion as to the weighting of these factors.

A very productive test was run during life testing to determine the effects of emission levels upon filament deterioration rates. At the 149th day, one each of the 75% W 25% Re, 97% W 3% Re and 74% W 24% Re 2% Th filaments emission levels was raised to 200 microamperes or double the previous level. It was thought that this might increase the resistance slope versus time. However, since an increase in slope did not occur this suggested that the major factor in filament degeneration of these materials was not ion bombardment of the emitter surface as has been suggested by other experimenters, but more a function of temperature since the temperature change required to achieve doubling the emission is only on the order of 1 to 2 percents. This can be seen in Figure 95.

MECHANICAL PROPERTIES

Concurrent with this study, a program to investigate filament short-term mechanical properties was being conducted on contract NAS 5-11076. This study looked into the elongation which occurs during filament warmup, and the relaxation of stresses which were inherent in the manufacturing processes. The filament assemblies were installed in a vacuum chamber with a viewing port and measurements were made with the filament both cold and hot. Filament mounting was similar to that of the two gas sensor system such that a tensioning spring maintained the filament straightness. Dimensional measurements were made using a cathodometer. The measurement method somewhat limited the absolute accuracy, however, relative measurements proved to be adequate. This testing was done only with the 75% W 25% Re wire. Table 25 illustrates the results of these measurements, which shows that the variations in length and elongation were within the experimental accuracy of the measurement equipment.

FILAMENT LIFE TESTING

Early in the program, life testing was done on Iridium and Tantalum and the life of these materials in this wire diameter was found to be extremely limited. Figure 106 is a plot of tantalum filament resistance versus time.

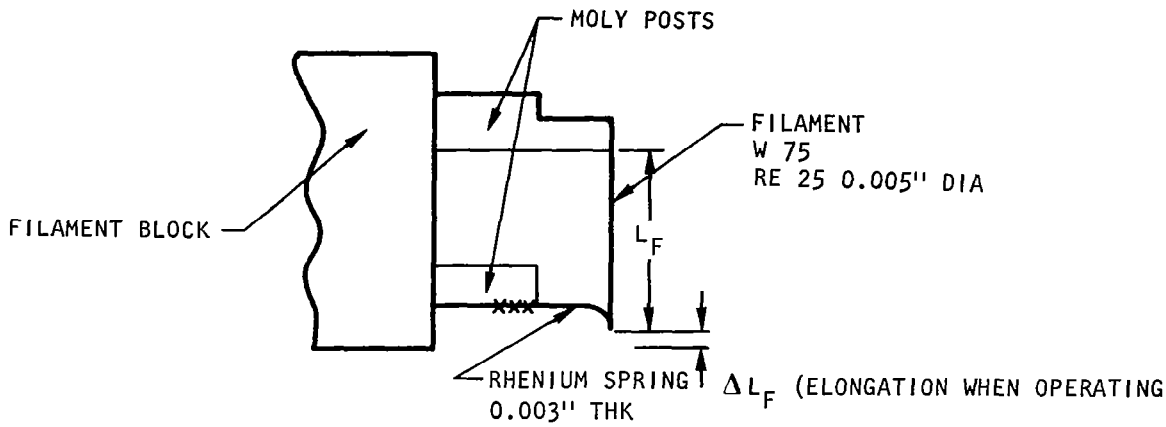

READING / TEST	OPERATING PRESSURE P (TORR)	OPERATING TIME	CURRENT IN FILAMENT I_{FIL} (AMPS)	MEASURED LENGTH OF FILAMENT L_F (IN)	ELONGATION ΔL_F (IN)
#1	5×10^{-7}	0	0	0.384	0
#2	5×10^{-7}	5 MIN.	1.82	0.3875	0.0035
#3	5×10^{-7}	10 MIN.	1.82	0.386	0.002
#4	5×10^{-7}	2 MIN.	1.90	0.3865	0.0025
#5	5×10^{-7}	8 HRS.	1.7	0.386	0.002
#6	5×10^{-7}	CYCLING (8 HRS) 5 MIN.ON/OFF	1.7	0.386	0.002

TABLE 25

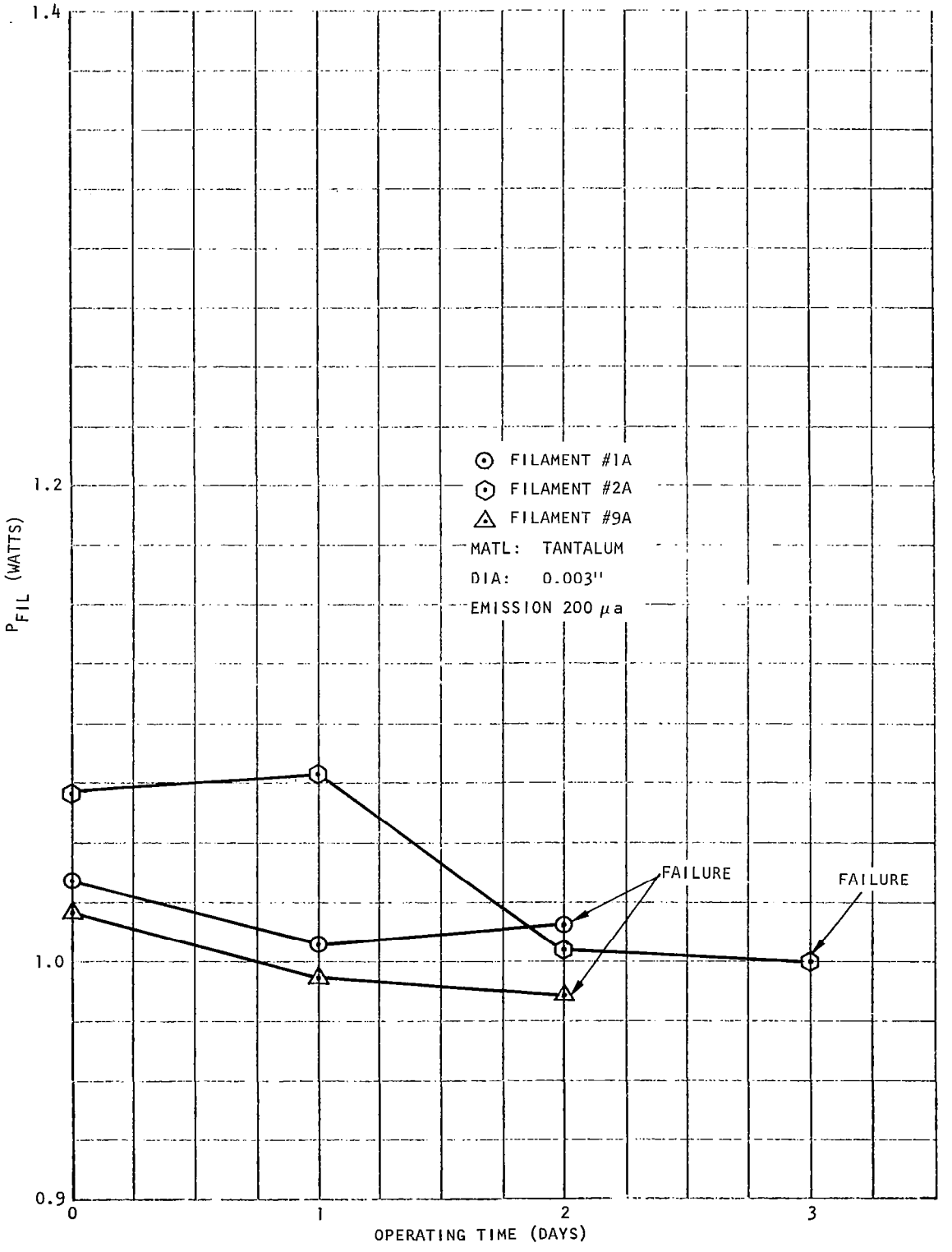
1.4
1.2
1.0
0.9
P_{FIL} (WATTS)
FILAMENT #1A
FILAMENT #2A
FILAMENT #9A
MATL: TANTALUM
DIA: 0.003"
EMISSION 200 μa
FAILURE
FAILURE
0
1
2
3
OPERATING TIME (DAYS)

FIGURE 106

Filament life testing over the major test period of 120 days with the aforementioned atmospheric environment yielded no filament failures due to burn-out. One filament, a 97% W 3% Re did, however, fail due to a defective spot weld. Power requirements on all filaments with the exception of the Thoriated Tungsten Rhenium filaments remained essentially the same over the operating period. The Thoriated filaments, after poisoning, also exhibited a leveling off of power. Figures 107 through 111 illustrate the filament power requirements plotted as a function of life test duration.

At the end of the test period photomicrographs were made of all of the filaments using a Unitrol Series N metalograph. Figures 112 through 118 are photographs made with a magnification factor of 100X with two of the detail photographs at 400X. For comparative purposes, a control sample of each material is also illustrated as a reference showing the nature of the samples prior to testing. At the time of photographing, filament dimensional data was also taken. This data shows the dimensional changes as listed below:

75% W 25% Re

Control-----New Wire-----	.00276 Inch	Diameter
#1	192 days operation---	.00256 Inch	Diameter
#2	192 days operation---	.00256 Inch	Diameter
#3	192 days operation---	.00256 Inch	Diameter

97% W 3% Re

Control-----New Wire-----	.00295 Inch	Diameter
#1	98 days operation---	.00295 Inch	Diameter
#2	192 days operation---	.00286 Inch	Diameter
#3	192 days operation---	.00276 Inch	Diameter

74% W 24% Re 2% Th

Control-----New Wire-----	.00286 Inch	Diameter
#1	192 days operation---	.00256 Inch	Diameter
#2	192 days operation---	.00256 Inch	Diameter
#3	192 days operation---	.00256 Inch	Diameter

These photographs show that the 75% W 25% Re was almost entirely crystaline and very irregular after the test period while the 97% W 3% Re remained more uniform and retained some of the original surface texture. These latter filaments also revealed no evidence of becoming crystaline. This suggests that, for mechanical resilience, the 97% W 3% Re probably is much more rugged, although no specific testing was done to confirm this.

The filament resistance versus time plots over the 192 day test period are shown in Figures 119 through 127 for the materials tested represent an excellent gauging technique for filament selection for several considerations. The first consideration of course is life expectancy. The relative slopes for each

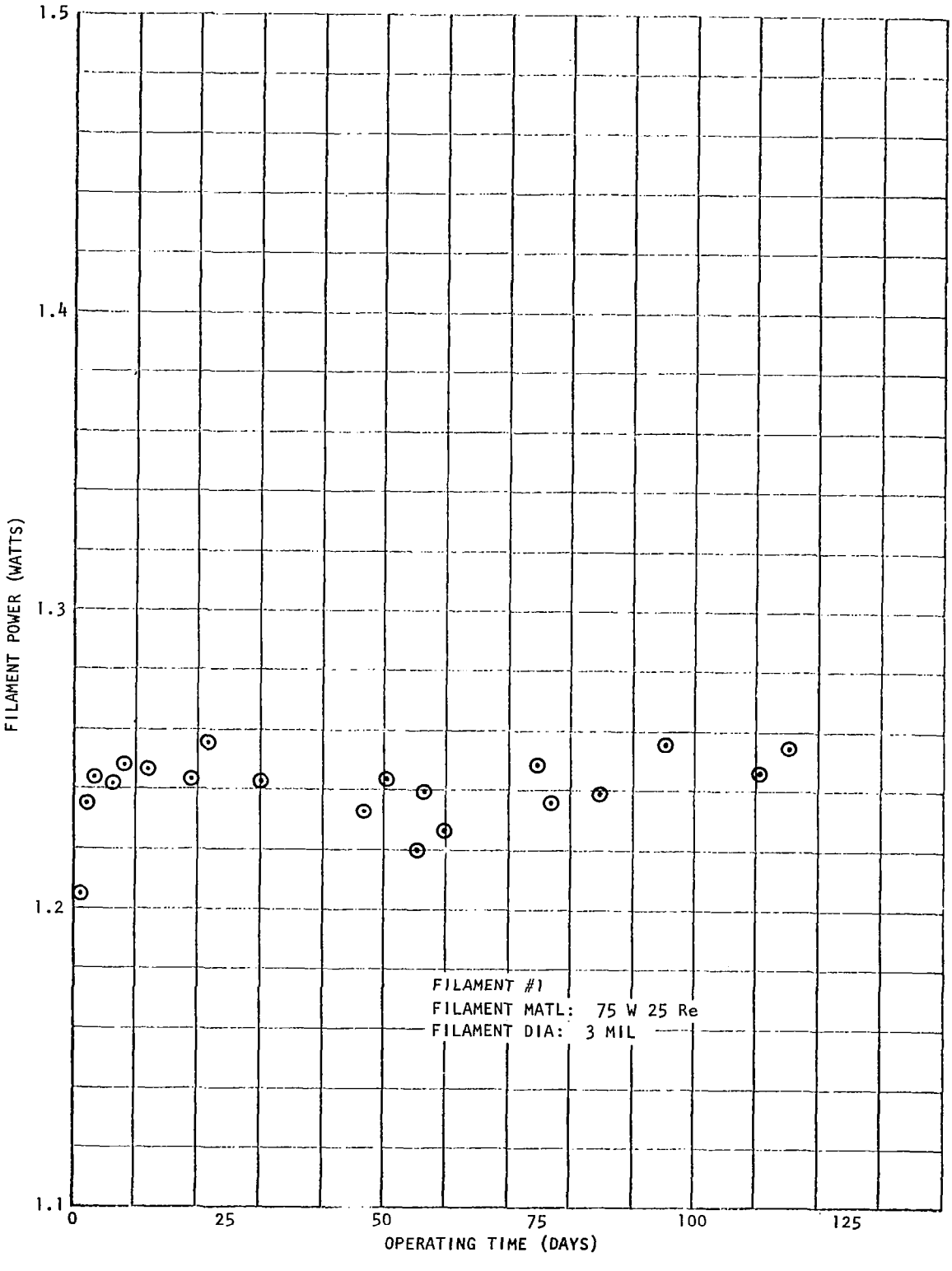
1.5
1.4
1.3
1.2
1.1
FILAMENT POWER (WATTS)
0
25
50
75
100
125
OPERATING TIME (DAYS)
FILAMENT #1
FILAMENT MATL: 75 W 25 Re
FILAMENT DIA: 3 MIL

FIGURE 107

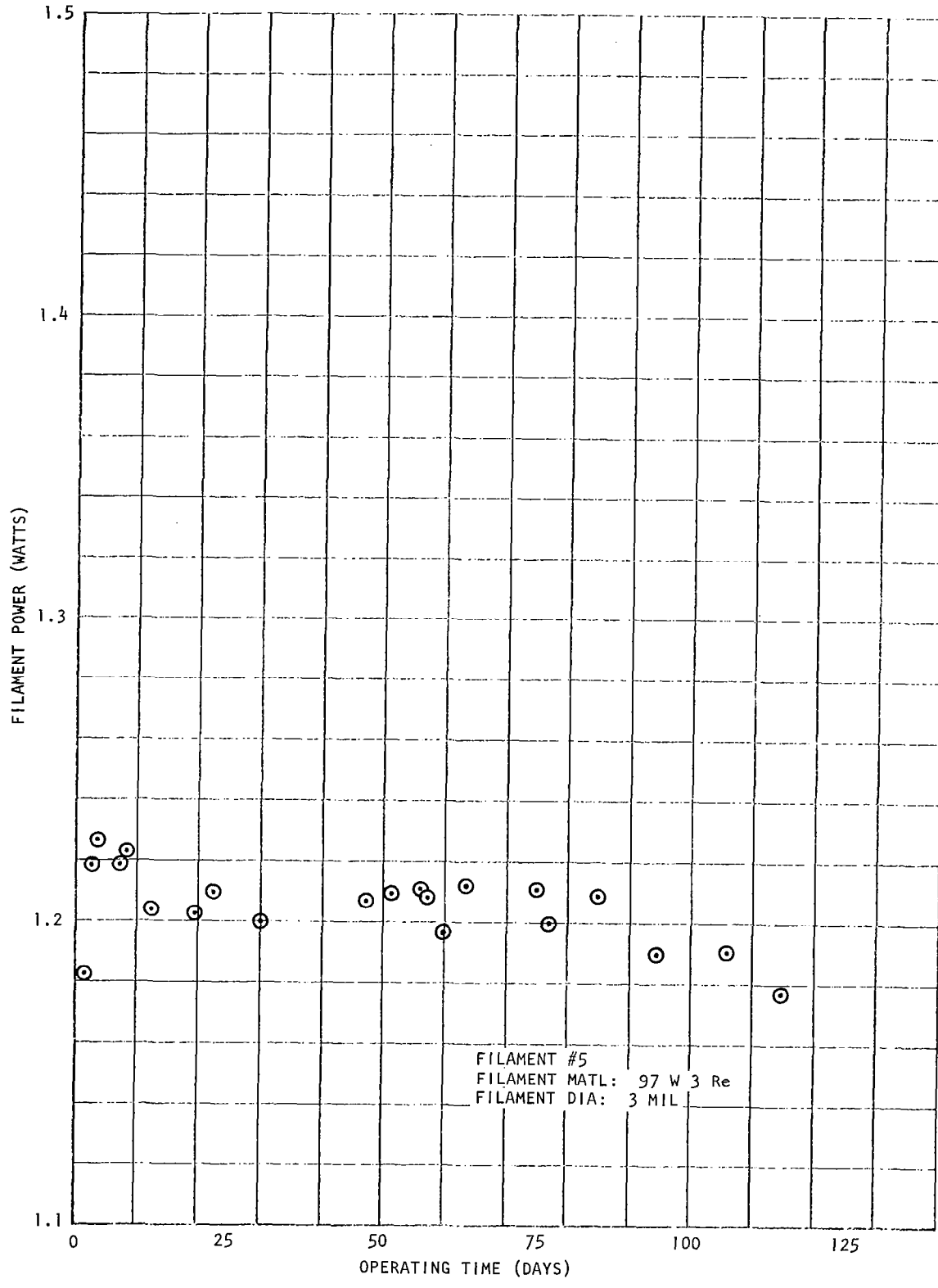
1.5
1.4
1.3
1.2
1.1
FILAMENT POWER (WATTS)
0
25
50
75
100
125
OPERATING TIME (DAYS)
FILAMENT #5
FILAMENT MATL: 97 W 3 Re
FILAMENT DIA: 3 MIL

FIGURE 108

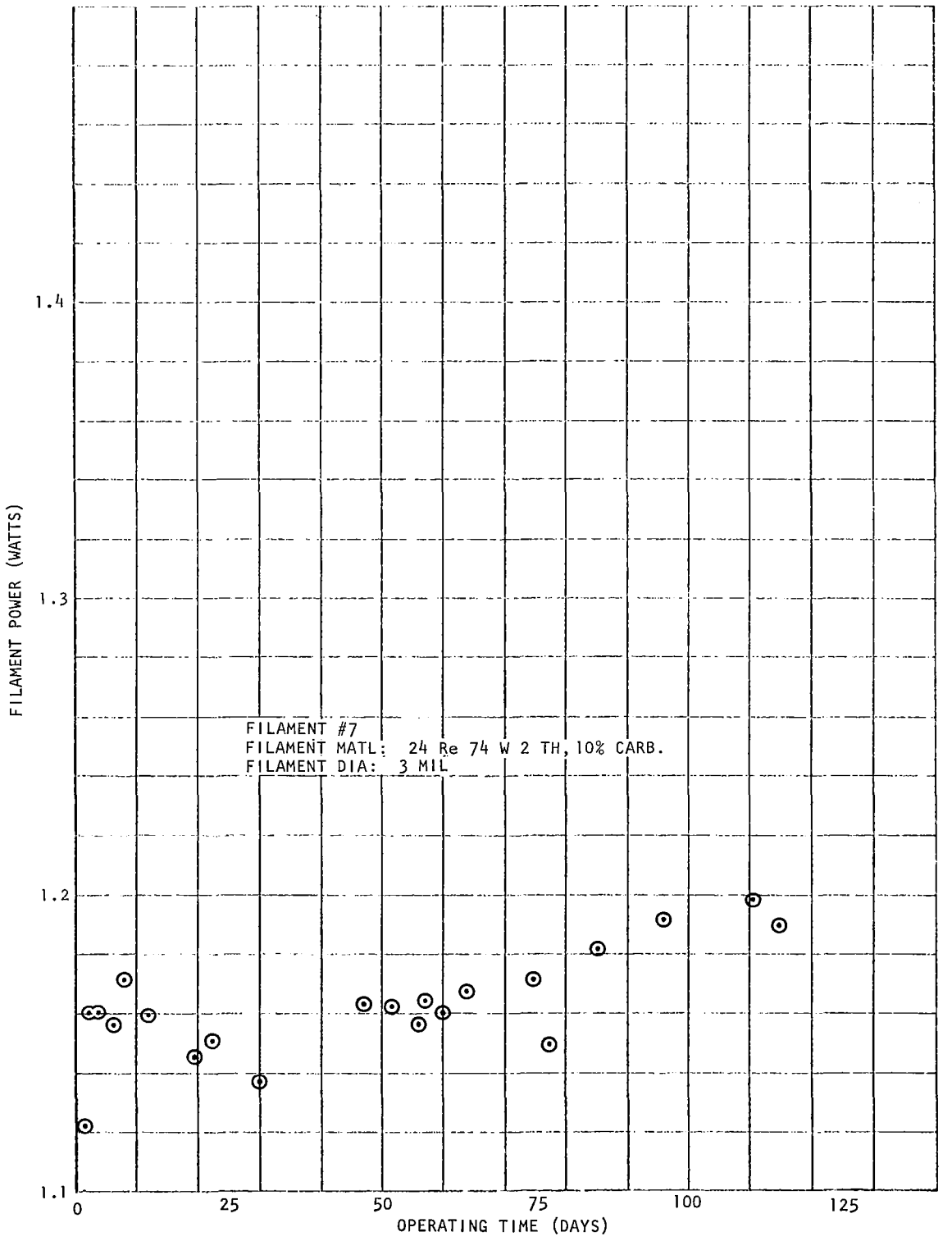
FILAMENT POWER (WATTS)
1.4
1.3
1.2
1.1
FILAMENT #7
FILAMENT MATL: 24 Re 74 W 2 TH, 10% CARB.
FILAMENT DIA: 3 MIL
0
25
50
75
100
125
OPERATING TIME (DAYS)

FIGURE 109

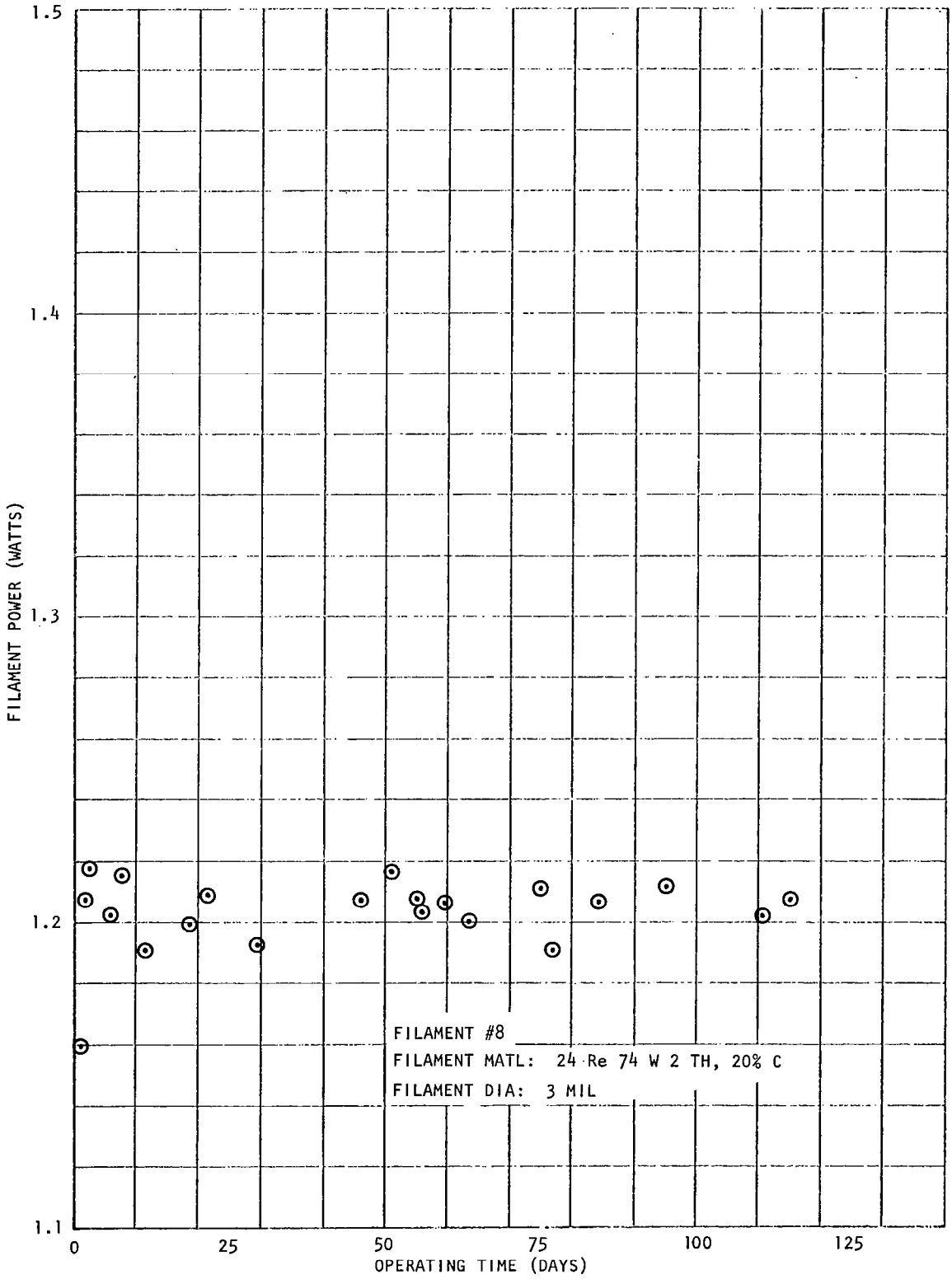
1.5
1.4
1.3
1.2
1.1
FILAMENT POWER (WATTS)
0
25
50
75
100
125
OPERATING TIME (DAYS)
FILAMENT #8
FILAMENT MATL: 24 Re 74 W 2 TH, 20% C
FILAMENT DIA: 3 MIL

FIGURE 110

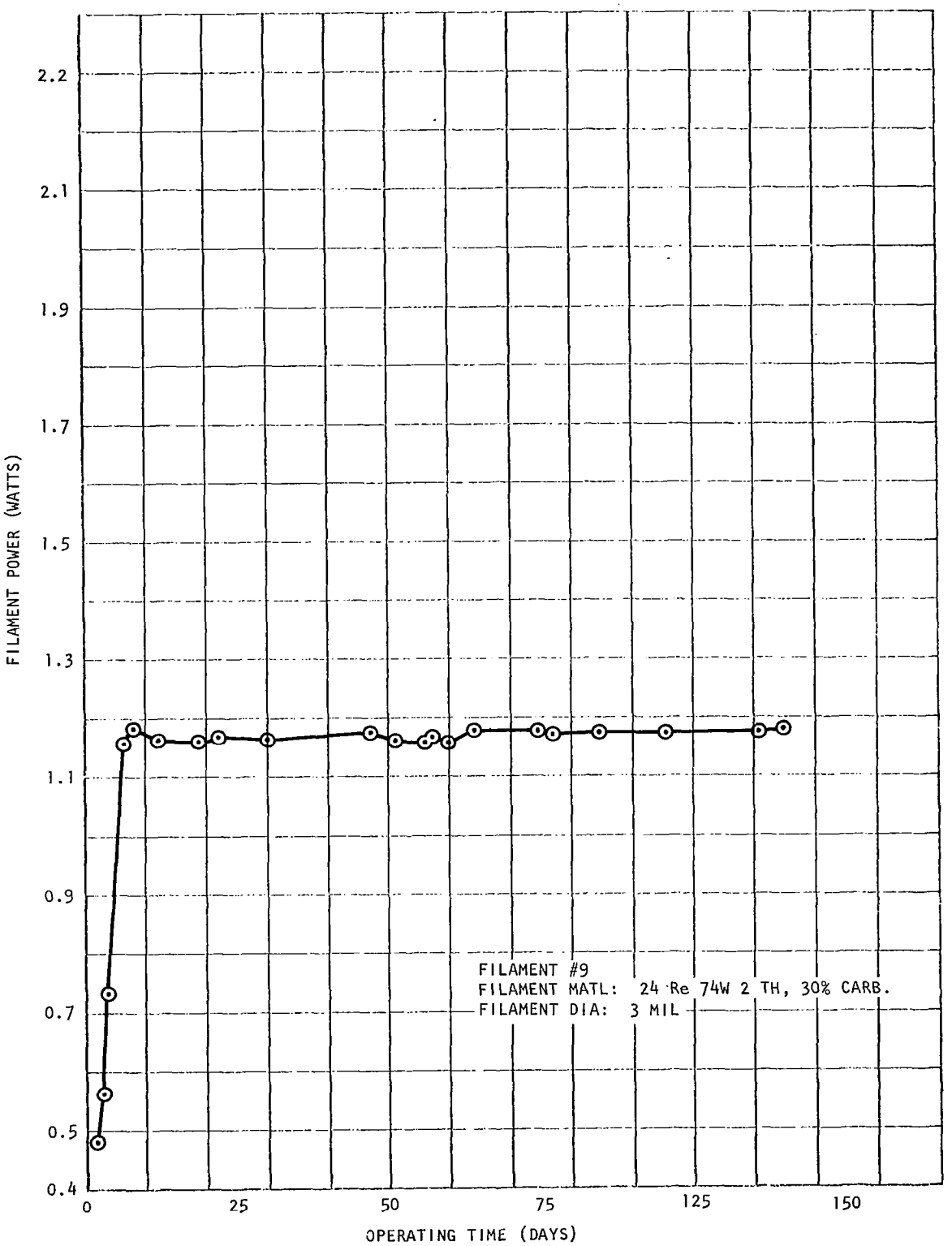
FILAMENT POWER (WATTS)
2.2
2.1
1.9
1.7
1.5
1.3
1.1
0.9
0.7
0.5
0.4
0
25
50
75
125
150
OPERATING TIME (DAYS)
FILAMENT #9
FILAMENT MATL: 24 Re 74W 2 TH, 30% CARB.
FILAMENT DIA: 3 MIL

FIGURE 111

FILAMENT #1
75% TUNGSTEN
25% RHENIUM
100 x MAGNIFICATION

FILAMENT #2
75% TUNGSTEN
25% RHENIUM
100 x MAGNIFICATION

FIGURE 112

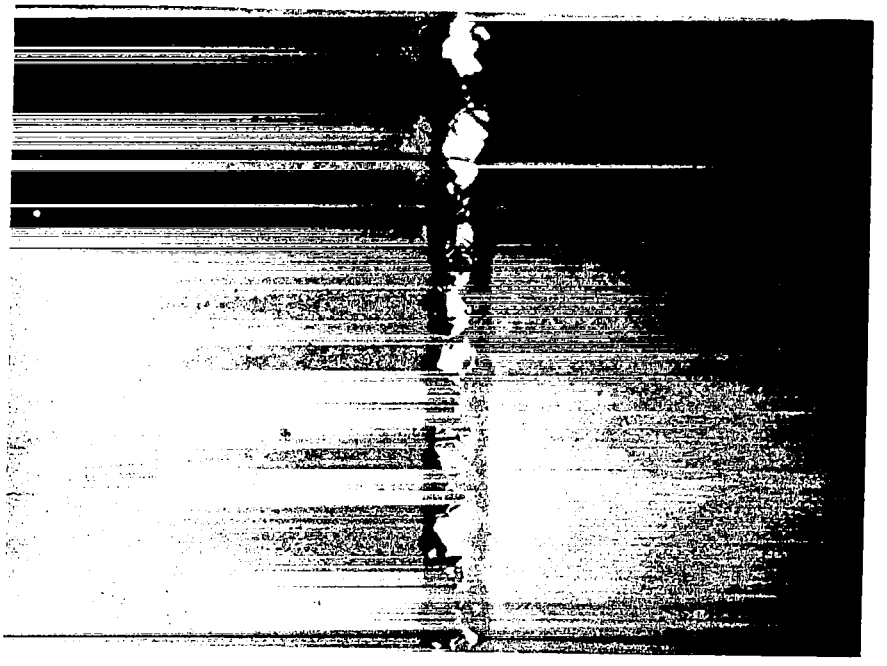

FILAMENT #3
75% TUNGSTEN
25% RHENIUM
100 x MAGNIFICATION

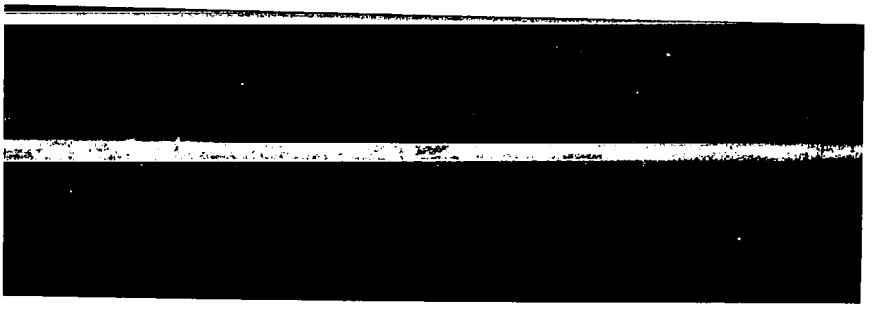

CONTROL SAMPLE
75% TUNGSTEN
25% RHENIUM
100 x MAGNIFICATION

FIGURE 113

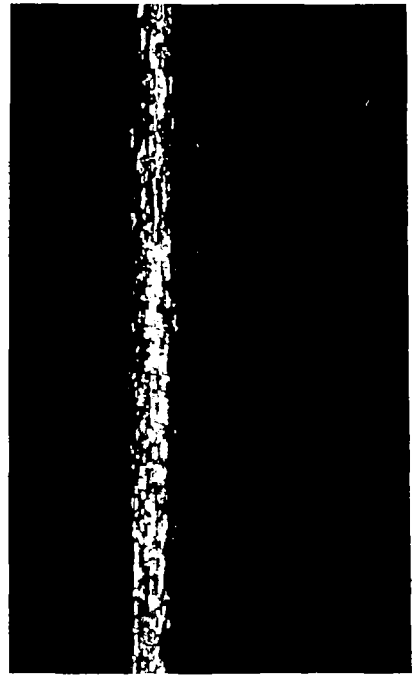

FILAMENT #4
97% TUNGSTEN
3% RHENIUM
100 x MAGNIFICATION

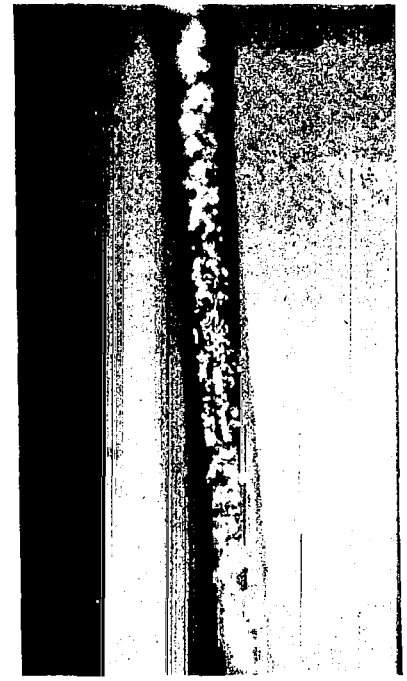

FILAMENT #5
97% TUNGSTEN
3% RHENIUM
100 x MAGNIFICATION

FIGURE 114

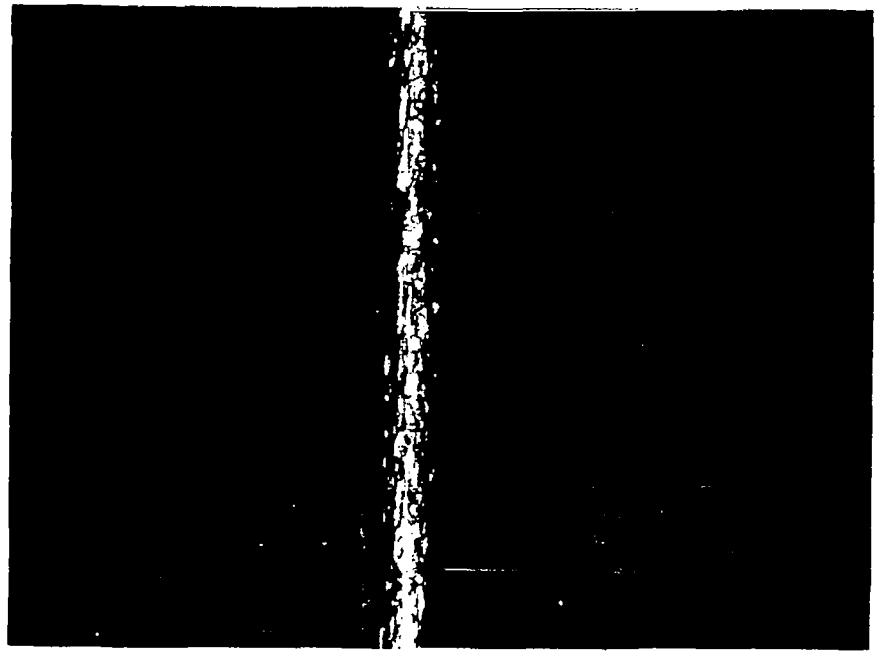

FILAMENT #6
97% TUNGSTEN
3% RHENIUM
100 x MAGNIFICATION

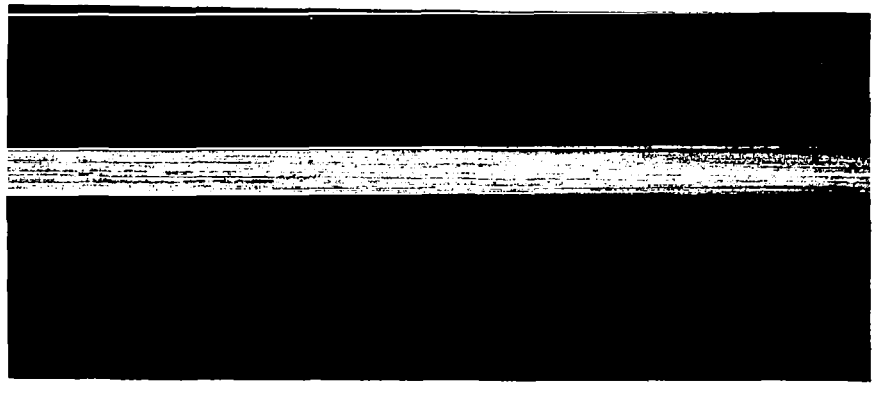

CONTROL SAMPLE
97% TUNGSTEN
3% RHENIUM
100 x MAGNIFICATION

FIGURE 115

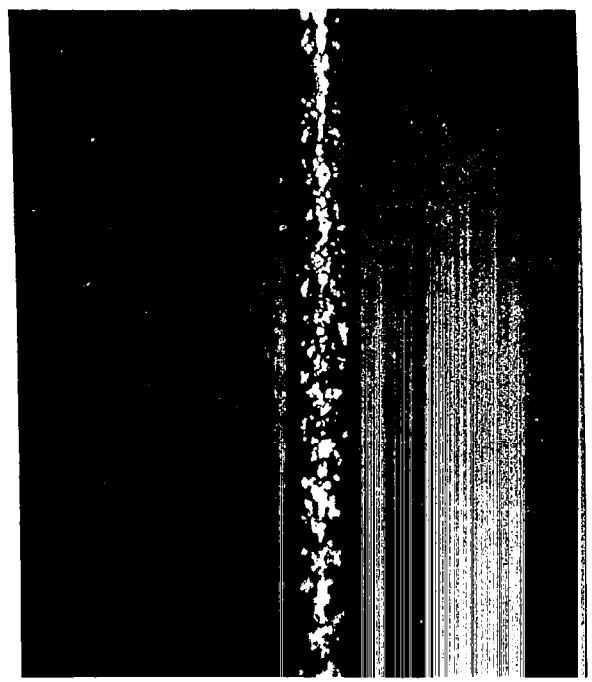

FILAMENT #7
74% TUNGSTEN
24% RHENIUM
2% THORIA
100 x MAGNIFICATION

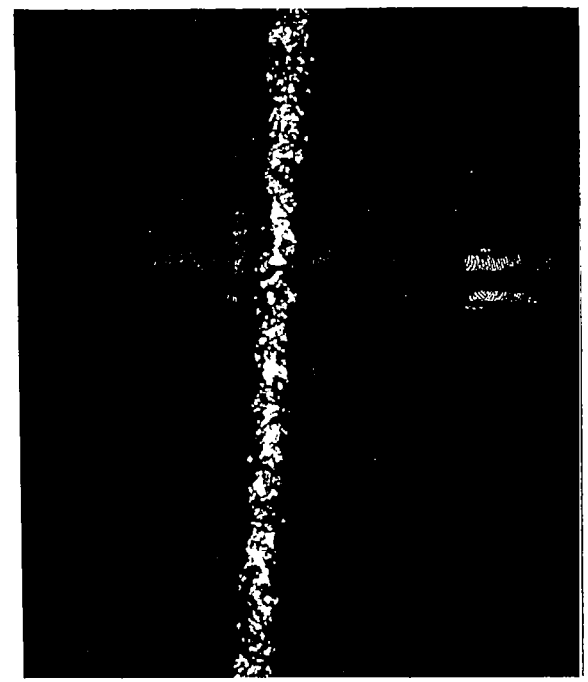

FILAMENT #8
74% TUNGSTEN
24% RHENIUM
2% THORIA

FIGURE 116

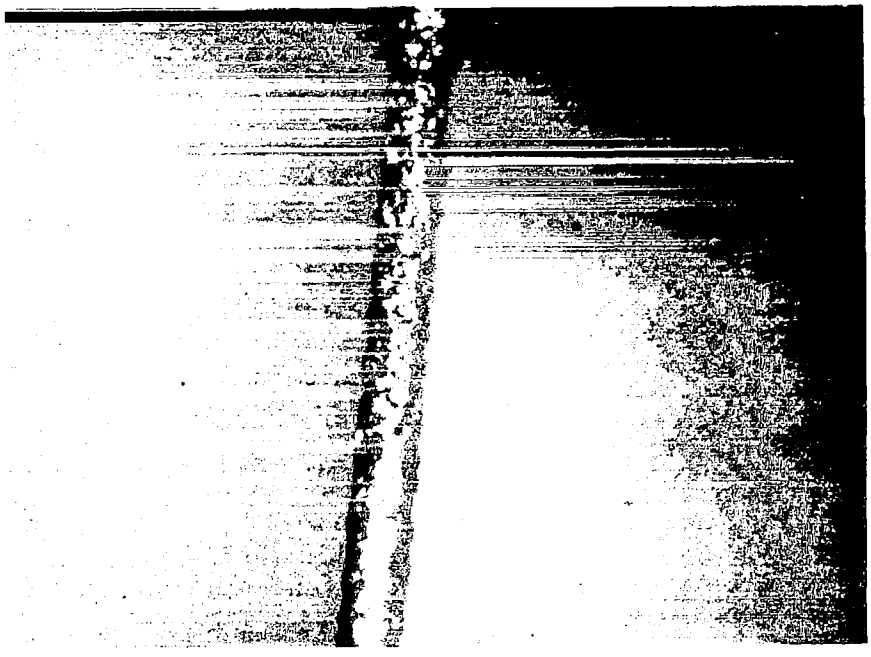

FILAMENT #9
74% TUNGSTEN
24% RHENIUM
2% THORIA
100 x MAGNIFICATION

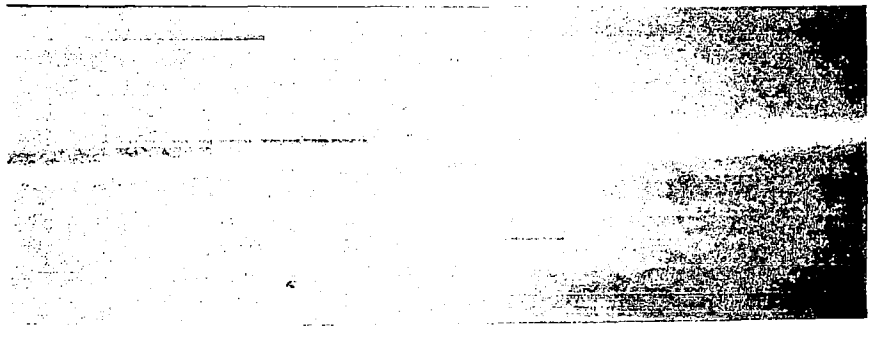

CONTROL SAMPLE
74% TUNGSTEN
24% RHENIUM
2% THORIA

FIGURE 117

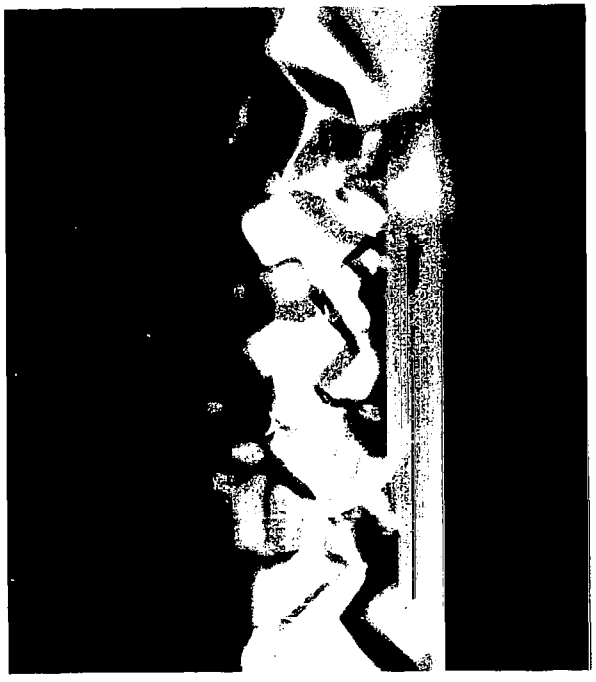

FILAMENT #3
75% TUNGSTEN
25% RHENIUM
400 x MAGNIFICATION

FILAMENT #6
97% TUNGSTEN
3% RHENIUM
400 x MAGNIFICATION

FIGURE 118

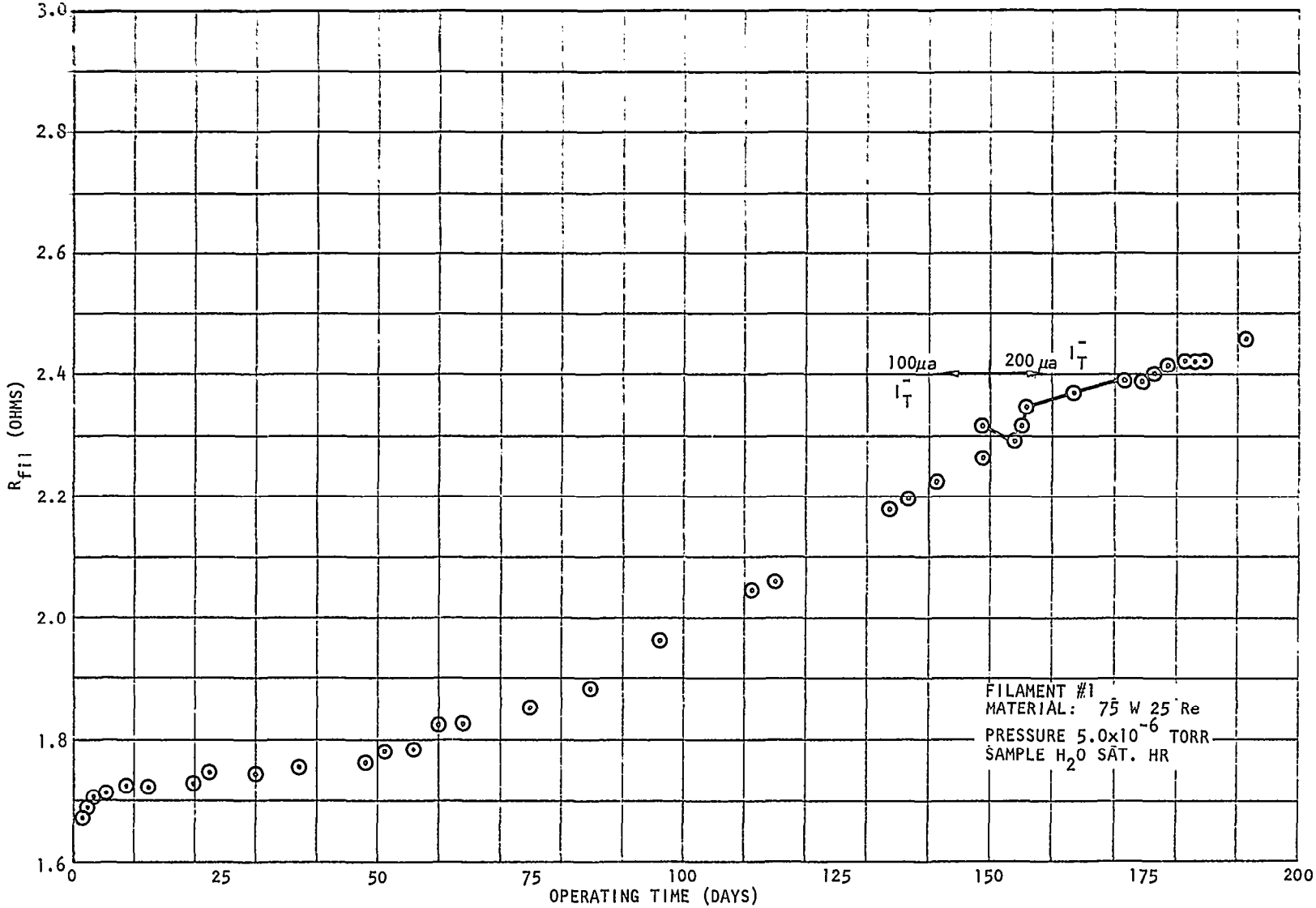
3.0
2.8
2.6
2.4
2.2
2.0
1.8
1.6
R_{Fil} (OHMS)
0
25
50
75
100
125
150
175
200
OPERATING TIME (DAYS)
100μa I_T^-
200 μa I_T^-
FILAMENT #1
MATERIAL: 75 W 25 Re
PRESSURE 5.0×10^{-6} TORR
SAMPLE H_2O SAT. HR

FIGURE 119

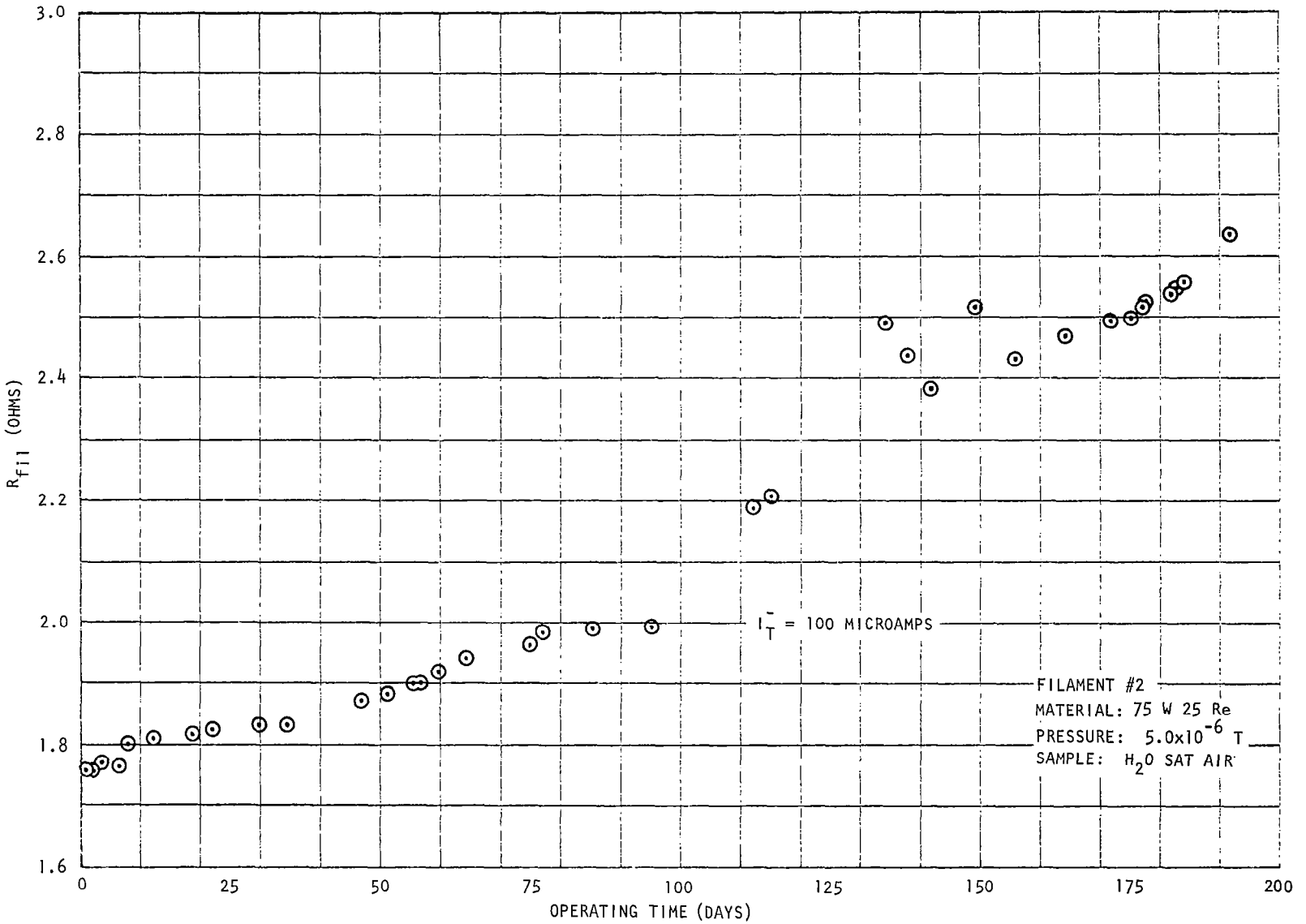
3.0
2.8
2.6
2.4
2.2
2.0
1.8
1.6
R_{fil} (OHMS)
0
25
50
75
100
125
150
175
200
OPERATING TIME (DAYS)
I_T^- = 100 MICROAMPS
FILAMENT #2
MATERIAL: 75 W 25 Re
PRESSURE: 5.0×10^{-6} T
SAMPLE: H_2O SAT AIR

FIGURE 120

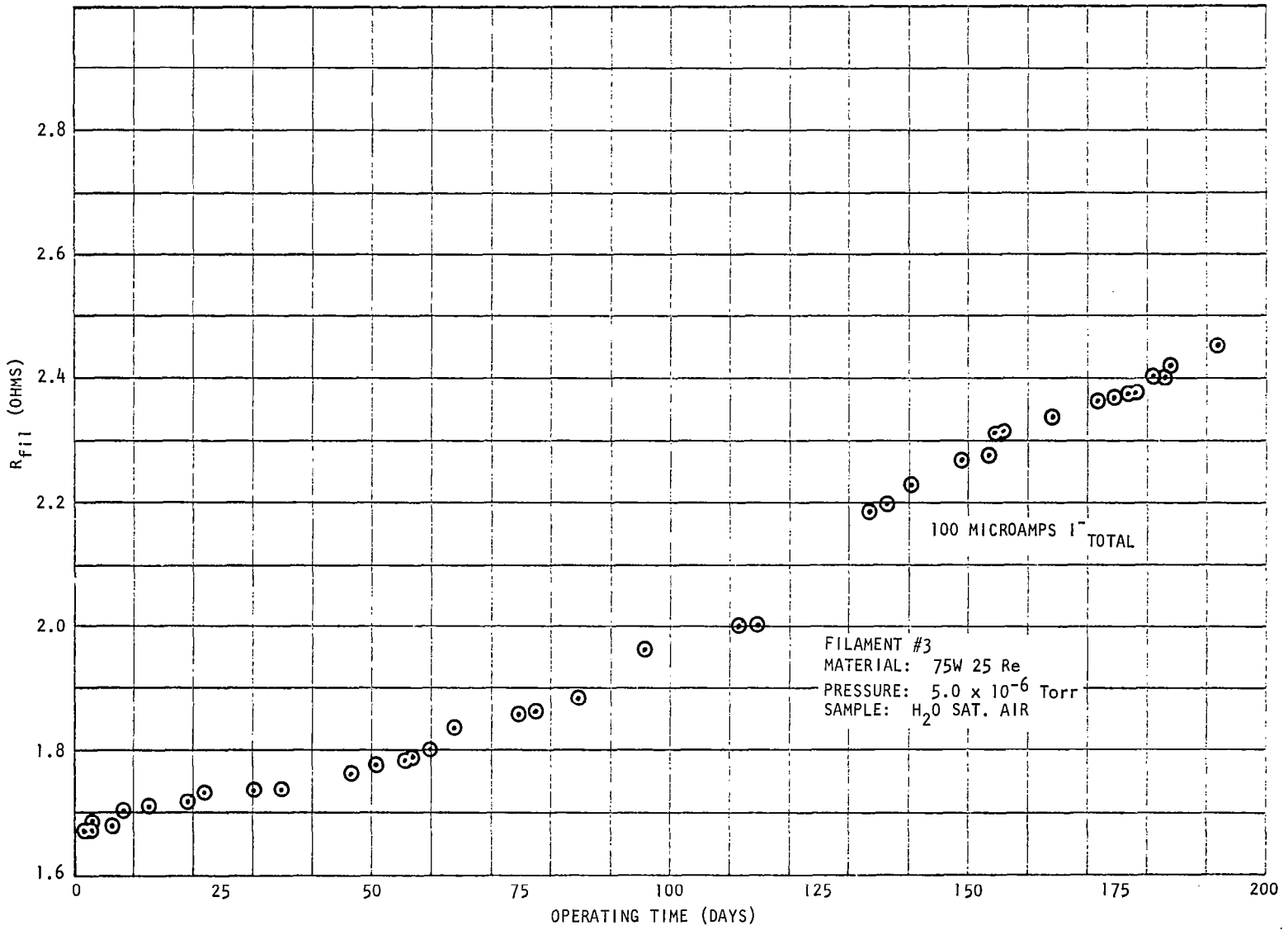
2.8
2.6
2.4
2.2
2.0
1.8
1.6
R_{Fil} (OHMS)
0
25
50
75
100
125
150
175
200
OPERATING TIME (DAYS)
100 MICROAMPS I^- TOTAL
FILAMENT #3
MATERIAL: 75W 25 Re
PRESSURE: 5.0×10^{-6} Torr
SAMPLE: H_2O SAT. AIR

FIGURE 121

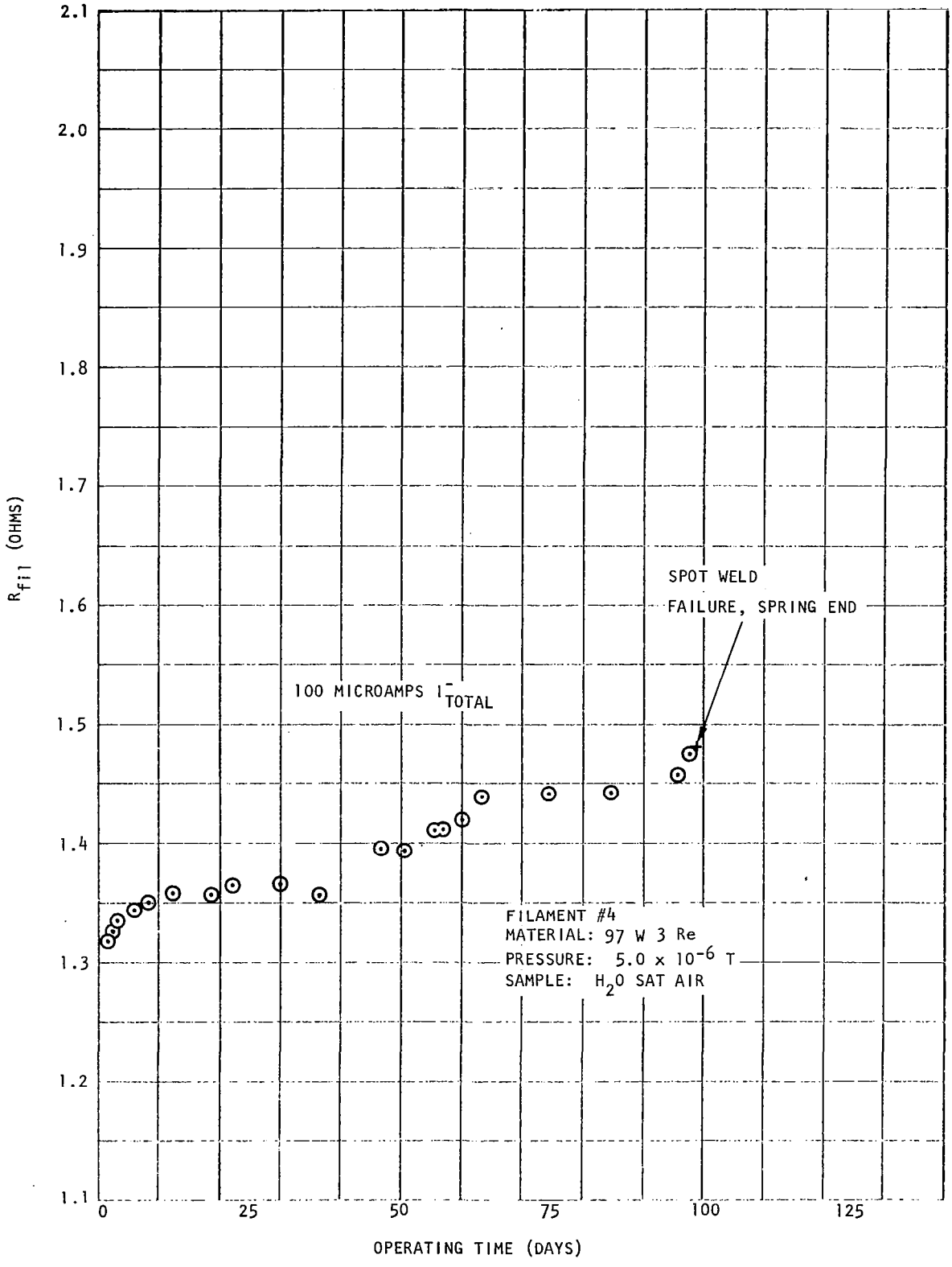
2.1
2.0
1.9
1.8
1.7
1.6
1.5
1.4
1.3
1.2
1.1
R_{fil} (OHMS)
0
25
50
75
100
125
OPERATING TIME (DAYS)
SPOT WELD
FAILURE, SPRING END
100 MICROAMPS I^-_{TOTAL}
FILAMENT #4
MATERIAL: 97 W 3 Re
PRESSURE: 5.0×10^{-6} T
SAMPLE: H_2O SAT AIR

FIGURE 122

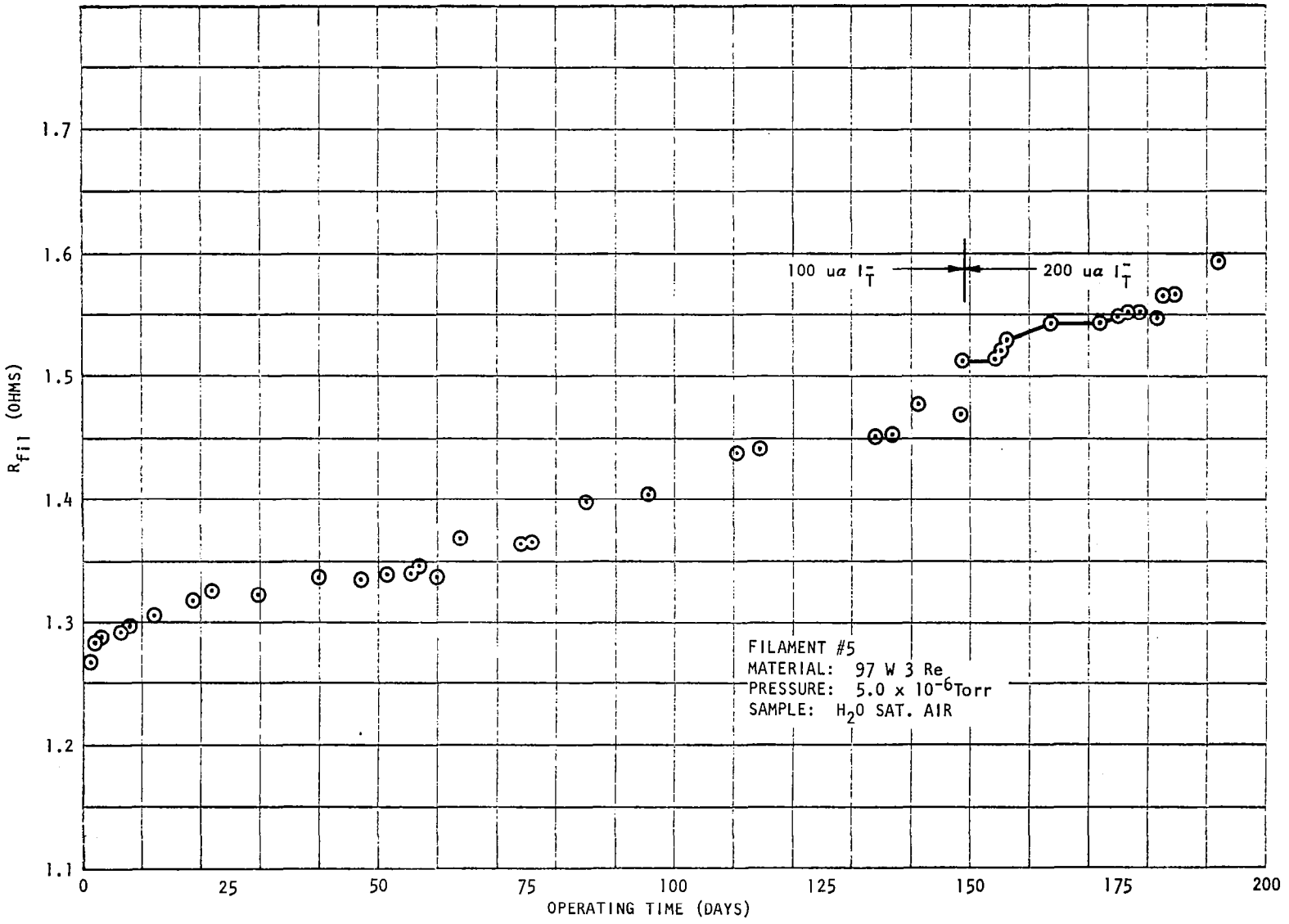
1.7
1.6
1.5
1.4
1.3
1.2
1.1
R_{Fil} (OHMS)
0
25
50
75
100
125
150
175
200
OPERATING TIME (DAYS)
100 ua I_T^-
200 ua I_T^-
FILAMENT #5
MATERIAL: 97 W 3 Re
PRESSURE: 5.0 x 10^{-6}Torr
SAMPLE: H_2O SAT. AIR

FIGURE 123

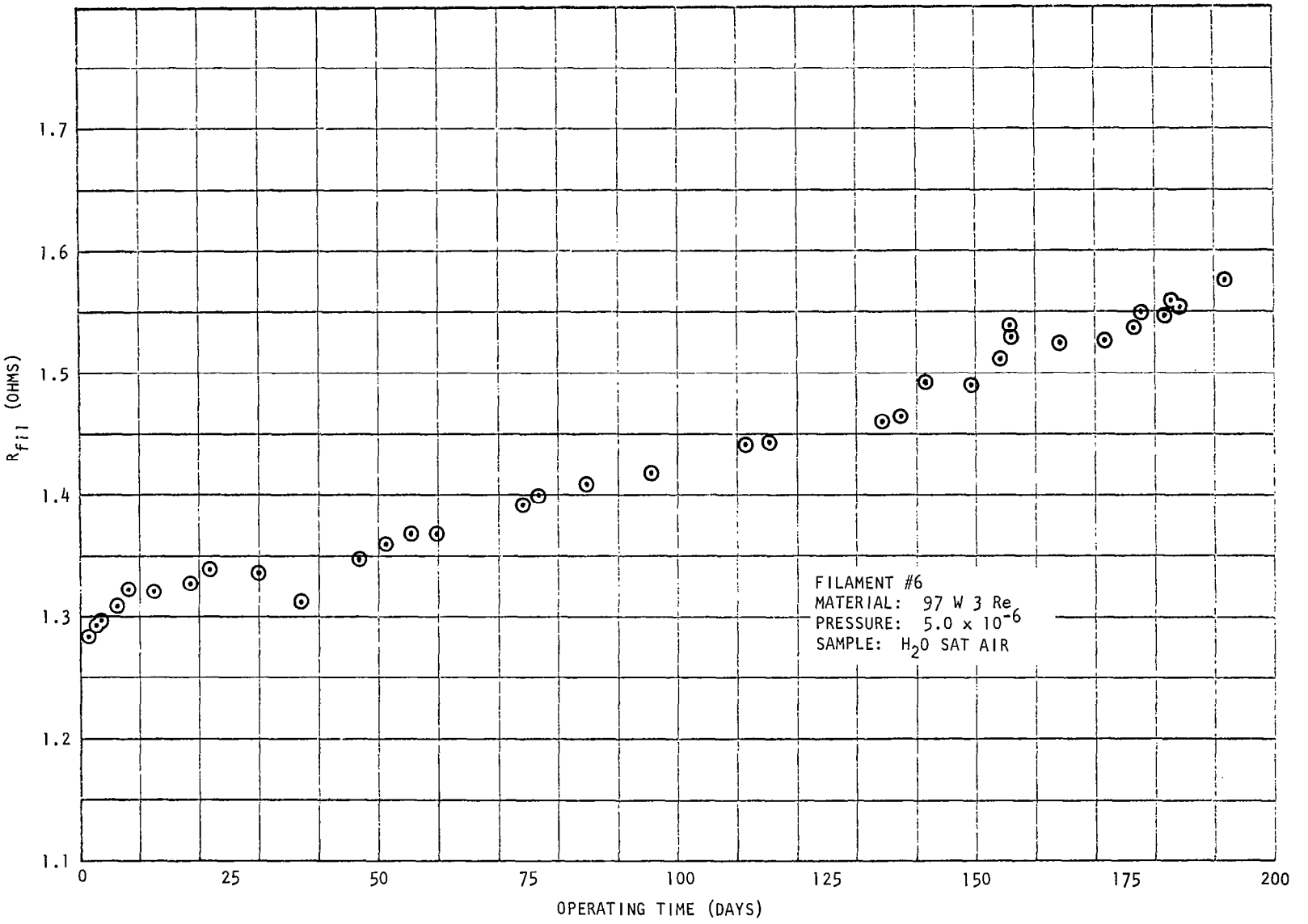
1.7
1.6
1.5
1.4
1.3
1.2
1.1
R_{fil} (OHMS)
0
25
50
75
100
125
150
175
200
OPERATING TIME (DAYS)
FILAMENT #6
MATERIAL: 97 W 3 Re
PRESSURE: 5.0 x 10^{-6}
SAMPLE: H_2O SAT AIR

FIGURE 124

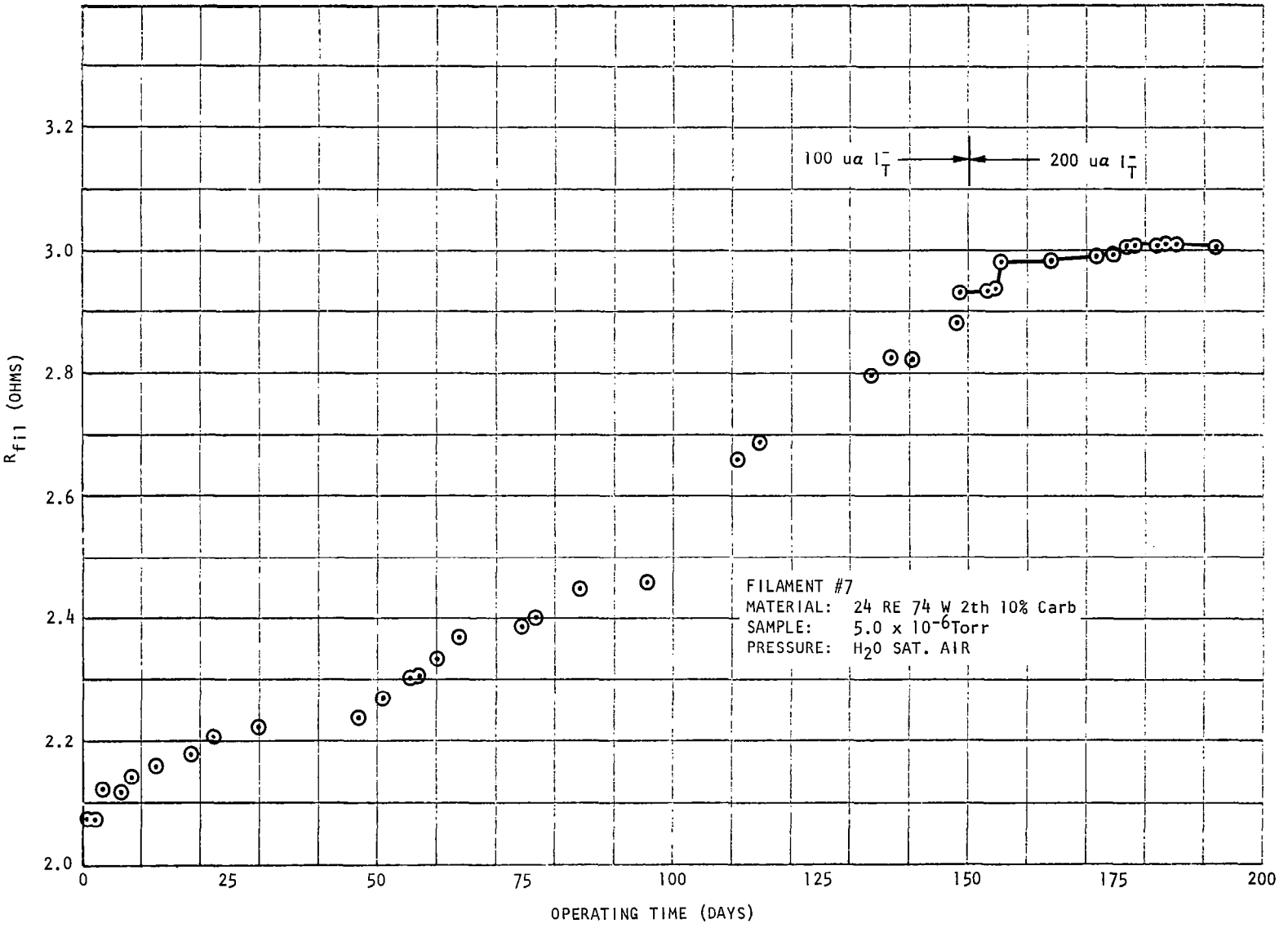
3.2
3.0
2.8
2.6
2.4
2.2
2.0
R_{Fil} (OHMS)
0
25
50
75
100
125
150
175
200
OPERATING TIME (DAYS)
100 ua I_T^-
200 ua I_T^-
FILAMENT #7
MATERIAL: 24 RE 74 W 2th 10% Carb
SAMPLE: 5.0 x 10^{-6}Torr
PRESSURE: H_2O SAT. AIR

FIGURE 125

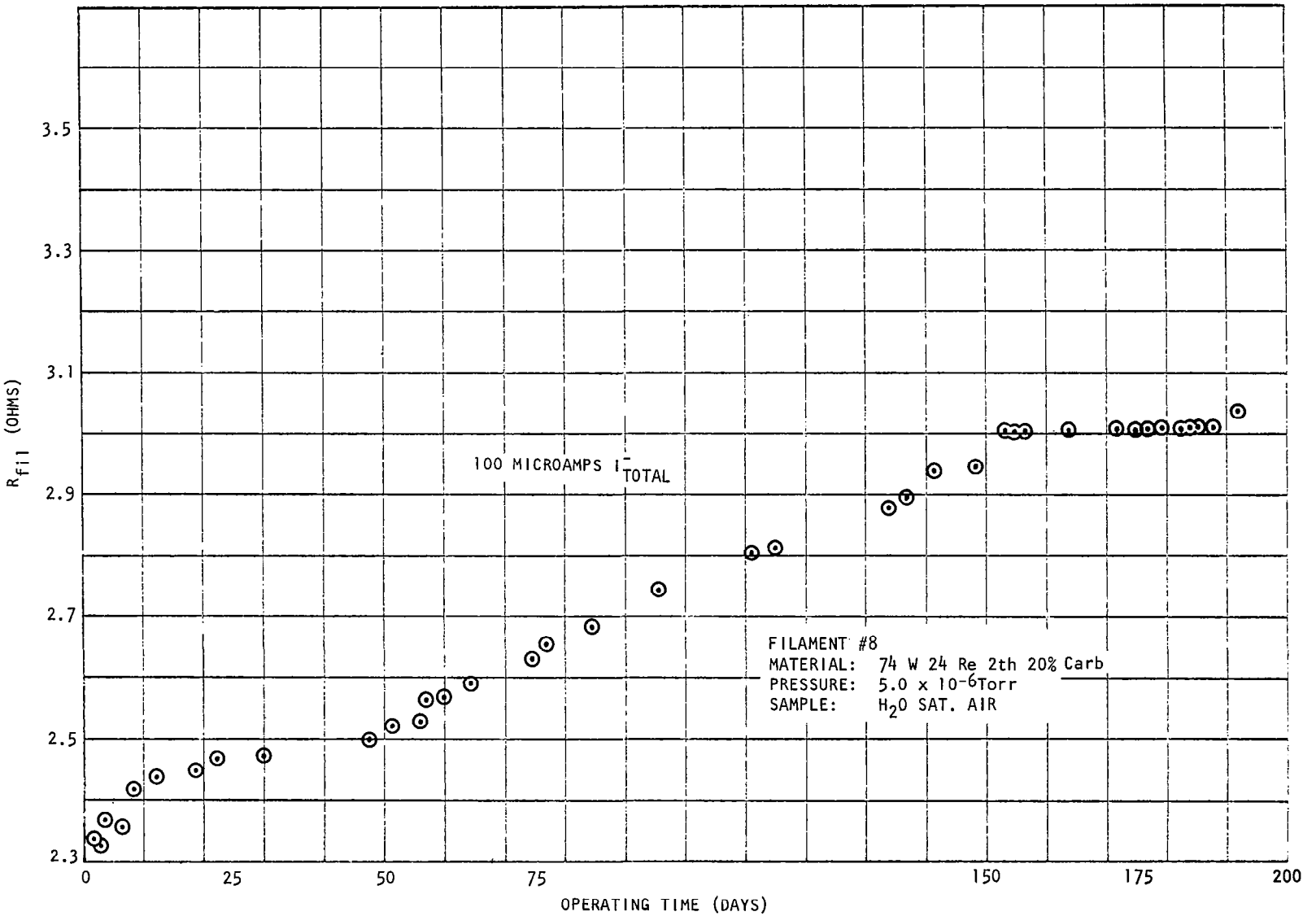
3.5
3.3
3.1
2.9
2.7
2.5
2.3
R_{Fil} (OHMS)
100 MICROAMPS I^-_{TOTAL}
FILAMENT #8
MATERIAL: 74 W 24 Re 2th 20% Carb
PRESSURE: 5.0 x 10^{-6}Torr
SAMPLE: H_2O SAT. AIR
0
25
50
75
150
175
200
OPERATING TIME (DAYS)

FIGURE 126

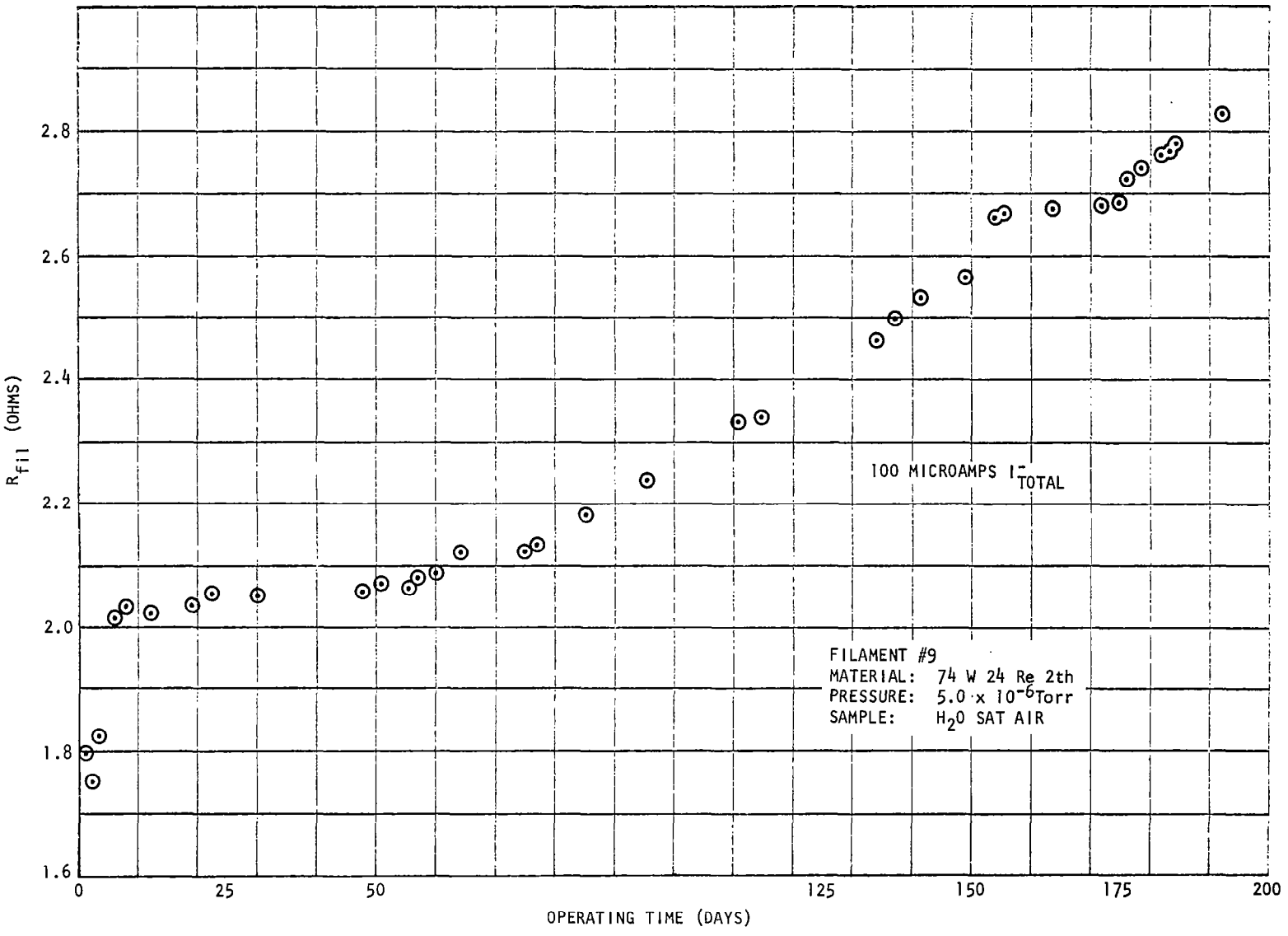
2.8
2.6
2.4
2.2
2.0
1.8
1.6
R_{Fil} (OHMS)
0
25
50
125
150
175
200
OPERATING TIME (DAYS)
100 MICROAMPS I^-_{TOTAL}
FILAMENT #9
MATERIAL: 74 W 24 Re 2th
PRESSURE: 5.0×10^{-6}Torr
SAMPLE: H_2O SAT AIR

FIGURE 127

material points out that the 97% W 3% Re is by far the best. This is supported by the photographs and diametric measurements. It would appear that if the slopes remained consistent until filament failure, the 97% W 3% Re material could have a life expectancy of better than twice that of the 75% W 25% Re wire under these environmental conditions. The Thoriated Tungsten Rhenium filaments were found to be the worst in this respect. This fact was supported by the diametric measurements under the microscope.

Another consideration is that of the support electronics design, specifically the emission regulator. From Figures 128 through 131 it is apparent that the resistance temperature coefficients for the non-thoriated filaments tested is approximately the same. However, the difference in power requirements at various emission levels for the different materials is not the same, as shown in Figure 132. This means that for the 75% W 25% Re, as opposed to the 97% W 3% Re, the emission regulator dynamic range requirement would be greater. More important, however, is the fact that a greater regulator dead band could be tolerated. This would be useful, if it were not for the extreme excursion of the 75% W 25% Re long-term resistance, which negates this effect by making the dynamic range requirements greater than desirable. This is because the dynamic range requirement could cause a dead band in the regulator greater than the short-term instability and power requirement deviations.

These facts all weigh heavily in filament selection and points toward the 97% W 3% Re emitter as being the best material investigated for this design consideration.

CONCLUSIONS

There have been several interesting results derived from this emitter study program. First, and most important, it has been shown that the 97% W 3% Re alloy wire is a more suitable filament material for the two gas sensor than is the 75% W 25% Re alloy which was originally selected. Fortunately this information was obtained just at a time when a potential problem was developing in the filament area. It is anticipated that changing to this more satisfactory material will eliminate any possible difficulty which might arise. Second, the study has shown that the thoriated filaments which might have given a power saving were poisoned by the simulated environment and consequently are not suitable for application to the two gas sensor. Third, the test program demonstrated the .003 inch diameter tantalum and iridium wires were not suitable for use as filaments under the existing conditions. Finally, it was shown that .003 inch diameter tungsten-rhenium alloy wire filaments can operate as emitters under simulated conditions for a period in excess of 190 days.

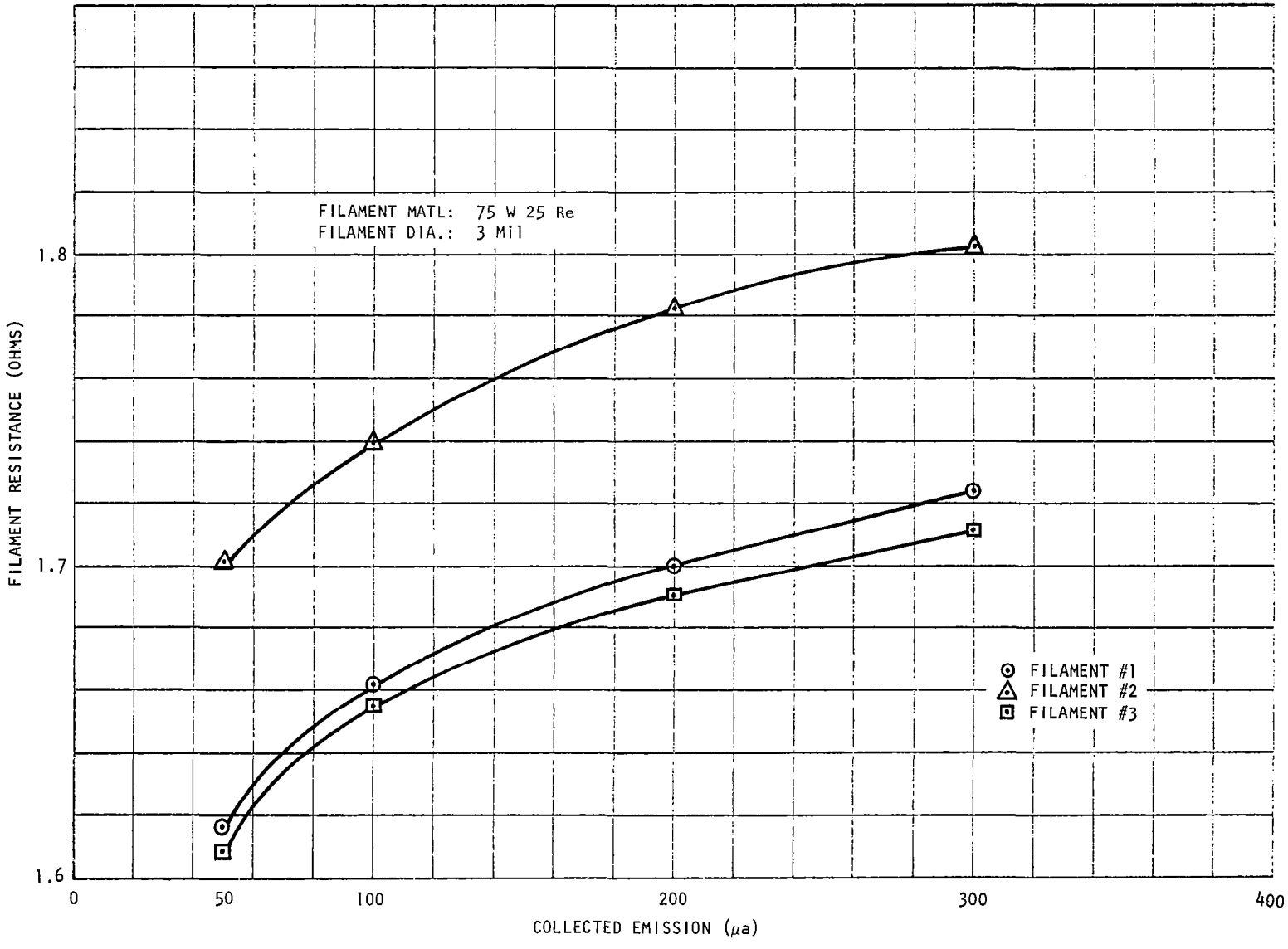
FILAMENT MATL: 75 W 25 Re
FILAMENT DIA.: 3 Mil
FILAMENT RESISTANCE (OHMS)
1.8
1.7
1.6
0
50
100
200
300
400
COLLECTED EMISSION (μa)
FILAMENT #1
FILAMENT #2
FILAMENT #3

FIGURE 128

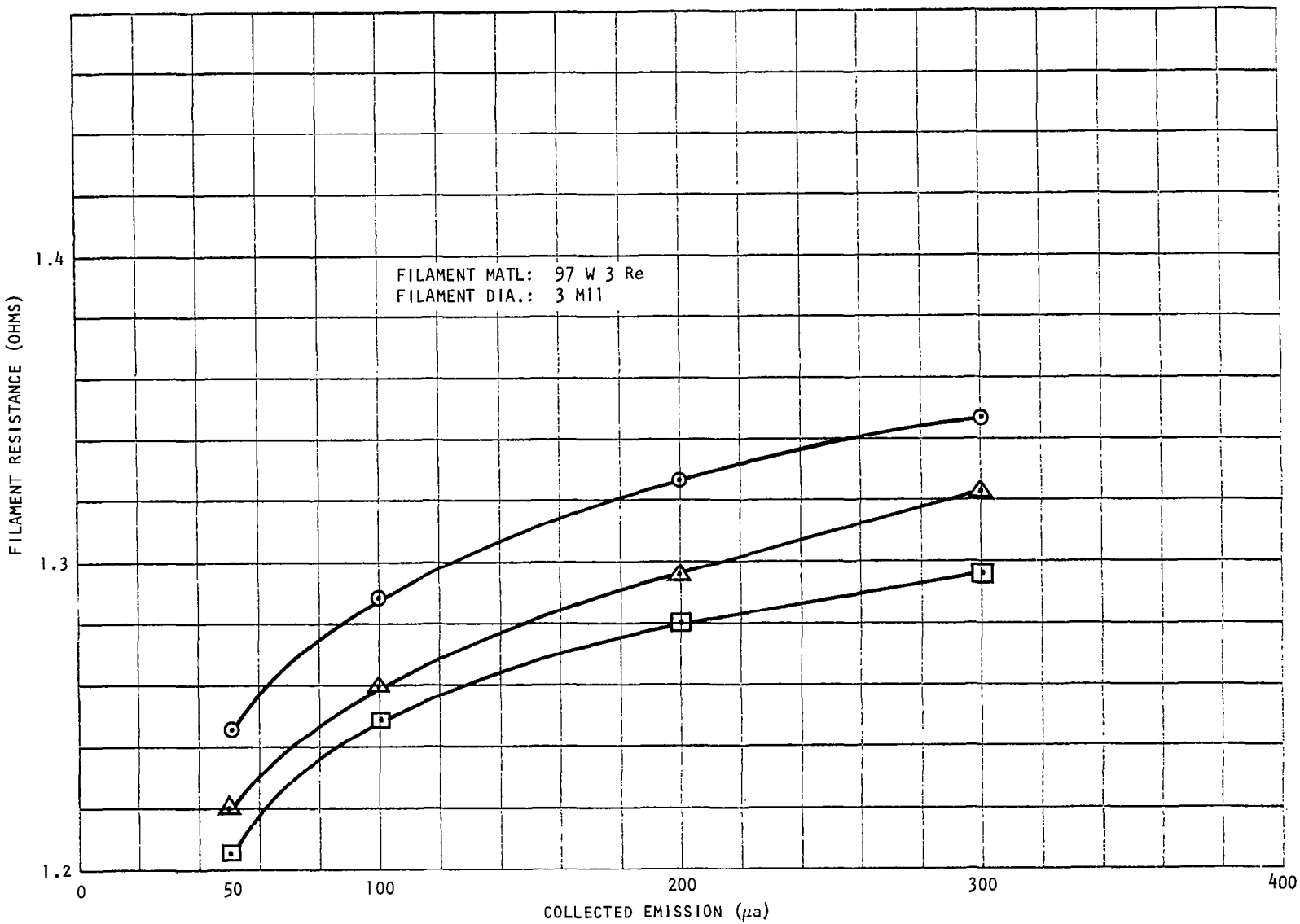
FILAMENT MATL: 97 W 3 Re
FILAMENT DIA.: 3 Mil
FILAMENT RESISTANCE (OHMS)
1.4
1.3
1.2
0
50
100
200
300
400
COLLECTED EMISSION (μa)

FIGURE 129

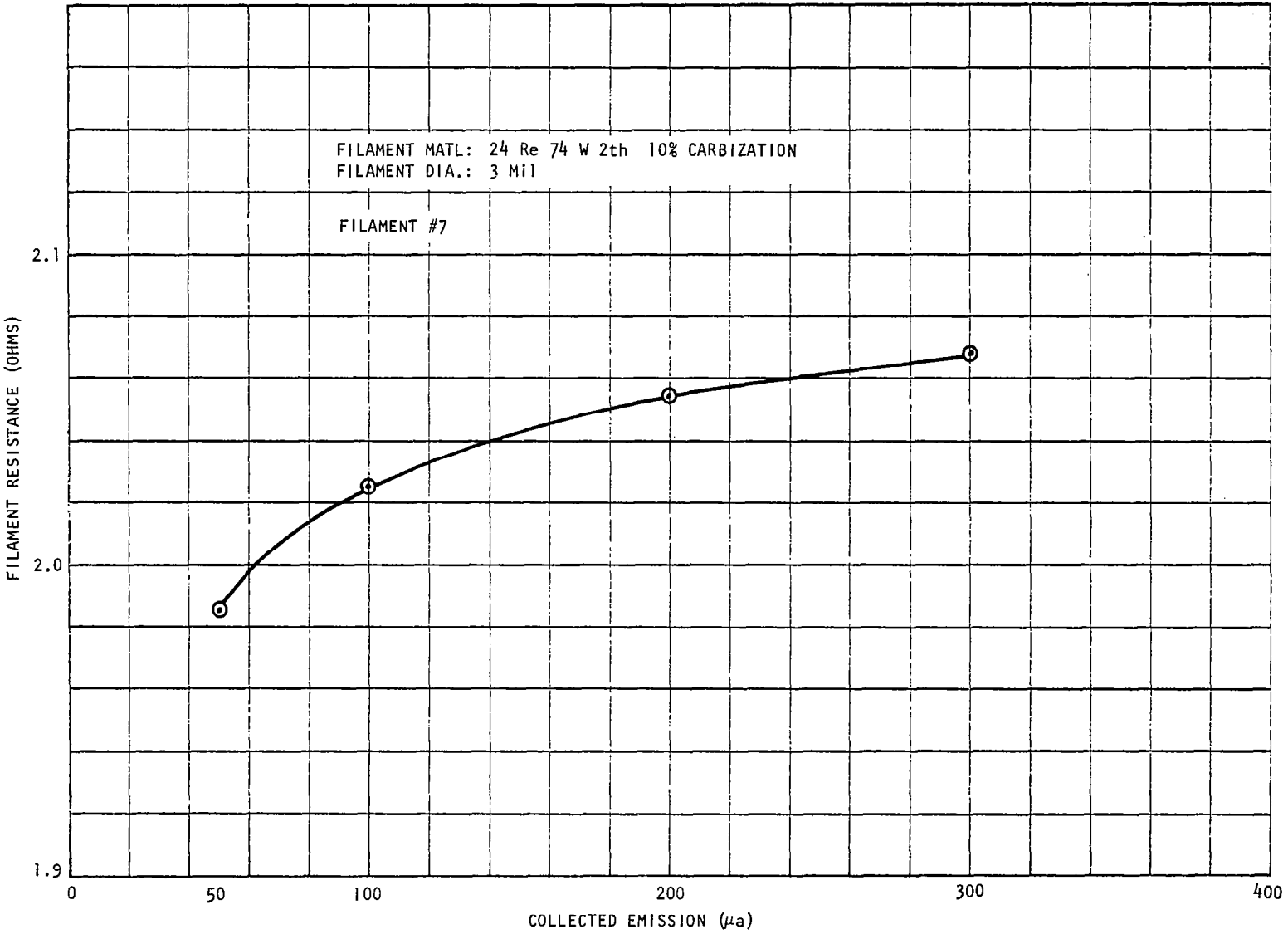
FILAMENT MATL: 24 Re 74 W 2th 10% CARBIZATION
FILAMENT DIA.: 3 Mil
FILAMENT #7
FILAMENT RESISTANCE (OHMS)
2.1
2.0
1.9
0
50
100
200
300
400
COLLECTED EMISSION (μa)

FIGURE 130

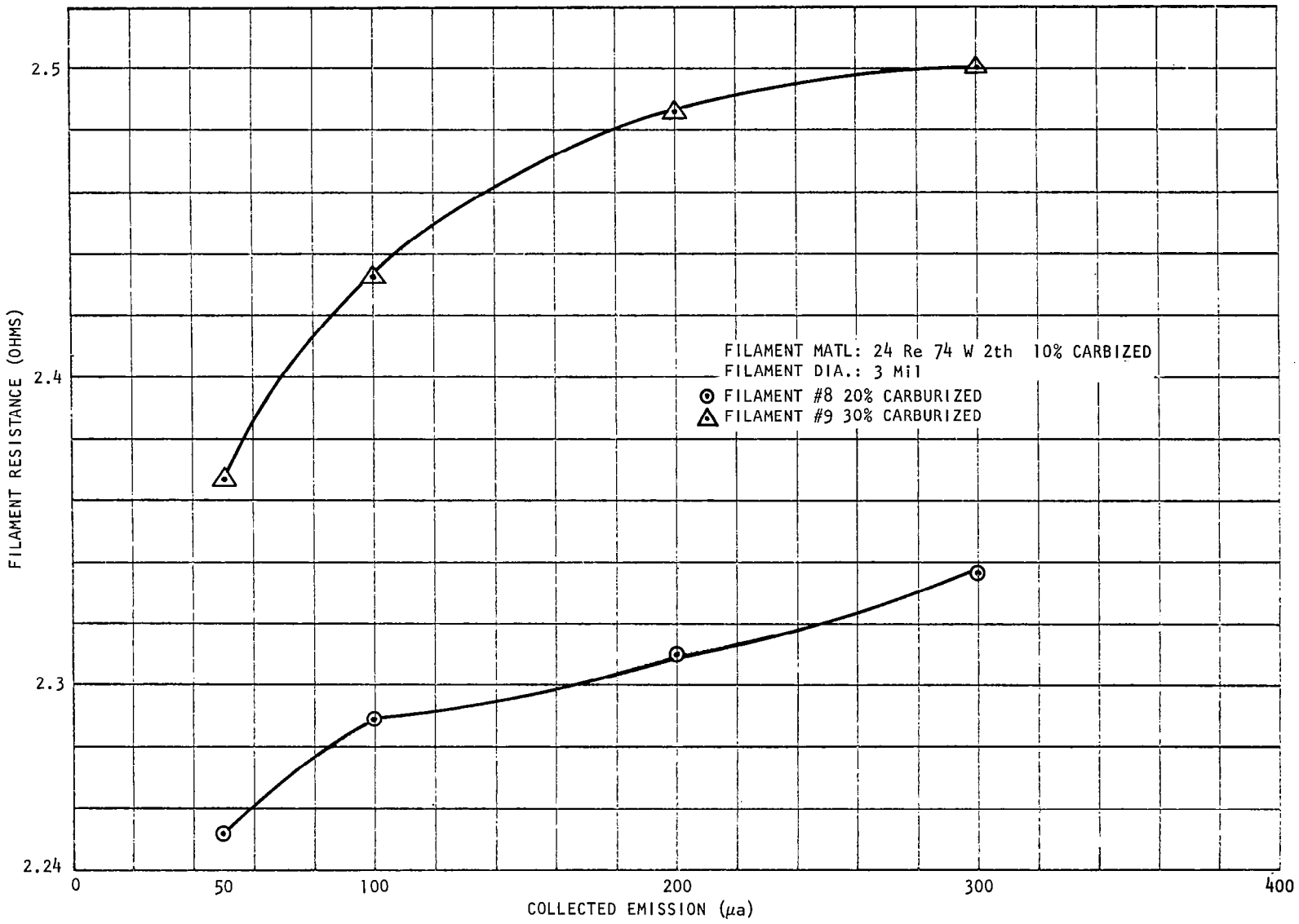
FILAMENT RESISTANCE (OHMS)
2.5
2.4
2.3
2.24
0
50
100
200
300
400
COLLECTED EMISSION (μa)
FILAMENT MATL: 24 Re 74 W 2th 10% CARBIZED
FILAMENT DIA.: 3 Mil
FILAMENT #8 20% CARBURIZED
FILAMENT #9 30% CARBURIZED

FIGURE 131

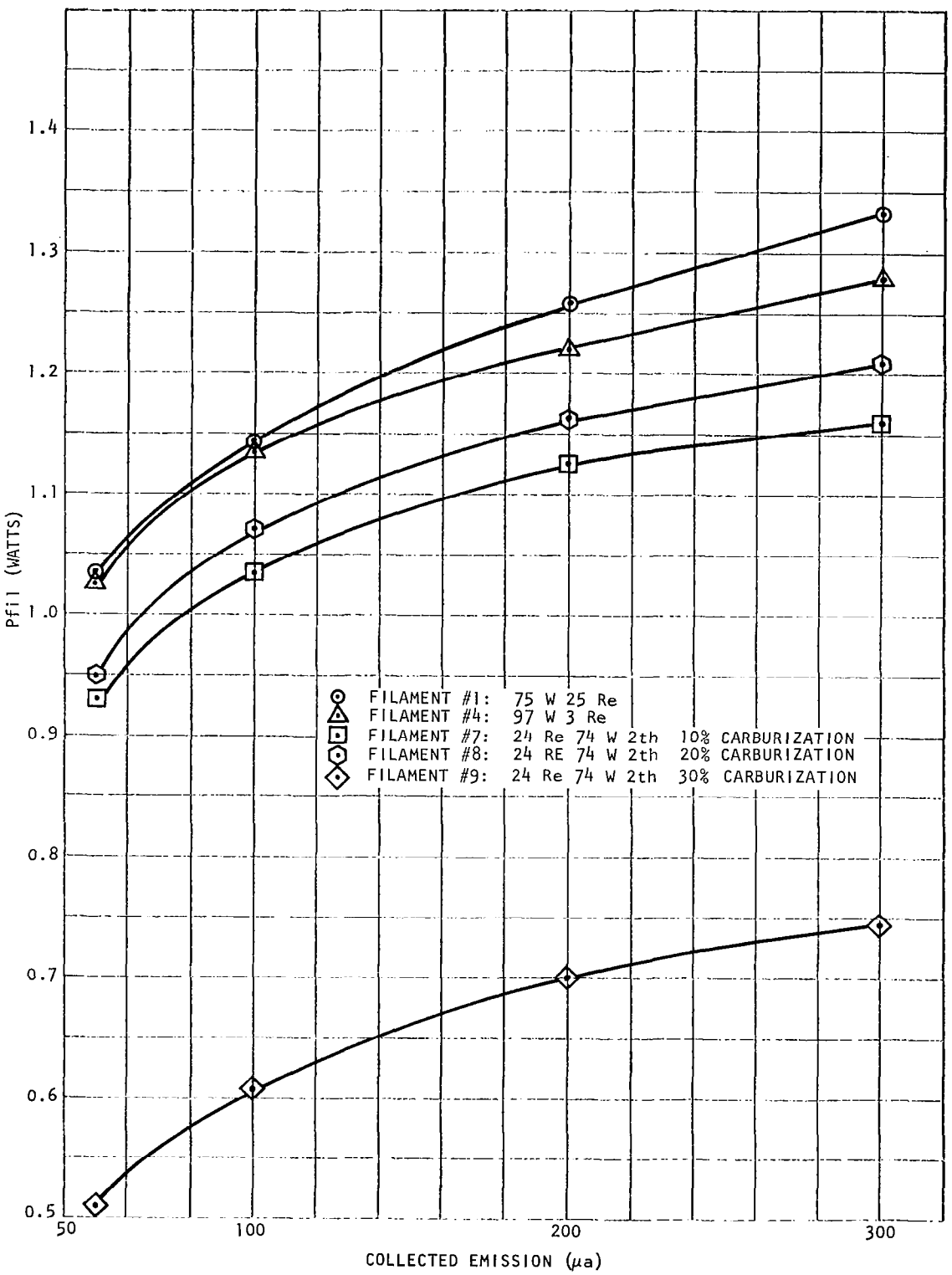
1.4
1.3
1.2
1.1
1.0
0.9
0.8
0.7
0.6
0.5
Pfil (WATTS)
50
100
200
300
COLLECTED EMISSION (μa)
FILAMENT #1: 75 W 25 Re
FILAMENT #4: 97 W 3 Re
FILAMENT #7: 24 Re 74 W 2th 10% CARBURIZATION
FILAMENT #8: 24 RE 74 W 2th 20% CARBURIZATION
FILAMENT #9: 24 Re 74 W 2th 30% CARBURIZATION

FIGURE 132

FLIGHT PROTOTYPE TESTING

Following the testing and modification of the ETM sensor system the four flight prototype units were also tested. This program is described in the following section and the test results are summarized. The test data records for S/N 01 of the flight prototype units is reproduced in Appendix C.

DESCRIPTION OF THE TEST PROGRAM

Each of the flight prototype sensor was tested by placing the analyzer (or mass spectrometer tube) on the laboratory vacuum system and pumping down. Each analyzer was tested with its own analyzer magnet. Only one set of shielding for the ion source was employed and this set was switched from one unit to the next. A single capillary line molecular inlet leak assembly was utilized during the test of the four flight prototypes. These procedures were instituted to obtain the maximum degree of consistency of operation between analyzers. The analyzers were tested utilizing a set of laboratory power supplies with the filament powered by a dc source.

The filament on each electron gun was burned in slowly to outgas it and give maximum filament life. Each electron gun was then tuned up to give the maximum transmission efficiency for electrons to the ionizing region. This tune up was conducted for a fixed filament to electron accelerator voltage which has been established as optimum during the ETM testing. The ionizing region was tuned by determining the voltage difference between the electron accelerators and the anodes for which the electron beam is centered over the accelerator aperture. The repeller-accelerator voltage was fixed at 10 volts to reduce the number of potentials to be varied. The analyzer was then briefly tuned to obtain an ion current output at the m/e 28 collector and the ion focusing electrodes and z axis focus electrode were tuned for maximum ion current output. The sensitivity of the analyzer (ion current output versus ion source pressure) for nitrogen was measured by introduction of the sample gas into the vacuum system itself so that there was no differential pumping.

Having established the operation of the ion source the analyzer was then tuned by varying the magnet position (two directions of translation and rotation). An optimum magnet position was found which minimized the m/e 17 - m/e 18 cross talk at the m/e 18 collector. The same was done for m/e 28 - m/e 32 on the m/e 28 collector. Then a compromise magnet position was found for which the m/e 28 - m/e 32 cross talk specification was met and which gave an acceptable m/e 18 peak in terms of the flatness of the top of the peak. The alignment of the buckets was then checked to see if each ion current to

be monitored was centered in its appropriate collector at the same ion accelerating voltage. Sufficient data was taken from which correct collector locations could be computed, where necessary.

A nitrogen sample was introduced into the sensor through the capillary line and the m/e 28 output was plotted up to 400 torr inlet pressure. This data was used to demonstrate linearity as well as for a measure of the total system transfer characteristic. Having shown the total analyzer to be operable and having measured the pertinent analyzer parameters, a final set of analyzer voltages were measured on the laboratory electronics system. These voltages were then set up on the voltage divider of the flight prototype electronics system.

Each set of flight prototype electronics was checked out on a board-by-board basis and then as a complete subsystem. The circuits were checked for regulation, ripple, input voltage extremes, voltage and current wave forms at critical points, etc. The electrometer amplifiers were checked for noise and drift and the emission regulator was tested with a dummy diode. After the complete electronics subsystem was shown to be operational and the voltage divider appropriately adjusted for the analyzer with which it was to be mated, the electronics were mated with the analyzer and each module was given a functional check. Mechanically, the electronics integration consisted of plugging the printed circuit modules onto the connectors of a test fixture which placed them in the approximate locations that they have in the flight package but slightly more separated to allow for the presence of flanges and access to the modules. The voltage divider potentiometers were adjusted, where required, to give the same analyzer operation as obtained with the laboratory supplies. Operation was checked at line voltage settings of 27.5 volts, 28.0 volts and 28.5 volts on the system power supply. Finally a sample gas mixture of CO_2, N_2 and O_2 was admitted to the system through the capillary line and outputs were simultaneously recorded for the m/e 44, m/e 28, and m/e 32 collectors. The operating voltages for the system were recorded along with the required magnet position and the system power was measured for all line voltages.

SUMMARY OF FLIGHT PROTOTYPE TEST RESULTS

This summary of test results was obtained on the four flight prototype instruments and describes the parameters which were tested. Those parameters which can be conveniently listed are shown in Table 26. Actual test scans and other plots are also shown in this section. In general it may be said that the instruments met the specifications which formed the initial design goals. In the few cases where the initial design goals were not completely met, it was attributable to specific difficulties in the system and remedies were usually identified.

ANALYZER SENSITIVITY

Typically the analyzer sensitivity was higher than the design goal of 5×10^{7} amperes/torr. In several cases it was as much as three times higher (See Table 26). These sensitivities were obtained at lower values of ionizing current than had originally been anticipated. This gives the instrument greater flexibility for various applications. It also should improve high pressure operation. In the case of S/N 4 the sensitivity on one gun was a little below specification.

	SENSITIVITY FOR N_2				CROSSTALK		N_2 LINEARITY DEVIATION IN OPERATING RANGE	SOURCE PRESSURE	SYSTEM POWER
	Analyzer Sensitivity		Sensitivity Thru Capillary	Adjusted System Sensitivity	m/e 28 - m/e 32	m/e 17 - m/e 18			
	Goal: 5×10^{-7} Amps/Torr		Goal: 2.5×10^{-13} Amps/Torr	Goal: 0.025 Volts/Torr	Goal: ≤ 0.5%	Goal: Detectible Valley for Equal Peak Amplitudes	Goal: ≤ 3% Deviation @ 400 Torr Inlet	Goal: 2×10^{-4} Torr @ 400 Torr Inlet	Goal: 3.5 Watts @ 28 Volts Input
	Gun #1	Gun #2	Gun #1	Gun #1	Gun #1				
Serial #01	1.7×10^{-6} Amps/Torr @ $I_{AN} = 21 \mu A$	—	2.3×10^{-12} Amps/Torr Inlet @ 400 Torr and $I_{AN} = 21 \mu A$	0.0252 Volts/Torr	< 0.5%	Very Slight Valley for 25% m/e 17	< 1%	5.4×10^{-4} Torr	3.36 Watts
Serial #02	7.7×10^{-7} Amps/Torr @ $I_{AN} = 15 \mu A$	9.8×10^{-7} Amps/Torr @ $I_{AN} = 15 \mu A$	8.0×10^{-13} Amps/Torr Inlet @ 400 Torr and $I_{AN} = 15 \mu A$	0.0270 Volts/Torr	~ 1%	Very Slight Valley for 25% m/e 17	< 1%	4.15×10^{-4} Torr	3.41 Watts
Serial #03	1.6×10^{-6} Amps/Torr @ $I_{AN} = 18 \mu A$	1.7×10^{-6} Amps/Torr @ $I_{AN} = 22 \mu A$	1.6×10^{-12} Amps/Torr Inlet @ 400 Torr and $I_{AN} = 18 \mu A$	0.0197 Volts/Torr	< 0.5%	Good Valley for 25% m/e 17	< 1%	4.0×10^{-4} Torr	3.47 Watts
Serial #04	4.3×10^{-7} Amps/Torr @ $I_{AN} = 20 \mu A$	5.3×10^{-7} Amps/Torr @ $I_{AN} = 15 \mu A$	3.98×10^{-13} Amps/Torr Inlet @ 400 Torr and $I_{AN} = 20 \mu A$	0.0281 Volts/Torr	< 0.5%	Good Valley for 25% m/e 17	< 1%	3.7×10^{-4} Torr	3.42 Watts

TABLE 26
Flight Prototype Operating Parameters

It is assumed that it could be raised, perhaps by realignment of the ion source electrodes. It is of interest to note that the biggest difference in sensitivity occur between instruments rather than between the electron guns on one instrument. This indicates that the majority of the variation is due to the ion focusing system rather than to the electron gun itself. For the specified application the sensitivity must be reduced, since if it is too high it will cause the electrometer amplifiers to saturate before the nominal ambient pressure is reached. This situation can be alleviated by detuning the ion focusing system by adjusting the voltage on ion focus B, or by turning down the emission current adjust potentiometer. Modifications could be made which would allow the instrument to take advantage of its excess sensitivity should this be desirable.

ELECTRON GUN OPERATION

All electron guns attained optimum operation at approximately the same electrode voltages. The operation appeared to be stable and the transmission efficiencies which were obtained varied between 15 and 20 percent. Less than 1 microampere was drawn by the repeller, accelerator, or side electrodes.

CROSS TALK AND PEAK SHAPE

The most important area for minimum cross talk is between m/e 28 and m/e 32. Data taken indicated that in three of the four instruments tested the value obtained was better than the specification of 0.5 percent. In the case of S/N 2 the specification was not met, because there was a significant variation in the magnetic flux density over the analyzer magnet pole face area. This variation was much greater than for the other magnets and probably was responsible for the poorer performance for this instrument.

Another parameter of importance is the peak shape which will determine the sensitivity of the analyzer output to voltage and magnet flux density variations. The wider the top of the peak when the spectrum is scanned for a given resolution the narrower is the ion beam in comparison with the corresponding collector slit width. In the case of m/e 28 and m/e 32 the peak top widths are fairly large. This may be taken advantage of either by having improved stability against magnet or voltage variations or the collector slits could be tabbed down to increase the resolution and decrease the cross talk.

Spectrum scans are shown for S/N 1, 3, and 4 in Figures 133, 134, and 135 and showing the resolution at m/e 28 - m/e 32 and m/e 17 - m/e 18 for magnet positions which are optimized for the collector on which the measurement was made. Figures 136 and 137 show typical spectrum scans taken on S/N 3 and S/N 4 for which the magnet is in a compromise position. These are the final magnet positions which were selected. Two points are in order. First, the m/e 28 and m/e 32 collectors were not designed to be at the optimum resolution points in order to reduce the size of the instrument. It is therefore to be expected that the magnet position can be altered to obtain improved m/e 28 - m/e 32 resolution. As a result it is necessary to select a compromise magnet position when one is attempting to optimize the resolution for m/e 28 - m/e 32 and m/e 17 -

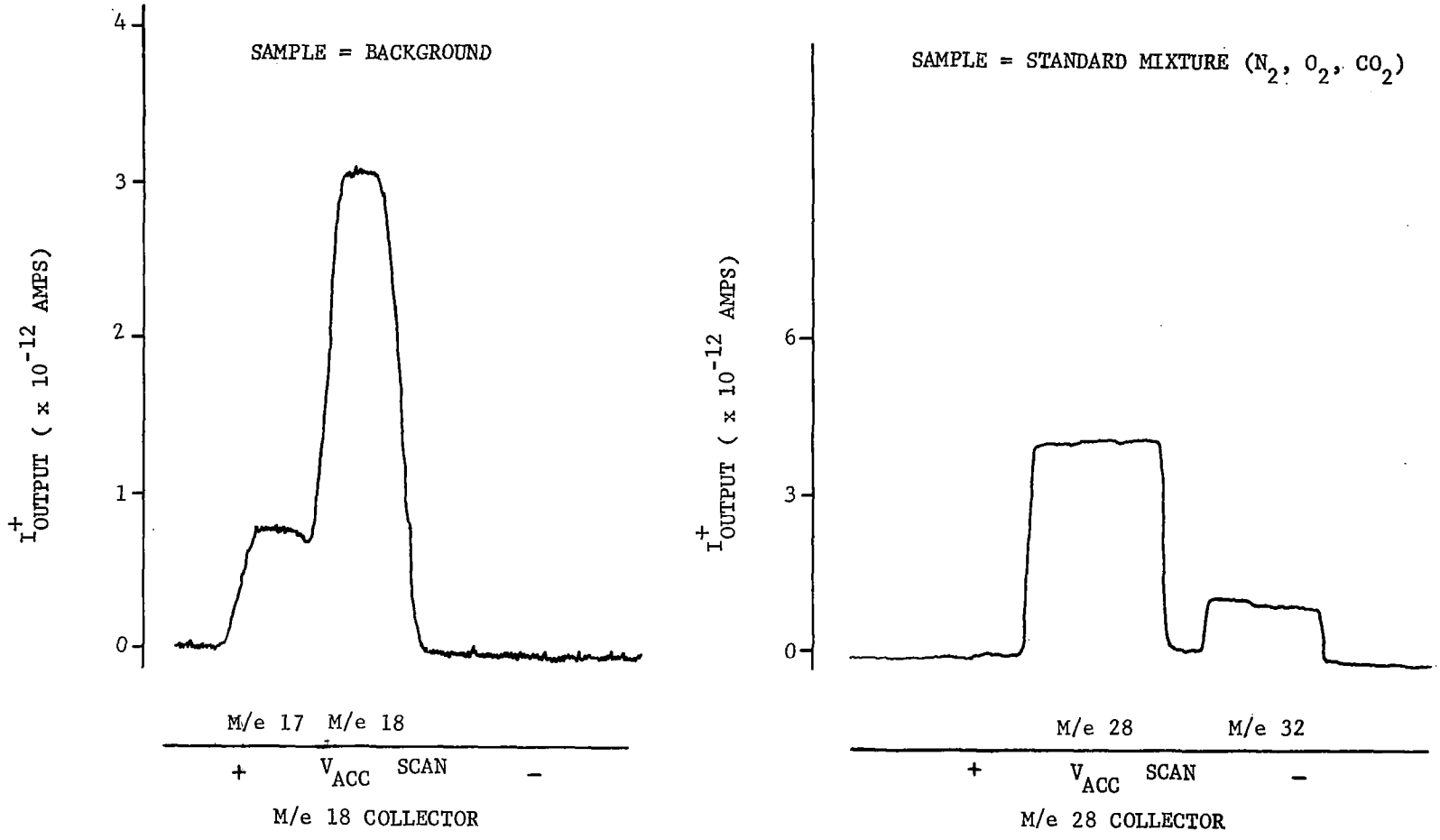

FIGURE 133
ANALYZER SN01
PEAK SHAPES WITH OPTIMIZED MAGNET LOCATIONS
FOR m/e 18 AND m/e 28 COLLECTORS

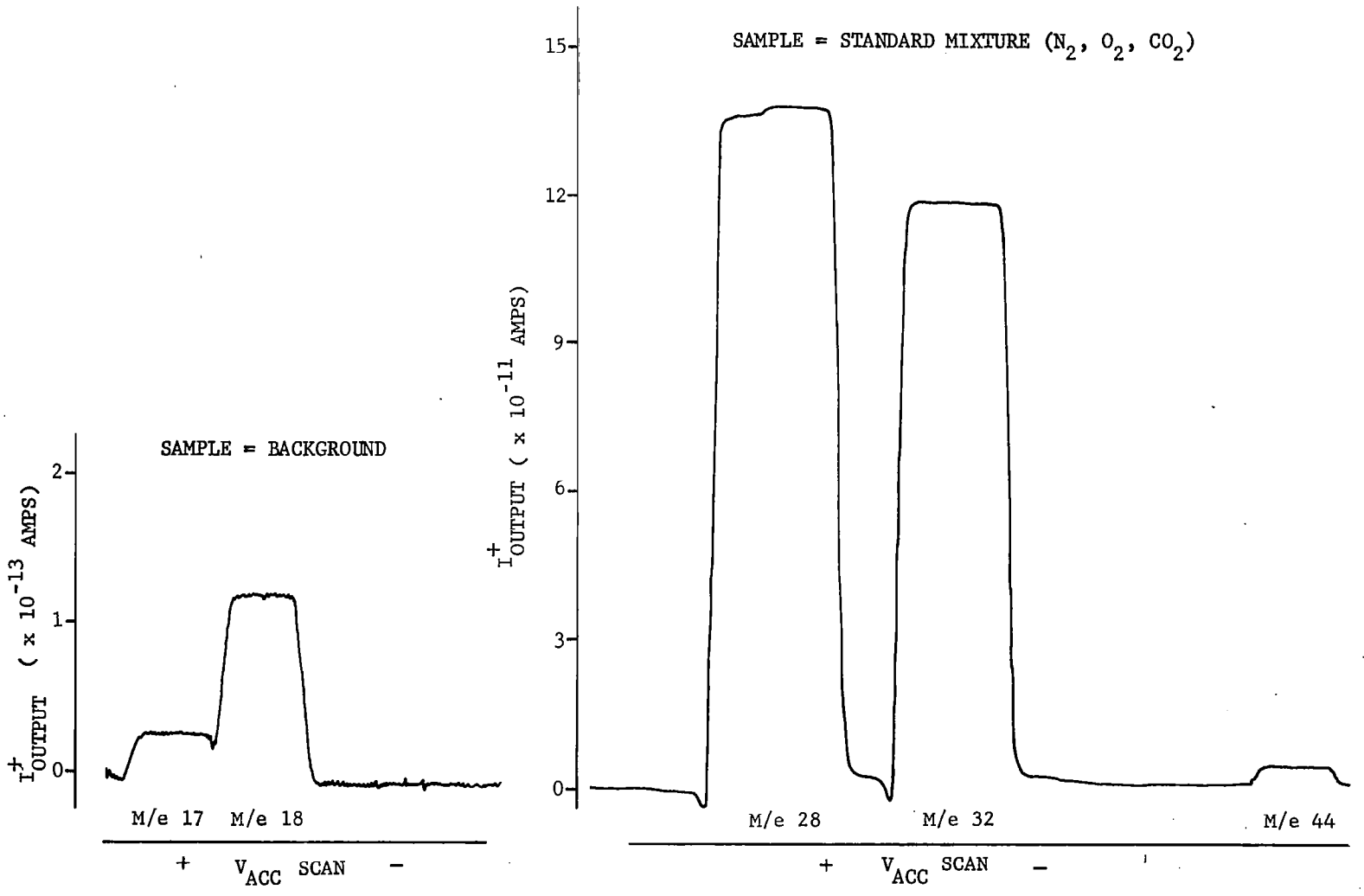

FIGURE 134
ANALYZER S/N 03
PEAK SHAPES WITH OPTIMIZED MAGNET LOCATIONS
FOR m/e 18 and m/e 28 COLLECTORS

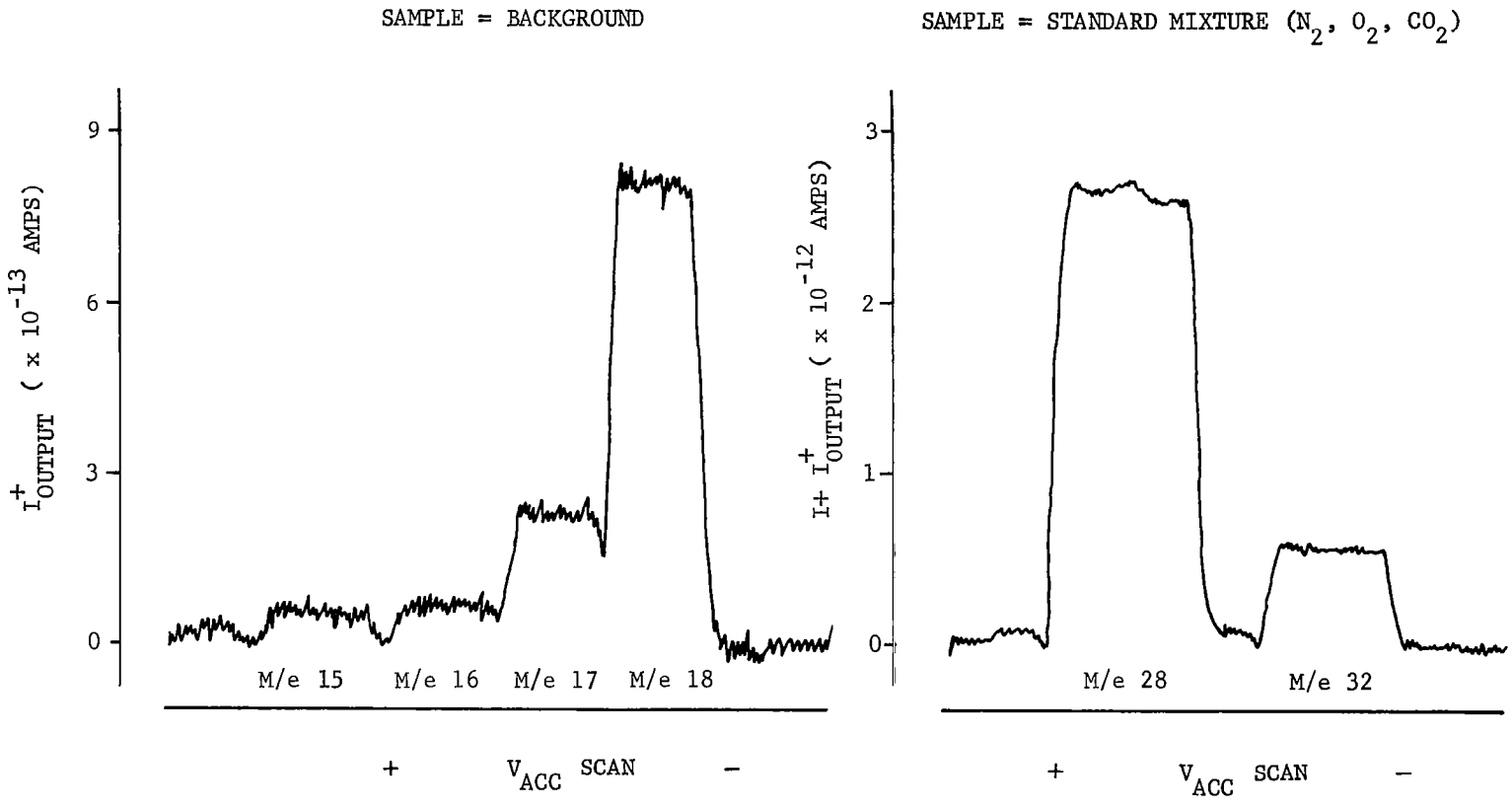

FIGURE 135
ANALYZER S/N 04

PEAK SHAPES WITH OPTIMIZED MAGNET LOCATIONS
FOR m/e 18 and m/e 28 COLLECTORS

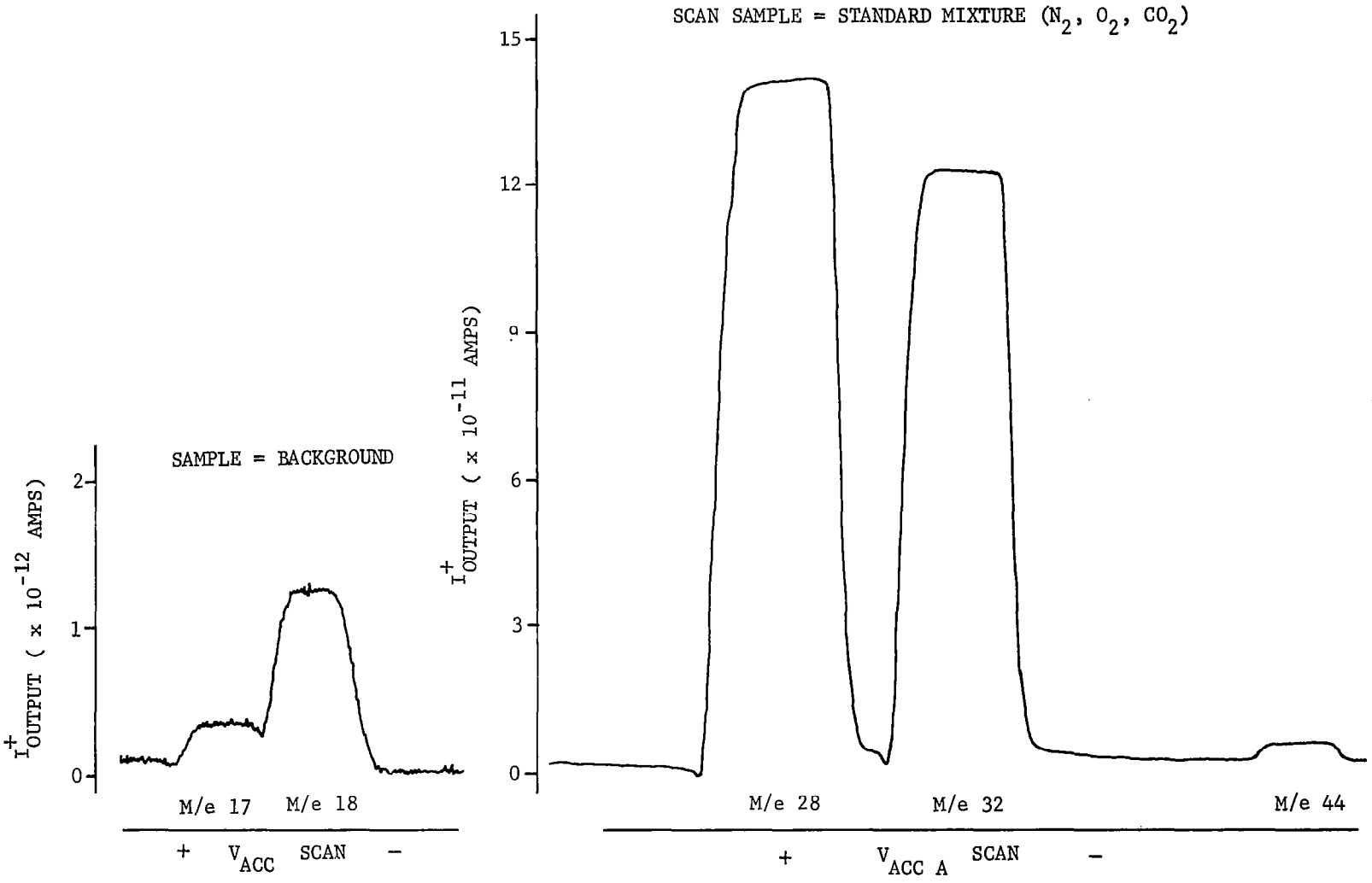

FIGURE 136
ANALYZER S/N 03
PEAK SHAPES WITH COMPROMIZED MAGNET LOCATION
FOR m/e 18 AND m/e 28 COLLECTORS

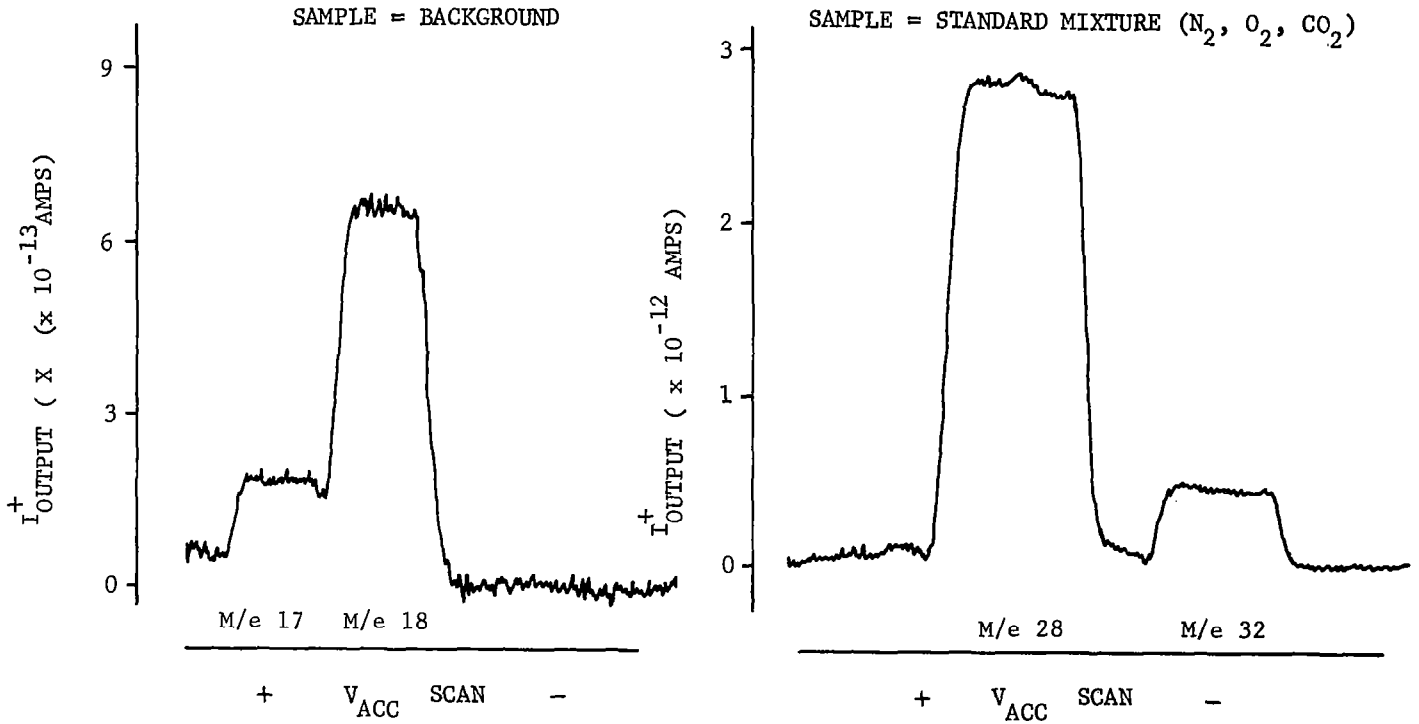

FIGURE 137
ANALYZER S/N04
PEAK SHAPES WITH COMPROMISED MAGNET LOCATION
FOR m/e 18 and m/e 28 COLLECTORS

m/e 18 simultaneously. The second point of interest is that the degree of the compromise in magnet position can be reduced by relocation of the collectors. This would improve the peak shapes at the compromise position. This operation was not carried out on the current test program, however, since the collectors are adjustable it can readily be accomplished.

In the case of m/e 17 - m/e 18 the only requirement is that the separation be sufficient to maintain a flat topped peak for m/e 18. This would be more than met if these were a slight valley between two equal sized peaks. The data indicated that in all cases there was a valley between m/e 17 and m/e 18 for a 25 to 30 percent m/e 17 peak height which is better than the requirements. In no case was there an apparent contribution if m/e 17 to the top of the m/e 18 peak. Data on the m/e 17 - m/e 18 resolution is shown in Figures 133 through 137.

Measurements of the resolution at m/e 44 were not made. As an initial design goal it was decided to resolve m/e 44 from m/e 40 in case some Argon was present in the atmosphere being sampled. Some data in which Argon was possibly present in the background indicated marginal separation. Relocation of the m/e 44 collector should improve this condition.

The peak shapes obtained were very good. The peak tops were flat over a reasonable voltage range. Some anomalies present in the data appear in the form of additional peaks. (See Figures 146 through 149.) The spurious peaks result from inadequate shielding of the ion current collectors from other ion beams than the one which is being collected at any given point in the scan. This situation is readily corrected by decreasing the collector slit widths which presently are wide for m/e 28 and m/e 32. Difficulty is not expected in this area.

SYSTEM SENSITIVITY AND LINEARITY

The overall system sensitivity is primarily dependent upon the product of the analyzer sensitivity which was discussed in Paragraph 5.2.1 and the ratio of the ion source pressure to the sample inlet pressure. More directly it is measured by recording the change in output current, usually at m/e 28 for a change in N_2 sample pressure. The transfer impedence of the detectors are also factors in the determination of the overall system gain but these are generally tightly controlled by the values of the feedback resistors. Two sets of measurements were therefore taken of the parameter. The first was taken with the laboratory electronics and is expressed in terms of amperes output per torr of sample inlet pressure. They appear in Table 26. Variations in these numbers are due to two factors. First, the analyzer sensitivities vary somewhat from one instrument to another as previously discussed; and second the ion source pressures are different for a given sample inlet pressure. The data given was for the maximum analyzer sensitivity and as a result the system sensitivity is higher than the design goal in every case. The analyzers may of course be detuned as described in Section 5.2.1 should this be required. The second set of data was taken with the complete system after the analyzer sensitivity was detuned. It can be seen

that the variation from instrument to instrument has been largely removed. These sensitivities were set by adjusting the analyzer sensitivity so that a 200 torr inlet pressure for N_2 gave approximately a five volt output on the N_2 channel.

The linearity of the systems was also checked by measuring a series of output ion currents at m/e 28 for a range of N_2 sample inlet pressures. Some non-linearity was noted over the entire pressure range from zero to 400 torr. See Figures 138 through 141. The exact source of this has not been determined. It could either be in the capillary inlet system or in the ion source. The capillary line linearity was not tested due to the difficulty of taking stable readings in a short period of time with the available test equipment. Since the length of the capillary line has been adjusted significantly from the initial design value in order to obtain a more nearly correct pressure division ratio it must be somewhat suspect. Direct data has been taken on an ion source similar to the Langley sources and they have been shown to be linear up to about 1×10^{-4} torr which was the last point sampled. Since the ion source pressures are considerably higher than this at the high and of the sample inlet pressure range it is possible that the difficulty is with the ion source. It must be remembered, however, that the data was taken at maximum sensitivity and that by reducing the electron beam current to obtain the appropriate sensitivity, and by increasing the repeller to accelerate voltage, the conditions contributing to ion source non-linearity can be virtually eliminated.

Before becoming too concerned with this, however, it is well to note that the linearity over the expected operating pressure range centered at 362 torr is well within the specification of 2% as indicated by Figures 142 through 145. The variations in these curves is due to the different system sensitivities for the various instruments when tuned for maximum output.

ION SOURCE PRESSURE

The ion source pressure may be determined from the analyzer sensitivity and the analyzer output. The ion source pressures for a 400 torr sample inlet pressures of N_2 are given in Table 26. It can be seen that those values run nominally a factor or two higher than the design value. It has not yet been determined whether this is due to the conductance in the inlet leak or the conductance of the ion source. Either conductance can be changed through mechanical modification or the capillary line may be adjusted to compensate appropriately. It is desirable to attempt to maintain the ion source pressure in the design range since it should improve linearity and stability. Efforts are currently underway on the engineering test model to determine where the necessary adjustment should be made.

COLLECTOR ALIGNMENT

During this effort no effort was made to adjust the positions of the collectors to obtain simultaneous centering of each ion beam in its appropriate collector. This condition is necessary if the maximum outputs for each constituent are to be obtained and so that the system will have maximum gain stability for all outputs. In other words it is not desirable to operate on the 'side of a mass

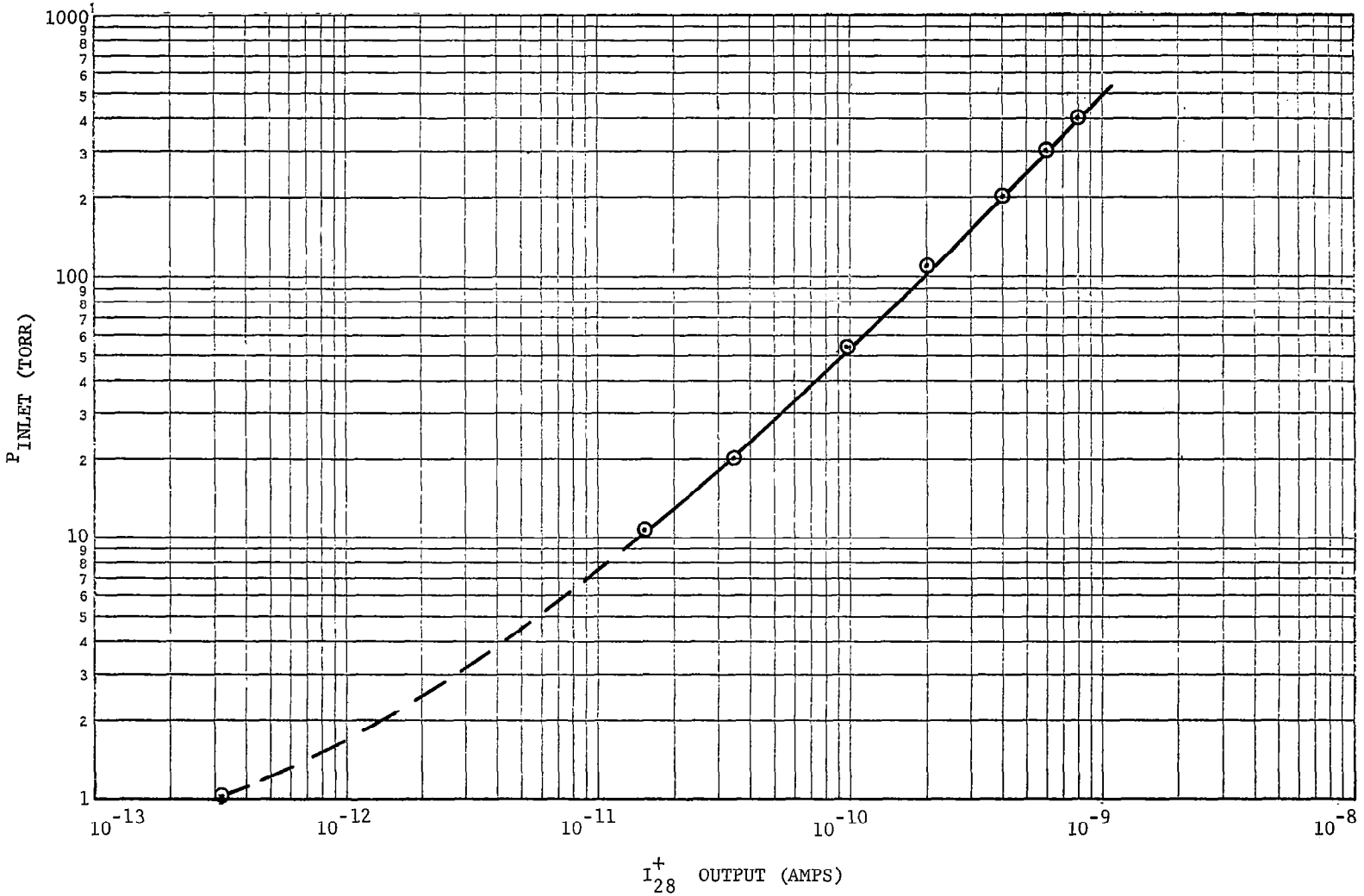

FIGURE 138
LINEARITY CURVE FOR ANALYZER S/N 01

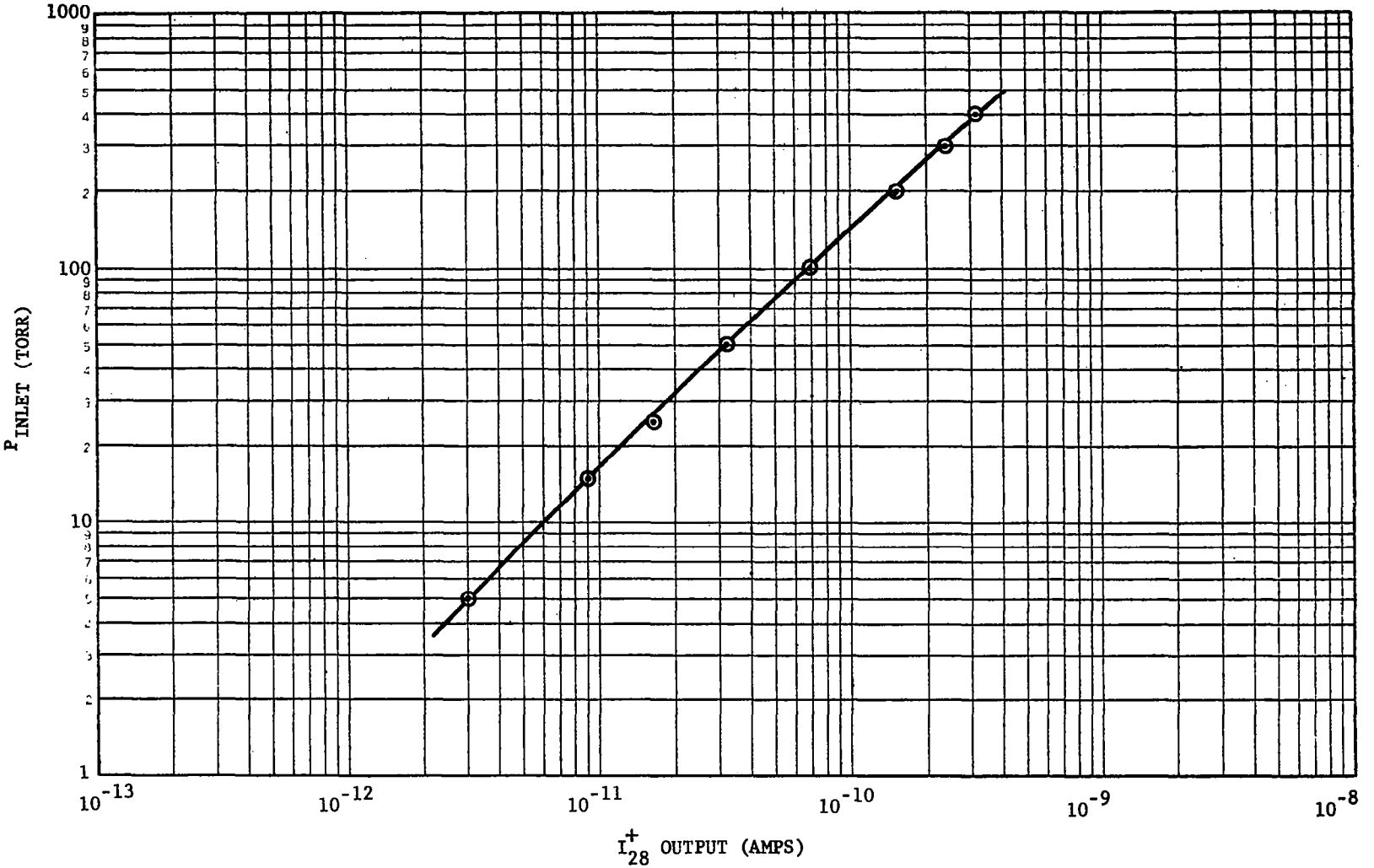

FIGURE 139

LINEARITY CURVE FOR ANALYZER S/N 02

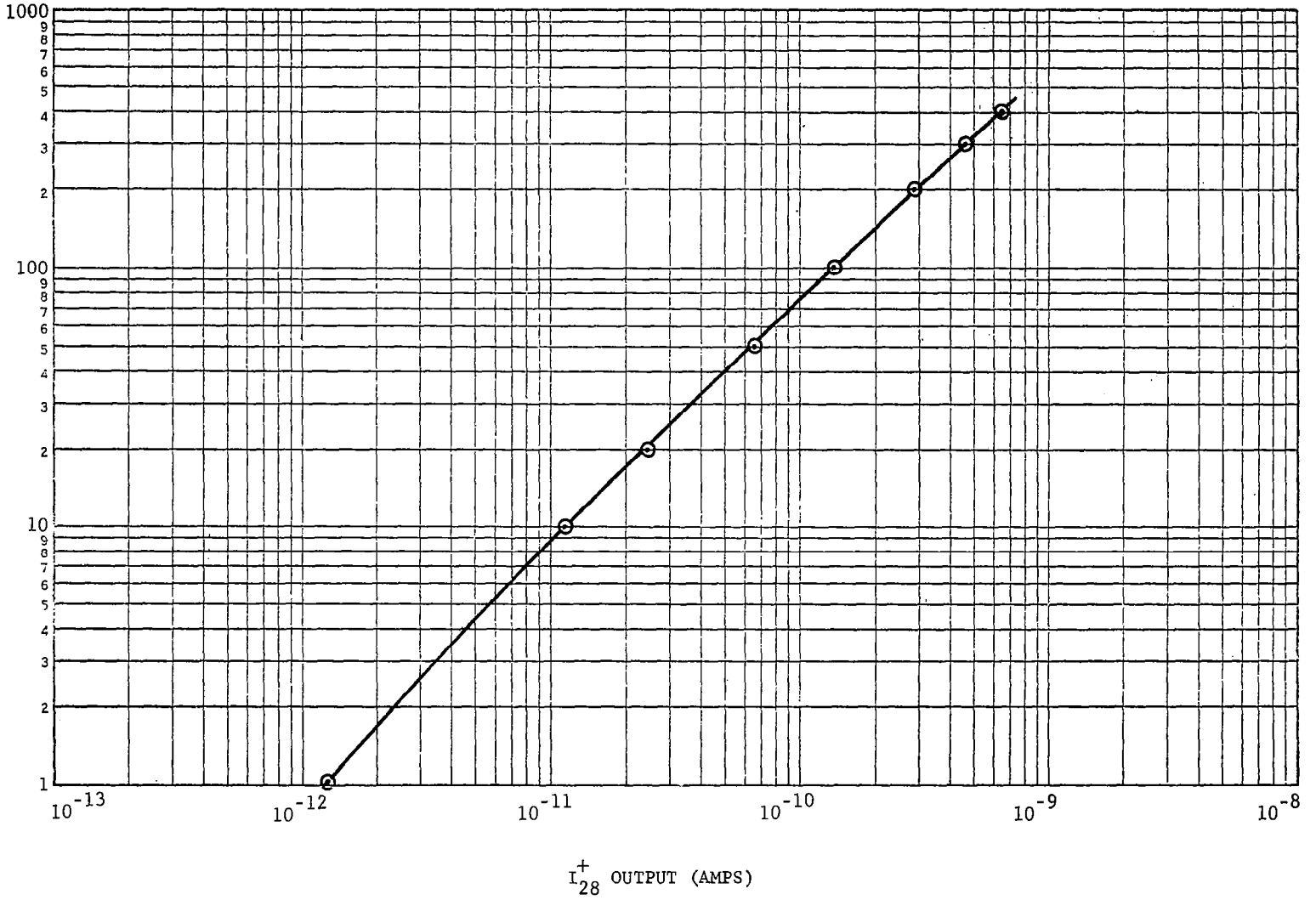

FIGURE 140
LINEARITY CURVE FOR ANALYZER S/N 03

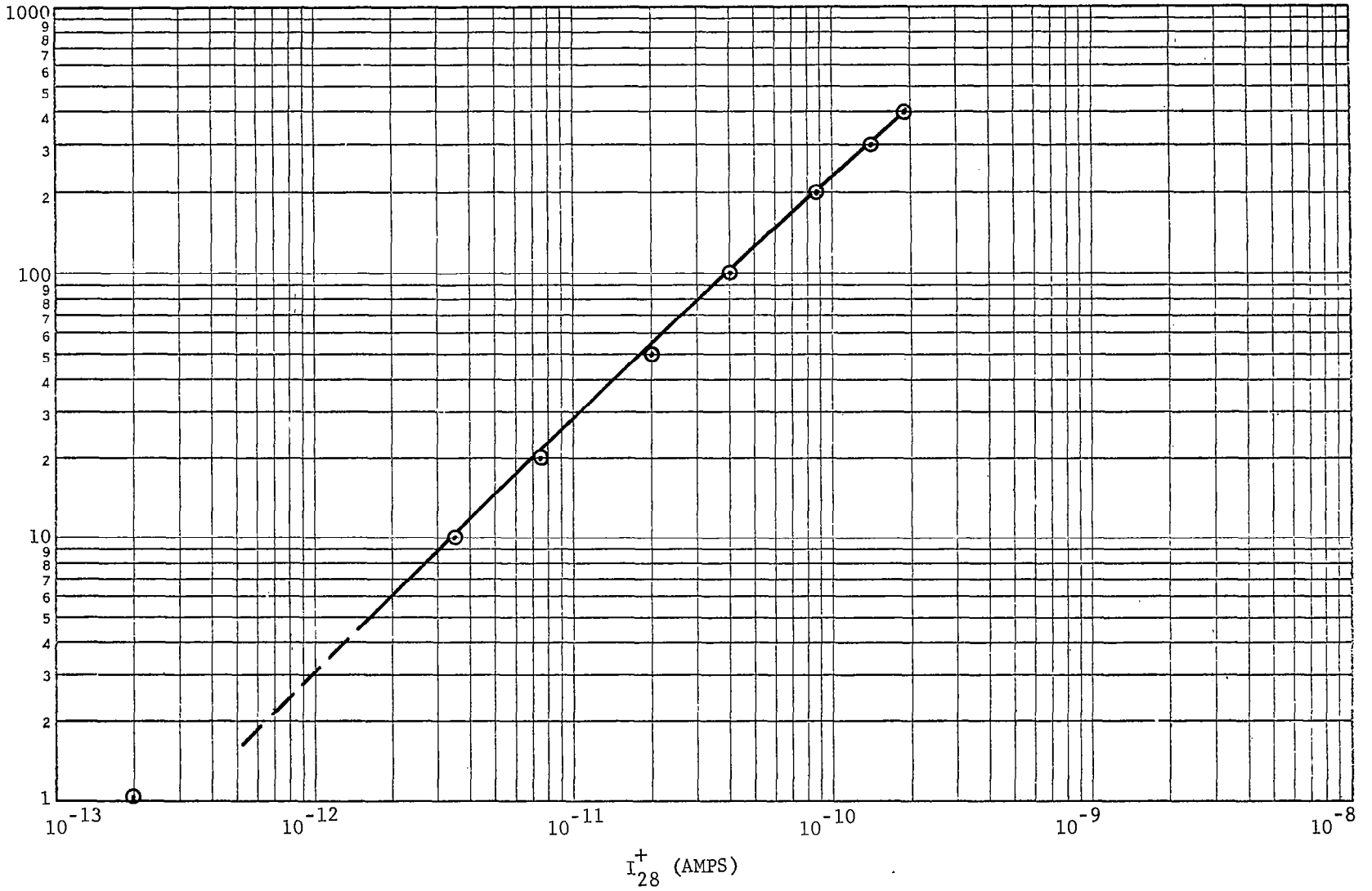

FIGURE 141
LINEARITY CURVE FOR ANALYZER S/N 04

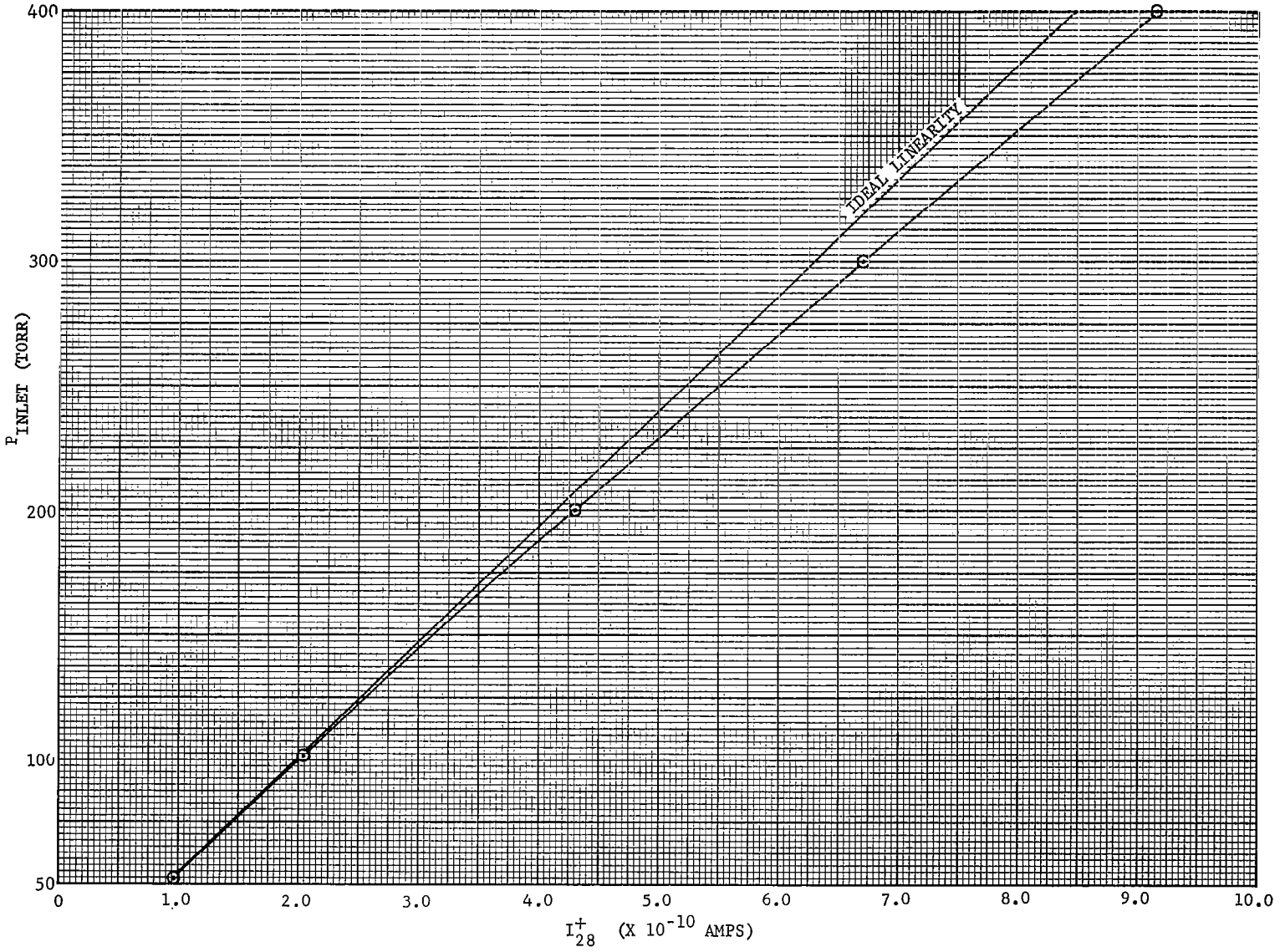

FIGURE 142
EXPANDED LINEARITY CURVE
ANALYZER S/N 01

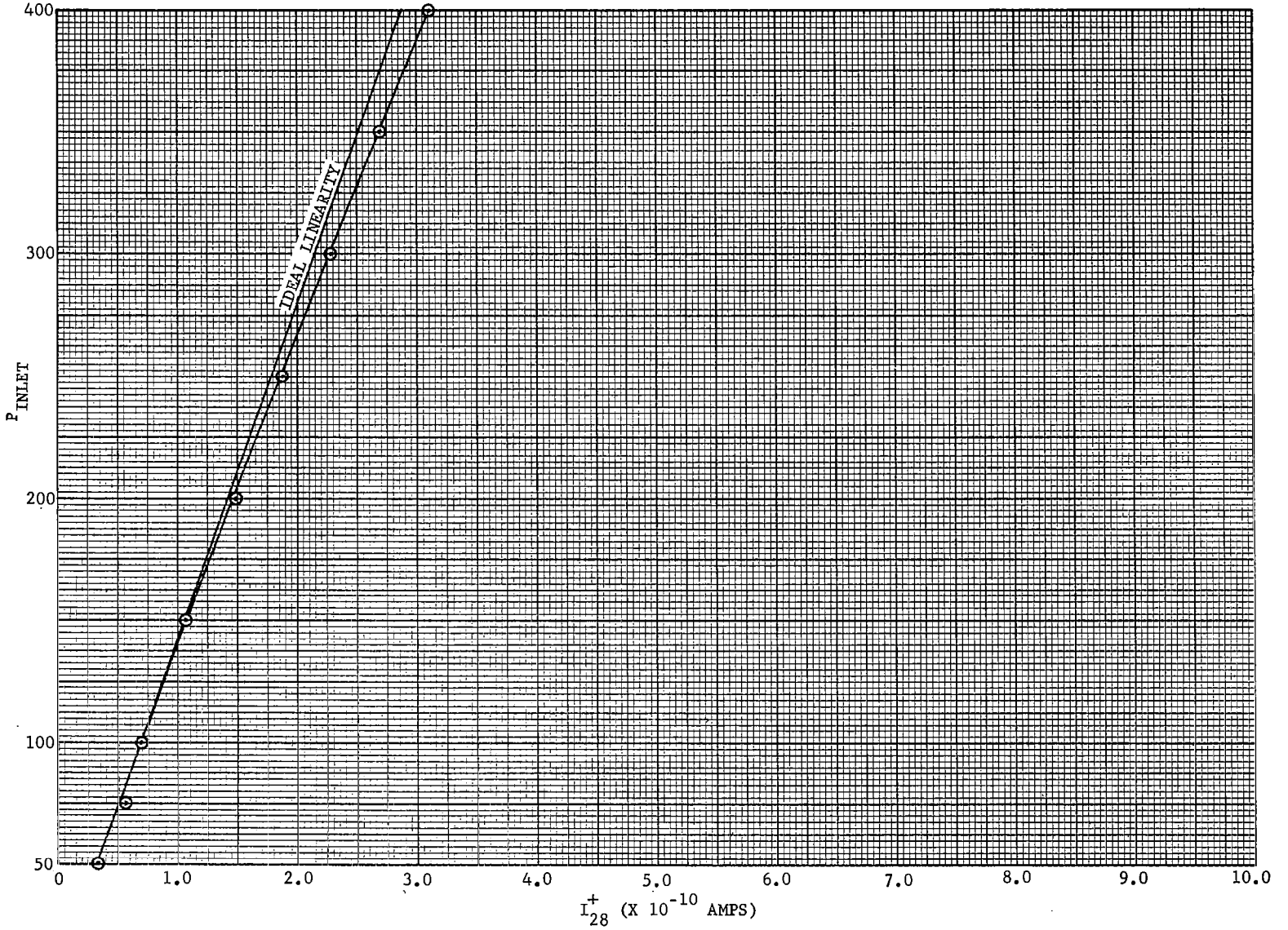

FIGURE 143
EXPANDED LINEARITY CURVE
ANALYZER S/N 02

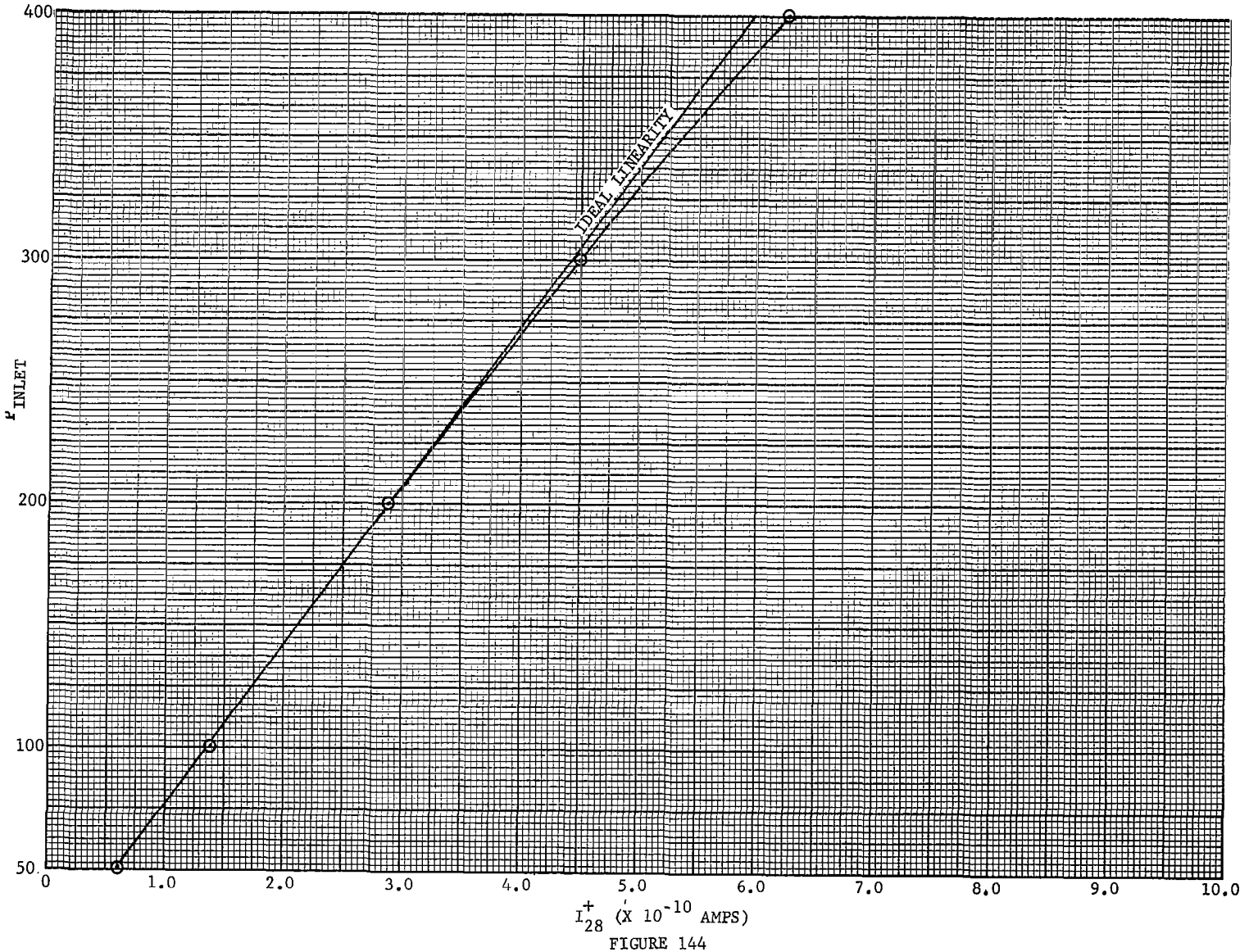

FIGURE 144
EXPANDED LINEARITY CURVE
ANALYZER S/N 03

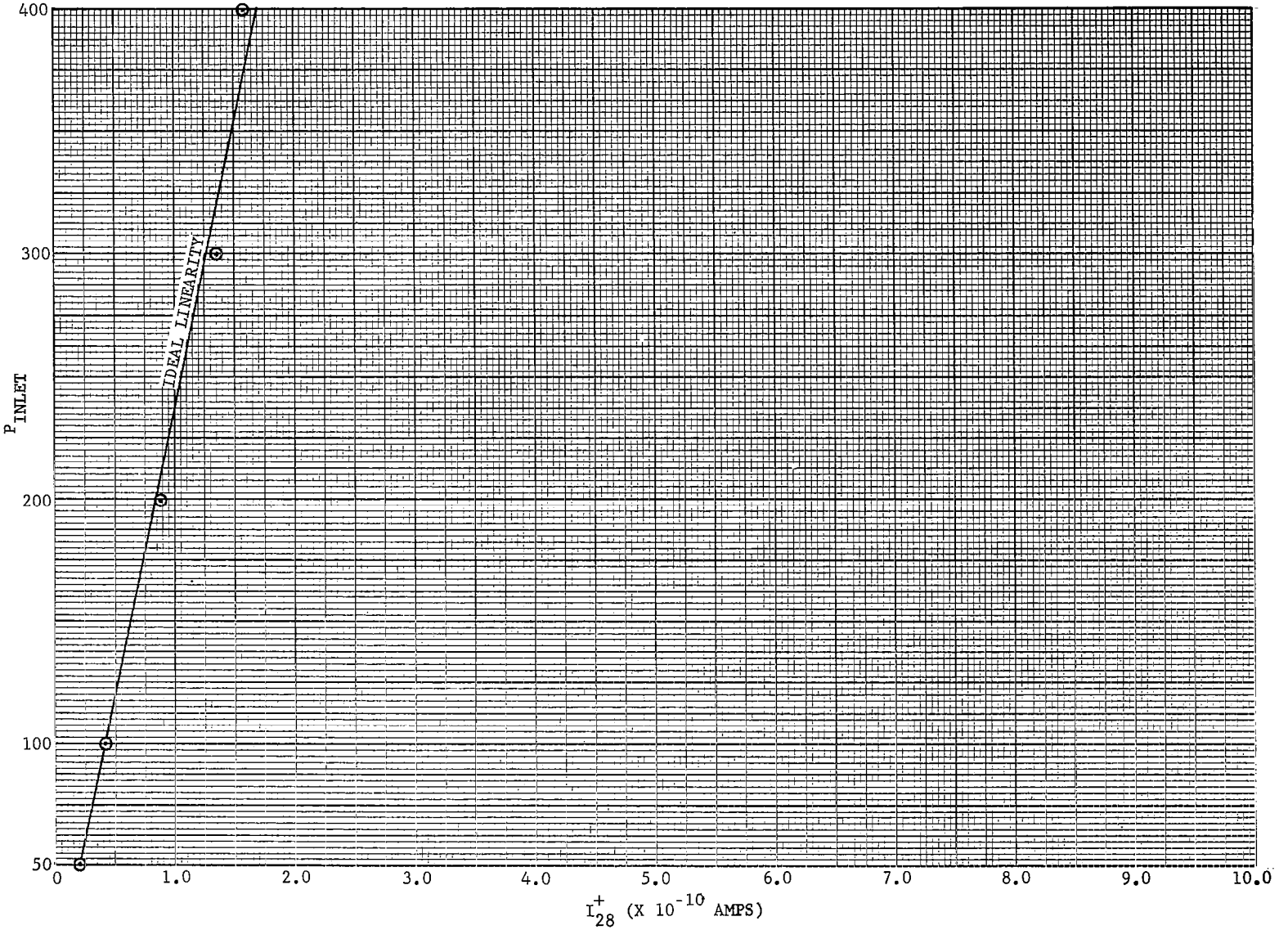

FIGURE 145
EXPANDED LINEARITY CURVE
ANALYZER S/N 04

peak'. Data was taken to the relative alignments of the collectors and is presented in Figures 146 through 149. It can be seen that while some adjustment is required that the peaks line up fairly well. Calculations have been performed which indicate that the required adjustment is well within the adjustable range of the collectors. It should be noted that in the case of m/e 28 and m/e 32, which are on the same collector assembly, that the peaks are well aligned.

DETECTIBLE LIMIT

The detectible limit for the system may be computed from a knowledge of the system sensitivity and the detector output noise and drift levels. The output noise and drift levels (after warmup) can be conservatively stated at ± 10 mV. Therefore with an adjusted sensitivity of 2.5×10^{-2} volts/torr for N_2 at m/e 28 the minimum detectible partial pressure of N_2 assuming a signal to noise ratio of unit is 0.4 torr. This is better than design goal by a factor of 2.5. This could be useful for applications in which a lower detectible limit is desirable or in case where an increased time response is necessary. It should further be pointed out that the 10 mV limit given above is dependent upon drift considerations and that this can be reduced significantly. As a result it is conceivable to talk about detectible limits a factor of 10 or more better than the design goal.

ELECTRONICS SUBSYSTEM

The electronics subsystem was checked out prior to mating with the analyzer. On all four systems all modules were functional and operating within requirements for output ranges, regulation and ripple. No difficulties were encountered in mating the electronics to the analyzer. The interface areas are the detectors, the electrode voltages, and at the filament-emission regulator. The performance of the detectors was not significantly affected by the collectors since original noise tests were done with a simulated collector capacitance of 10 pF. Some modification of the electrode bias supply system was required in order to interface with the desired electrode voltages but satisfactory performance resulted. Originally it had been assumed that the anodes and electron accelerators would be operated at the same potential. Tests conducted on the engineering test model revealed that improved ion source performance resulted if these voltages could be made unequal and therefore the voltage divider network had to be altered to allow the anode voltage to be obtained at a point somewhat below the electron accelerator potential. The required electrode voltages were sufficiently close for the four units that only minor differences were necessary in the wiring of the voltage divider networks and transformer winding jumpers in order to mate the supplies with the ion source electrodes. The emission regulators were found to perform satisfactorily with the filaments of the electron guns and the ion source operation was not appreciably affected by switching from the dc operation of the laboratory electronics to the ac operation of the flight emission regulator. The voltages on the filament shields and the electron focus electrodes required a slight adjustment in making this change but the resulting performance was comparable to that on the dc emission regulator.

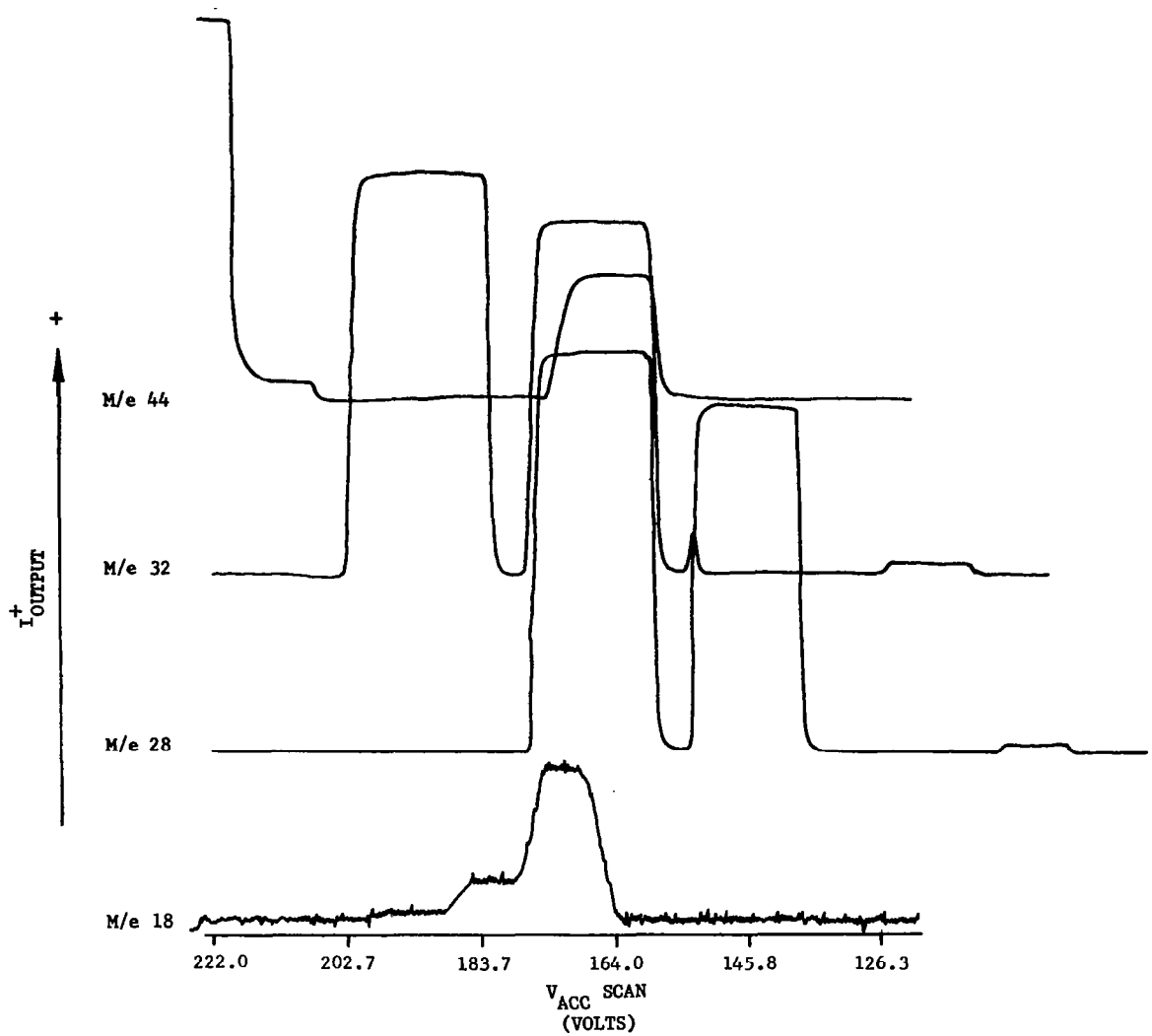

FIGURE 146
ANALYZER S/N 01
ALIGNMENT CHECK FOR EACH COLLECTOR

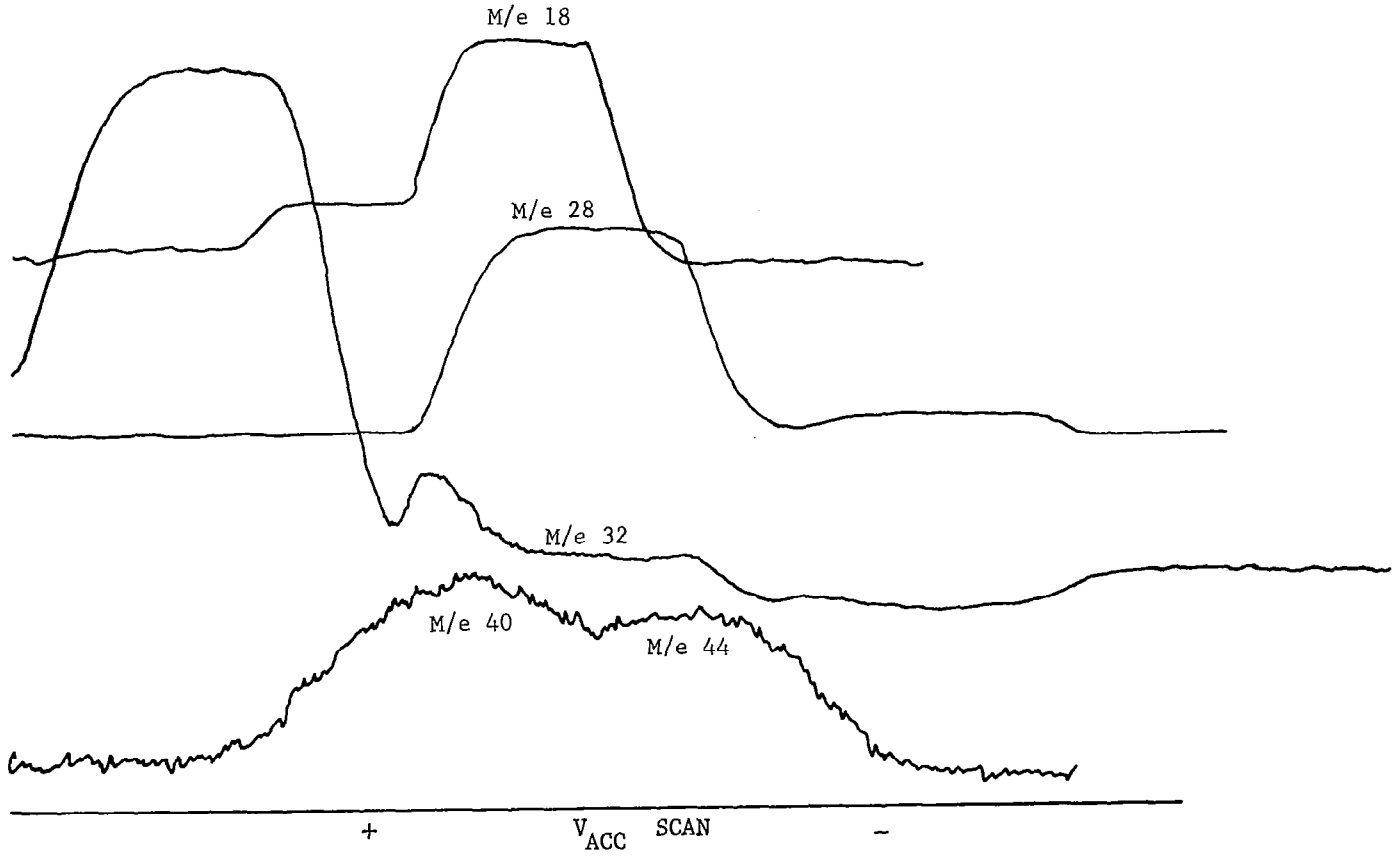

FIGURE 147
ALIGNMENT OF COLLECTORS FOR ANALYZER S/N 02

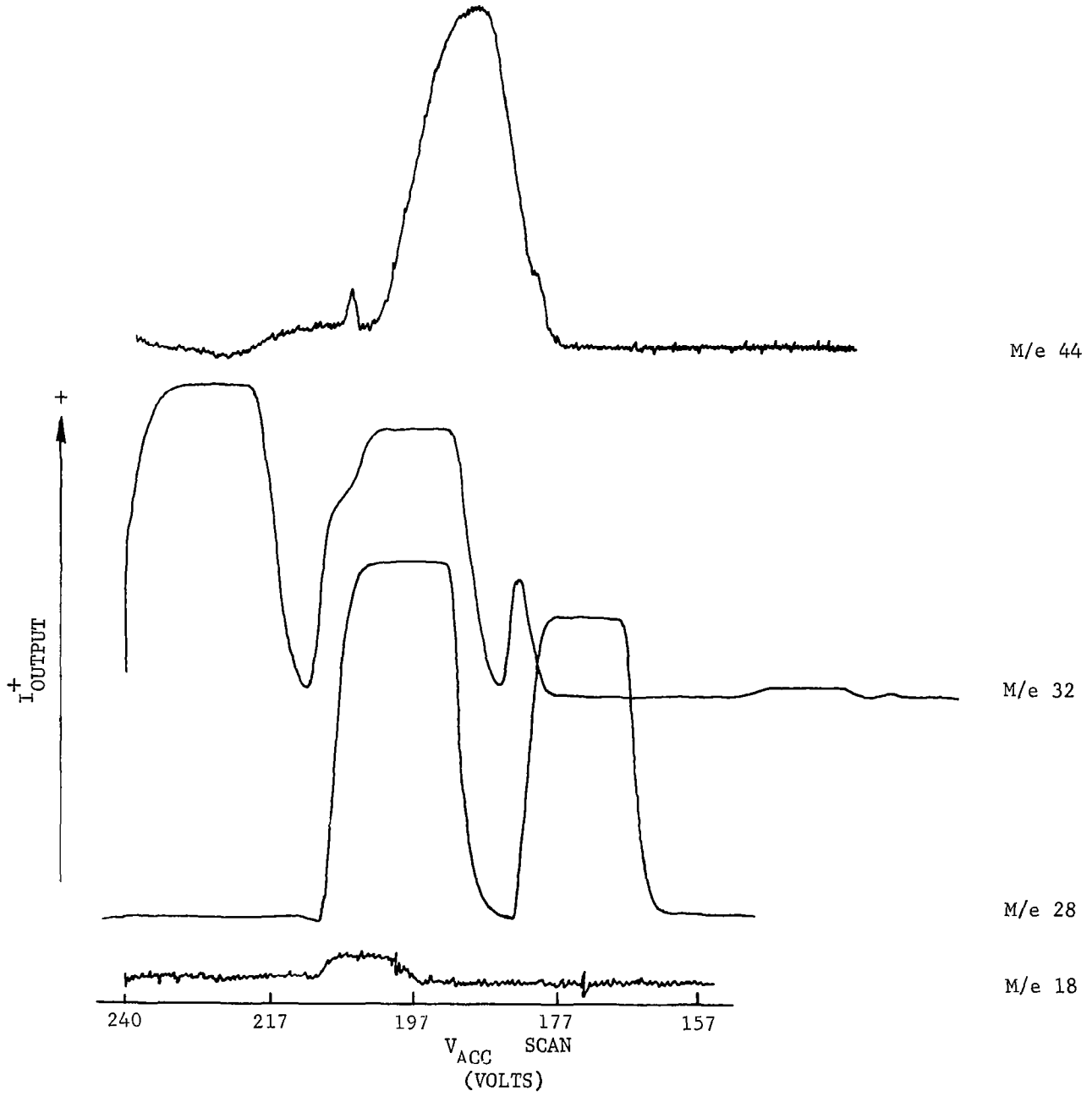

FIGURE 148
ALIGNMENT OF COLLECTORS FOR ANALYZER S/N 03

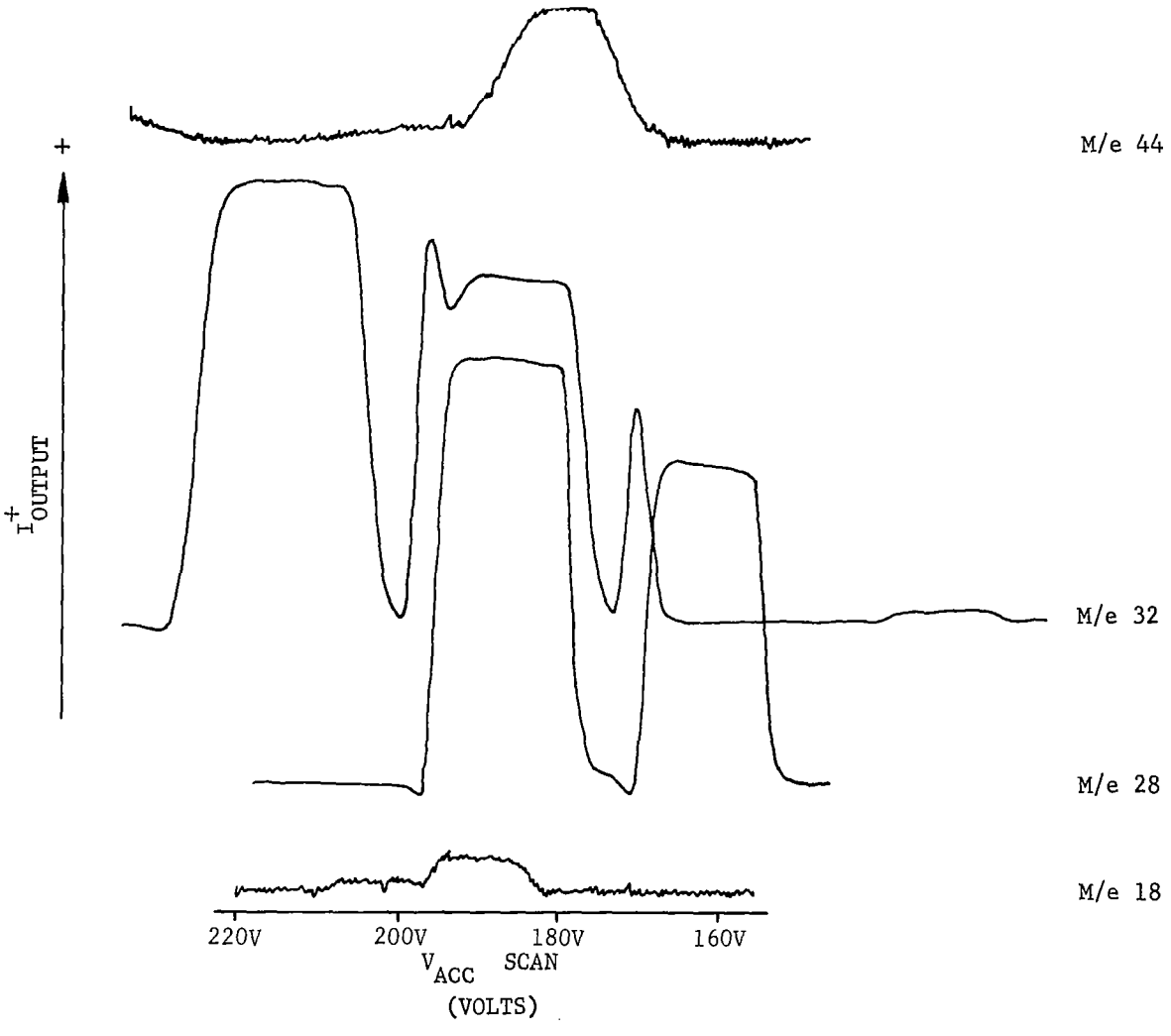

FIGURE 149
ALIGNMENT OF COLLECTORS FOR ANALYZER S/N 04

It was found that it would be desirable to have an increased upper range for adjustment of the emission current level. This can readily be obtained by increasing the number of turns on the secondary of the filament transformer. All of the electronics modules may be properly compensated for operation over the range of 40 to 90°F by replacing some metal film resistors with wire wound resistors and selecting a few components in test.

The power required for operation of the system was found to be less than the reduced design goal of 3.5 watts in all cases as shown in Table 26.

CONCLUSIONS

This report covers the extended testing of the engineering test model and the four flight prototype Two Gas Atmosphere Sensor Systems. Summary data from the testing of these units has been given in this report. In addition, the results of an emitter study have been presented showing an improved emitter material. The majority of the significant parameters have been examined and have been found to meet or better the design goals.

The demonstration of the performance of four instruments in addition to the engineering test model is a firm indication of the soundness of the design. In a few areas it has been necessary to limit testing for time and cost control purposes. It is anticipated that further testing will be carried out by Langley Research Center to supply information in these areas. Supporting programs are presently being carried out in several areas to improve the instrument beyond original contract requirements. These include the development of an ion pump and a direct molecular flow inlet leak as well as the improvement of the analyzer magnet.

The success of this development effort has demonstrated the value of carefully planned and sequenced programs. This program commenced with a study phase (Phase I) followed by a design phase which is verified by fabrication and testing of an engineering test model (Phase IIa), and concluded with the fabrication and test of several prototype units (Phase IIb). In addition, the program has been supported with study efforts in several key areas. The application of these instruments in simulated tests such as the 60 day test with the McDonnell Douglas Space Cabin Simulator is also providing valuable data for evaluation of the instrument. By establishing this firm base of design knowledge and test experience it will be possible to enter the flight phase of this program with a high degree of confidence and assurance of success.

ADDENDA

for

TWO GAS ATMOSPHERE SENSOR SYSTEM (MASS SPECTROMETER)

Phases IIa and IIb

ION PUMP DEVELOPMENT

The objective of the Ion Pump study was to obtain an adequate understanding of the Ion Pump System so that a 4 liter/second pump could be constructed which would have minimum size, weight, and power consumption. The steady state operation of the pump was expected to be in the pressure range of 5×10^{-7} torr to 5×10^{-6} torr.

The stated objective of this contract were initially based on the fact that published literature would supply the necessary understanding of the Penning Discharge Ion Pump. Consultations with the technical staff at the Ultek Division of Perkin-Elmer were expected to supply the design knowledge which was not adequately covered in the published literature. However, it was found that these two sources were inadequate to establish the required optionized analysis and design. For this reason it was necessary to utilize considerably more of the contract time in deriving a model for the ion pump operation. This model was then used to give criteria for ion pump optimization.

SPUTTER ION PUMP THEORY OF OPERATION

The theory of the Penning Discharge Ion Pump is very complex and a complete presentation of the technical development would be very lengthy. However, a brief discussion of the theory will be given along with the important equations and graphical presentations of fundamental relationships.

The physical construction of the Penning Discharge Cell is rather simple as can be seen in Figure 150. Although the physical construction is simple the discharge phenomena is very complex.

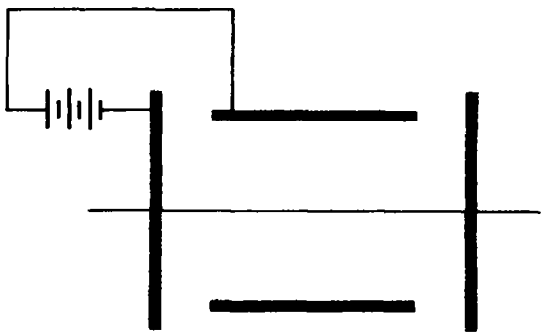

FIGURE 150

Penning Discharge Cell

Qualitatively, the discharge is explained by the following steps:

a. Electrons are initially produced byfield emission or by ionization from background radiation.

b. These electrons are accelerated toward the anode, but because of the magnetic field they are confined to a helical path that is parallel to the magnetic field.

c. The trapped electrons oscillate, between the two cathodes until they collide with a neutral particle.

d. Some of these collisions produce ions which make more electrons available to the discharge.

e. Elastic and inelastic collision allow the electrons to move toward the anode.

f. The ions are focused to the cathode where secondary electrons are released upon ion input.

g. The cathode secondary electrons enter the cell, but would be captured by the opposite cathode (because of the initial electron energy) if there were not a trapping mechanism.

h. A dynamic electrical field is established in the anode to cathode gap that causes energy to be removed from the secondary electrons. This allows the electrons to be trapped and sustains the discharge.

These eight steps present a closed loop, feedback system in which the ions and cathode secondary electrons form the feedback loop. Without the production and entrapment of secondary electrons the discharge would not be self-sustaining.

As the number of electrons in the discharge increases, a space charge potential develops which depresses the potential on the axis of the cell. This virtual cathode establishes a radial electric field, thus the Penning Discharge Ion Pump is converted into a cross field device. This cross field causes the electrons to travel in cycloidal paths, normal to the direction of the space charge field. The electrons that are in the cycloidal paths have lost most of their axial velocity so that their angular velocity is their major velocity component.

The gain of the discharge is high if each primary electron can ionize a neutral particle with resulting equal vector velocities for both the primary and secondary electrons. Such a well-ordered system is possible if the primary energy is equal to twice the binding energy of the electron in the neutral particle. Due to the loss of energy and the space charge field, the primary and the secondary electrons move toward the anode until they gain an average energy that is equal to twice the ionization potential. To obtain this well-ordered system the space charge potential must have the correct value. If the anode voltage is not adequate to obtain the required space charge potential then the

discharge is compressed toward the anode by the development of a hollow cylinder which is concentric with the axis of the cell. The radius of the hollow region will change in order to establish the correct space charge field. The radius of this neutral colum is designated r_k and the potential at this radius is designated V_k. To maintain this neutral colum the ions that are produced near the anode surface must be focused to impact with the cathode surface at the radius r_k. In this way the majority of the secondary electrons enter the discharge at this radius. This ion focusing requirement determines the value of V_k.

DEVELOPMENT OF A MODEL FOR ION PUMP OPERATION

When this model of the Penning Discharge is analyzed the following equation is obtained:

$$(V_a - V_k)\Phi = 2(Br_a)^2 \frac{e}{m_e} \qquad (1)$$

where:

V_a = anode potential

V_k = virtual cathode potential

B = magnetic flux density

r_a = anode radius

e = electron charge

m_e = electron mass

The function Φ defines the space charge potential distribution and is related to the geometric properties by:

$$\Phi = \frac{4}{1 - \delta^2 + 2\delta^2 \ell n\delta} \qquad (2)$$

where:

$$\delta = r_k / r_a$$

The term Φ is plotted in Figure 151 as a function of δ. The discharge potential drop, $V_a - V_k$, is plotted in Figure 152 as a function of Br_a, for various values of Φ.

Since no numerical values are used in these algebraic equations, any consistant set of units can be used. The graphic representations were computed in the MKS system of units; however, the display is in the units that are most commonly used in their respective fields of science.

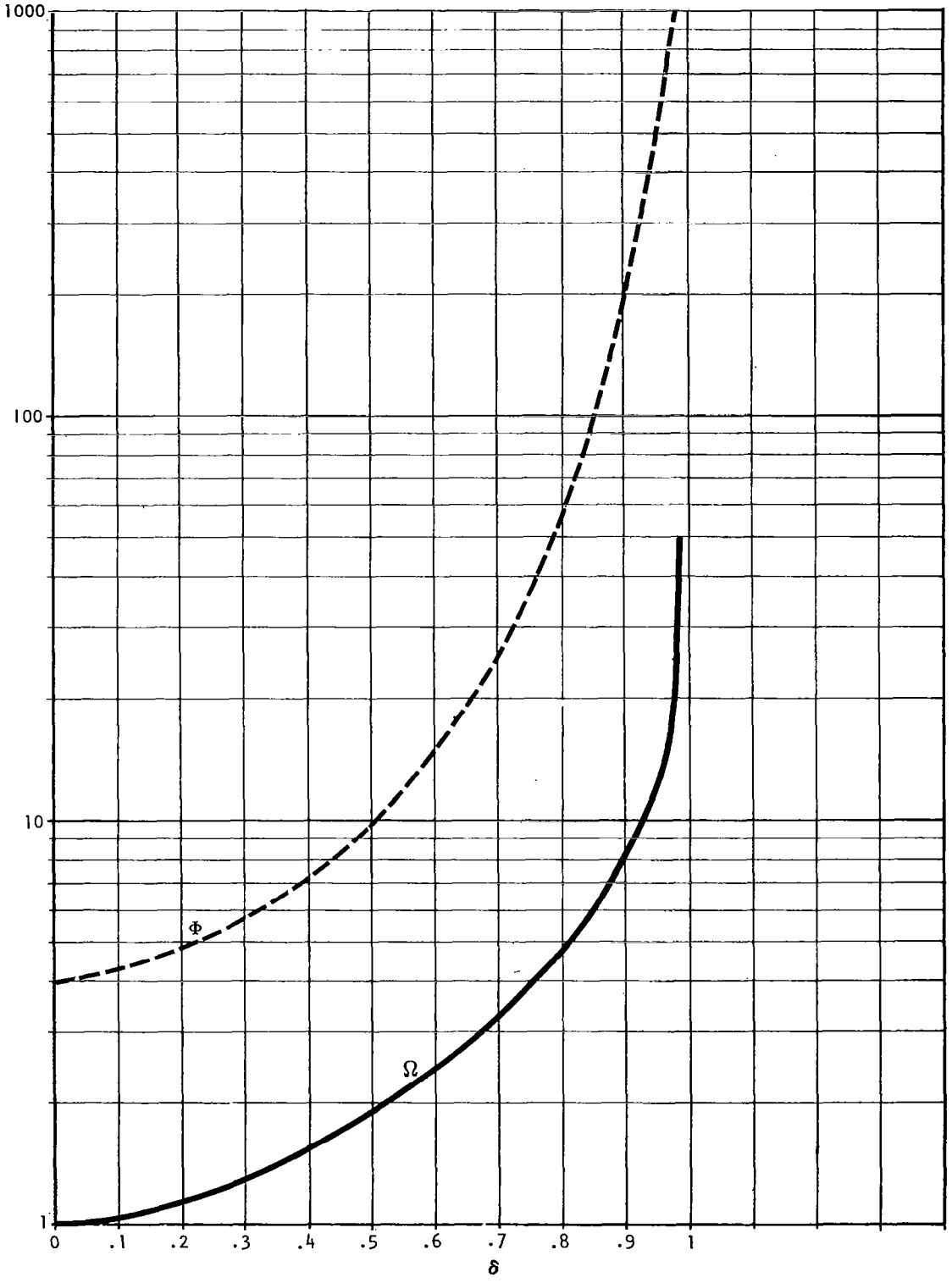

FIGURE 151

POTENTIAL AND FIELD DISTRIBUTIONS AS A FUNCTION OF δ FOR A PENNING DISCHARGE CELL

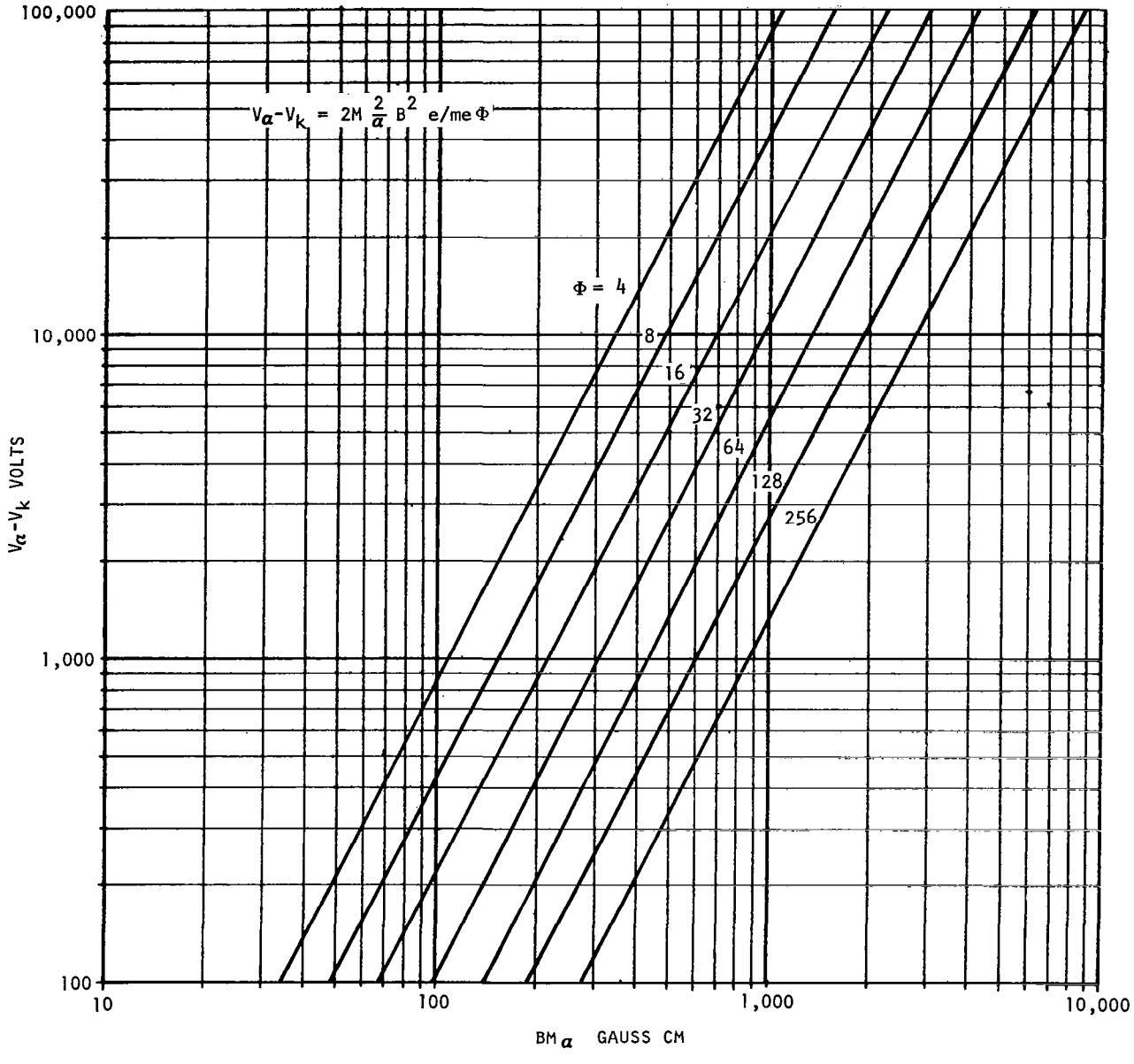

FIGURE 152

DISCHARGE POTENTIAL DROP AS A FUNCTION OF
THE PRODUCT OF THE MAGNETIC FLUX DENSITY AND
THE ANODE RADIUS WITH VARIOUS VALUES OF Φ

When the ion focusing requirements are analyzed, two limiting cases are found to exist:

$$V_k/V_a = \frac{1}{1 + \delta^2 \zeta^2} \qquad \text{(Case 1)}$$

$$= \frac{1}{1 + 1/4\, \zeta^2\, (\delta + 1)^2} \qquad \text{(Case 2)}$$

In Case 1 the focusing action of the electrostatic field brings the ions from the anode to a focus on the cathode at the radius r_k. In Case 2 the focusing takes the ions from the anode and returns them across the axis to the anode radius, r_a, where they impact the cathode surface.

Case 1 focusing gives the highest discharge gain and it may be required when the anode voltage is low. At anode voltages that are near the saturation levels, a high discharge gain is not required and the system shifts to Case 2 focusing. The ratio V_k/V_a is plotted in Figure 153 for both Case 1 and Case 2 focusing as a function of δ.

In a well ordered discharge the average electron velocities are about equal for all levels; thus the mean free path length would be achieved at about the same time, for all levels. This results in the average number of ions from each level being generated at about the same time. The ion current is obtained by considering the average number of ions that are produced in this time interval. The ion current is then obtained from the rate of charge production:

$$I_{ion} = dq/dt$$

$$= q/\tau$$

$$= \rho L_a r_a^2\, (1 - \delta^2) \Big/ \left(\frac{1}{2S\rho \sqrt{\frac{e}{m_e}\, V_b}} \right)$$

where:

ρ = space charge density

S = ionization probability at $2V_b$

V_b = ionization potential

p = pressure

L_a = length of the anode cell

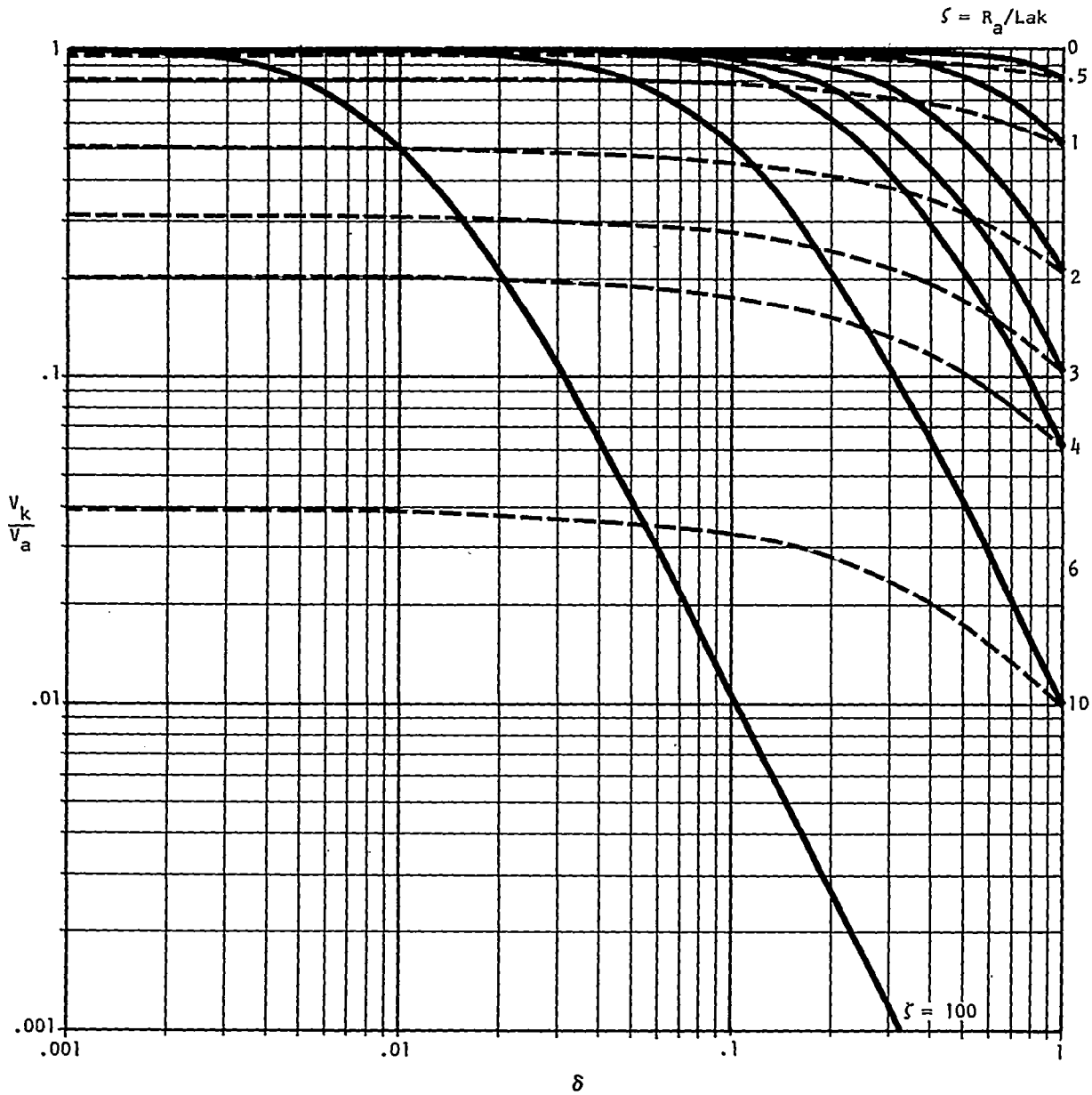

FIGURE 153

RATIO OF THE VIRTUAL CATHODE POTENTIAL TO THE ANODE POTENTIAL AS A FUNCTION OF δ FOR VARIOUS VALUES OF ζ

The ratio of the volume current density to cell pressure is given by:

$$\frac{J_v}{p} = 4 \epsilon_o B^2 \left(\frac{e}{m_e}\right)^{3/2} (1 - \delta^2) \quad S\sqrt{V_b} \qquad (3)$$

Since $\rho = 2 \epsilon_o B^2 \frac{e}{m_e}$

where ϵ_o = permitivity of free space

The ratio of volume ion current density to the pressure is plotted in Figure 154 as a function of the magnetic flux density, for various values of δ.

The current voltage relationship for the Penning cell can be obtained by the use of equations (1), (2) and (3). An explicit solution cannot easily be obtained because of the complicated function $\Phi(\delta)$; however, an approximate solution can be obtained for the case where the hollow region is near the anode.

If $\delta \rightarrow 1$

then $\frac{J_v}{p} = \delta \epsilon_o B \frac{e}{m_e} \quad S\sqrt{V_b} \quad \sqrt{2/3 \ (V_a - V_k)} \ / \ r_a$

This expression applies until saturation effect begins to apply. Saturation effects are expected to begin when $\delta \simeq 0.84$ and it occurs by slight increase in δ with a voltage increase but the effect on the current is cancelled by an anode separation. Anode separation is a condition where the discharge move inward away from the anode. The measured ion current-anode voltage relationship is presented in Figure 155.

The experimental data indicates that this calculated function is reasonably accurate at voltages that are near the saturation value for J_v; however, at low voltages the measured current is much lower than the calculated value. A closer agreement is obtained when the cell geometry allows a larger cathode penetration field. This penetration helps to remove the ions from the cell. The ion removal problem is severe for ions that are produced near the anode surface, since the axial component of the cathode penetration field is zero at the anode surface. The electron space charge produces an axial field that pull the ions toward the center of the cell and traps them unless the axial component of the cathode penetration is sufficient to overcome this space charge field. Inside the cell the axial component of the penetration field increases as the radius decreases; therefore, there is some radius, r_p, at which the axial component of the space charge and the penetration field are equal. For radii which are larger than r_p the ions become trapped and tend to neutralize the electronic space charge. This results in a limited area

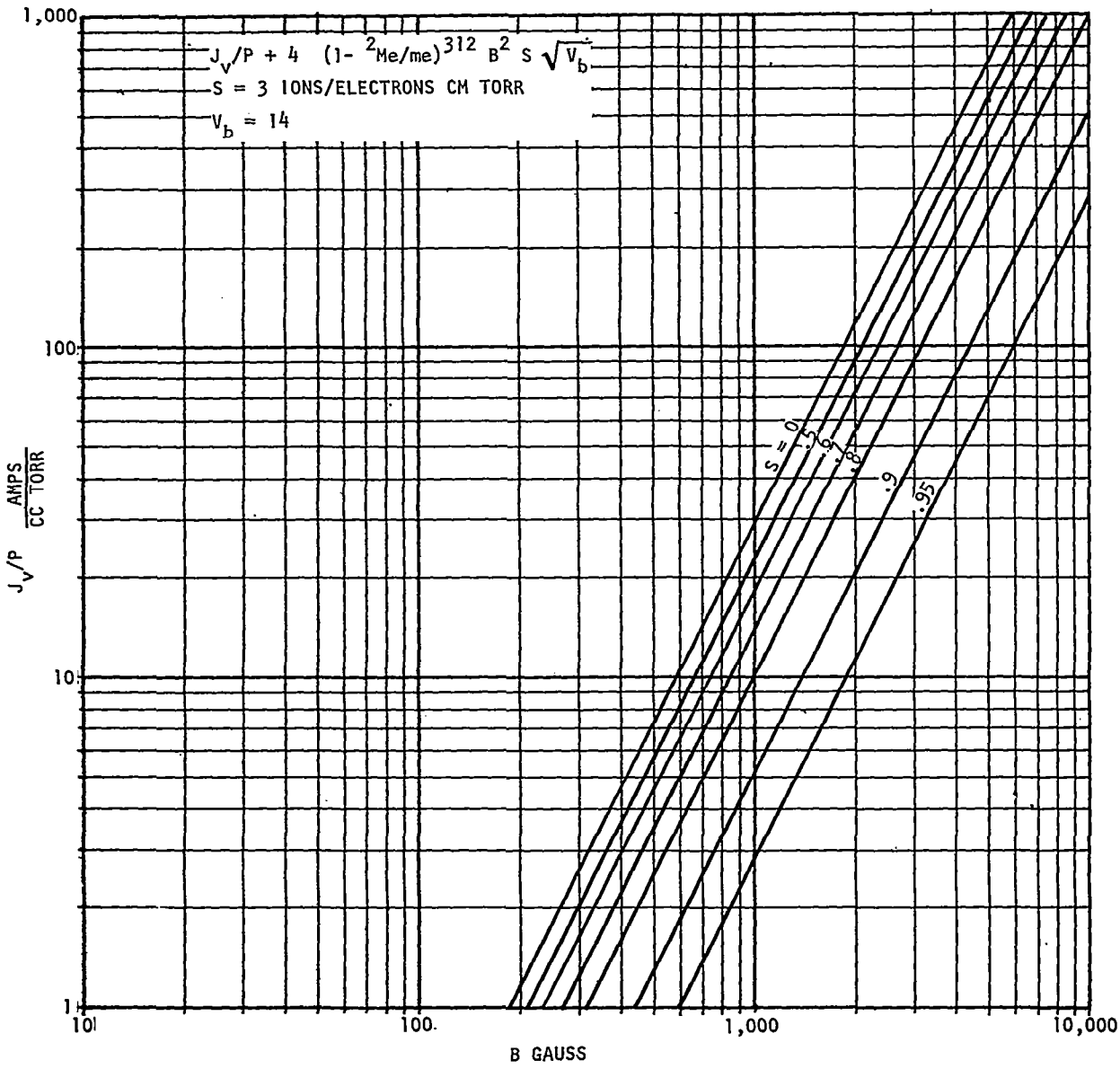

FIGURE 154

VOLUME CURRENT DENSITY PER UNIT PRESSURE AS A FUNCTION OF THE MAGNETIC FLUX DENSITY FOR VARIOUS VALUES OF δ

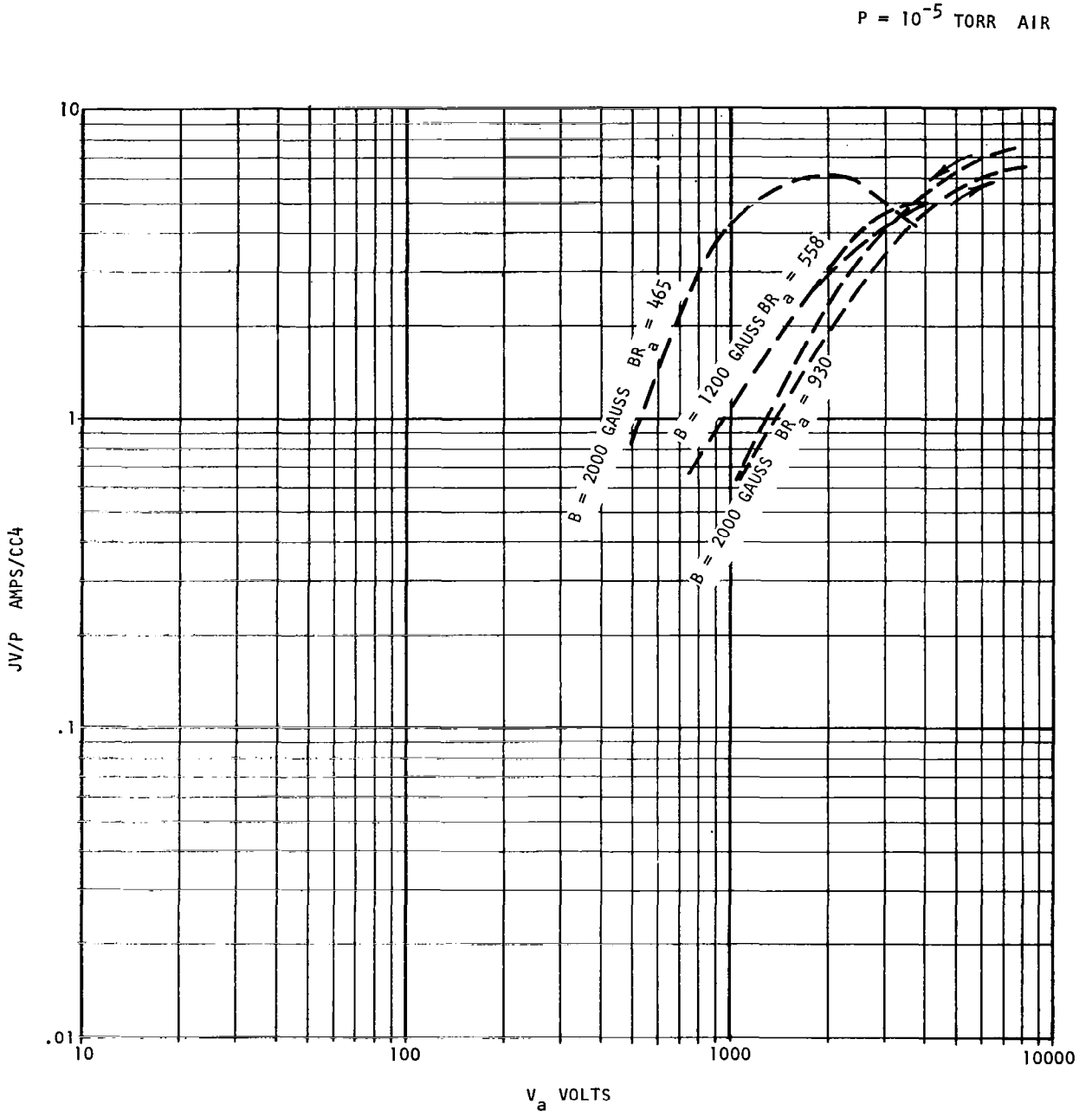

FIGURE 155

CURRENT VOLTAGE RELATIONSHIP FOR
A PENNING DISCHARGE CELL

from which an ion current can be extracted. The effective ion current production region becomes

$$A_{ion} = \pi(r_p^2 - r_k^2)$$

The radius r_p becomes the effective anode radius and it can be used in equations 1 and 3 and it is a function of the cell geometry and the anode voltage:

$$r_p = f(V_a, r_a, L_a, L_{ak})$$

where L_{ak} = cathode-anode spacing

The published experimental data indicates that the factor Br_a has an influence on the pressure dependence of the ratio I/p (where I is the anode current drawn by the cell). When Br_a is less than 1,000 gauss-cm, the ratio I/p decreases with a pressure decrease. A typical plot of I/p versus p has a region that is flat and a transition region where I/p drops to a new level. This transition extends over a pressure range which is about one decade. The pressure dependence can be explained by the secondary electron trapping mechanism. The trapping mechanism that seems to satisfy the requirements is a dynamic electrical field; it is necessary because many of the secondary cathode electrons, which are released from the cathode surfaces by ion impact, have enough initial energy to impact with the opposite cathode. The dynamic field must have the proper phase, frequency, and magnitude in order that the energy loss can be equal to the average initial energy of the secondary electrons. The power line serves to couple the two anode gaps. The gap potential would be the largest if the coupling line were to act as an anti-resonant transmission line. A transmission line which has a dynamic short at a distance equal to an odd multiple of a quarter wavelength ($[2n + 1]\ \lambda_e/4$), produces an anti-resonant line. The gap frequency is given by:

$$f_e = 1/4 \sqrt{2\frac{e}{me} V_k}\ (2n_f + 1)/(L_a + 2L_{ak})$$

where $n_f = 1, 2, 3 \ldots$

The potential of the dynamic gap field is given by:

$$V_w = 4 \sqrt{I_e \cdot p\ \overline{V}_o/C_T(1 + 1/Q)} \qquad (4)$$

where I_e = cathode electron current due to secondary emission

$\overline{V}_o$ = average initial energy for the secondary emission

Q = ratio of stored energy to the disipative energy

C_T = total line capacitance

I/p = pressure

The maximum trapping efficiency occurs when:

$$V_w \geq \overline{V}_o$$

If the above condition is not satisfied, the charge density would not be adequate to produce a well ordered system. With a low space charge density the ratio of the ion current to the pressure would be reduced. The only circumstance when the pressure has an influence on the I/p ratio is when the secondary electron trapping efficiency is not adequate to produce the maximum space charge density.

The Penning Discharge Ion Pump can be operated as a pump, if the cathode material has a high sputtering yield and can absorb the gases present in the cell. The sputtered cathode particles are released by an impacting ion and they combine with gaseous particles on some surface, preferably the anode surface. If the major pumping occurs on some region of the cathode, the pumped gases may be released when the discharge changes its focusing mode.

The actual receiver area is unimportant for the determination of the pumping speed as long as the desired pumping speed is less than the maximum pumping speed that could be obtained from the available receiver area.

The maximum pumping speed per unit area is obtained if all of the incident particles are absorbed on the surface.

$$S_m = \sqrt{\frac{KT}{2\pi M_g}} \qquad (5)$$

where K = Boltzmann's contant

T = absolute temperature

M_g = mass of the gas molecule

This expression is plotted in Figure 156 as a function of the molecular weight for several values of temperature.

The sputtering rate is directly related to the ion current and the pumping speed is directly related to the sputtering rate; therefore, the pumping speed is directly related to the ion current and is given by:

$$S_p = c\,\gamma\, m_s\, I/p\, e$$

The required I/p ratio is given by:

$$I/p = \frac{S_p e}{c\,\gamma\, m_s}$$

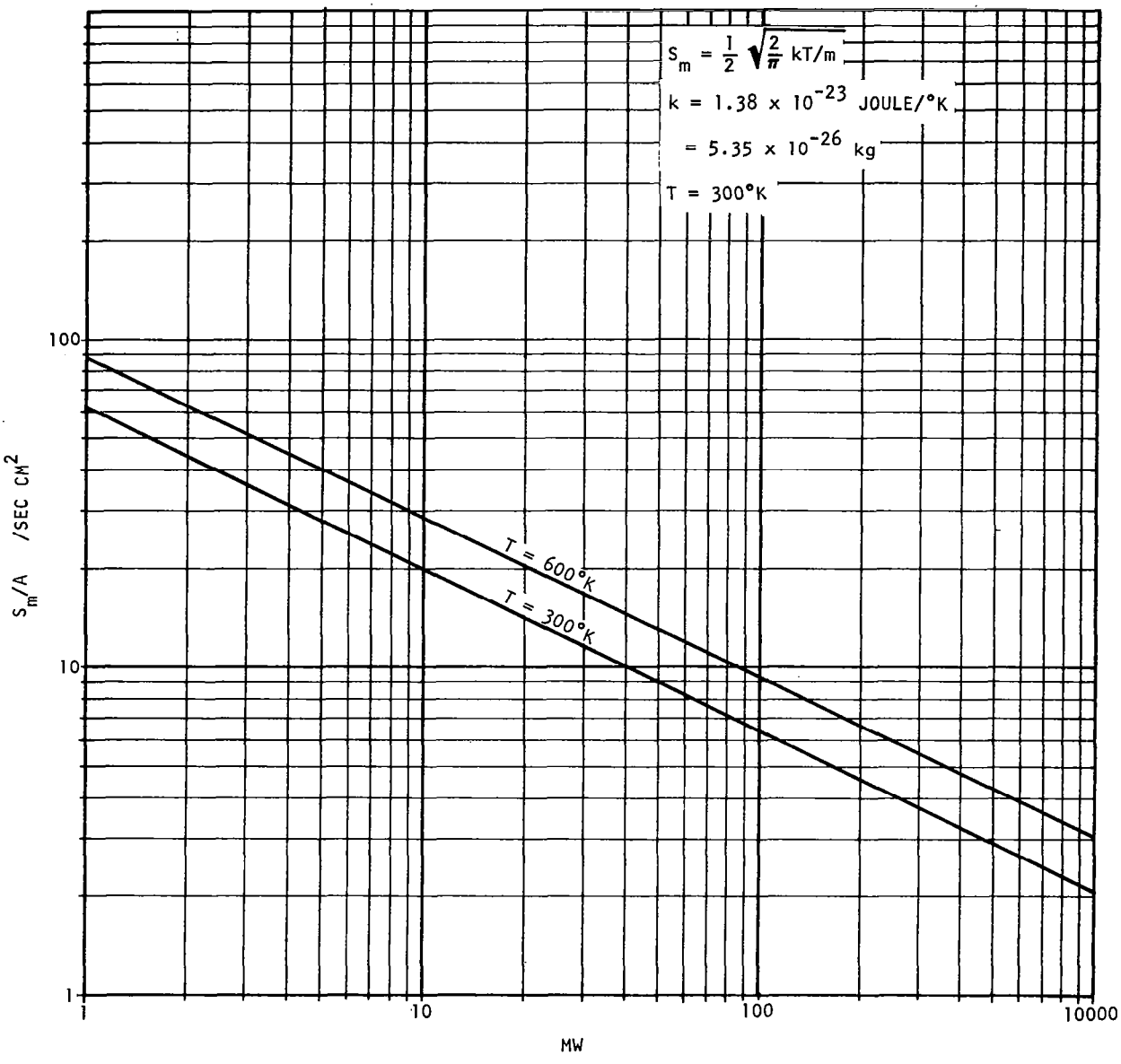

FIGURE 156

MAXIMUM PUMPING SPEED PER UNIT AREA
AS A FUNCTION OF MOLECULAR WEIGHT

c = getter capacity

m_s = mass of the sputtered atom

γ = coefficient of sputter yield

e = electronic charge

This expression is plotted in Figure 15.7 as a function of the pumping speed for several values of sputtering yield. For some materials the sputtering yield has an angular dependence; however, the published data indicates that titantium does not. When there is an angular dependence, the sputtering yield varies inversely with the cosine of the angle between the incident ion beam and the surface normal.

Ions that are produced near the hollow region have very little energy, 100 to 200 volts in some cases. Their energy is not sufficient to produce sputtering, but may penetrate the cathode deep enough to remain buried. Some ions may escape the discharge near the end and would not be focused. These ions would come from a region near the hollow center, but would impact the cathode at a radius which is larger than the radius of the hollow region. This cathode region is relatively free from sputtering, so that ions which are buried there remain buried. Ions which are buried below the hollow region are quite likely to be released by subsequent sputtering. Even the ions which are buried above the hollow region can be released by sputtering if a change in the discharge parameters causes the hollow region to expand.

Inert pumping is thought to be accomplished by ion burial. Recently, there have been proposals that explain the inert pumping by a back scatter mechanism where an ion is neutralized on impact with the cathode and back scattered with enough energy to be buried in the anode surface. In order that stable inert gas pumping may be obtained it is necessary to reduce the release of buried ions.

A slotted cathode and a triode pump have been used to enhance the inert pumping speed by providing a distinct ion burial region and a distinct sputtering region. Another technique, that has been used to improve the inert gas pumping speed is the use of different materials for the two cathodes; for example, titanium and tantalum. This pump has a higher pumping speed for pure inert gases and the best explanation for this increase seems to be that the tantalum has a much higher back-scatter coefficient for argon ions that titanium. This back scatter allows the inert atoms to be transported to the anode surface with sufficient energy for burial. Since there is no sputtering on the anode surface, the particle buried there would be stable.

The life time of an ion pump is determined by the thickness of the cathodes. When sputtering has progressed to a point where a hole is formed through the cathode, the cathodes should be replaced. The cathode volume that is required is given by:

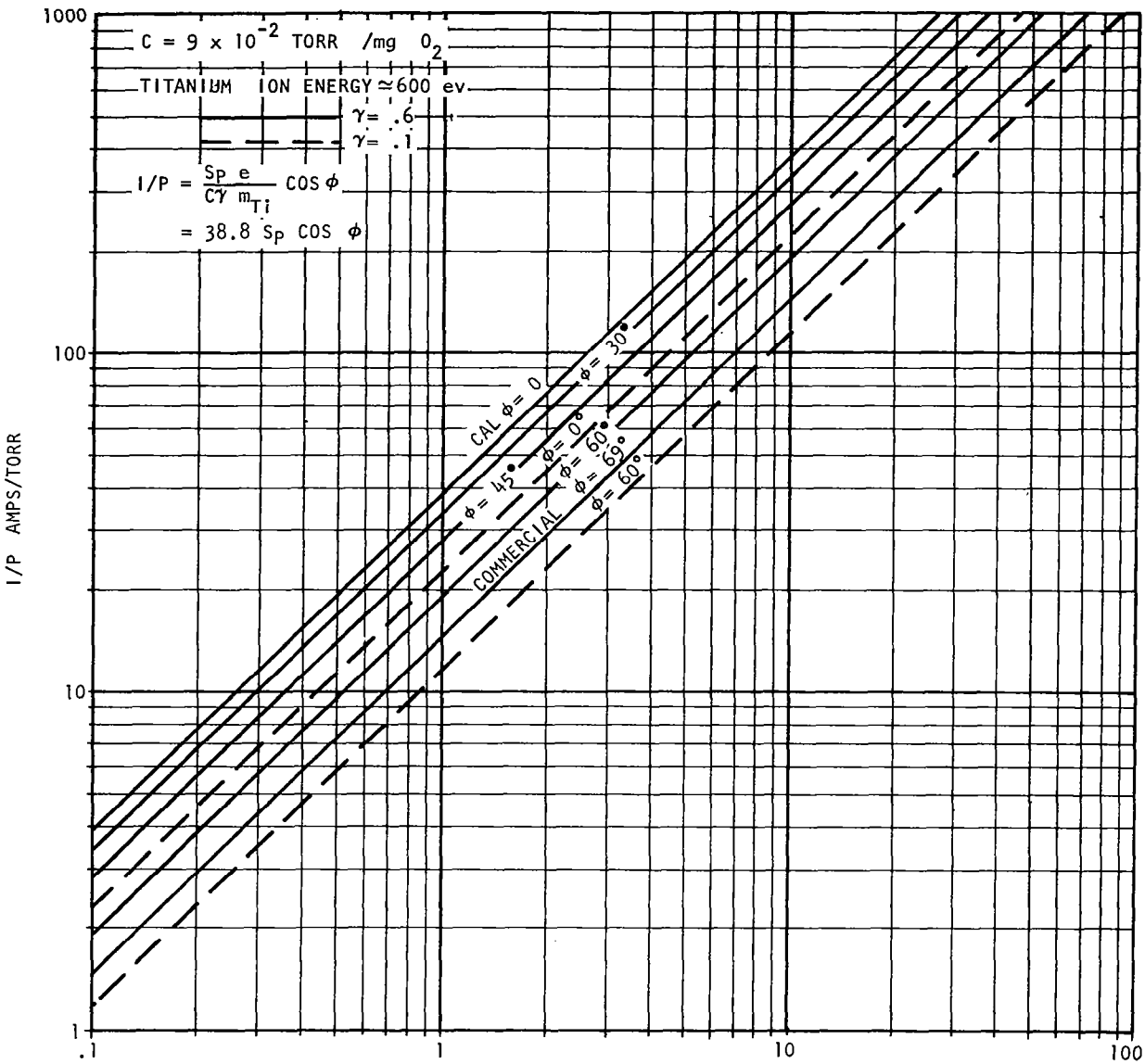

FIGURE 157

REQUIRED GAUGE CONSTANT
AS A FUNCTION OF PUMPING SPEED

$$U_c = \frac{p\ S_p t}{cD} \qquad \text{(Case 1 focusing)}$$

$$U_c = p\ S_p t/cD(1 - \delta^2) \qquad \text{(Case 2 focusing)}$$

where t = time required for a hole to be sputtered through the cathode

D = density of the cathode material.

The ratio of cathode volume to pressure is given in Figure 158 as a function of life time for various values of δ, and for case 1 ion focusing.

One of the most important aspects of the design of an optimized, lightweight ion pump is efficient magnet design.

The volume of the required magnet is given by:

$$U_m = \frac{f_1\ f_2}{H_d\ B_d}\ \Psi \frac{\Lambda\ k_1\ S_p}{(1 - \delta)}$$

Where f_1 = mmf leakage factor $\simeq 1.2$

f_2 = flux leakage factor $\simeq 2$

H_d = magnet field intensity at the point of maximum energy

B_d = magnet flux density at the point of maximum energy

$$k_1 = \frac{e}{4\,c\,\delta\,\epsilon_o \left(\frac{e}{m_e}\right)^{3/2} S \sqrt{V_b}}$$

$$\Lambda = \frac{4}{\pi}\left[1 + \sqrt{2}\ k_2^{3/2} \sqrt{\frac{\pi(1 - \delta^2)}{4k_1\ S_p B}} \left\{\frac{4}{\pi} + 0.03PB^2 + \frac{B^{3/4}\ S_p}{5.24}\left(\frac{\pi(1 - \delta^2)}{k_1\ k_2}\right)^{1/4}\right\}\right]$$

$$\Psi = \frac{4}{\pi} + 0.03pB^2 + \frac{B^{3/4}\ S_p^{1/4}}{5.24}\left(\frac{\pi(1 - \delta^2)}{k_1\ k_2}\right)^{1/4}$$

where $k_2 = Br_a$

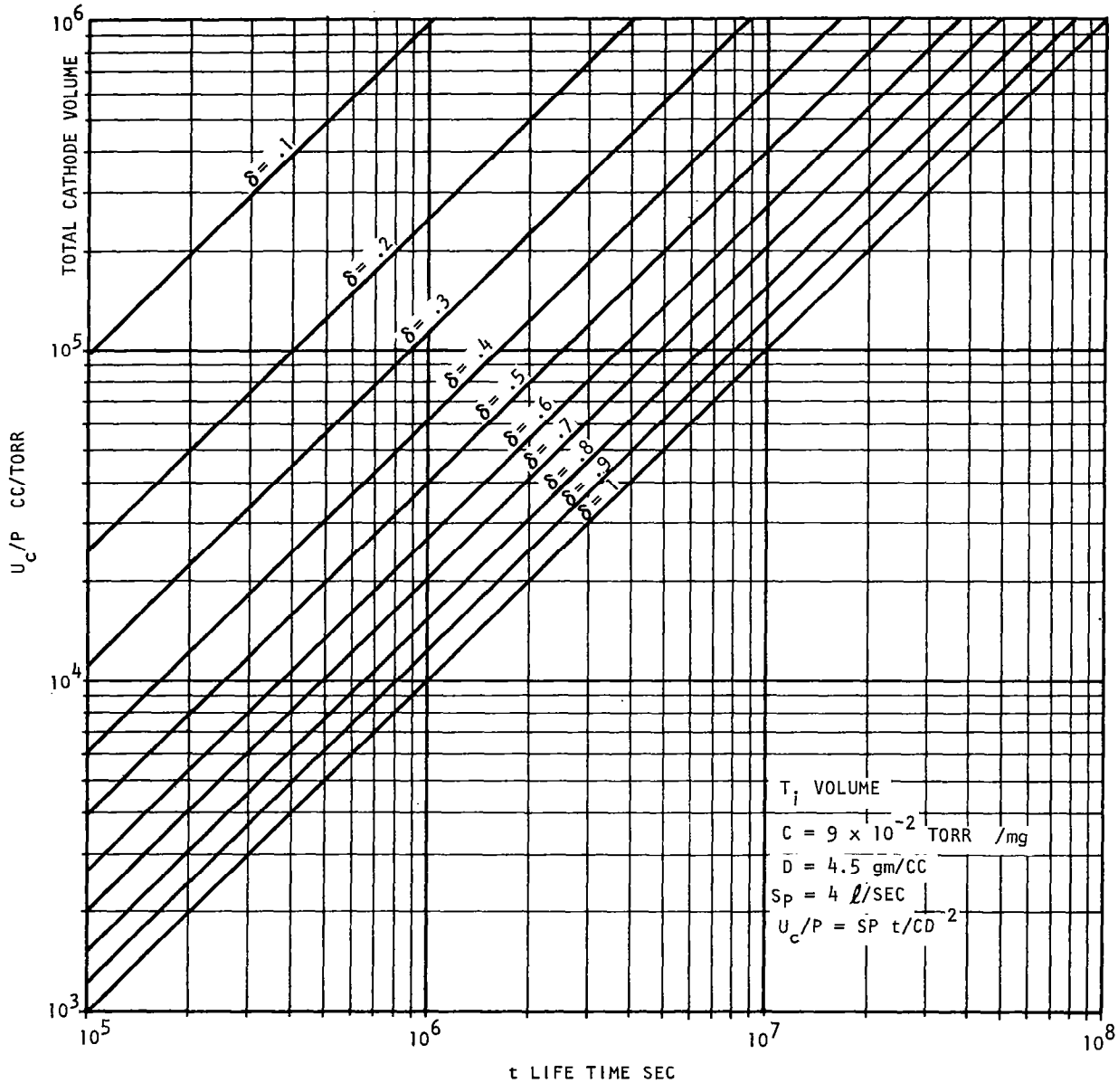

FIGURE 158

CATHODE VOLUME AS A FUNCTION OF PUMP LIFE

The minimum magnet size is obtained when the produce $\Psi \Lambda$ is a minimum. This product is referred to as the magnet utilization factor. It is obtained by a consideration of volume where the magnetic flux is wasted, such as the anode to cathode gap volume, the cathode volume and the volume of the fringe fields. The magnet energy factor $H_m B_m$ should be a maximum to obtain the minimum magnet volume. A comparison of the most common magnet materials is given in Table 27.

TABLE 27

Magnet Material	B_d Gauss	$H_d B_d$ Maximum Megagauss-Oersteds	D_m No./cu.in.	$D_m/H_d B_d$	H_d Oersteds
Alnico 5	10,000	5.5	.264	.048	550
Alnico 8	5,000	5	.262	.0524	1200
Platinum Cobalt	3,000	7.5 - 9.5	.565	.0595 .0753	2500
Oriented Barium Ferritez	1,850	3.25	.180	.0554	1775

From Table 27 it is clear that Alnico 5 has the maximum ratio of the energy density to the weight density, thus it should provide the least magnet weight.

The magnet volume is plotted in Figure 159 as a function of the pumping speed for various values for the product $\Psi \Lambda$. Figures 160 and 161 show a plot of slightly different forms for Ψ and Λ than are present in the text; however, they demonstrate the characteristics of these functions.

ION PUMP AND POWER SUPPLY DESIGN

Ion Pump Design

The first step in the design of an ion pump is the selection of the permanent magnet, since the magnet will probably be the heaviest item of the pump assembly. The expression for the magnet volume shows that a high energy density magnet is desirable.

The volume of magnetic material required can be expressed by the following:

$$U_m = k/H_d B_d$$

where U_m = volume of the magnet

k = constant

H_d = magnet field intensity at the point of maximum energy density

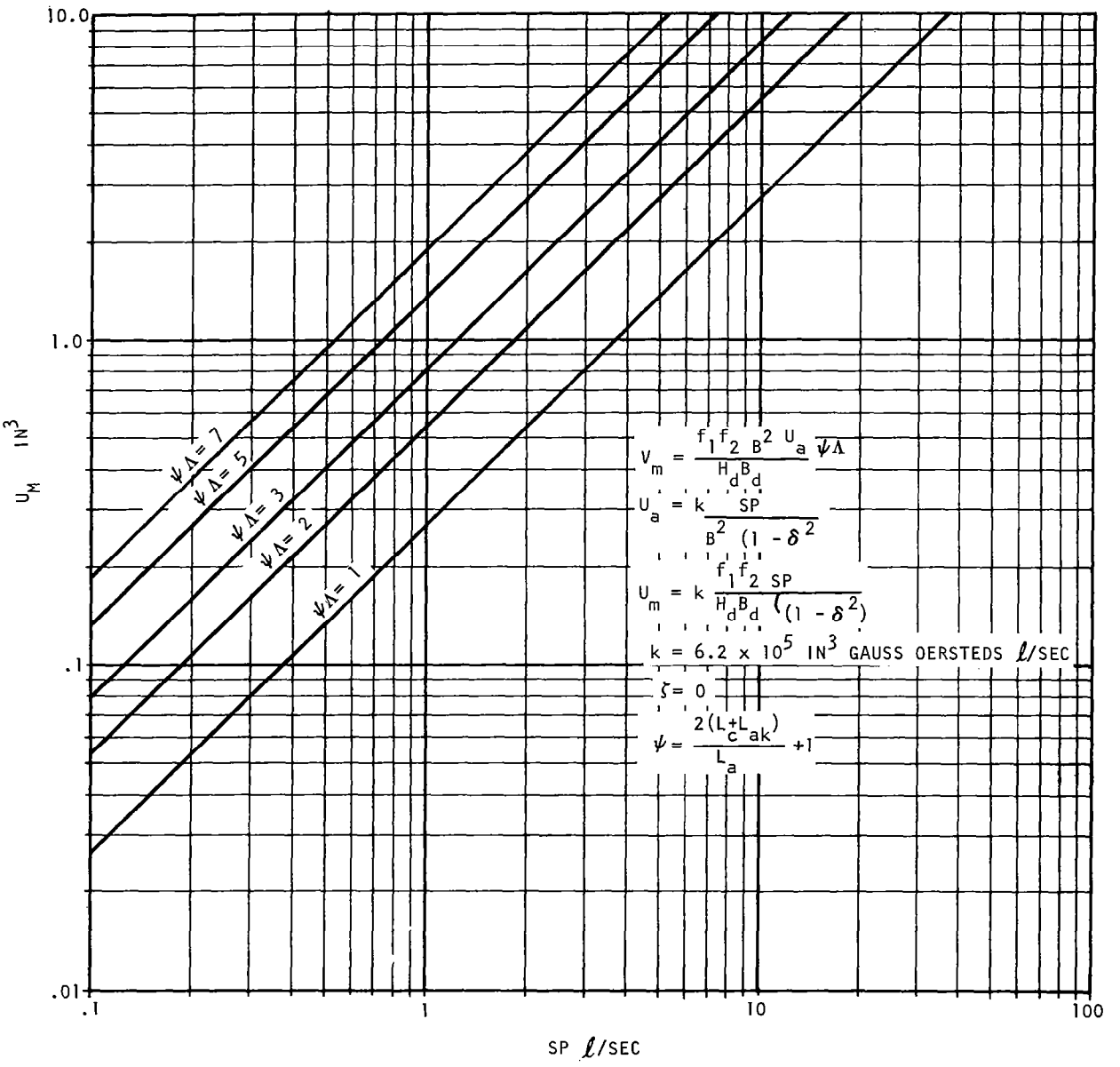

FIGURE 159

MAGNET VOLUME AS A FUNCTION OF
PUMPING SPEED FOR VARIOUS VALUES OF $\Psi\Lambda$

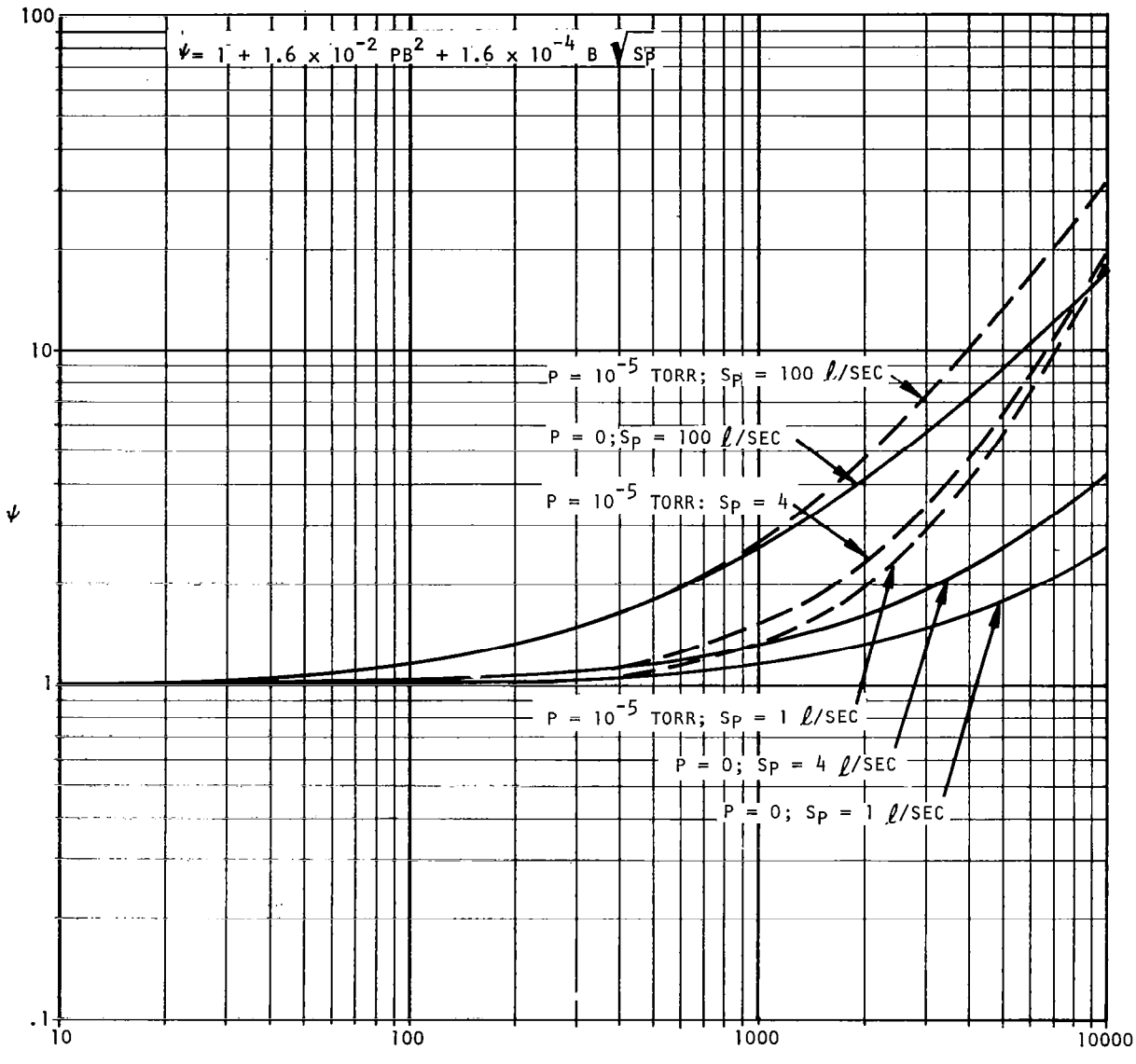

FIGURE 160

PLOT OF THE FUNCTION Ψ VS. THE MAGNETIC FLUX DENSITY
FOR VARIOUS VALUES OF PRESSURE AND PUMPING SPEED

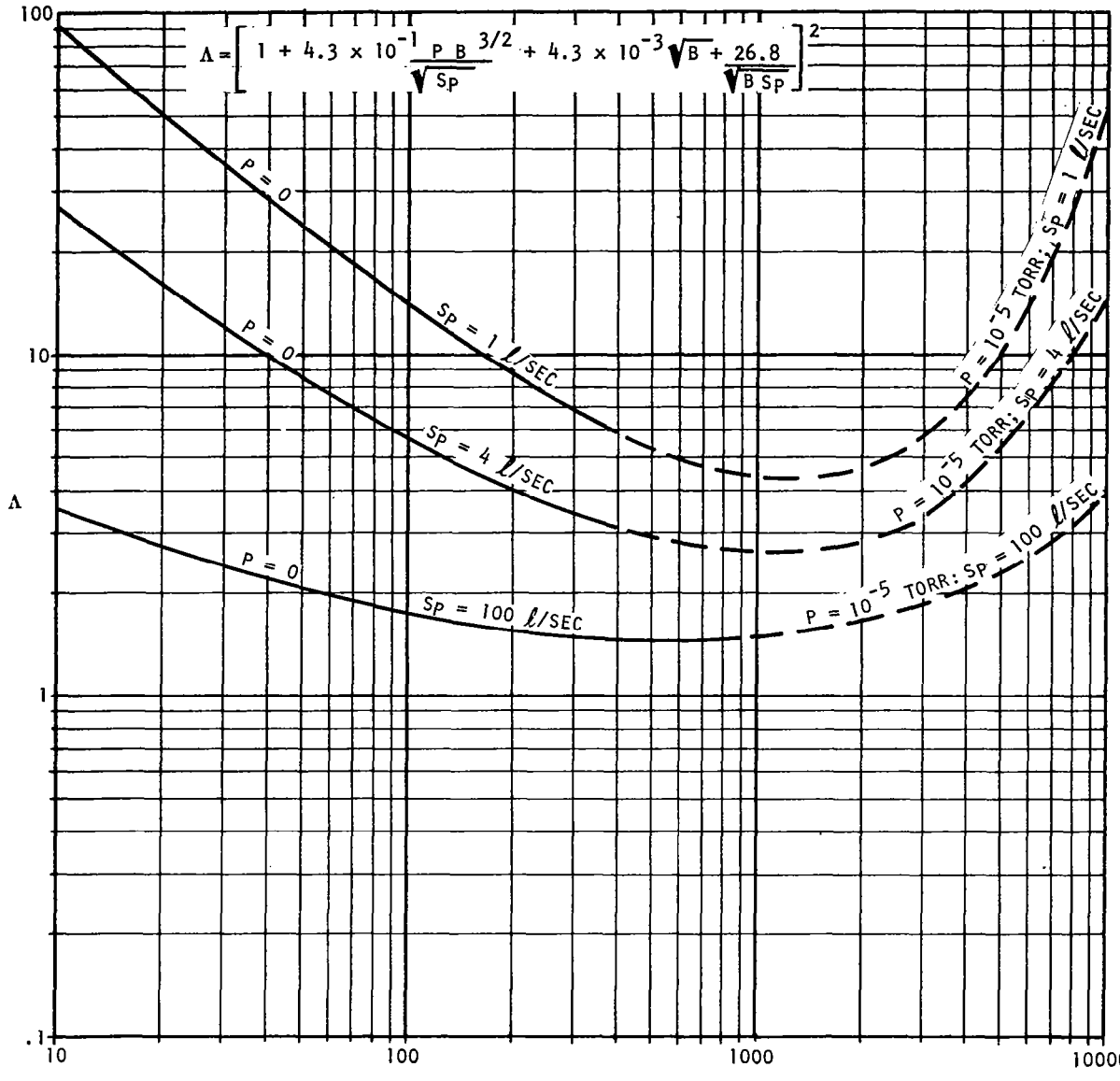

FIGURE 161

PLOT OF THE FUNCTION Λ VS. THE MAGNETIC FLUX DENSITY
FOR VARIOUS VALUES OF PRESSURE AND PUMPING SPEED

B_d = magnet flux density at the point of maximum energy density

$W_m = U_m D_m = k D_m/H_d B_d$

W_m = magnet weight

D_m = weight density of the magnet

The important properties of four possible magnet materials are listed in Table 27. For the design of the ion pump, weight considerations require the selection of Alnico 5. The selected magnetic material will determine the type of pump configuration since the magnet length will vary considerably for the various types of magnetic material. This is shown below:

$$\ell_m = B_g \ell_g f_1/H_d$$

where: ℓ_m = magnet length

B_g = flux density in the air gap

ℓ_g = air gas length

f_1 = mmf leakage factor

The cross sectional area of the magnet is given by:

$$A_m = B_g A_g f_2/B_d$$

where: A_g = cross sectional area of air gap

f_2 = flux leakage factor

If the magnet length is equal to or less than that of the air gap the flux leakage factor, f_2, will be very large. With this consideration the selection of Alnico 5 is further justified. In addition, it will be necessary to use a pole piece to allow the utilization of the high flux density of this magnetic material. The determination of the flux leakage factor is difficult, but by designing the magnetic circuit to minimize the flux leakage a leakage factor of 2 can usually be obtained. This means that for an Alnico 5 magnet:

$B_g \leq$ 5000 gauss

otherwise the cross section area of magnet would be larger than that of the pump.

The ion current of a cell is 75% of its maximum value when the space charge cloud extends to one half of the anode radius, therefore, the maximum values for δ is given by:

$$\delta \text{ max} \leq 0.5$$

A maximum anode potential of 1000 volts is adequate for the production of secondary electron emission and for the sputtering process.

Let $(V_a - V_k) \approx 1000$ volts

From Figure 155

$$Br_a = 600$$

To reduce the effect of the anode to cathode gap on the magnet volume the following conditions are imposed:

$$\zeta\gamma \geq 10$$

where $\zeta = \eta_a/ba_k$

$$\gamma = L_a/r_a$$

The anode to cathode spacing can be made small but should not be less than about 0.04 inch, since the possibility of whisker growth would make the probability of a short circuit very high for a closer spacing.

Let $L_{ak} = .04$ in.

$L_a \simeq .4$ in.

Let $L_a = 3/8$ in. $= 0.954$ cm.

$L_c = L_a + 2\,L_{ak}$

$= .375 + .03$

$= .455$

The distance between the ion pump and the pump voltage suppliy is assumed to be eight inches. The wavelength of the gap field becomes:

$\lambda_e/4 = 8$ in. $= 20.3$ cm

$\lambda_e \leq 161.2$ cm

$$f_e = v_c/\lambda_e = 3 \times 10^{10}/161.2 = 1.86 \times 10^8 \text{ cps}$$

from the text

$$V_r\, V_k \leq 150 \text{ volts}$$

It is desirable to limit the penetration of the electric field into the anode tube. From the potential equation the following condition should be satisfied.

$$\left(\frac{\pi \gamma_a}{2L_c}\right)^2 \leq .1$$

$$\frac{L_c}{r_a} \geq 4.96$$

$$L_c = L_a + 2L_{ak}$$

$$= L_a\,(1.212)$$

$$\nu = \frac{L_a}{r_a} \geq 4.1$$

It is common practice to have

$$3 < \nu < 4$$

Let $\nu = 4$

r_a = 3/32 in. = .238 cm

$d_a = 2r_a$ = 3/16 in.

The magnet flux density can now be computed

$$B_g = \frac{600}{r_a} = \frac{600}{.238} = \underline{2520 \text{ gauss}}$$

$$\zeta = r_a/L_{ak} = \frac{3}{32}/.04$$

$$= 2.34$$

From Figure 153

$$.23 < V_k/V_a \leq .4$$

$$V_a - V_k = 1000$$

$$V_a = \frac{1000}{.6}$$

$$= 1670 \text{ volts}$$

$$384 \text{ volts} \leq V_k \leq 666 \text{ volts}$$

From Figure 158 for a 4 ℓ/sec pumping speed

$$I/p = 65$$

From Figure 154

$$J_v/p = 10$$

The active volume of the pump is given by:

$$U_p = I/p \Big/ J_v/p = \frac{65}{10} = 6.5 \text{ cc}$$

$$U_p = n_c \pi r_a^2 L_a$$

where:

n_c = number of cells

$$n_c = \frac{U_p}{\pi r_a^2 L_a}$$

$$= \frac{6.5 \text{ cc}}{\pi (.238)^2 (.954)}$$

$$= 38.2$$

Let $n_c = 40$

From Figure 158

The total volume of the tilanium cathode for a life of one year is given by:

$$U_{c/p} = 1.3 \times 10^6 \text{ cc/torr} \qquad \text{(Case 1 focusing)}$$

$$U_{c/p} = 3.2 \times 10^5 \text{ cc/torr} \qquad \text{(Case 2 focusing)}$$

If $p = 10^{-5}$ torr (Case 2 focusing)

$U_c \geq 3.2$ cc

The volume of each cathode is

$$\frac{U_c}{2} \geq 1.6 \text{ cc}$$

The thickness of the cathode is given by

$$W_c \geq \frac{1.6}{n_c \pi} r_a^2$$

$$= \frac{1.6}{40 \pi (.238)^2}$$

$$= 22.5 \text{ cm}$$

$$= .0886 \text{ in.}$$

Let $W_c = .100$ in.

The magnet length is given by

$$\ell_m = \frac{B_g \ell_g f_i}{H_d}$$

$$\ell_g = L_a + 2 L_{ak} + W_c$$

$$= .375 + .08 + .2$$

$$= .655 \text{ in.}$$

$H_d = 550$

$B_g = 2520$ gauss

$f_i = 1.2$

$$\ell_m = \frac{.655 \times 1.2 \times 2520}{550}$$

$$= 3.6 \text{ in.}$$

The magnet cross sectional area is given by

$$A_m = \frac{B_g A_g f_2}{B_d}$$

$$B_d = 10{,}000 \text{ gauss}$$

$$f_2 = 2$$

A two air gap, ring magnetic circuit was selected, the reasons for which will be explained later. The air gap cross sectional area is given by:

$$A_g = 20 \left[\frac{3}{16} + \frac{1}{16}\right]^2 \times 10 \left[\frac{2}{16} + \frac{1}{16}\right]$$

$$= 1.25$$

This value is obtained by allowing a minimum thickness of material to be 1/32 inch around each cell.

$$A_m = \frac{2 \times 2520 \times 1.25}{10{,}000}$$

$$= .63 \text{ in.}^2$$

$$A_m = .5 \; Z_m$$

$$Z_m = \frac{.63}{5} = 1.26 \text{ in.}$$

where 2m = axial length of magnet.

The volume of the magnet is given by

$$U_m = \ell_m A_m$$

$$= 3.6 \times .63$$

$$= 2.26 \text{ cu. in.}$$

The weight of the magnet is given by

$$W_m = D_m U_m$$

$$= .264 \times 2.26$$

$$= .597 \text{ lb/per magnet}$$

$$W_m = 1.194 \text{ lb Total}$$

The power required is given by

$$P = 65p\ V_a$$

$$= 65p \times 1.67$$

$$= 1.08 \times p \times 10^5$$

$$p = 10^{-5}$$

$$p = 1.08 \text{ watts}$$

A ring magnetic circuit illustrated in Figure 162 was selected because of the following items:

a. No yoke is required.

b. Standard "C" magnets could be used.

c. Two pump units can be used and operated independently so that the reliability is improved.

d. The gas conductance can be improved by placing several long narrow pump units around a high conductance tube.

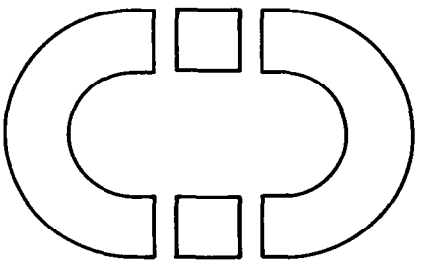

FIGURE 162

Magnetic Circuit

Ion Pump Power Supply

The ion pump requires a high positive voltage between the anode and cathode to establish a Penning discharge. A power supply is necessary for this purpose.

The design criteria for the ion pump power supply are as follows:

a. Inverter Frequency - 5 to 10Kc

b. Excitation Power - Regulated, 28 Vdc

c. Excitation Current - approximately 30 milliamps 60 microamps load

d. Output Current - 60 to 600 microamps at 4 to 5 KV

e. Operational Temperature Range - 0 to 70°C

f. Output Ripple - less than 2.5 volts

The first step in the design of the power supply is to design the transformer. The transformer was designed for a maximum efficiency. The design was completed on two types of transformers. The first used a Permaloy 80 core and the other used an Orthonol core. The efficiency of the Permaloy 80 core was much better than that of the Orthonol. Specifically, the magnetizing current would have been 50 milliamps whereas, in the Orthonol, the magnetizing current would have been 6.3 milliamps. Due to the low output power, a two transformer approach did not seem to be called for, although, the two transformer approach is more efficient at the higher power levels. A study was to be made which would define the point at which this trade off occurs. But due to a limitation of funds, this trade off study was not completed. For this reason the Permaloy 80 core was determined to be the most promising approach. Transformers were procurred, using this core for the systems, which was then breadboarded. The specification for the Permaloy 80 core type transformer is to be found under Aerospace SK A340837.

Figure 163 shows the schematic for the ion pump supply. This power supply uses available parts, with the exception of the transformer, the transistors, and the 3KV diodes which had to be special ordered. Initial tests were run on the circuit, with the result shown in Table 28. It can be seen that the output did not reach the expected level. A re-evaluation showed that the biasing resistor should have been 10 to 20K rather than the 260K originally defined. When the 260 resistor was replaced by a 10 resistor, the results were as expected. These results are shown in Table 29. It will be noted that at the point where the voltage has dropped off by approximately 50%, that the load current was running at 1.15 milliamps. A test was also run to see what the maximum load current could be obtained from the 2.5 KV tap. This data is shown in Table 30.

EXPERIMENTAL RESULTS

The experimental ion pump was designed before the analytical section, optimization of the magnet air gap, was written; therefore, the most efficient use of the magnet was not known. The original design called for the following parameters:

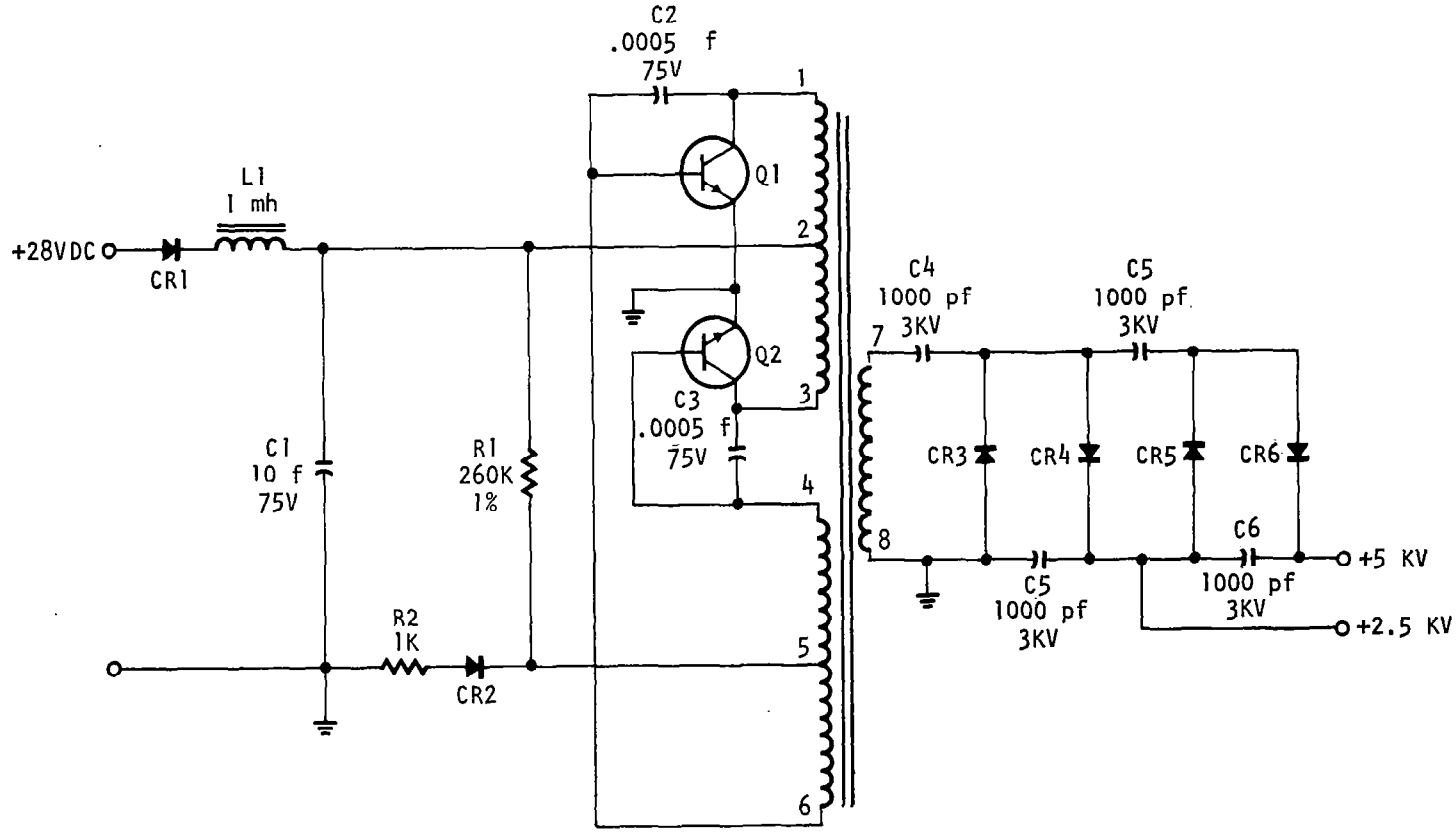

FIGURE 163

ION PUMP SUPPLY SCHEMATIC

TABLE 28

Initial Results of Ion Power Supply

E_{in}	I_{in}	V_o	I_{out} μ amps	Pressure Torr
28 Vdc	38	4.58 KV	39.0	3.5×10^{-8}
28 Vdc	38	4.58 KV	40.5	1.0×10^{-7}
28 Vdc	38	4.58 KV	42.3	2.0×10^{-7}
28 Vdc	40	4.55 KV	50.0	5.0×10^{-7}
28 Vdc	42	4.55 KV	72.0	1.0×10^{-6}
28 Vdc	45	4.53 KV	80.0	2.0×10^{-6}
28 Vdc	53	4.45 KV	135.0	5.0×10^{-6}
28 Vdc	66	4.30 KV	210.0	1.0×10^{-5}
28 Vdc	87	4.05 KV	355.0	2.0×10^{-5}
28 Vdc	98	2.57 KV	540.0	5.0×10^{-5}
28 Vdc	92	1.53 KV	615.0	1.0×10^{-4}

TABLE 29

Output V.S. Load from the 5KV Tap

B+ Volts	I_{in} (mA)	V_o (KV)	$I_o - I_m = I_p$ I_o (μA)	p_{pump} Sample = Air Pressure (torr)
28	46	4.60	59	8.6×10^{-7} T
28	47	4.60	70	1.0×10^{-6} T By air
28	50	4.60	90	2.0×10^{-6}
28	60	4.50	150	5.0×10^{-6}
28	76	4.35	250	1.0×10^{-5}
28	100	4.10	400	2.0×10^{-5}
28	158	3.30	830	5.0×10^{-5}
28	175	2.20	1200	1.0×10^{-4}
28	185	1.70	1400	2.0×10^{-4}

where I_o = Total Supply Output Current
I_m = 60 μA Load due to Meter
I_p = Current to the Ion Pump

TABLE 30

Output V.S. Load from the 2.5 KV Tap

B+ Volts	I_{in} (mA)	V_o (KV)	$I_o - I_m = I_p$ I_o (μA)	p_{pump} Sample = Air Pressure (torr)
28	39	2.40	27	8.6×10^{-7} T
28	39	2.40	28	1.0×10^{-6} T By air
28	40	2.40	35	2.0×10^{-6}
28	42	2.40	80	5.0×10^{-6}
28	45	2.40	120	1.0×10^{-5}
28	53	2.38	220	2.0×10^{-5}
28	78	2.30	540	5.0×10^{-5}
28	118	2.08	1040	1.0×10^{-4}
28	162	1.70	1500	2.0×10^{-4}

$k_2 = Br_a = 600$

$\zeta = .5$

$V_a - V_r = 1000$ *volts*

$B = 2500$ gauss

$r_a = 3/32$ in.

$L_a = 3/8$ in.

$n_c = 40$

$L_c = .100$ in.

$L_{ak} = .04$ in.

$V_a = 1670$ volts

$V_k = 670$ volts

$I/p = 65$ amps/torr

$S_p = 4$ /sec

$\ell_m = 3.6$ in.

$A_m = .63$ in.^{2}

$\delta = .5$ in. x 1.26 in.

The pump was constructed of two sections so that a ring magnetic circuit could be used. This ring eliminated the requirement of a yoke and provided two separate pump units which could be operated independent of each other. This independent operation allows the removal of a shorted section while the other unit can continue to operate. Each pump unit was attached to the side of a tube

opposite to each other and the pump area normal to the magnetic field, consisted of a longitudinal dimension which was larger than the radial dimension. This construction of the pump area does provide a high gas conductance; however, it increases the effects of the fringe field. The increase in the effective air gap cross sectional area due to the fringe field was overlooked both in the choice of the ring configuration and in the determination of the magnet volume. In addition to this oversight, the magnet drawing called for a magnet area to be 0.5 inch x 1 inch instead of the required are of 0.5 inch x 1.26 inches.

As a result of these two errors, the measured flux density in the pump air gap was 1.2 kilogauss. This resulted in a value of k_2 of

$$k_2 = Br_a$$

$$\approx 288 \text{ gauss-cm}$$

$$\zeta = 2$$

This gives a saturation voltage of 560 volts, $V_a - V_k$. The virtual cathode voltage, V_k, is equal to 0.5 V_a for Case 2 focusing:

$$V_a = .5\, V_a = 560 \text{ V.}$$

$$V_a = \frac{560}{.5} = 1120 \text{ volts}$$

if $\delta = 0$

After the pump was constructed it was found that an anode voltage of about 1000 volts was necessary to start the discharge. This makes the number of levels

$$n_g = \frac{1000 \times .5}{.156 \times V_b}$$

$$V_b = 15 \text{ volts}$$

$$n_g = \frac{500}{.156 \times 14}$$

$$= 228$$

This number of required levels is about constant for any geometric configuration; however, it may be a function of the cathode material. As the anode voltage is increased about the saturation value the inner radius of the space charge clouds become equal to the distance across one level. When this happens the approximations that were used in this analysis are no longer valid. The result is that a well ordered system cannot be obtained so the discharge gain drops. With the starting voltage so near the saturation voltage the discharge

can be extinguished when the voltage is increased above the saturation value. Another undesirable feature of this design was the inability of starting at low pressures. The discharge would start at pressures about 3×10^{-5} torr. The pressure dependence is obtained through the trapping efficiency of the cathode secondary electrons.

If the secondary electrons are all accelerated through the same potential, V_k, then only one gap frequency would be established. The trapping efficiency would be greatly reduced if there is a large frequency spread. The energy spread of the secondary electron is reduced when the ratio of the anode radius to the cathode spacing is large; that is, when r_a/L_{ak} is large. A large value for this ratio reduces the influence of the anode potential in the gap region at the space charge inner radius, r_k, so that the virtual cathode potential, V_k, is the accelerating potential for all of the secondary electrons. In addition, the ion focusing is better when the anode potential at the point r_k is small compared to V_k, a condition which is obtained when $r_a/L_{ak} \leq 1$.

Because of the difficulties described above, a new anode unit was constructed with five cells and a cell diameter of 3/8 inch. This resulted in

$$k_2 = 576 \text{ gauss cm}$$

$$\zeta = 4$$

The saturation voltage

$$V_a - V_k = 2200$$

For Case 2 focusing

$$V_k/V_a = .2$$

if $\delta = 0$

$V_a = 2750$ at saturation.

This cell assembly could maintain a discharge well below the region of 10^{-6} torr but the I/p at a pressure of 10^{-4} torr was 1.8 times that at 10^{-6} torr (see Figure 164). In addition, the pumping speed was low, 0.34 per second for air. This was to be expected because of the low magnetic flux density.

The magnet that was used in this design is a stock item which was ground from an axial length of 1.8 inch to 1 inch. An unground magnet was ordered and when applied to the pump the calculated magnetic flux density was

$$B = 1.97k \text{ gauss}$$

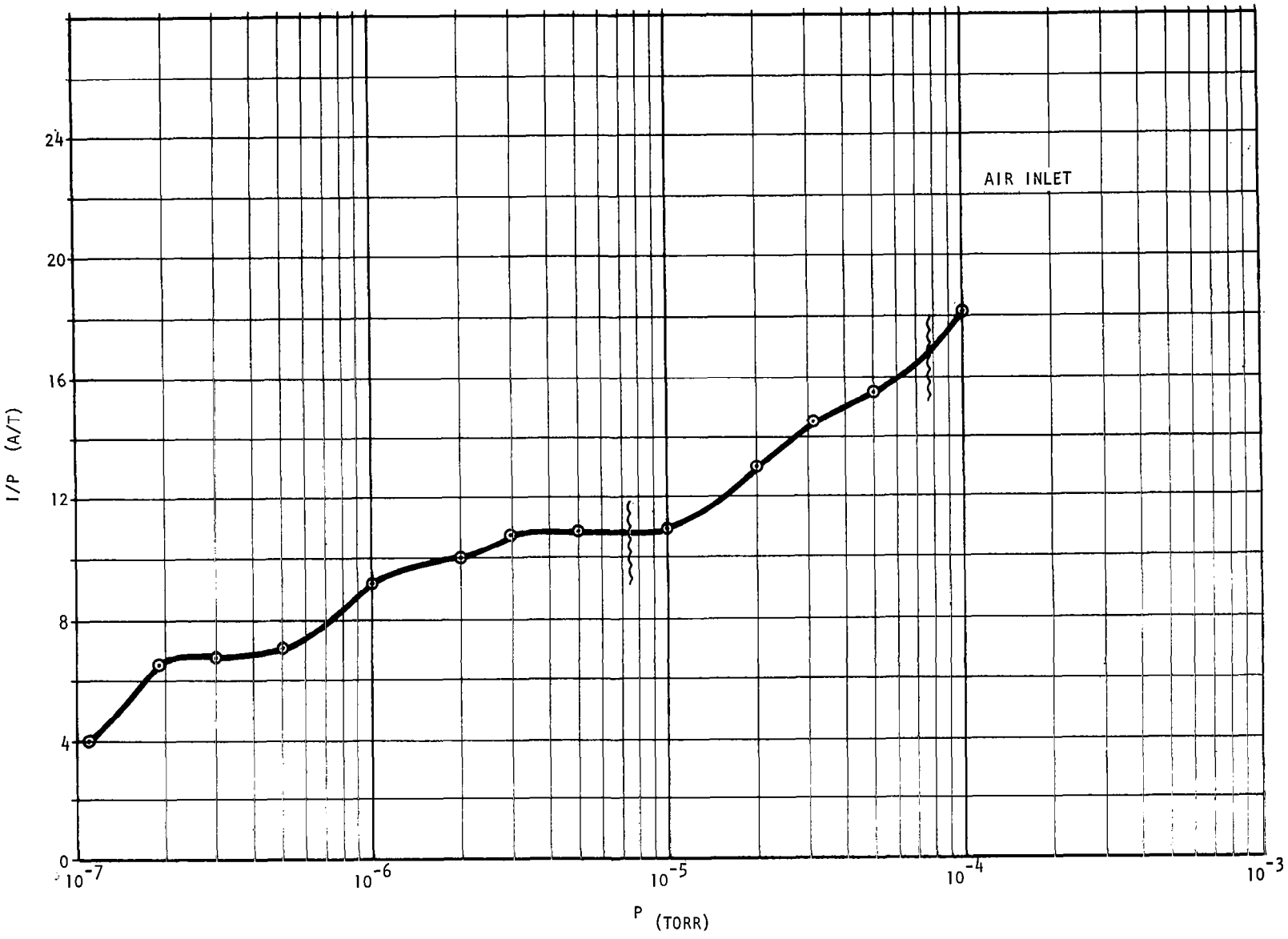

FIGURE 164

ION GAUGE CONSTANT AS A FUNCTION OF PRESSURE

This gives values of

$$k_2 = Br_a = 930 \text{ gauss cm}$$

$$\zeta = 4$$

$$(V_a - V_k) = 6k \text{ volts (saturation)}$$

For Case 2 focusing

$$V_a = 7.5k \text{ volts}$$

The I/p for this configuration was very constant over the pressure range 10^{-7} to 10^{-4} torr (see Figure 165). The dips that occurred at pressures of 10^{-5} and 2×10^{-7} torr can be attributed to a shift from Case 2 focusing to Case 1.

The pumping speed for air was measured by the standard two gauge technique and found to be

$$S_p = 1.34 \text{ } \ell/s \text{ (one anode assembly)}$$
(see Figure 166)

The total pumping speed would

$$S_p = 2.68 \text{ } \ell/s \text{ (total)}$$

This pumping speed is 67% of the desired value. An increase of 33% would be required to meet the design goal of 4 ℓ/s. The original design called for a magnetic flux density of 2.5k gauss and the value that was obtained was about 2 kilogauss, 20% less than the desired value. The pumping speed increases with the square of the magnetic flux density; therefore, the pumping speed should increase 40% if the magnetic flux density were increased to 2.5k gauss.

The weight of the magnet that was used to obtain the 2 kilogauss flux density is 1.8 pounds. With the aid of the optimization section of the analysis a tentative pump redesign has been established which would allow a better utilization of the magnet so that the same magnet weight could be used to obtain the desired pumping speed of 4 ℓ/second.

Additional experimental data is presented in Figures 167, 168, 169 and 170. The pumping speed for O_2 as a function of the anode voltage is shown in Figure 167. This gives an oxygen pumping speed which is 60% that of air at the saturation point. In general, it should be noted that the two gauge method of measuring the pumping speed is only accurate to ±20% unless a mass spectrometer is used to determine the composition of the gas sample. The I/p values are shown in Figure 168 as a function of anode voltage. The pumping speed for the smaller anode cells are shown in Figures 169 and 170 for air and oxygen, respectively, as a function of anode voltage.

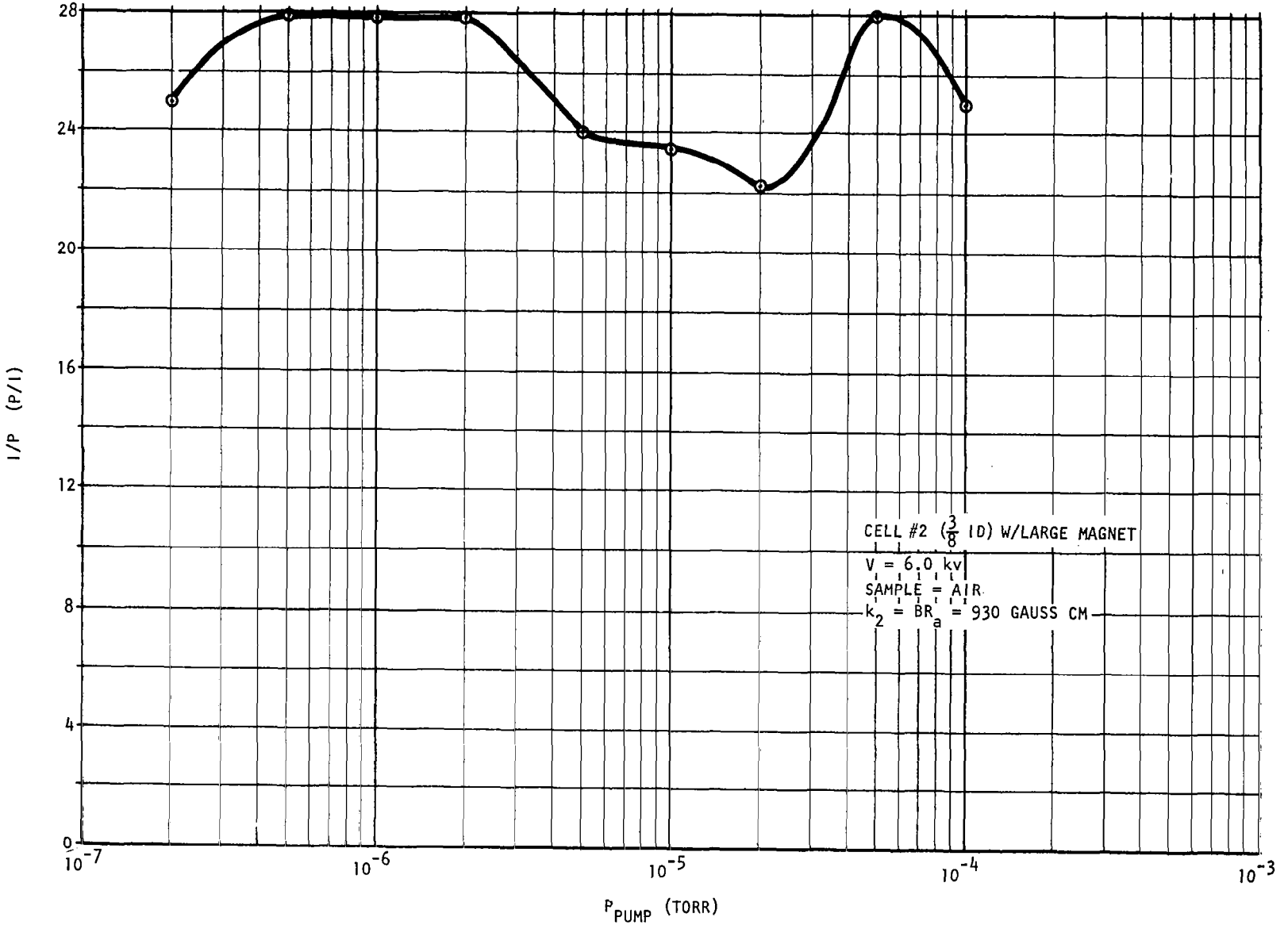

FIGURE 165

ION GAUGE CONSTANT AS A FUNCTION OF ANODE VOLTAGE

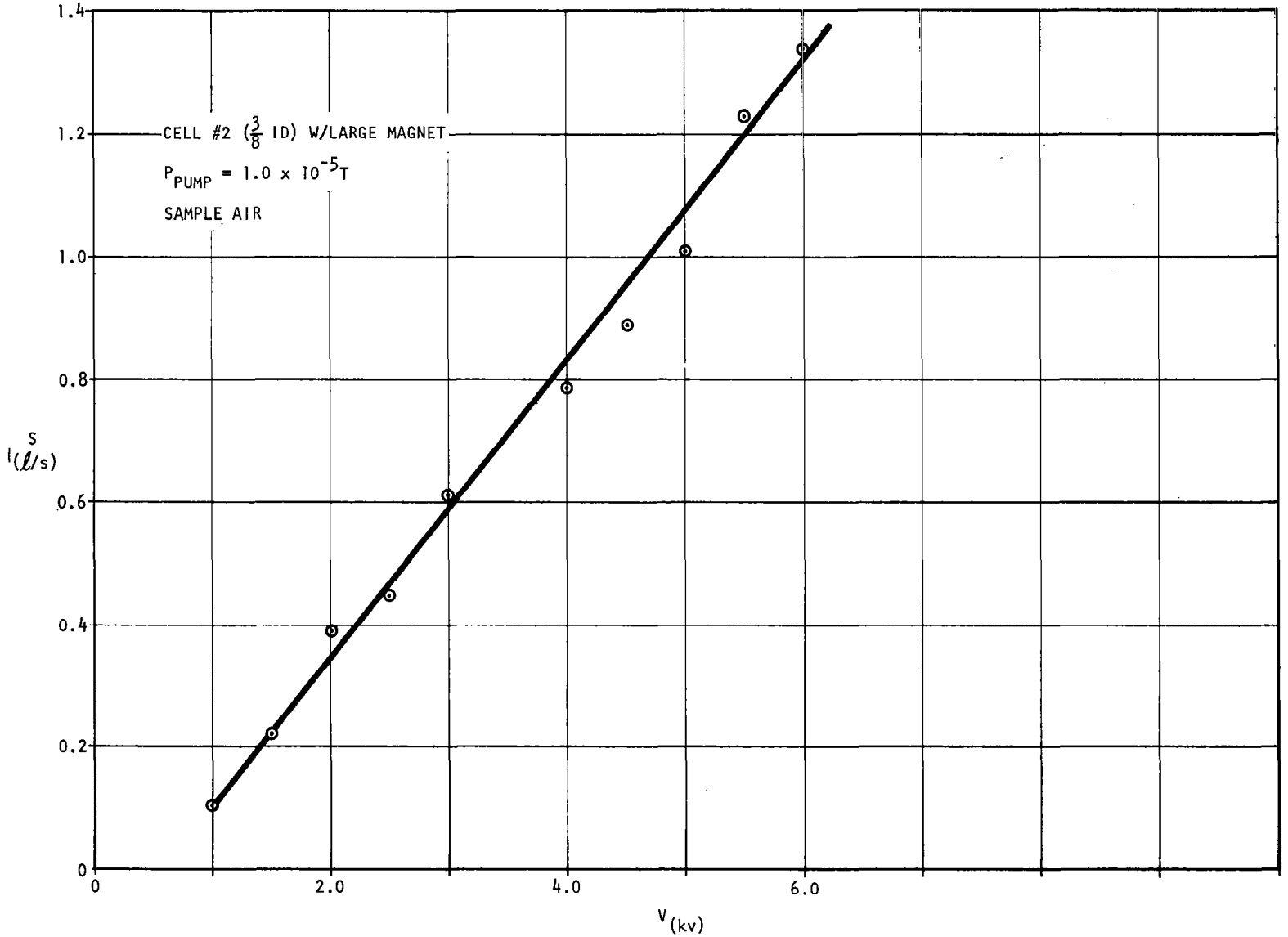

FIGURE 166

PUMPING SPEED AS A FUNCTION OF ANODE VOLTAGE

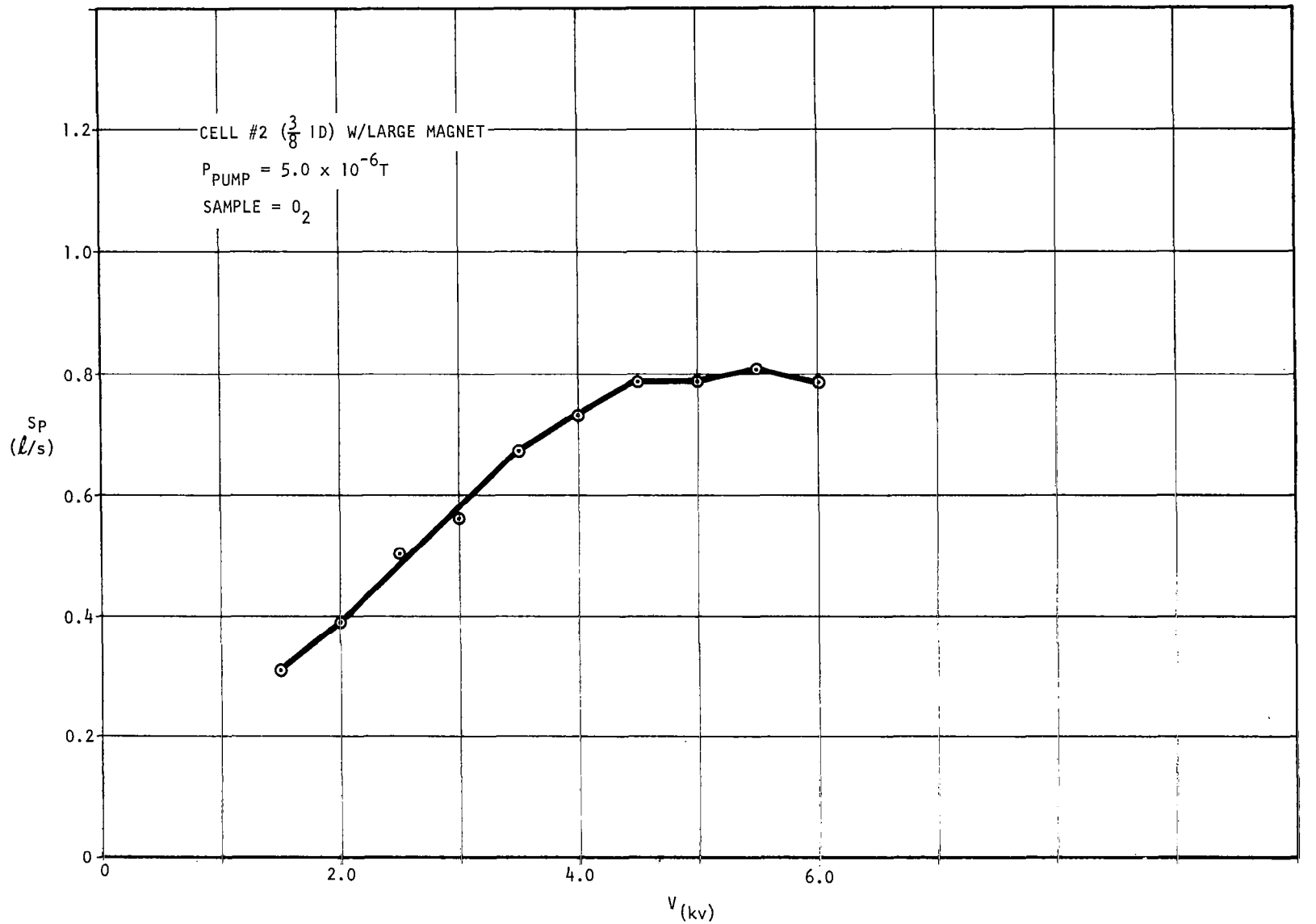

FIGURE 167

PUMPING SPEED AS A FUNCTION OF ANODE VOLTAGE

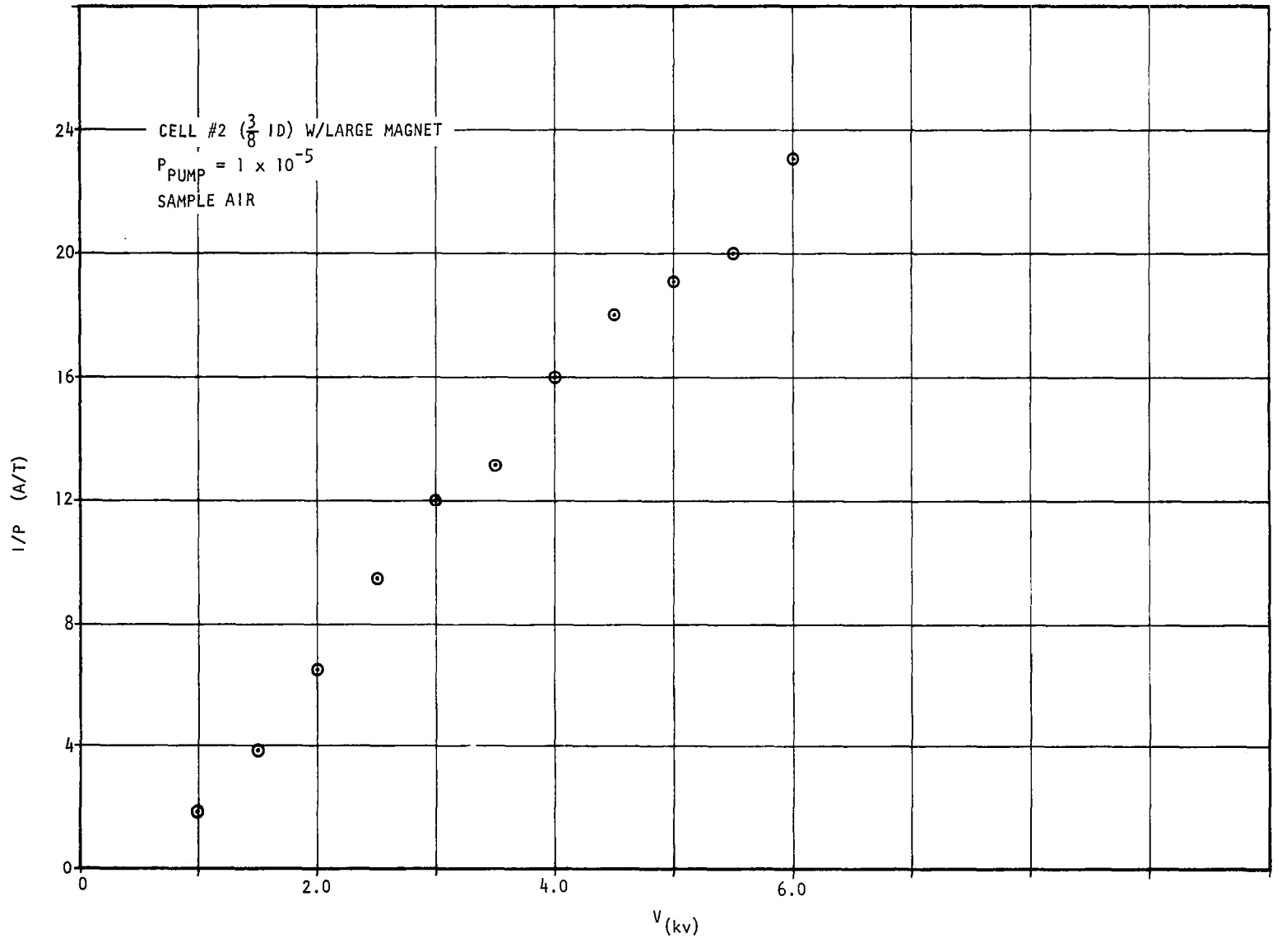

FIGURE 168

PUMPING SPEED AS A FUNCTION OF ANODE VOLTAGE

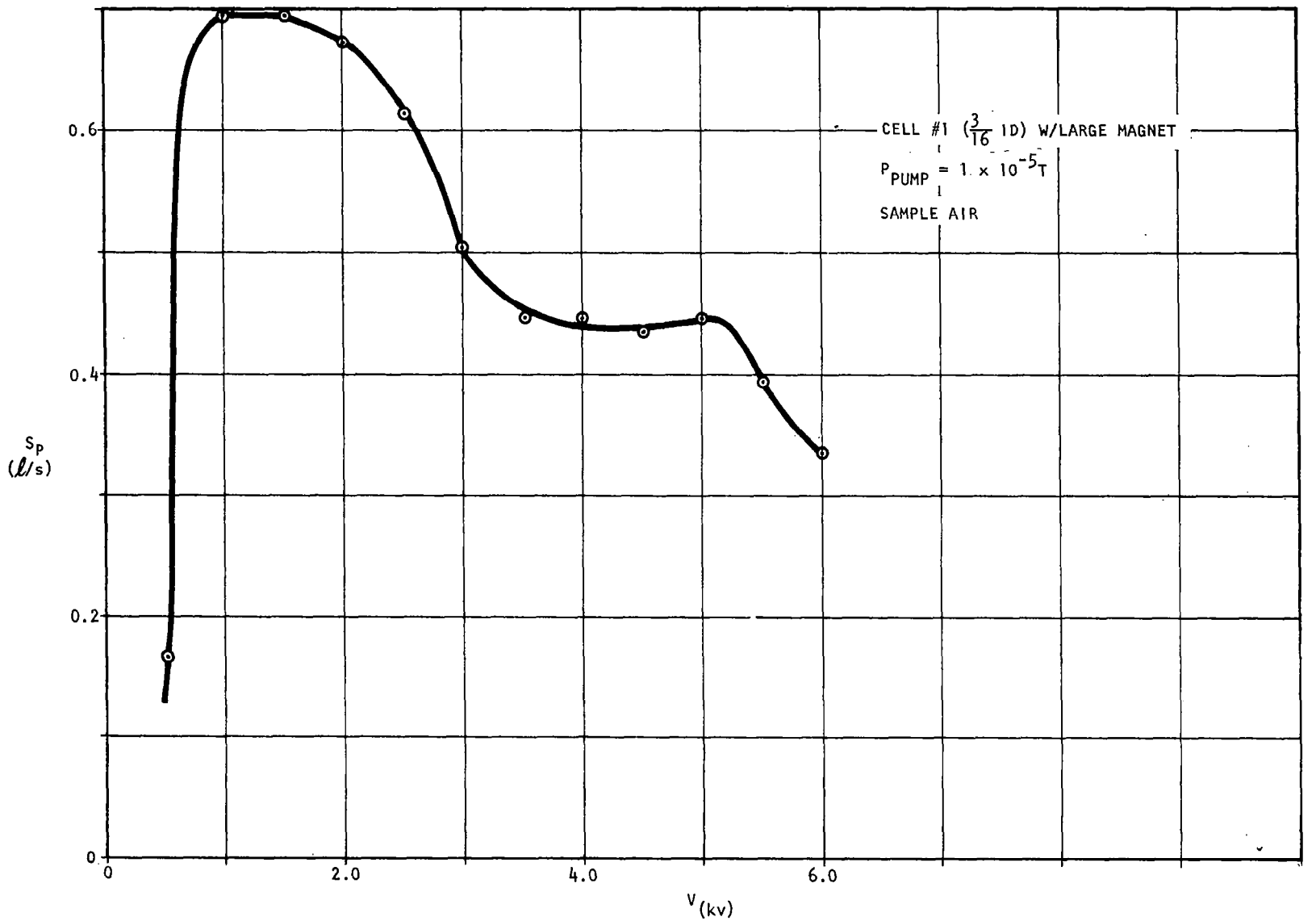

FIGURE 169

PUMPING SPEED AS A FUNCTION OF ANODE VOLTAGE

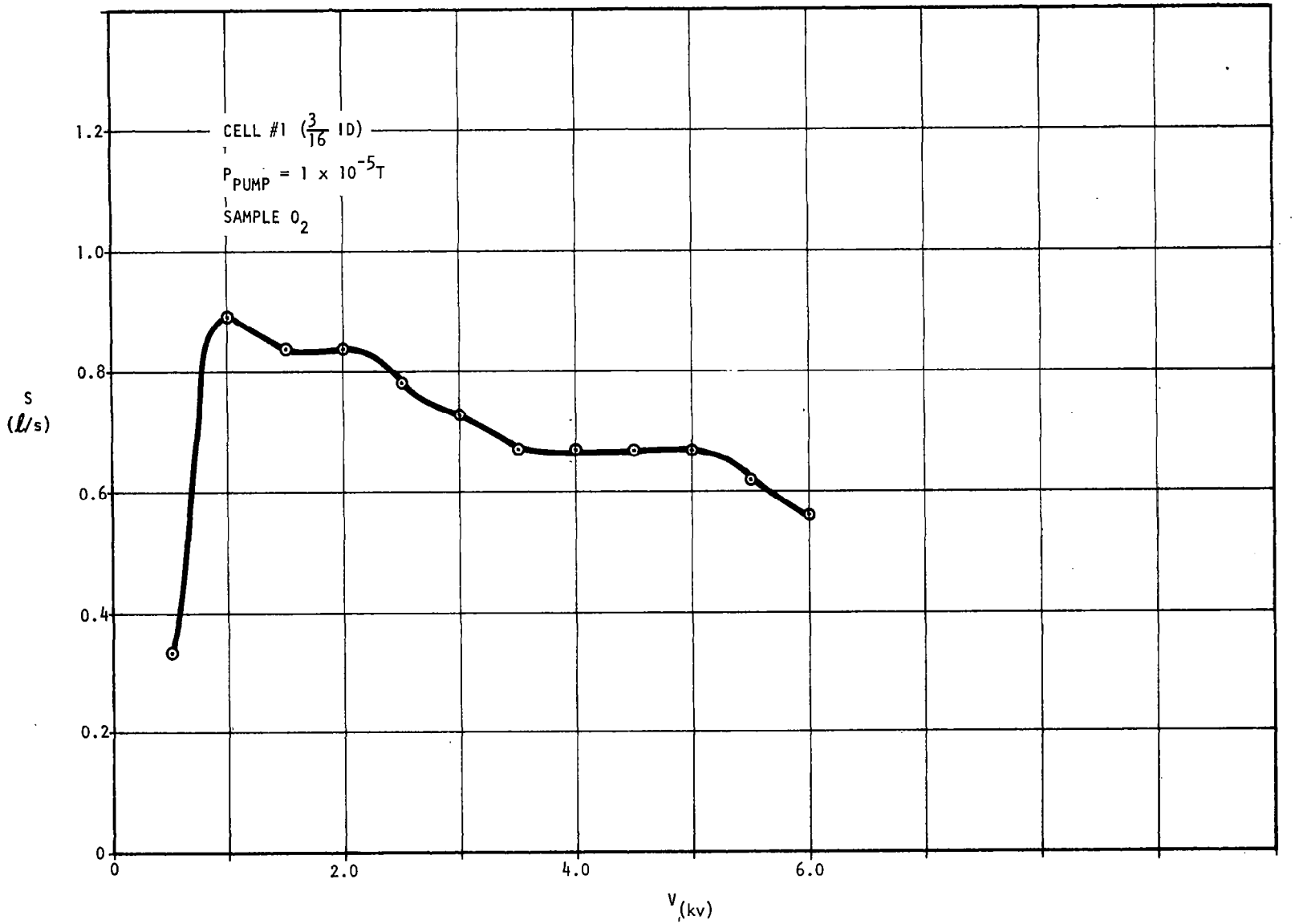

FIGURE 170

PUMPING SPEED AS A FUNCTION OF ANODE VOLTAGE

A comparison of the measured and calculated current-voltage dependence is illustrated in Figure 154. The agreement between the measured and the calculated current is within the accuracy that the ionization probability, S, can be obtained from the published curve that was used, if the anode potential is near the saturation value. At potentials which are less than the saturation value the anode current has a stronger voltage dependence than the calculated value. This occurs when the inner radius is less than half the anode radius. This current-voltage dependence is weaker for the larger cell diameter and it seems reasonable to expect a very close agreement when the ratio of the cell diameter to the cathode spacing becomes very large. The reason for the disagreement at low anode potential is to be found in the assumptions that were used for the model.

The first assumption states that the space charge density is constant over the region r_k to r_a. The influence of trapped ions causes an ionic space charge that cancels the electronic space charge near the anode surface. When the ions return to the radius at which they were produced their radial velocity is zero; therefore, the ions spend a large amount of time at the radius where they were produced. If the axial component of the cathode field is the basic mechanism for ion extraction, then the ions near the anode surface will have the difficulty in moving toward the ends of the cell for extraction since the axial component of the cathode field is zero at the anode surface. This can explain why the agreement between the measured and calculated current voltage relationship is better for a larger ratio of the anode radius to the cathode spacing, since for this condition the cathode field penetration is larger. This effect modified both the amount of ion current that reaches the cathodes and the voltage drop across the discharge region. The discharge potential is reduced since there is a small potential drop across the region of neutralized space charge; however, the greatest effect of this space charge neutralization is the loss of ion current. The ion current which is lost can be represented by an effective anode radius that is smaller than the actual anode radius.

In addition to the effects of space charge neutralization, the influence of the anode potential is the anode to cathode gap is more restricted when the ratio of the anode radius to the cathode spacing is large. A more restricted anode field allows the potential V_k to control the ion focus to obtain the maximum ion current density at the radius r_k.

The result of increasing the ratio of the cell radius to the cathode spacing changes the potential distribution, which effects both the ion focus and the ion trapping. If the ratio is increased by an increase in the anode radius, the discharge potential must be increased. This increase in the anode potential following from an increase in the anode radius would decrease the ion trapping efficiency but would also have the effect of mulifying the improvement in ion focusing. Therefore, the resultant effects of the increase in the ratio of the anode radius to the cathode spacing by an increase in the anode radius on the ion current-voltage relationship are due to ion trapping.

RECOMMENDED FUTURE EFFORT

The tentative redesign consists of one air gap, 0.995 inch wide, and a cross sectional area which is 1.57 inches x 1.57 inches. The anode assembly consists of 9 cells which have a diameter of 0.525 inch and a length of 0.524 inch. The anode to cathode gap is 0.141 inch.

The anode to cathode gap is 0.141 inch which gives a gas conductance of 1.2 ℓ/second for each gap or a total of 2.4 ℓ/second for both gaps at the last row of cells. The pumping speed of the last rwo would be 4/3 = 1.33 ℓ/second; therefore, the gap conductance of 2.4 ℓ/second should be adequate. The titanium cathodes would have a thickness of 0.094 inch each.

The magnetic flux density would be 1.5 kilogauss which would require a magnet length of 1.61 inches on each side of the air gap. A yoke of soft magnetic material would be used to connect the two magnets. The magnet area would be 1.409 inches x 1.409 inches, with a volume of 6.4 inches^3. The weight of the magnet would be 1.7 pounds. The weight of the yoke would be about 0.347 pound; therefore, the combined weight of the magnet and the yoke would be about 2.047 pounds.

The tentative redesign utilizes a magnetic pole piece that is inlayed into the wall of the pump housing. This technique was used on the experimental pump design. An anode mounting configuration was developed for the experimental unit that is both rugged and relatively free from shorting. This consists of ceramic rods that are slotted along the circumference so that sputtered metallic particles cannot produce a continuous shorting film on the surface of the rods. The redesign could have the two electrically separate anodes as the experimental unit had, to provide the capability to remove a short that might develope in one unit, while continuing pump operations.

The use of a single air gap for the pump makes it possible to integrate the pump magnet with the analyzer magnet when the pump is to be used with a magnetic mass spectrometer.

It is recommended that a modified ion pump along these lines be designed, fabricated and tested. The ion pump model which has been developed in conjunction with the experimental data obtained on the first ion pump will allow the required performance to be obtained on a second iteration.

INLET LEAK DEVELOPMENT

INTRODUCTION

The goal of the direct entry inlet leak development was to provide a molecular flow of sample gas from a sample environment of approximately one-half to one atmosphere, into the mass spectrometer ion source, at a maximum pressure of about 2×10^{-4} torr. The advantage is such a system is that it requires no auxilliary pump, such as that required for the existing capillary line pressure divider system. Molecular flow assures a linear relation between the pressure in the ion source and the pressure in the sample environment; and molecular flow allows each of the constituents in the sample gas mixture to flow independently of each other when they enter the ion source. As a result, the measurement of one constituent in the mixture is not affected by the amount of the other components which are present.

Molecular flow is characterized by conditions where there are many more wall collisions than there are molecule-molecule collisions. This occurs when the cross sectional dimensions are less than a mean free path. It has been found that acceptable flow conditions are obtained well into the transition flow region. At 25°C this relationship becomes:

$$d \leq \frac{5 \times 10^{-3}}{p}$$

where d = smallest leak dimension (cm)

p = pressure on the high pressure side of the leak (torr)

As an example of the dimensions which are involved, if the pressure is 500 torr, the leak dimensions must be less than or equal to 10^{-5} cm or 0.1 μ. This is an exceedingly small dimension and gives an indication of the difficulty which could be encountered in obtaining a molecular flow leak at these pressures.

It has been difficult to obtain a leak which could satisfy the conditions described above. An initial attempt at a successful design was made some time ago by the fabrication and test of a rough ball leak as described below.

BALL INLET LEAK

The rough ball leak utilizes tiny grooves on a stainless stell ball having a specified degree of roughness. This roughened ball is pressed against a circular knife-edge seat. When the knife-edge presses against the ball, the sample gas must flow through the grooves to enter the mass spectrometer. The flow rate can be controlled by the amount of pressure applied to the ball. This causes the knife-edge to deform the ball, resulting in a reduction of the average size of the grooves. The gas flow can be reduced to zero by the

application of sufficient pressure to the ball. The amount of depression required to stop the gas flow does not exceed the elastic limits of the steel ball.

The knife-edge seat is made by drilling a hole in a hard stainless steel block and grinding a spherical cup, on center with the drilled hole. A second spherical cup is ground over the first and with the same center but a larger diameter. The intersection of these two spherical cups forms a circular cusp. This circular cusp is used as a circular knife-edge.

The ball leak assembly uses a differential screw to allow a smooth application of pressure to the ball. To insure that the ball is properly centered with the seat, the ball shaft is loosely mounted. With the ball shaft free to move laterally about two-thousandths of an inch, the ball can be seated with laterial shocking during the adjustment of the leak conductance. A cross sectional view of this initial design is shown in Figure 171.

The molecular flow conductance of a long tube is given by

$$F_{in} = 30.48 \frac{r^3}{\ell} \sqrt{\frac{T}{M}} \quad \text{liters/second}$$

from which it is found that:

$$\frac{\Delta F_{in}}{F_{in}} = \frac{3\Delta r}{r} + 1/2 \frac{\Delta T}{T} - \frac{\Delta \ell}{\ell}$$

For an isotropic material, the thermal expansion yields

$$\frac{\Delta r}{r} = \frac{\Delta \ell}{\ell}$$

$$\frac{\Delta F_{in}}{F_{in}} - 2 \frac{\Delta r}{r} + 1/2 \frac{\Delta T}{T}$$

The ion source pressure is given approximately by

$$P_s = F_{in} P_a / F_s$$

where F_s is the conductance out of the ion source, then

$$\frac{\Delta P_s}{P_s} = \frac{\Delta F_{in}}{F_{in}}$$

Let the following variations be assumed for the present discussion

$$\frac{\Delta F}{F} = .01$$

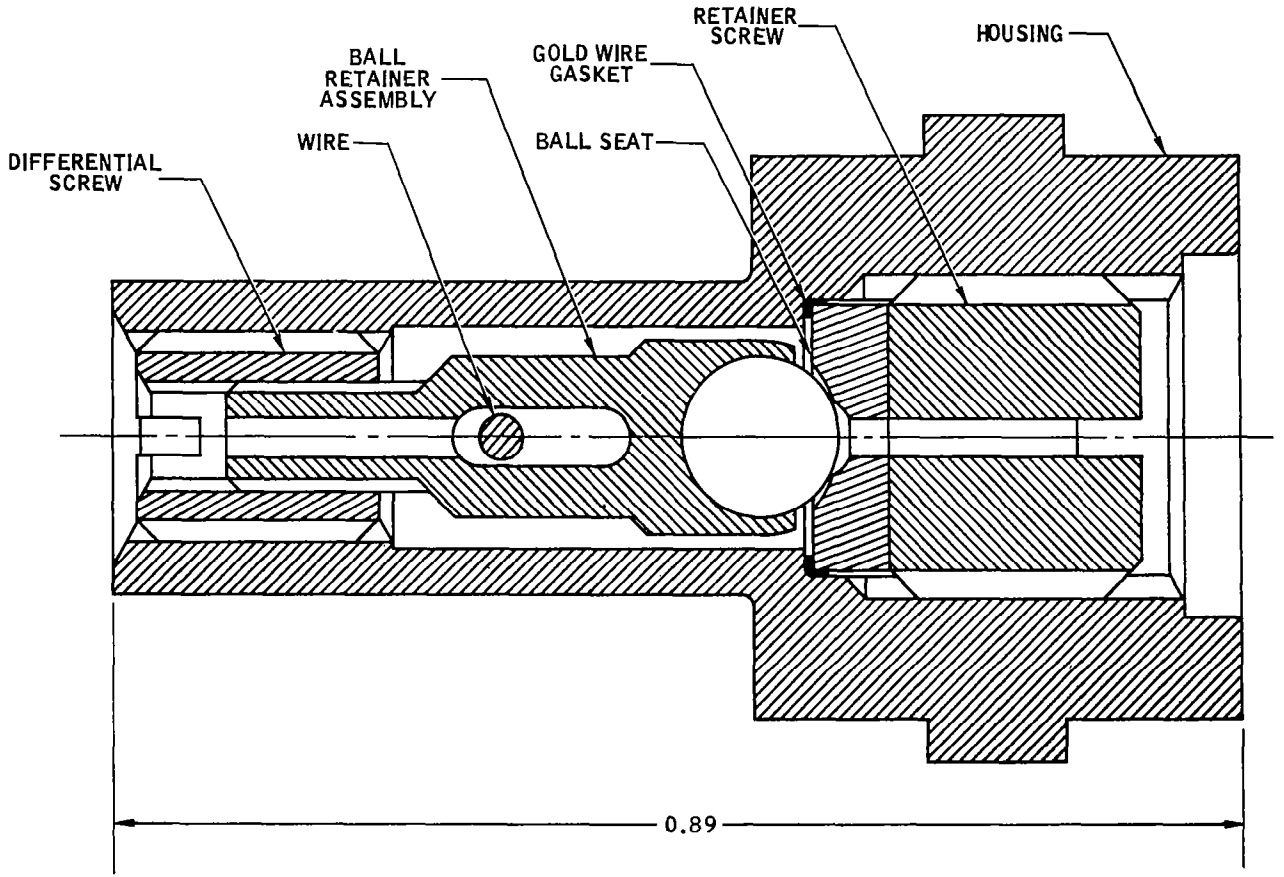

FIGURE 171
Ball Leak Assembly

therefore,

$$\frac{\Delta T}{T} = .02$$

or

$$\Delta T = 6°C$$

The expansion of the radius of the groove can be neglected since

$$\frac{\Delta r}{r} = 6.7 \times 10^{-6} \Delta t \ °F$$

$$= 3.7 \times 10^{-6} \Delta t \ °C$$

$$\frac{\Delta T}{T} = \Delta t/300$$

$$\frac{\Delta F_{in}}{F_{in}} = \frac{2\Delta r}{r} + 1/2 \frac{\Delta T}{T} = (7.4 \times 10^{-6} + 1.67 \times 10^{-3}) \Delta t$$

$$\simeq 1/2 \frac{\Delta t}{300}$$

The Apollo cabin temperature can vary as much as 20°C; therefore, it may be necessary to control the inlet leak's temperature. In addition, it may be necessary to heat the leak to prevent water condensation in the leak and the filter.

Since there is the possibility that the leak assembly may be heated, the assembly should be as small as possible to reduce the required heating power. The length of the tube on the high pressure side of the leak should be as short as possible to reduce the diffusion time of the sample entering the leak. The diffusion time determines the response time of the inlet system, unless there is forced circulation around the ball.

A unit of the original ball leak design was tested at the Goddard Space Flight Laboratory and three specific areas where improvement was necessary were: 1) the leak conductance was strongly influenced by the temperature of the assembly (7.6×10^{-5} / cc/sec at 21.6°C to 5.3×10^{-4} / cc/sec at 81.2°C); 2) the leak conductance varied by a factor of 2.35, under vibration about all three normal axis at thrust axis severity for the S-6A satellite neutral mass spectrometer prototype sub-assembly vibration loads. These levels were several times higher than those for the present requirement; and, 3) the adjustment mechanism was too coarse and did not allow accurate setting of the leak conductance.

Investigation of the temperature effects revealed that the ball leak assembly was constructed of two different grades of stainless steel. Type 440-C was used in the construction of the ball and the seat because of its hardness. The

rest of the assembly was constructed of Type 303 because of its machinability. The differential thermal expansions is given by

$$\Delta\ell = L(\alpha_1 - \alpha_2)\Delta t$$

where

L = length of ball and seat

α_1 = thermal coefficient and expansion for Type 303SS

α_2 = thermal coefficient of expansion

$\Delta\ell = 166\ (10.4 - 6.6) \times 10^{-6}/°F$ (inches)

$= 6.34 \times 10^{-7}/°F$ (inches)

$= 1.14 \times 10^{-6}/°C$ (inches)

For a temperature change as large as the one experienced in the tests at GSFC:

$\Delta t = 59.6°C$

$\Delta\ell = 6.8 \times 10^{-5}$ inches

= 68 micro inches

The diameters of the grooves in the ball should be

$d_g \leq 5.12$ micro inches

This represents the factor of 10 increase that was experienced in the leak conductance over this temperature, provided that the leak conductance varies linearly with the distance between the ball and the seat. The gas conductance of a short tube varies linearly with the cross sectional area. Rectangular, triangular, and eliptical tubes have cross sectional areas that vary linearly with two perpendicular dimensions. A circular tube can become eliptical when it is strained non-uniformly around the circumference. The actual shape of the grooves are irregular and indeterminate since they are formed by surface abrasion with a fine grit of a hard material. It is reasonable to expect the gas conductance to vary linearly with the displacement between the ball and the seat.

The obvious method of eliminating, or greatly reducing the temperature dependance of the leak conductance, is to make all of the parts that contribute to the loading of the ball to the seat of the same material or of materials that have about the same linear coefficient of thermal expansion. One possible combination would be 440-C stainless steel for the ball and seat and 416 stainless steel for the other parts.

The variation of the leak conductance with vibration is not surprising, since the design allowed for vibrational seating of the ball. The large change in leak conductance experienced at the GSFC laboratories could be due to a lack of proper seating at the time of adjustment of the leak. In general, the transverse vibrational levles (that is required for seating the ball) should be larger than that which the leak assembly is expected to experience after the leak conductance is adjusted.

The vibrational level that is required for seating the ball could be increased by making the shaft rigid and the ball loose on the shaft. The ball would move within its shaft mounting to obtain the proper seating position. The required vibration frequency and level would be increased since the mass of the parts which must move for proper seating has been reduced.

The adjustment mechanism was found to be excessively coarse both by test at Perkin-Elmer and at GSFC. The distance that the shaft moves per turn of the adjustment screw is given by

$$X = \frac{1}{\eta_1} - \frac{1}{\eta_2}$$

where

η_1 = number of threads per inch for the I.D. of the adjustment screw

η_2 = number of threads per inch for the O.D. of the adjustment screw

The number of turns required to close the grooves is given by

$$\eta = \frac{5.12 \times 10^{-6}}{.01316} = 3.9 \times 10^{-4} \text{ turns}$$

It would be desirable to have the screw turn 1° to obtain a complete stoppage of the gas flow

$$\eta_2 = \frac{1}{360} = 2.78 \times 10^{-3}$$

$$= \frac{5.12 \times 10^{-6}}{\frac{1}{\eta_1} - \frac{1}{\eta_2}}$$

$$\frac{1}{\eta_1} - \frac{1}{\eta_2} = \frac{5.12 \times 10^{-6}}{2.78 \times 10^{-3}}$$

$$\eta_1 - \eta_2 = 1.84 \times 10^{-3}\ \eta_1\eta_2$$

If

$$\eta_1 \simeq \eta_2 = \eta$$

$$\Delta\eta = \eta_1 - \eta_2 \simeq 1.84 \times 10^{-3}{}_2$$

Let $\eta_1 = 100$, then $\Delta\eta = 18.4$ and would require $\eta_2 = 118$

It will be necessary to allow for the possibility that the ball will not be in contact with the seat after the unit is assembled, therefore, a total movement of 0.005 inch is allowed to obtain initial contact.

$$L_T = .005 \text{ inch}$$

$$= N_T \left(\frac{1}{\eta_1} - \frac{1}{\eta_2}\right)$$

$$N_T = L_T \frac{\eta_1\eta_2}{\eta_2 - \eta_1}$$

$$= \frac{0.005\ (1.18 \times 10^4)}{18}$$

$$= 3.28 \text{ turns}$$

The total required movement of the adjustment screw along the shaft is given by

$$L_{ss} = N_T/\eta_2$$

$$= 3.28/118$$

$$= 0.0277 \text{ inch}$$

The total length of the adjustment screw is

$$L_s = 0.19 \text{ inch}$$

It is possible to experience erratic behavior of the leak conductance if solid particles collect in the leak. This is particularly true during the adjustment. After the leak is adjusted, the continuous collection of solid particles in or around the leak openings continuously decreases the leak conductance.

Because of the desirability of filtering the inlet gas during the adjustment, it is desirable to have the filter located between the ball and the adjustment screw with a sliding seal between the filter and the shaft. The filter and the seal should withstand the bakeout temperature of 400°C. The filter should

have a small volume and a large molecular gas conductance to keep the time constant of the filter small. The time constant is given by

$$\tau = 10 \text{ seconds}$$

$$\tau = \frac{V}{F_f}$$

where

V = volume

F_f = filter conductance

In general the closed volume ahead of the leak should be as small as possible, since the diffusion time is very long at atmospheric pressures.

DESIGN MODIFICATIONS

The design modifications were directed in the following areas:

a. Temperature stability

b. Adjustment

c. Alignment

d. Filter system

The temperature variation of the conductance of the initial leak design was attributed to the use of 440-C stainless steel for the ball and the seat with 303 stainless steel used for the loading mechanism. To improve the stability the same material should be used throughout the assembly; however, the ball and seat require a very hard material and the load mechanism requires an easily machinable material. These requirements are not compatible but the thermal expansion coefficient for all of the 400 series stainless steel are about the same. There is approximately a factor of two difference between the expansion coefficient for 300 and 400 series stainless steel.

The loading mechanism was constructed from 410 stainless steel which has a thermal expansion coefficient

$$\alpha_{410} = 5.5 \times 10^{-6}/°F$$

and the ball and seat were fabricated again of 440 stainless steel with a temperature coefficient of

$$\alpha_{440C} = 5.6 \times 10^{-6}/°F$$

With those two materials the differential expansion is given by

$$\Delta \ell = 0.2\ (\alpha_{440C} - \alpha_{410})\ \Delta t \text{ (inches)}$$

The ratio of the expansion for the present design to the previous design is given by

$$\frac{\Delta \ell_2}{\Delta \ell_1} = \frac{\alpha_{440C} - \alpha_{410}}{\alpha_{303} - \alpha_{440C}}$$

$$= \frac{5.6 - 5.5}{9.6 - 5.6}$$

$$\Delta \ell_2 / \Delta \ell_1 = 0.1/4$$

$$= 0.025$$

This represents a substantial improvement over the original design. Note also that the leak housing in the new design will expand somewhat less than will the ball and seat, where in the previous design the opposite was true. While a significant temperature variation was still indicated with the use of the new materials, it was believed that there should be experimentally verified before further corrective design measures were taken.

The adjustment improvement was provided by using a smaller pitch for the threads of the differential screw and making the ratio of the difference smaller. The outer thread was designed for 64 turns per inch and the inner thread for 72 turns per inch. This differential screw has a travel distance per turn that is given by

$$X = \frac{1}{\eta_1} - \frac{1}{\eta_2}$$

$$= \frac{1}{64} - \frac{1}{72}$$

$$= 1.7 \times 10^{-3} \text{ inches}$$

The ratio of the travel for the present design to that of the previous design is given by

$$\frac{X_2}{X_1} = \frac{1/64 - 1/72}{1/32 - 1/56}$$

$$= .13$$

Again, this is a significant improvement over the original design.

The previous design had the ball mounted in the drive screw shaft, which was difficult to center with the seat. Considerable transverse shock was required to seat the ball after it was assembled. For the present design the ball is fastened to the seat as a subassembly. The ball is placed on the seat while it is held in a horizontal position. The ball should be tapped on the sides to make sure that it is centered. A cap is placed over the ball and spot welded to the seat. A diaphragm on the top of the cap provides spring tension that can hold the ball in the centered position while it is being placed into the leak housing. The complete leak assembly is illustrated in Figure 172.

The filter was constructed with the following objectives:

a. Bakeable to 400°C;

b. Minimum volume between the filter and the leak;

c. Minimum particle size rejection between 0.1 to 0.5μ;

d. Filter assembly replacable by hand;

e. Minimum increase in the leak volume.

A cross section of the filter can be seen in Figure 172. The filter holder fits around the leak housing, with a gold "O" ring to seal the filter. The gold rings are driven against a conical surface so that they would be squeezed between the conical surface and the filter housing. The filter is a band of sinter stainless steel which is seam-welded around the filter housing. Four holes, located 90° apart in the filter and leak housings, allow the filter sample to enter the leak chamber. A knurled drive nut is used to seal the filter housing.

The leak assembly was designed to be as small as possible in the event that temperature stabilization is required and a smaller heater power would be needed. It is expected that the leak would be mounted on a ceramic feedthrough to reduce the heat conduction to the mass spectrometer.

FABRICATION AND ASSEMBLY

During the fabrication and assembly of the rough ball leak, several items were encountered which might have a bearing on a future design. First, severe difficulty was met in obtaining the precision ground seats for the leak. The vendor ran into several problems with the equipment which delayed delivery of the critical item. To a large extent, these problems are not believed to be of a recurring nature. However, this has lead to some thought that a different configuration might be employed which would be easier to manufacture. The present configuration was suggested by the vendor as the one which would give the truest seating surface with the required degree of sharpness. It is not believed that it should be modified unless considerable additional effort both in fabrication and testing of the leak is acceptable. This is particularly true due to the somewhat empirical nature of the leak design. Any significant

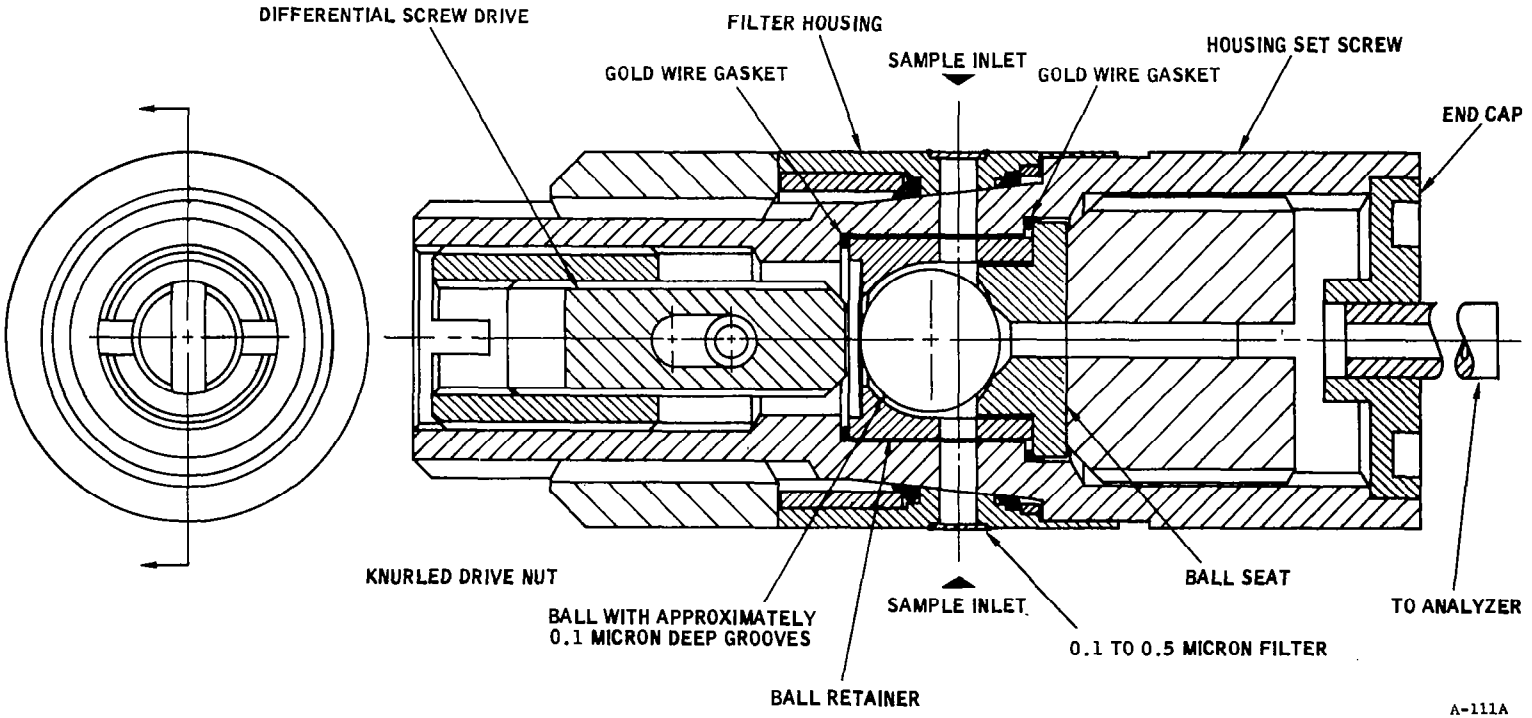

FIGURE 172
Improved Ball Leak Assembly

changes which are made, particularly in the area of the ball or seat, are likely to cause substantial changes in the performance of the leak.

During the assembly of the leak, it was not possible to electron-beam weld the diaphragm in place to hold the ball as was required by the original design. This seal was required not only to secure the diaphragm but also to make a gas-tight seal which would minimize the trapped volume between the ball leak and the filter. When one section of the diaphragm was electron-beam welded, it would pop up in another area making the continuation of the welding impossible. It was finally necessary to utilize an additional gold wire gasket seal to hold the diaphragm against the ball. While this method appeared to be satisfactory it should be reviewed before additional units are fabricated.

The design called for a heliarc welding process to be carried out on an end cap which attached the leak assembly to a small diameter connecting tube through which the sample gas was to flow to the mass spectrometer. This arrangement is shown in Figure 172. The purpose of the small diameter tube was to give some degree of thermal isolation between the leak and the mass spectrometer. In this method, the power required to heat the leak (should heating be necessary) would be minimized. However, it was found that in this method of construction that once the end cap is welded in place, it is no longer possible to tighten the screw holding the leak seat. This was found to be necessary on one occasion when a leak opened in the gold gasket seal between the seat and the leak housing. It was believed that the leak may have opened up when the end cup was welded into place. Further tests were conducted on the leak with an external welded flange in place of the end cap. This allowed adjustment of the screw for retightening the seat after welding.

EXPERIMENTAL RESULTS

In general, there was insufficient time remaining on the contract to obtain an adequate evaluation test but the limited testing that was accomplished seemed to verify the design objectives. Some transverse shock was required to seat the ball; however, the shock magnitude and the stabilization time were less for the initial design. The gas conductance decreased after the leak assembly was shocked which is the opposite effect observed on the previous design. As the ball moves toward the center of the seat, the diaphragm keeps the ball in close contact with the seat, whereas in the previous design, the ball would be less constrained as it moves toward the center. The leak assembly was shocked and readjusted until a selected leak rate was stabilized. It was found that helium conductance in the 10^{-6} cc/second range and above could be readily obtained. This range covered the expected range of required conductances for several possible applications of the Two Gas Sensor. Adjustability of the leak was also improved over the original design. It is still difficult to set a specific desired conductance.

The temperature testing on the leak was somewhat abbreviated and as a result it was not as conclusive as would have been desirable. A single temperature cycle was run from room temperature to approximately 90°C and back to room ambient. During the temperature rise leg the leak conductance dropped by about

a factor of two. When the temperature was restored to its initial value the conductance did not return to its initial value but raised only about fifteen percent. There was no time to run additional temperature cycles but it is believed that they would have repeated more closely.

While the observed temperature variations were larger than desirable, there were some encouraging aspects to the data. First, the initial leak design experienced conductance changes of a factor of ten over the same temperature range. Second, this variation had a positive temperature coefficient whereas the one experienced on the new design had a negative coefficient. Third, the variation exhibited a linear relationship with temperature. These factors lead to the following interpretation and conclusion. As the temperature increases there is an increase in the force on the ball which may cause a transverse movement toward the seat center. If this movement does occur it is expected that the ball would not move in a transverse direction when the assembly is returned to the ambient temperature. This would account for hysteresis in the data. Furthermore, it appears that since both positive and negative temperature coefficients have been obtained that a nearly zero temperature coefficient could be achieved with the proper combination of materials. It appears to be unlikely that this could be accomplished. The published thermal coefficient of expansion for the two materials differ by approximately 1.8%. Variation in thermal expansion coefficients for the same material are often greater than 2%.

The flow rate tests were conducted with a sample gas of helium and a helium leak detector was used as a partial pressure sensor. The flow rate was linearly related to the inlet pressure in the region of 100 to 760 torr. This indicated that molecular flow was being achieved in this range. At lower pressures some difficulties were experienced which are believed to be due to helium absorption in the vacuum system, perhaps in the hose that connected the leak detector to the vacuum system. This caused a deviation from linearity below 100 torr. A typical plot is shown in Figure 173.

The filter could not be tested, since the filter band was not welded properly to the filter housing. There were insufficient funds and time remaining in the contract to obtain a proper filter band weld.

At the conclusion of this test program, the leak was mounted to a Two Gas Sensor System to allow rapid breath-to-breath sampling. This system was then delivered to NASA/Manned Space Flight Center for extensive testing. It is believed that these tests will provide additional information on which the evaluation of the modified rough ball molecular leak can be based.

RECOMMENDED FUTURE EFFORT ON THE BALL LEAK

Due to brevity of the test program, it is not possible at this time to make recommendations on the further modifications and improvements of the ball leak. The first step in any future effort should be the fabrication and further test of additional leaks. One goal of such a program would be to evaluate the variations between leaks. This will be essential if a reasonable attempt is to be made at a more complete temperature compensation.

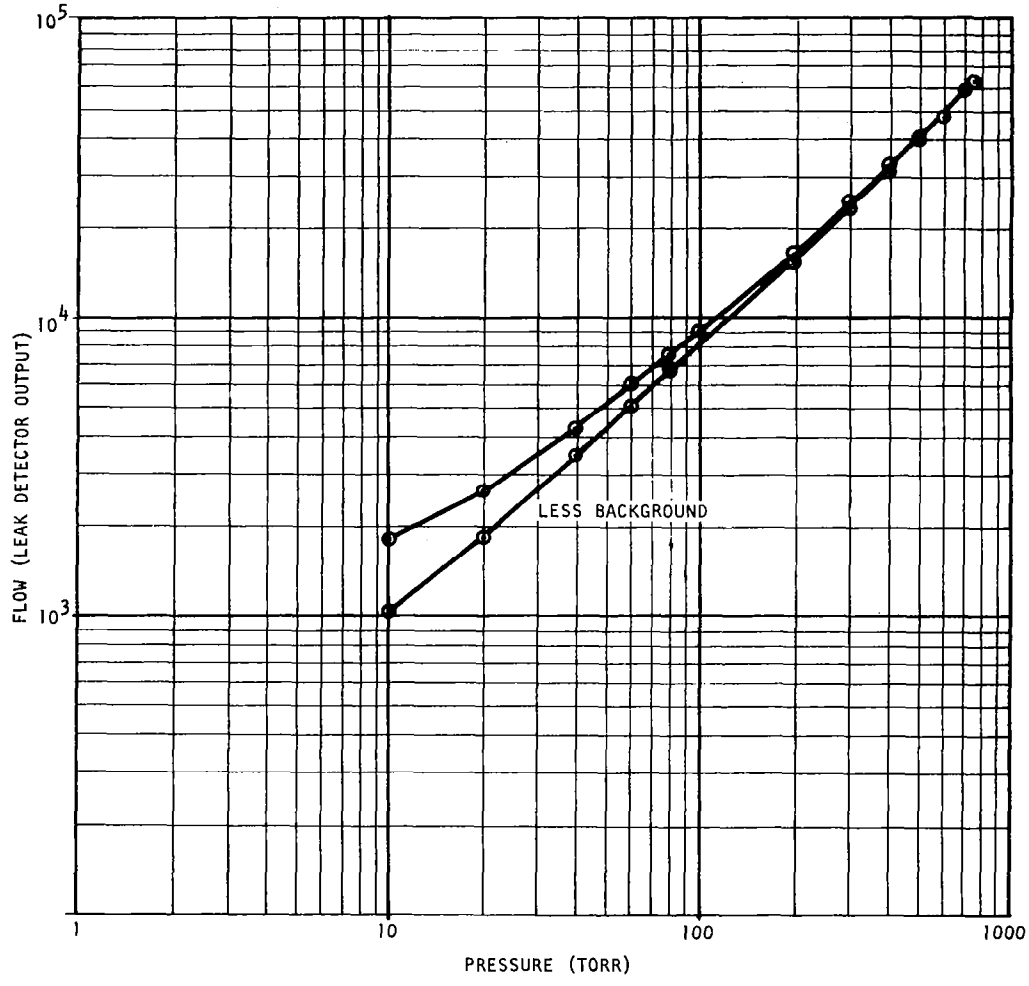

FIGURE 173
Performance Curve (Leak)

With respect to temperature compensation the data which has been taken indicates that a more complete temperature compensation is possible. Presently, the approach which would be adopted would be to add shims of material with different coefficients of thermal expansion to the drive screw. In this way, the proper combination of materials should be able to give a nearly constant pressure on the ball and thereby minimize the temperature coefficient.

An important area of further test is to establish the effects which water vapor in an unsaturated atmosphere have on the leak conductance. This will determine if the leak will have to be heated. Should this be necessary, additional effort may have to be expended to reduce the thermal mass after leak and to increase its insulation at the mounting interface.

ADDENDUM 2

TWO GAS ATMOSPHERE SENSOR SYSTEM
(MASS SPECTROMETER)

MAGNETIC STABILITY STUDY

INTRODUCTION

A space flight environment imposes stringent conditions for survival and successful mission completion upon both men and instrumentation. Unlike the human constituents of the vehicle, instrumentation is subject to strict weight, size and power requirements. When a magnetic mass spectrometer is designed for flight applications, the magnet is an area which demands a large amount of attention. The two major areas in the mass spectrometer magnet design which demanded attention were magnet stability and uniformity. Historically, the production of high performance magnets to meet the stringent requirements of mass spectrometers has been an empirical procedure. The need for better understanding and control prompted the initiation of this magnet study. Two generations of magnets were designed and constructed as improvements to the original analyzer magnet designed for the Two Gas Sensor. Methods of changing, stabilizing, and handling the magnets were also developed.

This report describes the design and fabrication of two magnet assemblies. The original analyzer magnet will be referred to as the first generation magnet, while the modified magnet made of Alnico V will be referred to as the second generation magnet. The magnet made of Alnico V-7 will be referred to as the third generation magnet.

MAGNET DESIGN

FIRST GENERATION MAGNET DESIGN

In the design of the first generation magnet, it was necessary to establish the pole face configuration. It was decided to make a conservative magnet design which would conform as closely as possible to the ideal magnet field. For this reason the pole face area was made sufficiently large so as to ensure a uniform field over most of the trajectory. The entrance and exit faces were established by the analyzer design calculations. The radial boundaries were placed two gap widths from the nearest trajectory. This should be a sufficient distance to ensure a uniform field. This configuration is shown in Figure 174. By specifying the pole face configuration, the area was computed and found to be 9.1 cm^2. The initial technical information applied to the magnet design is given in Table 31.

TABLE 31

Pole Face Area, A_g	9.1 cm^2
Gap Length, L_g	0.500 cm
Material	Alnico V
Maximum Gap Flux Density, $B_{g\ max}$	4500 gauss
Required Flux Density After Stabilization, B_g	4000 ±80 gauss
Reluctance Factor, f	1.2
Demagnetizing Force, H_d	550 oersteds
Flux Density at Peak Energy Product, B_d	10,000 gauss

Several comments are in order concerning the information presented in Table 31. First, the maximum gap flux density was specified to be greater than the required flux density so that the magnet could be stabilized by "knocking down" the field.

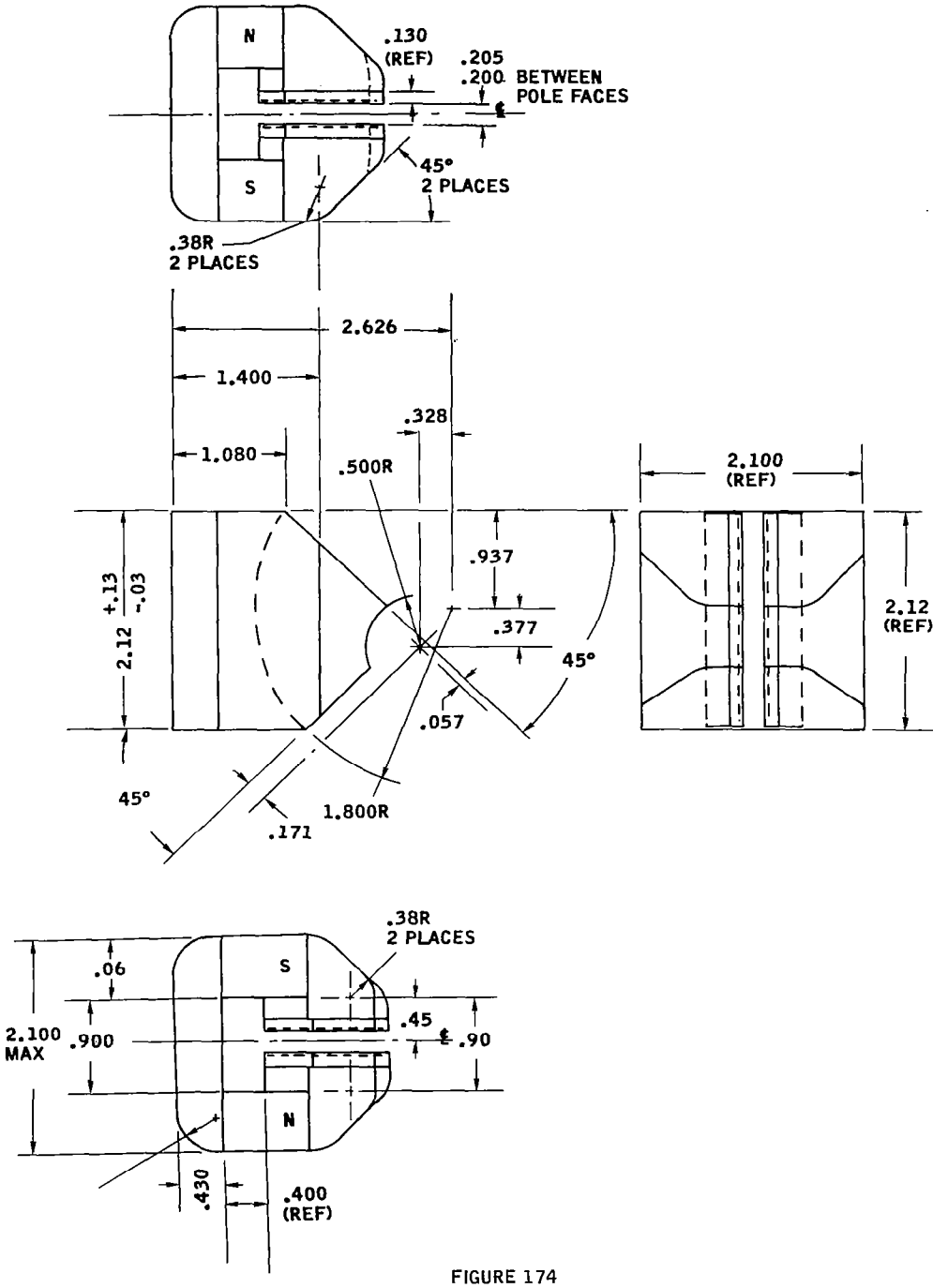

FIGURE 174
Initial Analyzer Magnet Design

A 7% reduction was adequate but a larger value is desirable. Second, a reluctance factor, f, is defined as:

$$f = \frac{MMF}{MMF_g} + 1 \qquad (1)$$

where

MMF = magnetomotive force required for soft iron pole faces and joints.

MMF_g = magnetomotive force required for the air gap.

The parameters B_d and H_d are determined from a demagnetization curve for Alnico V and represent the maximum energy product points. Increasing B_d above this value would require an increase in the amount of magnetic material used. Finally, the tolerance placed upon B_g will keep the ion energy and ion source sensitivity within the required range.

Several other constraints were placed upon the magnet design:

a. Due to the altered analyzer shape the magnet yoke must extend around the high mass side of the analyzer envelope rather than the low mass side as anticipated in the conceptual design.

b. The yoke geometry must be such that the magnet can be moved in over the analyzer envelope and not have the two interface. A motion of 0.400 inch is specified and thus becomes the minimum dimension between the inner edge of the yoke and the envelope. The envelope will fold at the pole piece surface when the magnet is in the theoretical position.

c. The outer dimensions of the magnet are limited in order that the magnet will fit into the space provided for it. Initially, this limited the magnet width (perpendicular to the pole faces) to 2.0 inches.

d. Variations in the cross-sectional area and shape from the pole faces to the yoke must be fairly gradual in order to minimize the leakage factor.

With this information, an initial design was carried out using the following design equations:[14]

$$L_m = \frac{fH_g L_g}{H_d} \qquad (2)$$

$$A_m = \frac{F B_g A_g}{B_d} \tag{3}$$

$$F = 1 + P_e/P_g \tag{4}$$

$$P_e = 1.24\sqrt{S} \tag{5}$$

$$S = (1/2)C L_m + A_g \tag{6}$$

where

L_m = length of magnetic material

A_m = cross-sectional area of magnetic material

F = leakage factor

P_e = leakage permeance

P_g = gap permeance

S = surface area of 1/2 of the magnetic material

C = perimeter of the pole face

The following values were obtained:

L_m = 4.909 cm

(A safety factor was added by letting L_m = 5 cm.)

A_g/L_g = 18.2

P_g = 19.5 (from Figure 28 of General Electric Manual)

S = 40.6 cm^2

P_e = 7.90

F = 1.405

A = 5.74 cm^2

Using these parameters as an initial guide and with the defined pole face configuration a magnet was designed. The cross-sectional area at the midpoint of the yoke was set at 0.5 x 2.12 in^2 or about 6.8 cm^2 which is greater than required. When the constraints outlined above were applied it was found that the length of magnetic material was about 9.1 cm which is considerably greater than the specified value of 5.0 cm.

Two things can be done with this extra length. First, it can be utilized by placing ridges on the pole pieces in order to improve the uniformity of the flux density over the pole face area. This will increase the value of L_g and therefore the required value of L_m. The other thing which may be done is to utilize a soft magnetic material as a yoke to fill in part of the magnet circuit. A material such as Armco iron has a much higher permeability than does Alnico V so that a smaller yoke cross-section may be utilized thereby saving weight.

Both of these methods were employed. Ridges 0.030 inch high were placed on the pole pieces. This actually amounted to dishing out the pole pieces so that at the edges the gap was 0.660 cm. This also reduced the pole piece thickness in the center from 0.130 inch to 0.100 inch. The length of magnetic material required to sustain the required gap flux density was then computed. It came out to about 6.5 cm which left some magnetic circuit length to be filled in by Armco iron. After consulting with General Electric Co. a new formula was applied to compute the leakage factor. The result was very close to F = 2.0. This value is exactly what the magnet designers at General Electric believed to be a reasonable value for a magnet of this size and shape. The area of the magnet was then computed to be 0.9 Ag. It should be pointed out that an iterative procedure must be followed in which A_m is computed with an assumed value of F and then F is computed using this value of A_m. Then A_m is recomputed and so forth. The effects of the yoke may be computed by using a modified form of equation (2):

$$H_d L_m = \frac{B_g L_g}{\mu_o} + \frac{B_y L_y}{\mu_y} \tag{7}$$

where

B_y = flux density in the yoke

L_y = length of yoke

μ_y = permeability of yoke material

In this case it is assumed that other contributions to the reluctance factor are negligible (i.e. f = 1.0). For B_y = 16,000 gauss, L_y = 2.1 inches and μ_y = 700 (reasonable for Armco iron), it can be shown that the second term on the right of equation (7) is about 4% of the first term and therefore the value of the reluctance factor assumed earlier (f = 1.2) will be more than enough to account for the reluctance of the yoke. The area required for the yoke is found from

$$A_y = \frac{B_d A_m}{B_y} \tag{8}$$

For B_y = 14,000 gauss and the other parameters are before A = 0.91 in^2 which establishes the yoke thickness for a given yoke width.

The magnet design shown in Figure 174 was submitted to General Electric for their comment. They returned a slightly modified and more conservative design. The principal changes which were made were increasing the magnet height by 0.320 inch to increase the length of magnetic material and to allow a larger 'window' inside of the yoke (for the purpose of reducing leakage losses), and simplifying the shape of the Alnico V pieces so that they could be more readily fabricated. This created a variance between the magnet cross-section and the pole face cross-section at their interface but there was full assurance from General Electric that this would create no problem in the resulting field. The first generation magnet is shown in Figure 175.

SECOND GENERATION MAGNET DESIGN

The second generation magnet was attained by modification of the first generation magnet. In the first generation magnet the arm and magnet were one piece of Alnico V. The shape of this arm magnet has a sharp bend. Difficulty has been reported in uniformity charging Alnico V which is bent. The cross-section of the arm magnet in the first generation magnet increases along the magnetic material from the yoke junction to the pole face junction. This non-rectangular shape was thought to be part of the uniformity problem because its shape did not lend itself to uniform charging. The decision was made to build the second generation magnet with the magnetic material in the shape of a rectangular block. This modification reduced the amount of magnetic material used. The curved part of the magnet which was originally Alnico V was replaced by Armco. The yoke was raised a small distance on the side of the magnet for better support as shown in Figure 176.

THIRD GENERATION MAGNET DESIGN

Evaluation of the second generation magnet design has led to a number of changes. The major changes are:

a. The use of Alnico V-7 instead of Alnico V.

b. Reduction in yoke size.

c. Modification of pole shape.

d. Reduction in air gap and the ridge on the magnet's face.

The choice of Alnico V-7 instead of Alnico V was made primarily because Alnico V-7 is believed to be more stable. The difference between Alnico V-7 and Alnico V is determined by when the magnetizing field is applied. When Alnico V is made the molten magnetic material is allowed to cool before the magnetizing field is applied. In making Alnico V-7 the magnetizing field is applied to magnetic material before it hardens. Application of the field to the material while it is in a molten state tends to better align the domains in respect to stability and energy product than the method used with Alnico V.

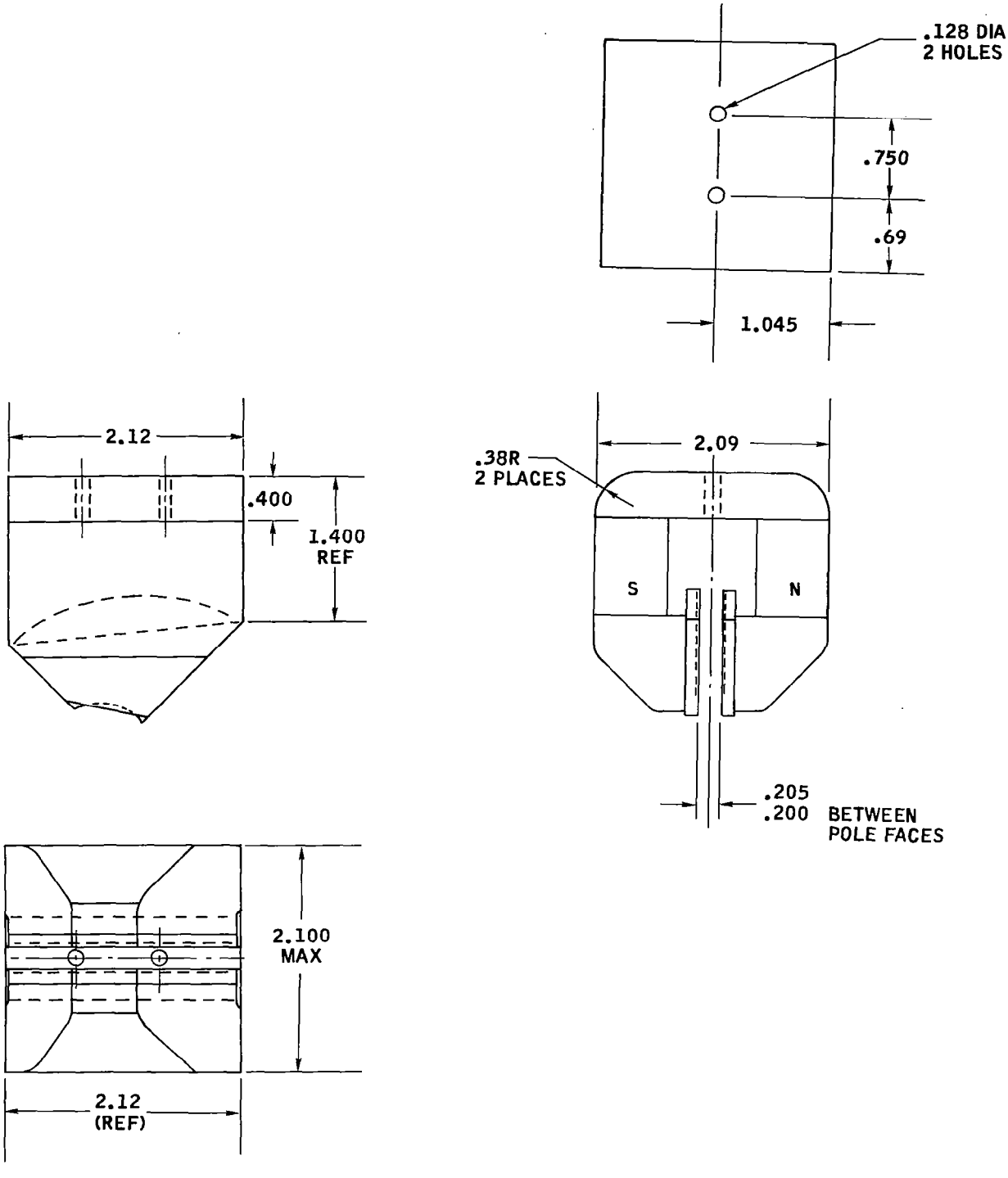

FIGURE 15
First Generation Magnet Design

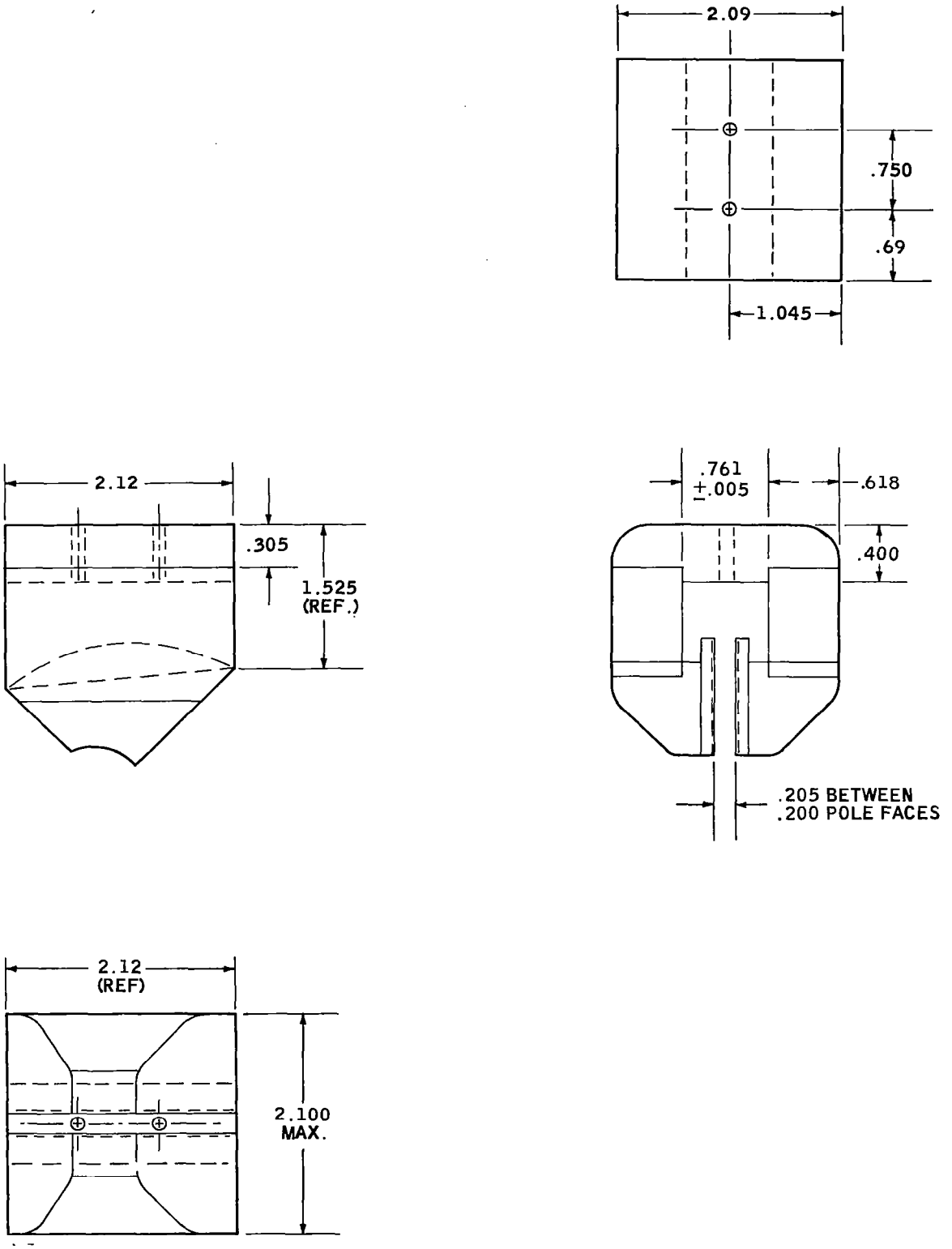

FIGURE 176
Second Generation Pole Pieces

The peak energy product of Alnico V-7 is 7.25 megagauss-oersteds and occurs at B and H values of 11,150 gauss and 650 oersteds. The peak energy product of Alnico V is 5.50 megagauss-oersteds and occurs at B and H values of 10,000 and 550 oersteds. The same design parameters for the magnetic material are to be used as in the second generation design. They are:

L_g = 0.200 inch (gap length)

A_m = 1.32 in^2 (magnet area)

L_m = 2.8 inch (magnet length)

A_g = 1.46 in^2 (gap area)

The slope of the operating line is determined by:

$$\frac{B_d}{H_d} = \frac{A_g L_m}{A_m L_g}$$

$$\frac{B_d}{H_d} = \frac{(1.46)(2.8)}{(1.32)(0.2)} = 15.4$$

where B_d = flux density of the magnet corresponding to the operating point on the demagnetization curve, and H_d = magnetizing force (oersteds) of magnet corresponding to the operating point on the demagnetization curve.

An estimate of the flux in the air gap can be obtained by:

$$B_g = \frac{A_m B_d}{A_g}$$

A B vs. H curve for Alnico V and V-7 is shown in Figure 177.

Evaluating B_g by taking values of where $\frac{B_d}{H_d}$ intercepts the curves for Alnico V

$$B_g = \frac{1.32}{1.46} (9,400) = 8,460 \text{ gauss}$$

for Alnico V-7

$$B_g = \frac{1.32}{1.46} (10,500) = 9,710 \text{ gauss}$$

The second generation magnet was built using Alnico V. The obtained field strength was 4100 gauss. Therefore, a field strength of approximately

$$B_g = \frac{4100}{8460} (9,710) = 4,700 \text{ gauss}$$

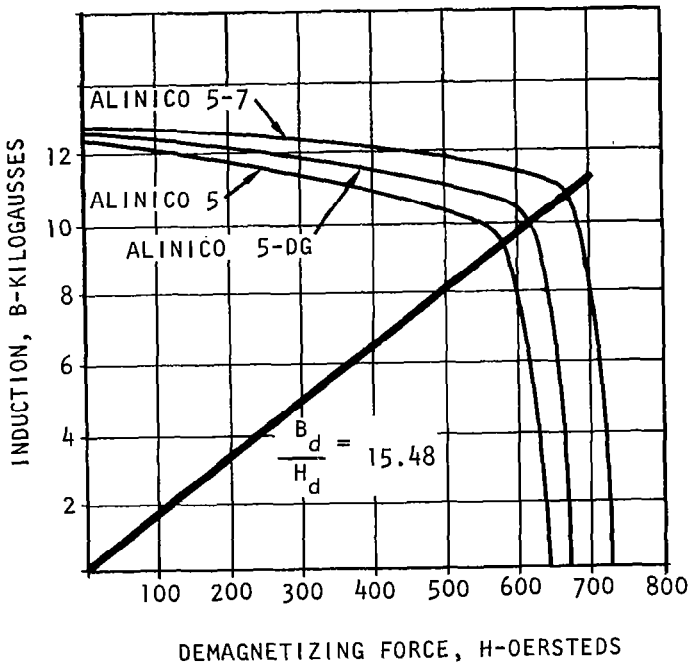

A-150C

FIGURE 177

B Versus H Curve for Alnico V and V-7

would be expected using the same design but substituting Alnico V-7 for Alnico V. Modifications two and three are primarily for additional stability. Armco is no longer on the sides of the magnet. The presence of Armco on the sides of the magnetic material would, as time passed, tend to realign the domains in the magnet particularly at the corners. For stability and uniformity it is essential that the magnetic domains remain fixed. The reduction in Armco is made at the yoke and at the pole piece section covering the sides of the magnet. (Figure 178)

The pole face contains a ridge which is raised 0.03 inch above the face of the magnet. In the magnet constructed of Alnico V a jump of about 300 gauss was measured at the ridge. A calculation of the field at the ridge, if fringing effects are neglected, gives:

$$B_1 L_1 = B_2 L_2$$

$$(4100)\ (2.6) = B_2\ (2.00)$$

$$B_2 = 5330 \text{ gauss}$$

The probe used to measure the field has an area larger than the ridge and, therefore, is integrating the flux over the length of the probe. It is assumed that the flux lies somewhere between the calculated and measured values. A jump in field of between 300 and 1300 gauss was judged too large for excellent instrument performance. The field should increase gradually from zero to its maximum value, the gap field value, as one transverses the fringe field towards the gap of the magnet. It was decided to half the height of the ridge thereby bringing the faces in by 0.030 inch. The calculated fields are now:

a. In the middle of the gap

$$10{,}650 = BL = B(2.3)$$

$$B = 4.63 \times 10^3 \text{ gauss}$$

b. Over the ridge B is still 5300 gauss (calculated). When Alnico V-7 is used, these values become:

$$B = \frac{(9710)}{(8460)}\ 4630 = 5280 \text{ gauss (in the gap)}$$

Over the ridge

$$B = \frac{(9710)}{(8460)}\ (5330) = 6040 \text{ gauss}$$

Saturation calculations were performed on the magnet system at the points of interest in the old design and the new design. Assuming the flux is constant throughout the magnetic circuit yields

$$\phi = \text{constant} = B_1 A_1 = B_2 A_2, \text{ etc.}$$

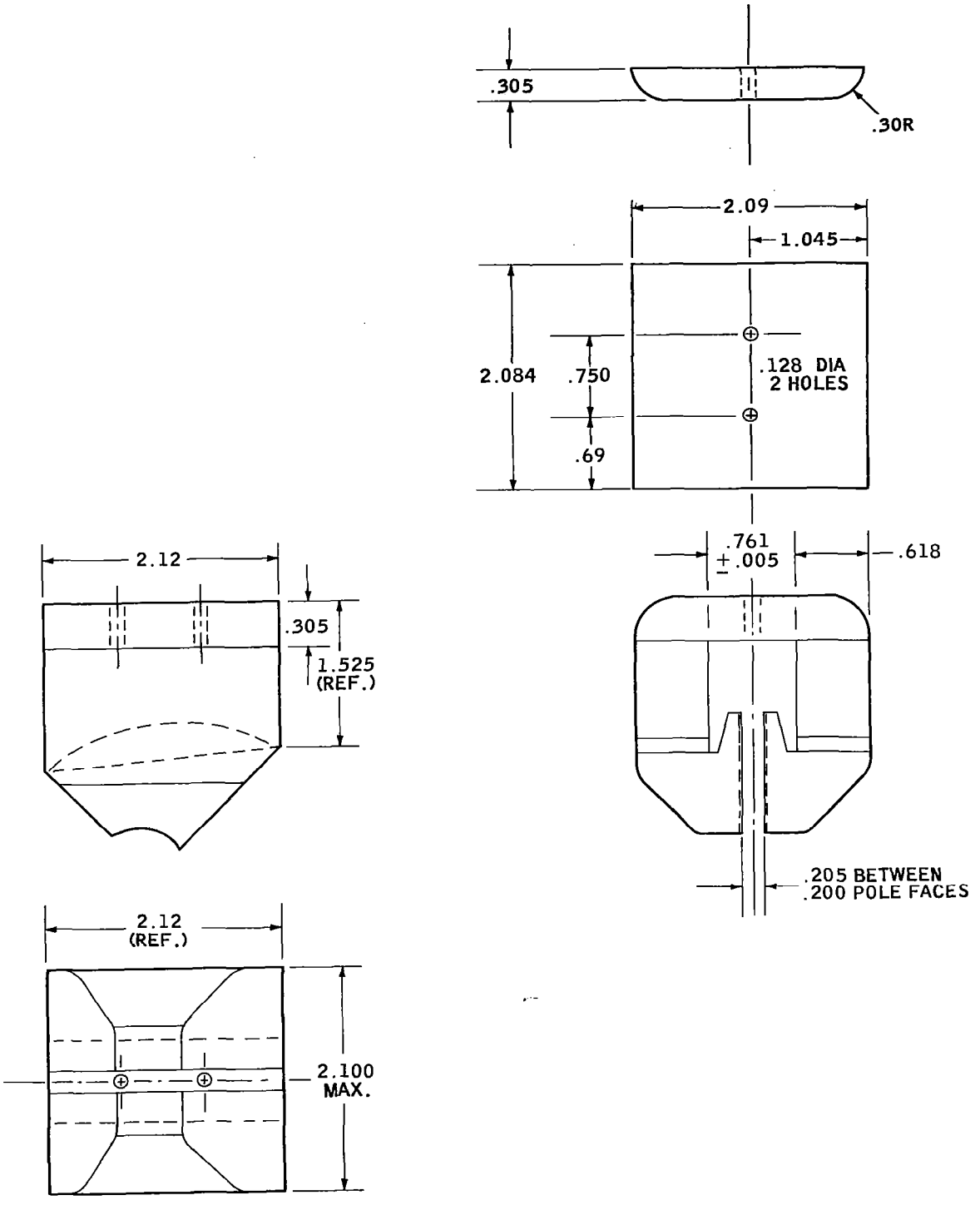

FIGURE 178
Third Generation Pole Pieces

The field across the gap is approximately 5200 gauss with Alnico V-7. By examining Armco saturation curves it was determined that a field of 14,000 gauss was well below saturation. At no place in the circuit was a field of 10,000 gauss found.

The method outlined for determining the flux density of a magnet of essentially the same design as the second generation magnet but made of Alnico V-7 utilizes the fact that the leakage is determined by the shape of the magnet. Therefore, the leakage factors should be essentially the same for magnets of generations two and three. The calculation predicts the third generation magnet should have a field of about 5200 gauss. The measured field of the magnet was 4850 gauss after a 10 percent knockdown. The second generation magnet was usually knocked down about 8 percent. This fact, together with the difficulty of imposing uniform control upon magnet construction and materials and the lack of accuracy in data furnished concerning magnetic materials, limits the accuracy of a theoretical or even semi-empirical prediction of magnet field strength. A reasonable estimate within 10 percent is obtainable.

STABILITY

The original Engineering Test Model (ETM) analyzer magnet was a five piece assembly which was held together by epoxy. The magnet was wrapped with a coil of wire at Aerospace Systems and taken to an outside vendor for charging. It was found that in handling the magnets at Aerospace Systems the flux level did not appear to be stable but would drop with time. While this problem did not seem to be too detrimental to the ETM testing it was more severe once testing of the flight prototype units began. Attempts to stabilize the magnet by shock treatment proved unsuccessful. While this technique had been useful in stabilizing earlier magnet designs it seemed to continually reduce the field of these magnet assemblies. Continued experimentation with the shock treatment led to another problem. The magnet assemblies were occasionally broken since the epoxy was not a sufficiently strong binding material to withstand the shock.

At this point several steps were taken. One of the magnets was sent to General Electric for analysis of the Alnico V material. Conversations with General Electric indicated that one of the problems might be the joining process which would not give adequate mechanical stability. General Electric recommended the pieces of the magnet assembly be soldered together. Various soldering techniques were investigated and a procedure for joining the magnet pieces was established. General Electric reported that the magnet material furnished by Aerospace Systems seemed to be normal in every respect. While discussing this it was brought out that a magnetically soft material had been used to strike the magnet during shock treatments. General Electric felt that this was the problem. They indicated that striking the surface of a permanent magnet with a magnetic material will cause a small additional pole to be created at the point of impact, which will effect the gap flux density. General Electric felt that great caution should be taken against striking the surface with the magnetic material and that when conducting any further shock treatments a rubber mallet should be used. It was then realized that during the handling of the ion source magnetic shields the bottom shield often slipped down and struck the magnet and it was reasoned that perhaps this caused a drop in the flux density. A coating material for the magnets was then obtained and all magnets from that point on were coated with approximately 1/8 inch thick protective resilient coating. At the same time steps were taken to purchase a magnet charger and magnet treater so that Aerospace Systems would have more control over the processing of the magnets. In the past the magnets were charged out of the plant. This gave Aerospace Systems much less control over the process and did not afford an opportunity to learn about the elements in the charging technique which might lead to magnet stability.

Aerospace Systems has recently acquired an R.F.L. magnet charger, Model 2470-350, and an R.F.L. magnet treater, Model 889B. The acquisition of this equipment allowed control over the complete charging and stabilization processes. The equipment was used on the third generation magnet.

The aging test has been running for seven weeks. Temperature cycling has been run between -20°C and 100°C for a three hour duration per temperature for over a week. No measurable change in magnetic field has been noticed. Further stability tests are to be performed but it now seems as if the stability problems are solved.

STABILIZATION

Permanent magnets do not naturally decay with time and no energy is required to maintain the magnetic field. Therefore, there is no theoretical reason for a permanent magnet to continually lose strength. Flux changes do occur in actual practices as a result of physical contact and environmental changes. Proper stabilization is needed to eliminate or reduce the effects of these factors.

METALLURGICAL CHANGES

The old magnetic materials such as cobalt-steel experience metallurgical changes as a function of time. If such a magnet is magnetized before these changes have stabilized, flux changes superimposed upon those to be described in Section 5 occur. Often this effect is reduced to a negligible factor by artificial aging. The newer materials such as the Alnicos and ceramics do not exhibit metallurgical changes to any reasonable degree at room temperature.

CHANGES DUE TO TIME

It is an established fact that freshly magnetized magnetic materials lose a percentage of its flux as a function of time. The loss is exponential as is shown by the experimental evidence that the flux loss plots linearly against time on a semi-log plot. Table 32[15] gives the results of laboratory measurements on some material. All losses are based on measurements made 0.1 hour after magnetizing.

The flux loss in Alnico is essentially eliminated by a partial demagnetization (called knockdown) of the freshly charged magnet. The accepted percentage of "knockdown" is from 7 to 15 percent. This can be accomplished crudely by merely striking the magnet with a non-magnetic mallet, such as hard rubber. This method besides being crude is generally unreliable because of the lack of control in determining the knockdown percentage as function of the amount of impact and number of impacts. The knockdown procedure is considerably more efficiently accomplished by an ac coil with the ac field in the same direction as was the magnetizing field. The knockdown is accomplished by gradually reducing the ac coil to zero by reducing the ac voltage to zero, by means of a variable auto-transformer. The function is performed in the lab using the R.F.L. magnet treater.

CHANGES DUE TO TEMPERATURE

Temperature effects can be said to fall into three categories.

a. Metallurgical changes may be caused by exposure to temperature changes above the curie temperature. Flux losses of this type are not recoverable by remagnetization.

TABLE 32

MATERIAL	LOSS PER LOG CYCLE (FIRST CYCLE IS 0.1 HOUR)	LOSS AT 100,000 HOURS 11.4 YEARS
Ceramic	Essentially zero	Essentially zero
Alnico III (near max. energy)	0.4%	2.4%
Alnico III (near coercive)	0.6%	3.6%
Alnico V (near residual)	0.01%	0.06%
Alnico V (near max. energy)	0.15%	0.9%
Alnico V (near coercive)	0.4%	2.4%
Alnico V-7 and Alnico VIII	Very similar to Alnico V	

The approximate maximum temperature which can be used without experiencing metallurgical changes is 550°C for Alnico V to 180°C for the ceramics. Often the effect of metallurgical changes can be avoided only by long-time exposure of the magnet to the temperature involved before magnetizing.

b. Irreversible losses are defined as a partially-demagnetization of the magnet caused by exposure to high or low temperatures. These losses are recoverable by remagnetization. Table 33[16] shows temperature losses for several magnetic materials.

TABLE 33

MATERIAL	350 C	200 C	-20 C	-60 C
Ceramic 5 (P_c 2 above max. energy)	0	0	0	0
Ceramic 6 (P_c 1.1 near max. energy)	0	0	0	0
Alnico V (near max. energy)	1.3%	0.8%	1%	2.5%
Alnico VI (near max. energy)	0.6%	0.4%	0.5%	1.3%
Alnico VIII (near max. energy)	0.3%	0.2%	0.1%	0.1%
Alnico VIII (near coercive)	3.5%	2.0%	0.5%	0.8%

The values shown in the table were obtained by measurement after the specimen had returned to room temperature after exposure to the indicated temperature. Percentages shown in the table are not additive for consecutive cycles above and below room temperature.

The method usually used for temperature stabilization is to install the magnet in the magnetic circuit for which they are intended, magnetize, then subject them to several temperature cycles between limits greater than the extremes they are to experience in service. This procedure is time consuming, taking several days for completion. An alternate method is available which uses an ac field as in the "time" section. A knockdown of 7 to 15 percent provides temperature stabilization. This fact has been tested at Aerospace Systems.

Seven temperature cycles have been run on the third generation magnet after it had been charged and knocked down 10 percent. A cycle consists of:

1. 3 hours at $-20^{o}C$
2. Return to room temperature
3. 3 hours at $100^{o}C$
4. Return to room temperature

After seven cycles no measurable change in flux has been observed.

c. Reversible losses are changes in flux which are reversible with temperature. For example, some ceramics lose as much as 0.19 percent at room temperature flux when heated $1^{o}C$. But when room temperature is reached the flux loss is regained. The Alnico has reversible losses on the order of 1/10 as great as that for ceramics, depending on the material and operating point on the demagnetization curve. These reversible variations cannot be eliminated by stabilization methods but fortunately these losses are very small for the Alnicos.

RELUCTANCE CHANGES

It is possible to have flux losses due to permance changes in the magnetic circuit. By permeance changes it is meant changes in the air gap or open circuiting the magnet. Whether or not a loss is experienced depends upon the properties of the materials and upon the extent of the permeance change.

Stabilization against such change may be accomplished by subjecting the magnet several times to reluctance changes of the same magnitude of those expected to be encountered in service. Stabilization against reluctance changes is also obtained by the ac field previously mentioned.

STRAY FIELDS

Partial demagnetization may occur if the magnet is subjected to stray magnetic fields. Stabilization against this hazard is also accomplished by the ac field previously mentioned.

SHOCK, VIBRATION, STRESS

Shock and vibration have a small percentage loss associated with them (a few tenths of a percent) and are not of major importance. The ac field stabilizes the magnet against shock and vibration.

FIELD UNIFORMITY

The uniformity of the magnetic field is a primary factor in determining the value of a magnet design to be used with a mass spectrometer. The dispersive and focusing properties of any lens system is greatly dependent upon the position of the ion in the magnetic field. A large variation in field uniformity can greatly limit the dispersive and focusing properties of the magnetic field, therefore, limiting the resolution. It is desirable to have the magnetic field as uniform as possible.

In order to readily compare the uniformity of the three magnets a field plot was taken along four lines for each of the three magnets. A table was prepared in which the end points of the line were neglected (none of the collected ions travel far enough to be influenced by the extreme points on the line) and fractions were formed by taking the largest value of the field along a line as the denominator and the difference between the largest field value and the smallest field value along the line as the numerator. This ratio is also expressed as a percentage. Values are not taken over the ridge. Average values are also given. (See Figure 179)

LINE	1st GENERATION	%	2nd GENERATION	%	3rd GENERATION	%
1	$\frac{400}{4400}$	9.1	$\frac{150}{4250}$	3.5	$\frac{300}{4800}$	6.3
2	$\frac{500}{4350}$	11.5	$\frac{300}{4150}$	7.2	$\frac{200}{4850}$	4.1
3	$\frac{250}{4400}$	5.7	$\frac{150}{4300}$	3.5	$\frac{200}{4700}$	4.3
4	$\frac{400}{4400}$	9.1	$\frac{350}{4300}$	8.2	$\frac{180}{4880}$	3.7
Ave	$\frac{390}{4390}$	8.9	$\frac{238}{4250}$	5.6	$\frac{220}{4810}$	4.6

By examining the table it is readily seen that the uniformity is improved with the newer magnet designs. This increase in uniformity is due primarily to the shape of the magnetic material used. In the first generation magnet a relatively large curved piece of Alnico V is used which is smaller at one end than the other.

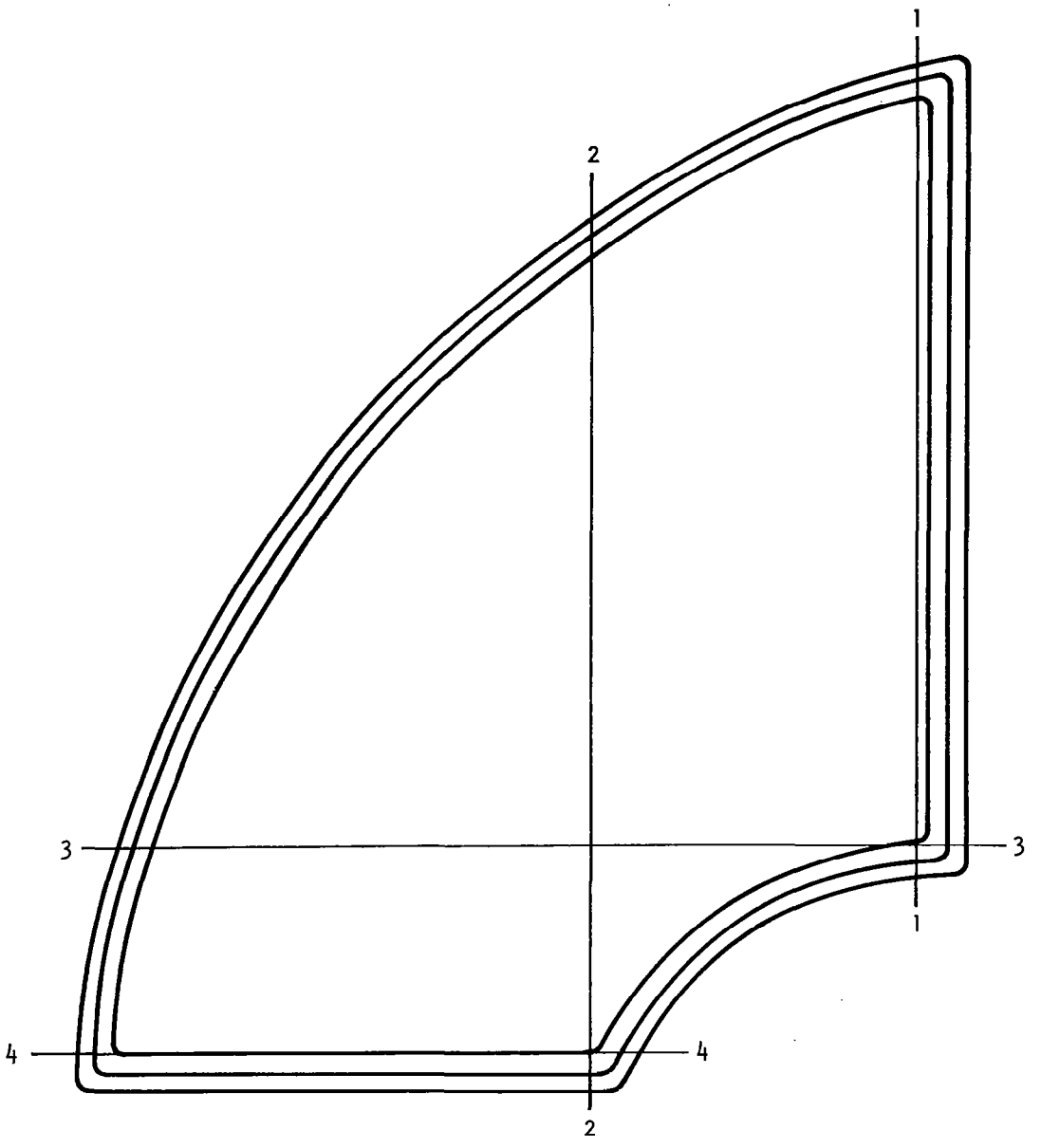

FIGURE 179
Pole Face Map

Uniformally charging such an awkwardly shaped piece of material presents problems in aligning the magnetic domains conformally. In the second and third generation magnets simple rectangular blocks of magnetic material are used and therefore better alignment is obtained. In general, even better alignment is expected when Alnico V-7 (as in the third generation magnet) is used because magnetization occurs when the material is still soft therefore making it easier for the domains to align uniformally. Also it should be noted that the third generation magnet is not superior to the second generation magnet along two of the four lines in the pole face map, but the average percentage deviation is better for the third generation magnet. Part of the increase in uniformity is probably due to a redesign of the pole pieces for the second and third generation magnet as shown in Figures 176 and 178, respectively. In general, a quite successful study was made in which the problems of magnet stability and uniformity were solved. A magnet system was developed capable of fulfilling all the present Two Gas Sensor performance requirements.

Pole face maps for the three generations of magnets are presented. They are shown in Figures 180, 181 and 182.

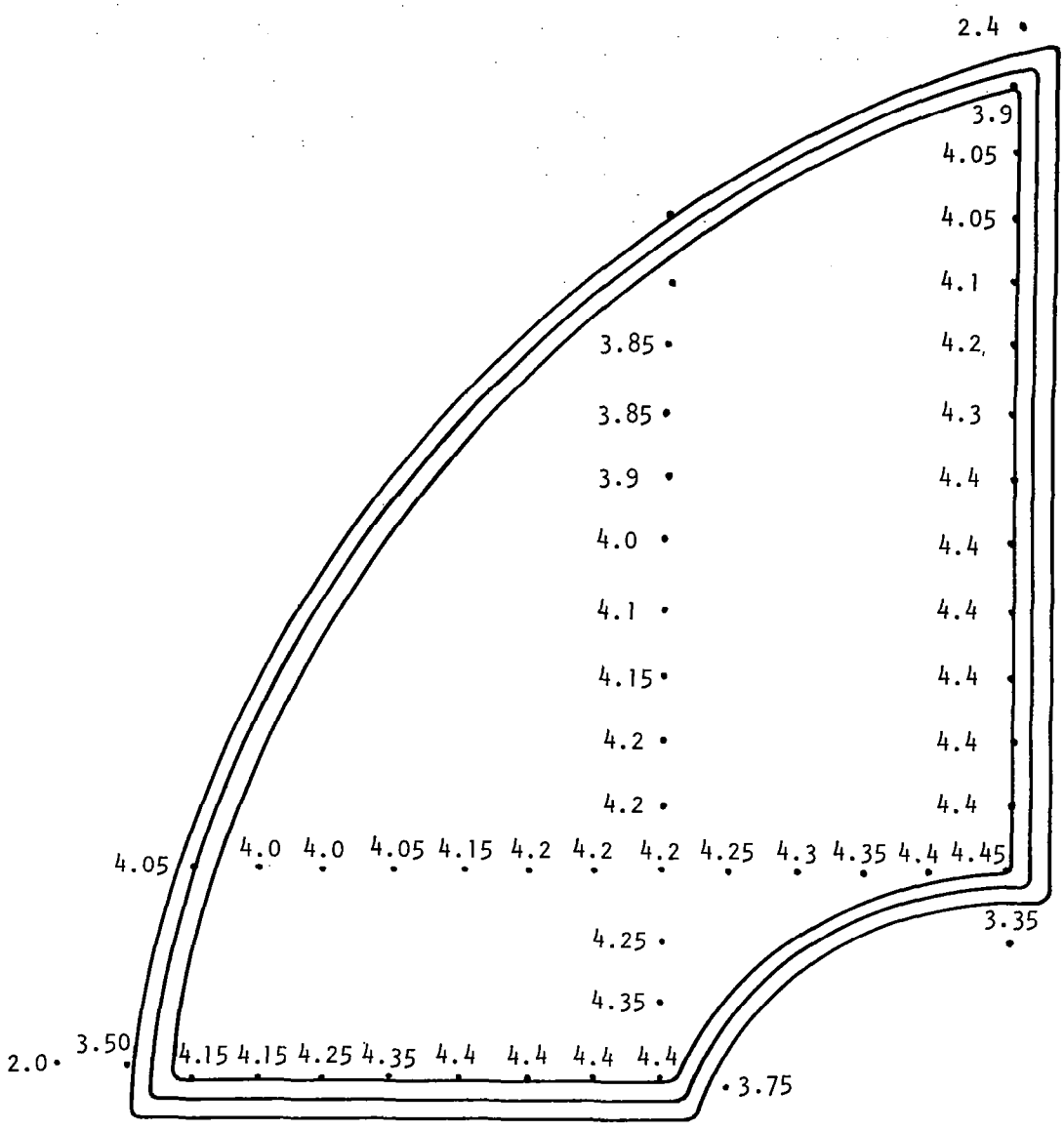

FIGURE 180

First Generation Magnet Pole
Face Map (Field in Kilogauss)

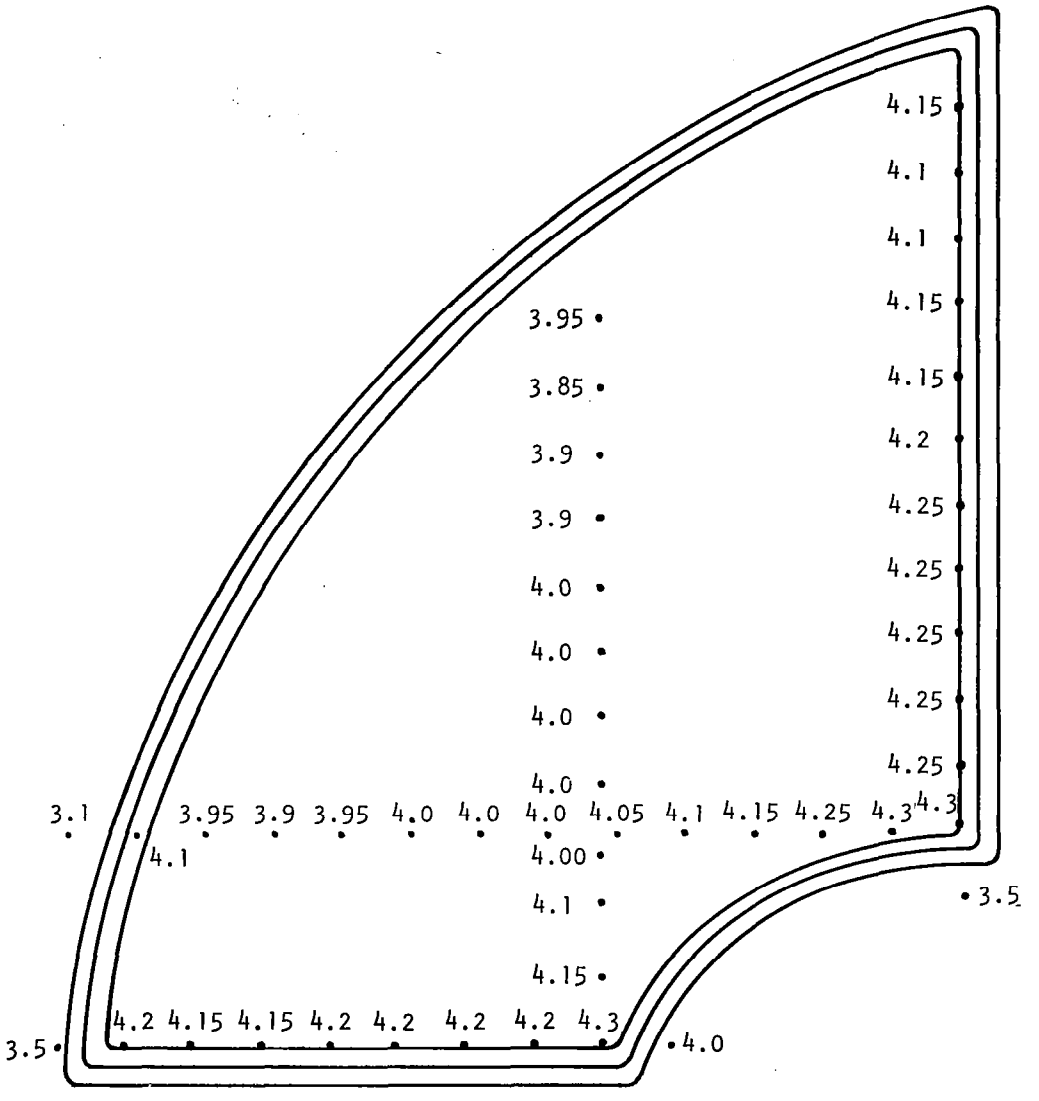

FIGURE 181

Second Generation Magnet Pole Face Map (Field in Kilogauss)

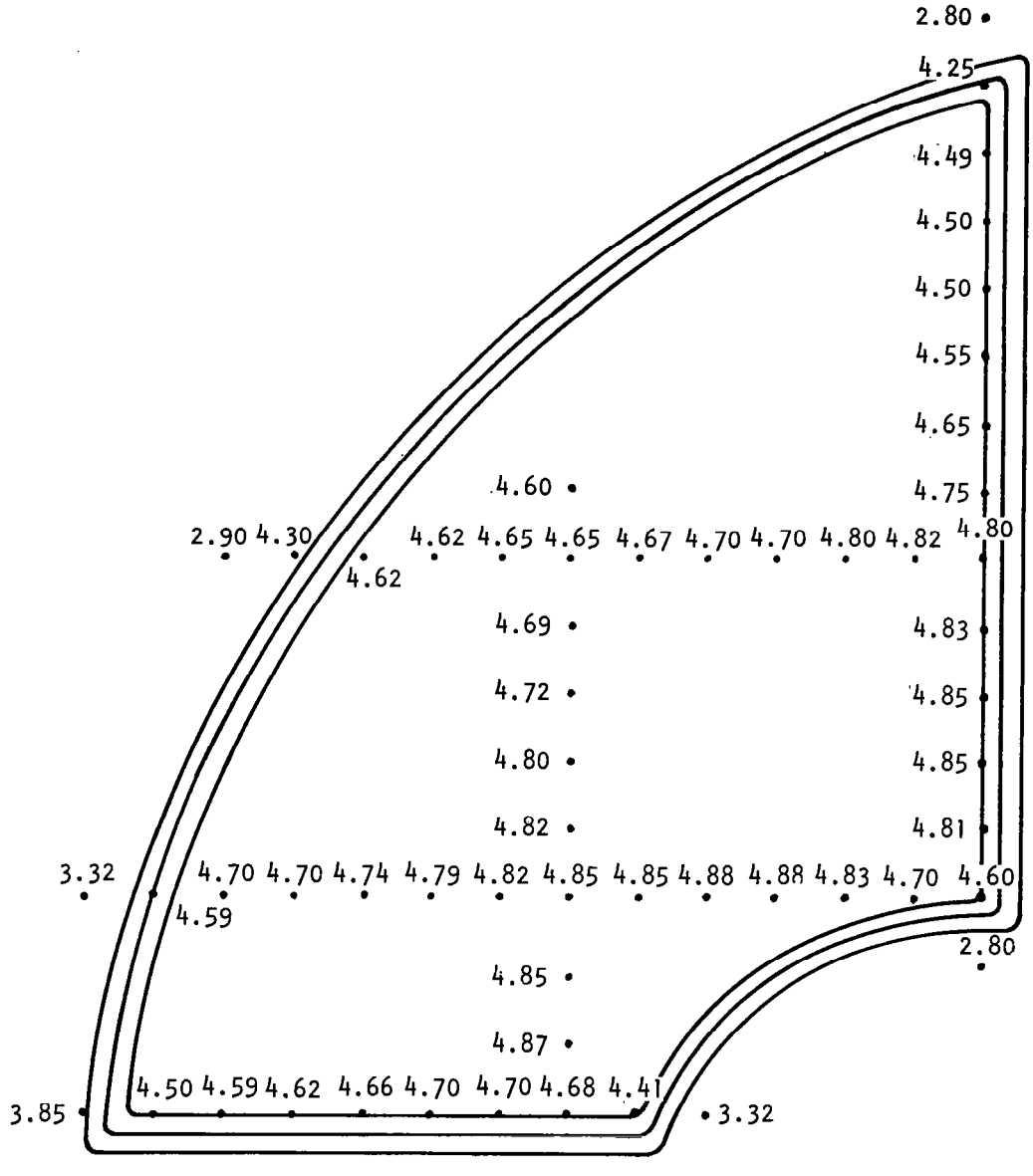

FIGURE 182

Third Generation Magnet Pole
Face Map (Field in Kilogauss)

FIELD STRENGTH

The size and weight for the three magnets are essentially the same. The original magnet design produced a field strength of about 4250 gauss. In the second magnet design the amount of magnetic material was reduced. Armco was substituted for Alnico at the pole pieces. A field of about 4100 gauss was obtained. The reduction or field strength between the first and second generation magnets was due to the reduction in magnetic material. The third generation magnet design utilized Alnico V-7 as the magnetic material. A field of 4850 was obtained. The attainment of such a high field with the third generation magnet means that the required field of 4100 can be obtained by a reduction in weight if the size of the window can be reduced. Also, this means that the magnet with its greater field can be used to increase the resolution of the mass spectrometer. The obtained field is about 20 percent greater than the required field. The use of this magnet can give a 44 percent increase in ion source sensitivity.

CONCLUSION

Improved techniques and knowledge in magnet design, manufacturing and stabilization were obtained. The primary point of interest, the magnet stabilization problem, was satisfactorily solved. The second generation magnet was used on a Two Gas Sensor during a 60 day space cabin simulator test held at McDonnell Douglas. The field the magnet charged by 0.6% in 67 days. Knowledge gained since the test allows the design and manufacture of a magnet which will have a change in field strength considerably smaller than 0.6%. The third generation magnet has not shown a measurable change in flux after seven weeks of charging and stabilization This study has produced a magnet sufficiently for operation with the Two Gas Sensor.

ADDENDUM 3

TWO GAS ATMOSPHERE SENSOR SYSTEM
(MASS SPECTROMETER)

SIXTY-DAY SPACE CABIN SIMULATOR TEST

INTRODUCTION

The 60 day, four man test of the McDonnell Douglas Space Cabin Simulator afforded an excellent opportunity for applying the Two Gas Atmosphere Sensor System developed by Perkin-Elmer Aerospace Systems for Langley Research Center in a long-term test. This test allowed the mass spectrometer sensor to be applied as an atmospheric monitor for nitrogen, oxygen, carbon dioxide and water vapor in a closed environmental system.

Since the sensor was located external to the closed cabin it was possible to carefully monitor the performance of the instrument during the 60 day continuous test. The McDonnell Douglas personnel were extremely helpful in obtaining a great deal of data from the mass spectrometer as well as the other atmospheric monitors. This data was reduced by computer and is presented in this report.

During the test the sensor was calibrated on a frequent basis in order to obtain a more absolute measure of its performance. This data indicates that the calibration repeatability for the instrument is approximately $\pm 2\%$. This is the best measure of its accuracy and stability. This number was obtained from calibration data by disregarding certain periods in which the performance was affected by abnormal external conditions which were not relevant to the evaluation of the two gas sensor. One internal condition existed which also created brief periods during which the instrument did not perform within the $\pm 2\%$ variation stated above. This was a change in the ion source filament resistance which could not adequately be compensated for by the emission regulator. This condition was rapidly diagnosed and interim corrective measures were taken during the test. At the same time data obtained during a parallel study effort has led to the determination of a permanent solution so that no recurrence of this condition is expected in future tests. It is indeed possible that the inherent stability of the mass spectrometer is better than the value given above since there were several limitations in the test conditions which possibly reduced the accuracy of the measurements. These factors are described in detail in this report.

The performance of the instrument can best be indicated on an absolute basis as well as in comparison with the other sensors, by the fact that during the fifteenth day of the test the control of the oxygen partial pressure was switched over to the sensor and during the twenty-ninth day the control of the nitrogen partial pressure was also switched over to the sensor. The sensor performed this primary monitoring function successfully for the remainder of the test program.

UPGRADING OF THE ENGINEERING TEST MODEL

Prior to initiation of the test with the Space Cabin Simulator the engineering test model (ETM) of the two gas sensor was upgraded, as required, to the flight prototype sensors status. The ETM sensor was completely disassembled, cleaned and reassembled. New 3 mil tungsten-rhenium (75%-25%) wire filaments were installed in the ion source. The sensor was then mounted on the vacuum system for initial testing without its capillary inlet system.

The original ETM magnet had been returned to General Electric for analysis and a new improved magnet design was used for this instrument. This magnet will be reported on at the conclusion of a magnet stability study which is now in process. The sensor employed straight bar elements of Alnico 5 instead of the shaped pieces which were used in the original design. Because the ETM sensor was not going to be welded closed, and therefore would not fit in the flight package configuration, a special expanded enclosure was designed and fabricated which would accept the analyzer, with its test flanges.

The analyzer and magnet assemblies were mounted in a chassis along with the electronics modules. The latter were mounted in the approximate locations which they occupy in the flight prototype package. A cover was placed over the total assembly during normal operation. The complete ETM system mounted on the laboratory vacuum system is shown in Figure 183.

The system support electronics were also upgraded to the flight prototype level. This primarily involved some modifications in the electrode bias supply which are discussed in detail in the Phase II(b) Final Report on contract NAS 1-6387.

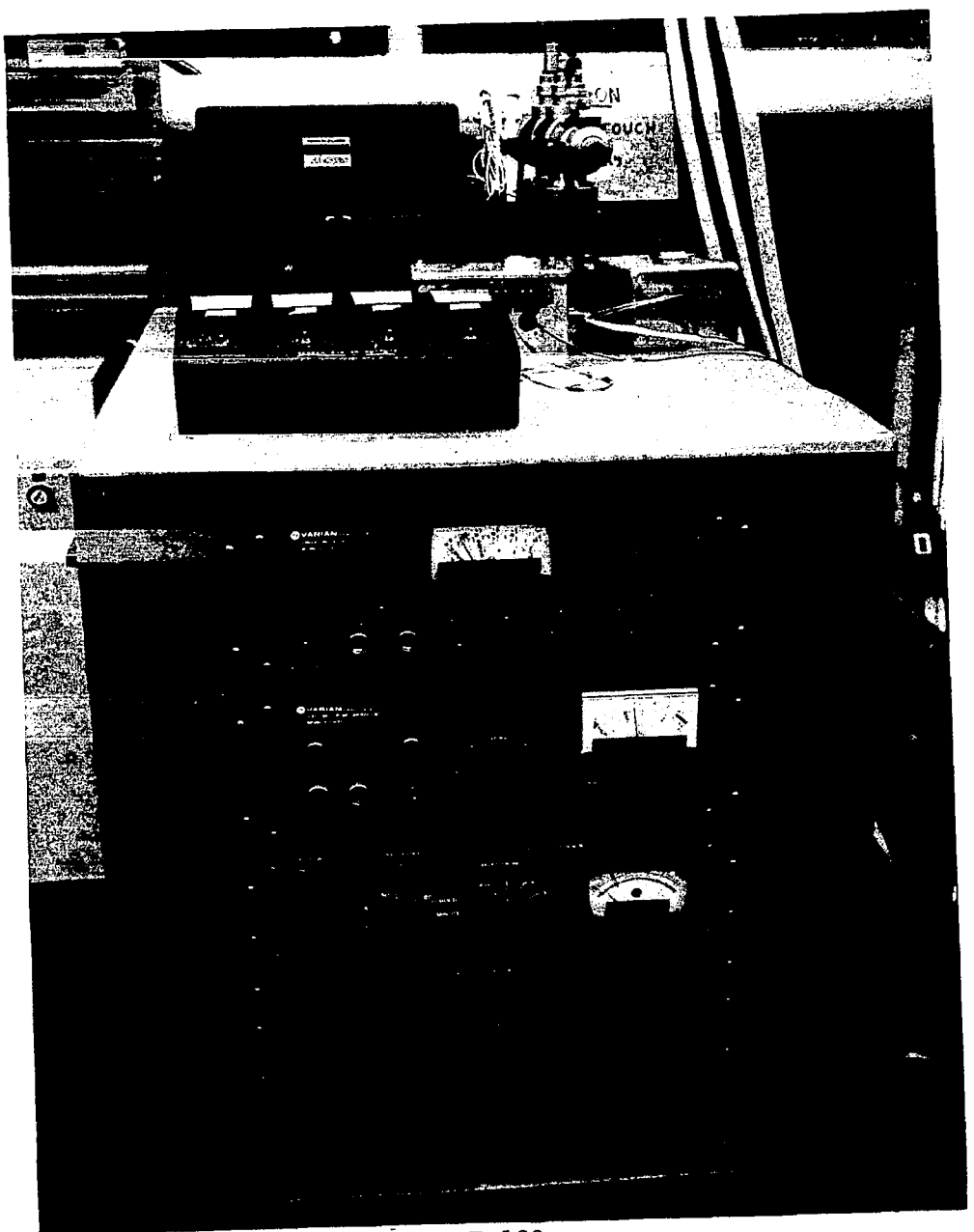

FIGURE 183

ETM System

ETM TESTING PRIOR TO INSTALLATION

The ETM analyzer was tested on the laboratory vacuum system utilizing a set of laboratory power supplies with the filament powered by a dc source. The filament on each electron gun was burned-in slowly to outgas it and give maximum filament life. Each electron gun was then tuned up to give the maximum electron transmission efficiency to the ionizing region. This tune up was conducted for a fixed filament to electron accelerator voltage which has been established as optimum during previous ETM testing. The electron beam was positioned in the ionizing region by determining the voltage difference between the electron accelerators and the anodes for which the output ion current is maximized. The repeller-accelerator voltage was fixed at 10 volts based on earlier test data to reduce the number of potentials to be varied. The analyzer was then briefly tuned to obtain an ion current output at the m/e 28 collector. The ion focusing electrodes and Z-axis focus electrodes were tuned for maximum ion current output. The basic sensitivity of the analyzer (ion current output versus ion source pressure) for nitrogen was measured by introduction of the sample gas into the vacuum system itself so that there was no differential pumping. A nitrogen sensitivity of 5.18×10^{-7} amps/torr at 10uA anode current was measured on electron gun No. 1. Thus the required sensitivity was achieved at approximately 50% of the normal operating anode current.

Having established the operation of the ion source the analyzer was then tuned by varying the magnet position (two directions of translation and rotation). An optimum magnet position was found which minimized the m/e 17 - m/e 18 cross talk at the m/e 18 collector. The same was done for m/e 28 - m/e 32 on the m/e 28 collector. Then a compromise magnet position was found for which the m/e 28 - m/e 32 cross talk specification was met and which gave an acceptable m/e 18 peak in terms of the flatness of the top of the peak. The alignment of the ion current collectors was then checked to see if each ion current to be monitored was centered in its appropriate collector at the same ion accelerating voltage. Sufficient data was taken from which correct collector locations could then be computed.

It took several iterations to arrive at the proper collector locations. With each iteration the sealing integrity of the collector to analyzer housing interface degraded. That is to say, the surfaces became warped and deformed with each iteration due to a deficiency in the clamp flange design which did not allow the clamping pressure to be applied directly over the gold wire gasket. This condition can be readily corrected by a redesign of the collector flange-envelope interface.

As an interim measure the test flange clamps were modified, but this did not completely alleviate the problem and on the final iteration it became necessary to weld the collector flange in place in the flight configuration. This was an excellent opportunity to check the effects of welding upon the alignment of the collectors.

After the flange was welded, the alignment was checked and found to be satisfactory. During this test it was found that the m/e 44 collector was open. That is, it was not connected to the feed through pin. This required that the flange be machined off. Provisions for cutting off the collector flange and rewelding it had been made in the design and this process was accomplished with full success, further demonstrating the feasibility of the welded collector flange.

The open connection which was repaired had resulted from a rework which had been required in order to properly position the m/e 44 ion current collector. This rework stemmed from the fact that the ETM housing which was being used had excessive dimensional variations which had to be accounted for. This condition did not exist on the flight prototype units and a reoccurance of this difficulty is not likely.

Once the collectors were properly located testing of the analyzer with the capillary inlet system began. It was found that the source pressure was higher than the design value which would cause a non-linearity in the sensor output with pressure. An investigation of this led to a modification of the inlet leak manifold such that a more reliable seal was made to the 5μ aperture which acts as the molecular leak. A means of visually inspecting the assembly was also included by means of a viewing port in the exposed surface of the manifold. When the new manifold was tested with the analyzer it was found that the source pressure was still too high. The resulting conclusion was that the 5μ aperture had a larger conductance than indicated by calculations which had been performed. Tests conducted on a leak detector in which the conductance of an aperture was measured for helium appeared to substantiate the conclusion. To adjust for this difference in the most expeditious manner it was decided to lengthen the capillary line by adding approximately 6 feet of 0.0065" I.D. capillary tubing which produced a source pressure of 1.93×10^{-4} torr which is almost exactly the design value of 2.0×10^{-4} torr.

The analyzer was then rapidly integrated with the electronics and the complete system was tested and tuned.

INTERFACE REQUIREMENTS AND INSTALLATION

Several trips to McDonnell Douglas Aircraft were made to establish the interface requirements with the Space Cabin Simulator. It was decided to use a 1/4 inch Swagelok feed through in a port about mid-way down the length of the capsule as the means for routing the capillary line. The sensor and support vacuum system were to remain outside the cabin. This would give a sampling point in the central equipment compartment. The external facilities (AC power, accessibility, etc.) for this location were also determined and found to be satisfactory. It was also felt that some additional filtering of the sampling capillary should be incorporated. While the capillary line has a Millipore filter housed in a holder at the inlet, the existing design does not allow the filter to be readily changed. It was therefore decided to add a large area Millipore filter in front of the capillary inlet. It was also desired that it be possible to calibrate the sensor with a known gas sample mixture from outside the cabin. This in turn requires that the sample gas be introduced at the head of the capillary line.

These various interface requirements led to the design of a coaxial feed through of the capillary line through the 1/4 inch Swagelok line which allowed the outer tube to be used to let the calibration sample into the capillary system. A schematic diagram of the complete sample inlet, calibration and vacuum system is shown in Figure 184. That part of the system which is inside the cabin is shown in Figure 185. It is shown in the calibration mode in which the sample part is flanged off and the sample is introduced to the head of the capillary. The valve for introducing the calibration sample is visible in the photographs. Figure 186 shows one of the occupants of the cabin removing the cover flange after a calibration.

The external calibration gas inlet system is an ordinary gas inlet system with a 2 liter expansion volume, although expansion techniques were not required as the calibration pressure was 360 torr.

Due to good planning and cooperation of McDonnell Douglas Aircraft personnel the installation of the Two Gas Atmosphere Sensor System went extremely smooth and fast with a very minimal amount of problems. The complete system was installed at McDonnell Douglas and made operational in a two day period just prior to the start of the sixty day test. The installation is shown in Figure 187. The vacuum station and calibration inlet system are visible in the center of the photograph.

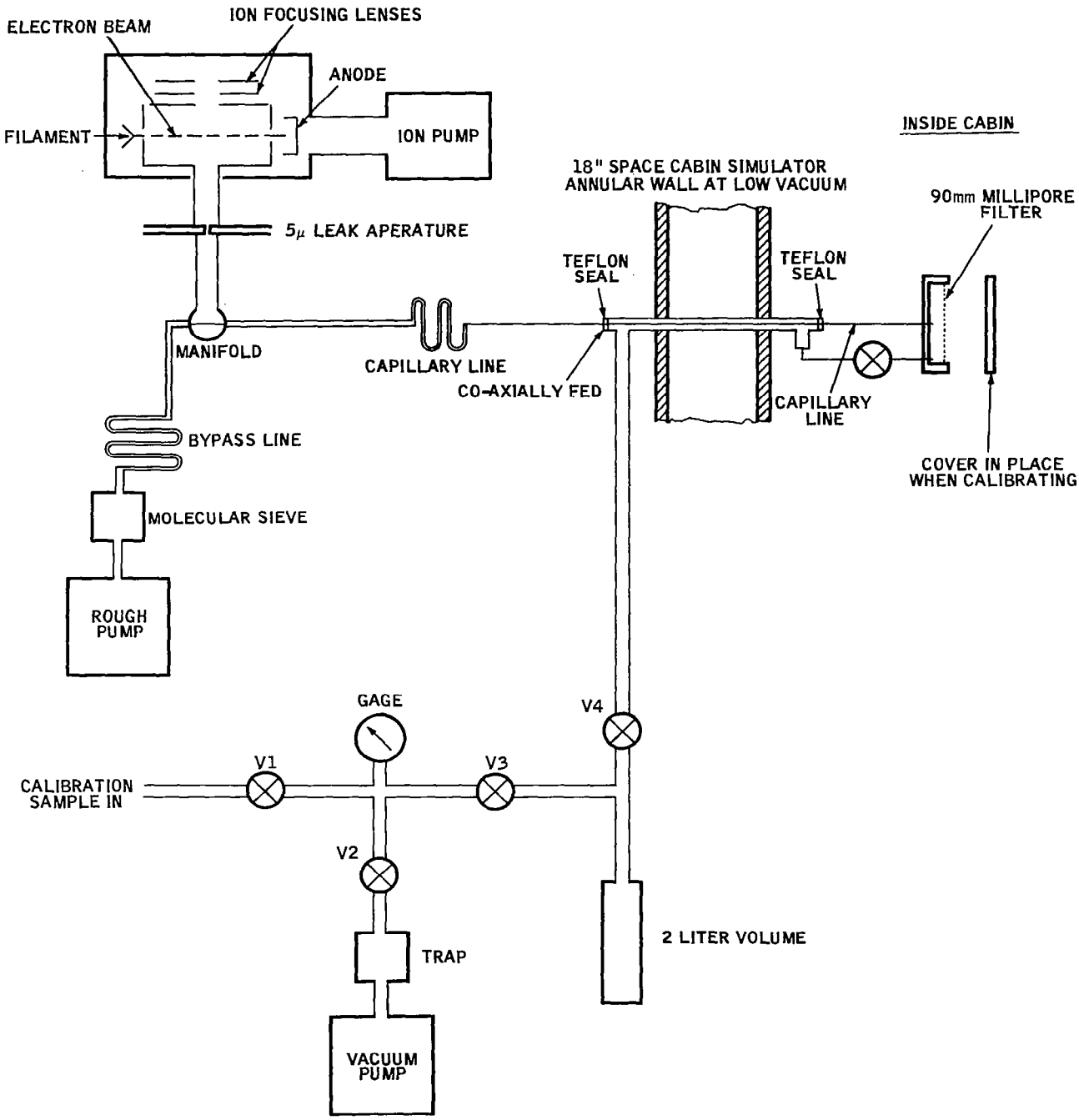

FIGURE 184
Calibration and Vacuum System Schematic Diagram

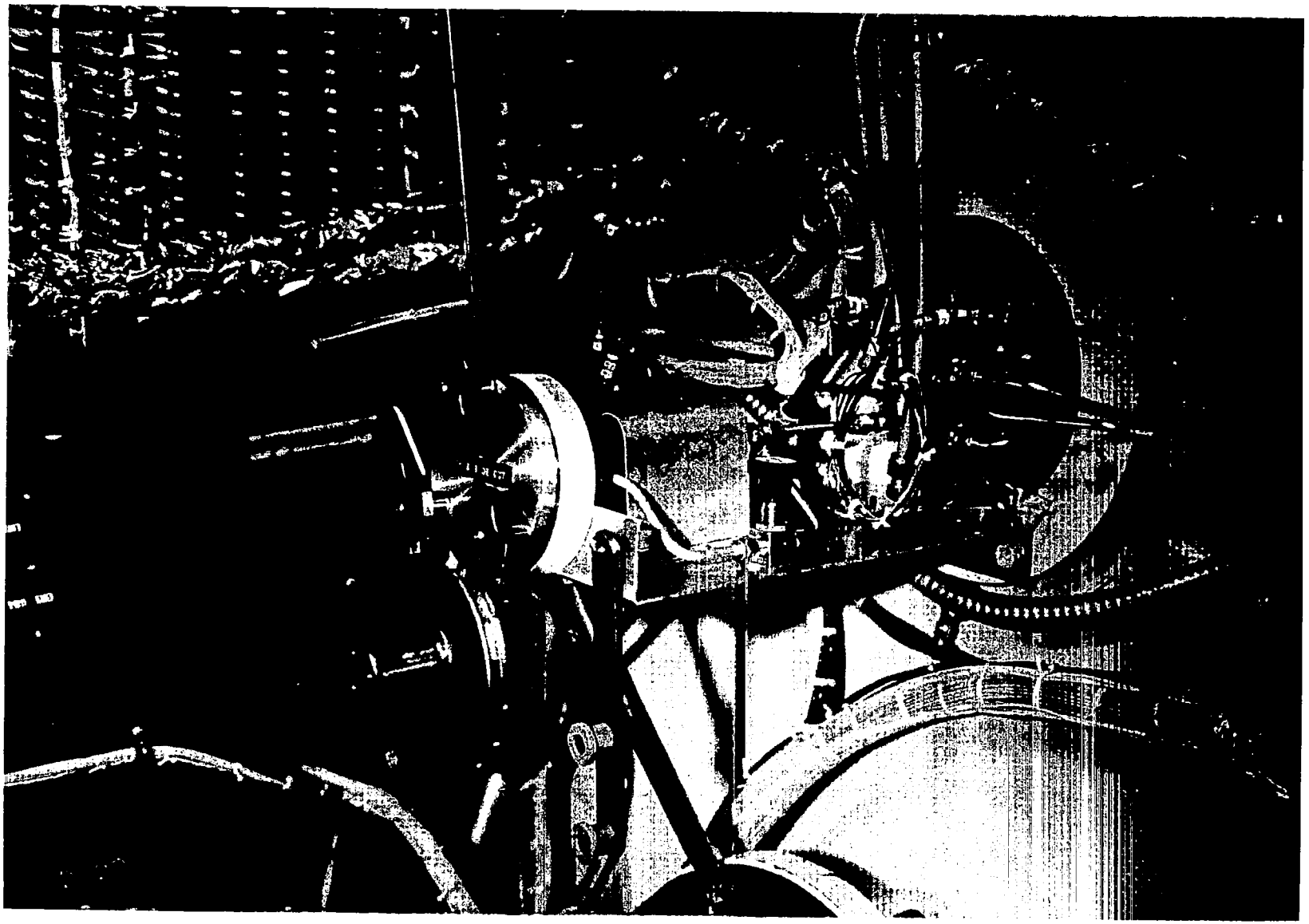

FIGURE 185

Equipment Inside the Space Cabin Simulator

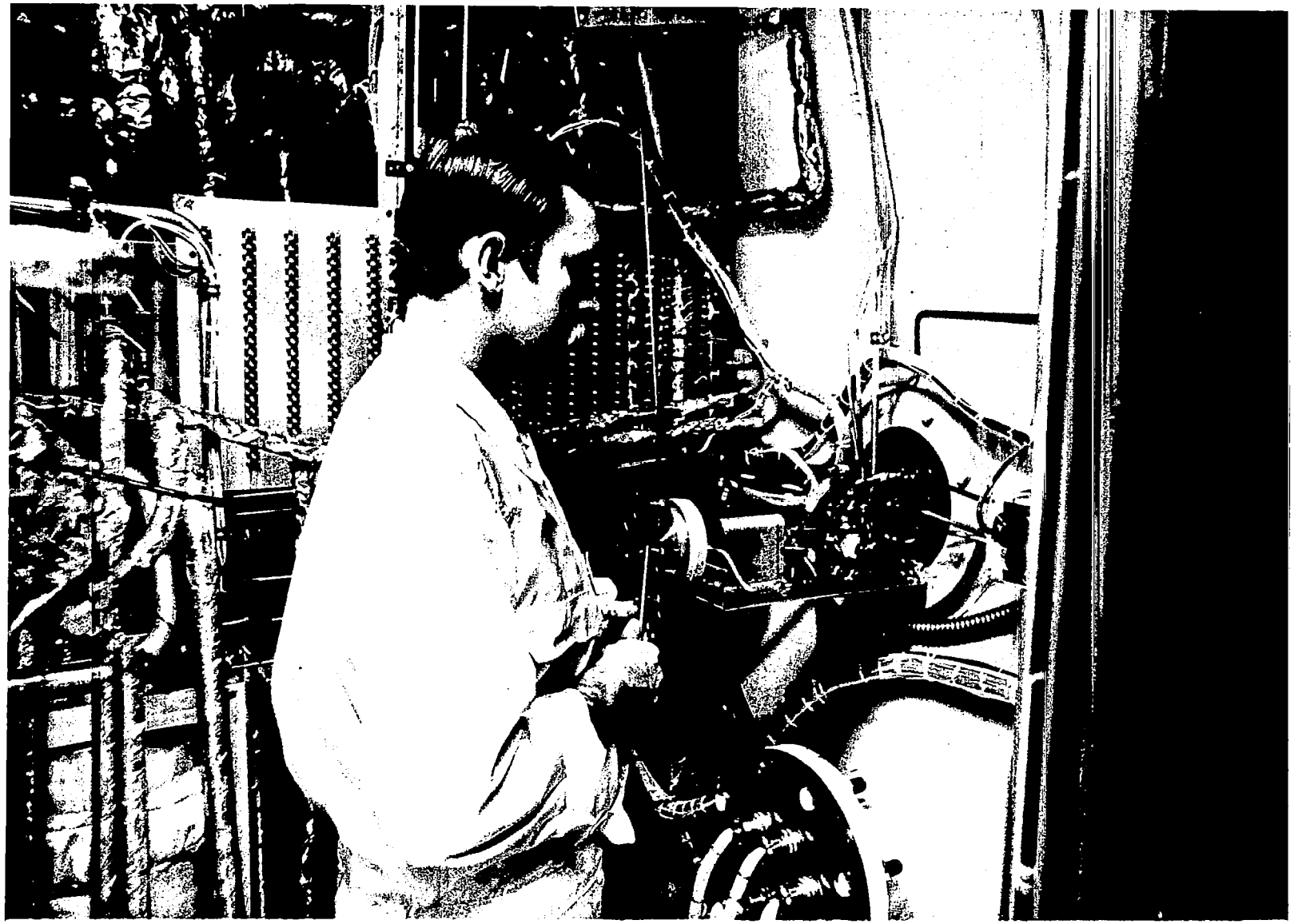

FIGURE 186

Calibration Sample Valve

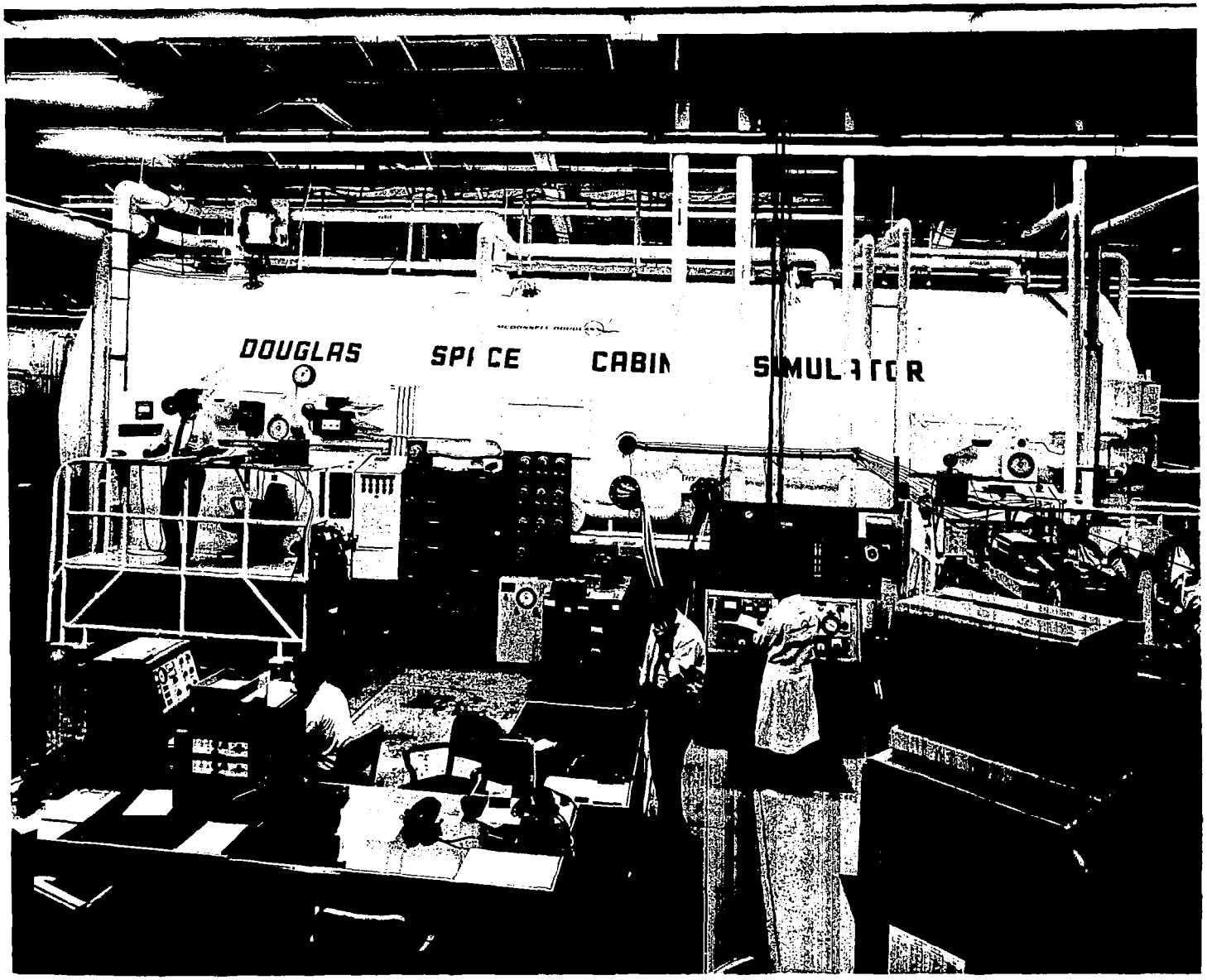

FIGURE 187

McDonnell Douglas Space Cabin Simulator

During installation a leak was encountered in the sampling port cover. This resulted from the manner in which the large diameter Millipore filter was held and could not be eliminated without substantial rework of the filter holder. The leak did not permit a good calibration of the system until the Space Cabin Simulator atmosphere was reduced to the operational pressure (362 torr ±3 torr).

It is not believed that the leak had a significant affect upon the calibration accuracy during the sixty day period.

SENSOR SYSTEM CALIBRATION

An integral part of the test program for the two gas sensor during the sixty day Space Cabin Simulator test was the periodic calibration of the unit. While a great deal of data was gathered while the instrument was monitoring the cabin atmosphere this could only be compared with the output of other sensors. Since those sensors often exhibited somewhat variable characteristics, it was generally difficult to assess the performance of the two gas sensor when comparing its outputs with this data. The only valid method by which the performance of the instrument could be evaluated was to calibrate it with a known sample and periodically monitor the repeatability of these measurements.

Calibration was performed by introducing a known pressure of a known sample mixture of nitrogen, oxygen, and carbon dioxide at the head of the capillary system. Water vapor could not be accurately handled with the calibration system and therefore no attempt was made to calibrate this channel. The outputs for the other three channels were read and calibration factors in torr/volt were computed. The complete calibration procedure which was followed is outlined in Table 34. A complete list of instruments used during calibration is given in Table 35. The calibrations were performed every day or every other day during the test with the exception of three intervals during which the calibrations were performed on the third day.

Two factors formed the primary limitations on the accuracy of this calibration technique. First, the output data from the two gas sensor was read on small ±2% accurate current meters which had been converted to read voltage. The meter panel is shown in Figure 188. Second, the instrument output versus time during the calibration period responded in varying ways to the changes in inlet pressure. In other words, after the system was evacuated and the calibration sample admitted the mass spectrometer outputs versus time did not respond in a consistent manner. There was some hesitancy about waiting any period of time for stabilization due to the leak which existed in the filter holder apparatus. This leak could cause some distortion of the sample with time. Therefore the mass spectrometer outputs were read at a fixed time after admission of the calibration sample. The exact cause of the variation was not determined. It is known that the mass spectrometer ion source has a thermal time constant and that the filament temperature varies with the oxygen partial pressure. This effect is noticable when the sample pressure is rapidly changed from zero to full pressure (~360 torr). There was also some indication that the capillary inlet system did not act in a fully consistent way when the pressure was rapidly changed. This is possible due to effects of water vapor in the line. These will be discussed in more detail in a later section. Both of these effects will be under continued investigation.

TABLE 34

CALIBRATION PROCEDURE OUTLINE

1. Warm up the John Fluke VTVM and X-Y plotter
2. Attach the X-Y plotter to the oxygen output channel
3. Determine the availability of cabin personnel to assist with the calibration.
4. Record the sensor output data and other comparative data prior to the initiation of calibration.
5. Attach the standard N_2, O_2, CO_2 mixture gas bottle to the calibration system and purge tne line by pumping through valves V1 and V2. Then close valve V1.
6. Verify the evacuation of the calibration system by opening valve V2 (See Figure 4-1)
7. Request the inspection of the large filter and the covering of the sample part with the flange cover.
8. Request the opening of the internal calibration sample admitting valve
9. Evacuate the region at the head of the capillary line and the calibration system
10. Close valve V2 and verify that the flange cover is properly in place by looking for a pressure rise at the gauge
11. Record the detector zeros for each output channel
12. Record other supporting data such as ionization gauge pressure, thermocouple gauge pressure, ion pump current, system temperature, filament voltage and anode current.
13. Turn on the time scan on the X-Y plotter at low speed
14. Admit the standard mixture to the calibration pressure
15. When the oxygen output has stabilized record the sensor outputs, filament voltage and anode current
16. Evacuate the calibration system by opening valve V2
17. Repeat steps 14, 15 and 16 at a second calibration pressure if two pressure levels are desired
18. Recheck the detector zero levels
19. Readmit the calibration mixture to a pressure approximately five torr in excess of the current cabin pressure
20. Close the internal valve.
21. Request the removal of the flange cover from the sample part.
22. Allow for restabilization of outputs and record the levels
23. Verify the closure of the internal valve by evacuating the calibration system.
24. Compute calibration factors for the nitrogen, oxygen and carbon dioxide channels.

TABLE 35

DATA MEASUREMENT EQUIPMENT

MEASUREMENT	EQUIPMENT USED
Two Gas Sensor System Output Voltages	4 - Simpson Model 1212 0 - 50 microamp meters with series resistors to provide measurements in 0 - 0.5 and 0 - 5.0 volts
Calibration Sample Gas Pressure	Wallace and Tiernan Gauge Model FA 160, 0 - 800 torr
Capillary Bypass Line Pressure	Hastings Raydist thermocouple gauge, Model DV-6, 0 - 1000 microns
Ion Pump Current	Varian Associates ion pump control unit, Model 921-0013
Vacuum System Pressure	Varian Associates ionization gauge control unit, Model 971-0003
Cabin Pressure	Wallace and Tiernan Gauge, Model FA 129
Cabin Temperature	Barber Colman, Model TP 101-0-2
Two Gas Sensor System Temperature	Simpson Instruments, Model 388 Temperature probe
Two Gas Sensor System Filament Voltage	Tripplet VOM, Model 630-A, set on 3 VAC range but measured on the 3 vdc range for greater resolution
Two gas Sensor System Voltages	John Fluke VTVM, Model 803
Calibration Sample	49.3% nitrogen, 49.7% oxygen, and 1.0% carbon dioxide
Two Gas Sensor System Anode Current	Tripplet VOM, Model 630-A, 0 - 60 microamp scale
System 28 Volt Power Supply	Universal Electronics, Model M28-0.5
McDonnell Douglas Oxygen Sensor	Beckman Instruments, Model F-3
McDonnell Douglas Carbon Dioxide Sensor	Mine Safety Appliances, LIRA 300
McDonnell Douglas Dew Point Sensor	Cambridge Instruments, Model 992
Time	Mission primary wall clock

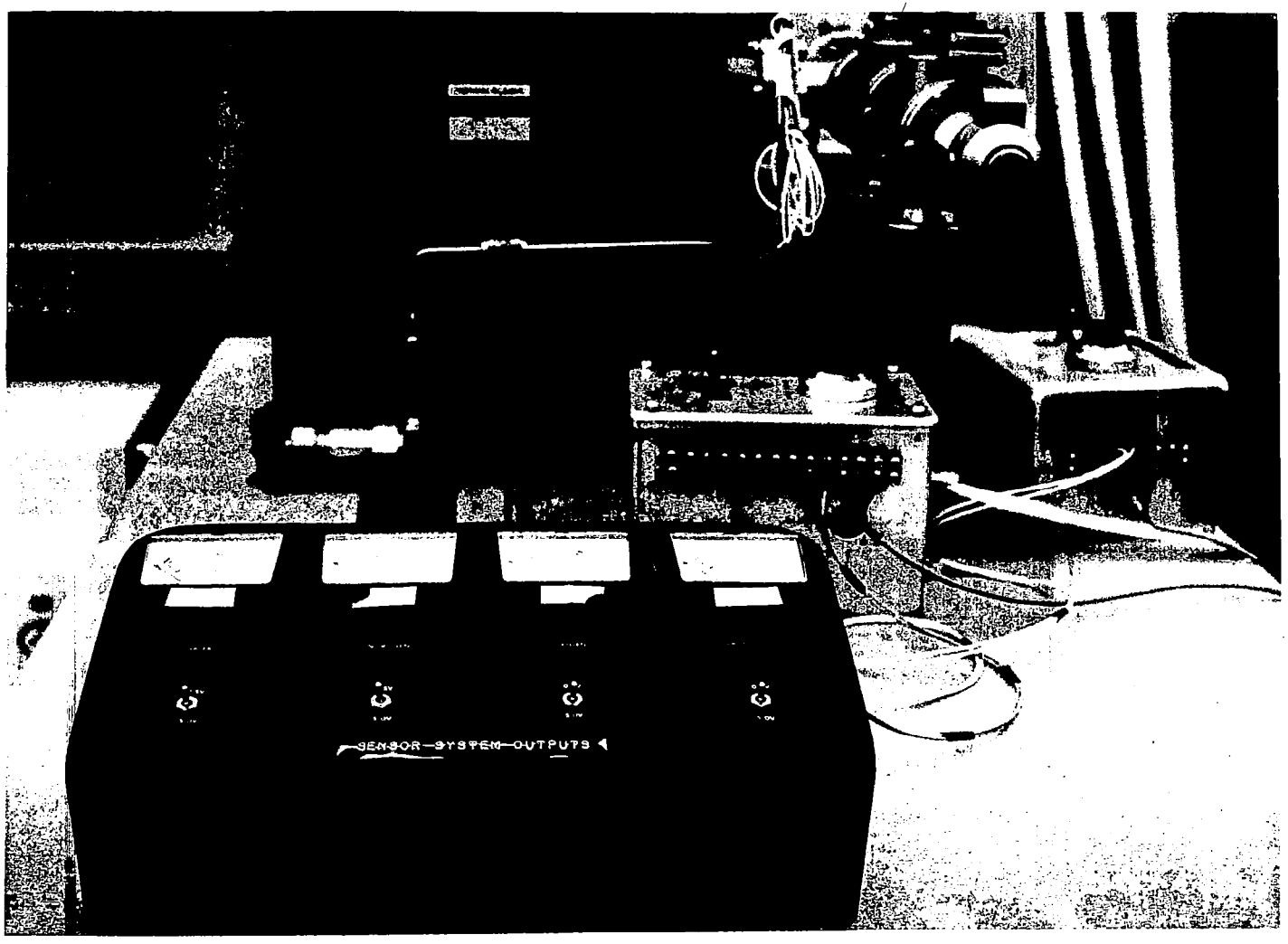

FIGURE 188

Meter Panel

The best indication of the accuracy of the calibration method is given by the data in Figure 189. Here the last set of mass spectrometer outputs before each calibration was measured and converted to torr by using the calibration factors obtained during the immediately following calibration. By minimizing the time between that moment when the readings were made and the subsequent calibration cycle, the variations in the instrument were minimized. Furthermore, by using readings taken just prior to calibration rather than just after, any effects due to the calibration cycle itself can be eliminated. The partial pressures as indicated by the mass spectrometer were summed and compared against the total pressure as indicated by the primary space cabin pressure monitor which was a double revolution 0-800 torr Wallace-Tiernan gauge. It can be seen that, with the exception of two points which are assumed to be erroneous due to some variation in the calibration cycle, the other thirty-nine points fall within a ±1.6% error band. This indicates that the calibrations were generally more accurate than the variations in the instrument performance but that a substantial amount of the apparent variation in the instrument performance may be accounted for by inaccuracies in the calibration procedure.

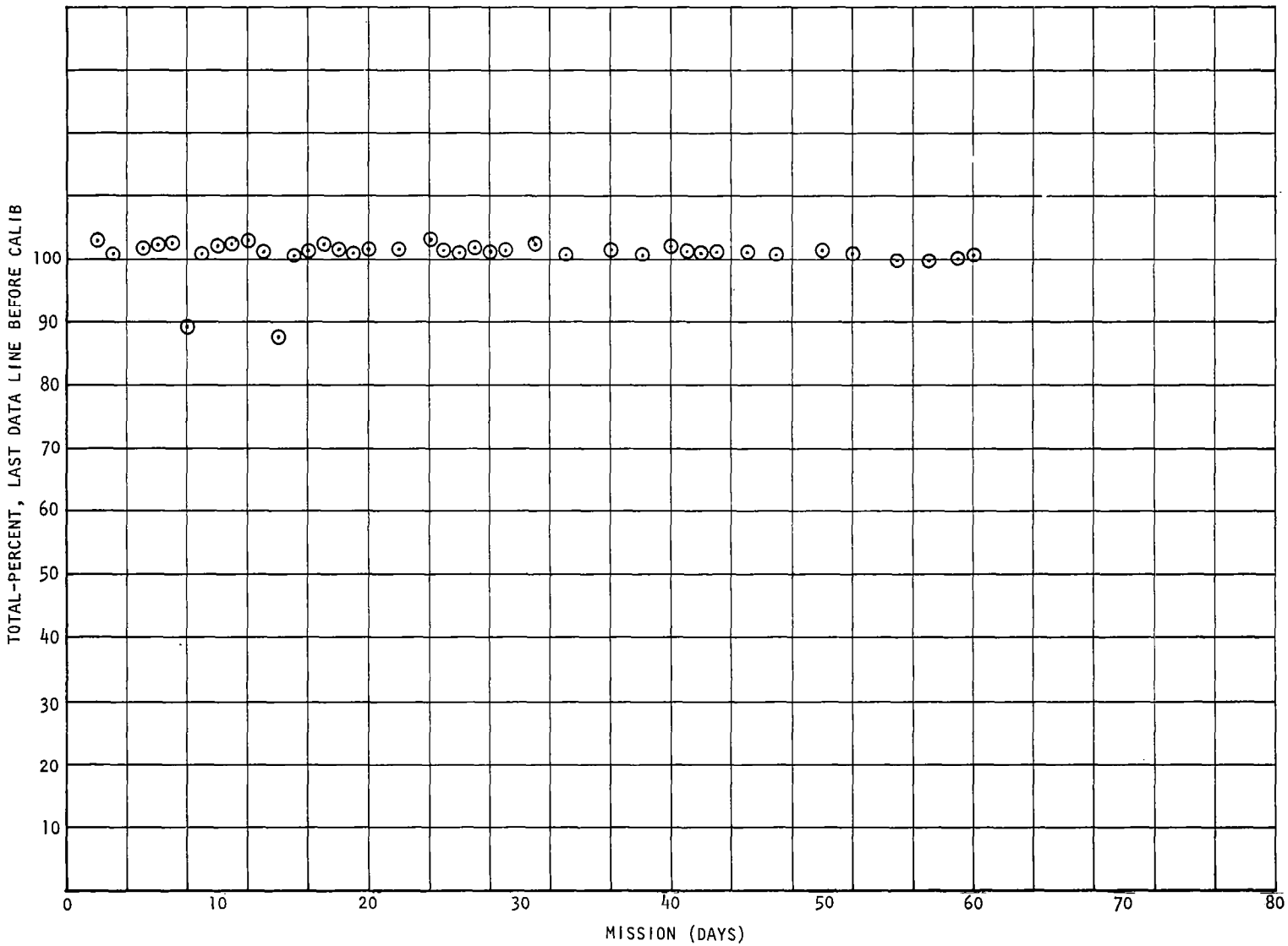

FIGURE 189

Case 1 Data

INSTRUMENT OPERATION DURING THE 60 DAY TEST

At the beginning of the sixty day test, it immediately became clear that the emission regulator was not holding the ionizing electron beam current constant. Measurements taken of the filament voltage indicated that the voltage required to obtain a fixed emission current level had increased rapidly during the tests prior to beginning the sixty day run. This increase was due to an increase in the filament resistance. (This was indicated since the filament power required to give a fixed emission current level remains approximately constant as the filament resistance changes and therefore the drive voltage must go up.) The filament resistance had increased to the point where the emission regulator did not have sufficient voltage drive to maintain regulation.

At this time efforts were initiated to provide a modification to the emission regulator to resolve this anomaly. The modification was a minor one which involved only the addition of turns to the filament transformer secondary to provide higher filament drive voltage. This required about ten days since all of the existing transformers were sealed in potting resin and a new transformer core had to be ordered, wound and installed. For this reason the first 13 days of operation exhibited instrument sensitivity shifts of about plus or minus 11.5%. On the eleventh mission day the regulator was replaced with a temporary unit while the original was modified to cope with the higher filament resistance.

Figure 190 is a plot of the filament voltage during the mission. These data points were taken during calibration and with a fixed sample pressure. As the filament voltage required to maintain a set emission level increases, it varies as the square root of the filament resistance. A parallel program to study these aging effects on various filament materials, in an environment similar to that of the mission, was being concluded at this time on Contract NAS 1-6387. The relatively rapid resistance change noted in the Two Gas Sensor System was also found to be true in this study. It was found however, that a filament material of 97% Tungsten, 3% Rhenium exhibited only 38% of the resistance changes observed with the 75% Tungsten, 25% Rhenium alloy during the same period ($\sim$ 200 days). A full report of this filament investigation will be included in the Phase IIb Final Report on NAS 1-6387. After the completion of the test at McDonnell Douglas all of the existing Two Gas Sensor System analyzers were changed incorporating the superior filament material. With the new material and a modification of the emission regulator to give load regulation over a wider load range it is not expected that this difficulty will be encountered again during future long term operation. It is important to note

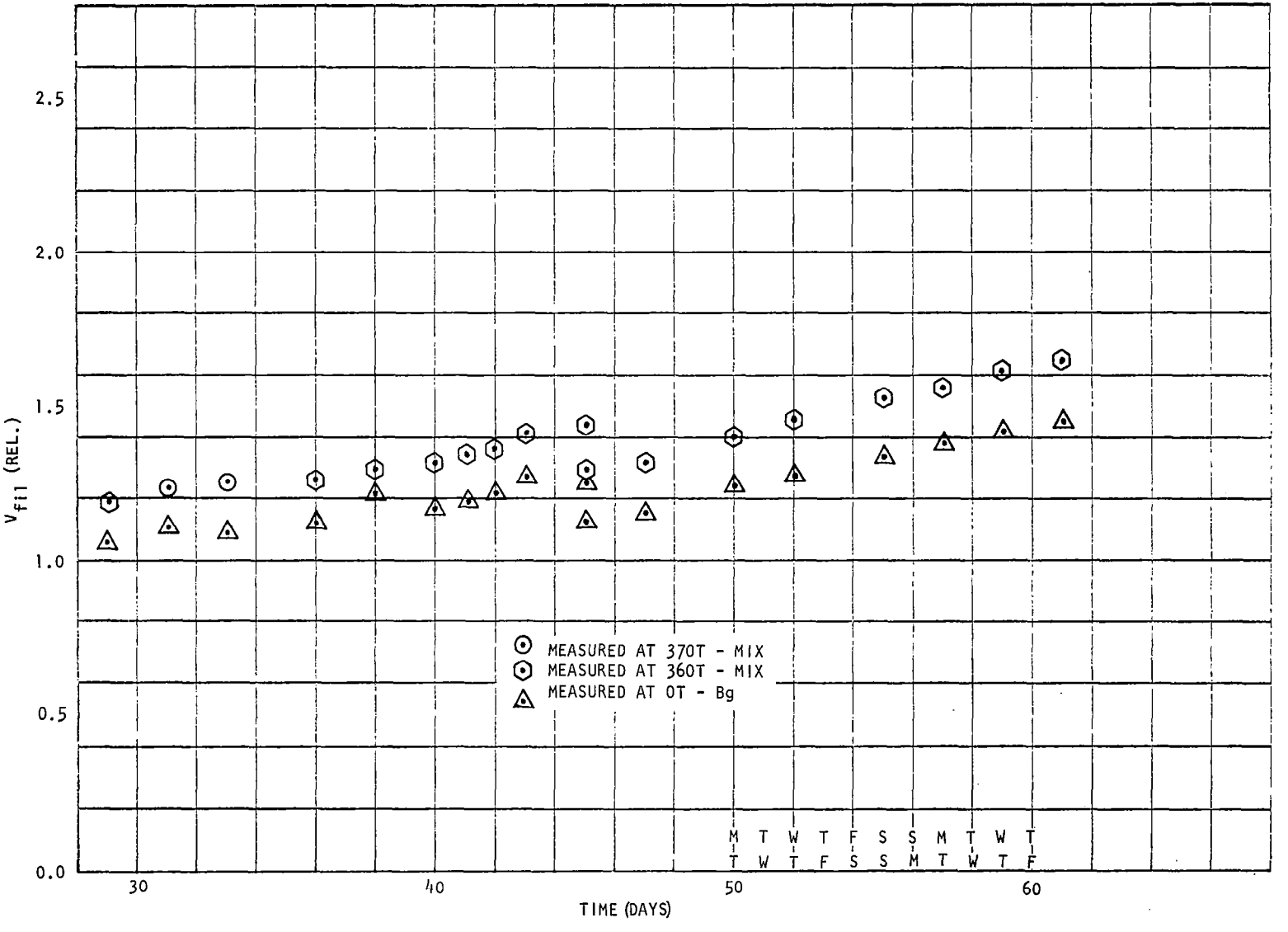

FIGURE 190
Filament Voltage vs Time (Sheet 1 of 2)

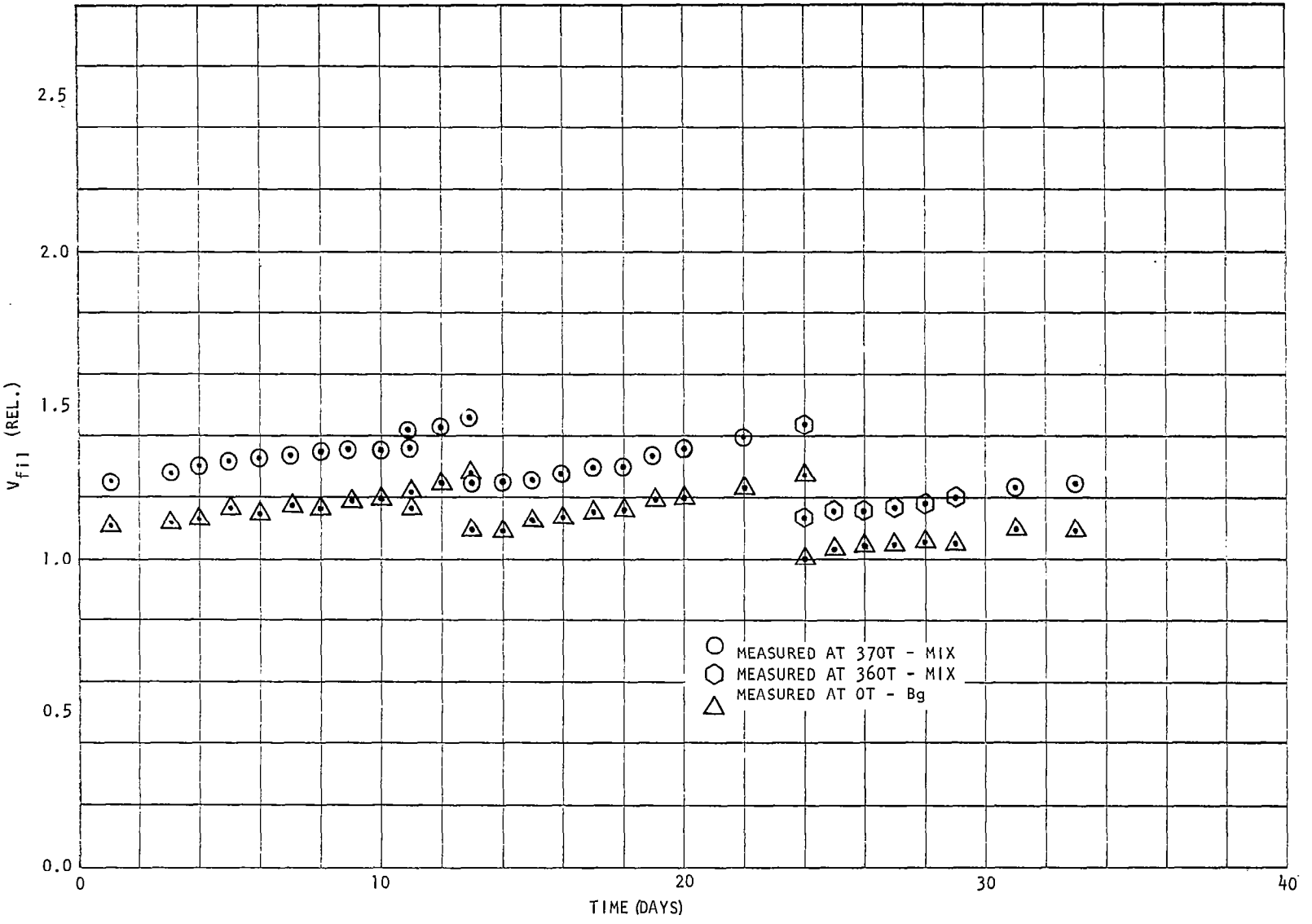

FIGURE 190
Filament Voltage vs Time (Sheet 2 of 2)

that in spite of the difficulty described above, at no time during the test were the filaments in danger of burning out.

On the thirteenth day, the original emission regulator with the aforementioned modifications was put back into the system replacing the temporary unit. The emission regulation was then found to be satisfactory. During the 13th, 14th, and 15th days, three external power failures occurred which completely shut down the sensor system and laboratory vacuum system causing some variation in calibration factors during this period. Calibration factors for the next nine days were within $\pm$1.25%.

On the twenty-fourth mission day the operation of the instrument was switched to the second filament and electron gun as part of the program to analyze all aspects of instrument performance and demonstrate the utility of the redundant electron gun. After a one day stabilization period it can be seen that for the next thirteen days the calibration factors were within about $\pm$2%. The numbers quoted are for nitrogen. The variations in the calibration factors are presented in Figures 191 through 193 for N_2, O_2 and CO_2. No calibration data was taken on H_2O.

An extreme change in the analyzer sensitivity on day 40 resulted when the belt on on the capillary bypass line roughing pump failed. This caused a subsequent pressure rise in the analyzer. This day's data was stable, however, the analyzer sensitivity at the next calibration was much different suggesting that the sensitivity changes seemed to occur during calibration. The suspected area in which the change occurred was in the capillary divider inlet system. This can be supported by comparing the bypass line pressures from before and after this calibration. The pressure before calibration was approximately seven microns and after about eight microns.

At this point it is worth mentioning that throughout the sixty day test there appeared to be some correlation between the changes in the instrument calibration factors and the performance of the capillary line inlet system. This was noted by correlating the nitrogen calibration factor with the pressure measured by the thermocouple pressure gauge at the end of the bypass line. While this pressure may reflect changes in pumping speed of the rough pump as much as changes in the conductance of the capillary and bypass line pressure divider system it was noted that some correlation existed. It is therefore suggested that those changes which occured in the instrument sensitivity (other than during the periods of non-regulation of the emission regulator) were primarily due to the inlet system. Since it is currently anticipated that this system will be replaced by a direct molecular leak it is expected that this source of difficulty can be eliminated.

From mission day 41 until the termination of the mission the nitrogen calibration factors remained within $\pm$2%, however, on mission day 45, the filament resistance was again beyond the emission regulators range necessitating the replacement of the regulator with one having increased voltage drive.

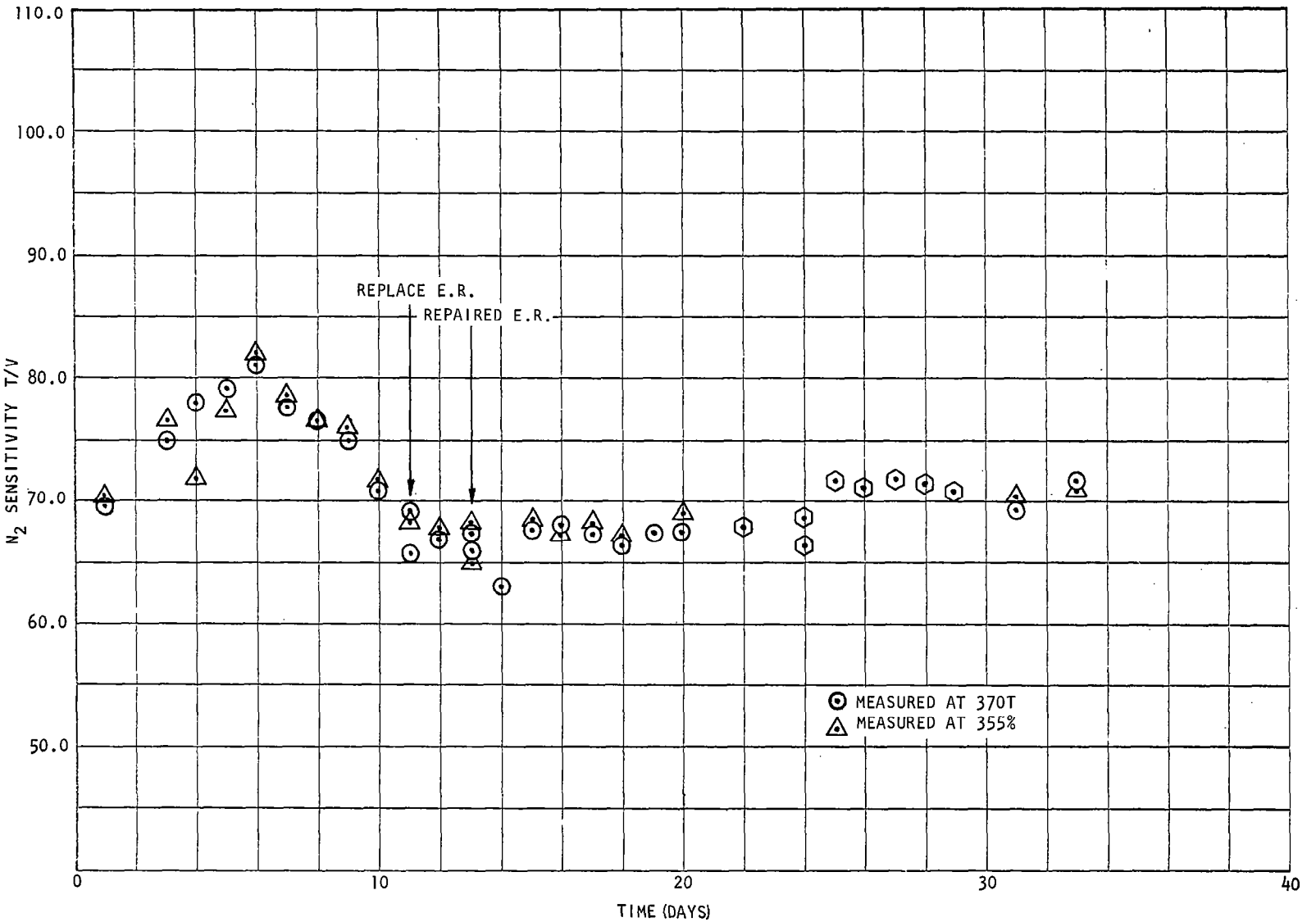

FIGURE 191
N_2 Sensitivity vs Time (Sheet 1 of 2)

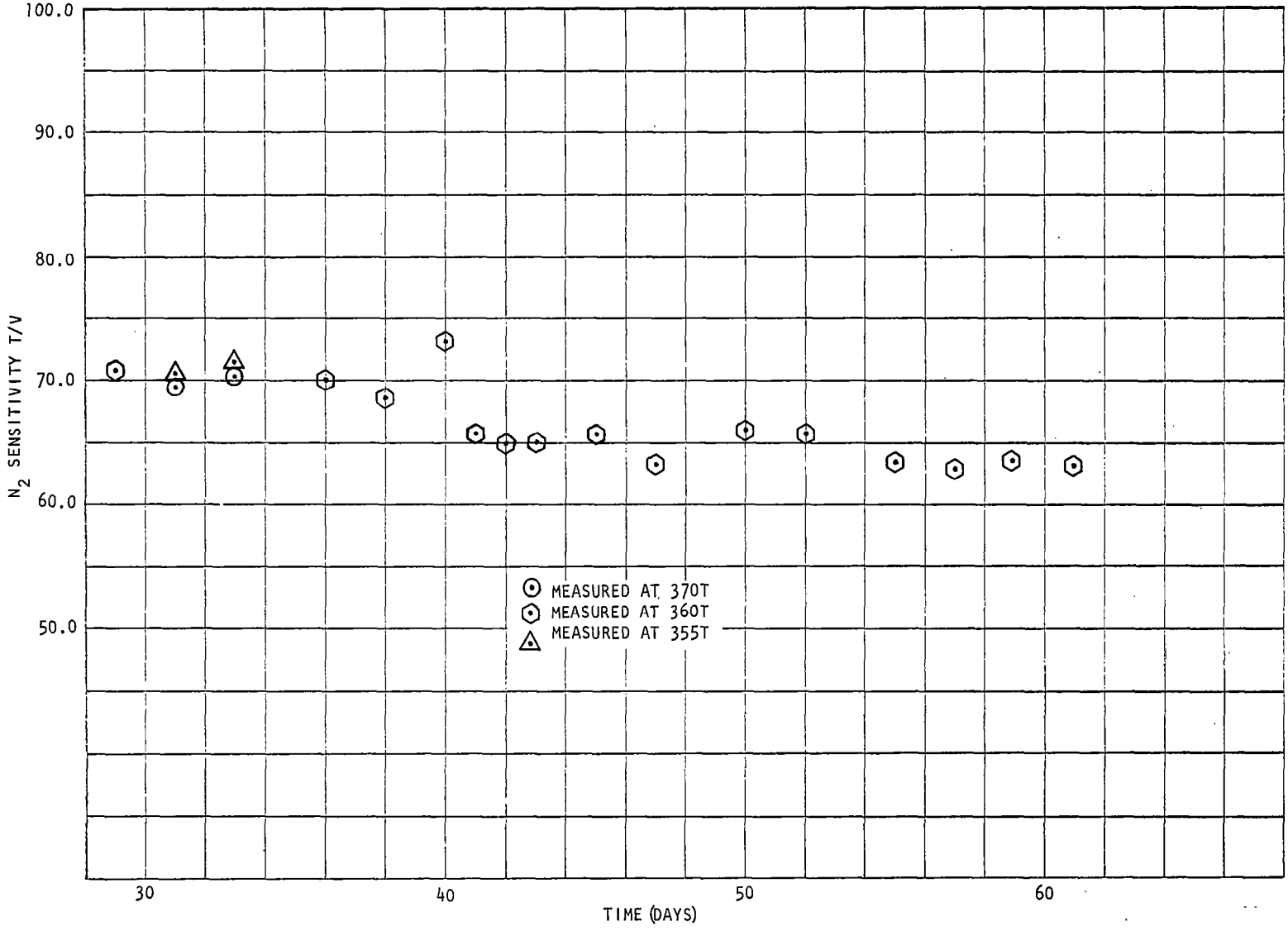

FIGURE 191
N_2 Sensitivity vs Time (Sheet 2 of 2)

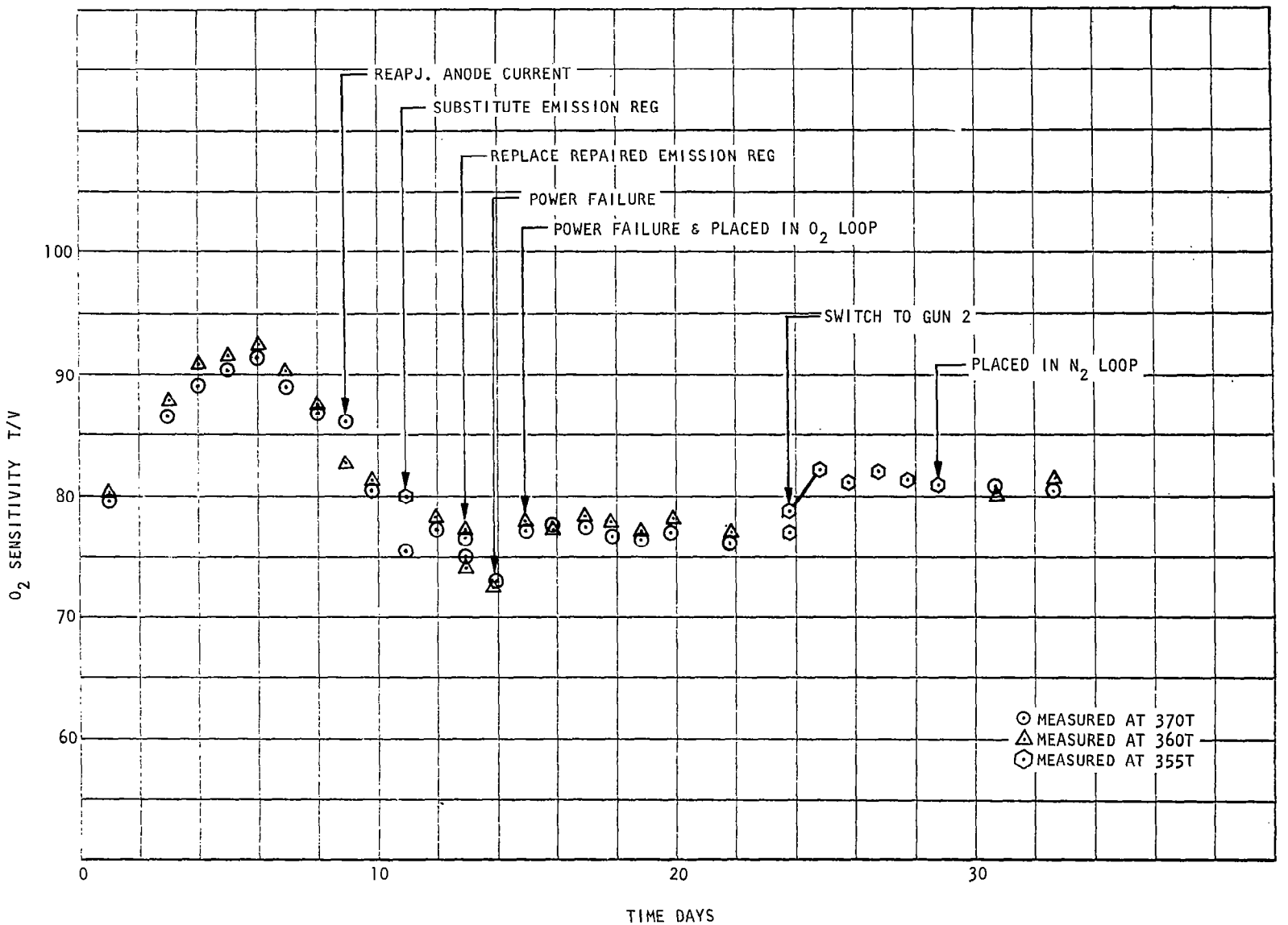

FIGURE 192
O_2 Sensitivity vs Time (Sheet 1 of 2)

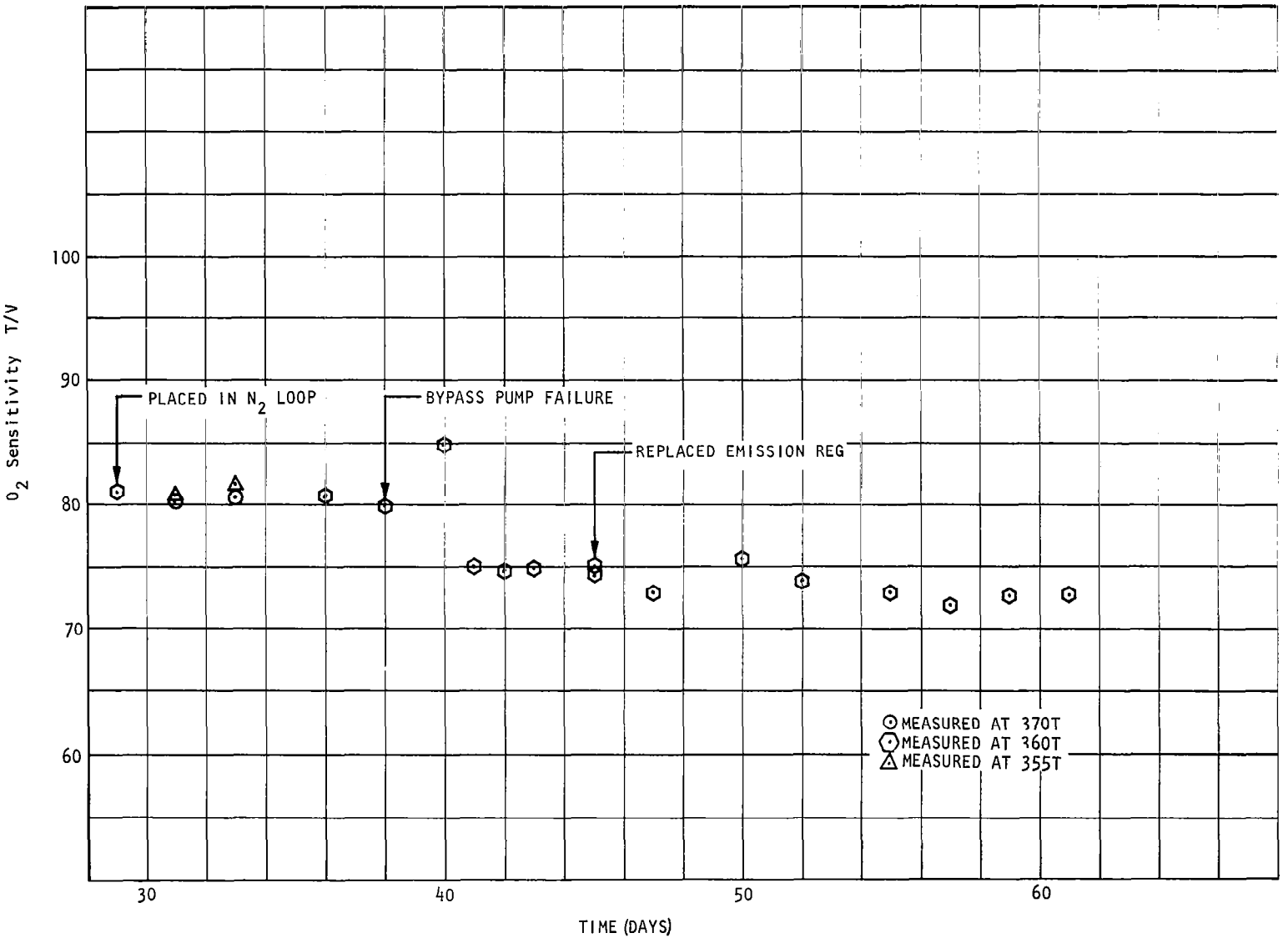

FIGURE 192
O_2 Sensitivity vs Time (Sheet 2 of 2)

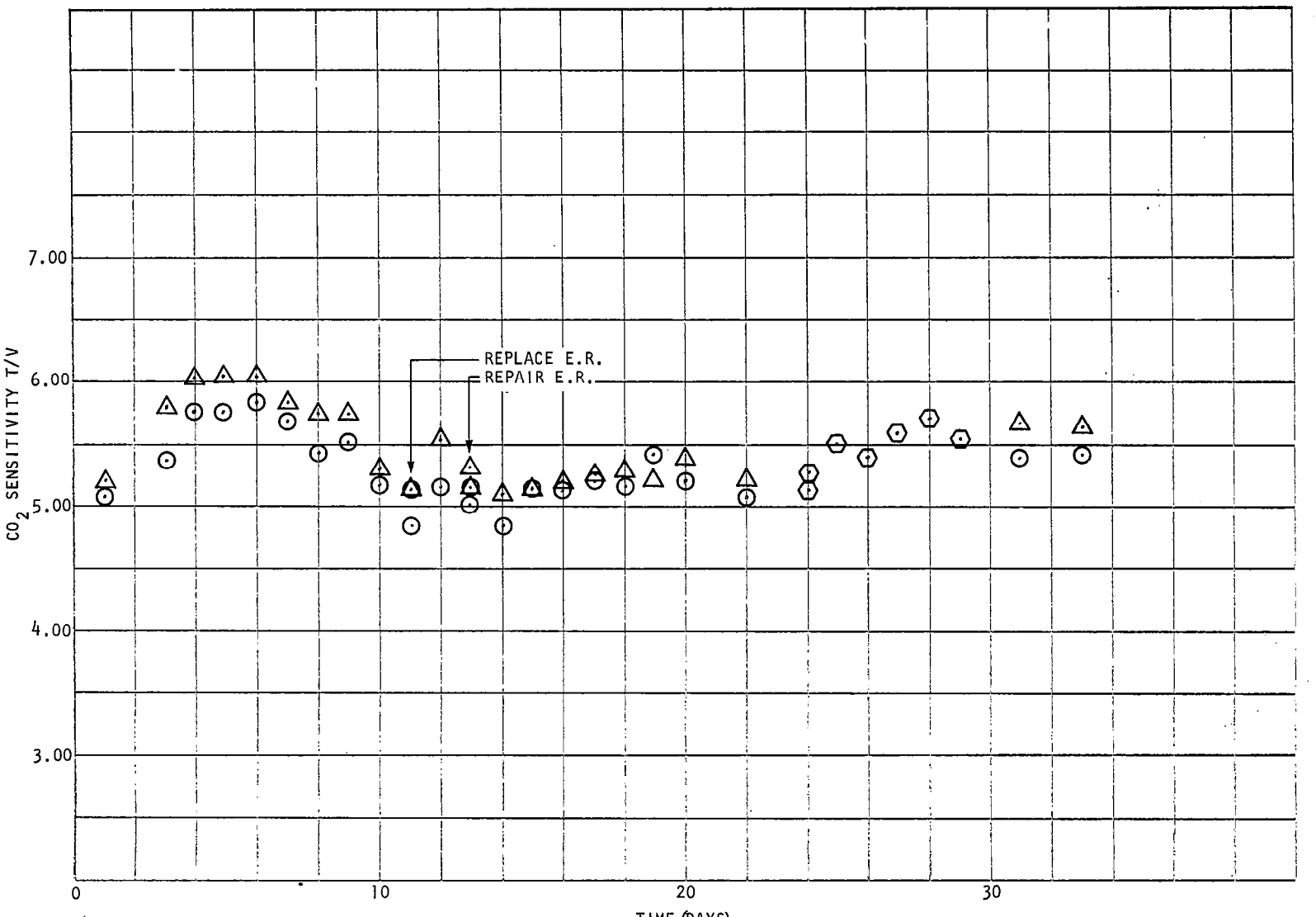

FIGURE 193
CO_2 Sensitivity vs Time (Sheet 1 of 2)

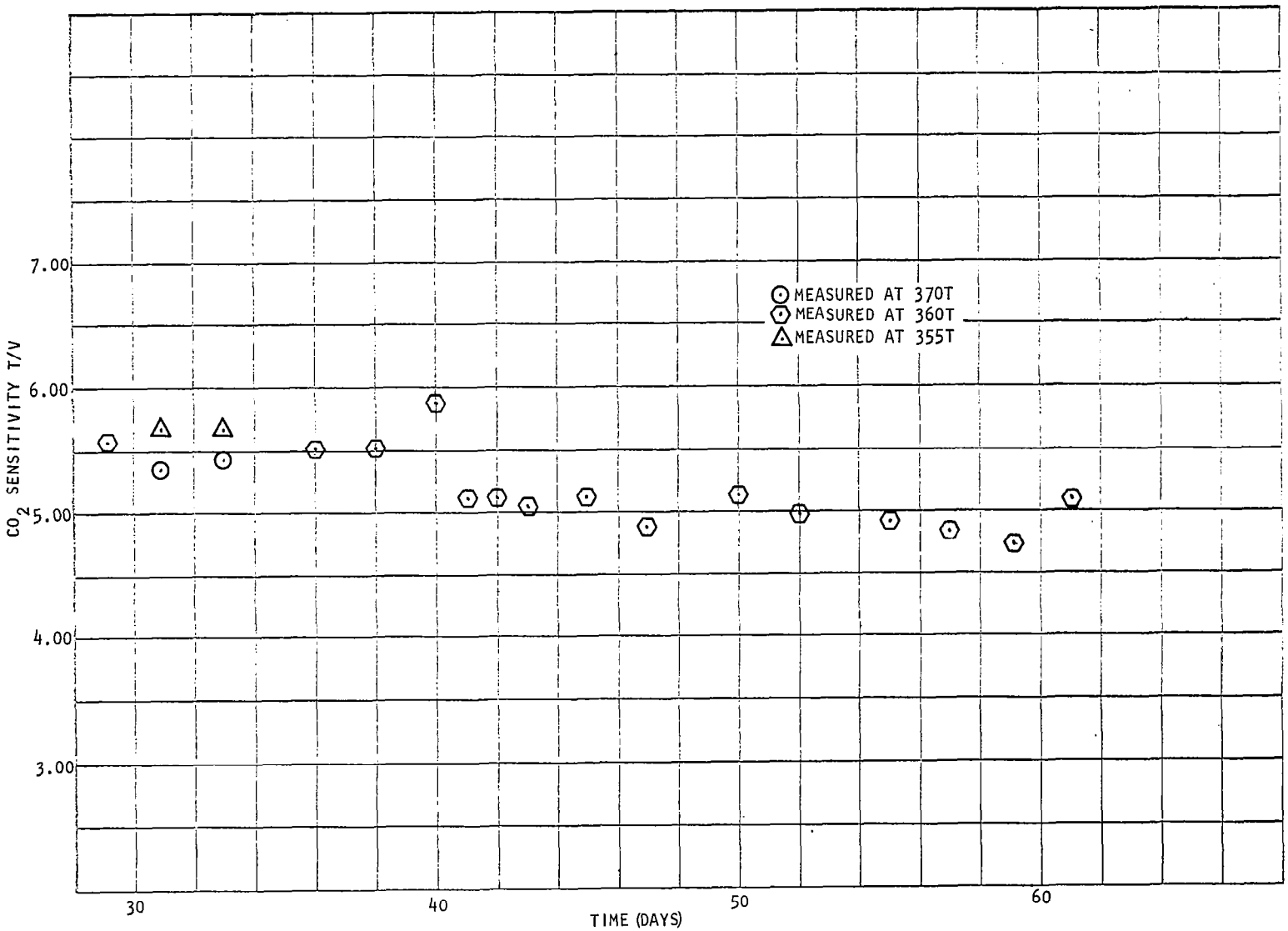

FIGURE 193
CO_2 Sensitivity vs Time (Sheet 2 of 2)

In summary, except for periods when external factors or the emission regulator affected the stability, the variations in calibration factors remained within ±2%. The performance of the Two Gas Sensor is summarized in Table 36.

TABLE 36
Description of Daily Data

CALIBRATION PERIOD	MISSION DAY	DATA DESCRIPTION
1-6	1-6	Emission current anomally due to high filament resistance beyond the range of the emission regulator. This anomally continues till period 10. The Two Gas Sensor System and the McDonnell Douglas oxygen measurements were not in agreement because the McDonnell Douglas analyzer was calibrated using air. This continues till period 9 when MCD began using the Perkin-Elmer standard calibration mix.
6	7	During calibration, a special test was made in an attempt to evaluate the calibration method. This test has some deleterious effects upon the calibration accuracy which biased the entire period's data.
7-9	8-10	Emission current anomally due to the high filament resistance continues.
10	11	The emission regulator was replaced with a temporary regulator so that the original could be modified to accommodate the high filament resistance.
11	12	Emission current anomally due to the high filament resistance continues.
12	13	The temporary emission regulator was replaced with the original which had been modified for extended dynamic range. The emission regulation was then normal. Same restabilization time was required for the system. An external power failure was the cause for the short period duration.
13	14	After restarting the system another external power failure occurred. This again biased the data until restabilization.
14	15	System operation satisfactory. An external power failure occurred after the first data line, however it was of short duration and the analyzer was promptly restarted. This caused a biasing of the next several data lines and until the analyzer could restabilize.

TABLE 36 (Continued)

CALIBRATION PERIOD	MISSION DAY	DATA DESCRIPTION
		The Two Gas Sensor System was employed in the McDonnell Douglas cabin oxygen control loop at 4:53 p.m. and remained in the O_2 control loop for the remainder of the mission.
15-19	16-20	System operation satisfactory.
20	22	System operation satisfactory. There were several data points in which the sensitivity appeared to have changed. It may be erroneous data or may possibly be due to short term variations in the capillary inlet line characteristics.
21	24	At this time the instrument was switched to electron gun #2. The emission regulation was satisfactory. Some restabilization was evidently required.
22-25	25-28	System operation satisfactory.
26	29	System operation satisfactory. At 2:52 p.m. the Two Gas Sensor System was integrated in the cabin atmosphere control loop using the nitrogen output to control the balance of the cabin atmosphere.
27-29	31-36	System operation satisfactory.
30	37-38	At the end of this period the capillary bypass line roughing pump belt was found to be slipping badly. The belt was replaced but changes in the bypass line pressure contributed heavily to the apparent system sensitivity changes. This roughing pump is a support system only and would not be used during an actual space mission.
31	39-40	The ending calibration factor was found to be in error. The cause is not fully known. Therefore, the beginning calibration factor should be used to reduce the entire period's data. The system stability was satisfactory.
32-33	41-42	System operation satisfactory.
34	43-44	Instrument stability appears good however upon calibration it was found that the filament resistance was outside the emission regulator's dynamic range.

TABLE 36 (Continued)

CALIBRATION PERIOD	MISSION DAY	DATA DESCRIPTION
35	45-46	The emission regulator was replaced with a modified unit to accommodate the filament resistance value. The modified unit provided satisfactory operation.
36-41	47-60	System operation satisfactory. At the end of period 41 the test was terminated.

DISCUSSION OF THE DATA AND DATA REDUCTION

There were four types of data taken during the sixty day test. These included: 1) calibration data (as described in Section 5); 2) monitoring data (consisting of the sensor system outputs during the cabin monitoring periods); 3) housekeeping data (pressures, voltages, etc. related to the sensor performance); and 4) comparative data from the other partial and total pressure sensors. The accumulation and subsequent reduction of the data provided a definitive day to day and long term qualative analysis of the instruments operation. Each time the system was calibrated data was acquired concerning the analyzer temperature, emission current, filament voltage, vacuum system pressure at background and with the standard sample, detector zeros, ion pump current, bypass line pressure, calibration sample gas pressure, analyzer output at background and with the standard sample, and the corresponding time of measurement. After calibration additional data was noted regarding the cabin temperature, pressure, emission level, and filament voltage. The calibration each time was then checked against the previous calibration and all analyzer outputs compared with the various McDonnell Douglas systems.

During the normal operating time, McDonnell Douglas personnel recorded pertinent system data including: All Two Gas Sensor System outputs, vacuum system pressure, ion pump current, capillary bypass line pressure, cabin pressure, cabin temperature; and the McDonnell Douglas oxygen, carbon dioxide, and water vapor analyzer measurements. These measurements were done generally every two hours. Measurements were made from the equipment listed in Table 35.

It must be pointed out that all of the raw data, pertinent to the Two Gas Sensor System, taken at the mission site, was done in a manner which inherently involved some measurement error. That is, most measurements were visual readings on small meters generally without antiparallax mirrors and which, for the most part, could be considered no better than indications with two to three percent accuracies. Inconsistency of measurements was also incurred by the fact that they were made by a variety of individuals who possibly had various techniques for reading meters. It therefore is not surprising that the deviations in the reduced data are a few percent at various times.

During those periods when the emission regulator was not holding the emission current constant it was decided to calibrate the Two Gas Sensor at two pressure levels so that any resultant effects due to total pressure variation could be eliminated. The calibration data (Figures 191 through 193) therefore show dual values at certain times. It was found, however, that the variation in the calibration factor with pressure level did not always act consistently. This may have been partially due to the effect which the first calibration had on the second one. In any case as soon as the emission regulator difficulties were

corrected the system was calibrated at a single point. It is likely that there was some non-linearity in the output signals with total pressure which may have had some effect upon the data taken in the monitoring mode. This was due to a slightly higher pressure than normal in the ionizing region and can be corrected either by modifying the inlet system to reduce the pressure or by increasing the repeller-accelerator potential to minimize the effects of ion space charge.

There were, of course, several anomalous occurrences during the mission which affected the analyzer performance. An example of this would be that during calibration period six, the calibration standard sample pressure surged and caused an immediate loss in analyzer sensitivity or at least the apparent analyzer sensitivity. The system did recover as may be seen in the data of the following calibration period. The various occurrences during the mission which did have significant effects upon the reduced data can be found in Table 36.

Data taken during the monitoring mode is presented in Appendix D. Two data reduction methods were used. In the Case 1 data the calibration factors were linearly interpolated between pairs of calibrations. In the Case 2 data only the calibration preceding the period was used. This is more representative of what might occur in actual use. In both cases when calibrations were made at two pressures the factors were linearly interpoled between these points as dictated by the pressure gauge measurement. This was done during periods when the emission regulator was not controlling as previously discussed. In the reduced data, each calibration period is correlated with the McDonnell Douglas mission day which is noted as: MISSION TOTAL ELAPSED TIME IN DAYS. There was 41 calibration periods and the duration of each is indicated by: ELAPSED TIME BETWEEN CALIBRATION. It must be pointed out that if one were to total all of these period elapsed hours the total would not exactly equal the total mission time. This is due to the fact that calibration typically requires 30 minutes to one hour and this time is not included in the Elapsed Time Between Calibration. Additionally, there were facility power failures during the mission in which there was no data. These times also are not included in the Elapsed Time Between Calibration.

The calibration factors in torr/volt are listed with the reduced data. In the Case 1 data these factors are shown for both the sensitivities at the beginning and ending of a calibration period whereas in the Case 2 data only the sensitivities at the beginning of a period are listed. Both the Case 1 and 2 reduced data refer to the Two Gas Sensor System as MS while McDonnell Douglas data are listed in columns headed MDA.

In the Case 1 reduced data CABIN TOR is the cabin pressure in torr. The N_2, O_2 CO_2 and H_2O data are compiled as partial pressure in percent and T.C. MICR. is the capiallary bypass pressure in microns. TOTAL is the sum of the Two Gas Sensor System's N_2, O_2, CO_2 and H_2O measurements and is a good measure of the analyzer performance when compared against the Wallace Tiernan gauge.

In Case 2 the format differs. The N_2, O_2, CO_2 and H_2O data, listed under the major heading TWO GAS SENSOR, are partial pressures in torr. Under the major heading, COMPARATIVE DATA, the O_2 and CO_2 have been reduced to partial pressure in percent for comparison to the McDonnell Douglas Aircraft company analyzer

outputs which are in percent. The TOTAL TOR subheading shows, for comparison, the sum of the Two Gas Sensor's outputs in torr which can be compared to the actual MDA measured cabin pressure in torr. TOTAL PCT is the ratio of the Two Gas Sensor TOTAL in torr and the measured cabin pressure.

In some cases the first data line after calibration has a higher total percentage than the following data. This is due to effects of the residual water in the inlet system during calibration which biases the measurements. The time required for calibration with the numerous measurements the residual water in the inlet system to continuously decrease whereupon return to the cabin, a water lag occurs until the system again reaches equilibrium. This then causes a biasing of the first measurements made after calibration and until equilibrium is reached. An inverse effect takes place due to competition between the water and other molecules in the capillary line in the region of the molecular leak.

This leads to a high total pressure reading when the summation of partial pressures is monitored shortly after calibration. It also acts to shift the calibration factor so that the average reading for the total pressure should be greater than the actual pressure by some small amount. These effects are not well understood at this time but there is substantial evidence that they are due to the time delay of water transmission in the capillary line.

The significance of the first data line therefore should be somewhat discounted. At times the first data line was not taken immediately after calibration and this biasing affect does not appear. There were also, during several calibration periods, events where, after calibration, the H_2O output continued to drop for several data lines before returning to the "normal" level. This probably was due to the slow migration of water on the walls of the capillary with the corresponding low water level from calibration. In the Case 1 reduced data the last line of a calibration period is most significant and variations here are a measure of the calibration accuracy as previously mentioned.

It is also possible to account for many of the variations in the data by referring to Table 36 which gives a brief profile of the complete sixty day test period. It should be noted that the elapsed times between the data are somewhat variable. This is due to the fact that the measurements were made on an irregular basis by McDonnell Douglas personnel who were fitting this task in with their other duties. All of the data which was taken is presented in the appendix.

SENSOR TESTING AFTER RETURN TO AEROSPACE SYSTEMS

After the last calibration and just prior to pressurizing the cabin the two gas sensor was turned off. The supporting pumping systems were left on. Four days later the instrument was returned to Perkin-Elmer by van. The mass spectrometer was re-evacuated and turned on. First, the power supply voltages were checked and found to be within 0.1 volts of their values at the beginning of the sixty day test. A test was performed to determine the change in the flux density of the analyzer magnet. Rather than attempt to measure the flux a test was set up to measure the shift in the ion beam position. This was done by tuning the filament reference power supply and 'scanning' the m/e 28 peak by changing the ion energy. This data was compared with similar data taken at the start of the sixty day test. The results indicated that the flux density had falled 0.6% during approximately sixty-seven days. Two points are worth noting. First, the magnet used during this test had not been subjected to the full set of stabilizing procedures prior to installation on the analyzer, and second, the flux density shift could have been four times as large as it was before the ion beam would start to miss the current collector. Therefore, no problem is indicated in this area.

Another important test was performed to measure the pressure in the region surrounding the filament. This information was important since it was suspected that one reason for the relatively rapid increase in filament current was an excessive pressure in the region around the filament. This was believed to be due to gas streaming from the ionizing region (which is at 100 times the pressure of the analyzer) through the electron accelerator aperture. At the same time the electrodes surrounding the filament do not allow this gas to be rapidly dispersed. In order to measure the pressure in the region of the filament, use was made of the increase in filament drive voltage with O_2 partial pressure. This effect had been previously observed.

By admitting the standard calibration mixture into the vacuum system, in the same way that is done for N_2 ion source sensitivity measurements, the pressure can be adjusted until the same filament drive voltage is obtained as for the normal inlet mode of operation. It is then assumed that equality of filament drive implies equal pressures in the filament region. Since the entire vacuum system pressure is raised when the sample is introduced through the inlet leak valve rather than the inlet system. Therefore, pressure level may be measured on the vacuum system ionization gauge. These measurements indicated that during the sixty day test the pressure in the vicinity of the filament was between 7×10^{-6} and 9×10^{-6} torr and suggests that if the pressure level can be reduced that the filament resistance increase can be reduced. By modifying the region surrounding the filament and by modifying the sample inlet system it should be possible to reduce this pressure sufficiently to inhance filament life.

The ion source was then switched to dc operation in order to accurately check the filament resistances. The results of this measurement are given in Table 37 along with the measurements made prior to the sixty day run. The measurements were made at background pressure in both cases. The increases in resistance shown compare with value of from 43% to 47% which were experienced during a parallel filament study without filament fialure. There is, therefore, every reason to believe that if it were necessary, the filaments could be allowed to increase their resistance up to 50% without fear of failure provided that the emission regulator could supply the necessary additional voltage drive. It is also important to notice that the test filaments required a 195 day period to experience these resistance changes. Since they were operated at a lower oxygen partial pressure ($\sim 1 \times 10^{-6}$ torr) this suggests the importance of using the pressure in the vicinity of the filament.

TABLE 37

	Gun No. 1	Gun No. 2
Before 60 Day Test		
Volts	1.365	1.36
Amps	0.78	0.74
Ohms	1.75	1.84
Watts	1.06	1.01
After 60 Day Test		
Volts	1.57	1.83
Amps	0.72	0.66
Ohms	2.18	2.77
Watts	1.13	1.21
Percent Change		
Volts	+14.6%	+34.5%
Amps	- 7.7%	-10.8%
Ohms	+24.6%	+50.5%
Watts	+ 6.6%	+19.8%

After these tests the ion source was disassembled. The most significant result of this was obtained by the inspection of the anodes. There had been some concern that after an extended period of operation the surfaces which had been under continuous electron bombardment might form insulating deposits. It was found that the anode for electron gun number two had no visible deposit even

though it had been operated for a longer period of time. There was some visible discoloration on electron gun number one which suggested that since it was the electron gun which was operated most during the early test phases of the program that there may have been some source of contamination which was ultimately pumped away. This indicates the importance of proper initial cleaning and also shows that contamination during the run did not occur.

CONCLUSION

The overall performance of the Two Gas Atmosphere Sensor System during the 60 day Space Cabin Simulator test was very encouraging. The only significant problem associated with the instrument was the filament resistance variation in conjunction with the limited range of the load regulation of the emission regulator. Both of these areas are readily correctable and in fact the necessary changes are being implemented on the following sensor units. If the periods of non-regulation are eliminated along with those where external failures or changes affected the instrument it was found that the calibration factors for the primary constituents held within ±2%. When the accuracy of the calibration technique and the associated measurements are considered it is realized that the actual accuracy of the sensor is likely to be much better than this figure indicates. This is remarkable considering that the unit tested was not potted or hermetically sealed.

The successful performance of the Two Gas Atmosphere Sensor System is demonstrated by the fact that after a trail period it was given the job of primary oxygen monitor.

REFERENCES

1. "Angular Aberrations in Sector-Shaped Electromagnetic Lenses for Focusing Beams of Charged Particles" Physical Review, Volume 91, No. 1, July 1, 1953, by E. G. Johnson and A. O. Nier.

2. Ionen-und electronenoptische Zylinderlinsen und Prismen I., Von Richard Herzog. Zeitschrift Fin Physik, Volume 89, p. 447.

3. Mass Spectrometry, Edited by C. A. McDowell.

4. "Image Curvature Caused by Fringing Fields in Magnetic Sector Mass Spectrometers", C. E. Berry, RSI Vol 27, No. 10, October 1956.

5. See the Phase I report for a derivation of this equation.

6. "Numerical Determination of Ion Paths in Nonhomogeneous Magnetic Fields" by A. C. Lilly, Jr., T. J. Weismann, and D. A. Lowitz M.A.P., Vol. 34, No. 3, March 1963.

7. These equations are taken from General Electric Co. Permanent Magnet Manual PM - 125.

8. U.S. Patent No. 2,569,032.

9. Designed by the Space Physics Research Laboratory, Department of Electrical Engineering, University of Michigan, Ann Arbor, Michigan.

10. Jolly, James A., "Thoriated Rhenium Tungsten as a Thermionic Emitter", Given at the Sixth National Conference on Tube Techniques, New York City, New York.

11. Jenkins, R. O,, Trodden, W. G., "The Poisoning of Thoriated Tungsten Cathodes", Brit. J. Appl. Phys.

12. These equations are taken from General Electric Co. Permanent Magnet Manual PM - 125.

13. Permanent Magnet Guidelines, Part II, March 1968, Electromechanical Design.

APPENDIX A

Project Notes

Project Note	
5	The Angular Relationships for Non-Normal Entry Into a Triangular Magnetic Field
6	Detailed Derivation of Herzog's Optical Analogy for Ion Trajectories in a Magnetic Field
13	Derivation for Ion Trajectories in a Magnetic Fringe Field
14	The Location of an Effective Object Point to be Used with Herzog's Equation in a Magnet with Fringing Fields
15	Effects of Z-Axis Focus on X-Y Plane Focusing
16	Ion Source Conductance Calculations
17	Inlet and Pump Out Line System
18	Mechanical Design Considerations
19	Ion Source Non-Linearity Due to the Influence of Space Charge in the Ionizing Region
20	Reduced Image Distances in the 60° and 90° Magnetic Sector Analyzers
21	Derivation of the Position for an Effective Magnet Boundary

Project: 20207 S. S. Berg

Project Note Number 5

The Angular Relationships For Non-Normal Entry Into a Triangular Magnetic Field

INTRODUCTION

It is shown that the sector angle is

$$\Phi = \sin^{-1}\left(\frac{y_o}{a}\sin\Omega - \frac{x_o}{a}\cos\Omega\right) + \Omega + \epsilon'$$

where

$$y_o = y' - a\cos\epsilon'$$

$$x_o = a\sin\epsilon'$$

The angles are defined as:

Φ = Arc angle of trajectory in field

Ω = Sector angle of magnet

ϵ' = Angular displacement from normal on entrance to field

ϵ'' = Angular displacement from normal on exit from field.

The angles are positive if the normals to the magnet fail in the positive quadrant of the coordinates describing the trajectory and its arc. In the diagram these angles are constructed negative.

The coordinates x', y', give the intersection of the normal from the source to the magnet face. The origin of the coordinates, in this system is the apex angle of the magnet. The entry face of the magnet falls on the coordinate x = 0. The distance is ℓ' from the source to the magnet face at x = 0.

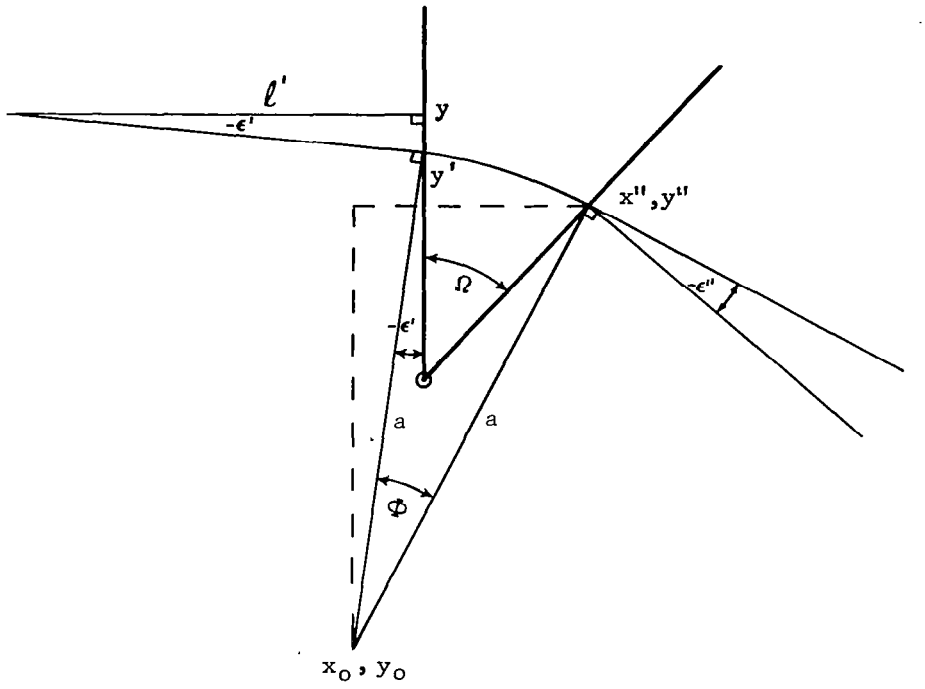

Given:

ℓ' ≡ Perpendicular distance from the face of the magnet to object

ϵ' ≡ Angle of entry (negative by definition)

a ≡ Radius of curvature for ion

y = Distance from magnet apex angle to line perpendicular from source to magnet

Ω = Magnet apex angle

Φ ≡ Apex angle of magnetic force deflection

ϵ'' ≡ Exact angle

Statement	Justification
1) $y' = y + \ell' \tan[-\epsilon']$	1) $\frac{\Delta y}{\ell'} = \tan \epsilon'$
2) $y_o = y' - a \cos[-\epsilon']$	2) $\frac{\Delta y}{a} = \cos \epsilon'$, and equal angles created by $\perp$.
3) $x_o = a \sin[-\epsilon']$	3) $\frac{\Delta x}{a} = \sin \epsilon'$
4) $y'' = a \cos(\phi - \epsilon') + y_o$	4) $\frac{\Delta y}{a} = \cos(\phi + \epsilon')$
5) $x'' = a \sin(\phi - \epsilon') + x_o$	5) $\frac{\Delta x}{a} = \sin(\phi + \epsilon')$
6) $\frac{a \sin(\phi - \epsilon') + x_o}{a \cos(\phi - \epsilon') + y_o} = \tan\Omega$	6) $\frac{\Delta x}{\Delta y} = \tan\Omega$

Hence, Φ may be found from 6. To put it in a tractable form of $\Phi = f(a, \epsilon', \ell', \Omega)$, we do the following:

$$a \sin(\phi - \epsilon') + x_o = [a \cos(\phi - \epsilon') + y_o] \tan\Omega$$

$$\sin(\phi - \epsilon') - \cos(\phi - \epsilon') \tan\Omega = \frac{y_o \tan\Omega - x_o}{a}$$

Using the double angle formula:

$$\sin\phi \cos[-\epsilon'] + \cos\phi \sin[-\epsilon']$$

$$- \tan\Omega \left[\cos\phi \cos[-\epsilon'] - \sin\phi \sin[-\epsilon']\right]$$

$$= \frac{y_o \tan\Omega - x_o}{a}$$

Expanding the tangent:

$$\sin\phi \cos[-\epsilon'] \cos\Omega + \cos\phi \sin[-\epsilon'] \cos\Omega$$

$$- \cos\phi \cos[-\epsilon'] \sin\Omega + \sin\phi \sin[-\epsilon'] \sin\Omega$$

$$= \frac{\cos\Omega}{a} (y_o \tan\Omega - x_o)$$

The triple angle formula is:

$$\sin(-\alpha + \beta + \gamma) =$$

$$- \sin\alpha \cos\beta \cos\gamma + \sin\alpha \sin\beta \sin\gamma$$

$$+ \cos\alpha \sin\beta \cos\gamma + \cos\alpha \cos\beta \sin\gamma$$

Identifying terms, it is found that:

$$\sin\ (-\Omega - \epsilon' + \phi) = \frac{\cos\ \Omega}{a}\ (y_o \tan \Omega - x_o)$$

Hence:

$$\phi = \sin^{-1}\left(\frac{y_o}{a}\sin\Omega - \frac{x_o}{a}\cos\Omega\right) + \Omega + \epsilon'$$

Note that if $x_o = y_o = 0$, which occurs if $\epsilon' = 0$, $\phi = \Omega$. Therefore, to find ϕ, first find:

$$y_o = y' - a\cos\epsilon' ,$$

then:

$$x_o = -a\sin\epsilon ;$$

and plug into:

$$\phi = \sin^{-1}\left(\frac{y_o}{a}\sin\Omega - \frac{x_o}{a}\cos\Omega\right) + \Omega + \epsilon'$$

To find ϵ'', since Σ (angles) = 360°, then:

$$\phi - \epsilon' + (360 - \Omega) - \epsilon'' = 360 ,$$

or:

$$\epsilon'' = \phi - \epsilon' - \Omega$$

Note that:

$$\Omega = \Phi - \epsilon' - \epsilon''$$

Project: 20207 S. S. Berg

Project Note Number 6

Detailed Derivation of Herzog's Optical Analogy for Ion Trajectories in a Magnetic Field

INTRODUCTION

The equations given in this report were originally developed by Herzog in Zeitschrift Fur Physik, Vol.89, p. 447. The advantage of Herzog's approach is the simple formulation for object-image position and sizes for both normal and oblique entry into the field. The derivation is first order in terms of the angular divergence of the beam.

DEFINITION OF TERMS - NORMAL ENTRY

For sake of clarity, the normal case will be done first. Figure 1 is a diagram of the geometry of interest. Regions I and II are field free. Region III has a homogeneous magnetic field which causes the ion to describe a radius of curvature.

$$a = \frac{m_o v_o c}{eH} = \frac{144\sqrt{m_o V}}{H} \text{ cm} \tag{1}$$

where

c = velocity of light
e = ionic charge
H = field strength
m_o = ionic mass
v_o = mean ion speed
V = accelerator voltage

Note the origin of the x', y', and x", and y" is at 0', and 0" respectively. In Region I, the ion path is

$$y' = y_1 + \alpha' x' \tag{2}$$

where α' is the angular divergence of the ray from a normal to the magnet and intersects the magnet at height, y_1. In Region III, the path radius is

$$r = a_1 + y_1 \tag{3}$$

Assuming a first order approximation and $y_1 \ll a$ and $y' \approx y$. The radius, a, varies slightly from $\phi = 0$ to $\phi = \Phi$, and is almost equal to 'a' defined in equation (1).

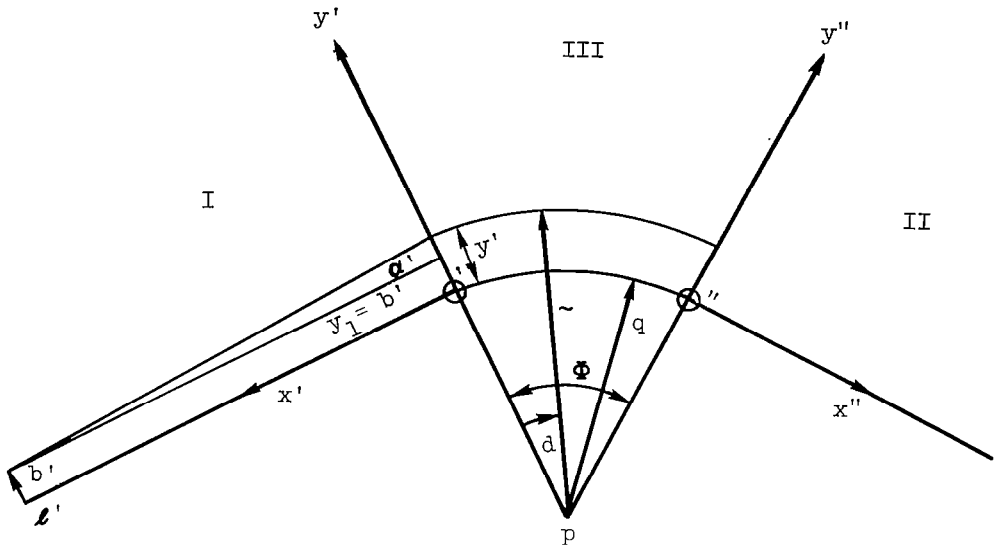

FIGURE 1
Normal Entry Diagram

On the exit side of the magnet (interface III - II) there is a divergence angle α'', image height y", etc. The field apex angle at exit has $\phi = \Phi$.

EQUATION OF MOTION

The kinetic energy for the ion is

$$T = \tfrac{1}{2}\, m\, (r^2\dot{\phi}^2 + \dot{r}^2)$$

The potential, for $v \ll c$, is

$$U = \int_o^r \frac{Be\dot{\phi}}{c}\, r dr = \tfrac{1}{2}\, Be\dot{\phi} r^2/c$$

Hence, the Lagrangian is

$$L = \tfrac{1}{2}\left[m(r^2\dot{\phi}^2 + \dot{r}^2) - \frac{Be\dot{\phi}}{c}\, r^2\right]$$

The equations of motion, relative to the generalized coordinate, ϕ is

$$\frac{d}{dt}\,(rmr\dot{\phi}) = \frac{Be}{c}\, r\dot{r} \tag{4}$$

and, relative to the generalized coordinate, r r

$$\frac{d}{dt}\,(m\dot{r}) = mr\dot{\phi}^2 - \frac{Be}{c}\, r\dot{\phi} \tag{5}$$

Integrating equation (4), then

$$\int_{mr_1^2\dot{\phi}_o}^{mr^2\dot{\phi}} d(r^2 m\dot{\phi}) = \int_{r_1}^{r} \frac{He}{c}\, r dr$$

gives

$$\dot{\phi} = \frac{r_1^{\,2}\,\dot{\phi}_o}{r^2} + \tfrac{1}{2}\,\frac{He}{mc}\left(1 - \frac{r_1^{\,2}}{r^2}\right) \tag{6}$$

SOLUTION OF EQUATIONS

Since variations from a fiducial point is of interest, assume a first order Maclauren expansion of

$$r = a(1 + z) \tag{7}$$

so $z \ll 1$.

To set up r_1^2/r^2 as a first order approximation by using equations (3) and (7).

$$\frac{r_1^2}{r^2} = \frac{(a + y_1)^2}{a^2(1 + z)^2} \approx \frac{a^2 + 2y_1 a}{a^2(1 + 2z)} \tag{8}$$

or

$$\frac{r_1^2}{r^2} = 1 + \frac{2y_1}{a} - 2z \tag{8}$$

Now put equations (1) and (8) into equations (6), and get

$$\dot{\phi} = \dot{\phi}_o \left(1 + \frac{2y_1}{a}\right) + \frac{v_o y_1}{a^2} - \frac{y_1}{a}\left(\frac{v_o}{a} - 2\dot{\phi}_o\right) z \tag{9}$$

From the definition of angular velocity and equation (3),

$$\dot{\phi}_o = \frac{v_{III}}{a + y_1}$$

where v_{III} is speed of the ion in the field region, and equal to

$$v_{III} = v_o (1 + \beta)$$

where v_o is the mean ion beam velocity and β is the velocity dispersion. Hence,

$$\dot{\phi}_o = \frac{v_o}{a}\left(1 + \beta - \frac{y_1}{a}\right) \tag{10}$$

Putting equation (10) into equation (9), and using only first order terms,

$$\dot{\phi} \approx \frac{v_o}{a}(1 + \beta - z)$$

Hence

$$\left(\frac{a}{v_o}\dot{\phi}\right) = 1 + \beta - z \tag{11}$$

Now setting up equation (5) and substituting equations (1) and (7),

$$\ddot{z} = \left(\frac{v_o}{a}\right)^2 \left\{\left[\left(\frac{a}{v_o}\dot{\phi}\right)^2 - \frac{1}{1+\gamma}\left(\frac{a}{v_o}\dot{\phi}\right)\right] + z\left[\left(\frac{a}{v_o}\dot{\phi}\right)^2 - \frac{1}{1+\gamma}\left(\frac{a\dot{\phi}}{v_o}\right)\right]\right\} \qquad (12)$$

where

$$m = m_o(1+\gamma)$$

Since

$$\gamma \ll 1, \quad \frac{1}{1+\gamma} \approx 1 - \gamma$$

Examining the expression in brackets and substituting equation (11), equation (12) then becomes, to a first order

$$\ddot{z} = \left(\frac{v_o}{a}\right)^2 (\beta + \gamma - z) \qquad (13)$$

and letting $\beta + \gamma = \delta$,

$$\ddot{z} = \left(\frac{v_o}{a}\right)^2 (\delta - z) \qquad (14)$$

If one substitutes $q = \delta - z$

$$-\ddot{q} = \left(\frac{v_o}{a}\right) q$$

which is the familiar SHM equation. The solution is

$$z = -A \sin \frac{v_o}{a} t - B \cos \frac{v_o}{a} t + \delta$$

The boundary conditions, which determine A and B are

A. At $t = 0$

$$z_o = \frac{r - a}{a} = \frac{y_1}{a}$$

and

B.

$$\dot{z} = \frac{\dot{r}}{a} = \frac{\alpha v_o}{a}$$

Hence

$$z = -\alpha' \sin \frac{v_o}{a} t + \delta\left(1 - \cos \frac{v_o}{a} t\right) + \frac{y_1}{a} \cos \frac{v_o}{a} t \tag{15}$$

To eliminate t, use the approximation,

$$\dot{\phi} = \frac{v_o}{a} (1 + \beta - z) \approx \frac{v_o}{a}$$

so

$$\phi = \frac{v_o}{a} t \tag{16}$$

Now substituting equations (7) and (16) into equation (15),

$$\frac{r}{a} - 1 = -\alpha' \sin\phi + \delta(1 - \cos\phi) + \frac{y_1}{a} \cos\phi \tag{17}$$

Since $r = a + y_2$ at the interface II-III, when $\phi = \Phi$, then equation (17) becomes

$$y_2 = a\left[-\alpha' \sin\Phi + \delta(1 - \cos\Phi) + \frac{y_1}{a} \cos\Phi\right] \tag{18}$$

To determine the trajectory in Region III, recall that $z = \frac{r}{a} - 1$, so

$$\frac{dz}{d\phi} = \frac{\left(\frac{dr}{d\phi}\right)}{a}$$

and geometrically

$$\frac{\Delta z}{\Delta \phi} \approx \alpha'' \text{ at } \phi = \Phi$$

so

$$\alpha'' = \frac{\left(\frac{dr}{d\phi}\right)\Phi}{a}$$

Applying this to equation (17)

$$\alpha'' = -\alpha' \cos\Phi + \delta \sin\Phi - \frac{y_1}{a} \sin\Phi \tag{19}$$

Since the trajectory in II is

$$y'' = y_2 + \alpha'' x'' \tag{20}$$

Putting equations (18) and (19) into (20)

$$y'' = \alpha' \left\{ - a \sin\Phi - \ell' \cos\Phi + x'' \left[- \cos\Phi + \frac{\ell'}{a} \sin\Phi \right] \right\}$$
$$+ \delta a \left[\frac{x''}{a} \sin\Phi + 1 - \cos\Phi \right] \qquad (21)$$
$$- b' \left[\frac{x''}{a} \sin\Phi - \cos\Phi \right]$$

FOCAL POINTS

The above expression gives the size, y", of any image at x", with object at $\ell' = x'$, and entering perpendicular to a homogeneous magnetic field of apex angle Φ. If we make the coefficient of α' equal to zero by finding the appropriate value of $x' = \ell'$, the image distance we get is:

$$-a \sin\Phi - (\ell' + \ell'') \cos\Phi + \frac{\ell'\ell''}{a} \sin\Phi$$

TRAJECTORY EQUATIONS FOR OBLIQUE RAYS

As seen in Figure 2, the rays enter the field region at an angle ϵ' to the normal, and leave at an angle ϵ'' from the normal. The angles ϵ are considered positive if the normals to the field fall in the positive X, Y quadrants. The angles ϵ' and ϵ'', shown in the figure in such a manner to clarify its definition, are the deviation of the off-axis ray from the normal to the trajectory (x' and x"). A second angle of interest, again illustrated for clarity in Figure 2, is designated as A and is the angle between the X axis and the off-axis ray. It can easily be seen that

$$\alpha' = A' - \Delta\phi' = A' - \frac{y_1}{a} \tan\epsilon' \qquad (22a)$$

and

$$\alpha'' = A'' - \Delta\phi'' = A'' - \frac{y_2}{a} \tan\epsilon'' \qquad (22b)$$

because

$$a\Delta\phi = y \tan\varepsilon$$

The program for the solution is now clear. We find y_1 and y_2. Let's proceed. We see

$$Y' = y_1 + A'X' \qquad (22c)$$

and

$$Y' = y_2 + A''X''$$

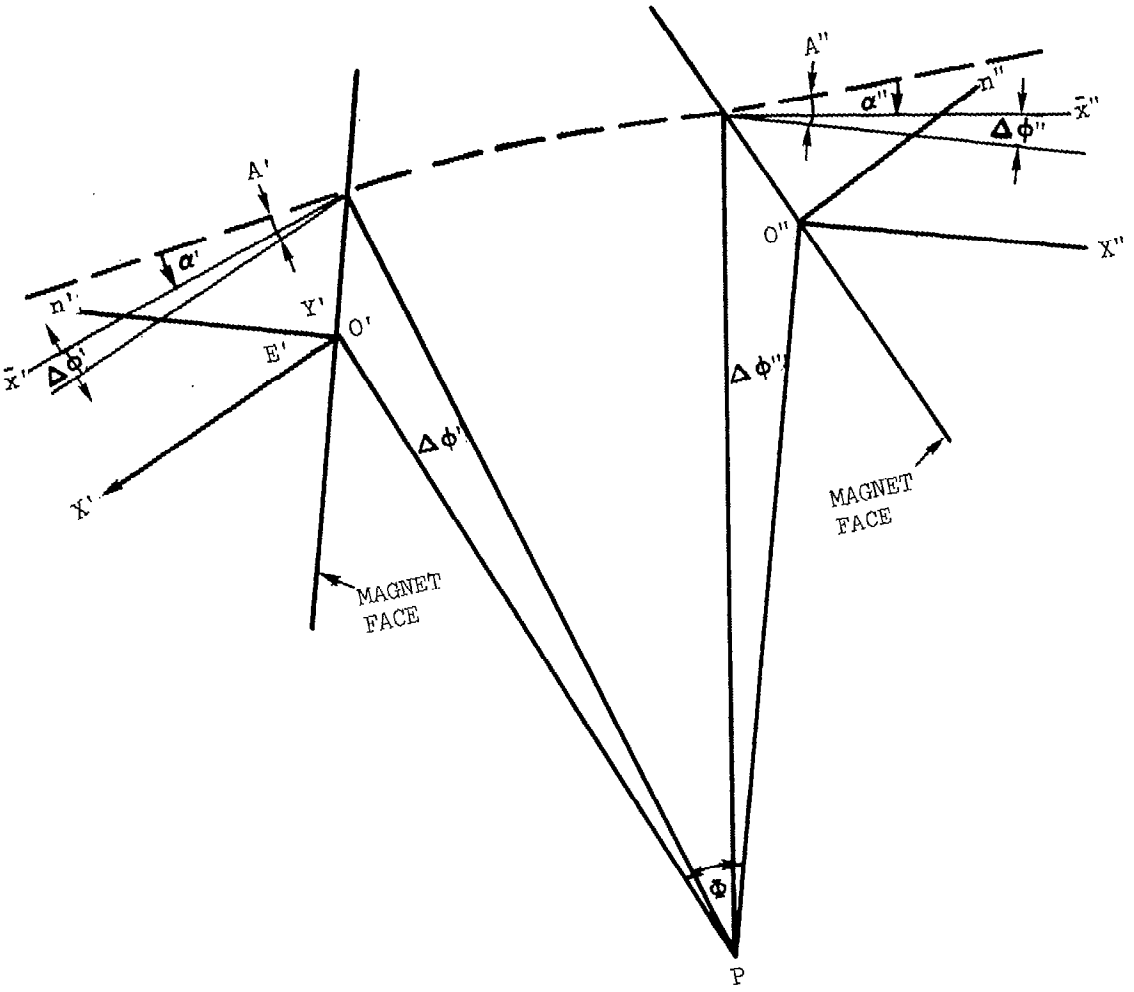

FIGURE 2
Oblique Entry Diagram

Substituting equation (18) for y_2 and equation (22) for A", one gets

$$Y'' = a\left[-a\sin\Phi + \delta\,(1 - \cos\Phi) + \frac{y_1}{a}\cos\Phi\right] + \left(\alpha'' + \frac{y_2}{a}\tan\epsilon''\right) X''$$

Now using equation (19) for α'' and equation (18) again

$$\begin{aligned} Y'' = -a\left[\left(A' - \frac{y_1}{a}\tan\epsilon''\right)\sin\Phi - \frac{y_1}{a}\cos\Phi\right] \\ -X''\left[\alpha'(\cos\Phi + \sin\Phi\tan\epsilon'') + \frac{y_1}{a}(\sin\Phi - \cos\Phi\tan\epsilon''\right] \\ + \delta\left\{a(1 - \cos\Phi) + X''\left[\sin\Phi + (1 - \cos\Phi)\tan\epsilon''\right]\right\} \end{aligned} \tag{23}$$

And substituting α' from equation (22a) into equation (23) and manipulating gives:

$$\begin{aligned} Y'' = -a\,A'\sin\Phi + y_1\frac{\cos(\Phi - \epsilon')}{\cos\epsilon'} \\ -X''\left[A'\frac{\cos(\Phi - \epsilon'')}{\cos\epsilon''} + \frac{y_1}{a}\frac{\sin(\Phi - \epsilon' - \epsilon'')}{\cos\epsilon'\cos\epsilon''}\right] \\ + \delta\left\{a\,(1 - \cos\Phi) + X''\left[\sin\Phi + (1 - \cos\Phi)\tan\epsilon''\right]\right\} \end{aligned} \tag{24}$$

Equation (24) gives the value of the size of the image at Y" for a given object size, y_1, oblique entry and exit angle, ϵ' and ϵ'', magnetic sector deflection angle, Φ, which is a function of magnet size and radius of curvature, a, and object position X". The angle, A', is the beam divergence.

FOCUSING FOR BEAM ENTERING MAGNET OBLIQUELY

For a focus condition, the coefficient of A' must be zero. Now calling $X' = \ell'$ and $X'' = \ell''$, and recalling from equation (22c), $y = b' - A'\ell'$, then,

$$0 = -a\sin\Phi - \ell'\frac{\cos(\Phi - \epsilon')}{\cos\epsilon'} - \ell''\left[\frac{\cos(\Phi - \epsilon'')}{\cos\epsilon''} - \frac{\ell'}{a}\frac{\sin(\Phi - \epsilon' - \epsilon'')}{\cos\epsilon'\cos\epsilon''}\right]$$

This may be expressed as:

$$(\ell' - g')(\ell'' - g'') = f^2 \tag{25}$$

where

$$g' = \frac{a \cos \epsilon' \cos (\Phi - \epsilon'')}{\sin (\Phi - \epsilon' - \epsilon'')} \tag{26}$$

$$g'' = \frac{a \cos \epsilon'' \cos (\Phi - \epsilon')}{\sin (\Phi - \epsilon' - \epsilon'')} \tag{27}$$

and

$$f = \frac{a \cos \epsilon' \cos \epsilon''}{\sin (\Phi - \epsilon' - \epsilon'')} \tag{28}$$

To obtain the focused image size, using equation (24) , one gets,

$$b'' = b' \left(\frac{g'' - \ell''}{f} \right) + \delta \left\{ a(1 - \cos\Phi) + \ell'' \left[\sin\Phi + \tan \epsilon'' \, (1 - \cos\Phi) \right] \right\} \tag{29}$$

Project: 20207 M. Ruecker

Project Note Number 13

Derivation For Ion Trajectories in a Magnetic Fringe Field

INTRODUCTION

The coordinates of this problem are defined below:

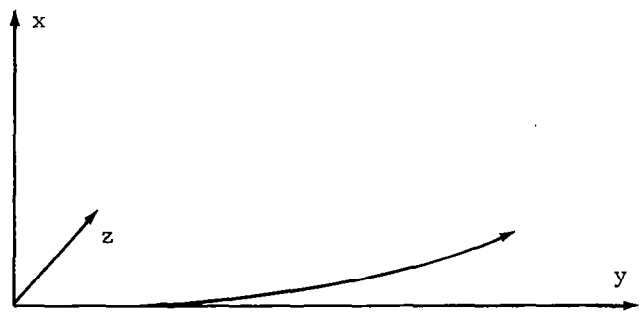

An ion starts at the origin with a velocity V_o which is y directed.

$$\vec{F} = q\vec{v} \times \vec{B}$$

Let

$$\vec{B} = B_z(y)\vec{K}$$

$$V_o^2 = \dot{x}^2 + \dot{y}^2$$

The equations of motion are:

$$\ddot{x} = \frac{qB(y)\dot{y}}{m} \qquad \ddot{y} = \frac{-q}{m} B(y)\dot{x}$$

$$\dot{x} = \frac{q}{m}\int B(y)\dot{y}\, dt = \frac{q}{m}\int B(y)dy$$

$$B(y) = B_o\, b(y)$$

$$\dot{x} = \frac{qB_o}{m}\int b(y)dy \qquad \dot{x}_o = o$$

$$\dot{y} = (V_o^2 - \dot{x}^2)^{\frac{1}{2}}$$

$$\dot{y} = \left(V_o^2 - \left[\frac{qB_o}{m}\int b(y)dy\right]^2\right)^{\frac{1}{2}}$$

But

$$\frac{qB_o}{m} = \frac{V_o}{r_o}$$

Hence

$$\dot{y} = \frac{V_o}{r_o}\left(r_o^2 - \left[\int h(y)dy\right]^2\right)^{\frac{1}{2}}$$

$$\frac{dx}{dy} = \frac{\dot{x}}{\dot{y}} = \frac{\int h(y)dy}{\left(r_o^2 - \left[\int h(y)dy\right]^2\right)^{\frac{1}{2}}} \tag{1}$$

and

$$x = \int_o^y \frac{\int h(y)dy}{\left(r_o^2 - \left[\int h(y)dy\right]^2\right)^{\frac{1}{2}}} dy \tag{2}$$

The latter two equations may be numerically integrated using available magnetic field data. In many cases the denominator of (1) may be approximated by r_o giving

$$\frac{dx}{dy} = \frac{1}{r_o}\int h(y)dy \tag{3}$$

and

$$x = \frac{1}{r_o}\iint h(y)dy \tag{4}$$

These equations will be utilized.

Project: 20207 M. Ruecker

Project Note Number 14

The Location of An Effective Object Point to Be Used With Herzog's Equations in a Magnet With Fringing Fields

One of the significant problems in magnetic sector design is the proper interfacing of the sector equations with the deflection and focusing effects of the fringe field. Several workers including Coggeshall, Nier, Bainbridge, and Kerwin have developed methods by which they attempt to fudge in the effects of the boundary field, however, all of these methods are lacking in some element of exactness and logic. The technique given below can be made exact. It is based on equations which are extensions of those developed by Coggeshall.

Consider the x-y plane in which there exists a fringe field $\bar{B} = - B(y)\bar{K}$. Two trajectories begin at 0 and travel to the boundary $y=y_1$, which is chosen as one gap width inside of the real magnet boundary. From this point on the field is uniform, so Herzog's equations may be applied.

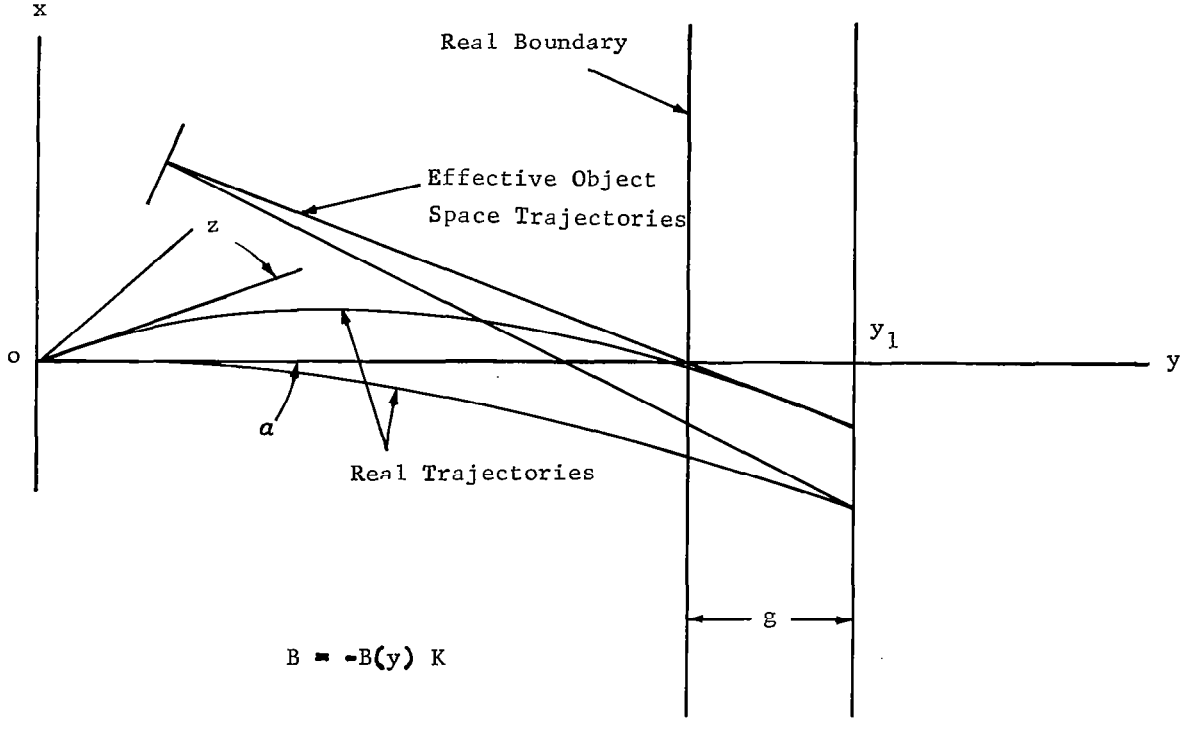

$$\ddot{x} = \frac{-qB(y)}{m}\,\dot{y}$$

$$\ddot{y} = \frac{+q}{m}\,B(y)\dot{x}$$

$$\dot{x}^2 + \dot{y}^2 = V_o^2$$

Integration of the x equation gives:

$$\dot{x} = \frac{-q}{m}\int B(y)dy + \dot{x}_o = \frac{-qB_o}{m}\int b(y)dy + \dot{x}_o$$

$$\dot{y} = \left(V_o^2 - \left[\frac{-qB_o}{m}\int b(y)dy + \dot{x}_o\right]^2\right)^{\frac{1}{2}}$$

$$\frac{qB_o}{m} = \frac{V_o}{r_o}$$

$$\dot{y} = \frac{V_o}{r_o}\left(r_o^2 - \left[-\int h(y)dy + \frac{\dot{x}_o r_o}{V_o}\right]^2\right)^{\frac{1}{2}}$$

$$\frac{dx}{dy} = \frac{\dot{x}}{\dot{y}} = \frac{-\int b(y)dy + \frac{\dot{x}_o r_o}{V_o}}{\left(r_o^2 - \left[-\int h(y)dy + \frac{\dot{x}_o r_o}{V_o}\right]^2\right)^{\frac{1}{2}}} \qquad (1)$$

and

$$x = \int \frac{-\int b(y)dy + \frac{\dot{x}_o r_o}{V_o}}{\left(r_o^2 - \left[-\int h(y)dy + \frac{\dot{x}_o r_o}{V_o}\right]^2\right)^{\frac{1}{2}}}\,dy \qquad (2)$$

But $\dot{x}_o/V_o = \sin\alpha$. For small angles $\sin\alpha \approx \alpha$, then:

$$\frac{dx}{dy} \doteq \frac{-\int b(y)dy + r_o\alpha}{\left(r_o^2 - \left[-\int b(y)dy + r_o\alpha\right]^2\right)^{\frac{1}{2}}} \qquad (3)$$

and

$$x = \int \frac{-\int b(y)dy + r_o\alpha}{\left(r_o^2 - \left[-\int b(y)dy + r_o\alpha\right]^2\right)^{\frac{1}{2}}}\, dy \qquad (4)$$

These equations are similar to those developed by Coggashell but are for the case where there is an initial angle α. Using these equations, it is possible to project the effective object space trajectories shown below:

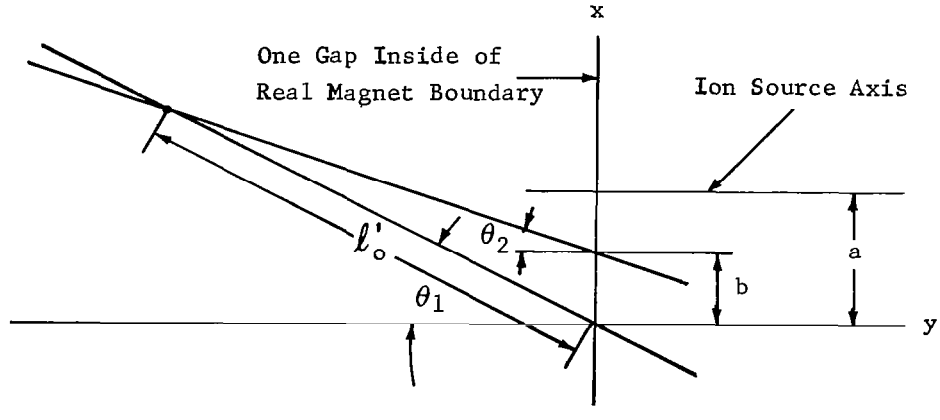

The equations of these trajectories are:

$$x = y \tan\theta_1 \qquad (5)$$

$$x = b + y \tan\theta_2 \qquad (6)$$

Where θ_1, θ_2 and b are given by appropriate evaluations of equations (3) and (4) as given below:

$$\tan\theta_1 = \frac{dx}{dy}\Bigg|_{\substack{y=y_1 \\ \alpha=0}} \qquad (7)$$

$$\tan\theta_2 = \frac{dx}{dy}\Bigg|_{\substack{y=y_1 \\ \alpha=\alpha}} \qquad (8)$$

$$b = x\Big|_{\substack{y=y_1 \\ \alpha=\alpha}} - x\Big|_{\substack{y=y_1 \\ \alpha=0}} \qquad (9)$$

Solving equations (5) and (6) for the intersection gives:

$$y = \frac{b}{\tan \theta_1 - \tan \theta_2} \tag{10}$$

which can be evaluated with (7), (8) and (9).

This substitution yields:

$$y = -\frac{\int \left\{ \frac{r_o \alpha - \int b(y)dy}{\left(r_o^2 - \left[r_o \alpha - \int b(y)dy\right]^2\right)^{\frac{1}{2}}} + \frac{\int b(y)dy}{\left(r_o^2 - \left[\int b(y)dy\right]^2\right)^{\frac{1}{2}}} \right\} dy}{\frac{r_o \alpha - \int b(y)dy}{\left(r_o^2 - \left[r_o \alpha - \int b(y)dy\right]^2\right)^{\frac{1}{2}}} + \frac{\int b(y)dy}{\left(r_o^2 - \left[\int b(y)dy\right]^2\right)^{\frac{1}{2}}}} \tag{11}$$

We are interested in finding an effective focal distance. This should be independent of α. Since α is small in any case, it seems reasonable to find the limit of the above expression as $\alpha \longrightarrow 0$. The first attempt leads to a value of 0/0. Applying I'Hospital's rule gives:

$$y\Big|_{\alpha=0} = -\frac{\int_o^{y_1} \frac{1}{\left(r_o^2 - \left[\int b(y)dy\right]^2\right)^{\frac{1}{2}}} \left[1 - \frac{\int b(y)dy}{r_o^2 - \left[\int b(y)dy\right]^2}\right] dy}{\frac{1}{\left(r_o^2 - \left[\int_o^{y_1} b(y)dy\right]^2\right)^{\frac{1}{2}}} \left[1 - \frac{\int_o^{y_1} b(y)dy}{r_o^2 - \left[\int_o^{y_1} b(y)dy\right]^2}\right]} \tag{12}$$

The effective object length ℓ_o' is then:

$$\ell_o' = \frac{y\Big|_{\alpha=0}}{\sin \theta_1} \tag{13}$$

where θ_1 is determined by equation (7).

Similar effects occur at the exit face and may be computed in the same way.

Project: 20207 M. Ruecker

Project Note Number 15

Effects of the Z Axis Focus on X-Y Plane Focusing

Consider an ion traveling in a Cartesian coordinates system in a field free region of zero potential with a velocity:

$$\bar{V}_o = \dot{x}_o \bar{i} + \dot{y}_o \bar{j} + \dot{z}_o \bar{k} \tag{1}$$

Assume that the ion passes through a Z axis focusing system which exerts no forces in the x direction and into a second field free region of zero potential with a velocity given by:

$$\bar{V}_1 = \dot{x}_1 \bar{i} + \dot{y}_1 \bar{j} + \dot{z}_1 \bar{k} \tag{2}$$

Let two angles be defined:

Ω = ion trajectory angle with respect to the y axis in the X-Y plane

Θ = ion trajectory angle with respect to the y axis in the Z-Y plane

Then

$$\tan \Omega_o = \dot{x}_o/\dot{y}_o, \quad \tan \Omega_1 = \dot{x}_1/\dot{y}_1 \tag{3), (4}$$

$$\tan \Theta_o = \dot{z}_o/\dot{y}_o, \quad \tan \Theta_1 = \dot{z}_1/\dot{y}_1 \tag{5), (6}$$

From conservation of energy:

$$\frac{1}{2}m (\dot{x}_o^2 + \dot{y}_o^2 + \dot{z}_o^2) = \frac{1}{2}m (\dot{x}_1^2 + \dot{y}_1^2 + \dot{z}_1^2) \tag{7}$$

Since there is no x gradient

$$\dot{x}_o = \dot{x}_1 \tag{8}$$

Therefore

$$\dot{y}_o^2 + \dot{z}_o^2 = \dot{y}_1^2 + \dot{z}_1^2 \tag{9}$$

This equation may be manipulated with the use of (3), (4), (5), (6) and (8) as follows:

$$\dot{y}_o^2 \ (1 + \tan^2 \theta_o) = \dot{y}_1^2 \ (1 + \tan^2 \theta_1)$$

$$\frac{\dot{x}_o^2}{\tan^2 \Omega_o}(1 + \tan^2 \theta_o) = \frac{\dot{x}_1^2}{\tan^2 \Omega_1}(1 + \tan^2 \theta_1)$$

$$\tan^2 \Omega_1 = \tan^2 \Omega_o \ \frac{(1 + \tan^2 \theta_1)}{(1 + \tan^2 \theta_o)}$$

All angles are sufficiently small that the tangents may be replaced by the angles:

$$\Omega_1 = \Omega_o \sqrt{\frac{1 + \theta_1^2}{1 + \theta_o^2}}$$

The θ angles are sufficiently small that further approximations are valid giving:

$$\Omega_1 = \Omega_o \left[1 + \frac{1}{2}\left(\theta_1^2 - \theta_o^2\right)\right]$$

In the z axis focusing system the greatest difference between θ_1^2 and θ_o^2 will result when $\theta_1 = 2^o$ and $\theta_o = 0^o$. In this case $\theta_1 = 0.035$, and $\theta_1^2 = 1.225 \times 10^{-3}$, giving

$$\Omega_1 = 1.0006125\,\Omega_o$$

This effect is clearly neglegible.

Project: 20207 M. Ruecker

Project Note Number 16

Ion Source Conductance Calculation

For a long tube:

$$F = \frac{4}{3} V_a \Big/ \int_o^{\ell} \frac{H}{A^2} \, d\ell$$

For 50-50 N_2-O_2 at 300°K

$$F_D = 61.4 \Big/ \int_o^{\ell} \frac{H}{A^2} \, d\ell \quad \frac{\text{liters}}{\text{sec}} \tag{1}$$

where H = perimeter (cm) and A = area $(\text{cm})^2$ and F_D = duct conductance

$$\frac{1}{F} = \frac{1}{F_D} + \frac{1}{F_{ap}} \tag{2}$$

$$F_{ap} = 11.6 \, w_o t_o \quad \text{liters/sec} \tag{3}$$

For a tapered duct:

$$\begin{aligned} w &= w_o + 2\ell \tan\alpha = \text{width (cm)} \\ t &= t_o + 2\ell \tan\alpha = \text{thickness (cm)} \end{aligned} \tag{4}$$

Then

$$\begin{aligned} H &= 2(w + t) = 2(w_o + t_o) + 8\ell \tan\alpha \\ A &= w_o t_o + 2\ell \tan\alpha \quad (w_o + t_o) + 4\ell^2 \tan^2\alpha \end{aligned} \tag{5}$$

These values are substituted into the F_D equation and integrated. There is also a correction factor, K, which is a function of t/w. Values are tabulated for constant dimensional ducts which should be fairly close.

$$F_D = \frac{30.7 \, w_o t_o \left[w_o t_o + 2 (w_o + t_o) \ell \tan\alpha + 4\ell^2 \tan^2\alpha \right]}{\left[(w_o + t_o) + 2\ell \tan\alpha \right] \ell} K \tag{6}$$

Combinint equations (2), (3) and (6) conductances may be calculated. Results are tabulated below for both the electron accelerator and ion exit apertures.

	w_o	t_o	ℓ	α	
E.A.	.040	.010	.050	5°	43.1 cc/sec
Ion Exit	.020	.012	.100	5°	
E.A.	.040	.010	.050	10°	45.5 cc/sec
Ion Exit	.020	.012	.050	5°	
E.A.	.040	.010	.025	10°	49.3 cc/sec
Ion Exit	.020	.012	.050	5°	

Select 45.5 cc/sec values.

The conductance will be somewhat less than shown due to rounded corners. Probably the total conductance will be close to 40 cc/sec.

Project: 20207 J. B. Chang

Project Note Number 17

Inlet and Pump Out Line System

ATMOSPHERIC SAMPLING

The sampling of the atmosphere is an important factor in determining the ultimate performance of the sensor system. Sampling is accomplished by a continuous-flow inlet system which serves the function of transporting a small but representative quantity of the atmospheric gas to the mass spectrometer ion source which is at a pressure 10^{-6} times that of the cabin.

The key variables of the sampling system are the quantity of gas consumed, the time taken to produce a change in gas composition in the ion source of the mass spectrometer after a change in the original mixture, and the accuracy of the composition in the ion source. Size, weight and reliability are also factors in the design. While the inlet and sampling system introduce time and accuracy factors, the performance and design are, except in the fastest response - time problems, separable from the basic analyzer design. This is due to the fact that the time constants of gas flow in the ion source and the flow of ions are generally short and not a function of the inlet system. The large pressure drop from the inlet system to the ion source precludes any upstream reflection of flow characteristics, and the inlet leak can be set to any desired flow for ion chamber pressure.

The time constant of the sensor system is a result of the following three significant time factors which are additive and non-interacting.

a. The sample transport time Δt_g

b. The ion source time constant $\tau_s = \frac{V_s}{S_s}$, where V_s is the ion source volume and S_s, the pumping speed out of the ion source.

c. The time constant, τ_a, of the ion current amplifying system. The sample transport time is often the dominant time factor and will be discussed later for both the constant diameter flow line and tapered flow lines.

GENERAL INLET SYSTEM CHARACTERISTICS

It is important to first establish the nature of flow into the mass spectrometer necessary for accurate analysis. There are three types of flow to be considered: molecular flow; viscous non-critical flow; and viscous critical flow.

If molecular flow could be achieved directly from the atmosphere, the inlet flow problem would reduce to only a temperature measurement. The number of molecules passing through an aperture A cm^2 per unit time is:

$$Q_i = \frac{n_i \bar{C}_i A_i}{4} \text{ molecules/sec}$$

where n is the density in molecules/cm^3:

$$\bar{C} = \left(\frac{8KT}{m\pi}\right)^{\frac{1}{2}} \text{ is the mean molecular speed in cm/sec}$$

If this flow takes place directly into the ionizing region of the mass spectrometer and the flow out of the source is molecular, then

$$Q_s = \frac{n_s \bar{C}_s A_s}{4} = \frac{n_i \bar{C}_i A_i}{4} \text{ molecules/sec}$$

or

$$n_s = \frac{A_i}{A_s}\left(\frac{T_i}{T_s}\right)^{\frac{1}{2}} n_i \text{ molecules/cm}^3$$

where subscript i and s refer to inlet and ion source respectively.

Thus if the mass spectrometer is accurately calibrated as a function of molecular density (equivalent to partial pressure), the density of each species in the atmosphere is known by the knowledge of the temperature ratio T_i/T_s.

Viscous, non-critical flow may be achieved through a single narrow channel. For isothermal flow in a long constant-diameter capillary channel, the boundary layer thickness grows rapidly and in approximately 8 diameters fills the opening at the entrance. When the intake region is a negligible part of the channel, the flow can be expressed as the well known poiseuille equation.

$$Q_i = \left(\frac{1}{KT}\right)\frac{a_i^2\left(p_1^2 - p_2^2\right)}{16\eta\ell} A_i \text{ molecules/sec}$$

where

Q_i = Inlet flow, molecules/sec

K = Boltzman constant, 1.38×10^{-16} ergs/molecules/°K

T = Temperature, °K

a = Radius of the capillary, cm

p_1 = Inlet pressure, dynes/cm^2

p_2 = Exit pressure, dynes/cm^2

η = Viscosity of mixture, dyne-sec/cm^2

ℓ = Capillary length, cm

A = Capillary cross-section, cm^2

For direct flow into the spectrometer $p_1 \gg p_2$, and p_2 is neglected. Converting to density, $p_1 = n_i KT_i$ and thus

$$Q_i = \frac{a_i^2 n_i^2 A_i KT_i}{16\eta\ell}$$

The source density for each species is then

$$n_s = \frac{a_i^2 KT_i}{4\,\bar{C}_s \eta\ell} \left(\frac{A_i}{A_s}\right) n_i^2 \quad \text{molecules/sec}$$

First it is observed that the density in the ionizing region increases as the square of the external density. Thus, a wider dynamic range of operation is required, for a given range of inlet densities. Secondly, the flow is a function of viscosity which is a complex empirical relationship depending on the gases, temperature, and mixture. The chief difficulty here is that a pure gas calibration has little meaning when that gas is to be analyzed in a mixture. Due to these factors, it is virtually impossible to analyze a mixture except by post-synthesis.

Thus, it is clear that regardless of the techniques used to transport and reduce the inlet pressure (while preserving the accuracy of the composition), the flow into the mass spectrometer should be molecular in nature.

The equation of molecular conductance through long circular pipe is

$$C = \frac{1}{6} \sqrt{\frac{2\pi KT}{m}} \frac{D^3}{L} \quad \text{cgs units}$$

This is reduced from the general Knudsen equation for a long circular pipe for a very low pressure.

The general Knudsen flow equation for a long circular pipe is

$$C = \left(\frac{\pi}{128} \frac{D^4 \bar{P}}{\eta L}\right) + \left(\frac{1}{6} \sqrt{\frac{2\pi KT}{m}} \frac{D^3}{L}\right)\left(\frac{1 + \sqrt{\frac{m}{KT}} \frac{D\bar{P}}{\eta}}{1 + 1.24 \sqrt{\frac{m}{KT}} \frac{D\bar{P}}{\eta}}\right)$$

where D is the diameter of the pipe, $\bar{P}$ is the average pressure in the pipe, L is the length of the pipe, η is the viscosity of the gas, K is the Boltzmann constant, T is the absolute temperature, and m is the mass of the molecule.

For simplification, the Knudsen equation may be written in the form for a short segment ΔL.

$$C = \frac{1}{\Delta L}\left(ap + b\,\frac{1 + cp}{1 + fp}\right)$$

then the flow through that segment is

$$\Delta Q = \left(ap + b\,\frac{1 + cp}{1 + fp}\right)\frac{\Delta p}{\Delta L}$$

The total flow through the capillary line in a steady state becomes

$$Q = \frac{1}{L}\int_{p_2}^{p_1}\left(ap + b\,\frac{1 + cp}{1 + fp}\right)dp$$

$$= \frac{1}{L}\left[\frac{a}{2}\,p^2 + \frac{bc}{f}\,p + \frac{b\,(d-c)}{f^2}\,\ln(1 + fp)\right]_{p_2}^{p_1}$$

where p_1 is the entrance pressure, p_2 the exit pressure.

Since $p_2 \ll p_1$ in the case to be considered, by letting the lower integration limit p_2 equal 0, we have

$$QL = \frac{a}{2}\,p_1^2 + bp_1\left[\frac{c}{f}\left(1 - \frac{\ln(1 + fp_1)}{fp_1}\right) + \frac{\ln(1 + fp_1)}{fp_1}\right]$$

Related to the general Knudsen flow equation, we have

$$a = \frac{\pi}{128}\,\frac{D^4}{\eta L}$$

$$b = \frac{1}{6}\sqrt{\frac{2\pi KT}{m}}\,\frac{D^3}{L}$$

$$c = \sqrt{\frac{m}{KT}}\ \frac{D}{\eta}$$

$$f = 1.24\ \sqrt{\frac{m}{KT}}\ \frac{D}{\eta}$$

therefore, $a = 0.0476\ bf$, $\frac{c}{f} = 0.807$.

Then

$$QL = 0.024\ bfp_1^2 + bp_1\ \left[0.807\ \left(1 - \frac{\ln\ (1 + fp_1)}{fp_1}\right) + \frac{\ln\ (1 + fp_1)}{fp_1}\right]$$

Let

$$y' = QL/bp_1$$

We have

$$y' = 0.024\ fp_1 + 0.807\ \left[1 - \frac{\ln\ (1 + fp_1)}{fp_1}\right] + \frac{\ln\ (1 + fp_1)}{fp_1}$$

$$= 0.024\ x + 0.807\ \left(1 - \frac{\ln\ (1 + x)}{x}\right) + \frac{\ln\ (1 + x)}{x}$$

where

$$x = fp = (m/KT)^{\frac{1}{2}}\ \frac{D}{\eta}\ p_1$$

as $x \longrightarrow 0$, $\frac{\ln\ (1 + x)}{x} \longrightarrow 1$, and $QL = bp_1 = \frac{1}{6}\ \sqrt{\frac{2\pi KT}{m}}\ D^3\ p_1$ ergs/sec which is equivalent to the molecular flow equation,

$$Q = \frac{\pi}{3}\ \left(\frac{KT}{2\pi m}\right)^{\frac{1}{2}}\ \frac{D^3}{L}\ \Delta p \quad \text{ergs/sec}$$

Now, we may plot the deviation from molecular flow as a function of $x = fp_1$ vs y'. See Table

x = fp	A = 0.024x	B = $\frac{\ln (1 + x)}{x}$	(1-B)	C=0.807 (1-B)	γ' = A+B+C
0.01	0.00024	0.99500	0.00500	0.00404	0.99928
0.03	0.00072	0.98533	0.01467	0.01184	0.99789
0.06	0.00144	0.96794	0.03206	0.02587	0.99525
0.08	0.00192	0.96200	0.03800	0.03067	0.99999
0.10	0.00240	0.95310	0.04690	0.03785	0.99335
0.30	0.00720	0.87453	0.12547	0.10125	0.98298
0.70	0.01680	0.75804	0.24196	0.19526	0.97010
1.00	0.02400	0.69315	0.30685	0.24763	0.96478
1.30	0.03120	0.64065	0.35935	0.29000	0.96185
3.00	0.07200	0.46210	0.53790	0.43409	0.96819
5.00	0.12000	0.35835	0.64165	0.51781	0.99616
6.00	0.14400	0.32432	0.67568	0.54523	1.01355
10.00	0.24000	0.23797	0.76203	0.61496	1.09293
30.00	0.72000	0.11447	0.88553	0.71462	1.54909
70.00	1.68000	0.06090	0.93910	0.75785	2.49875
100.00	2.40000	0.04605	0.95395	0.76984	3.21589
200.00	4.80000	0.02652	0.97348	0.78560	5.61212
500.00	12.00000	0.01243	0.98757	0.79697	12.80940
700.00	16.80000	0.00936	0.99064	0.79945	17.60881
1,000.00	24.00000	0.00691	0.99309	0.80142	24.80833
2,000.00	48.00000	0.00380	0.99620	0.80393	48.80773

ANALYTIC DESIGN FORMULAS

The differential equation of poiseuille flow is

$$Q_n = \frac{-\pi a^4}{8\eta KT} \; p \; \frac{dp}{dx}$$

where

Q_n = Flow in molecules/sec

K = Boltzman constant, 1.38×10^{-16} ergs/molecule/K°

T = Temperature in Kelvin (°K)

a = Radius of the capillary in cm

η = Viscosity of mixture in dyne-sec/cm^2

p = Pressure in dynes/cm^2

In the constant diameter line region:

$$Q_n dx = -\frac{\pi a^4}{8\eta KT}\, p\,dp$$

$$\int_o^{\ell} Q_n dx = -\int_{p_o}^{p_1} \frac{\pi a^4}{8\eta KT}\, p\,dp$$

$$Q_n x \Big|_o^{\ell} = -\frac{\pi a^4}{16\eta KT}\, p^2 \Big|_{p_o}^{p_1}$$

$$Q_n \ell = \frac{\pi a^4}{16\eta KT}\left(p_o^2 - p_1^2\right)$$

$$Q_n = \frac{\pi a^4 \left(p_o^2 - p_1^2\right)}{16\eta KT\ell}$$

$$Q = \rho VA$$

$$= pVA$$

Hence

$$V_o = \frac{Q_o}{p_o \pi a_o^2}$$

$$V = \frac{dx}{dt}$$

$$dt = \frac{dx}{V} \qquad \text{(Transport Time)}$$

$$\int_o^t dt = \int_o^{\ell} \frac{dx}{Q_p/p_{xA}} = \frac{Q_p}{A}\int_o^{\ell} \frac{dx}{\left[1 - \frac{x}{\ell}\left(1 - \left(\frac{p_1}{p_o}\right)^2\right)\right]^{\frac{1}{2}}}$$

Hence

$$t = \frac{2\ell}{3V_o}\left(1 + \frac{(P_1/P_o)^2}{1 + (P_1/P_o)}\right)$$

$$\frac{V_x}{V_o} = \left[1 - x\left(1 - \left(\frac{p_1}{p_o}\right)^2\right)\right]^{-\frac{1}{2}}$$

Hence

$$V_x = \left[1 - x\left(1 - \left(\frac{p_1}{p_o}\right)^2\right)\right]^{-\frac{1}{2}} V_o$$

where $x = x/\ell$

In the constant velocity region:

Let

$$a^2 = \frac{K_2}{p}$$

$$Q_n = \frac{-\pi\left(\frac{K_2}{p}\right)^2 p \frac{dp}{dx}}{8\eta KT} = -\pi \frac{K_2^2}{p} \frac{dp}{dx} \quad /8\eta KT$$

$$\frac{8\eta KTQ_n}{\pi} dx = -K_2^2 \frac{dp}{p}$$

$$\int_o^{\ell} \frac{8\eta KTQ_n}{\pi} dx = -\int_{p_o}^{P_1} K_2^2 \frac{dp}{p}$$

$$\frac{8\eta KT\ell}{\pi} Q_n = -K_2^2 (\ln p_1 - \ln p_o)$$

Hence

$$Q_n = \frac{\pi K_2^2 \ln (P_o/P_1)}{8\eta KT\ell}$$

$$= \frac{\pi a_o^4 p_o^2}{8\eta KT\ell} \ln (p_o/p_1)$$

$$t = \frac{\ell}{V}$$

In the constant D/λ region:

Let $a = k_3/p$

$$Q_n = -\frac{\pi\left(\frac{k_3}{p}\right)^4 p \frac{dp}{dx}}{8\eta KT} = -\frac{\pi k_3^4}{p^3} \frac{dp}{dx} / 8\eta KT$$

$$\int_o^\ell \frac{8K\eta TQ_n}{\pi} dx = -\int_{p_o}^{p_1} \frac{k_3^4 dp}{p^3}$$

$$\frac{8K\eta T\ell}{\pi} Q_n = \frac{k_3^4}{2} \frac{\left(p_o^2 - p_1^2\right)}{p_o^2 p_1^2}$$

$$Q_n = \frac{\pi k_3^4 \left(p_o^2 - p_1^2\right)}{16K\eta T\ell\, p_o^2 p_1^2}$$

$$= \frac{\pi a_o^2 a_1^2 \left(p_o^2 - p_1^2\right)}{16K\eta T\ell}$$

$$V_x = \left\{1 + x\left[\frac{1}{\left(p_1/p_o\right)^2} - 1\right]\right\}^{-\frac{1}{2}} V_o$$

$$t = \frac{2\ell}{3V_o\left(p_1/p_o\right)}\left(1 + \frac{\left(p_1/p_o\right)^2}{1 + \left(p_1/p_o\right)}\right)$$

ANALYTIC CALCULATIONS

Aperture Design

Length to diameter relations

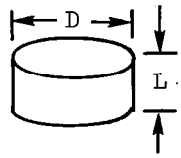

L	D
20μ	5μ
30	10
30	20
30	30
30	50
30	100

$$QL = \left\{ 0.024fp + 0.807 \left[1 - \frac{\ln (1 + fp)}{fp} \right] + \frac{\ln(1 + fp)}{fp} \right\} bp$$

where

$$f = \sqrt{\frac{m}{KT}} \frac{D}{\eta}$$

$$b = \frac{1}{6} \sqrt{\frac{2K\pi T}{m}} D^3$$

From γ' vs x curve, $x = fp \leq 5$ can be considered as pure molecular flow.

For air at 293.2°K

$$f = 0.316D, \quad b = 12.1D^3$$

$$f_p = 0.316Dp \Longrightarrow p = \frac{5}{0.316D}$$

Let

$$QL = \gamma' bp$$

D 10^{-4}cm	L 10^{-4}cm	p μHg	fp	A = 0.024fp	B = $\frac{\ln (1+fp)}{fp}$	0.807 (1-B)	γ'	bp	QL	Q μ-liters /sec
5	20	32×10^{3}	5	0.1200	0.3584	0.5178	0.9962	4.84×10^{-5}	4.82×10^{-5}	0.024
10	30	16×10^{3}	5	0.1200	0.3584	0.5178	0.9962	1.94×10^{-4}	1.93×10^{-4}	0.064
20	30	8×10^{3}	5	0.1200	0.3584	0.5178	0.9962	7.74×10^{-4}	7.71×10^{-4}	0.257
30	30	5.3×10^{3}	5	0.1200	0.3584	0.5178	0.9962	1.73×10^{-3}	1.72×10^{-3}	0.575
50	30	3.2×10^{3}	5	0.1200	0.3584	0.5178	0.9962	4.84×10^{-3}	4.82×10^{-3}	1.607

For molecular conductance in short circular pipe in air at 293.2°K we have

$$C = 12.1 \frac{D^3}{L} \alpha \text{ liters/sec}$$

Where

$$\alpha = \frac{15\left(\frac{L}{D}\right) + 12\left(\frac{L}{D}\right)^2}{20 + 38\left(\frac{L}{D}\right) + 12\left(\frac{L}{D}\right)^2}$$

D 10^{-4}cm	L 10^{-4}cm	$\frac{L}{D}$	$\left(\frac{L}{D}\right)^2$	α	$\frac{D^3}{L}$	C liters/sec.
5	20	4	16	0.692	6.25×10^{-8}	0.523×10^{-6}
10	30	3	9	0.632	33.3×10^{-8}	2.55×10^{-6}
20	30	1.5	2.25	0.476	2.67×10^{-6}	15.4×10^{-6}
30	30	1	1	0.386	9×10^{-6}	42.1×10^{-6}
50	30	0.6	0.36	0.283	41.7×10^{-6}	142.8×10^{-6}

The maximum flow in the ion source is

$$Q_3 = C_s p_s$$

$$= 35 \times 10^{-3} \text{ liter/sec} \times 2 \times 10^{-4} \text{ torr} \times \frac{10^3 \mu}{\text{torr}}$$

$$= 7 \times 10^{-3} \mu \text{ - liters/sec}$$

Choose the aperture with the size

$$D = 5\mu = 5 \times 10^{-4}\text{cm}$$

$$L = 20\mu = 20 \times 10^{-4}\text{cm}$$

The molecular conductance is

$$C_3 = 0.523 \times 10^{-6} \text{ liters/sec}$$

Since

$$Q_3 = C_3 \Delta p$$

it implies

$$\Delta p = \frac{7 \times 10^{-3}}{0.523 \times 10^{-6}} = 13.4 \times 10^{3}\mu = 13.4 \text{ torr}$$

or

$$p_1 \approx 13.4 \text{ torr}$$

INLET CAPILLARY LINE DESIGN

Choose a combination of the constant diameter line and a constant velocity line.

$Q_o = 10 \text{ torr}^{-cc/sec} = 1 \times 10^{4}\mu\text{-cc/sec}$

$p_o = 400 \text{ torr} = 5.37 \times 10^{5} \text{ dyne/cm}^2$

$T = 293.2°K$

$\eta = 1.8 \times 10^{-4} \text{ gm-sec/cm}$

$K = 1.38 \times 10^{-16} \text{ dyne-cm/molecule } °K$

$p_1 = 13.5 \text{ torr} = 18.12 \times 10^{3} \text{ dyne/cm}^2$

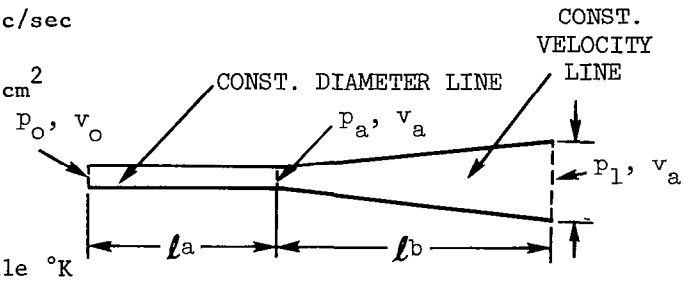

Since

$$\lambda_1 = \frac{5}{p_1} = \frac{5}{18.12 \times 10^{3}} = 0.37 \times 10^{-3} \text{cm}$$

Let

$$\frac{D_1}{\lambda_1} \geq 200$$

or

$$D_1 = 74 \times 10^{-3} \text{cm}$$

Choose

$$D_1 = 76.2 \times 10^{-3} \text{cm}$$

In the constant velocity region, we have

$$\ln\left(\frac{p_a}{p_1}\right) = \ln\left(\frac{a_1^2}{a_o^2}\right)$$

Hence

$$p_a = \frac{a_1^2}{a_o^2} \; p_1$$

$$= \frac{26.3}{a_o^2} \text{ dyne/cm}^2$$

$$Q_a = \frac{\pi a_o^4 \; p_a^2 \; \ln \; (p_a/p_1)}{8KT\eta \ell_b}$$

The flow in constant diameter line region is

$$Q_o = \frac{\pi a_o^4 \left(p_o^2 - p_a^2\right)}{16KT\eta \ell_a}$$

Matching flows in the two regions leads to

$$\frac{2 \; p_a^2 \; \ln \left(\frac{p_a}{p_1}\right)}{\ell_b} = \frac{p_o^2 - p_a^2}{\ell_a}$$

Let

$$p_a = \frac{26.3}{a_o^2} \leq 5.36 \times 10^5 \text{ dyne/cm}^2$$

Then

$$a_o^2 \geq 49.072 \times 10^{-6} \text{ cm}^2$$

or

$$a_o \geq 7 \times 10^{-3} \text{cm}$$

Choose

$$d_o = 20.32 \times 10^{-3} \text{cm}$$

$$a_o = 10.16 \times 10^{-3} \text{cm} > 7 \times 10^{-3} \text{cm}$$

$$p_a = \frac{26.3}{a_o^2} = 2.55 \times 10^5 \text{ dyne/cm}^2$$

$$2 \; p_a^2 \; \ln \left(\frac{p_a}{p_1}\right) = \frac{\ell_b}{\ell_a} \left(p_o^2 - p_a^2\right)$$

Assume that the total inlet capillary line is two meters long. Therefore,

$$\ell_b = (200 - \ell_a) \text{ cm}$$

$$2 \times (2.55 \times 10^5)^2 \ln\left(\frac{255}{18.1}\right)\ell_a = (200 - \ell_a)\left[(5.36 \times 10^5)^2 - (2.55 \times 10^5)^2\right]$$

It implies

$$\ell_a = 78.562 \text{ cm}$$

$$\ell_b = 200 - \ell_a = 121.438 \text{ cm}$$

Check for D/λ

At Entrance:

$$D_o = 20.32 \times 10^{-3} \text{ cm}$$

$$\lambda_o = \frac{5}{4 \times 10^5} = 1.25 \times 10^{-5} \text{ cm}$$

$$D_o/\lambda_o = 1{,}626 \gg 200$$

At Aperture:

$$D_1 = 76.2 \times 10^{-3} \text{ cm}$$

$$\lambda_1 = \frac{5}{13.5 \times 10^3} = 0.37 \times 10^{-3} \text{ cm}$$

$$D_1/\lambda_1 = 206 > 200$$

Check for velocity

At Entrance:

$$V_o = \frac{Q_o}{p_o \pi a_o^2} = 77 \text{ cm/sec}$$

At Aperture:

$$V_1 = V_a = \left(\frac{p_o}{p_a}\right) V_o = 162 \text{ cm/sec} \quad << \frac{1}{10} V_{sound}$$

Check for maximum transport time

$$\tau = \Delta t_1 + \Delta_2$$

In the constant diameter region

$$\Delta t_1 = \frac{2\ell_a}{3V_o}\left(1 + \frac{(p_a/p_o)^2}{1 + (p_a/p_o)}\right)$$

$$= \frac{2 \times 78.562}{3 \times 77}\left(1 + \frac{0.2304}{1.48}\right)$$

$$= 0.78 \text{ sec}$$

In the constant velocity region

$$\Delta t_2 = \frac{\ell_b}{V_a} = \frac{121.438}{162} = 0.75 \text{ sec}$$

$$\tau = 1.53 \text{ sec}$$

PUMP OUT LINE DESIGN

Choose the combination of a constant velocity line and a constant D/λ line.

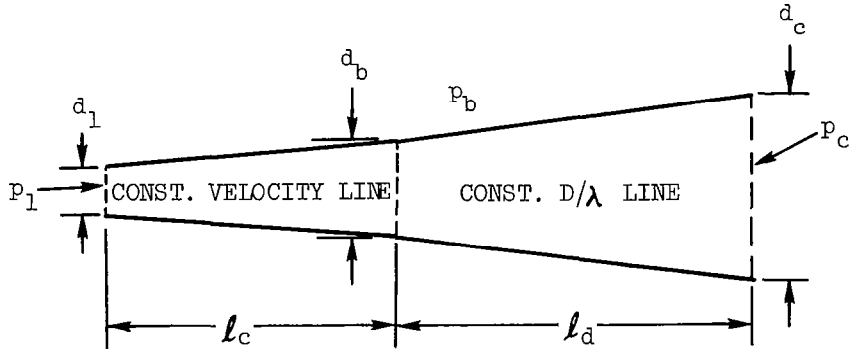

$Q_2 = 3.532 \times 10^{17}$ molecules/sec

$p_1 = 13.5$ torr

$T = 293.2°K$

$\eta = 1.8 \times 10^{-4}$ gm-sec/cm

$K = 1.38 \times 10^{-16}$ dyne-cm/molecule °K

$d_1 = 76.2 \times 10^{-3}$ cm

In the constant velocity region, choose

$$d_b = 127 \times 10^{-3} \text{ cm}$$

Thus

$$P_b = \frac{a_1^2}{a_b^2} \quad P_1 = \frac{(38.1 \times 10^{-3})^2}{(63.5 \times 10^{-3})^2} \times 13.5$$

$$= 4.86 \text{ torr} = 6.52 \times 10^3 \text{ dyne/cm}^2$$

$$\lambda_b = \frac{5}{P_b} = \frac{5}{4.86 \times 10^3} = 1.03 \times 10^{-3} \text{ cm}$$

The ratio of the tube diameter D_b to mean free path of molecule λ_b is

$$\frac{D_b}{\lambda_b} = \frac{127 \times 10^{-3}}{1.03 \times 10^{-3}} = 124$$

Since

$$Q_2 = \frac{\pi a_1^4 P_1^2}{8KT\eta \ell_c} \ln (P_1/P_b) = 3.532 \times 10^{17} \text{ molecules/sec}$$

Thus

$$\ell_c = \frac{\pi a_1^4 P_1^2}{8LT \eta Q_2} \ln (P_1/P_b)$$

$$= 105.03 \text{ cm}$$

In the constant D/λ region, keep $D/\lambda = 124$; let the pressure drop to one fifth of P_1 then

$$P_c = \frac{1}{5} P_1 = 2.7 \text{ torr} = 3.63 \times 10^3 \text{ dyne/cm}^2$$

Hence

$$\lambda_c = \frac{5}{P_c} = \frac{5}{3.63 \times 10^3} = 1.85 \times 10^{-3} \text{ cm}$$

Therefore, we should choose

$$D_c = 124 \lambda_c = 124 \times 1.85 \times 10^{-3} = 229.4 \times 10^{-3} \text{ cm}$$

Since

$$Q_2 = \frac{\pi a_b^2 a_c^2 (P_b^2 - P_c^2)}{16KT \eta \ell_d}$$

Therefore

$$\ell_d = \frac{\pi a_b^2 a_c^2 (P_b^2 - P_c^2)}{16KT \eta Q_2}$$

$$= 115.81 \text{ cm}$$

CRITICAL ORIFICE DESIGN

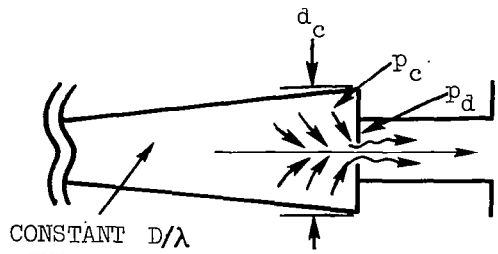

$p_c = 2.7$ torr

$d_c = 229.4 \times 10^{-3}$ cm

The critical ratio is

$$\gamma_c = \left(\frac{p_d}{p_c}\right)_{\text{critical}} = \left(\frac{2}{\nu+1}\right)^{\frac{\nu}{\nu-1}} = 0.525 \text{ for air}$$

Let

$$\gamma_c \geq 0.5$$

(for critical flow)

Therefore

$$p_d = 0.5\ p_c = 1.35 \text{ torr}$$

The conductance of the orifice is given by the equation

$$C_o = 20 \frac{A}{1-\gamma} \quad (\gamma \leq 0.52)$$

$$= 40A \text{ liters/sec}$$

where A is the cross-section area of the orifice

Since

$$Q_2 = C_o \Delta p = C_o(p_c - p_d)$$

Therefore

$$C_o = \frac{Q_2}{(p_c - p_d)}$$

Finally, we have

$$A = \frac{Q_2}{40(p_c - p_d)} = 1.8474 \times 10^{-4} \text{ cm}^2$$

Choose A circular cross-section orifice

$$A = \frac{\pi}{4} D_{co}^2$$

Thus

$$\frac{\pi}{4} D_{co}^2 = 1.8474 \times 10^{-4}$$

$$D_{co} = 15.34 \times 10^{-3} \text{ cm}$$

VALVE DESIGN

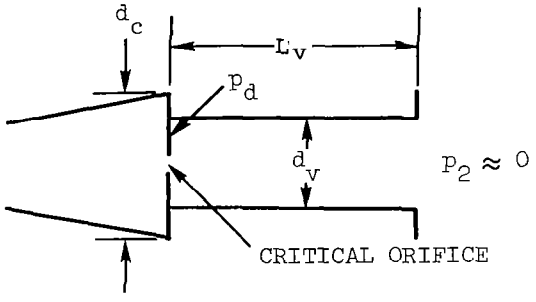

$p_d = 1.35$ torr

$Q_2 = 3.532 \times 10^{17}$ molecules/sec

$d_c = 229.4 \times 10^{-3}$ cm

$K = 1.38 \times 10^{-16}$ dyne-cm/molecule °K

$T = 293.2$°K

$\eta = 1.8 \times 10^{-4}$ gm-sec/cm

Choose

$$d_v = 158.75 \times 10^{-3} \text{ cm}$$

At Entrance:

$$\lambda_v = \frac{5}{p_d} = \frac{5}{1.35 \times 10^3} = 3.7 \times 10^{-3} \text{ cm}$$

$$\frac{D_v}{\lambda_v} = \frac{158.75 \times 10^{-3}}{3.7 \times 10^{-3}} \approx 43 \text{ (transient flow region)}$$

At Exit:

$$\lambda_v \approx \infty$$

$$D/\lambda \approx o \quad \text{(pure molecular flow)}$$

Expressions for the conductance of a long circular pipe is readily found and solving for L_v one obtains

$$L_v = 15.97 \text{ cm}$$

This indicates that, if required, a length of tubing L_v may be incorporated after the critical orifice in order to facilitate the design or possible valve requirements.

Project: 20207

Project Note Number 18

Mechanical Design Considerations

OBJECTIVE

Summarize the mechanical design considerations to date leading to the design of the two Gas Atmosphere Sensor System. The mechanical design considerations consisted of stress analysis as well as vibration analysis.

GENERAL DESCRIPTION

Analytical methods are employed to perform the stress analysis, vibration analysis at a number critical areas as far as mechanical design is concerned. Such areas include the pump out tube assembly, the thickness of the object slit mounting plate, the welding section of the analyzer housing, the magnet assembly, etc. The results of the analyses showed that both the individual parts and the total mechanical packaging are mechanically rigid and structurally sound.

NOMENCLATURE

Stress:	Internal force exerted by either of two adjacent parts of a body upon the other, across an imagined plane of separation. $S = \frac{F}{A}$ psi
Normal Stress:	When the force is normal to the imagined plane of separation. $\sigma = \frac{N}{A}$ psi
Shearing Stress:	When the force is tangential, it is called shearing stress. $\tau = \frac{T}{A}$ psi
Buckling Load:	The smallest load to cause buckling, F_a.
Critical Stress:	The stress while the load is critical, $\sigma_{ci} = \frac{F_a}{A}$ psi
Modulus of Elasticity:	The rate of change of unit tensile or compressive stress with respect to unit tensile or compressive strain for the condition of uniaxial stress within the proportional limit. E, psi
Deflection:	The relative change in location of a specific point of a structure. δ, in

Moment of Inertia: The sum of the products obtained by multiplying each element of the area dA by the square of its distance from the x_i axis, $I_{x_i} = \int x_i^2 \, dA \ in^4$

Shearing Modulus: The rate of change of unit shear stress with respect to unit shear strain, for the condition of pure shear within the proportional limit. G, psi

Natural Frequency: The frequency of free vibration of a system, ω_n, cps

Vibration: An oscillation wherein the quantity is a parameter that defines the motion of a mechanical system.

Resonant Frequency: A frequency at which resonance exists.

ASSUMPTIONS

A. STRESS ANALYSIS

1. Pump Out Tube Assembly

Consider that the externally projecting pump out tube is rigidly clamped to a bracket at one end and free at the other end.

Total Weight of the Cantilever Portion

W = 0.1062 x 2.148 x 0.29 = 0.0662 lbs
ω = 0.0662/2.148 = 0.031 lb/in
p = 0.114 lbs

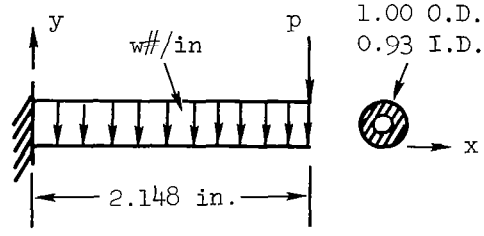

Maximum bending moment at the root is

$$M_{max} = \frac{1}{2} W\ell + p\ell$$

$$= \frac{1}{2} \times 0.0662 \times 2.148 + 0.114 \times 2.148$$

$$= 0.316 \text{ in-lb}$$

Moment of Inertia $I_x = \frac{1}{64}\pi(1.00^4 - 0.93^4)$

$$= \frac{3.1416}{64}(1-0.7481)$$

$$= 1.24 \times 10^{-2} \text{ in}^4$$

Maximum bending stress is thus

$$\sigma_{max} = \frac{M_{max} C}{I} = \frac{0.316 \times 0.5}{1.24 \times 10^{-2}} = .3 \text{ psi}$$

Assume that the structure is subjected to 25 g inertia forces together with a superimposed factor 1.5, the corresponding bending stress is

$$\sigma_{max} = 13 \times 25 \times 1.5 = 487.5 \text{ psi} << \sigma_{yield}$$

No failure due to bending at a high G-load will occur.

2. The Analyzer Assembly

The approximate weight of the ion source, the housing, the headers, etc., is about 0.8#

$$q_3 = 0.8\#/2 \text{ in} = 0.4\#/\text{in}$$

The approximate weight of the thin flat envelope section is about 0.2#

$$q_2 = 0.2\#/2.7 \text{ in} = 0.074\#/\text{in}$$

The approximate weight of the thick flat envelope section is about 0.4#

$$q_1 = 0.4\#/1.8 \text{ in} = 0.23\#/\text{in}$$

Assume that end conditions are fixed at one end, multiply simply supported at the other end.

Moment of inertias are

$$I_1 = \frac{1}{12} b_1 h^3 - (b_1 - 2t)(h-2t)^3$$

$$= \frac{1}{12} 0.6 \times 2^3 - (0.6-0.080)(2-0.080)^3$$

$$= 9.33 \times 10^{-2} \text{ in}^4$$

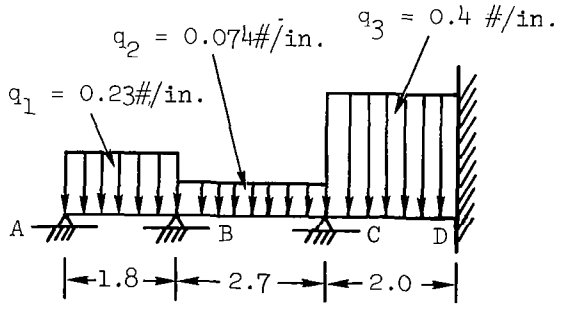

$$I_2 = \frac{1}{12} b_2 h^3 - (b_2 - 2t)(h-2t)^3$$

$$= \frac{1}{12} 0.2 \times 2^3 - (0.2-0.080)(2-0.080)^3$$

$$= 6.25 \times 10^{-2} \text{ in}^4$$

$$I_3 = \frac{1}{64} (D_o^4 - D_{in}^4)$$

$$= \frac{1}{64} (1.82^4 - 1.74^4)$$

$$= 8.86 \times 10^{-2} \text{ in}^4$$

Stiffness factors

$$K_1 = I_1/L_1 = 5.183 \times 10^{-2}, \quad K_2 = \frac{I_2}{L_2} = 2.315 \times 10^{-2},$$

$$K_3 = \frac{I_3}{L_3} = 4.43 \times 10^{-2}$$

Distributed factors are

B

$$R_1 = \frac{I_1/L_1}{I_1/L_1 + I_2/L_2} = 0.691$$

$$R_2 = 0.309$$

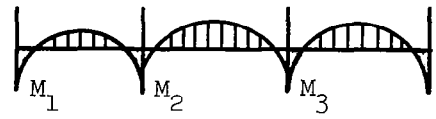

C

$$R_3 = \frac{I_2/L_2}{I_3/L_3 + I_2/L_2} = 0.343$$

$$R_4 = 0.657$$

Fixed end moments are

$$M_1 = \frac{1}{12} q_1 L_1^2 = \frac{1}{12} \times 0.23 \times 1.8^2$$

$$= 6.2 \times 10^{-2} \text{ in-lb}$$

$$M_2 = \frac{1}{12} q_2 L_2^2 = \frac{1}{12} \times 0.074 \times 2.7^2$$

$$= 4.5 \times 10^{-2} \text{ in-lb}$$

$$M_3 = \frac{1}{12} q_3 L_3^2 = \frac{1}{12} \times 0.4 \times 2^2$$

$$= 13.3 \times 10^{-2} \text{ in-lb}$$

	(A)	SPAN 1	(B)	SPAN 2	(C)	SPAN 3	(D)
L,in		1.8		2.7		2.0	
I,in^4		9.33×10^{-2}		6.25×10^{-2}		8.86×10^{-2}	
$K=\frac{I}{L}$		5.183×10^{-2}		2.315×10^{-2}		4.43×10^{-2}	
R		0.691	0.309	0.343	0.657		
F.E.M,	-6.2×10^{-2}	-6.2×10^{-2}	-4.5×10^{-2}	-4.5×10^{-2}	-13.3×10^{-2}		-13.3×10^{-2}
		$\Delta M=1.7\times10^{-2}$					
		$+1.2\times10^{-2}$	-0.5×10^{-2}				
		$+0.6\times10^{-2}$		-0.25×10^{-2}			
				$\Delta M=8.7\times10^{-2}$			
	$+5.6\times10^{-2}$			-3×10^{-2}	$+5.7\times10^{-2}$		
		$+2.8\times10^{-2}$	-1.5×10^{-2}			$+2.8\times10^{-2}$	
		$\Delta M=4.3\times10^{-2}$					
		-3×10^{-2}	$+1.3\times10^{-2}$				
		-1.5×10^{-2}		$+0.6\times10^{-2}$			
	$+1.5\times10^{-2}$			-0.2×10^{-2}	$+0.4\times10^{-2}$		
		$+0.8\times10^{-2}$				$+0.2\times10^{-2}$	
		-0.4×10^{-2}	$+0.4\times10^{-2}$				
	o	-5.6×10^{-2}	-5.6×10^{-2}	-7.2×10^{-2}	-7.2×10^{-2}		-10.3×10^{-2}

Maximum bending moment at the flange is then

$$M_3 = 0.103 \text{ in-lb}$$

Maximum bending stress is

$$\sigma_{max} = \frac{M_{max} C}{I}$$

$$= \frac{0.103 \times 0.81}{8.86 \times 10^{-2}}$$

$$= 1 \text{ psi}$$

Assume that the structure is subjected to 25g inertia force together with a superimposed factor 1.5, the corresponding maximum bending stress is

$$\sigma_{max} = 1 \times 25 \times 1.5 = 37.5 \text{ psi} \ll \sigma_{yield}$$

3. Lateral Support to Analyzer Housing Assembly

Assume that when the G-loading is acting laterally, i.e., perpendicular to the plane of the drawing, the reacting forces at the supports will be then proportional to the cross-sectional area of each support.

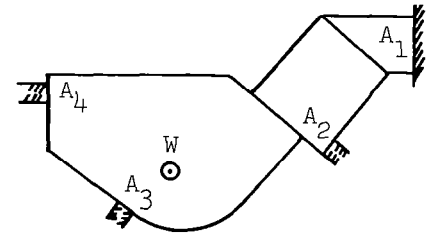

The approximate weight of the analyzer is assumed to be

$$W = 6 \text{ lbs}$$

Cross-section area of the pump out tube

$$A_1 = (D_o^2 - D_{in}^2) = 0.104 \text{ in}^2$$

Stress area of No. 6 bolt

$$A_2 = A_3 = A_4 = 0.009 \text{ in}^2$$

total area

$$A = A_1 + A_2 + A_3 + A_4 = 0.104 + 3\ (0.009) = 0.131 \text{ in}^2$$

shearing stress

$$\tau = \frac{W}{A} = \frac{6}{0.131} = 45.8 \text{ psi}$$

consider a 25g inertia force together with a factor of safety 1.5, the corresponding maximum shearing stress is

$$\tau_{max} = 45.8 \times 25 \times 1.5 = 1.718 \text{ psi} \ll \tau_{yield}$$

the housing assembly is structurally strong enough for lateral loading.

4. Welding Section of the Analyzer Housing Assembly

Assume that in the worst condition, the housing is supported on one side only.

Take W = 6 lbs
d = 1 in

section ① - ① is the considered welding section.

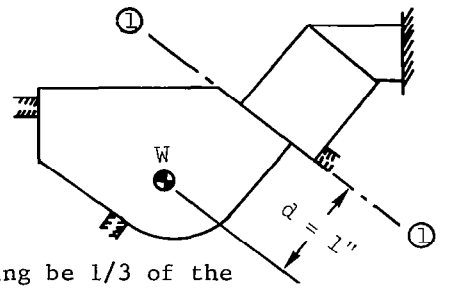

let the allowable stress by arc welding be 1/3 of the regular allowable stress. For stainless steel allow =40,000 psi

$$\tau'_{allow} = \frac{1}{3}\tau_{allow} = \frac{1}{3}(40{,}000)$$

$$= 13{,}000 \text{ psi}$$

effective arc welding area

$A_w = 0.020 \times 1.25 = 0.25 \text{ in}^2$

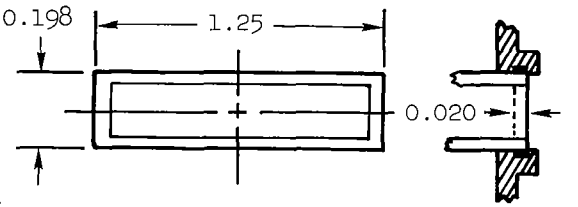

shearing stress $\tau = (\frac{Wxd}{b})/A_w$

$$= \frac{6x1}{0.198}/0.25$$

$$= 120 \text{ psi}$$

consider a 25g inertia force together with a factor of safety 1.5, the corresponding maximum shearing stress is

$$\tau_{max} = 120 \times 25 \times 1.5 = 4{,}000 \text{ psi} < \tau'_{allow}$$

the welding section is considered to be rigid enough to take 25g loading.

5. Object Slit Mounting Plate

Material = 304 stainless steel

Yield strength = σ_y = 30,000 psi

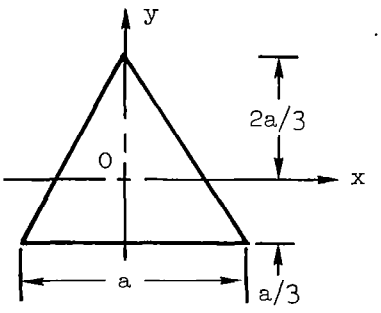

Consider an equilateral plate subjected to uniformly distributed load and simply supported.

Maximum stress is

$$\sigma_{max} = 0.1554 \frac{\omega a^2}{t^2} \qquad y = 0,\ x = 0.129\ a$$

where $\omega = \frac{W}{A} = \frac{0.2\#}{0.66 in^2} = 0.303$ lbs/in^2 is the weight of the ion source.

$$t^2 = \frac{0.1554\ \omega a^2}{\sigma} = \frac{0.1554 \times 0.303 \times 1.069^2}{3 \times 10^4}$$

$$= 180 \times 10^{-8}\ in^2$$

$$t = 1.342 \times 10^{-3}\ in$$

Choose a factor of 2.5 for possible stress concentration and a factor of safety 1.5, together with 25g inertia force, the minimum plate thickness should be

$$t = 2.5 \times 1.5 \times 25 \times 1.342 \times 10^{-3}$$

$$t = 126 \times 10^{-3}\ in$$

6. <u>O-Ring Sealing Assembly</u>

Use No. 2-123 O-Ring

$t_o = 0.103$ in (Nominal)

$t_s = 0.077$ in (Nominal)

Maximum deflection $= t_{o_{max}} - t_{s_{min}}$

$= 0.106 - 0.074$

$= 0.032$ in

Compression - % of cross-section $= \frac{0.032}{0.106} \times 100\% = 30.2\%$

It is found that in order to get a 30% compression for a compound with shore a hardness 80, 0.070 in cross-section, a force 12 lbs per inch of circumference is needed. Therefore, for a 0.103 in cross-section, a force 20 lbs/in of circumference is a suitable assumption.

$$C_{max} = 2\pi R = 6.2832 \times (1.180 \times 0.106)$$

$$= 8.08\ in.$$

thus the total force needed is

$$F = 8.08 \times 20 = 162 \text{ lbs}$$

assume that the total force is evenly distributed to the eight screws

$$F_{min} = \frac{162}{8} = 20.2 \text{ lbs per screw}$$

choose a factor of safety 1.5, $p_{min} = 20.2 \times 1.5 = 30$ lbs per screw

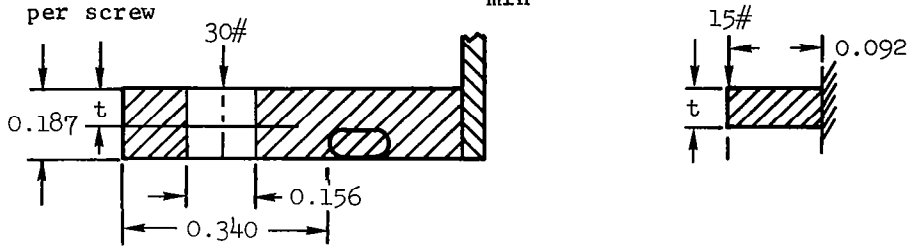

Assume that the total force is evenly supported by two ends.
Maximum bending moment = $15 \times 0.092 = 1.38$ in-lb @ corner
yield strength $\sigma_{yield} = 30 \times 10^3$ psi (304 stainless steel)
Moment if inertia $I = \frac{1}{12} bt^3 = \frac{1}{12} \times 0.34t^3 = 2.8 \times 10^{-2} t^3$

Maximum stress $\sigma_{max} = \frac{M_{max} C}{I}$

this $I = \frac{M_{max} C}{\sigma_{max}}$

or $2.8 \times 10^{-2} t^3 = \frac{1.38 \times 0.5t}{3 \times 10^4}$

$$t^2 = \frac{0.69}{3 \times 10^4 \times 2.8 \times 10^{-2}}$$

$$= 8.2 \times 10^{-4}$$

$$t = 28.64 \times 10^{-3} \text{ in}$$

Choose a factor of safety 2, minimum t should be

$$t_{min} = 57 \times 10^{-3} \text{ in}$$

7. System Package, Outside Thin Wall Box

Assume that the total weight of the analyzer assembly and electronic modules is W = 8 lbs.

Also assume that at the worst condition, the total 8 lbs load are all applied on wall BDFH, and are then transmitted to the cover ABEF. Thus the maximum shear load applied on wall ABCD is one half of the total and equals

$$p = \frac{1}{2} w = 4 \text{ lbs}$$

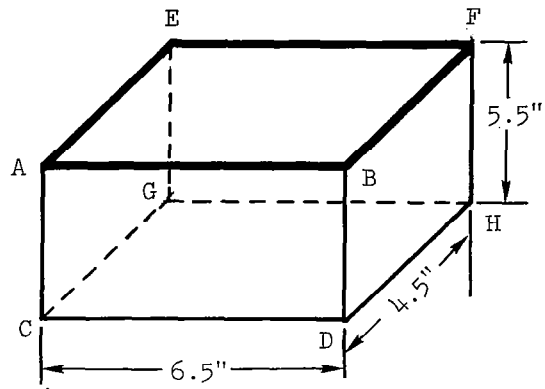

Consider a 25-g inertia force, it gives

$$p_{max} = 4 \times 25 = 100\#$$

Maximum shearing stress is

$$\tau_{max} = \frac{p_{max}}{A} = \frac{100}{6.5xt}$$

consider the case of buckling of rectangular plate under the action of shearing stresses. Assume that the plate is simply supported at four edges

$$\beta = \frac{a}{b} = \frac{6.5}{5.5} = 1.2$$

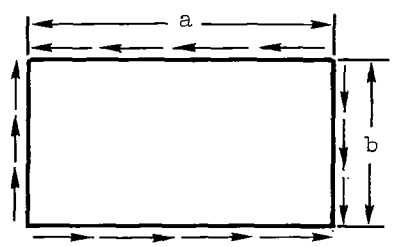

$$k = 8$$

$$\tau_{cr} = k \frac{\pi^2 D}{b^2 t}$$

where $D = \frac{Et^3}{12(1-\nu^2)}$

therefore, $\tau_{cr} = k \frac{\pi^2 E t^3}{12b^2(1-\nu^2)t} = \frac{\pi^2 E k t^2}{12(1-\nu^2)b^2} = \alpha_1 t^2$

choose a high-strength aluminum, say, 7079 aluminum alloy

$E = 10.3 \times 10^6$ psi

$\nu = 0.3$

Thus $\alpha_1 = \frac{\pi^2 E k}{12(1-\nu^2)b^2}$

$$= \frac{3.146)^2 x 10.3 x 10^6 x 8}{12(1-0.3^2)x5.5^2}$$

$$= 2.462 \times 10^6$$

$$\tau_{cr} = 2.462 \times 10^6 \, t^2$$

choose a $\frac{1}{32}$ in wall-thickness, $t = 31 \times 10^{-3}$ in

the critical stress is

$$\tau_{cr} = 2.462 \times 10^{6} \times (31 \times 10^{-3})^{2}$$

$$= 2.366 \text{ psi}$$

Comparing this critical stress with the maximum shearing stress, it shows for a wall thickness of 0.031", no buckling will occur.

8. Mounting Bolts and Legs, System Packaging

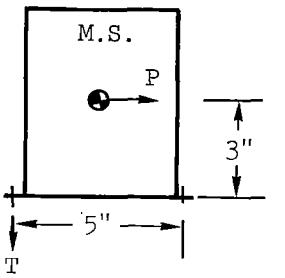

Force acting at a single bolt

$$T = \frac{1}{2}\left(\frac{px3}{5}\right) = 3p$$

For 1g loading $p = \frac{}{w} = 8$ lb

Consider 25g loading and 1.5 factor of safety T = 90#

Bolt

#8-32 bolts were used

stress area = .014 in^2

$\sigma_t = \frac{90}{.014} = 6{,}420$ psi $\quad \tau_y = 30{,}000$ psi

Legs

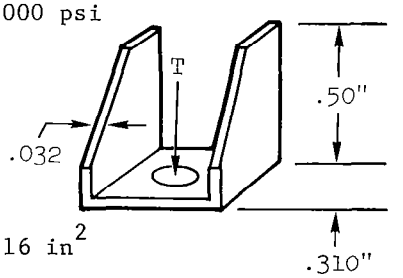

Assume that the force acting from bolt will be resisted by shearing section .25" on each side. Total shearing area

$$A = (.25 \times .032) \times 2 = .016 \text{ in}^2$$

Shear stress

$$\tau = \frac{30}{.020} = 1{,}500 \text{ psi} < \tau_{allowable} = 30{,}000 \text{ psi}$$

So the mounting connections are sound and rigid.

B. VIBRATION ANALYSIS

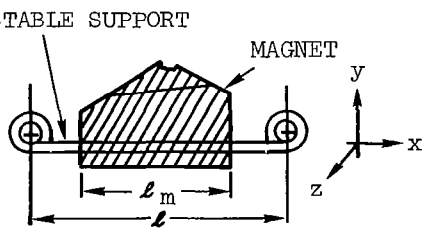

1. Magnet Assembly

Weight of magnet $W = 1.7$ lbs

Elastic Modulus $E = 30 \times 10^{6}$ psi

Length of magnet $\ell_m = 2.12$"

Section properties of adjustable support:

ℓ = 2.7"

t = 0.090"

b = 0.625 - 0.112 = 0.512"

$I_x = \frac{1}{12} bt^3 = \frac{(0.512)\ (0.090)^3}{12} = 31 \times 10^{-6}\ in^4$

$I_y = \frac{1}{12} b^3 t = \frac{(0.512)^3\ (0.09)}{12} = 1.01 \times 10^{-3}\ in^4$

W_b = 0.06 lbs

CASE I: Assume that the support has the magnet attached at center, hinged-hinged.

Lateral vibration of the adjustable support about x-axis

$$\omega_1 = 4\sqrt{\frac{3EI_x}{M\ell^3}} = 4\sqrt{\frac{3x30x10^6x31x10^{-6}}{1.7/32.2x12(2.7)^3}}$$

$$= 4\sqrt{\frac{3x3x10^7x3.1x10^{-5}x386}{1.7x19.88}}$$

$$= 4\sqrt{\frac{107.7}{33.80}} \times 10^2$$

$$= 4\sqrt{3.284} \times 10^2$$

$$= 725 \text{ rad/sec}$$

$$= 115 \text{ cps}$$

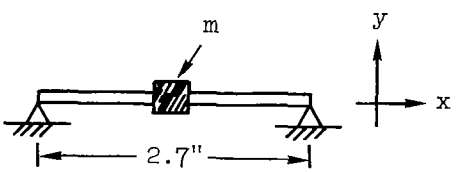

Lateral vibration of the adjustable support about y-axis

$$\omega_1 = 4\sqrt{\frac{3EI_x}{M\ell^3}} = 4\sqrt{\frac{3x30x10^6x1.01x10^{-3}}{1.7/32.2x12)(2.7)^3}}$$

$$= 4\sqrt{\frac{3x3x10^7x1.01x10^{-3}x.386x10^3}{33.80}}$$

$$= 4\sqrt{\frac{3509}{33.80}} \times 10^2$$

$$= 400\sqrt{103.82}$$

$= 400 \times 10.19$ rad/sec

$= 650$ cps

CASE II: Clamped-Clamped

Lateral vibration of the adjustable support about x-axis

$$\omega_1 = 8\sqrt{\frac{3EI_x}{M\ell^3}} = 8\sqrt{\frac{3x30x10^6x31x10^{-6}}{1.7/32.2x12(2.7)^3}}$$

$$= 8\sqrt{\frac{3x3x10^7x3.1x10^{-5}x386}{1.7x19.88}}$$

$$= 8\sqrt{\frac{107.7}{33.80}} \times 10^2$$

$$= 8\sqrt{3.284} \times 10^2$$

$= 1450$ rad/sec

$= 230$ cps

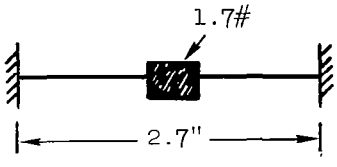

Lateral vibration of the adjustable support about y-axis

$$\omega_1 = 8\sqrt{\frac{3EI_y}{M\ell^3}} = 8\sqrt{\frac{3x30x10^6x1.01x10^{-3}}{1.7/(32.2x12)(2.7)^3}}$$

$$= 8\sqrt{\frac{3x3x10^7x1.01x10^4x386}{33.80}}$$

$$= 8\sqrt{\frac{3509}{33.80}} \times 10^2$$

$$= 800\sqrt{103.82}$$

$= 800 \times 10.19$ rad/sec $= 1298$ cps

CASE III: Assume that the magnet lays across the adjustable support hinged-hinged.

Lateral vibration of the adjustable support about x-axis

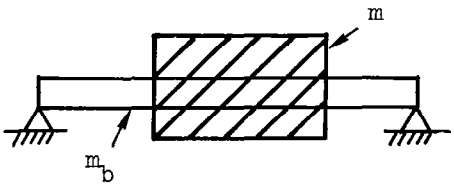

$$\omega_1 = \frac{\pi^2}{\sqrt{1+2m/m_b}} \sqrt{\frac{EI_x g}{S\gamma\ell^4}}$$

$$= \frac{\pi^2}{\sqrt{1+2(1.7)0.06}} \sqrt{\frac{30\times10^6\times31\times10^{-6}\times386}{0.0461\times0.29\times(2.7)^4}}$$

$$= \frac{\pi^2}{\sqrt{1+56.7}} \quad \frac{1}{(2.7)^2} \sqrt{26.851 \times 10^3}$$

$$= \frac{1.30}{7.29} \times 5.183 \times 10^3$$

$$= 925 \text{ rad/sec}$$

$$= 147 \text{ cps}$$

Lateral vibration of the adjustable support about y-axis

$$\omega_1 = \frac{\pi^2}{\sqrt{1+2m/m_b}} \sqrt{\frac{EI_y g}{S\gamma\ell^4}}$$

$$= \frac{\pi^2}{\sqrt{1+2(1.7)/0.06}} \sqrt{\frac{30\times10^6\times1.01\times10^{-3}\times386}{0.0461\times0.29\times(2.7)^4}}$$

$$= \frac{\pi^2}{\sqrt{1+56.7}} \quad \frac{1}{(2.7)^2} \sqrt{8.75 \times 10^4}$$

$$= \frac{1.30}{7.29} \times 2.958 \times 10^4$$

$$= 5275 \text{ rad/sec}$$

$$= 845 \text{ cps}$$

The above analyses show that the fundamental natural frequencies of the magnet assembly are a little bit low. However, it can be improved by increasing the stiffness of the structure for airborne units.

2. Ion Collector Assembly

The natural frequency of this system can be considered as a cantilever beam subjected to a weight W_1 at the free end.

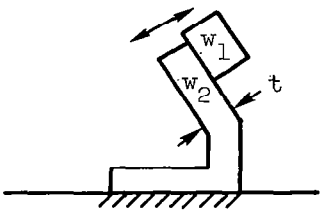

ION COLLECTOR

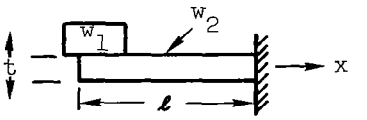

ℓ = 0.51 in

t = 0.10 in

b = 0.40 in

W_1 = 0.144 lbs

W_2 = 0.006 lbs

E = 29×10^6 psi (304 stainless steel)

$I_x = \frac{1}{12} b t^3 = 33 \times 10^{-6}$ in^4

The natural frequency of this system having both concentrated and distributed mass is

$$\omega = \sqrt{\frac{3EI}{\ell^3(M+0.23m)}}$$

$$= \sqrt{\frac{3 \times 29 \times 10^6 \times 33 \times 10^{-6}}{(0.51)^3 \times (0.144+0.23 \times 0.006)}}$$

= 22,985 rad/sec

= 3,660 cps

This value is considered to be high enough to avoid problems.

Project: 20207 R. B. Lehotsky

Project Note Number 19

Ion Source Non-Linearity Due to the Influence of Space Charge in the Ionizing Region

The spacial potential of the ionizing region of mass spectrometer ion sources is a function of the following parameters:

a. Ion extraction potential

b. Electron current reaching the anode

c. Spacing of the ion extraction electrodes

d. Position of the electron beam between these electrodes

e. Energy of the ionizing electrons

f. Width of the electron beam

g. Molecular weight of the gas

The potential distribution in the ionizing region thus becomes affected by space charge created by both the electron current passing through to the anode, and the ion current formed by the electron beam within the ion extraction area. This phenomena has been treated by W. M. Brubaker [1], from which he defines a critical pressure expressed by

$$P_c = \frac{3}{4dS} \left(\frac{V_r \, m_e}{a \, V_{el} \, M} \right)^{\frac{1}{2}} \qquad (1)$$

where

P_c = critical pressure (torr)

V_r = ion extraction potential - $\left[V \text{ (repeller)} - V \text{ (accelerator)} \right]$ (volts)

d = repeller - accelerator distance (meters)

a = fraction of repeller - accelerator distance at which the ionizing electron beam is located

V_{el} = ionizing electron energy (electron volts)

S = number of ion pairs formed per electron per meter of electron path length at a pressure of 1 torr

m_e = electron mass (kg.)

M = ion mass (kg)

1. Brubaker, W.M., Influence of Space Charge on the Potential Distribution in Mass Spectrometer Ion Sources, J.App.Phys., Vol. 26, No. 8, August 1955.

This pressure is defined as the pressure at which the spacial potential of the ionizing region becomes independent of the electron current reaching the anode, for a defined extraction potential, V_r. Normalizing the anode current and the potential of the ionizing plane with respect to the extraction potential, such that

$$\alpha = \frac{V_{\text{ionizing plane}}}{V_r} \tag{2}$$

$$i_v = \frac{I^-_{\text{anode}\ (\mu\text{amps})}}{V_r} \tag{3}$$

then Figure 1 , which is reproduced from Brubaker's paper, illustrates a plot of the defined parameter α with respect to i_v, for various ion source pressure to critical pressure ratios, since

$$x = \frac{P_s}{P_c} \tag{4}$$

where

P_s = ionizing region pressure (torr)

It is thus seen from the curve, that when the ion source pressure equals the critical pressure, i.e., $x = 1$, that for small values of i_v, the potential of the ionizing plane is independent of i_v.

The non-linearlity of the ion source can be related to the change in the spacial potential from the ionizing plane to the accelerator electrode, and for small i_v, α is expressed by

$$\alpha = a\,[1 + A\, i_v\, (x - 1)] \tag{5}$$

where A is defined by

$$A = \frac{(1 - a)\, d \times 10^{-6}}{\epsilon_o w} \left(\frac{m_e}{2\, V_{e1}\, e}\right)^{\frac{1}{2}} \tag{6}$$

In this expression,

- w = width of the ionizing electron beam (meters)
- ϵ_o = permittivity of free space, 8.85×10^{-12} farads/meter
- e = electronic charge, 1.6×10^{-19} coulombs

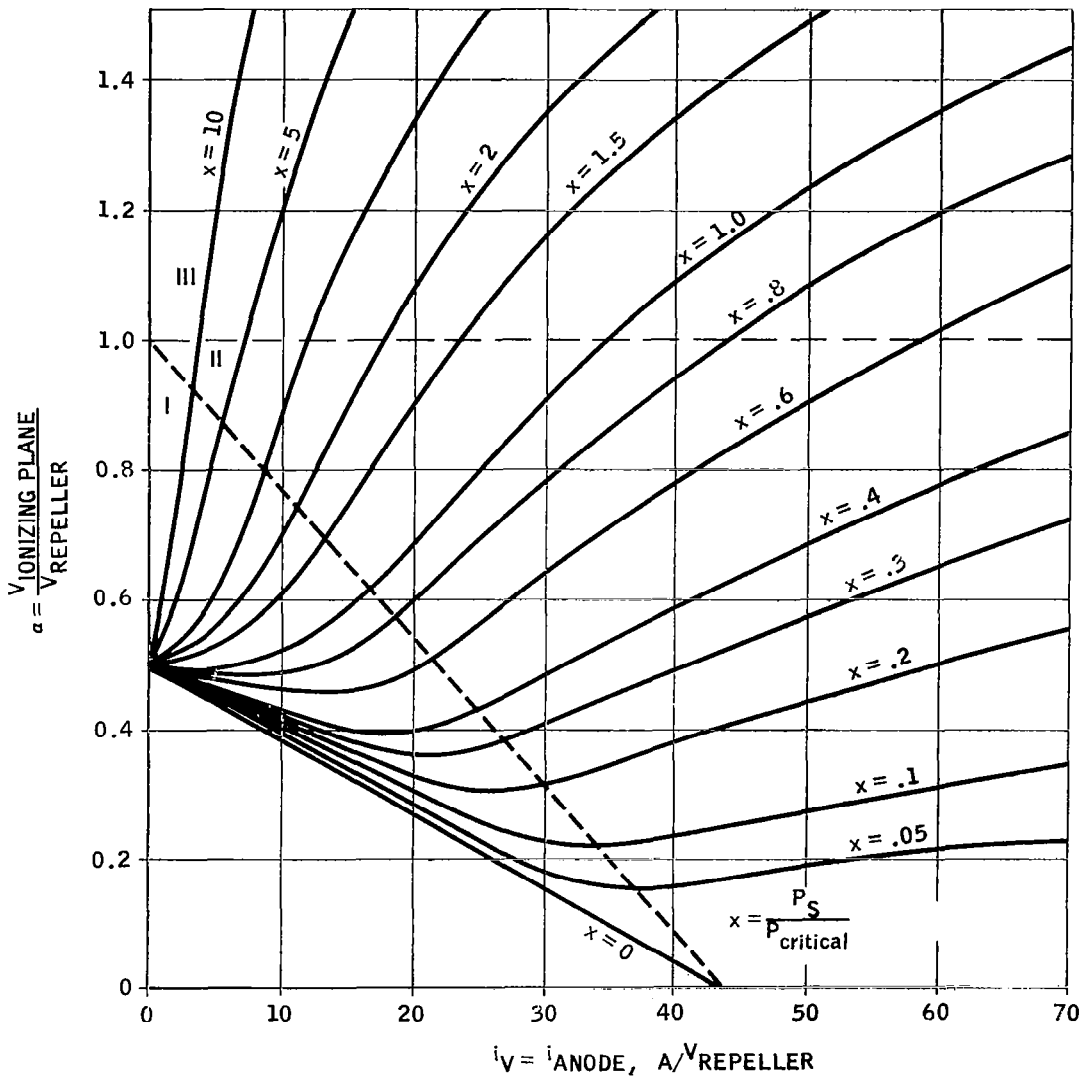

FIGURE 1
Potential of Ionizing Region as a Function of i_V

Differentiating equation (5) gives

$$\Delta a = a\, A i_V\, \Delta x$$

However, since the ion source pressure will vary the value of x from x = o to x = x, then $\Delta x = x$, and thus

$$\Delta a = a\, A i_V\, x \tag{7}$$

The percentage change of this potential can then be expressed by

$$\frac{\Delta a}{a} = \frac{A i_V\, x}{1 + A i_V (x-1)} \tag{8}$$

Previous data taken on analytical instrumentation has determined a value of the $\Delta a / a$ ratio for degrees of non-linearity, such that it is convenient to rewrite equation (8) in the form

$$x = \frac{\left[\frac{1}{A i_V} - 1\right]}{\left[\frac{a}{\Delta a} - 1\right]} \tag{9}$$

The dual filament ion source being utilized was designed on a previous NASA contract, however, the ion source parameters were determined such that the instrument would be compatible with the two-gas atmosphere analyzer. Consequently, to determine the maximum ion source pressure at a defined non-linearity, it can be written that

$$P_s = \frac{3}{4dS} \left(\frac{V_r\, m_e}{a\, V_{e1} M}\right)^{\frac{1}{2}} (x) \tag{10}$$

The design parameters of the source to ensure operation with the two-gas atmosphere analyzer are listed below:

$d = 2.54 \times 10^{-3}$ meters

$a = 0.5$

$w = 1.27 \times 10^{-3}$ meters

$V_r = 10$ volts

$V_{e1} = 100$ volts

$M = 30\,(1.66 \times 10^{-27})$ kg [2]

$S = 1200$ amp/amp-meter-torr

2. The average mass-to-charge ratio of 30 is used since the designed atmosphere is to have equal parts of nitrogen and oxygen ($^m/_e$'s 28 and 32), and the ionization crossection is nearly the same for both gases using electrons having 100 ev, of energy.

Substituting these values into equation (10), the ion source pressure at which a defined non-linearity will occur is thus

$$P_s = (4.71 \times 10^{-4})(x) \quad \text{(torr)} \tag{11}$$

Experimental values determined on an analytical instrument gives a 3% non-linearity which occurs when $\Delta\alpha/\alpha = .023$, and the probable range of electron current reaching the anode will be 20 to 30 microamperes. Evaluating the constant A, and computing the value of i_v at both 20 and 30 microamperes enables the computation of the ion source to critical pressure ratio, such that

$x = .394$ for $I^-_{anode} = 30\ \mu a$ at 3% non-linearity

and

$x = .601$ for $I^-_{anode} = 20\ \mu a$ at 3% non-linearity

Substituting these values into equation (11) gives the ion source pressure at which a 3% non-linearity will occur as

$$P_s = 1.85 \times 10^{-4} \text{ torr} \quad (I^- = 30\ \mu a)$$

$$P_s = 2.83 \times 10^{-4} \text{ torr} \quad (I^- = 20\ \mu a)$$

Project: 20207 M. Ruecker

Project Note Number 20

Reduced Image Distances in The
60° and 90° Magnetic Sector Analyzers

INTRODUCTION

During the Phase I study it became obvious that it was not necessary to have the m/e 28, m/e 32, m/e 40 and m/e 44 collector buckets at the image point for zero alpha aberration. This restriction was lifted since lower resolution could be tolerated for these masses. It was not possible to take full advantage of this liberty during the Phase I period and therefore was one of the first areas of study on Phase II. It was of particular importance since the primary criticism of the 60° magnetic sector was its large overall dimensions which could be reduced if X_{44} could be diminished.

CALCULATION

Two analyzers were investigated; the 90° sector chosen on the Phase I effort, and the smallest magnet in the 60° sector group of computer selections. Their important parameters are listed below:

Parameter	$\theta = 60°$	$\theta = 90°$
Ion Energy	200v	225v
$r_o/18$	2.159 cm	2.290 cm
$r_o/28$	2.693 cm	2.857 cm
$r_o/44$	3.376 cm	3.580 cm
ϕ_{18}	78.7°	104.5°
ϕ_{28}	60.0°	90.0°
ϕ_{44}	51.2°	78.3°
S_o = object slit	0.0210 cm	0.0307 cm
ΔV = energy spread	3v	3v
Z = half gap width	0.200 cm	0.200 cm
$n_o/28$	1.5	1.0
$n_o/44$	1.197	0.796

The following resolution requirements were then assumed: at m/e 18, dm/m = 1/18; at m/e 28, dm/m = 1/10; and at m/e 44, dm/m = 1/11. These are sufficient to resolve the masses of interest from other expected components.

Then equations were evaluated for the actual and required ion beam widths at the collector points. These were based upon the work in the Phase I report:

$$B_{req} = r_o K_2 (0.5 \text{ dm/m} - \psi) - 2\Delta y$$

where

B_{req} = required ion beam width
$K_2 = 1 - \cos\phi + n_i \sin\phi$
ψ = fractional variation in the accelerator voltage = .0075
Δy = slit misalignment = 0.005 cm

and

$$B_{act} = M S_o + 0.5 K_2 r_o \Delta V/V + Z^2/r_o$$

$$+ 2 r_o \alpha \left\{(1 - n_o n_i) \sin\phi + (n_o + n_i) \cos\phi\right\} + B_x$$

where

B_{act} = actual beam width
$M = |\cos\phi - n_i \sin\phi|$
α = half angle divergence of ion beam at source exit
B_x = other less important aberrations (given in Phase I report)

In the m/e 18 cases n_i was chosen for zero α aberration since this was the most severe aberrant component. This was done by setting

$$(1 - n_o n_i) \sin\phi + (n_o + n_i) \cos\phi = 0$$

which gives:

$$n_i = \frac{n_o + \tan\phi}{n_o \tan\phi - 1}$$

For m/e 28 and m/e 44 the above equations for B_{req} and B_{act} were equated and n_i was solved. The following results were found:

θ	$n_{i_{18}}$	$n_{i_{28}}$	$n_{i_{44}}$
60°	0.792	1.17	2.085
90°	0.450	0.365	0.784

From these values the analyzer geometry may be constructed.

Project: 20207 M. Ruecker

Project Note Number 21

Derivation of the Position For An Effective Magnet Boundary

Let a criteria be established for an effective magnet boundary so that an ion starting at the effective magnet boundary and traveling to a point one gap width within the real boundary in a field B_o will undergo the same angular deflection as the ion which traveled in the fringe field from a real magnet of strength B_o starting from the object plane and going to the same point.

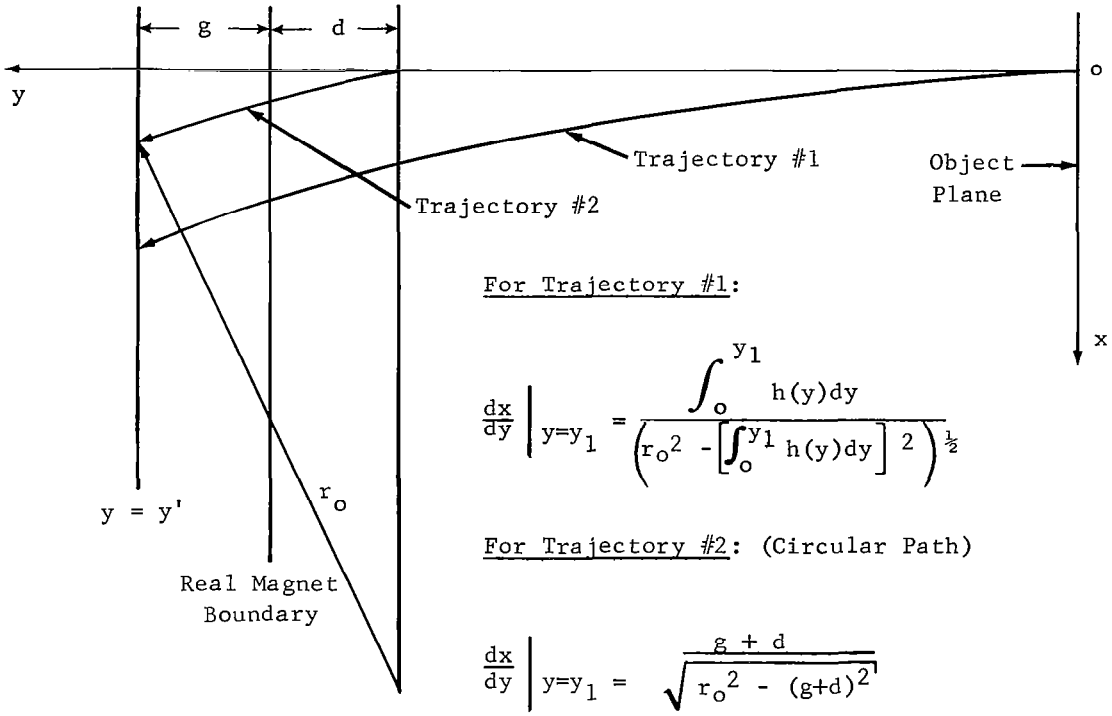

For Trajectory #1:

$$\left.\frac{dx}{dy}\right|_{y=y_1} = \frac{\int_o^{y_1} h(y)dy}{\left(r_o^2 - \left[\int_o^{y_1} h(y)dy\right]^2\right)^{\frac{1}{2}}}$$

For Trajectory #2: (Circular Path)

$$\left.\frac{dx}{dy}\right|_{y=y_1} = \frac{g+d}{\sqrt{r_o^2 - (g+d)^2}}$$

Equating slopes at $y=y_1$ gives

$$d = \int_o^{y_1} h(y)dy - g$$

Typically, all units are expressed in terms of gap widths giving:

$$d = \int_o^{y_1} h(y)dy - 1$$

APPENDIX B

SYMBOLS

APPENDIX B

Symbols

A	circuit gain
e_{in}	input voltage (variable)
e_{out} or e_o	output voltage (variable)
e(t)	signal voltage as a function of t
f	frequency in Hertz
f	current gain - bandwidth product
G(S)	forward transfer function in terms of S
H(S)	reverse transfer function in terms of S
I	current (dc)
i	current (instantaneous)
$I_{(Cn)}$, $i_{(Cn)}$	current thru capacitor Cn
$I_{(Ln)}$, $i_{(Ln)}$	current thru inductor Ln
I_{in}	input current
I_{out} or I_o	output current
I_P	peak current
$I_{(Rn)}$, $i_{(Rn)}$	current thru resistor Rn
j	$\sqrt{-1}$
k	Boltzmann's constant = 8.63×10^{-5} ev/°K
S	stability factor

t	time (with descriptive subscript or letters)
T	temperature (absolute)
T_A	temperature (ambient)
TC	temperature
t_D	pulse duration
t_d	delay time
t_f	fall time
T_J	junction temperature
t_{pd}	propagation delay
t_r	rise time
T(S)	closed loop transfer function in terms of S
τ	lifetime or time constant
V_{in}	input voltage
V_{out} or V_o	output voltage
$V_{(Rn)}$	voltage drop across resistor Rn
V_{REF}	reference voltage (usually a precision supply)
V_{REG}	regulated voltage
V_{ac}	ac voltage - rms
V_{p-p}	ac voltage - peak-to-peak
V_{dc}	dc voltage
X_C	capacitive reactance
X_L	inductive reactance

Y	admittance
Z	impedance
α	$\frac{I_C}{I_E}$ Common base forward transfer ratio
β	$\frac{I_C}{I_B}$ Common emitter current gain in transition region
β_f	$\frac{I_C}{I_B}$ Common emitter current gain in saturation region
Δ	(Delta) indicates a small change in the variable with which it is associated
θ_J	thermal resistance
ω_α	alpha cutoff frequency (rad/sec)
∞	infinity

SEMICONDUCTOR PARAMETER SYMBOLS

The following symbols will be used as standard symbols:

BV_{CBO}	Measured breakdown voltage, collector-to-base, emitter open
BV_{CEO}	Measured breakdown voltage, collector-to-emitter, base open
C_{ib}	Transistor input capacitance (Common base)
C_{ob}	Transistor output capacitance (Common base)
f_r	Current Gain - Bandwidth Product
G_{fs}	Forward Transconductance (FET)
h_{FE} or β	dc forward current transfer ratio (common emitter)
H_{FE} or β_f	Forced current gain of circuit
h_{fe}	Incremental (small signal) gain of transistor
I_B	Base current (dc)
i_B	Base current (instantaneous)
I_{BL}	Base leakage current
I_C	Collector current (dc)
i_C	Collector current (instantaneous)
I_{CBO}	Collector cutoff current, emitter open
I_{CL}	Collector leakage current
I_D	Drain current (FET)

I_D	Diode forward current
I_{DSS}	Drain current (FET) with source shorted to gate
I_E	Emitter current (dc)
i_E	Emitter current (instantaneous)
I_{EBO}	Emitter cutoff current, collector open
I_F	Forward Current (dc)
I_G	Gate current (FET)
I_R	Reverse current
pC	Pico-coulombs
P_C	Transistor collector dissipation
q	Electron charge = 1.6×10^{-19} coulombs
Q_S	Total stored charge
Q_T	Total control charge
R_{DS}	Drain-to-source resistance (FET)
SV_{BE}	Base-to-emitter saturation voltage
SV_{CE}	Collector-to-emitter saturation voltage
t_{rr}	Reverse recovery time
t_s	Storage time
t_t	Total switching time
V_{BB} (±)	Base supply voltage
V_{BE}	Base-emitter on voltage

V_{CB}	Voltage, collector-to-base (dc)
V_{CC} (±)	Collector supply voltage
V_{CE}	Collector-to-emitter voltage (dc)
V_{D}	Drain voltage (FET) (dc)
V_{DS}	Drain-to-source voltage (FET)
V_{EB}	Voltage, emitter-to-base (dc)
V_{EE} (±)	Emitter supply voltage
V_{F}	Forward voltage of a diode
V_{G}	Gate voltage (FET)
V_{GS}	Gate-to-source voltage (FET)
V_{P}	Pinchoff voltage (FET)
V_{R}	Reverse voltage

APPENDIX C

TEST DATA RECORDS FOR FLIGHT PROTOTYPE TWO GAS ATMOSPHERE SENSOR SYSTEMS

THE PERKIN-ELMER CORPORATION
AEROSPACE SYSTEMS
2855 Metropolitan Place Pomona, California

TWO GAS ATMOSPHERE SENSOR SYSTEM (MASS SPECTROMETER)

TEST DATA RECORD FOR SYSTEM SERIAL NO. 01

Contract NAS 1-6387
Perkin-Elmer Aerospace Systems
Contract No. 20207

Prepared for
NATIONAL AERONAUTICS AND SPACE ADMINISTRATION
Langley Research Center
Hampton, Virginia

Approved by M. R. Ruecker
M. Ruecker, Manager
Space Physics

Approved by J. C. Bemis
J. Bemis, Manager
Quality Assurance

TEST DATA RECORD

This section provides for all of the test data taken in Section 5, to be recorded. In addition, some computational work is included to reduce the data to a more meaningful form. The section numbers in parenthesis refer to the section of this document in which the instructions for the measurements are given. Where specifications apply, the data is compared with it to see if the specifications are met.

PREPARATIONS

SENSOR SYSTEM SETUP

		Completed
a.	Sensor System fully assembled and operational with laboratory vacuum system.*	16 Nov 1967
b.	Capillary line attached to laboratory sample inlet system and pumped down to < 1.0 torr.	
c.	Bypass line connected to Vacsorb pump with critical orifice and Vacsorb pump pumped down to < 2 x 10^{-3} torr.	
d.	Background pressure in vacuum system is 2 x 10^{-7} torr. To be 1 x 10^{-7} before turning on filaments.	
	NOTE: Prior to analyzer bake-out	
e.	Ion source to be operated on gun # 1. Gun # 2 used only as specifically called for.	

OUTPUT MONITORING SETUP

a.	Each electrometer output attached to X-Y type Moseley 7030 as required.	16 Nov 1967
b.	For accurate output levels digital voltmeter type Fairchild M 7000 is to be used.	

* Assembled in flight configuration with clamped flanges, instrument system mounted to Laboratory Vacuum System less flight enclosure for test convenience.

SENSOR SYSTEM POWER SUPPLY SETUP

Completed

a. Power Supply type Universal Electronics M25-5 is being used. _____

b. With simulated load power supply output is:

R = 234 ohms, 120 mA measured value

Switch Position 27.5 V = 27.53
Switch Position 28.0 V = 27.99
Switch Position 28.5 V = 28.45 _____

c. Sensor System attached to power supply with power turned off. 16 Nov 1967

EMISSION ADJUSTMENT (PRE-SET)

a. Emission adjust pot previously set and IF_A defocused to give 4.907 volts out on m/e 28 channel with 430 torr N_2 sample. Mixture 50.5% O_2, 1.1% CO_2, bal. % N_2.* 16 Nov 1967

SYSTEM COOL DOWN (NOT APPLICABLE)

a. Sensor System has been turned off for _____ minutes/hours. (at least 30 minutes) _____

TEST PARAMETERS

a. Only system inputs and outputs monitored with the following exceptions:

All analyzer electrode currents monitored on laboratory meter panel. This is necessary to measure internal currents as compared with external input/output characteristics 16 Nov 1967

EQUIPMENT WARM-UP

a. Recorder and other equipment warmed up for >1 hours. 16 Nov 1967

EQUIPMENT IDENTIFICATION

a. Equipment other than previously noted:

Fluke diff. VTVM - Model 803

_____ —

* This mixture is used throughout this test where called for.

b. Record gas purity and composition — Completed

N_2 is 99.7% - 0.2% O_2 **

O_2 is (Not Used)

CO_2 is (Not Used)

Standard Mixture is O_2 50.5% CO_2 1.1% N_2 Balance ** — 16 Nov 1967

ION SOURCE CHECKOUT

a. Electron guns last checked on laboratory electronics setup 15 Nov 1967. — 16 Nov 1967

b. Anode current level for output of m/e 28 collector with mixture sample. @ 400 torr

Gun No.	I_{AN}	m/e 28 V	N_2 Pressure	
1	10 μA	4.907	48.4% of 400T = 193.6 torr	
2	10 μA	2.534	48.4% of 400T = 193.6 torr	16 Nov 1967

SOURCE VOLTAGES (C-340290)

a. The following source voltages were measured on laboratory electronic setup on 11-15-67 w/Fluke 803.

P101

1.	Filament - Gun 2 - Spring	89.7 Volts
2.	Filament - Gun 2 - Post	88.1 Volts
3.	Z axis B	183.0 Volts
4.	Open	
5.	Open	
6.	Z axis A	183.0 Volts
7.	Filament - Gun 1 - Spring	88.1 Volts
8.	Filament - Gun 1 - Post	89.7 Volts
9.	Open	

P102

1.	Electron Accelerator - 2	274.7 Volts
2.	Electron Focus 2B	87.1 Volts
3.	Electron Focus 2A	93.5 Volts
4.	Anode 1	216.0 Volts

** Matheson certified analysis

			Completed
5.	Accelerator	183.5 Volts	
6.	Ion Focus B	0.0 Volts	
7.	Filament Shiled - 2	62.9 Volts	
8.	Open		
9.	Ground - Internal	0.0 Volts	

P103

1.	Filament Shiled 1	68.4 Volts	
2.	Electron Focus - 1B	93.0 Volts	
3.	Electron Focus - 1A	97.6 Volts	
4.	Exit Slit (Normally ground)	0.0 Volts	
5.	Ion Focus A	174.6 Volts	
6.	Anode - 2	215.3 Volts	
7.	Repeller	193.5 Volts	
8.	Electron Accelerator - 1	279.3 Volts	
9.	Open		15 Nov 1967

ACCEPTANCE TEST OUTLINE

TURN-ON TESTS

a. Set recorder for 100 mV full scale and speed such that a 5 minute run will be meaningful. —

Depress sensor system zero check button. —

Turn on system power and monitor zero levels of all detectors until they reach 10 mV of zero. —

Time for all zeros to be within 10 mV of zero is 1 hour as measured on bench checkout of detector. —

Check recorder zero. —

b. With zero check button depressed the peak-to-peak noise as seen on Type 531A Tektronix oscilloscope with CA preamp set at _____ mV/cm is:

m/e 18 - 5 mV
m/e 28 - 2 mV
} Detector bench test w/flight power supply

Completed

m/e 32 - 2 mV } Detector bench test w/flight power supply
m/e 44 - 5 mV }
28 V power 100 mV

c. With zero check button released, the measured background levels on each channel with DVM are:

m/e 18 - 0.040 V
m/e 28 - 0.020 V
m/e 32 - 0.006 V
m/e 44 - 0.070 V

16 Nov 1967

d. The rms noise on each channel on background is:

m/e 18 - < 10 mV } Typical
m/e 28 - < 10 mV }
m/e 32 - < 10 mV }
m/e 44 - < 10 mV }

Turn system power off for at least 30 minutes prior to the next step. —

e. The sensor system has been off for _____ min/hr. —

The "standard gas mixture" admitted to _____ torr in the reservoir. —

Recorder scales reset as follows in anticipation of the output levels from the "standard mixture".

m/e 18 _____/_____
m/e 28 _____/_____
m/e 32 _____/_____
m/e 44 _____/_____ —

Sample admitted to capillary line _____ minutes and reservoir pressure now is _____ torr. With recorder running, turn on system power at _____ (time).

Record outputs for one hour noting the following items on recorder chart at 5 minute intervals except as noted.

Completed

1. Time
2. Inlet pressure
3. Recorder zero (if applicable)
4. Outputs with DVM (15 minute intervals)
5. Vacuum system pressure

Using the inlet pressure normalize the output data as follows:

Sensitivity in amps/torr inlet =

$$\frac{E_o/R_{FB}}{\text{inlet pressure in torr}}$$

Gun 1 N_2 S(ADJ) = 2.04 x 10^{-4} amps/torr N_2

E_o = Volts out of particular channel

R_{FB} = Feedback resistor value for particular electrometer.

Make a graph of this output data versus time in minutes for each channel. —

f. In the following test the system power was turned off but the system was allowed to warm up for the indicated minutes/hours:

Date	Reason	Min/Hr Warmed Up

—

NITROGEN SENSITIVITY, LINEARITY AND TIME RESPONSE TESTS

a. The sample inlet system pumped down to < 1 torr and a nitrogen sample admitted to 400 torr. (Mixture)

16 Nov 1967

Completed

Nitrogen sample admitted to capillary and emission adjusted until the m/e 28 output is 4.907 volts. The inlet pressure at this point is 406 torr. (Mixture) 16 Nov 1967

b. Sample inlet system pumped down to <1.0 torr. Admit nitrogen in the following steps and record this output of each channel on a DVM and the vacuum system pressure from the ionization gage.

The following data is from laboratory electronics setup

P_{inlet}	P_{inlet} (Actual)	m/e 28 Amps (Output)	~~m/e 28 Noise Level~~	P_{ig}	Outputs m/e 18, 32, 44
0	<1.0 T	3.3×10^{-13}	*		
10	11 T	1.62×10^{-11}			
30	20 T	3.4×10^{-11}			
50	52 T	9.8×10^{-11}			
100	101 T	2.05×10^{-10}			
150	—	—			
200	200 T	4.3×10^{-10}			
	300 T	6.75×10^{-10}			
	400 T	9.15×10^{-10}			

c. Sample inlet system pumped down to _____ torr. Nitrogen admitted to _____ torr with capillary closed off. _____

Set up the X-Y recorder with m/e 28 output on the Y axis and 20 seconds/inch on the X axis. Quickly open capillary to the N_2 sample and record the m/e 28 output as it responds to the N_2 sample. _____

The m/e 28 output reaches 97% of its final value in _____ seconds. _____

The sample inlet system pumped down to _____ torr. _____

STANDARD MIXTURE SENSITIVITY AND LINEARITY TEST

a. Admit standard mixture in the following steps and record the output of each channel on a DVM and the vacuum system pressure from the ionization gage.

* Not usefully observable during this measurement as bandwidth of Fethly model ≠ electrometer is narrow and varies with range switch position

P_{inlet}	P_{inlet} (Actual)	m/e 28 Volts (Output) *	m/e 28 Noise Level	P_{ig}	Complete Outputs m/e 18*, 32, 44*
0	< 1 T	-0.020	10 mV typical		-0.040 -0.006 -0.070
10	10 T	-0.087			-0.048 -0.074 -0.070
20	20 T	-0.199			-0.032 -0.170 -0.073
30	30 T	-0.319			-0.035 -0.276 -0.096
50	50 T	-0.547			-0.034 -0.471 -0.156
100	100	-1.140			-0.036 -1.005 -0.327
~~150~~ 200	200	-2.370			-0.040 -2.110 -0.760
~~200~~ 300	300	-3.643			-0.049 -3.226 -1.106
~~250~~ 400	400	-4.907	↓		-0.061 -4.426 -1.527

CARBON DIOXIDE SENSITIVITY AND LINEARITY TESTS

a. Sample reservoir pumped down to < 1.0 torr. Admit carbon dioxide sample in the following steps and record the output of each channel on the DVM and the vacuum system pressure from the ionization gage.

P_{inlet}	P_{inlet} (CO_2 ppl) (Actual)	m/e 44	m/e 18	m/3 28	m/e 32	m/e 44 Noise	P_{ig}
0	0.2 T	-0.070 -0.073 V				10 mV Typical	
50	0.6 T	-0.156 V					
100	1.1 T	-0.327 V					
200	2.2 T	-0.760 V					
300	3.3 T	-1.166 V					
400	4.4 T	-1.527 V				↓	

Sample reservoir pumped out to < 1.0 torr. 16 Nov 1967

WATER SATURATED NITROGEN SENSITIVITY, LINEARITY AND TIME RESPONSE TESTS

a. Set up completed as described in 5.2.5 preface. —

Saturated nitrogen admitted slowly to sample reservoir. —

Using two X-Y recorders with the Y axis set at 1 volt/inch attach to the m/e 18 and m/e 28 output. —

* Flight electrometer detector amplifiers

	Completed
Quickly open the inlet valve to record the pressure transient.	_____
Note when each channel reaches 97% of its final value.	_____
Record the capillary inlet pressure at two minute intervals.	_____
At end of test sample reservoir pumped down to _____ torr.	_____

b. Admit the saturated nitrogen samples to the inlet system in the following steps and record the output of each channel on the DVM. (Be sure m/e 18 has stabilized at each step.)

P_{inlet}	P_{inlet} (Actual)	m/e 18	m/e 28	m/e 32	m/e 44	m/e 18 Noise	P_{ig}
0							
20							
50							
100							
150							
200							
300							
400							
500							

When completed inlet system pumped out to _____ torr. _____

INTERFERENCE AND OVER PRESSURE TEST

a. Admit the nitrogen to the inlet system in the following steps which monitor the output on a DVM.

P_{inlet}	P_{inlet} (Actual)	m/e 18	m/e 28	m/e 32	m/e 44	P_{ig}
100						
200						

Completed

P_{inlet}	P_{inlet} (Actual)	m/e 18	m/e 28	m/e 32	m/e 44	P_{ig}
400						
600						
800	Analyzer operationally checked with laboratory electronics and found to be functional					

b. Reduce the sample pressure slowly bact to _____ torr and record the outputs.

P_{inlet}	P_{inlet} (Actual)	m/e 18	m/e 28	m/e 32	m/e 44	P_{ig}
Instrument performed in a normal manner after the over pressure exposure.						

STABILITY TESTS

a. Inlet system pumped out to _____ torr. —

Admit sample mixture _____ torr. Set up multichannel recorder for 4 hour run and record outputs with DVM and inlet pressure at 30 minute intervals. Maintain the inlet pressures to 360 torr _10 torr by readjusting periodically. Note any instabilities in outputs of 1% or more of full scale. —

P_{inlet}	P_{inlet} (Actual)	m/e 18	m/e 28	m/e 32	m/e 44	P_{ig}

b. At the end of 4 hour run measure output with DVM. —

Completed

Then pump out sample to _____ torr at reservoir. Readmit new sample mixture to 360 ±2 torr and allow output to stabilize. Record outputs of each channel on DVM and inlet pressure.

Inlet Pressure	m/e 18	m/e 28	m/e 32	m/e 44

ELECTRICAL TESTS

a. With sample mixture still at _____ torr, monitor the m/e 28 output on X-Y recorder with X axis on _____ in/sec. Rapidly switch the system power supply to 27.5 V position and record for 1 minute noting any m/e 28 change. Repeat for 28.5 V position. Verify readings with DVM and record inlet pressures.

Quick tests of Ampl. P.S. indicated that detectors are not affected by input variations and no variation in electron gun currents are seen with input voltage variations.

Return to 28.0 V position.

b. With sample mixture still at 400 torr, record the output of each channel then switch to the other filament while monitoring the m/e 28 channel on Fairchild DVM record on time base, noting difference in output levels.

Filament #	m/e 18	m/e 28	m/e 32	m/e 44	P_{inlet}
1	0.061	4.907	4.420	1.527	400 ī
2	0.037	2.53	2.293	0.781	400 ī

c. Adjust emission potentiometer until the same output level is obtained for m/e 28 as with other filament. Note pressure and outputs for 15 minutes.

Time	m/e 18	m/e 28	m/e 32	m/e 44	P_{inlet}

Completed

d. Turned system power off at _____.

Insert current meter in power lead and turn on power again. Record current required for each power supply setting.

Switch Position	Actual Voltage	Current	Watts
27.5 V	27.53	124 mA	3.411
28.0 V	27.99	124 mA	3.470
28.5 V	28.45	124 mA	3.528

Return to 28.0 V position. 14 DEC 1967

e. Turned power off at _____ and removed current meter. Attach system to programmed transient power source; turn system back on. With sample mixture at _____ torr, record outputs on DVM and record. Apply transient and immediately measure.

Before Transient

m/e 18	m/e 28	m/e 32	m/e 44	P_{inlet}

After Transient

m/e 18	m/e 28	m/e 32	m/e 44	P_{inlet}

Turn power off and reconnect to normal power source. Do not turn power on.

FINAL ION SOURCE CHECK

a. Set up completed as described in 5.2.9. Turned on system power at _____ and warmed up for > 1 hr. Admit nitrogen sample to 406 torr. Allow m/e 28 to stabilize for 1 minutes. Record anode current, pressures and m/e 28 output.

Completed

I_{an}	P_{inlet}	P_{ig}	m/e 28
10	400 T mixture		-4.907

16 Nov 1967

b. Switch to other filament and readjust for -5 V output on m/e 28. Allow to stabilize for 15 minutes and then record pressures, m/e 28 output and anode current.

Time	P_{inlet}	P_{ig}	m/e 28	I_{an}

c. Measure and record ion source voltages on flight electronics with fluke 803.

P101

1. Filament - Gun 2 - Spring 89.2 Volts
2. Filament - Gun 2 - Post 89.2 Volts
3. Z axis B 185.0 Volts
4. Open
5. Open
6. Z axis A 185.0 Volts
7. Filament - Gun 1 - Spring 89.2 Volts
8. Filament - Gun 1 - Post 89.2 Volts
9. Open

P102

1. Electron Accelerator - 2 275.5 Volts
2. Electron Focus 2B 87.4 Volts

Completed

P102

3.	Electron Focus 2A	94.3 Volts	
4.	Anode 1	215.6 Volts	
5.	Acceleratoe	185.0 Volts	
6.	Ion Focus B	0.0 Volts	
7.	Filament Shield - 2	64.6 Volts	
8.	Open		
9.	Ground - internal	0.0 Volts	

P103

1.	Filament Shiled 1	69.5 Volts	
2.	Electron Focus - 1B	93.4 Volts	
3.	Electron Focus - 1A	98.5 Volts	
4.	Exit Slit (Normally ground)	0.0 Volts	
5.	Ion Focus A	174.6 Defocused / 193.3 Volts Focused	
6.	Anode - 2	215.5 Volts	
7.	Repeller	193.9 Volts	
8.	Electron Accelerator - 1	215.5 Volts	
9.	Open		16 Nov 1967

Inlet system pumped out to < 1.0 torr. 16 Nov 1967

System power turned off at 16 Nov 1967 P.M. . 16 Nov 1967

Disconnect power supply. 16 Nov 1967

WEIGHT MEASUREMENT

System vented with Dry nitrogen at 17 Nov 1967.

Remove sensor system from vacuum system and weigh and record.

Sensor system weight: with estimates where necessary 7 lbs. 1.1 oz

w/o flight → source shield
nT6 Tabs w/4 -4-40 × 1/4" screws 5.9 ozs

APPENDIX D

CASE 1

MISSION TOTAL ELAPSED TIME 1 DAYS

CALIB. PERIOD 1 ELAPSED TIME BETWEEN CALIB. 40.48 HOURS

CALIBRATION FACTORS (SENSITIVITY, TORR/VOLT)

		355T	360T	370T
NITROGEN	BEGIN	70.01	.00	69.62
	END	76.43	.00	75.07
OXYGEN	BEGIN	80.20	.00	80.30
	END	88.66	.00	87.15
CO2	BEGIN	5.14	.00	5.07
	END	5.82	.00	5.44

E. TIME HOURS	PCABIN TORR	T.C. MICR.	N2-PCT MS	O2-PCT MS/MDA	CO2-PCT MS/MDA	H2O-PCT* MS	TOTAL-PCT MS
.4	369.0	7.6	56.6	45.0/42.7	.9/ .6	.8	103.2
.5	369.0	7.5	56.0	44.4/42.7	.9/ .6	1.8	103.0
1.8	370.0	7.5	55.3	43.8/42.5	.9/ .7	2.2	102.1
4.9	380.0	7.5	53.9	42.8/42.0	.9/ .7	2.0	99.6
9.1	370.1	7.5	55.6	44.4/42.0	.9/ .7	2.2	103.0
14.1	374.1	7.5	54.8	42.3/42.0	1.1/ .9	2.1	100.4
26.1	376.0	7.5	55.1	43.9/40.5	1.1/1.0	2.1	102.2
31.6	371.5	7.5	55.2	45.6/41.5	1.2/1.0	2.2	104.2
35.1	370.2	7.5	54.3	45.6/41.8	1.3/1.0	2.2	103.4
37.1	368.5	7.5	53.5	45.3/41.5	1.4/ .7	2.4	102.6
39.8	368.5	7.8	53.5	46.0/41.4	1.5/1.2	2.4	103.5

*COMPUTED USING THE N2 CAL. FACTOR AND
THE KNOWN IONIZATION PROBABILITY OF H2O.

MISSION TOTAL ELAPSED TIME 3 DAYS

CALIB. PERIOD 2 ELAPSED TIME BETWEEN CALIB. 21.17 HOURS

CALIBRATION FACTORS (SENSITIVITY, TORR/VOLT)

		355T	360T	370T
NITROGEN	BEGIN	76.43	.00	75.07
	END	72.02	.00	76.32
OXYGEN	BEGIN	88.66	.00	87.15
	END	91.42	.00	89.70
CO2	BEGIN	5.82	.00	5.44
	END	6.02	.00	5.78

E. TIME HOURS	PCABIN TORR	T.C. MICR.	N2-PCT MS	O2-PCT MS/MDA	CO2-PCT MS/MDA	H2O-PCT* MS	TOTAL-PCT MS
.5	368.0	8.0	55.3	47.6/42.0	1.6/1.2	.7	105.2
1.0	367.0	7.8	53.4	46.3/ .0	1.5/ .0	2.5	103.7
1.9	368.2	8.0	53.2	46.5/43.2	1.6/1.5	2.4	103.7
2.9	365.0	7.5	53.0	45.8/42.8	1.6/1.5	2.6	103.0
3.3	364.2	7.5	52.3	45.4/42.8	1.6/ .7	2.7	101.9
5.3	362.1	7.0	53.3	46.5/41.9	1.6/ .0	2.5	103.8
9.5	359.3	7.0	53.6	45.7/42.4	1.3/1.3	2.2	102.9
16.3	366.5	7.0	50.7	44.4/42.0	1.1/ .9	2.5	98.7
17.7	364.8	7.0	50.4	46.6/42.2	1.0/ .9	2.5	100.5
19.9	362.2	7.3	50.7	46.2/41.8	1.1/ .8	2.8	100.7
20.3	361.0	7.3	50.7	46.0/41.9	1.1/ .6	2.7	100.5
20.6	359.5	7.3	51.1	45.9/41.7	1.1/ .8	2.7	100.8

*COMPUTED USING THE N2 CAL. FACTOR AND
THE KNOWN IONIZATION PROBABILITY OF H2O.

MISSION TOTAL ELAPSED TIME 4 DAYS

CALIB. PERIOD 3 ELAPSED TIME BETWEEN CALIB. 27.03 HOURS

CALIBRATION FACTORS (SENSITIVITY, TORR/VOLT)

		355T	360T	370T
NITROGEN	BEGIN	72.02	.00	76.32
	END	72.62	.00	78.62
OXYGEN	BEGIN	91.42	.00	89.70
	END	92.37	.00	91.03
CO2	BEGIN	6.02	.00	5.78
	END	6.02	.00	5.78

E. TIME HOURS	PCABIN TORR	T.C. MICR.	N2-PCT MS	O2-PCT MS/MDA	CO2-PCT MS/MDA	H2O-PCT* MS	TOTAL-PCT MS
.5	361.6	7.7	52.5	48.5/32.7	1.2/ .9	.6	102.8
1.6	362.2	7.7	49.7	46.8/42.5	1.1/1.0	2.4	100.0
2.3	356.2	7.7	51.3	46.2/42.0	1.2/1.2	2.2	101.0
2.7	356.0	7.8	51.2	46.5/42.1	1.2/1.3	2.1	101.0
3.7	363.2	7.8	50.2	47.5/43.0	1.1/1.0	2.6	101.5
4.7	358.0	7.8	51.2	46.6/42.7	1.2/1.1	2.2	101.3
5.8	356.5	7.7	51.2	46.3/42.1	1.2/1.4	2.1	100.7
6.0	359.5	7.3	51.0	46.6/43.1	1.2/1.2	2.1	100.8
8.4	354.0	7.1	52.2	47.8/43.7	1.1/1.1	2.1	103.3
24.0	356.6	7.5	51.2	46.5/43.5	1.3/1.2	2.4	101.4
26.4	357.2	7.8	52.2	46.2/42.9	1.3/1.4	2.1	101.8

* COMPUTED USING THE N2 CAL. FACTOR AND
THE KNOWN IONIZATION PROBABILITY OF H2O.

MISSION TOTAL ELAPSED TIME 5 DAYS

CALIB. PERIOD 4 ELAPSED TIME BETWEEN CALIB. 23.45 HOURS

CALIBRATION FACTORS (SENSITIVITY, TORR/VOLT)

		355T	360T	370T
NITROGEN	BEGIN	72.62	.00	78.62
	END	77.44	.00	76.97
OXYGEN	BEGIN	92.37	.00	91.03
	END	93.35	.00	92.41
CO2	BEGIN	6.02	.00	5.78
	END	6.02	.00	5.87

E. TIME HOURS	PCABIN TORR	T.C. MICR.	N2-PCT MS	O2-PCT MS/MDA	CO2-PCT MS/MDA	H2O-PCT* MS	TOTAL-PCT MS
.3	358.5	8.0	53.6	47.9/42.5	1.4/1.2	.7	103.6
1.4	362.0	8.0	51.4	46.4/42.6	1.3/1.2	2.1	101.1
3.0	364.5	8.1	51.1	47.2/42.9	1.5/ .5	1.3	101.1
11.2	366.2	8.1	51.2	47.8/43.0	1.4/1.3	2.1	102.5
15.5	367.1	8.1	51.9	48.0/43.0	1.3/1.3	2.1	103.3
19.4	367.7	8.1	52.6	47.3/43.0	1.3/1.2	2.1	103.3
22.7	367.2	8.3	52.4	46.4/42.7	1.4/ .7	2.1	102.3
23.0	367.2	8.2	52.4	46.4/42.9	1.4/1.2	2.1	102.3

* COMPUTED USING THE N2 CAL. FACTOR AND
THE KNOWN IONIZATION PROBABILITY OF H2O.

MISSION TOTAL ELAPSED TIME 6 DAYS

CALIB. PERIOD 5 ELAPSED TIME BETWEEN CALIB. 24.52 HOURS

CALIBRATION FACTORS (SENSITIVITY, TORR/VOLT)

		355T	360T	370T
NITROGEN	BEGIN	77.44	.00	76.97
	END	78.48	.00	78.29
OXYGEN	BEGIN	93.35	.00	92.41
	END	90.95	.00	89.70
CO2	BEGIN	6.02	.00	5.87
	END	5.82	.00	5.69

E. TIME HOURS	PCABIN TORR	T.C. MICR.	N2-PCT MS	O2-PCT MS/MDA	CO2-PCT MS/MDA	H2O-PCT* MS	TOTAL-PCT MS
2.2	367.4	8.6	52.9	46.6/42.0	1.4/1.2	.5	101.4
2.6	367.5	8.5	52.5	46.0/ .0	1.4/ .0	.4	100.3
2.7	367.6	8.4	51.0	45.5/ .0	1.4/ .0	1.9	99.8
18.3	363.8	7.0	55.0	46.3/41.9	1.5/ .6	2.2	104.9
20.6	364.0	7.4	54.6	46.9/41.9	1.3/1.3	2.2	105.0
21.6	365.0	7.6	54.5	46.8/41.9	1.3/1.3	2.3	104.8
23.3	365.7	7.7	53.6	46.1/42.0	1.2/1.2	2.1	103.1
23.9	365.8	8.0	53.6	46.3/41.8	1.2/1.2	2.3	103.4
24.0	365.8	7.9	53.4	45.8/41.8	1.3/1.2	2.3	102.7

* COMPUTED USING THE N2 CAL. FACTOR AND
THE KNOWN IONIZATION PROBABILITY OF H2O.

MISSION TOTAL ELAPSED TIME 7 DAYS

CALIB. PERIOD 6 ELAPSED TIME BETWEEN CALIB. 27.03 HOURS

CALIBRATION FACTORS (SENSITIVITY, TORR/VOLT)

		355T	360T	370T
NITROGEN	BEGIN	78.48	.00	78.29
	END	76.76	.00	76.32
OXYGEN	BEGIN	90.95	.00	89.70
	END	88.22	.00	87.57
CO2	BEGIN	5.82	.00	5.69
	END	5.73	.00	5.44

E. TIME HOURS	PCABIN TORR	T.C. MICR.	N2-PCT MS	O2-PCT MS/MDA	CO2-PCT MS/MDA	H2O-PCT* MS	TOTAL-PCT MS
.6	366.3	7.0	46.9	40.3/ .0	1.1/ .0	.6	88.9
.9	357.0	6.9	48.0	41.0/ .0	1.0/ .0	.5	90.4
.9	357.0	6.9	48.0	41.0/ .0	1.0/ .0	.5	90.4
2.0	366.2	6.8	46.2	39.5/42.5	1.1/1.2	1.9	88.7
10.6	367.5	6.2	47.2	40.0/42.5	1.1/1.2	2.1	90.4
13.6	367.0	6.0	47.1	39.5/42.0	1.1/1.2	2.0	89.6
16.0	366.7	6.1	47.1	39.4/43.8	1.1/1.1	1.8	89.3
21.3	369.8	6.4	46.1	40.1/43.8	1.0/1.1	2.0	89.2
21.5	370.0	6.4	46.1	40.3/43.8	1.1/1.1	2.0	89.4

* COMPUTED USING THE N2 CAL. FACTOR AND
THE KNOWN IONIZATION PROBABILITY OF H2O.

MISSION TOTAL ELAPSED TIME 8 DAYS

CALIB. PERIOD 7 ELAPSED TIME BETWEEN CALIB. 26.60 HOURS

CALIBRATION FACTORS (SENSITIVITY, TORR/VOLT)

		355T	360T	370T
NITROGEN	BEGIN	76.76	.00	76.32
	END	73.85	.00	75.07
OXYGEN	BEGIN	88.22	.00	87.57
	END	86.91	.00	86.74
CO2	BEGIN	5.73	.00	5.44
	END	5.73	.00	5.52

E. TIME HOURS	PCABIN TORR	T.C. MICR.	N2-PCT MS	O2-PCT MS/MDA	CO2-PCT MS/MDA	H2O-PCT* MS	TOTAL-PCT MS
.3	370.8	7.8	53.8	47.1/43.8	1.3/1.1	.7	102.9
.8	371.0	7.6	52.5	45.9/43.8	1.3/1.2	2.3	101.9
.9	371.2	7.8	52.3	43.5/43.8	1.3/1.2	2.3	99.3
5.1	365.2	7.5	51.7	44.5/44.5	1.3/1.3	2.2	99.7
7.3	365.2	7.5	51.6	46.1/43.5	1.4/1.3	2.4	101.5
8.7	363.5	7.5	51.8	46.0/43.5	1.3/1.3	2.2	101.4
10.7	363.2	7.5	51.7	46.2/43.5	1.3/1.2	2.1	101.3
12.7	362.0	7.5	52.0	46.1/43.5	1.2/1.2	2.1	101.4
18.8	363.0	7.2	51.5	45.9/43.5	1.2/1.1	2.1	100.7
22.7	362.7	7.3	51.9	46.8/43.0	1.2/1.1	2.2	102.1
26.0	364.0	7.6	51.3	45.8/42.5	1.3/1.2	2.2	100.6
26.1	364.2	7.5	51.5	46.0/ .0	1.3/ .0	2.2	101.0

* COMPUTED USING THE N2 CAL. FACTOR AND
THE KNOWN IONIZATION PROBABILITY OF H2O.

MISSION TOTAL ELAPSED TIME 9 DAYS

CALIB. PERIOD 8 ELAPSED TIME BETWEEN CALIB. 29.47 HOURS

CALIBRATION FACTORS (SENSITIVITY, TORR/VOLT)

		355T	360T	370T
NITROGEN	BEGIN	73.85	.00	75.07
	END	69.73	.00	69.36
OXYGEN	BEGIN	86.91	.00	86.74
	END	82.06	.00	81.37
CO2	BEGIN	5.73	.00	5.52
	END	5.30	.00	5.21

E. TIME HOURS	PCABIN TORR	T.C. MICR.	N2-PCT MS	O2-PCT MS/MDA	CO2-PCT MS/MDA	H2O-PCT* MS	TOTAL-PCT MS
.4	363.8	7.7	54.9	48.9/42.2	1.4/1.3	.6	105.9
.9	363.5	7.6	53.9	47.7/42.1	1.4/1.3	2.2	105.2
11.0	364.5	7.1	52.3	47.1/43.0	1.4/1.4	2.2	103.1
16.3	364.5	7.0	51.7	46.6/42.5	1.4/1.4	2.3	102.0
22.5	364.0	7.5	51.1	46.0/43.0	1.4/1.3	2.3	100.8
24.5	364.2	8.0	50.0	45.4/43.0	1.4/1.4	2.2	99.0
28.3	364.1	8.0	52.5	47.5/43.2	1.6/1.4	.7	102.3
29.1	363.5	8.0	51.5	47.0/45.9	1.4/1.5	2.1	102.1

*COMPUTED USING THE N2 CAL. FACTOR AND
THE KNOWN IONIZATION PROBABILITY OF H2O.

MISSION TOTAL ELAPSED TIME 10 DAYS

CALIB. PERIOD 9 ELAPSED TIME BETWEEN CALIB. 18.23 HOURS

CALIBRATION FACTORS (SENSITIVITY, TORR/VOLT)

		355T	360T	370T
NITROGEN	BEGIN	69.73	.00	69.36
	END	69.73	.00	69.36
OXYGEN	BEGIN	82.06	.00	81.37
	END	80.56	.00	80.30
CO2	BEGIN	5.30	.00	5.21
	END	5.14	.00	5.14

E. TIME HOURS	PCABIN TORR	T.C. MICR.	N2-PCT MS	O2-PCT MS/MDA	CO2-PCT MS/MDA	H2O-PCT* MS	TOTAL-PCT MS
.4	362.9	8.0	52.5	47.5/45.5	1.4/1.5	.6	102.1
8.6	358.7	7.0	53.8	47.0/44.2	1.3/1.3	2.1	104.2
11.4	358.9	7.1	53.8	46.4/44.3	1.3/1.4	2.2	103.7
13.7	358.5	7.0	54.0	46.8/44.5	1.3/1.3	2.1	104.2
17.8	359.0	7.4	53.8	45.5/43.8	1.3/1.3	2.3	102.9
17.8	358.7	7.2	53.6	45.3/43.8	1.3/1.4	2.2	102.5

* COMPUTED USING THE N2 CAL. FACTOR AND
THE KNOWN IONIZATION PROBABILITY OF H2O.

MISSION TOTAL ELAPSED TIME 11 DAYS

CALIB. PERIOD 10 ELAPSED TIME BETWEEN CALIB. 22.48 HOURS

CALIBRATION FACTORS (SENSITIVITY, TORR/VOLT)

		355T	360T	370T
NITROGEN	BEGIN	65.80	.00	65.62
	END	68.10	.00	67.81
OXYGEN	BEGIN	75.08	.00	75.99
	END	78.77	.00	77.92
CO2	BEGIN	5.07	.00	4.87
	END	5.55	.00	5.14

E. TIME HOURS	PCABIN TORR	T.C. MICR.	N2-PCT MS	O2-PCT MS/MDA	CO2-PCT MS/MDA	H2O-PCT* MS	TOTAL-PCT MS
.2	357.7	7.8	52.1	43.7/43.9	1.4/1.4	.5	97.7
6.6	359.8	7.2	51.3	42.5/43.5	1.5/1.5	2.2	97.4
13.2	357.0	7.0	53.8	43.9/43.5	1.4/1.4	2.1	101.2
16.7	355.9	7.0	54.8	44.4/43.2	1.3/1.2	2.0	102.5
18.8	357.0	7.0	55.0	45.3/43.5	1.2/1.2	2.0	103.5
21.5	358.2	7.0	54.7	45.5/43.5	1.1/1.1	2.5	103.8
21.9	358.0	7.0	54.5	44.9/43.5	1.2/1.4	2.5	103.1

* COMPUTED USING THE N2 CAL. FACTOR AND
THE KNOWN IONIZATION PROBABILITY OF H2O.

MISSION TOTAL ELAPSED TIME 12 DAYS

CALIB. PERIOD 11 ELAPSED TIME BETWEEN CALIB. 14.92 HOURS

CALIBRATION FACTORS (SENSITIVITY, TORR/VOLT)

		355T	360T	370T
NITROGEN	BEGIN	68.10	.00	67.56
	END	67.57	.00	67.31
OXYGEN	BEGIN	78.77	.00	77.92
	END	77.72	.00	77.26
CO2	BEGIN	5.55	.00	5.00
	END	5.07	.00	5.00

E. TIME HOURS	PCABIN TORR	T.C. MICR.	N2-PCT MS	O2-PCT MS/MDA	CO2-PCT MS/MDA	H2O-PCT* MS	TOTAL-PCT MS
.3	358.0	7.3	55.0	45.6/43.5	1.1/1.1	.8	102.5
.5	358.0	7.1	54.2	44.9/43.5	1.1/1.1	.5	100.8
3.9	360.8	7.2	54.8	46.3/44.0	1.1/1.1	2.1	104.2
6.3	361.0	7.3	55.4	46.8/44.0	1.1/1.0	2.0	105.4
8.3	361.5	7.3	55.3	46.9/44.0	1.1/1.0	2.0	105.4
13.7	362.9	7.7	53.6	44.9/43.5	1.1/1.0	2.2	101.7
13.9	362.9	7.8	53.9	44.9/43.5	1.1/1.0	2.1	102.0
14.5	362.9	7.8	53.5	44.7/43.4	1.1/1.0	2.1	101.4

* COMPUTED USING THE N2 CAL. FACTOR AND
THE KNOWN IONIZATION PROBABILITY OF H2O.

MISSION TOTAL ELAPSED TIME 11 DAYS

CALIB. PERIOD 10 ELAPSED TIME BETWEEN CALIB. 22.48 HOURS

CALIBRATION FACTORS (SENSITIVITY, TORR/VOLT)

		355T	360T	370T
NITROGEN	BEGIN	65.80	.00	65.62
	END	68.10	.00	67.81
OXYGEN	BEGIN	75.08	.00	75.99
	END	78.77	.00	77.92
CO2	BEGIN	5.07	.00	4.87
	END	5.55	.00	5.14

E. TIME HOURS	PCABIN TORR	T.C. MICR.	N2-PCT MS	O2-PCT MS/MDA	CO2-PCT MS/MDA	H2O-PCT* MS	TOTAL-PCT MS
.2	357.7	7.8	52.1	43.7/43.9	1.4/1.4	.5	97.7
6.6	359.8	7.2	51.3	42.5/43.5	1.5/1.5	2.2	97.4
13.2	357.0	7.0	53.8	43.9/43.5	1.4/1.4	2.1	101.2
16.7	355.9	7.0	54.8	44.4/43.2	1.3/1.2	2.0	102.5
18.8	357.0	7.0	55.0	45.3/43.5	1.2/1.2	2.0	103.5
21.5	358.2	7.0	54.7	45.5/43.5	1.1/1.1	2.5	103.8
21.9	358.0	7.0	54.5	44.9/43.5	1.2/1.4	2.5	103.1

* COMPUTED USING THE N2 CAL. FACTOR AND
THE KNOWN IONIZATION PROBABILITY OF H2O.

MISSION TOTAL ELAPSED TIME 12 DAYS

CALIB. PERIOD 11 ELAPSED TIME BETWEEN CALIB. 14.92 HOURS

CALIBRATION FACTORS (SENSITIVITY, TORR/VOLT)

		355T	360T	370T
NITROGEN	BEGIN	68.10	.00	67.56
	END	67.57	.00	67.31
OXYGEN	BEGIN	78.77	.00	77.92
	END	77.72	.00	77.26
CO2	BEGIN	5.55	.00	5.00
	END	5.07	.00	5.00

E. TIME HOURS	PCABIN TORR	T.C. MICR.	N2-PCT MS	O2-PCT MS/MDA	CO2-PCT MS/MDA	H2O-PCT* MS	TOTAL-PCT MS
.3	358.0	7.3	55.0	45.6/43.5	1.1/1.1	.8	102.5
.5	358.0	7.1	54.2	44.9/43.5	1.1/1.1	.5	100.8
3.9	360.8	7.2	54.8	46.3/44.0	1.1/1.1	2.1	104.2
6.3	361.0	7.3	55.4	46.8/44.0	1.1/1.0	2.0	105.4
8.3	361.5	7.3	55.3	46.9/44.0	1.1/1.0	2.0	105.4
13.7	362.9	7.7	53.6	44.9/43.5	1.1/1.0	2.2	101.7
13.9	362.9	7.8	53.9	44.9/43.5	1.1/1.0	2.1	102.0
14.5	362.9	7.8	53.5	44.7/43.4	1.1/1.0	2.1	101.4

* COMPUTED USING THE N2 CAL. FACTOR AND
THE KNOWN IONIZATION PROBABILITY OF H2O.

MISSION TOTAL ELAPSED TIME 13 DAYS

CALIB. PERIOD 12 ELAPSED TIME BETWEEN CALIB. 9.68 HOURS

CALIBRATION FACTORS (SENSITIVITY, TORR/VOLT)

		355T	360T	370T
NITROGEN	BEGIN	60.56	.00	59.03
	END	63.64	.00	63.78
OXYGEN	BEGIN	70.29	.00	68.11
	END	73.21	.00	73.26
CO2	BEGIN	4.80	.00	4.74
	END	5.07	.00	4.87

E. TIME HOURS	PCABIN TORR	T.C. MICR.	N2-PCT MS	O2-PCT MS/MDA	CO2-PCT MS/MDA	H2O-PCT* MS	TOTAL-PCT MS
.6	363.8	8.0	48.8	41.0/43.4	1.2/1.2	.4	91.3
.6	363.8	8.0	48.8	41.0/43.4	1.2/1.2	.4	91.3
1.5	364.1	8.2	46.2	38.5/43.0	1.2/1.2	2.0	87.9

* COMPUTED USING THE N2 CAL. FACTOR AND THE KNOWN IONIZATION PROBABILITY OF H2O.

MISSION TOTAL ELAPSED TIME 14 DAYS

CALIB. PERIOD 13 ELAPSED TIME BETWEEN CALIB. 9.02 HOURS

CALIBRATION FACTORS (SENSITIVITY, TORR/VOLT)

		355T	360T	370T
NITROGEN	BEGIN	63.64	.00	63.78
	END	68.90	.00	68.32
OXYGEN	BEGIN	73.21	.00	73.26
	END	78.42	.00	77.92
CO2	BEGIN	5.07	.00	4.87
	END	5.14	.00	5.14

E. TIME HOURS	PCABIN TORR	T.C. MICR.	N2-PCT MS	O2-PCT MS/MDA	CO2-PCT MS/MDA	H2O-PCT* MS	TOTAL-PCT MS
.2	362.0	8.0	52.7	42.4/43.2	1.5/1.4	.8	97.3
.4	362.0	7.7	51.6	41.4/43.4	1.5/1.3	.6	95.0
1.4	361.6	7.4	51.4	40.5/43.3	1.0/1.1	1.8	94.8
4.7	362.1	7.4	52.7	41.7/43.3	1.0/ .9	1.9	97.2
6.6	362.2	7.4	53.9	42.4/43.3	1.0/ .9	2.0	99.3
8.5	362.4	7.5	54.5	43.2/43.0	1.0/ .9	2.1	100.8

* COMPUTED USING THE N2 CAL. FACTOR AND
THE KNOWN IONIZATION PROBABILITY OF H2O.

MISSION TOTAL ELAPSED TIME 15 DAYS

CALIB. PERIOD 14 ELAPSED TIME BETWEEN CALIB. 22.15 HOURS

CALIBRATION FACTORS (SENSITIVITY, TORR/VOLT)

		355T	360T	370T
NITROGEN	BEGIN	68.90	.00	68.32
	END	67.84	.00	68.06
OXYGEN	BEGIN	78.42	.00	77.92
	END	78.07	.00	78.25
CO2	BEGIN	5.14	.00	5.14
	END	5.14	.00	5.14

. TIME HOURS	PCABIN TORR	T.C. MICR.	N2-PCT MS	O2-PCT MS/MDA	CO2-PCT MS/MDA	H2O-PCT* MS	TOTAL-PCT MS
.4	363.0	7.9	55.2	43.7/43.2	1.0/ .9	.6	100.6
.6	362.1	8.0	62.1	49.2/43.6	1.2/1.0	3.2	115.8
.9	361.0	8.0	57.7	45.4/42.8	1.2/1.0	2.6	106.9
1.2	360.9	8.0	55.2	43.5/43.0	1.2/1.0	2.5	102.4
3.8	360.4	8.0	53.4	42.9/ .0	1.2/ .0	2.1	99.6
4.0	360.8	8.0	53.3	42.9/44.0	1.2/1.1	2.1	99.4
11.4	356.6	7.0	54.9	42.7/43.6	1.1/1.1	2.0	100.7
21.3	364.6	7.5	54.8	42.9/43.5	1.0/1.0	2.1	100.8
21.5	364.3	7.6	55.0	42.9/43.4	1.0/1.0	2.1	101.1

*TED USING THE N2 CAL. FACTOR AND
DOWN IONIZATION PROBABILITY OF H2O.

MISSION TOTAL ELAPSED TIME 16 DAYS

CALIB. PERIOD 15 ELAPSED TIME BETWEEN CALIB. 17.78 HOURS

CALIBRATION FACTORS (SENSITIVITY, TORR/VOLT)

		355T	360T	370T
NITROGEN	BEGIN	67.84	.00	68.06
	END	68.90	.00	68.32
OXYGEN	BEGIN	78.07	.00	78.25
	END	78.77	.00	78.25
CO2	BEGIN	5.14	.00	5.14
	END	5.22	.00	5.21

E. TIME HOURS	PCABIN TORR	T.C. MICR.	N2-PCT MS	O2-PCT MS/MDA	CO2-PCT MS/MDA	H2O-PCT* MS	TOTAL-PCT MS
.2	365.0	7.8	55.3	43.2/43.2	1.1/1.0	.8	100.3
.5	364.5	7.7	54.6	43.1/43.0	1.1/1.0	.5	99.3
14.9	365.7	7.2	55.9	43.8/43.0	1.0/ .9	2.1	102.8
16.9	365.2	7.5	56.0	43.5/42.8	1.0/ .9	2.0	102.5
17.2	365.0	7.5	56.1	43.5/42.6	1.0/ .9	2.1	102.7

*COMPUTED USING THE N2 CAL. FACTOR AND
THE KNOWN IONIZATION PROBABILITY OF H2O.

MISSION TOTAL ELAPSED TIME 17 DAYS

CALIB. PERIOD 16 ELAPSED TIME BETWEEN CALIB. 21.77 HOURS

CALIBRATION FACTORS (SENSITIVITY, TORR/VOLT)

		355T	360T	370T
NITROGEN	BEGIN	68.90	.00	68.32
	END	68.10	.00	67.56
OXYGEN	BEGIN	78.77	.00	78.25
	END	78.42	.00	77.26
CO2	BEGIN	5.22	.00	5.21
	END	5.22	.00	5.14

E. TIME HOURS	PCABIN TORR	T.C. MICR.	N2-PCT MS	O2-PCT MS/MDA	CO2-PCT MS/MDA	H2O-PCT* MS	TOTAL-PCT MS
.2	365.2	.0	57.0	43.5/42.5	1.0/1.0	.8	102.3
.5	364.9	7.6	55.7	43.1/42.5	1.0/1.0	1.1	100.9
.6	366.0	7.9	55.0	43.0/42.5	1.0/ .9	1.9	100.9
4.3	366.2	7.7	54.7	42.9/43.0	1.1/1.0	1.9	100.6
6.3	366.8	7.6	54.9	42.8/44.5	1.1/1.0	2.1	100.9
8.8	366.1	7.6	55.0	42.8/44.0	1.1/1.1	2.1	101.1
11.5	365.0	7.4	55.2	42.9/44.0	1.1/1.1	2.1	101.3
13.5	363.7	7.3	55.9	43.0/44.0	1.1/1.1	2.0	101.9
15.2	363.1	7.2	55.9	43.0/44.0	1.1/1.0	2.0	102.0
17.5	363.3	7.0	55.8	43.0/44.0	1.0/1.0	2.1	101.8
19.5	361.8	7.0	55.9	43.0/45.0	1.0/1.0	2.1	102.1
21.2	361.8	7.4	55.5	42.8/44.9	1.1/1.1	2.2	101.5

*COMPUTED USING THE N2 CAL. FACTOR AND
THE KNOWN IONIZATION PROBABILITY OF H2O.

MISSION TOTAL ELAPSED TIME 18 DAYS

CALIB. PERIOD 17 ELAPSED TIME BETWEEN CALIB. 24.98 HOURS

CALIBRATION FACTORS (SENSITIVITY, TORR/VOLT)

		355T	360T	370T
NITROGEN	BEGIN	68.10	.00	67.56
	END	67.84	.00	67.56
OXYGEN	BEGIN	78.42	.00	77.26
	END	77.72	.00	77.26
CO2	BEGIN	5.22	.00	5.14
	END	5.22	.00	5.14

E. TIME HOURS	PCABIN TORR	T.C. MICR.	N2-PCT MS	O2-PCT MS/MDA	CO2-PCT MS/MDA	H2O-PCT* MS	TOTAL-PCT MS
.3	361.3	7.5	56.8	44.1/ .0	1.1/1.1	.7	102.8
1.0	360.8	7.3	54.8	42.4/43.9	1.1/1.1	2.2	100.6
3.0	362.1	7.5	54.9	42.5/42.3	1.1/1.1	2.1	100.7
6.2	365.0	7.4	54.7	43.8/42.3	1.1/1.0	2.0	101.6
10.0	366.8	7.3	55.5	43.1/41.7	1.0/ .9	1.9	101.6
11.9	367.8	7.3	55.4	43.2/41.7	1.0/ .9	2.0	101.6
13.9	367.8	7.2	55.4	43.4/41.8	1.0/1.0	2.0	101.8
16.9	367.8	7.3	55.4	44.0/41.7	1.0/1.0	2.1	102.5
18.4	367.9	7.3	55.1	43.8/41.7	1.0/ .9	2.0	101.9
20.5	368.0	7.3	54.9	43.5/42.0	1.0/ .9	.7	100.2
22.4	368.3	7.1	54.9	43.5/42.0	1.0/ .8	1.8	101.2
24.0	369.2	7.7	54.7	43.4/42.0	1.0/ .8	1.9	101.0

*COMPUTED USING THE N2 CAL. FACTOR AND
THE KNOWN IONIZATION PROBABILITY OF H2O.

MISSION TOTAL ELAPSED TIME 19 DAYS

CALIB. PERIOD 18 ELAPSED TIME BETWEEN CALIB. 26.47 HOURS

CALIBRATION FACTORS (SENSITIVITY, TORR/VOLT)

		355T	360T	370T
NITROGEN	BEGIN	67.84	.00	67.56
	END	69.18	.00	68.06
OXYGEN	BEGIN	77.72	.00	77.26
	END	78.77	.00	77.59
CO2	BEGIN	5.22	.00	5.14
	END	5.38	.00	5.14

E. TIME HOURS	PCABIN TORR	T.C. MICR.	N2-PCT MS	O2-PCT MS/MDA	CO2-PCT MS/MDA	H2O-PCT* MS	TOTAL-PCT MS
.3	369.8	7.8	55.8	43.9/ .0	1.1/ .0	.7	101.5
1.1	370.1	7.8	54.7	42.9/42.3	1.1/1.1	2.0	100.6
2.4	371.2	8.0	54.6	43.0/42.0	1.1/1.1	2.1	100.8
4.9	366.8	7.4	54.1	43.1/43.0	1.2/1.2	2.0	100.3
7.2	364.5	7.4	54.5	43.3/43.0	1.2/1.2	2.1	101.0
8.7	360.9	7.3	54.4	43.5/43.5	1.1/1.2	2.1	101.1
11.2	360.0	7.3	54.6	43.8/43.3	1.1/1.1	2.0	101.4
15.0	361.2	7.3	54.9	44.8/43.4	1.1/1.1	2.2	103.0
17.2	361.4	7.3	54.9	44.8/43.0	1.1/1.1	2.2	103.0
20.4	361.8	7.0	55.2	45.0/42.5	1.0/1.0	2.2	103.4
23.9	363.2	7.2	54.6	44.1/42.0	1.0/1.0	2.1	101.9
25.9	365.0	7.8	54.7	44.0/42.5	1.1/1.0	2.0	101.7

*COMPUTED USING THE N2 CAL. FACTOR AND
THE KNOWN IONIZATION PROBABILITY OF H2O.

MISSION TOTAL ELAPSED TIME 20 DAYS

CALIB. PERIOD 19 ELAPSED TIME BETWEEN CALIB. 42.15 HOURS

CALIBRATION FACTORS (SENSITIVITY, TORR/VOLT)

		355T	360T	370T
NITROGEN	BEGIN	69.18	.00	68.06
	END	67.31	.00	67.31
OXYGEN	BEGIN	78.77	.00	77.59
	END	77.05	.00	76.94
CO2	BEGIN	5.38	.00	5.14
	END	5.14	.00	5.07

E. TIME HOURS	PCABIN TORR	T.C. MICR.	N2-PCT MS	O2-PCT MS/MDA	CO2-PCT MS/MDA	H2O-PCT* MS	TOTAL-PCT MS
.3	366.0	8.0	55.5	44.8/42.5	1.1/1.4	.7	102.2
.6	365.8	8.0	54.6	43.9/42.5	1.1/1.4	1.9	101.6
2.6	367.3	7.8	54.6	44.0/42.0	1.0/1.2	2.1	101.7
4.2	365.7	7.6	55.4	43.7/42.7	1.2/1.2	2.1	102.5
6.0	362.5	7.4	55.5	43.7/43.0	1.2/1.2	2.0	102.4
7.4	359.5	7.3	55.0	43.5/43.0	1.2/1.2	2.0	101.7
8.8	360.0	7.3	55.1	43.6/42.5	1.2/1.1	2.1	102.0
10.7	360.4	7.2	55.4	43.6/43.0	1.1/1.1	2.0	102.2
12.7	361.6	7.2	55.1	43.7/43.0	1.1/1.1	2.0	101.9
14.5	361.2	7.2	54.9	43.7/43.0	1.1/1.1	2.0	101.6
16.9	362.2	7.7	54.7	43.3/42.7	1.1/1.0	2.1	101.2
19.6	364.3	7.9	54.0	43.1/42.5	1.1/1.1	2.1	100.4
21.7	366.1	8.0	53.7	42.9/42.5	1.1/1.1	2.1	99.9
23.7	366.3	8.0	53.5	42.8/43.3	1.2/1.1	2.0	99.4
25.7	367.5	7.8	53.8	43.1/43.3	1.1/1.1	1.9	100.0
28.7	367.0	7.6	54.9	43.3/42.8	1.1/1.1	2.1	101.4
31.5	365.6	7.4	55.2	43.0/42.8	1.1/1.1	2.3	101.6
32.7	361.5	7.4	55.0	43.2/43.0	1.1/1.1	2.1	101.4
34.7	361.8	7.3	55.1	43.3/42.5	1.1/1.1	2.1	101.5
36.7	362.6	7.2	55.1	43.2/42.8	1.1/1.1	2.1	101.4
38.6	362.4	7.2	55.1	43.2/42.8	1.0/1.1	2.0	101.3
40.5	362.9	7.5	55.3	43.1/42.7	1.1/1.1	2.2	101.6
41.1	363.0	7.6	55.3	43.1/ .0	1.1/ .0	2.2	101.6
41.2	363.0	7.6	55.1	42.9/ .0	1.1/ .0	2.2	101.2
41.8	362.5	7.7	55.2	42.9/42.4	1.1/1.1	2.2	101.3

*COMPUTED USING THE N2 CAL. FACTOR AND
THE KNOWN IONIZATION PROBABILITY OF H2O.

MISSION TOTAL ELAPSED TIME 22 DAYS

CALIB. PERIOD 20 ELAPSED TIME BETWEEN CALIB. 47.50 HOURS

CALIBRATION FACTORS (SENSITIVITY, TORR/VOLT)

		355T	360T	370T
NITROGEN	BEGIN	67.31	.00	70.16
	END	66.55	.00	69.36
OXYGEN	BEGIN	77.05	.00	80.30
	END	76.38	.00	79.61
CO2	BEGIN	5.14	.00	5.36
	END	5.14	.00	5.36

E. TIME HOURS	PCABIN TORR	T.C. MICR.	N2-PCT MS	O2-PCT MS/MDA	CO2-PCT MS/MDA	H2O-PCT* MS	TOTAL-PCT MS
.4	362.2	7.8	56.6	44.3/42.4	1.2/1.1	.8	102.9
1.4	362.5	7.8	55.2	43.6/42.6	1.2/1.2	2.0	101.9
3.4	364.1	7.8	54.3	43.0/43.0	1.2/1.2	2.1	100.6
4.9	366.0	7.8	53.9	43.0/ .0	1.3/ .0	2.1	100.2
5.7	366.0	7.5	53.9	43.0/ .0	1.3/ .0	2.1	100.2
8.7	364.0	7.5	54.4	43.4/42.0	1.4/1.3	2.4	101.6
11.4	364.0	7.5	54.4	43.4/42.0	1.4/1.4	2.4	101.6
14.3	365.5	7.3	54.8	43.2/42.0	1.3/1.3	2.1	101.5
16.1	363.0	7.3	55.6	43.8/42.0	1.2/1.2	2.0	102.6
17.1	369.2	7.5	53.9	44.4/43.8	1.1/1.2	2.0	101.5
17.9	370.5	7.5	53.5	44.5/43.8	1.1/1.2	2.0	101.1
19.7	365.0	7.3	54.4	45.2/43.5	1.2/1.2	2.0	102.8
23.9	357.8	7.3	55.7	44.8/42.0	1.2/1.1	2.3	104.0
25.9	357.9	7.3	55.5	44.8/42.0	1.2/1.1	2.3	103.7
27.9	358.2	7.0	55.2	44.7/42.0	1.2/1.1	2.0	103.0
29.7	358.7	7.3	55.0	44.5/43.0	1.2/1.1	2.0	102.7
31.9	358.5	7.3	55.4	44.8/42.8	1.2/1.1	2.0	103.3
33.9	358.5	7.3	55.4	44.5/42.8	1.1/1.0	2.1	103.2
37.2	359.2	7.3	55.1	44.3/43.0	1.1/1.0	2.2	102.8
39.4	359.0	7.8	55.5	44.8/42.8	1.1/1.0	2.2	103.6
40.7	358.4	7.0	55.7	44.7/42.5	1.1/1.0	2.1	103.6
42.7	358.2	7.0	55.7	44.8/42.5	1.0/1.0	2.2	103.7
45.2	357.8	7.0	56.0	44.8/42.5	1.0/1.0	2.2	104.1
46.9	357.8	7.2	56.0	44.6/42.3	1.0/1.0	2.2	103.8
47.2	357.8	7.1	55.8	44.6/42.2	1.0/1.0	2.2	103.6

* COMPUTED USING THE N2 CAL. FACTOR AND THE KNOWN IONIZATION PROBABILITY OF H2O.

MISSION TOTAL ELAPSED TIME 24 DAYS

CALIB. PERIOD 21 ELAPSED TIME BETWEEN CALIB. 18.45 HOURS

CALIBRATION FACTORS (SENSITIVITY, TORR/VOLT)

		355T	360T	370T
NITROGEN	BEGIN	.00	68.79	.00
	END	.00	71.85	.00
OXYGEN	BEGIN	.00	79.17	.00
	END	.00	82.83	.00
CO2	BEGIN	.00	5.14	.00
	END	.00	5.54	.00

E. TIME HOURS	PCABIN TORR	T.C. MICR.	N2-PCT MS	O2-PCT MS/MDA	CO2-PCT MS/MDA	H2O-PCT* MS	TOTAL-PCT MS
.5	363.0	7.2	53.3	44.1/43.3	1.1/1.1	.5	99.1
.7	363.0	7.2	53.1	44.1/43.1	1.1/1.1	.5	98.9
1.9	365.0	7.3	51.3	43.2/43.5	1.1/1.1	1.9	97.5
4.7	364.1	7.0	51.2	43.6/44.0	1.2/1.2	2.0	98.0
7.3	362.0	7.0	51.8	44.3/44.0	1.1/1.1	1.9	99.2
8.3	362.8	7.0	51.8	44.6/44.0	1.1/1.1	1.9	99.4
10.1	364.2	6.8	51.9	45.3/44.5	1.1/1.1	1.9	100.1
11.6	364.4	6.8	52.2	45.4/44.5	1.1/1.0	1.8	100.5
13.4	364.4	6.8	52.4	45.6/44.5	1.0/1.0	1.8	100.8
16.1	364.2	6.9	53.0	45.7/44.3	1.1/1.0	1.9	101.6
17.9	364.8	7.2	52.9	45.8/44.5	1.1/1.0	2.0	101.8

* COMPUTED USING THE N2 CAL. FACTOR AND THE KNOWN IONIZATION PROBABILITY OF H2O.

MISSION TOTAL ELAPSED TIME 25 DAYS

CALIB. PERIOD 22 ELAPSED TIME BETWEEN CALIB. 22.23 HOURS

CALIBRATION FACTORS (SENSITIVITY, TORR/VOLT)

		355T	360T	370T
NITROGEN	BEGIN	.00	71.85	.00
	END	.00	70.71	.00
OXYGEN	BEGIN	.00	82.83	.00
	END	.00	81.70	.00
CO2	BEGIN	.00	5.54	.00
	END	.00	5.45	.00

E. TIME HOURS	PCABIN TORR	T.C. MICR.	N2-PCT MS	O2-PCT MS/MDA	CO2-PCT MS/MDA	H2O-PCT* MS	TOTAL-PCT MS
.3	364.0	7.3	53.5	46.4/44.4	1.0/1.1	.9	101.8
1.0	363.4	7.3	52.6	45.6/44.9	1.1/1.1	1.5	100.8
2.8	362.3	7.1	52.5	45.2/44.5	1.1/1.1	1.9	100.7
1.8	362.1	6.8	53.5	44.3/43.7	1.1/1.1	1.9	100.9
5.4	362.0	6.8	53.6	44.5/43.5	1.2/1.1	1.9	101.1
9.1	361.2	6.8	53.6	44.5/43.7	1.1/1.1	1.9	101.1
10.9	361.0	6.8	53.5	44.4/43.7	1.1/1.0	1.9	100.9
15.6	360.7	6.8	53.6	44.1/43.5	1.0/1.0	1.9	100.6
18.5	360.4	6.8	53.9	44.1/43.5	1.0/1.0	2.0	101.0
19.8	359.8	6.8	53.9	44.1/43.3	1.0/ .9	2.0	101.0
21.6	359.6	7.0	54.1	43.9/43.4	1.0/1.0	2.1	101.0

*COMPUTED USING THE N2 CAL. FACTOR AND
THE KNOWN IONIZATION PROBABILITY OF H2O.

MISSION TOTAL ELAPSED TIME 26 DAYS

CALIB. PERIOD 23 ELAPSED TIME BETWEEN CALIB. 25.03 HOURS

CALIBRATION FACTORS (SENSITIVITY, TORR/VOLT)

		355T	360T	370T
NITROGEN	BEGIN	.00	70.71	.00
	END	.00	71.85	.00
OXYGEN	BEGIN	.00	81.70	.00
	END	.00	82.45	.00
CO2	BEGIN	.00	5.45	.00
	END	.00	5.62	.00

E. TIME HOURS	PCABIN TORR	T.C. MICR.	N2-PCT MS	O2-PCT MS/MDA	CO2-PCT MS/MDA	H2O-PCT* MS	TOTAL-PCT MS
.2	359.5	7.0	54.7	44.8/43.0	1.1/1.0	1.1	101.6
.6	359.5	7.0	54.1	43.6/43.6	1.1/1.0	1.9	100.7
2.5	360.5	7.0	53.2	43.6/43.3	1.1/1.1	2.0	99.9
2.6	360.5	7.0	53.2	43.6/43.3	1.1/1.1	2.0	99.9
4.7	361.4	7.1	53.2	43.7/43.5	1.2/1.1	2.0	100.1
7.0	362.0	7.0	53.0	43.7/43.3	1.2/1.2	2.2	100.1
9.0	361.5	7.0	53.1	43.8/43.3	1.3/1.3	2.3	100.5
10.7	361.0	7.0	53.4	43.9/43.3	1.3/1.3	2.1	100.7
12.5	361.3	6.9	53.5	43.8/43.3	1.3/1.2	2.2	100.7
15.0	361.2	6.9	53.6	43.9/43.3	1.2/1.2	2.1	100.8
16.7	361.0	6.9	53.7	44.2/43.0	1.2/1.2	2.0	101.1
18.7	361.0	7.0	53.9	44.2/43.0	1.2/1.1	2.0	101.3
20.5	361.2	6.8	54.3	44.7/43.0	1.2/1.1	2.1	102.4
24.6	363.0	7.2	54.8	43.8/43.0	1.1/1.1	2.1	101.9

*COMPUTED USING THE N2 CAL. FACTOR AND
THE KNOWN IONIZATION PROBABILITY OF H2O.

MISSION TOTAL ELAPSED TIME 27 DAYS

CALIB. PERIOD 24 ELAPSED TIME BETWEEN CALIB. 25.92 HOURS

CALIBRATION FACTORS (SENSITIVITY, TORR/VOLT)

		355T	360T	370T
NITROGEN	BEGIN	.00	71.85	.00
	END	.00	71.28	.00
OXYGEN	BEGIN	.00	82.45	.00
	END	.00	82.07	.00
CO2	BEGIN	.00	5.62	.00
	END	.00	5.71	.00

E. TIME HOURS	PCABIN TORR	T.C. MICR.	N2-PCT MS	O2-PCT MS/MDA	CO2-PCT MS/MDA	H2O-PCT* MS	TOTAL-PCT MS
.3	363.3	7.4	55.2	44.5/42.7	1.2/1.1	1.0	101.9
.6	363.0	7.5	54.4	43.6/42.5	1.2/1.1	1.9	101.1
3.8	364.0	7.4	54.0	43.5/42.7	1.2/1.1	2.1	100.7
5.1	364.8	7.4	54.1	43.6/42.7	1.2/1.1	2.2	101.0
7.3	365.2	7.2	54.0	43.5/42.8	1.2/1.1	2.2	100.9
9.4	365.0	7.0	54.2	43.8/42.8	1.2/1.2	2.3	101.4
11.3	364.0	7.0	54.7	43.9/42.8	1.2/1.1	2.1	101.8
13.3	363.2	7.0	54.8	44.2/42.5	1.2/1.2	2.1	102.2
16.1	362.2	6.8	55.1	44.0/42.5	1.2/1.2	2.1	102.4
19.8	361.1	6.5	55.2	43.7/42.0	1.2/1.2	2.0	102.1
21.8	362.0	6.8	55.2	43.8/42.3	1.2/1.2	2.1	102.2
23.8	363.1	7.0	54.8	44.1/42.3	1.2/1.1	2.0	102.1
25.3	364.0	7.2	54.3	43.7/42.5	1.2/1.1	2.0	101.2
25.6	364.0	7.2	54.2	43.7/42.5	1.2/1.1	1.9	101.1

* COMPUTED USING THE N2 CAL. FACTOR AND THE KNOWN IONIZATION PROBABILITY OF H2O.

MISSION TOTAL ELAPSED TIME 28 DAYS

CALIB. PERIOD 25 ELAPSED TIME BETWEEN CALIB. 21.63 HOURS

CALIBRATION FACTORS (SENSITIVITY, TORR/VOLT)

		355T	360T	370T
NITROGEN	BEGIN	.00	71.28	.00
	END	.00	70.43	.00
OXYGEN	BEGIN	.00	82.07	.00
	END	.00	81.33	.00
CO2	BEGIN	.00	5.71	.00
	END	.00	5.54	.00

E. TIME HOURS	PCABIN TORR	T.C. MICR.	N2-PCT MS	O2-PCT MS/MDA	CO2-PCT MS/MDA	H2O-PCT* MS	TOTAL-PCT MS
.3	365.0	7.5	54.3	43.8/42.5	1.2/1.1	.9	100.2
.4	364.9	7.3	54.3	43.9/42.5	1.2/1.1	1.4	100.8
2.4	366.0	7.2	53.9	43.9/42.3	1.2/1.1	2.1	101.2
4.4	366.0	7.0	54.4	43.9/42.3	1.4/1.2	2.2	101.8
7.4	365.5	7.0	54.4	43.9/42.3	1.4/1.3	2.1	101.8
9.4	365.5	7.0	54.5	43.8/42.3	1.3/1.2	2.1	101.7
11.4	365.0	7.0	54.5	43.9/42.2	1.3/1.2	2.1	101.7
13.8	364.8	6.9	54.9	43.8/42.1	1.2/1.2	2.0	102.0
15.9	364.2	6.8	55.3	43.9/42.1	1.2/1.1	2.0	102.4
17.9	364.5	6.8	55.4	43.8/42.0	1.2/1.1	2.0	102.4
19.9	364.0	6.8	55.4	43.8/42.4	1.2/1.1	2.0	102.4
21.2	364.4	7.0	55.1	43.1/ .0	1.2/ .0	2.2	101.6

* COMPUTED USING THE N2 CAL. FACTOR AND
THE KNOWN IONIZATION PROBABILITY OF H2O.

MISSION TOTAL ELAPSED TIME 29 DAYS

CALIB. PERIOD 26 ELAPSED TIME BETWEEN CALIB. 48.10 HOURS

CALIBRATION FACTORS (SENSITIVITY, TORR/VOLT)

		355T	360T	370T
NITROGEN	BEGIN	.00	70.43	.00
	END	.00	71.28	.00
OXYGEN	BEGIN	.00	81.33	.00
	END	.00	82.07	.00
CO2	BEGIN	.00	5.54	.00
	END	.00	5.71	.00

E. TIME HOURS	PCABIN TORR	T.C. MICR.	N2-PCT MS	O2-PCT MS/MDA	CO2-PCT MS/MDA	H2O-PCT* MS	TOTAL-PCT MS
.2	363.3	7.3	54.3	42.8/ .0	1.2/ .0	2.0	100.3
.9	364.7	7.5	53.9	42.6/42.7	1.3/1.2	2.2	100.0
2.0	365.0	7.5	53.7	42.6/42.3	1.3/1.2	1.9	99.4
3.2	366.0	7.5	53.5	42.9/42.1	1.3/1.3	2.0	99.8
3.3	366.0	7.5	53.5	42.9/42.1	1.3/1.3	2.1	99.9
5.5	367.0	7.5	53.4	43.3/42.0	1.2/1.3	1.9	99.8
9.4	367.0	7.5	53.9	44.0/42.0	1.2/1.2	2.0	101.0
11.6	367.0	7.0	53.9	44.0/42.0	1.2/1.2	2.0	101.1
13.6	366.2	7.0	54.6	43.4/42.3	1.2/1.2	2.1	101.4
15.7	368.0	7.0	54.8	43.4/42.0	1.2/1.2	2.2	101.6
17.7	367.2	7.0	55.1	43.3/42.0	1.3/1.3	2.4	102.2
19.7	366.1	7.0	55.3	43.5/42.0	1.3/1.3	2.3	102.3
25.5	365.4	7.5	54.3	43.2/42.3	1.4/1.3	2.1	100.9
28.2	367.5	7.8	53.8	42.9/ .0	1.5/ .0	2.1	100.4
30.3	368.0	7.8	54.2	43.6/42.0	1.5/1.5	2.1	101.4
32.3	367.8	7.3	54.2	43.6/42.0	1.5/1.5	2.3	101.6
35.8	366.7	7.1	54.6	44.0/42.3	1.4/1.4	2.1	102.1
37.8	365.2	7.0	55.1	44.0/42.1	1.3/1.3	2.0	102.4
39.8	364.0	7.0	55.5	44.1/42.1	1.2/1.2	2.0	102.9
41.9	363.1	7.0	55.7	44.0/42.1	1.1/1.1	2.0	102.8
44.0	363.0	7.0	55.7	44.1/42.1	1.1/1.1	2.2	103.1
46.8	362.0	7.2	55.7	44.0/42.0	1.1/1.0	2.0	102.8
47.6	362.0	7.2	55.5	43.8/42.0	1.1/1.0	2.2	102.5

* COMPUTED USING THE N2 CAL. FACTOR AND
THE KNOWN IONIZATION PROBABILITY OF H2O.

MISSION TOTAL ELAPSED TIME 31 DAYS

CALIB. PERIOD 27 ELAPSED TIME BETWEEN CALIB. 48.87 HOURS

CALIBRATION FACTORS (SENSITIVITY, TORR/VOLT)

		355T	360T	370T
NITROGEN	BEGIN	70.29	.00	69.89
	END	70.86	.00	70.43
OXYGEN	BEGIN	80.93	.00	79.95
	END	81.68	.00	81.01
CO2	BEGIN	5.63	.00	5.36
	END	5.63	.00	5.44

E. TIME HOURS	PCABIN TORR	T.C. MICR.	N2-PCT MS	O2-PCT MS/MDA	CO2-PCT MS/MDA	H2O-PCT* MS	TOTAL-PCT MS
.5	362.2	7.4	55.5	43.5/42.0	1.1/1.1	.7	100.9
.8	361.4	7.3	54.3	42.5/41.9	1.1/1.1	1.6	99.5
1.0	361.5	7.3	54.1	42.3/41.9	1.1/1.1	2.1	99.5
6.9	364.2	7.8	53.6	43.2/42.8	1.1/1.1	2.0	99.9
11.2	363.0	7.0	54.2	43.3/43.0	1.1/1.0	2.0	100.6
14.2	362.0	7.0	54.5	43.7/43.0	1.1/1.0	1.9	101.2
15.9	361.4	7.0	54.8	43.8/42.7	1.0/1.0	1.9	101.6
17.9	360.5	7.0	55.1	43.6/42.5	1.0/1.0	1.9	101.7
19.9	360.5	7.0	55.3	43.6/42.5	1.1/1.0	2.1	102.1
21.7	360.0	7.0	55.2	43.5/42.5	1.0/1.0	2.0	101.8
23.4	360.7	7.1	55.2	43.7/42.2	1.1/1.0	2.0	101.9
25.4	360.7	7.5	54.4	43.0/42.8	1.1/1.1	2.0	100.5
29.4	362.6	7.5	54.0	43.3/42.8	1.3/1.3	1.9	100.5
32.9	363.2	7.3	54.3	43.8/42.2	1.3/1.4	1.9	101.3
35.2	363.0	7.0	54.4	43.6/42.0	1.3/1.4	2.0	101.3
38.4	361.0	7.0	55.1	43.8/42.0	1.2/1.2	2.0	102.0
40.4	360.8	7.0	55.1	44.1/41.8	1.1/1.1	2.0	102.2
43.9	362.0	7.1	54.6	44.4/42.5	1.1/1.1	2.0	102.0
45.4	362.7	7.1	54.7	44.4/42.5	1.1/1.1	2.0	102.2
47.4	362.3	7.2	54.4	44.7/42.5	1.0/1.0	1.9	101.9
47.9	362.5	7.4	54.4	44.9/52.7	1.0/ .9	1.9	102.1
48.6	362.7	7.4	53.8	44.2/42.8	1.0/1.0	1.9	100.8

*COMPUTED USING THE N2 CAL. FACTOR AND
THE KNOWN IONIZATION PROBABILITY OF H2O.

MISSION TOTAL ELAPSED TIME 33 DAYS

CALIB. PERIOD 28 ELAPSED TIME BETWEEN CALIB. 71.40 HOURS

CALIBRATION FACTORS (SENSITIVITY, TORR/VOLT)

		355T	360T	370T
NITROGEN	BEGIN	70.86	.00	70.43
	END	69.18	.00	72.10
OXYGEN	BEGIN	81.68	.00	81.01
	END	79.83	.00	83.21
CO2	BEGIN	5.63	.00	5.44
	END	5.46	.00	5.69

E. TIME HOURS	PCABIN TORR	T.C. MICR.	N2-PCT MS	O2-PCT MS/MDA	CO2-PCT MS/MDA	H2O-PCT* MS	TOTAL-PCT MS
.1	362.8	7.5	54.3	44.6/42.8	1.0/1.0	1.1	101.0
.5	362.7	7.5	54.1	44.4/42.8	1.0/1.0	.6	100.2
1.1	362.6	7.6	53.4	43.5/43.7	1.0/1.0	1.9	99.8
1.1	363.2	7.6	53.3	43.5/43.7	1.0/1.0	1.9	99.7
3.4	362.2	7.5	53.0	43.3/43.0	1.1/1.1	1.9	99.4
6.7	362.0	7.0	53.3	43.4/43.0	1.1/1.1	2.0	99.7
9.4	361.0	8.0	54.4	43.5/43.0	1.1/1.0	2.0	100.9
12.1	361.9	7.0	54.3	43.2/43.0	1.0/1.0	1.8	100.3
13.7	361.5	7.0	54.5	43.2/43.0	1.0/1.0	1.9	100.7
15.7	360.0	6.9	55.0	43.4/42.5	.9/1.0	1.8	101.1
20.5	361.6	6.9	55.9	43.2/42.0	.9/ .9	1.9	102.0
22.5	362.1	7.0	55.6	43.2/41.8	1.0/1.0	2.0	101.7
24.5	365.0	7.3	54.3	43.4/42.0	1.1/1.0	1.9	100.7
26.2	365.1	7.3	54.3	43.0/42.0	1.2/1.1	1.9	100.4
28.5	366.9	7.2	53.9	42.7/42.0	1.3/1.4	2.2	100.1
30.9	375.3	7.2	55.2	41.2/40.3	1.4/1.5	2.2	100.0
35.8	364.0	7.5	56.8	40.6/40.0	1.7/ .5	1.9	101.1
39.3	362.0	6.9	56.2	42.8/41.0	1.5/1.6	1.9	102.4
41.9	363.0	6.9	56.0	43.1/41.5	1.2/1.2	1.9	102.1
44.3	366.0	7.0	55.3	43.8/42.0	1.1/1.0	1.9	102.1
46.3	364.1	7.0	55.3	43.5/41.8	1.1/1.0	2.0	101.9
48.4	363.3	7.3	54.9	43.2/41.6	1.0/ .9	1.9	101.1
50.8	365.9	7.6	53.9	43.2/42.0	1.0/ .8	1.9	99.9
52.4	365.5	7.3	54.0	43.2/42.0	1.0/ .8	1.9	100.1
54.7	365.1	7.1	53.9	43.1/42.0	.9/ .9	2.0	99.9
57.4	362.5	6.9	55.9	44.1/42.0	.9/ .8	2.2	103.1
59.9	361.9	7.0	55.5	44.0/42.0	.8/ .7	2.0	102.2
63.9	362.4	7.0	55.2	44.3/42.1	.8/ .7	2.0	102.3
65.9	365.0	7.0	54.4	44.2/42.1	.9/ .7	2.0	101.5
67.9	365.5	7.0	54.3	44.3/42.3	.8/ .7	2.0	101.3
70.1	365.3	7.0	54.3	44.3/42.5	.8/ .6	2.1	101.4
70.8	365.5	7.0	54.8	44.2/42.5	.8/ .7	2.0	101.8

COMPUTED USING THE N2 CAL. FACTOR AND
THE KNOWN IONIZATION PROBABILITY OF H2O.

MISSION TOTAL ELAPSED TIME 36 DAYS

CALIB. PERIOD 29 ELAPSED TIME BETWEEN CALIB. 49.50 HOURS

CALIBRATION FACTORS (SENSITIVITY, TORR/VOLT)

		355T	360T	370T
NITROGEN	BEGIN	.00	70.15	.00
	END	.00	69.06	.00
OXYGEN	BEGIN	.00	80.96	.00
	END	.00	79.87	.00
CO2	BEGIN	.00	5.54	.00
	END	.00	5.54	.00

E. TIME HOURS	PCABIN TORR	T.C. MICR.	N2-PCT MS	O2-PCT MS/MDA	CO2-PCT MS/MDA	H2O-PCT* MS	TOTAL-PCT MS
.2	365.5	7.0	55.3	44.3/43.0	.8/ .7	1.1	101.5
.7	365.0	7.0	54.4	43.9/43.6	.8/ .7	2.0	101.1
2.5	362.9	7.2	54.3	43.5/42.8	.9/ .8	2.1	100.7
4.7	362.5	7.2	54.3	43.5/43.0	.9/ .8	2.1	100.8
6.4	363.5	7.0	53.9	43.4/42.5	.9/ .9	2.2	100.4
8.5	362.5	6.9	54.4	43.9/42.8	.9/ .9	2.0	101.3
10.5	361.2	6.8	55.2	43.8/42.8	.9/ .8	2.0	101.9
13.7	360.9	6.8	55.0	44.0/42.5	.8/ .7	1.9	101.7
15.7	359.4	6.9	55.4	44.2/42.3	.8/ .7	2.0	102.4
17.7	359.0	6.8	55.2	43.8/42.7	.8/ .7	2.0	101.8
19.7	359.0	6.6	55.0	44.0/42.5	.8/ .7	1.9	101.6
21.9	359.2	6.7	54.9	43.7/42.5	.8/ .7	2.0	101.3
23.9	359.1	6.8	54.9	43.7/42.5	.8/ .7	2.1	101.4
26.0	358.5	7.0	54.5	43.3/42.5	.8/ .7	2.1	100.7
27.9	361.3	7.0	53.7	43.4/43.5	1.0/ .9	2.1	100.1
30.6	362.3	7.0	53.5	43.9/43.2	1.0/ .9	2.0	100.3
33.2	362.2	7.0	53.7	43.9/43.5	1.0/ .0	2.3	100.8
35.3	359.5	6.9	54.2	43.7/42.7	1.0/1.0	2.3	101.3
37.8	359.0	6.9	54.3	44.0/42.8	1.0/ .9	2.2	101.4
39.4	359.8	6.8	54.1	44.1/43.0	1.0/ .9	1.9	101.1
42.7	359.0	6.5	54.7	44.6/43.0	1.0/ .9	1.9	102.2
44.8	358.5	6.5	55.0	44.2/43.0	1.0/ .9	1.9	102.1
47.8	359.0	7.0	54.5	43.6/42.0	1.1/1.0	2.0	101.1
49.1	360.0	7.0	53.9	43.9/42.8	1.1/1.0	1.9	100.8

* COMPUTED USING THE N2 CAL. FACTOR AND THE KNOWN IONIZATION PROBABILITY OF H2O.

MISSION TOTAL ELAPSED TIME 38 DAYS

CALIB. PERIOD 30 ELAPSED TIME BETWEEN CALIB. 46.53 HOURS

CALIBRATION FACTORS (SENSITIVITY, TORR/VOLT)

		355T	360T	370T
NITROGEN	BEGIN	.00	69.06	.00
	END	.00	73.34	.00
OXYGEN	BEGIN	.00	79.87	.00
	END	.00	84.80	.00
CO2	BEGIN	.00	5.54	.00
	END	.00	5.90	.00

E. TIME HOURS	PCABIN TORR	T.C. MICR.	N2-PCT MS	O2-PCT MS/MDA	CO2-PCT MS/MDA	H2O-PCT* MS	TOTAL-PCT MS
.7	359.4	7.0	53.7	43.8/43.4	1.1/1.1	1.9	100.5
3.3	358.9	7.3	53.7	43.4/43.0	1.1/1.1	2.0	100.2
5.8	359.0	7.2	53.9	43.5/43.5	1.2/1.0	2.0	100.6
8.1	358.8	7.0	54.5	44.1/42.8	1.2/1.2	2.0	101.8
10.5	357.0	6.9	55.1	44.5/43.0	1.2/1.1	2.0	102.8
12.5	356.8	6.9	55.3	44.8/43.0	1.2/1.1	2.0	103.3
14.8	358.0	6.7	55.3	45.0/43.5	1.2/1.1	2.0	103.5
16.8	358.0	6.7	55.4	45.4/43.5	1.2/1.1	2.0	104.0
18.3	357.7	6.7	55.6	45.5/43.5	1.1/1.1	2.0	104.2
19.6	357.5	6.6	55.9	45.8/43.5	1.1/1.1	2.0	104.9
22.3	356.9	7.0	55.4	45.4/43.5	1.2/1.1	2.1	104.0
24.0	356.5	7.1	55.2	45.1/43.0	1.2/1.1	2.0	103.4
26.3	358.3	7.0	54.7	45.2/43.5	1.1/1.1	2.0	103.0
28.3	360.4	7.0	55.1	46.0/43.5	1.3/1.2	2.1	104.5
30.3	360.0	7.0	55.7	45.9/43.7	1.2/1.1	1.9	104.7
32.6	359.8	7.1	55.9	46.1/43.5	1.2/1.2	2.2	105.4
33.8	359.2	7.0	56.1	46.2/43.5	1.2/1.1	2.2	105.6
36.0	359.0	6.9	56.2	46.6/43.3	1.2/1.1	2.2	106.2
37.8	358.7	6.8	56.6	46.8/43.0	1.2/1.1	2.2	106.7
39.7	357.9	6.7	56.9	47.0/43.0	1.2/1.1	2.2	107.2
41.5	357.6	6.6	57.1	46.9/43.0	1.1/1.1	2.3	107.4
43.4	358.1	6.7	57.3	46.9/43.0	1.2/1.1	2.5	108.0
46.1	361.9	6.7	53.9	45.0/43.5	1.1/1.1	2.3	102.2

*COMPUTED USING THE N2 CAL. FACTOR AND
THE KNOWN IONIZATION PROBABILITY OF H2O.

MISSION TOTAL ELAPSED TIME 40 DAYS

CALIB. PERIOD 31 ELAPSED TIME BETWEEN CALIB. 23.90 HOURS

CALIBRATION FACTORS (SENSITIVITY, TORR/VOLT)

		355T	360T	370T
NITROGEN	BEGIN	.00	73.34	.00
	END	.00	73.34	.00
OXYGEN	BEGIN	.00	84.80	.00
	END	.00	84.80	.00
CO2	BEGIN	.00	5.90	.00
	END	.00	5.90	.00

E. TIME HOURS	PCABIN TORR	T.C. MICR.	N2-PCT MS	O2-PCT MS/MDA	CO2-PCT MS/MDA	H2O-PCT* MS	TOTAL-PCT MS
.4	361.5	6.6	54.2	45.0/43.2	1.2/1.2	.5	100.9
1.7	361.5	6.9	53.0	44.1/44.2	1.2/1.2	2.1	100.3
2.3	361.0	7.0	52.6	44.4/43.8	1.3/1.2	2.0	100.3
3.8	360.0	6.8	53.0	44.3/43.0	1.3/1.3	2.0	100.6
5.4	359.0	6.7	53.3	44.4/43.7	1.3/1.3	2.0	101.1
6.4	359.9	6.8	53.2	44.1/43.5	1.3/1.3	2.4	100.9
7.4	359.0	6.8	53.5	44.4/43.5	1.3/1.3	2.1	101.4
9.8	357.4	6.7	53.8	44.4/43.5	1.3/1.3	2.1	101.5
10.4	357.0	6.7	53.8	44.4/43.5	1.3/1.3	2.1	101.6
11.4	357.2	6.7	53.8	44.4/43.3	1.3/1.4	2.2	101.7
12.4	357.1	6.7	53.8	44.2/43.2	1.3/1.4	2.2	101.5
13.4	356.8	6.6	53.9	44.2/43.2	1.3/1.3	2.0	101.4
14.4	356.2	6.5	54.1	44.5/43.2	1.3/1.3	2.0	102.0
16.9	355.5	6.6	54.3	44.6/43.2	1.3/1.3	2.0	102.1
18.9	355.2	6.5	54.3	44.6/43.2	1.2/1.2	1.9	102.1
21.5	355.5	6.1	54.3	45.1/43.5	1.1/1.1	2.0	102.5
23.4	355.8	6.7	54.0	44.3/43.4	1.1/1.1	2.2	101.6

*COMPUTED USING THE N2 CAL. FACTOR AND
THE KNOWN IONIZATION PROBABILITY OF H2O.

MISSION TOTAL ELAPSED TIME 41 DAYS

CALIB. PERIOD 32 ELAPSED TIME BETWEEN CALIB. 25.08 HOURS

CALIBRATION FACTORS (SENSITIVITY, TORR/VOLT)

		355T	360T	370T
NITROGEN	BEGIN	.00	65.25	.00
	END	.00	65.01	.00
OXYGEN	BEGIN	.00	75.18	.00
	END	.00	74.86	.00
CO2	BEGIN	.00	5.14	.00
	END	.00	5.14	.00

E. TIME HOURS	PCABIN TORR	T.C. MICR.	N2-PCT MS	O2-PCT MS/MDA	CO2-PCT MS/MDA	H2O-PCT* MS	TOTAL-PCT MS
.3	356.0	7.7	54.6	44.3/43.4	1.2/1.2	.8	100.9
.5	356.0	7.8	53.7	43.9/43.2	1.2/1.2	2.0	100.7
1.5	356.0	7.8	53.5	43.9/43.5	1.2/1.1	2.1	100.7
3.5	356.0	7.6	54.0	42.6/42.2	1.2/1.1	2.0	99.8
5.5	354.0	7.4	54.7	42.9/42.5	1.1/1.1	2.0	100.7
6.5	354.1	7.5	54.9	42.6/42.3	1.2/1.2	2.1	100.7
8.9	354.0	7.5	55.2	42.4/42.0	1.2/1.1	2.1	100.9
12.3	355.0	7.5	55.4	42.7/41.0	1.1/1.0	2.0	101.2
13.3	356.0	7.5	55.2	42.8/41.4	1.1/1.0	2.0	101.2
15.0	361.0	7.7	54.5	44.0/42.1	1.1/1.0	2.0	101.6
17.5	360.5	7.7	55.1	43.2/41.8	1.1/1.1	2.1	101.6
19.5	362.0	7.7	54.8	43.7/42.0	1.2/1.1	2.1	101.7
21.0	362.6	7.8	54.7	43.8/42.0	1.1/1.1	2.1	101.8
23.8	364.5	7.8	54.6	43.6/42.0	1.1/1.0	2.0	101.3
24.7	364.2	7.8	54.4	43.6/42.2	1.1/1.0	2.0	101.1

*COMPUTED USING THE N2 CAL. FACTOR AND
THE KNOWN IONIZATION PROBABILITY OF H2O.

MISSION TOTAL ELAPSED TIME 42 DAYS

CALIB. PERIOD 33 ELAPSED TIME BETWEEN CALIB. 22.52 HOURS

CALIBRATION FACTORS (SENSITIVITY, TORR/VOLT)

		355T	360T	370T
NITROGEN	BEGIN	.00	65.01	.00
	END	.00	64.77	.00
OXYGEN	BEGIN	.00	74.86	.00
	END	.00	74.86	.00
CO2	BEGIN	.00	5.14	.00
	END	.00	5.07	.00

E. TIME HOURS	PCABIN TORR	T.C. MICR.	N2-PCT MS	O2-PCT MS/MDA	CO2-PCT MS/MDA	H2O-PCT* MS	TOTAL-PCT MS
.2	364.1	7.9	55.0	44.0/42.1	1.1/1.0	.9	101.0
2.1	365.1	8.0	53.8	43.5/42.0	1.1/1.1	2.0	100.4
6.3	367.2	8.0	52.9	43.2/42.0	1.2/1.1	2.0	99.4
8.6	367.2	7.9	53.6	43.2/42.0	1.2/1.1	2.1	100.1
11.7	366.0	7.8	53.9	43.8/42.2	1.2/1.1	1.9	100.8
13.7	365.5	7.7	54.3	43.8/42.2	1.2/1.1	1.9	101.2
16.2	364.5	7.7	54.4	44.0/42.1	1.2/1.1	1.9	101.4
18.2	363.8	7.7	54.5	44.0/42.2	1.1/1.1	1.9	101.6
20.0	363.7	7.5	54.7	44.0/42.7	1.1/1.0	1.9	101.7
20.5	363.4	7.6	54.6	43.9/42.5	1.1/1.1	2.0	101.5
22.4	364.0	7.7	54.3	43.8/43.2	1.1/1.1	2.0	101.2

*COMPUTED USING THE N2 CAL. FACTOR AND
THE KNOWN IONIZATION PROBABILITY OF H2O.

MISSION TOTAL ELAPSED TIME 43 DAYS

CALIB. PERIOD 34 ELAPSED TIME BETWEEN CALIB. 45.97 HOURS

CALIBRATION FACTORS (SENSITIVITY, TORR/VOLT)

		355T	360T	370T
NITROGEN	BEGIN	.00	64.77	.00
	END	.00	65.25	.00
OXYGEN	BEGIN	.00	74.86	.00
	END	.00	75.18	.00
CO2	BEGIN	.00	5.07	.00
	END	.00	5.14	.00

E. TIME HOURS	PCABIN TORR	T.C. MICR.	N2-PCT MS	O2-PCT MS/MDA	CO2-PCT MS/MDA	H2O-PCT* MS	TOTAL-PCT MS
.5	363.8	7.7	54.0	43.4/42.6	1.2/1.2	2.0	100.5
1.2	363.5	7.8	53.8	43.5/42.3	1.2/1.2	2.0	100.5
2.7	364.7	7.8	54.0	43.7/42.0	1.3/1.3	2.1	101.2
9.0	365.0	7.8	53.3	43.3/42.0	1.3/1.3	2.0	99.9
12.5	364.2	7.5	53.6	43.8/42.5	1.2/1.2	1.9	100.6
15.4	365.2	7.5	53.5	44.5/43.0	1.2/1.1	1.9	101.2
17.2	365.5	7.5	53.5	44.3/42.8	1.2/1.2	1.9	100.9
19.2	363.0	7.5	53.9	44.4/42.5	1.2/1.2	2.0	101.5
21.6	362.4	7.8	53.8	44.1/42.8	1.2/1.2	1.9	101.0
26.0	362.8	7.8	52.9	44.1/44.0	1.3/1.3	2.0	100.2
28.2	364.3	7.8	52.9	43.9/43.5	1.4/1.4	2.3	100.4
31.5	362.2	7.5	53.4	44.2/43.5	1.3/1.3	2.0	100.8
33.2	361.6	7.5	53.7	44.2/43.5	1.2/1.3	2.0	101.1
34.7	360.8	7.5	53.8	44.8/43.5	1.2/1.2	1.9	101.7
37.2	360.7	7.5	53.8	44.8/43.5	1.2/1.3	1.9	101.7
39.2	359.0	7.2	54.1	45.0/43.5	1.2/1.2	1.9	102.2
41.5	358.2	7.3	54.4	45.1/43.5	1.1/1.1	1.9	102.5
44.0	358.0	7.2	54.3	44.5/43.5	1.1/1.2	2.0	102.0
45.5	358.3	7.6	53.9	44.3/43.5	1.2/1.2	2.0	101.3

*COMPUTED USING THE N2 CAL. FACTOR AND
THE KNOWN IONIZATION PROBABILITY OF H2O.

MISSION TOTAL ELAPSED TIME 45 DAYS

CALIB. PERIOD 35 ELAPSED TIME BETWEEN CALIB. 43.65 HOURS

CALIBRATION FACTORS (SENSITIVITY, TORR/VOLT)

		355T	360T	370T
NITROGEN	BEGIN	.00	65.25	.00
	END	.00	63.84	.00
OXYGEN	BEGIN	.00	75.18	.00
	END	.00	73.63	.00
CO2	BEGIN	.00	5.14	.00
	END	.00	4.93	.00

E. TIME HOURS	PCABIN TORR	T.C. MICR.	N2-PCT MS	O2-PCT MS/MDA	CO2-PCT MS/MDA	H2O-PCT* MS	TOTAL-PCT MS
.2	357.9	7.6	54.0	44.7/43.7	1.3/1.3	.8	100.8
3.7	359.5	7.6	54.2	44.5/43.5	1.3/1.3	2.0	101.9
7.6	358.6	7.6	54.2	44.5/43.3	1.2/1.2	1.9	101.8
8.7	358.4	7.4	54.4	44.5/43.3	1.3/1.3	2.0	102.1
11.1	357.5	7.3	54.8	45.0/43.4	1.3/1.3	1.9	103.0
13.6	356.9	7.2	55.0	44.6/43.2	1.4/1.4	2.1	103.1
15.7	355.5	7.1	55.2	44.7/43.2	1.3/1.3	2.2	103.4
17.1	355.0	7.2	55.0	44.5/43.3	1.3/1.3	2.0	102.8
19.0	358.0	7.6	53.8	44.3/43.7	1.2/1.3	2.0	101.3
20.1	358.0	7.7	53.2	43.9/43.7	1.3/1.3	1.9	100.3
21.3	359.0	7.7	52.9	43.9/ .0	1.2/ .0	1.9	100.0
24.2	361.0	7.7	52.1	43.6/43.7	1.3/1.3	1.8	98.9
25.2	361.1	7.7	52.5	43.8/43.8	1.3/1.4	1.9	99.5
27.1	361.2	7.5	52.9	43.8/43.7	1.3/1.3	2.0	100.0
29.1	360.7	7.5	53.1	44.0/43.9	1.4/1.4	2.0	100.5
31.1	359.1	7.5	53.3	44.4/43.9	1.3/1.4	1.9	100.9
33.1	357.9	7.5	53.6	44.5/44.0	1.3/1.3	1.9	101.3
35.4	357.2	7.4	53.7	44.1/43.2	1.3/1.3	1.8	100.9
37.6	356.9	7.4	53.6	44.1/42.8	1.2/1.3	1.9	100.8
39.8	356.2	7.3	53.7	44.1/43.0	1.2/1.2	1.9	101.0
41.8	356.0	7.4	53.8	44.1/43.3	1.1/1.2	1.9	101.0
42.8	357.8	7.5	53.4	44.3/ .0	1.1/ .0	1.9	100.7

*COMPUTED USING THE N2 CAL. FACTOR AND
THE KNOWN IONIZATION PROBABILITY OF H2O.

MISSION TOTAL ELAPSED TIME 47 DAYS

CALIB. PERIOD 36 ELAPSED TIME BETWEEN CALIB. 70.33 HOURS

CALIBRATION FACTORS (SENSITIVITY, TORR/VOLT)

		355T	360T	370T
NITROGEN	BEGIN	.00	63.84	.00
	END	.00	64.07	.00
OXYGEN	BEGIN	.00	73.63	.00
	END	.00	74.86	.00
CO2	BEGIN	.00	4.93	.00
	END	.00	5.14	.00

E. TIME HOURS	PCABIN TORR	T.C. MICR.	N2-PCT MS	O2-PCT MS/MDA	CO2-PCT MS/MDA	H2O-PCT* MS	TOTAL-PCT MS
.9	357.5	7.7	52.5	43.3/ .0	1.1/ .0	1.8	98.7
2.2	358.0	7.6	52.1	43.6/43.5	1.2/1.2	1.9	98.8
3.2	358.0	7.6	51.9	43.4/43.3	1.2/1.2	1.8	98.4
5.2	358.9	7.4	51.8	43.5/43.5	1.2/1.3	1.9	98.4
7.4	357.0	7.3	53.0	44.2/43.3	1.2/1.2	1.9	100.3
9.9	356.0	7.3	52.9	44.4/43.5	1.2/1.1	1.9	100.4
11.7	355.0	7.3	53.3	44.5/43.5	1.2/1.1	1.9	100.8
12.8	355.0	7.2	53.6	44.7/43.5	1.2/1.1	1.9	101.4
14.7	358.0	7.2	53.2	45.4/44.0	1.2/1.2	2.0	101.8
15.8	357.9	7.3	53.4	45.2/43.8	1.2/1.2	2.0	101.8
17.1	357.3	7.3	53.3	45.1/43.5	1.3/1.3	2.1	101.8
19.2	355.0	7.1	53.8	45.2/43.2	1.3/1.3	2.0	102.3
20.6	355.4	7.2	53.8	44.6/43.0	1.2/1.2	2.0	101.5
22.5	355.0	7.4	53.5	44.2/44.0	1.2/1.2	2.0	100.9
23.9	356.2	7.5	52.8	43.9/43.8	1.3/1.3	2.1	100.0
25.6	357.1	7.5	52.5	44.0/44.0	1.2/1.2	2.0	99.7
26.7	357.8	7.6	52.2	43.9/44.0	1.2/1.2	1.9	99.2
28.7	359.0	7.5	52.2	44.0/44.0	1.3/1.3	2.1	99.5
31.1	358.0	7.5	53.0	44.5/44.0	1.3/1.2	2.0	100.8
33.2	359.7	7.5	53.0	45.0/44.3	1.3/1.3	2.0	101.3
36.2	362.2	7.4	53.5	44.7/44.0	1.3/1.2	2.2	101.7
38.6	360.2	7.2	54.5	45.0/43.7	1.3/1.2	2.2	103.0
41.4	358.9	7.2	54.9	44.5/43.3	1.4/1.3	1.9	102.8
43.8	357.3	7.2	55.3	44.6/43.3	1.2/1.2	1.9	103.0
45.7	357.0	7.3	54.7	44.2/43.0	1.2/1.1	1.9	101.9
47.7	358.2	7.5	53.2	43.7/43.0	1.1/1.1	2.0	100.0
52.3	362.5	7.5	52.6	44.2/43.7	1.1/1.0	1.9	99.9
54.3	362.6	7.7	53.0	44.4/43.7	1.2/1.1	2.0	100.6
56.2	361.0	7.3	53.9	44.6/43.5	1.1/1.1	2.0	101.7
58.6	360.3	7.5	54.2	44.5/43.2	1.1/1.1	2.5	102.4
60.5	358.9	7.5	54.4	44.5/43.0	1.1/1.1	2.0	102.0
62.7	357.1	7.4	54.5	44.8/43.0	1.1/1.1	2.0	102.5
65.3	357.1	7.3	54.7	44.6/43.2	1.2/1.2	2.0	102.5
67.2	357.0	7.3	54.9	44.6/43.2	1.2/1.2	2.0	102.8
69.2	356.5	7.3	54.5	44.7/43.0	1.2/1.1	2.0	102.4
69.9	357.0	7.7	54.0	44.2/43.3	1.2/1.1	2.1	101.5

*COMPUTED USING THE N2 CAL. FACTOR AND
THE KNOWN IONIZATION PROBABILITY OF H2O.

MISSION TOTAL ELAPSED TIME 50 DAYS

CALIB. PERIOD 37 ELAPSED TIME BETWEEN CALIB. 47.95 HOURS

CALIBRATION FACTORS (SENSITIVITY, TORR/VOLT)

		355T	360T	370T
NITROGEN	BEGIN	.00	64.07	.00
	END	.00	65.01	.00
OXYGEN	BEGIN	.00	74.86	.00
	END	.00	75.49	.00
CO2	BEGIN	.00	5.14	.00
	END	.00	5.00	.00

E. TIME HOURS	PCABIN TORR	T.C. MICR.	N2-PCT MS	O2-PCT MS/MDA	CO2-PCT MS/MDA	H2O-PCT* MS	TOTAL-PCT MS
.4	357.3	7.8	51.7	44.0/43.0	1.2/1.1	2.2	99.0
.6	357.4	7.7	52.9	43.4/43.0	1.2/1.1	2.5	99.9
3.6	368.0	8.2	51.8	43.2/44.2	1.2/1.3	2.3	98.4
5.3	370.8	8.2	51.2	42.8/43.5	1.1/1.1	2.9	98.1
9.5	364.0	8.0	52.4	43.7/43.0	1.2/1.1	2.5	99.8
11.1	361.7	7.8	53.0	43.5/42.8	1.2/1.2	2.7	100.4
12.8	358.8	7.8	53.2	43.5/42.8	1.2/1.1	2.4	100.4
14.6	356.8	7.7	53.9	44.0/42.5	1.2/1.1	2.3	101.4
15.7	356.0	7.7	54.1	44.3/42.7	1.2/1.1	2.3	101.8
17.6	358.4	7.8	53.7	45.5/43.5	1.1/1.0	2.1	102.5
18.7	357.4	7.7	53.7	45.4/43.5	1.1/1.0	2.1	102.3
20.5	358.8	7.8	53.5	45.6/44.0	1.1/ .9	2.1	102.4
22.2	359.0	8.0	52.8	45.6/44.5	1.1/ .9	2.1	101.7
25.1	362.0	8.3	51.0	44.9/45.0	1.1/1.1	2.1	99.0
27.1	360.8	8.5	50.5	44.4/45.0	1.1/1.2	2.1	98.1
29.1	360.5	8.5	50.6	44.2/44.8	1.1/1.3	2.1	98.0
31.2	359.0	8.0	51.5	44.9/44.0	1.1/1.2	2.1	99.6
34.5	356.2	8.0	51.1	45.2/44.0	1.1/1.1	2.1	99.5
35.8	356.0	7.8	53.9	45.3/43.8	1.1/1.1	2.1	102.3
37.7	357.0	7.7	54.5	45.0/73.5	1.1/1.1	2.1	102.7
38.8	357.3	7.7	54.6	44.7/42.8	1.1/1.2	2.1	102.6
40.8	361.0	7.6	55.0	45.1/42.8	1.1/1.2	2.0	103.3
42.8	362.0	7.5	55.2	45.4/43.0	1.2/1.3	2.3	104.1
44.7	361.1	7.8	55.0	45.3/42.8	1.2/1.2	2.1	103.7
46.8	362.3	8.0	53.8	44.4/43.5	1.1/1.1	2.2	101.5
47.3	362.8	8.3	53.4	44.3/ .0	1.1/ .0	2.1	101.0

*COMPUTED USING THE N2 CAL. FACTOR AND
THE KNOWN IONIZATION PROBABILITY OF H2O.

MISSION TOTAL ELAPSED TIME 52 DAYS

CALIB. PERIOD 38 ELAPSED TIME BETWEEN CALIB. 73.60 HOURS

CALIBRATION FACTORS (SENSITIVITY, TORR/VOLT)

		355T	360T	370T
NITROGEN	BEGIN	.00	65.01	.00
	END	.00	63.39	.00
OXYGEN	BEGIN	.00	75.49	.00
	END	.00	73.33	.00
CO2	BEGIN	.00	5.00	.00
	END	.00	4.93	.00

E. TIME HOURS	PCABIN TORR	T.C. MICR.	N2-PCT MS	O2-PCT MS/MDA	CO2-PCT MS/MDA	H2O-PCT* MS	TOTAL-PCT MS
.6	362.5	7.5	53.4	44.3/43.2	1.2/1.1	.7	99.6
3.7	367.5	8.8	50.5	43.5/44.5	1.1/ .0	2.0	97.1
5.4	369.5	9.0	50.2	43.2/44.3	1.2/1.0	2.1	96.8
8.2	367.5	8.9	50.8	43.4/43.9	1.2/1.3	2.1	97.5
10.9	365.8	8.6	52.1	43.6/43.9	1.2/1.3	2.1	98.9
13.7	363.2	8.0	53.1	44.0/43.5	1.2/1.3	2.1	100.4
14.8	362.4	8.0	53.4	43.9/43.0	1.2/1.2	2.1	100.6
16.9	360.8	7.9	53.9	44.5/43.0	1.1/1.2	2.0	101.6
19.1	360.8	7.7	54.8	45.3/43.0	1.1/1.2	2.0	103.2
20.6	360.5	7.5	55.0	45.3/43.0	1.1/1.2	2.2	103.6
22.9	360.0	7.5	54.3	44.7/43.0	1.1/1.2	2.3	102.3
25.0	361.8	7.9	52.7	44.0/ .0	1.2/ .0	2.3	100.2
26.7	361.7	7.7	52.7	44.0/43.0	1.2/1.2	2.2	100.2
28.4	360.9	7.5	52.8	43.4/43.0	1.2/1.2	2.3	99.8
32.2	359.0	8.0	53.4	43.8/42.5	1.2/1.2	2.3	100.7
34.4	358.0	7.9	53.5	43.7/42.2	1.2/1.1	2.2	100.5
36.5	357.1	7.9	53.8	43.8/42.3	1.1/1.1	2.1	100.8
38.8	358.0	7.7	53.8	44.2/42.7	1.2/1.2	2.2	101.3
41.8	359.0	7.7	53.7	45.1/43.0	1.1/1.1	2.1	102.0
44.7	360.8	7.7	53.6	45.0/43.2	1.2/1.2	2.3	102.1
46.7	360.2	7.8	53.5	44.9/43.2	1.2/1.2	2.2	101.7
50.1	362.0	7.7	52.6	44.6/43.4	1.2/1.2	2.3	100.6
52.1	362.0	7.5	52.7	44.7/43.5	1.2/1.2	2.1	100.7
54.2	362.2	7.5	52.7	44.9/43.5	1.2/1.2	2.3	101.1
56.3	362.3	7.7	52.8	44.8/43.7	1.2/1.2	2.3	101.1
60.2	361.2	7.5	52.9	44.9/43.8	1.2/1.2	2.3	101.3
62.6	360.5	7.6	53.1	44.7/43.7	1.2/1.2	2.2	101.3
64.6	360.8	7.6	52.9	44.7/43.3	1.2/1.2	2.3	101.1
66.7	359.9	7.5	53.0	44.7/43.7	1.2/1.2	2.1	101.0
68.7	359.5	7.5	53.0	44.8/44.0	1.1/1.1	2.1	100.9
70.8	360.3	7.8	52.8	44.6/44.1	1.1/1.1	2.2	100.7
73.0	362.0	7.6	52.0	44.4/44.1	1.1/1.1	2.3	99.8

*COMPUTED USING THE N2 CAL. FACTOR AND
THE KNOWN IONIZATION PROBABILITY OF H2O.

MISSION TOTAL ELAPSED TIME 55 DAYS

CALIB. PERIOD 39 ELAPSED TIME BETWEEN CALIB. 48.48 HOURS

CALIBRATION FACTORS (SENSITIVITY, TORR/VOLT)

		355T	360T	370T
NITROGEN	BEGIN	.00	63.39	.00
	END	.00	62.94	.00
OXYGEN	BEGIN	.00	73.33	.00
	END	.00	72.44	.00
CO2	BEGIN	.00	4.93	.00
	END	.00	4.86	.00

E. TIME HOURS	PCABIN TORR	T.C. MICR.	N2-PCT MS	O2-PCT MS/MDA	CO2-PCT MS/MDA	H2O-PCT* MS	TOTAL-PCT MS
.1	361.5	7.7	52.8	45.0/44.1	1.1/1.1	.9	99.8
1.8	362.2	7.7	51.8	44.1/44.2	1.1/1.1	2.1	99.1
3.5	362.3	7.5	52.1	44.5/44.2	1.1/1.2	2.2	99.9
5.7	362.0	7.2	52.8	44.7/44.2	1.2/1.1	2.3	100.9
7.6	360.0	7.2	53.6	44.7/44.0	1.1/1.1	2.2	101.7
9.6	359.1	7.3	53.9	44.8/43.6	1.1/1.0	2.1	101.9
12.6	359.0	7.3	53.8	44.8/43.5	1.1/1.1	2.2	101.8
14.6	358.6	7.2	53.8	44.8/43.5	1.1/1.1	2.2	102.0
16.6	358.0	7.3	54.0	44.9/43.5	1.1/1.1	2.1	102.2
18.6	357.5	7.2	54.1	44.9/43.5	1.1/1.1	2.1	102.2
20.6	357.5	7.5	53.4	44.5/43.5	1.1/1.0	2.2	101.1
23.4	360.0	7.7	52.3	43.9/43.5	1.1/1.0	2.2	99.5
25.4	361.5	7.7	51.7	43.7/43.5	1.1/1.0	2.2	98.7
27.5	362.1	7.7	51.6	43.8/43.8	1.1/1.1	2.1	98.7
29.9	361.9	7.5	52.1	44.2/43.9	1.1/1.1	2.2	99.7
31.6	360.6	7.6	52.3	44.2/43.9	1.2/1.1	2.3	100.0
33.7	359.3	7.6	52.7	44.1/43.5	1.2/1.2	2.2	100.2
35.9	358.8	7.2	52.5	44.4/43.5	1.2/1.2	2.2	100.3
38.0	357.2	7.3	53.5	44.3/43.1	1.2/1.1	2.3	101.3
40.1	356.0	7.2	53.6	44.5/43.2	1.2/1.1	2.2	101.4
42.2	356.1	7.2	53.6	44.4/43.1	1.3/1.3	2.3	101.6
45.5	356.8	7.2	53.5	44.1/43.2	1.2/1.2	2.1	100.9
47.6	356.5	7.2	53.1	43.7/43.0	1.3/1.2	2.2	100.3
47.8	356.4	7.5	53.0	43.5/ .0	1.2/ .0	2.2	99.9

*COMPUTED USING THE N2 CAL. FACTOR AND
THE KNOWN IONIZATION PROBABILITY OF H2O.

MISSION TOTAL ELAPSED TIME 57 DAYS

CALIB. PERIOD 40 ELAPSED TIME BETWEEN CALIB. 47.58 HOURS

CALIBRATION FACTORS (SENSITIVITY, TORR/VOLT)

		355T	360T	370T
NITROGEN	BEGIN	.00	62.94	.00
	END	.00	63.84	.00
OXYGEN	BEGIN	.00	72.44	.00
	END	.00	73.93	.00
CO2	BEGIN	.00	4.86	.00
	END	.00	4.93	.00

E. TIME HOURS	PCABIN TORR	T.C. MICR.	N2-PCT MS	O2-PCT MS/MDA	CO2-PCT MS/MDA	H2O-PCT* MS	TOTAL-PCT MS
.2	356.2	7.6	53.5	44.5/ .0	1.3/ .0	.8	100.2
3.2	358.5	7.6	52.2	43.3/44.0	1.2/1.3	2.1	98.9
5.0	359.0	7.7	52.0	43.7/43.2	.0/1.2	2.2	97.8
7.0	359.0	7.7	52.2	44.1/43.7	1.2/1.2	2.2	99.7
9.0	358.0	7.6	52.4	44.3/43.8	1.2/1.1	2.1	99.9
11.0	357.0	7.5	52.7	44.4/43.5	1.1/1.1	2.0	100.3
12.8	357.9	7.4	52.4	44.6/43.5	1.1/1.1	2.1	100.3
15.0	357.2	7.4	52.7	44.9/43.5	1.1/1.1	2.0	100.8
17.0	357.0	7.3	52.8	45.0/43.5	1.2/1.2	2.2	101.2
19.0	356.5	7.2	52.9	45.1/44.0	1.2/1.1	2.1	101.2
21.0	356.0	7.2	52.8	45.0/44.0	1.1/1.1	2.1	101.0
23.3	359.8	7.8	52.1	44.3/43.6	1.2/1.1	2.3	99.9
25.1	362.2	7.8	51.6	43.9/43.8	1.2/1.2	2.2	98.9
27.1	361.0	7.6	52.2	44.1/43.5	1.2/1.2	2.1	99.6
29.2	359.6	7.7	52.4	44.1/43.7	1.2/1.2	2.1	99.8
31.8	357.8	7.5	53.1	44.3/43.7	1.2/1.2	2.1	100.8
33.8	357.0	7.4	53.4	44.5/43.1	1.2/1.3	2.1	101.2
35.8	357.0	7.3	53.6	44.9/42.7	1.3/1.3	2.1	101.9
38.0	357.1	7.1	54.0	45.0/42.7	1.3/1.3	2.2	102.4
40.0	358.8	7.1	53.8	45.6/43.2	1.2/1.2	2.2	102.8
41.8	359.5	7.2	53.7	45.7/43.2	1.2/1.2	2.2	102.9
43.7	360.0	7.3	53.3	45.7/43.4	1.2/1.2	2.2	102.4
46.4	362.0	7.8	52.4	45.1/43.8	1.2/ .0	2.2	100.8
47.0	361.1	7.7	52.0	44.8/ .0	1.2/ .0	2.1	100.1

* COMPUTED USING THE N2 CAL. FACTOR AND THE KNOWN IONIZATION PROBABILITY OF H2O.

MISSION TOTAL ELAPSED TIME 59 DAYS

CALIB. PERIOD 41 ELAPSED TIME BETWEEN CALIB. 42.93 HOURS

CALIBRATION FACTORS (SENSITIVITY, TORR/VOLT)

		355T	360T	370T
NITROGEN	BEGIN	.00	63.39	.00
	END	.00	63.39	.00
OXYGEN	BEGIN	.00	73.33	.00
	END	.00	72.73	.00
CO2	BEGIN	.00	4.80	.00
	END	.00	5.07	.00

E. TIME HOURS	PCABIN TORR	T.C. MICR.	N2-PCT MS	O2-PCT MS/MDA	CO2-PCT MS/MDA	H2O-PCT* MS	TOTAL-PCT MS
.2	361.0	8.0	52.3	44.9/43.6	1.2/1.2	.7	99.0
3.3	361.8	7.9	51.0	44.2/44.2	1.2/1.2	2.1	98.4
5.2	359.8	7.8	51.8	44.2/44.6	1.2/1.2	2.1	99.3
7.3	358.0	7.7	52.4	44.2/44.5	1.2/1.2	2.1	99.9
9.5	358.4	7.7	52.7	44.5/43.6	1.1/1.1	2.2	100.6
11.6	358.0	7.5	52.9	44.6/43.5	1.1/1.1	2.3	100.9
13.1	357.4	7.3	53.0	44.6/43.3	1.1/1.1	2.3	101.0
15.3	358.5	7.2	52.9	44.5/43.1	1.1/1.1	2.3	100.7
17.3	358.8	7.2	53.2	44.8/43.1	1.1/1.1	2.3	101.4
19.3	359.2	7.2	52.9	44.7/43.2	1.1/1.1	2.3	101.1
21.8	360.0	7.2	52.6	44.4/ .0	1.1/ .0	2.3	100.5
23.5	359.8	7.5	52.1	43.6/43.5	1.2/1.1	2.2	99.2
27.6	361.5	7.6	51.9	43.4/43.0	1.3/1.2	2.2	98.8
29.3	362.0	7.5	52.0	43.7/43.5	1.4/1.3	2.3	99.4
31.4	361.8	7.6	52.2	43.9/43.5	1.4/1.3	2.2	99.7
33.5	361.0	7.6	52.5	44.0/43.6	1.3/1.3	2.3	100.2
35.5	359.9	7.6	52.8	44.3/43.6	1.3/ .0	2.1	100.6
37.2	359.0	7.4	53.1	44.2/43.0	1.3/1.2	2.2	100.9
39.4	359.0	7.2	53.1	44.0/43.0	1.3/1.2	2.1	100.6
40.8	358.2	7.3	53.6	44.1/42.8	1.3/1.2	2.1	101.1
41.9	357.2	7.3	53.6	44.0/43.8	1.2/1.1	2.1	100.9
42.7	357.3	7.3	53.6	44.0/43.2	1.2/1.1	2.1	100.9

*COMPUTED USING THE N2 CAL. FACTOR AND
THE KNOWN IONIZATION PROBABILITY OF H2O.

CASE 2

MISSION TOTAL ELAPSED TIME 1 DAYS

CALIB. PERIOD 1 ELAPSED TIME BETWEEN CALIB. 40.48 HOURS

CALIBRATION FACTORS (SENSITIVITY, TORR/VOLT)

		355T	360T	370T
NITROGEN	BEGIN	70.01	.00	69.62
OXYGEN	BEGIN	80.20	.00	80.30
CO2	BEGIN	5.14	.00	5.07

TWO GAS SENSOR COMPARATIVE DATA

TIME HR	N2 TOR	O2 TOR	CO2 TOR	H2O* TOR	O2-PCT MS/MDA	CO2-PCT MS/MDA	TOTAL-TOR MS/MDA	TOTAL-PCT MS
.4	207.1	166.0	3.2	2.8	45.0/42.7	.9/ .6	379.2/369.0	102.8
.5	205.0	163.6	3.2	6.5	44.3/42.7	.9/ .6	378.4/369.0	102.5
1.8	202.3	161.2	3.2	8.0	43.6/42.5	.9/ .7	374.7/370.0	101.3
4.9	200.9	160.3	3.4	7.5	42.2/42.0	.9/ .7	372.1/380.0	97.9
9.1	200.2	160.4	3.3	7.8	43.3/42.0	.9/ .7	371.7/370.1	100.4
14.1	197.0	152.3	4.0	7.7	40.7/42.0	1.1/ .9	361.1/374.1	96.5
26.1	193.6	153.9	3.6	7.5	40.9/40.5	1.0/1.0	358.7/376.0	95.4
31.6	189.8	156.4	3.9	7.5	42.1/41.5	1.0/1.0	357.6/371.5	96.2
35.1	184.8	154.8	4.3	7.5	41.8/41.8	1.2/1.0	351.4/370.2	94.9
37.1	180.5	152.4	4.6	8.3	41.4/41.5	1.2/ .7	345.8/368.5	93.8
39.8	179.8	154.0	4.9	8.2	41.8/41.4	1.3/1.2	346.9/368.5	94.1

*COMPUTED USING THE N2 CAL. FACTOR AND
THE KNOWN IONIZATION PROBABILITY OF H2O.

MISSION TOTAL ELAPSED TIME 3 DAYS

CALIB. PERIOD 2 ELAPSED TIME BETWEEN CALIB. 21.17 HOURS

CALIBRATION FACTORS (SENSITIVITY, TORR/VOLT)

		355T	360T	370T
NITROGEN	BEGIN	76.43	.00	75.07
OXYGEN	BEGIN	88.66	.00	87.15
CO2	BEGIN	5.82	.00	5.44

TWO GAS SENSOR COMPARATIVE DATA

TIME HR	N2 TOR	O2 TOR	CO2 TOR	H2O* TOR	O2-PCT MS/MDA	CO2-PCT MS/MDA	TOTAL-TOR MS/MDA	TOTAL-PCT MS
.5	202.0	175.1	5.8	2.6	47.6/42.0	1.6/1.2	385.6/368.0	104.8
1.0	195.0	169.6	5.6	9.0	46.2/ .0	1.5/ .0	379.2/367.0	103.3
1.9	195.2	170.8	5.7	8.8	46.4/43.2	1.6/1.5	380.5/368.2	103.4
2.9	193.0	166.6	5.8	9.5	45.6/42.8	1.6/1.5	374.8/365.0	102.7
3.3	189.7	164.7	5.6	9.8	45.2/42.8	1.5/ .7	369.8/364.2	101.5
5.3	192.3	166.9	5.6	9.2	46.1/41.9	1.5/ .0	374.0/362.1	103.3
9.5	191.7	162.0	4.5	8.1	45.1/42.4	1.3/1.3	366.3/359.3	101.9
16.3	190.3	159.0	3.9	9.6	43.4/42.0	1.1/ .9	362.7/366.5	99.0
17.7	187.6	165.7	3.6	9.3	45.4/42.2	1.0/ .9	366.2/364.8	100.4
19.9	185.5	162.6	3.7	10.2	44.9/41.8	1.0/ .8	362.0/362.2	99.9
20.3	183.7	161.5	3.7	10.1	44.7/41.9	1.0/ .6	359.0/361.0	99.4
20.6	183.4	160.3	3.7	9.8	44.6/41.7	1.0/ .8	357.3/359.5	99.4

*COMPUTED USING THE N2 CAL. FACTOR AND
THE KNOWN IONIZATION PROBABILITY OF H2O.

MISSION TOTAL ELAPSED TIME 4 DAYS

CALIB. PERIOD 3 ELAPSED TIME BETWEEN CALIB. 27.03 HOURS

CALIBRATION FACTORS (SENSITIVITY, TORR/VOLT)

		355T	360T	370T
NITROGEN	BEGIN	72.02	.00	76.32
OXYGEN	BEGIN	91.42	.00	89.70
CO2	BEGIN	6.02	.00	5.78

TWO GAS SENSOR COMPARATIVE DATA

TIME HR	N2 TOR	O2 TOR	CO2 TOR	H2O* TOR	O2-PCT MS/MDA	CO2-PCT MS/MDA	TOTAL-TOR MS/MDA	TOTAL-PCT MS
.5	188.3	175.5	4.3	2.1	48.5/32.7	1.2/ .9	370.2/361.6	102.4
1.6	178.2	169.3	4.1	8.8	46.7/42.5	1.1/1.0	360.4/362.2	99.5
2.3	180.8	164.4	4.3	7.9	46.2/42.0	1.2/1.2	357.5/356.2	100.4
2.7	180.2	165.3	4.2	7.6	46.4/42.1	1.2/1.3	357.3/356.0	100.4
3.7	180.5	172.2	4.1	9.5	47.4/43.0	1.1/1.0	366.4/363.2	100.9
4.7	181.1	166.6	4.3	7.9	46.5/42.7	1.2/1.1	359.9/358.0	100.5
5.8	179.9	164.5	4.2	7.5	46.1/42.1	1.2/1.4	356.0/356.5	99.9
6.0	180.8	166.9	4.2	7.5	46.4/43.1	1.2/1.2	359.5/359.5	100.0
8.4	181.6	168.4	4.0	7.4	47.6/43.7	1.1/1.1	361.4/354.0	102.1
24.0	176.8	163.6	4.5	8.4	45.9/43.5	1.3/1.2	353.2/356.6	99.1
26.4	180.1	162.8	4.5	7.4	45.6/42.9	1.3/1.4	354.9/357.2	99.3

* COMPUTED USING THE N2 CAL. FACTOR AND THE KNOWN IONIZATION PROBABILITY OF H2O.

MISSION TOTAL ELAPSED TIME 5 DAYS

CALIB. PERIOD 4 ELAPSED TIME BETWEEN CALIB. 23.45 HOURS

CALIBRATION FACTORS (SENSITIVITY, TORR/VOLT)

		355T	360T	370T
NITROGEN	BEGIN	72.62	.00	78.62
OXYGEN	BEGIN	92.37	.00	91.03
CO2	BEGIN	6.02	.00	5.78

TWO GAS SENSOR COMPARATIVE DATA

TIME HR	N2 TOR	O2 TOR	CO2 TOR	H2O* TOR	O2-PCT MS/MDA	CO2-PCT MS/MDA	TOTAL-TOR MS/MDA	TOTAL-PCT MS
.3	190.7	171.7	4.8	2.5	47.9/42.5	1.4/1.2	369.9/358.5	103.2
1.4	184.2	167.7	4.8	7.5	46.3/42.6	1.3/1.2	364.2/362.0	100.6
3.0	184.1	171.8	5.4	4.6	47.1/42.9	1.5/ .5	365.9/364.5	100.4
11.2	182.4	173.9	5.1	7.4	47.5/43.0	1.4/1.3	368.8/366.2	100.7
15.5	183.0	175.0	4.8	7.4	47.7/43.0	1.3/1.3	370.2/367.1	100.8
19.4	183.9	172.4	4.8	7.6	46.9/43.0	1.3/1.2	368.6/367.7	100.2
22.7	182.1	168.6	5.0	7.5	45.9/42.7	1.4/ .7	363.2/367.2	98.9
23.0	182.1	168.6	5.0	7.3	45.9/42.9	1.4/1.2	363.0/367.2	98.9

*COMPUTED USING THE N2 CAL. FACTOR AND
THE KNOWN IONIZATION PROBABILITY OF H2O.

MISSION TOTAL ELAPSED TIME 6 DAYS

CALIB. PERIOD 5 ELAPSED TIME BETWEEN CALIB. 24.52 HOURS

CALIBRATION FACTORS (SENSITIVITY, TORR/VOLT)

		355T	360T	370T
NITROGEN	BEGIN	77.44	.00	76.97
OXYGEN	BEGIN	93.35	.00	92.41
CO2	BEGIN	6.02	.00	5.87

TWO GAS SENSOR COMPARATIVE DATA

TIME HR	N2 TOR	O2 TOR	CO2 TOR	H2O* TOR	O2-PCT MS/MDA	CO2-PCT MS/MDA	TOTAL-TOR MS/MDA	TOTAL-PCT MS
2.2	192.6	171.5	5.2	1.8	46.7/42.0	1.4/1.2	371.0/367.4	101.0
2.6	191.1	169.6	5.2	1.4	46.2/ .0	1.4/ .0	367.3/367.5	99.9
2.7	185.7	167.8	5.1	7.0	45.6/ .0	1.4/ .0	365.5/367.6	99.4
18.3	196.2	172.0	5.5	7.8	47.3/41.9	1.5/ .6	381.5/363.8	104.9
20.6	194.7	174.8	4.9	8.0	48.0/41.9	1.3/1.3	382.3/364.0	105.0
21.6	194.8	174.9	4.8	8.2	47.9/41.9	1.3/1.3	382.7/365.0	104.8
23.3	191.7	173.1	4.7	7.7	47.3/42.0	1.3/1.2	377.2/365.7	103.2
23.9	191.7	174.1	4.7	8.2	47.6/41.8	1.3/1.2	378.6/365.8	103.5
24.0	190.9	172.2	4.7	8.2	47.1/41.8	1.3/1.2	376.1/365.8	102.8

* COMPUTED USING THE N2 CAL. FACTOR AND
THE KNOWN IONIZATION PROBABILITY OF H2O.

MISSION TOTAL ELAPSED TIME 7 DAYS

CALIB. PERIOD 6 ELAPSED TIME BETWEEN CALIB. 27.03 HOURS

CALIBRATION FACTORS (SENSITIVITY, TORR/VOLT)

		355T	360T	370T
NITROGEN	BEGIN	78.48	.00	78.29
OXYGEN	BEGIN	90.95	.00	89.70
CO2	BEGIN	5.82	.00	5.69

TWO GAS SENSOR COMPARATIVE DATA

TIME HR	N2 TOR	O2 TOR	CO2 TOR	H2O* TOR	O2-PCT MS/MDA	CO2-PCT MS/MDA	TOTAL-TOR MS/MDA	TOTAL-PCT MS
.6	170.2	147.7	4.1	2.1	40.3/ .0	1.1/ .0	324.2/366.3	88.5
.9	169.9	146.5	3.5	1.7	41.0/ .0	1.0/ .0	321.6/357.0	90.1
.9	169.9	146.5	3.5	1.7	41.0/ .0	1.0/ .0	321.6/357.0	90.1
2.0	167.8	145.0	4.0	7.1	39.6/42.5	1.1/1.2	323.9/366.2	88.5
10.6	173.4	148.8	4.0	7.9	40.5/42.5	1.1/1.2	334.0/367.5	90.9
13.6	173.4	146.9	4.0	7.3	40.0/42.0	1.1/1.2	331.6/367.0	90.3
16.0	173.4	146.9	4.0	6.7	40.1/43.8	1.1/1.1	331.0/366.7	90.3
21.3	171.9	151.9	3.9	7.5	41.1/43.8	1.1/1.1	335.1/369.8	90.6
21.5	171.9	152.8	4.0	7.5	41.3/43.8	1.1/1.1	336.1/370.0	90.8

* COMPUTED USING THE N2 CAL. FACTOR AND
THE KNOWN IONIZATION PROBABILITY OF H2O.

MISSION TOTAL ELAPSED TIME 8 DAYS

CALIB. PERIOD 7 ELAPSED TIME BETWEEN CALIB. 26.60 HOURS

CALIBRATION FACTORS (SENSITIVITY, TORR/VOLT)

		355T	360T	370T
NITROGEN	BEGIN	76.76	.00	76.32
OXYGEN	BEGIN	88.22	.00	87.57
CO2	BEGIN	5.73	.00	5.44

TWO GAS SENSOR COMPARATIVE DATA

TIME HR	N2 TOR	O2 TOR	CO2 TOR	H2O* TOR	O2-PCT MS/MDA	CO2-PCT MS/MDA	TOTAL-TOR MS/MDA	TOTAL-PCT MS
.3	196.1	174.7	4.7	2.5	47.1/43.8	1.3/1.1	380.0/370.8	102.5
.6	193.5	170.3	4.7	8.5	45.9/43.8	1.3/1.2	377.0/371.0	101.6
.9	192.8	161.5	4.7	8.6	43.5/43.8	1.3/1.2	367.5/371.2	99.0
5.1	188.5	162.8	4.8	8.0	44.6/44.5	1.3/1.3	364.1/365.2	99.7
7.3	188.5	169.0	5.0	8.9	46.3/43.5	1.4/1.3	371.3/365.2	101.7
8.7	188.4	168.0	4.9	8.2	46.2/43.5	1.3/1.3	369.4/363.5	101.6
10.7	188.3	168.8	4.6	7.7	46.5/43.5	1.3/1.2	369.4/363.2	101.7
12.7	189.0	167.8	4.5	7.6	46.4/43.5	1.2/1.2	368.9/362.0	101.9
18.6	189.1	167.9	4.5	7.8	46.3/43.5	1.2/1.1	369.3/363.0	101.7
22.7	191.4	171.4	4.4	8.2	47.3/43.0	1.2/1.1	375.3/362.7	103.5
26.0	190.7	168.9	4.8	8.2	46.4/42.5	1.3/1.2	372.6/364.0	102.4
26.1	191.5	169.8	4.8	8.4	46.6/ .0	1.3/ .0	374.5/364.2	102.8

* COMPUTED USING THE N2 CAL. FACTOR AND
THE KNOWN IONIZATION PROBABILITY OF H2O.

MISSION TOTAL ELAPSED TIME 9 DAYS

CALIB. PERIOD 8 ELAPSED TIME BETWEEN CALIB. 29.47 HOURS

CALIBRATION FACTORS (SENSITIVITY, TORR/VOLT)

		355T	360T	370T
NITROGEN	BEGIN	73.85	.00	75.07
OXYGEN	BEGIN	86.91	.00	86.74
CO2	BEGIN	5.73	.00	5.52

TWO GAS SENSOR COMPARATIVE DATA

TIME HR	N2 TOR	O2 TOR	CO2 TOR	H2O* TOR	O2-PCT MS/MDA	CO2-PCT MS/MDA	TOTAL-TOR MS/MDA	TOTAL-PCT MS
.4	198.5	178.0	5.2	2.2	48.9/42.1	1.4/1.3	384.0/363.8	105.5
.9	194.9	173.7	5.1	8.1	47.8/42.1	1.4/1.3	381.8/363.5	105.0
11.0	193.9	175.4	5.4	8.3	48.1/43.0	1.5/1.4	383.0/364.5	105.1
16.3	193.9	175.4	5.4	8.5	48.1/42.5	1.5/1.4	383.2/364.5	105.1
22.5	194.0	175.4	5.4	8.8	48.2/43.0	1.5/1.3	383.6/364.0	105.4
24.5	191.0	173.7	5.3	8.5	47.7/43.0	1.5/1.4	378.5/364.2	103.9
28.3	202.2	183.2	6.2	2.7	50.3/43.2	1.7/1.4	394.3/364.1	105.2
29.1	198.6	181.5	5.5	8.2	49.9/45.9	1.5/1.5	393.8/363.5	108.3

*COMPUTED USING THE N2 CAL. FACTOR AND
THE KNOWN IONIZATION PROBABILITY OF H2O.

MISSION TOTAL ELAPSED TIME 10 DAYS

CALIB. PERIOD 9 ELAPSED TIME BETWEEN CALIB. 18.23 HOURS

CALIBRATION FACTORS (SENSITIVITY, TORR/VOLT)

		355T	360T	370T
NITROGEN	BEGIN	69.73	.00	69.36
OXYGEN	BEGIN	82.06	.00	81.37
CO2	BEGIN	5.30	.00	5.21

TWO GAS SENSOR COMPARATIVE DATA

TIME HR	N2 TOR	O2 TOR	CO2 TOR	H2O* TOR	O2-PCT MS/MDA	CO2-PCT MS/MDA	TOTAL-TOR MS/MDA	TOTAL-PCT MS
.4	189.2	172.5	5.2	2.2	47.5/45.5	1.4/1.5	369.0/362.9	101.7
8.6	191.7	169.6	4.8	7.4	47.3/44.2	1.3/1.3	373.5/358.7	104.1
11.4	191.7	168.0	4.9	7.9	46.8/44.3	1.4/1.4	372.5/358.9	103.8
13.7	192.4	169.6	4.7	7.4	47.3/44.5	1.3/1.3	374.1/358.5	104.4
17.8	191.7	165.6	4.9	8.2	46.1/43.8	1.4/1.3	370.4/359.0	103.2
17.8	191.0	164.7	4.9	7.9	45.9/43.8	1.4/1.4	368.6/358.7	102.7

* COMPUTED USING THE N2 CAL. FACTOR AND
THE KNOWN IONIZATION PROBABILITY OF H2O.

MISSION TOTAL ELAPSED TIME 11 DAYS

CALIB. PERIOD 10 ELAPSED TIME BETWEEN CALIB. 22.48 HOURS

CALIBRATION FACTORS (SENSITIVITY, TORR/VOLT)

		355T	360T	370T
NITROGEN	BEGIN	65.80	.00	65.62
OXYGEN	BEGIN	75.08	.00	75.99
CO2	BEGIN	5.07	.00	4.87

TWO GAS SENSOR COMPARATIVE DATA

TIME HR	N2 TOR	O2 TOR	CO2 TOR	H2O* TOR	O2-PCT MS/MDA	CO2-PCT MS/MDA	TOTAL-TOR MS/MDA	TOTAL-PCT MS
.2	185.1	156.2	4.9	1.8	43.7/43.9	1.4/1.4	348.0/357.7	97.3
6.6	181.3	151.4	5.2	7.9	42.1/43.5	1.4/1.5	345.7/359.8	96.1
13.2	187.1	154.0	4.8	7.4	43.1/43.5	1.3/1.4	353.3/357.0	99.0
16.7	189.0	154.9	4.3	7.0	43.5/43.2	1.2/1.2	355.2/355.9	99.8
18.8	189.7	157.8	4.0	7.0	44.2/43.5	1.1/1.2	358.6/357.0	100.4
21.5	188.4	158.4	3.9	8.5	44.2/43.5	1.1/1.1	359.3/358.2	100.3
21.9	187.8	156.2	3.9	8.5	43.6/43.5	1.1/1.4	356.3/358.0	99.5

* COMPUTED USING THE N2 CAL. FACTOR AND
THE KNOWN IONIZATION PROBABILITY OF H2O.

MISSION TOTAL ELAPSED TIME 12 DAYS

CALIB. PERIOD 11 ELAPSED TIME BETWEEN CALIB. 14.92 HOURS

CALIBRATION FACTORS (SENSITIVITY, TORR/VOLT)

		355T	360T	370T
NITROGEN	BEGIN	68.10	.00	67.56
OXYGEN	BEGIN	78.77	.00	77.92
CO2	BEGIN	5.55	.00	5.00

TWO GAS SENSOR COMPARATIVE DATA

TIME HR	N2 TOR	O2 TOR	CO2 TOR	H2O* TOR	O2-PCT MS/MDA	CO2-PCT MS/MDA	TOTAL-TOR MS/MDA	TOTAL-PCT MS
.3	195.6	163.2	4.0	2.7	45.6/43.5	1.1/1.1	365.5/358.0	102.1
.5	192.9	160.9	4.0	1.9	44.9/43.5	1.1/1.1	359.7/358.0	100.5
3.9	196.5	167.4	4.1	7.5	46.4/44.0	1.1/1.1	375.6/360.8	104.1
6.3	199.3	169.8	4.0	7.4	47.0/44.0	1.1/1.0	380.5/361.0	105.4
8.3	199.3	170.7	3.9	7.4	47.2/44.0	1.1/1.0	381.3/361.5	105.5
13.7	194.0	164.6	4.0	7.9	45.3/43.5	1.1/1.0	370.5/362.9	102.1
13.9	195.4	164.6	4.1	7.7	45.3/43.5	1.1/1.0	371.7/362.9	102.4
14.5	194.0	163.8	4.2	7.8	45.1/43.4	1.2/1.0	369.8/362.9	101.9

* COMPUTED USING THE N2 CAL. FACTOR AND
THE KNOWN IONIZATION PROBABILITY OF H2O.

MISSION TOTAL ELAPSED TIME 13 DAYS

CALIB. PERIOD 12 ELAPSED TIME BETWEEN CALIB. 9.68 HOURS

CALIBRATION FACTORS (SENSITIVITY, TORR/VOLT)

		355T	360T	370T
NITROGEN	BEGIN	60.56	.00	59.03
OXYGEN	BEGIN	70.29	.00	68.11
CO2	BEGIN	4.80	.00	4.74

TWO GAS SENSOR COMPARATIVE DATA

TIME HR	N2 TOR	O2 TOR	CO2 TOR	H2O* TOR	O2-PCT MS/MDA	CO2-PCT MS/MDA	TOTAL-TOR MS/MDA	TOTAL-PCT MS
.6	175.6	148.5	4.2	1.5	40.8/43.4	1.2/1.2	329.8/363.8	90.7
.6	175.6	148.5	4.2	1.5	40.8/43.4	1.2/1.2	329.8/363.8	90.7
1.5	165.5	138.9	4.3	7.3	38.1/43.0	1.2/1.2	315.9/364.1	86.8

* COMPUTED USING THE N2 CAL. FACTOR AND THE KNOWN IONIZATION PROBABILITY OF H2O.

MISSION TOTAL ELAPSED TIME 14 DAYS

CALIB. PERIOD 13 ELAPSED TIME BETWEEN CALIB. 9.02 HOURS

CALIBRATION FACTORS (SENSITIVITY, TORR/VOLT)

		355T	360T	370T
NITROGEN	BEGIN	63.64	.00	63.78
OXYGEN	BEGIN	73.21	.00	73.26
CO2	BEGIN	5.07	.00	4.87

TWO GAS SENSOR COMPARATIVE DATA

TIME HR	N2 TOR	O2 TOR	CO2 TOR	H2O* TOR	O2-PCT MS/MDA	CO2-PCT MS/MDA	TOTAL-TOR MS/MDA	TOTAL-PCT MS
.2	189.2	153.1	5.4	2.7	42.3/43.2	1.5/1.4	350.4/362.0	96.8
.4	184.8	149.4	5.3	2.2	41.3/43.4	1.5/1.3	341.6/362.0	94.4
1.4	182.2	145.0	3.7	6.5	40.1/43.3	1.0/1.1	337.4/361.6	93.3
4.7	182.2	145.7	3.5	6.6	40.2/43.3	1.0/ .9	338.1/362.1	93.4
6.6	183.5	146.5	3.4	6.8	40.4/43.3	.9/ .9	340.2/362.2	93.9
8.5	182.9	147.2	3.4	7.1	40.6/43.0	.9/ .9	340.6/362.4	94.0

* COMPUTED USING THE N2 CAL. FACTOR AND
THE KNOWN IONIZATION PROBABILITY OF H2O.

MISSION TOTAL ELAPSED TIME 15 DAYS

CALIB. PERIOD 14 ELAPSED TIME BETWEEN CALIB. 22.15 HOURS

CALIBRATION FACTORS (SENSITIVITY, TORR/VOLT)

		355T	360T	370T
NITROGEN	BEGIN	68.90	.00	68.32
OXYGEN	BEGIN	78.42	.00	77.92
CO2	BEGIN	5.14	.00	5.14

TWO GAS SENSOR COMPARATIVE DATA

TIME HR	N2 TOR	O2 TOR	CO2 TOR	H2O* TOR	O2-PCT MS/MDA	CO2-PCT MS/MDA	TOTAL-TOR MS/MDA	TOTAL-PCT MS
.4	199.0	158.7	3.7	2.4	43.7/43.2	1.0/ .9	363.7/363.0	100.2
.6	223.6	178.2	4.5	11.6	49.2/43.6	1.2/1.0	417.9/362.1	115.4
.9	207.0	164.0	4.2	9.2	45.4/42.8	1.2/1.0	384.5/361.0	106.5
1.2	198.1	157.0	4.2	8.9	43.5/43.0	1.2/1.0	368.2/360.9	102.0
3.8	191.2	154.6	4.2	7.7	42.9/ .0	1.2/ .0	357.7/360.4	99.3
4.0	191.2	154.7	4.2	7.6	42.9/44.0	1.2/1.1	357.7/360.8	99.1
11.4	194.9	152.0	3.9	7.0	42.6/43.6	1.1/1.1	357.8/356.6	100.3
21.3	200.6	156.5	3.7	7.9	42.9/43.5	1.0/1.0	368.6/364.6	101.1
21.5	201.2	156.5	3.7	7.9	42.9/43.4	1.0/1.0	369.2/364.3	101.4

*COMPUTED USING THE N2 CAL. FACTOR AND
THE KNOWN IONIZATION PROBABILITY OF H2O.

MISSION TOTAL ELAPSED TIME 16 DAYS

CALIB. PERIOD 15 ELAPSED TIME BETWEEN CALIB. 17.78 HOURS

CALIBRATION FACTORS (SENSITIVITY, TORR/VOLT)

		355T	360T	370T
NITROGEN	BEGIN	67.84	.00	68.06
OXYGEN	BEGIN	78.07	.00	78.25
CO2	BEGIN	5.14	.00	5.14

	TWO GAS SENSOR				COMPARATIVE DATA			
TIME HR	N2 TOR	O2 TOR	CO2 TOR	H2O* TOR	O2-PCT MS/MDA	CO2-PCT MS/MDA	TOTAL-TOR MS/MDA	TOTAL-PCT MS
.2	200.3	157.8	3.9	2.8	43.2/43.2	1.1/1.0	364.8/365.0	100.0
.5	197.6	157.1	3.9	1.9	43.1/43.0	1.1/1.0	360.5/364.5	98.9
14.9	201.0	159.4	3.5	7.8	43.6/43.0	1.0/ .9	371.6/365.7	101.6
16.9	201.0	157.8	3.5	7.4	43.2/42.8	1.0/ .9	369.8/365.2	101.2
17.2	201.0	157.8	3.6	7.6	43.2/42.6	1.0/ .9	370.0/365.0	101.4

*COMPUTED USING THE N2 CAL. FACTOR AND
THE KNOWN IONIZATION PROBABILITY OF H2O.

MISSION TOTAL ELAPSED TIME 17 DAYS

CALIB. PERIOD 16 ELAPSED TIME BETWEEN CALIB. 21.77 HOURS

CALIBRATION FACTORS (SENSITIVITY, TORR/VOLT)

		355T	360T	370T
NITROGEN	BEGIN	68.90	.00	68.32
OXYGEN	BEGIN	78.77	.00	78.25
CO2	BEGIN	5.22	.00	5.21

TWO GAS SENSOR COMPARATIVE DATA

TIME HR	N2 TOR	O2 TOR	CO2 TOR	H2O* TOR	O2-PCT MS/MDA	CO2-PCT MS/MDA	TOTAL-TOR MS/MDA	TOTAL-PCT MS
.2	206.8	158.8	3.8	2.9	43.5/42.5	1.0/1.0	372.3/365.2	101.9
.5	202.0	157.2	3.8	3.9	43.1/42.5	1.0/1.0	366.9/364.9	100.5
.6	200.1	157.3	3.8	7.1	43.0/42.5	1.0/ .9	368.1/366.0	100.6
4.3	199.4	157.3	3.9	7.1	42.9/43.0	1.1/1.0	367.6/366.2	100.4
6.3	200.8	157.3	3.9	7.7	42.9/44.5	1.1/1.0	369.7/366.8	100.8
8.8	200.8	157.3	4.1	7.9	43.0/44.0	1.1/1.1	370.0/366.1	101.1
11.5	201.3	157.2	4.0	7.7	43.1/44.0	1.1/1.1	370.1/365.0	101.4
13.5	203.2	157.1	3.9	7.4	43.2/44.0	1.1/1.1	371.6/363.7	102.2
15.2	203.2	157.1	3.9	7.5	43.3/44.0	1.1/1.0	371.5/363.1	102.3
17.5	203.2	157.1	3.8	7.6	43.2/44.0	1.0/1.0	371.6/363.3	102.3
19.5	203.0	157.0	3.8	7.6	43.4/45.0	1.0/1.0	371.4/361.8	102.6
21.2	201.6	156.2	3.9	7.9	43.2/44.9	1.1/1.1	369.6/361.8	102.2

*COMPUTED USING THE N2 CAL. FACTOR AND
THE KNOWN IONIZATION PROBABILITY OF H2O.

MISSION TOTAL ELAPSED TIME 18 DAYS

CALIB. PERIOD 17 ELAPSED TIME BETWEEN CALIB. 24.98 HOURS

CALIBRATION FACTORS (SENSITIVITY, TORR/VOLT)

		355T	360T	370T
NITROGEN	BEGIN	68.10	.00	67.56
OXYGEN	BEGIN	78.42	.00	77.26
CO2	BEGIN	5.22	.00	5.14

TWO GAS SENSOR COMPARATIVE DATA

TIME HR	N2 TOR	O2 TOR	CO2 TOR	H2O* TOR	O2-PCT MS/MDA	CO2-PCT MS/MDA	TOTAL-TOR MS/MDA	TOTAL-PCT MS
.3	204.0	159.4	4.0	2.6	44.1/ .0	1.1/1.1	370.1/361.3	102.4
1.0	196.5	153.1	4.0	7.8	42.4/43.9	1.1/1.1	361.5/360.8	100.2
3.0	197.3	154.1	4.1	7.8	42.5/42.3	1.1/1.1	363.3/362.1	100.3
6.2	198.3	160.0	3.9	7.5	43.8/42.3	1.1/1.0	369.7/365.0	101.3
10.0	202.6	158.7	3.7	7.1	43.3/41.7	1.0/ .9	372.1/366.8	101.4
11.9	202.7	159.6	3.8	7.2	43.4/41.7	1.0/ .9	373.3/367.8	101.5
13.9	202.7	160.4	3.8	7.2	43.6/41.8	1.0/1.0	374.1/367.8	101.7
16.9	202.7	162.8	3.8	7.6	44.3/41.7	1.0/1.0	376.8/367.8	102.4
18.4	202.0	162.0	3.8	7.3	44.0/41.7	1.0/ .9	375.1/367.9	102.0
20.5	201.4	161.2	3.6	2.6	43.8/42.0	1.0/ .9	368.9/368.0	100.2
22.4	201.4	161.3	3.5	6.8	43.8/42.0	1.0/ .8	373.0/368.3	101.3
24.0	201.5	161.4	3.7	7.1	43.7/42.0	1.0/ .8	373.7/369.2	101.2

*COMPUTED USING THE N2 CAL. FACTOR AND
THE KNOWN IONIZATION PROBABILITY OF H2O.

MISSION TOTAL ELAPSED TIME 19 DAYS

CALIB. PERIOD 18 ELAPSED TIME BETWEEN CALIB. 26.47 HOURS

CALIBRATION FACTORS (SENSITIVITY, TORR/VOLT)

		355T	360T	370T
NITROGEN	BEGIN	67.84	.00	67.56
OXYGEN	BEGIN	77.72	.00	77.26
CO2	BEGIN	5.22	.00	5.14

TWO GAS SENSOR COMPARATIVE DATA

TIME HR	N2 TOR	O2 TOR	CO2 TOR	H2O* TOR	O2-PCT MS/MDA	CO2-PCT MS/MDA	TOTAL-TOR MS/MDA	TOTAL-PCT MS
.3	204.9	162.4	4.1	2.4	43.9/ .0	1.1/ .0	373.8/369.8	101.1
1.1	200.8	158.6	4.1	7.3	42.8/42.3	1.1/1.1	370.7/370.1	100.2
2.4	200.9	159.4	4.2	7.8	42.9/42.0	1.1/1.1	372.2/371.2	100.3
4.9	196.6	157.6	4.2	7.2	43.0/43.0	1.1/1.2	365.5/366.8	99.7
7.2	196.4	157.4	4.3	7.5	43.2/43.0	1.2/1.2	365.6/364.5	100.3
8.7	194.2	156.4	4.1	7.5	43.3/43.5	1.1/1.2	362.2/360.9	100.4
11.2	194.2	157.2	3.9	7.1	43.7/43.3	1.1/1.1	362.3/360.0	100.6
15.0	195.6	161.1	4.0	7.7	44.6/43.4	1.1/1.1	368.5/361.2	102.0
17.2	195.6	161.1	4.0	7.7	44.6/43.0	1.1/1.1	368.4/361.4	101.9
20.4	196.3	161.9	3.7	7.7	44.8/42.5	1.0/1.0	369.6/361.8	102.2
23.9	194.3	158.9	3.7	7.6	43.8/42.0	1.0/1.0	364.6/363.2	100.4
25.9	195.1	159.0	4.0	7.1	43.6/42.5	1.1/1.0	365.2/365.0	100.1

*COMPUTED USING THE N2 CAL. FACTOR AND
THE KNOWN IONIZATION PROBABILITY OF H2O.

MISSION TOTAL ELAPSED TIME 20 DAYS

CALIB. PERIOD 19 ELAPSED TIME BETWEEN CALIB. 42.15 HOURS

CALIBRATION FACTORS (SENSITIVITY, TORR/VOLT)

		355T	360T	370T
NITROGEN	BEGIN	69.18	.00	68.06
OXYGEN	BEGIN	78.77	.00	77.59
CO2	BEGIN	5.38	.00	5.14

	TWO GAS SENSOR				COMPARATIVE DATA			
TIME HR	N2 TOR	O2 TOR	CO2 TOR	H2O* TOR	O2-PCT MS/MDA	CO2-PCT MS/MDA	TOTAL-TOR MS/MDA	TOTAL-PCT MS
.3	201.8	164.0	4.2	2.7	44.8/42.5	1.1/1.4	372.6/366.0	101.8
.6	198.3	160.8	4.2	7.0	44.0/42.5	1.1/1.4	370.3/365.8	101.2
2.6	199.3	161.8	3.8	7.6	44.1/42.0	1.0/1.2	372.6/367.3	101.4
4.2	201.8	160.0	4.6	7.9	43.8/42.7	1.2/1.2	374.2/365.7	102.3
6.0	200.4	158.7	4.3	7.3	43.8/43.0	1.2/1.2	370.6/362.5	102.2
7.4	197.0	156.7	4.2	7.1	43.6/43.0	1.2/1.2	365.0/359.5	101.5
8.8	197.8	157.5	4.2	7.4	43.8/42.5	1.2/1.1	366.9/360.0	101.9
10.7	199.2	157.6	4.1	7.3	43.7/43.0	1.1/1.1	368.3/360.4	102.2
12.7	198.8	158.6	4.1	7.5	43.8/43.0	1.1/1.1	369.0/361.6	102.0
14.5	198.0	158.5	3.9	7.2	43.9/43.0	1.1/1.1	367.6/361.2	101.8
16.9	198.2	157.9	3.9	7.6	43.6/42.7	1.1/1.0	367.6/362.2	101.5
19.6	197.3	158.2	4.2	7.9	43.4/42.5	1.1/1.1	367.6/364.3	100.9
21.7	197.7	158.5	4.3	7.9	43.3/42.5	1.2/1.1	368.3/366.1	100.6
23.7	197.1	158.5	4.3	7.4	43.3/43.3	1.2/1.1	367.3/366.3	100.3
25.7	199.4	160.3	4.3	7.2	43.6/43.3	1.2/1.1	371.1/367.5	101.0
28.7	203.4	161.0	4.2	7.8	43.9/42.8	1.1/1.1	376.4/367.0	102.6
31.5	203.8	159.2	4.2	8.7	43.5/42.8	1.1/1.1	375.8/365.6	102.8
32.7	200.2	157.8	4.1	7.8	43.6/43.0	1.1/1.1	369.8/361.5	102.3
34.7	200.9	158.6	4.0	7.6	43.8/42.5	1.1/1.1	371.2/361.8	102.6
36.7	201.8	158.7	3.9	7.8	43.8/42.8	1.1/1.1	372.2/362.6	102.6
38.6	201.7	158.7	3.9	7.6	43.8/42.8	1.1/1.1	371.9/362.4	102.6
40.5	203.2	158.8	3.9	8.0	43.7/42.7	1.1/1.1	374.0/362.9	103.0
41.1	203.2	158.8	4.1	8.1	43.7/ .0	1.1/ .0	374.1/363.0	103.1
41.2	202.5	158.0	4.1	8.1	43.5/ .0	1.1/ .0	372.6/363.0	102.7
41.8	202.4	157.9	4.0	8.0	43.6/42.4	1.1/1.1	372.4/362.5	102.7

*COMPUTED USING THE N2 CAL. FACTOR AND
THE KNOWN IONIZATION PROBABILITY OF H2O.

MISSION TOTAL ELAPSED TIME 22 DAYS

CALIB. PERIOD 20. ELAPSED TIME BETWEEN CALIB. 47.50 HOURS

CALIBRATION FACTORS (SENSITIVITY, TORR/VOLT)

		355T	360T	370T
NITROGEN	BEGIN	67.31	.00	70.16
OXYGEN	BEGIN	77.05	.00	80.30
CO2	BEGIN	5.14	.00	5.36

	TWO GAS SENSOR				COMPARATIVE DATA			
TIME HR	N2 TOR	O2 TOR	CO2 TOR	H2O* TOR	O2-PCT MS/MDA	CO2-PCT MS/MDA	TOTAL-TOR MS/MDA	TOTAL-PCT MS
.4	203.6	160.6	4.2	3.0	44.3/42.4	1.2/1.1	371.5/362.2	102.6
1.4	198.6	158.1	4.3	7.2	43.6/42.6	1.2/1.2	368.3/362.5	101.6
3.4	196.4	156.7	4.4	7.8	43.0/43.0	1.2/1.2	365.3/364.1	100.3
4.9	196.0	157.4	4.6	7.6	43.0/ .0	1.3/ .0	365.7/366.0	99.9
5.7	196.0	157.4	4.7	7.7	43.0/ .0	1.3/ .0	365.8/366.0	99.9
8.7	197.1	158.3	5.0	8.7	43.5/42.0	1.4/1.3	369.1/364.0	101.4
11.4	197.1	158.3	5.0	8.8	43.5/42.0	1.4/1.4	369.2/364.0	101.4
14.3	199.7	158.4	4.8	7.8	43.3/42.0	1.3/1.3	370.7/365.5	101.4
16.1	201.1	159.5	4.5	7.5	43.9/42.0	1.2/1.2	372.5/363.0	102.6
17.1	198.3	164.5	4.2	7.5	44.5/43.8	1.1/1.2	374.6/369.2	101.5
17.9	197.6	165.4	4.2	7.5	44.6/43.8	1.1/1.2	374.7/370.5	101.1
19.7	198.0	165.6	4.3	7.4	45.4/43.5	1.2/1.2	375.3/365.0	102.8
23.9	199.1	161.0	4.2	8.2	45.0/42.0	1.2/1.1	372.5/357.8	104.1
25.9	198.4	160.9	4.3	8.3	45.0/42.0	1.2/1.1	371.8/357.9	103.9
27.9	197.5	160.8	4.3	7.1	44.9/42.0	1.2/1.1	369.6/358.2	103.2
29.7	197.3	160.6	4.2	7.3	44.8/43.0	1.2/1.1	369.3/358.7	103.0
31.9	198.8	161.5	4.1	7.1	45.0/42.8	1.2/1.1	371.4/358.5	103.6
33.9	198.8	160.7	4.0	7.8	44.8/42.8	1.1/1.0	371.2/358.5	103.5
37.2	198.4	160.4	3.8	8.1	44.6/43.0	1.1/1.0	370.7/359.2	103.2
39.4	199.9	162.0	3.8	7.9	45.1/42.8	1.1/1.0	373.7/359.0	104.1
40.7	200.2	161.5	3.8	7.8	45.1/42.5	1.1/1.0	373.3/358.4	104.2
42.7	200.3	161.6	3.7	8.0	45.1/42.5	1.0/1.0	373.6/358.2	104.3
45.2	201.2	161.8	3.7	7.9	45.2/42.5	1.0/1.0	374.5/357.8	104.7
46.9	201.2	161.0	3.7	8.0	45.0/42.3	1.0/1.0	373.9/357.8	104.5
47.2	200.5	161.0	3.7	8.0	45.0/42.2	1.0/1.0	373.2/357.8	104.3

*COMPUTED USING THE N2 CAL. FACTOR AND
THE KNOWN IONIZATION PROBABILITY OF H2O.

MISSION TOTAL ELAPSED TIME 24 DAYS

CALIB. PERIOD 21 ELAPSED TIME BETWEEN CALIB. 18.45 HOURS

CALIBRATION FACTORS (SENSITIVITY, TORR/VOLT)

		355T	360T	370T
NITROGEN	BEGIN	.00	68.79	.00
OXYGEN	BEGIN	.00	79.17	.00
CO2	BEGIN	.00	5.14	.00

	TWO GAS SENSOR				COMPARATIVE DATA			
TIME HR	N2 TOR	O2 TOR	CO2 TOR	H2O* TOR	O2-PCT MS/MDA	CO2-PCT MS/MDA	TOTAL-TOR MS/MDA	TOTAL-PCT MS
.5	191.9	159.9	4.1	2.0	44.1/43.3	1.1/1.1	357.9/363.0	98.6
.7	191.2	159.9	4.1	1.7	44.1/43.1	1.1/1.1	356.9/363.0	98.3
1.9	185.0	156.8	4.1	7.1	42.9/43.5	1.1/1.1	353.0/365.0	96.7
4.7	183.0	156.8	4.2	7.2	43.1/44.0	1.2/1.2	351.1/364.1	96.4
7.3	183.0	157.5	4.0	6.7	43.5/44.0	1.1/1.1	351.2/362.0	97.0
8.3	183.0	158.3	4.0	6.6	43.6/44.0	1.1/1.1	351.9/362.8	97.0
10.1	183.0	160.7	3.9	6.6	44.1/44.5	1.1/1.1	354.1/364.2	97.2
11.6	183.7	160.7	3.7	6.4	44.1/44.5	1.0/1.0	354.5/364.4	97.3
13.4	183.7	160.7	3.5	6.4	44.1/44.5	1.0/1.0	354.3/364.4	97.2
16.1	184.4	159.9	3.6	6.5	43.9/44.3	1.0/1.0	354.4/364.2	97.3
17.9	183.7	159.9	3.7	6.9	43.8/44.5	1.0/1.0	354.2/364.8	97.1

*COMPUTED USING THE N2 CAL. FACTOR AND
THE KNOWN IONIZATION PROBABILITY OF H2O.

MISSION TOTAL ELAPSED TIME 25 DAYS

CALIB. PERIOD 22 ELAPSED TIME BETWEEN CALIB. 22.23 HOURS

CALIBRATION FACTORS (SENSITIVITY, TORR/VOLT)

		355T	360T	370T
NITROGEN	BEGIN	.00	71.85	.00
OXYGEN	BEGIN	.00	82.83	.00
CO2	BEGIN	.00	5.54	.00

TWO GAS SENSOR COMPARATIVE DATA

TIME HR	N2 TOR	O2 TOR	CO2 TOR	H2O* TOR	O2-PCT MS/MDA	CO2-PCT MS/MDA	TOTAL-TOR MS/MDA	TOTAL-PCT MS
.3	193.3	169.0	3.6	3.4	46.4/44.4	1.0/1.1	369.3/364.0	101.4
1.0	189.7	165.7	4.1	5.5	45.6/44.9	1.1/1.1	365.0/363.4	100.4
2.8	189.0	164.0	4.2	6.8	45.3/44.5	1.1/1.1	363.9/362.3	100.4
1.8	192.6	160.7	4.2	7.0	44.4/43.7	1.1/1.1	364.4/362.1	100.6
5.4	193.3	161.5	4.2	7.0	44.6/43.5	1.2/1.1	366.0/362.0	101.1
9.1	193.3	161.5	4.0	7.0	44.7/43.7	1.1/1.1	365.8/361.2	101.3
10.9	193.3	161.5	3.9	7.0	44.7/43.7	1.1/1.0	365.7/361.0	101.3
15.6	194.0	160.7	3.8	7.0	44.6/43.5	1.0/1.0	365.5/360.7	101.3
18.5	195.4	160.7	3.8	7.2	44.6/43.5	1.0/1.0	367.1/360.4	101.9
19.8	195.4	160.7	3.5	7.3	44.7/43.3	1.0/ .9	367.0/359.8	102.0
21.6	196.2	159.9	3.7	7.5	44.5/43.4	1.0/1.0	367.2/359.6	102.1

*COMPUTED USING THE N2 CAL. FACTOR AND
THE KNOWN IONIZATION PROBABILITY OF H2O.

MISSION TOTAL ELAPSED TIME 26 DAYS

CALIB. PERIOD 23 ELAPSED TIME BETWEEN CALIB. 25.03 HOURS

CALIBRATION FACTORS (SENSITIVITY, TORR/VOLT)

		355T	360T	370T
NITROGEN	BEGIN	.00	70.71	.00
OXYGEN	BEGIN	.00	81.70	.00
CO2	BEGIN	.00	5.45	.00

TWO GAS SENSOR COMPARATIVE DATA

TIME HR	N2 TOR	O2 TOR	CO2 TOR	H2O* TOR	O2-PCT MS/MDA	CO2-PCT MS/MDA	TOTAL-TOR MS/MDA	TOTAL-PCT MS
.2	195.2	160.9	3.9	3.8	44.8/43.0	1.1/1.0	363.8/359.5	101.2
.6	193.0	156.9	3.8	6.9	43.6/43.6	1.1/1.0	360.6/359.5	100.3
2.5	190.2	156.9	4.0	7.1	43.5/43.3	1.1/1.1	358.2/360.5	99.4
2.6	190.2	156.9	4.0	7.3	43.5/43.3	1.1/1.1	358.3/360.5	99.4
4.7	190.2	157.7	4.2	7.2	43.6/43.5	1.2/1.1	359.3/361.4	99.4
7.0	189.5	157.7	4.5	7.9	43.6/43.3	1.2/1.2	359.5/362.0	99.3
9.0	189.5	157.7	4.6	8.3	43.6/43.3	1.3/1.3	360.1/361.5	99.6
10.7	190.2	157.7	4.6	7.5	43.7/43.3	1.3/1.3	360.0/361.0	99.7
12.5	190.2	157.7	4.5	7.8	43.6/43.3	1.2/1.2	360.1/361.3	99.7
15.0	190.2	157.7	4.4	7.4	43.7/43.3	1.2/1.2	359.7/361.2	99.6
16.7	190.2	158.5	4.3	7.3	43.9/43.0	1.2/1.2	360.3/361.0	99.8
18.7	190.9	158.5	4.2	7.2	43.9/43.0	1.2/1.1	360.8/361.0	99.9
20.5	192.3	160.1	4.3	7.6	44.3/43.0	1.2/1.1	364.3/361.2	100.9
24.6	194.5	157.7	4.0	7.6	43.4/43.0	1.1/1.1	363.7/363.0	100.2

*COMPUTED USING THE N2 CAL. FACTOR AND
THE KNOWN IONIZATION PROBABILITY OF H2O.

MISSION TOTAL ELAPSED TIME 27 DAYS

CALIB. PERIOD 24 ELAPSED TIME BETWEEN CALIB. 25.92 HOURS

CALIBRATION FACTORS (SENSITIVITY, TORR/VOLT)

		355T	360T	370T
NITROGEN	BEGIN	.00	71.85	.00
OXYGEN	BEGIN	.00	82.45	.00
CO2	BEGIN	.00	5.62	.00

TWO GAS SENSOR COMPARATIVE DATA

TIME HR	N2 TOR	O2 TOR	CO2 TOR	H2O* TOR	O2-PCT MS/MDA	CO2-PCT MS/MDA	TOTAL-TOR MS/MDA	TOTAL-PCT MS
.3	199.0	161.6	4.3	3.7	44.5/42.7	1.2/1.1	368.6/363.3	101.5
.6	196.2	158.3	4.3	6.9	43.6/42.5	1.2/1.1	365.6/363.0	100.7
3.8	195.4	158.3	4.3	7.5	43.5/42.7	1.2/1.1	365.6/364.0	100.4
5.1	196.2	159.1	4.3	7.9	43.6/42.7	1.2/1.1	367.5/364.8	100.7
7.3	196.2	159.1	4.2	8.0	43.6/42.8	1.2/1.1	367.5/365.2	100.6
9.4	196.9	160.0	4.4	8.4	43.8/42.8	1.2/1.2	369.6/365.0	101.3
11.3	198.3	160.0	4.3	7.5	43.9/42.8	1.2/1.1	370.1/364.0	101.7
13.3	198.3	160.8	4.3	7.7	44.3/42.5	1.2/1.2	371.1/363.2	102.2
16.1	199.0	160.0	4.4	7.5	44.2/42.5	1.2/1.2	370.9/362.2	102.4
19.8	199.0	158.3	4.4	7.4	43.8/42.0	1.2/1.2	369.2/361.1	102.2
21.8	199.8	159.1	4.2	7.5	44.0/42.3	1.2/1.2	370.6/362.0	102.4
23.8	199.0	160.8	4.2	7.3	44.3/42.3	1.1/1.1	371.3/363.1	102.3
25.3	197.6	160.0	4.3	7.3	43.9/42.5	1.2/1.1	369.1/364.0	101.4
25.6	197.6	160.0	4.3	7.0	43.9/42.5	1.2/1.1	368.8/364.0	101.3

*COMPUTED USING THE N2 CAL. FACTOR AND
THE KNOWN IONIZATION PROBABILITY OF H2O.

MISSION TOTAL ELAPSED TIME 28 DAYS

CALIB. PERIOD 25 ELAPSED TIME BETWEEN CALIB. 21.63 HOURS

CALIBRATION FACTORS (SENSITIVITY, TORR/VOLT)

		355T	360T	370T
NITROGEN	BEGIN	.00	71.28	.00
OXYGEN	BEGIN	.00	82.07	.00
CO2	BEGIN	.00	5.71	.00

	TWO GAS SENSOR				COMPARATIVE DATA			
TIME HR	N2 TOR	O2 TOR	CO2 TOR	H2O* TOR	O2-PCT MS/MDA	CO2-PCT MS/MDA	TOTAL-TOR MS/MDA	TOTAL-PCT MS
.3	196.7	160.0	4.5	3.2	43.8/42.5	1.2/1.1	364.4/365.0	99.8
.4	196.7	160.0	4.5	5.1	43.9/42.5	1.2/1.1	366.4/364.9	100.4
2.4	196.0	160.9	4.6	7.8	44.0/42.3	1.2/1.1	369.3/366.0	100.9
4.4	198.2	160.9	5.0	8.0	44.0/42.3	1.4/1.2	372.0/366.0	101.6
7.4	198.2	160.9	5.1	7.7	44.0/42.3	1.4/1.3	371.9/365.5	101.8
9.4	198.9	160.9	4.9	7.5	44.0/42.3	1.3/1.2	372.2/365.5	101.8
11.4	198.9	160.9	4.7	7.5	44.1/42.2	1.3/1.2	372.0/365.0	101.9
13.8	200.3	160.9	4.6	7.4	44.1/42.1	1.3/1.2	373.2/364.8	102.3
15.9	201.7	160.9	4.6	7.4	44.2/42.1	1.3/1.1	374.6/364.2	102.9
17.9	202.4	160.9	4.5	7.4	44.1/42.0	1.2/1.1	375.2/364.5	102.9
19.9	202.4	160.9	4.5	7.4	44.2/42.4	1.2/1.1	375.2/364.0	103.1
21.2	201.7	158.4	4.5	8.2	43.5/ .0	1.2/ .0	372.8/364.4	102.3

* COMPUTED USING THE N2 CAL. FACTOR AND
THE KNOWN IONIZATION PROBABILITY OF H2O.

MISSION TOTAL ELAPSED TIME 29 DAYS

CALIB. PERIOD 26 ELAPSED TIME BETWEEN CALIB. 48.10 HOURS

CALIBRATION FACTORS (SENSITIVITY, TORR/VOLT)

		355T	360T	370T
NITROGEN	BEGIN	.00	70.43	.00
OXYGEN	BEGIN	.00	81.33	.00
CO2	BEGIN	.00	5.54	.00

	TWO GAS SENSOR				COMPARATIVE DATA			
TIME HR	N2 TOR	O2 TOR	CO2 TOR	H2O* TOR	O2-PCT MS/MDA	CO2-PCT MS/MDA	TOTAL-TOR MS/MDA	TOTAL-PCT MS
.2	195.8	155.3	4.4	7.4	42.8/ .0	1.2/ .0	362.9/363.3	99.9
.9	195.1	155.3	4.6	8.1	42.6/42.7	1.3/1.2	363.1/364.7	99.6
2.0	194.4	155.3	4.6	7.0	42.6/42.3	1.3/1.2	361.4/365.0	99.0
3.2	194.4	157.0	4.9	7.5	42.9/42.1	1.3/1.3	363.7/366.0	99.4
3.3	194.4	157.0	4.9	7.6	42.9/42.1	1.3/1.3	363.8/366.0	99.4
5.5	194.4	158.6	4.4	7.0	43.2/42.0	1.2/1.3	364.5/367.0	99.3
9.4	195.8	161.0	4.5	7.2	43.9/42.0	1.2/1.2	368.5/367.0	100.4
11.6	195.8	161.0	4.5	7.2	43.9/42.0	1.2/1.2	368.5/367.0	100.4
13.6	197.9	158.6	4.4	7.7	43.3/42.3	1.2/1.2	368.6/366.2	100.6
15.7	199.3	159.4	4.5	8.1	43.3/42.0	1.2/1.2	371.3/368.0	100.9
17.7	200.0	158.6	4.9	8.9	43.2/42.0	1.3/1.3	372.3/367.2	101.4
19.7	200.0	158.6	4.7	8.3	43.3/42.0	1.3/1.3	371.6/366.1	101.5
25.5	195.8	157.0	4.9	7.5	43.0/42.3	1.3/1.3	365.1/365.4	99.9
28.2	195.1	157.0	5.4	7.8	42.7/ .0	1.5/ .0	365.2/367.5	99.4
30.3	196.5	159.4	5.4	7.7	43.3/42.0	1.5/1.5	369.0/368.0	100.3
32.3	196.5	159.4	5.5	8.3	43.3/42.0	1.5/1.5	369.6/367.8	100.5
35.8	197.2	160.2	5.0	7.5	43.7/42.3	1.4/1.4	369.9/366.7	100.9
37.8	197.9	159.4	4.7	7.3	43.6/42.1	1.3/1.3	369.3/365.2	101.1
39.8	198.6	159.4	4.3	7.3	43.8/42.1	1.2/1.2	369.6/364.0	101.5
41.9	198.6	158.6	4.0	7.3	43.7/42.1	1.1/1.1	368.4/363.1	101.5
44.0	198.6	158.6	4.0	7.8	43.7/42.1	1.1/1.1	368.9/363.0	101.6
46.8	197.9	157.8	3.7	7.3	43.6/42.0	1.0/1.0	366.6/362.0	101.3
47.6	197.2	157.0	3.8	7.9	43.4/42.0	1.0/1.0	365.8/362.0	101.0

*COMPUTED USING THE N2 CAL. FACTOR AND
THE KNOWN IONIZATION PROBABILITY OF H2O.

MISSION TOTAL ELAPSED TIME 31 DAYS

CALIB. PERIOD 27 ELAPSED TIME BETWEEN CALIB. 48.87 HOURS

CALIBRATION FACTORS (SENSITIVITY, TORR/VOLT)

		355T	360T	370T
NITROGEN	BEGIN	70.29	.00	69.89
OXYGEN	BEGIN	80.93	.00	79.95
CO2	BEGIN	5.63	.00	5.36

TWO GAS SENSOR COMPARATIVE DATA

TIME HR	N2 TOR	O2 TOR	CO2 TOR	H2O* TOR	O2-PCT MS/MDA	CO2-PCT MS/MDA	TOTAL-TOR MS/MDA	TOTAL-PCT MS
.5	199.7	157.6	4.1	2.5	43.5/42.0	1.1/1.1	364.0/362.2	100.5
.8	194.8	153.5	4.0	5.7	42.5/41.9	1.1/1.1	358.0/361.4	99.1
1.0	194.1	152.7	3.9	7.4	42.2/41.9	1.1/1.1	358.1/361.5	99.1
6.9	193.6	157.1	4.1	7.2	43.1/42.8	1.1/1.1	362.0/364.2	99.4
11.2	194.9	156.9	4.0	7.3	43.2/43.0	1.1/1.0	363.1/363.0	100.0
14.2	195.5	157.6	3.8	6.8	43.5/43.0	1.1/1.0	363.8/362.0	100.5
15.9	196.2	157.5	3.8	7.0	43.6/42.7	1.0/1.0	364.5/361.4	100.9
17.9	196.8	156.6	3.7	6.8	43.4/42.5	1.0/1.0	363.9/360.5	100.9
19.9	197.5	156.6	3.8	7.4	43.4/42.5	1.1/1.0	365.3/360.5	101.3
21.7	196.8	155.7	3.8	7.1	43.3/42.5	1.0/1.0	363.4/360.0	100.9
23.4	196.8	156.6	3.8	7.2	43.4/42.2	1.1/1.0	364.5/360.7	101.0
25.4	194.0	154.2	4.0	7.2	42.8/42.8	1.1/1.1	359.4/360.7	99.6
29.4	193.5	156.1	4.7	6.8	43.0/42.8	1.3/1.3	361.0/362.6	99.6
32.9	194.9	157.8	4.8	6.8	43.4/42.2	1.3/1.4	364.3/363.2	100.3
35.2	194.9	156.9	4.8	7.2	43.2/42.0	1.3/1.4	363.8/363.0	100.2
38.4	196.1	156.7	4.3	7.0	43.4/42.0	1.2/1.2	364.1/361.0	100.9
40.4	196.1	157.4	4.0	7.0	43.6/41.8	1.1/1.1	364.6/360.8	101.1
43.9	194.8	159.2	3.8	7.0	44.0/42.5	1.0/1.1	364.8/362.0	100.8
45.4	195.6	159.3	3.8	7.3	43.9/42.5	1.0/1.1	366.0/362.7	100.9
47.4	194.1	160.1	3.5	6.7	44.2/42.5	1.0/1.0	364.4/362.3	100.6
47.9	194.1	160.9	3.5	6.8	44.4/52.7	1.0/ .9	365.3/362.5	100.8
48.6	192.1	158.5	3.5	6.9	43.7/42.8	1.0/1.0	360.9/362.7	99.5

*COMPUTED USING THE N2 CAL. FACTOR AND
THE KNOWN IONIZATION PROBABILITY OF H2O.

MISSION TOTAL ELAPSED TIME 33 DAYS

CALIB. PERIOD 28 ELAPSED TIME BETWEEN CALIB. 71.40 HOURS

CALIBRATION FACTORS (SENSITIVITY, TORR/VOLT)

		355T	360T	370T
NITROGEN	BEGIN	70.86	.00	70.43
OXYGEN	BEGIN	81.68	.00	81.01
CO2	BEGIN	5.63	.00	5.44

TWO GAS SENSOR COMPARATIVE DATA

TIME HR	N2 TOR	O2 TOR	CO2 TOR	H2O* TOR	O2-PCT MS/MDA	CO2-PCT MS/MDA	TOTAL-TOR MS/MDA	TOTAL-PCT MS
.1	195.7	161.9	3.7	3.8	44.6/42.8	1.0/1.0	365.1/362.8	100.6
.5	195.0	161.1	3.7	2.3	44.4/42.8	1.0/1.0	362.1/362.7	99.8
1.1	192.2	157.8	3.7	6.9	43.5/43.7	1.0/1.0	360.5/362.6	99.4
1.1	192.2	157.9	3.7	7.1	43.5/43.7	1.0/1.0	360.8/363.2	99.3
3.4	190.7	157.0	3.9	7.0	43.3/43.0	1.1/1.1	358.6/362.2	99.0
6.7	191.4	157.0	4.1	7.1	43.4/43.0	1.1/1.1	359.6/362.0	99.3
9.4	194.9	156.9	3.8	7.1	43.5/43.0	1.1/1.0	362.6/361.0	100.4
12.1	194.9	156.1	3.6	6.6	43.1/43.0	1.0/1.0	361.2/361.9	99.8
13.7	195.6	156.1	3.6	6.9	43.2/43.0	1.0/1.0	362.2/361.5	100.2
15.7	196.2	156.0	3.4	6.5	43.3/42.5	.9/1.0	362.0/360.0	100.5
20.5	200.6	156.1	3.4	7.0	43.2/42.0	.9/ .9	367.0/361.6	101.5
22.5	199.9	156.1	3.6	7.1	43.1/41.8	1.0/1.0	366.7/362.1	101.3
24.5	197.3	158.8	3.9	7.1	43.5/42.0	1.1/1.0	367.1/365.0	100.6
26.2	197.3	157.2	4.6	7.1	43.1/42.0	1.3/1.1	366.2/365.1	100.3
28.5	197.4	157.4	4.8	8.1	42.9/42.0	1.3/1.4	367.7/366.9	100.2
30.9	209.5	157.3	5.5	8.4	41.9/40.3	1.5/1.5	380.7/375.3	101.4
35.8	205.7	148.2	6.3	7.1	40.7/40.0	1.7/ .5	367.3/364.0	100.9
39.3	202.0	154.5	5.3	7.0	42.7/41.0	1.5/1.6	368.8/362.0	101.9
41.9	202.1	156.2	4.4	6.8	43.0/41.5	1.2/1.2	369.5/363.0	101.8
44.3	202.3	161.4	4.0	7.1	44.1/42.0	1.1/1.0	374.8/366.0	102.4
46.3	200.8	158.8	3.9	7.3	43.6/41.8	1.1/1.0	370.7/364.1	101.8
48.4	198.6	157.1	3.6	7.1	43.2/41.6	1.0/ .9	366.3/363.3	100.8
50.8	197.4	158.9	3.5	7.1	43.4/42.0	1.0/ .8	366.9/365.9	100.3
52.4	197.3	158.9	3.5	7.1	43.5/42.0	1.0/ .8	366.8/365.5	100.4
54.7	196.6	158.0	3.4	7.3	43.3/42.0	.9/ .9	365.3/365.1	100.1
57.4	201.3	159.4	3.3	8.0	44.0/42.0	.9/ .8	372.0/362.5	102.6
59.9	199.2	158.6	2.9	7.1	43.8/42.0	.8/ .7	367.7/361.9	101.6
63.9	198.5	160.2	2.9	7.2	44.2/42.1	.8/ .7	368.8/362.4	101.8
65.9	198.7	162.1	3.2	7.4	44.4/42.1	.9/ .7	371.4/365.0	101.8
67.9	198.7	163.0	3.1	7.3	44.6/42.3	.8/ .7	372.1/365.5	101.8
70.1	198.7	162.9	2.8	7.6	44.6/42.5	.8/ .6	372.0/365.3	101.8
70.8	200.9	163.0	2.8	7.4	44.6/42.5	.8/ .7	374.0/365.5	102.3

* COMPUTED USING THE N2 CAL. FACTOR AND THE KNOWN IONIZATION PROBABILITY OF H2O.

MISSION TOTAL ELAPSED TIME 36 DAYS

CALIB. PERIOD 29 ELAPSED TIME BETWEEN CALIB. 49.50 HOURS

CALIBRATION FACTORS (SENSITIVITY, TORR/VOLT)

		355T	360T	370T
NITROGEN	BEGIN	.00	70.15	.00
OXYGEN	BEGIN	.00	80.96	.00
CO2	BEGIN	.00	5.54	.00

TWO GAS SENSOR COMPARATIVE DATA

TIME HR	N2 TOR	O2 TOR	CO2 TOR	H2O* TOR	O2-PCT MS/MDA	CO2-PCT MS/MDA	TOTAL-TOR MS/MDA	TOTAL-PCT MS
.2	200.6	161.9	3.0	4.0	44.3/43.0	.8/ .7	369.6/365.5	101.1
.7	197.1	160.3	3.0	7.2	43.9/43.6	.8/ .7	367.7/365.0	100.7
2.5	195.7	157.9	3.1	7.5	43.5/42.8	.9/ .8	364.2/362.9	100.4
4.7	195.7	157.9	3.3	7.5	43.6/43.0	.9/ .8	364.4/362.5	100.5
6.4	195.0	157.9	3.4	8.1	43.4/42.5	.9/ .9	364.4/363.5	100.2
8.5	196.4	159.5	3.4	7.3	44.0/42.8	.9/ .9	366.6/362.5	101.1
10.5	198.5	158.7	3.3	7.3	43.9/42.8	.9/ .8	367.8/361.2	101.8
13.7	197.8	159.5	3.0	6.9	44.2/42.5	.8/ .7	367.3/360.9	101.8
15.7	198.5	159.5	3.0	7.3	44.4/42.3	.8/ .7	368.3/359.4	102.5
17.7	197.8	157.9	2.9	7.2	44.0/42.7	.8/ .7	365.9/359.0	101.9
19.7	197.1	158.7	2.8	6.9	44.2/42.5	.8/ .7	365.5/359.0	101.8
21.9	197.1	157.9	2.8	7.2	44.0/42.5	.8/ .7	365.0/359.2	101.6
23.9	197.1	157.9	2.8	7.5	44.0/42.5	.8/ .7	365.3/359.1	101.7
26.0	195.7	156.3	2.9	7.5	43.6/42.5	.8/ .7	362.4/358.5	101.1
27.9	194.3	157.9	3.6	7.6	43.7/43.5	1.0/ .9	363.4/361.3	100.6
30.6	194.3	160.3	3.6	7.2	44.2/43.2	1.0/ .9	365.4/362.3	100.9
33.2	195.0	160.3	3.8	8.3	44.3/43.5	1.0/ .0	367.4/362.2	101.4
35.3	195.7	158.7	3.7	8.4	44.1/42.7	1.0/1.0	366.5/359.5	102.0
37.8	195.7	159.5	3.5	7.9	44.4/42.8	1.0/ .9	366.7/359.0	102.1
39.4	195.7	160.3	3.6	6.9	44.6/43.0	1.0/ .9	366.5/359.8	101.9
42.7	197.8	161.9	3.6	6.9	45.1/43.0	1.0/ .9	370.3/359.0	103.1
44.8	198.5	160.3	3.6	6.9	44.7/43.0	1.0/ .9	369.3/358.5	103.0
47.8	197.1	158.7	3.8	7.2	44.2/42.0	1.1/1.0	366.8/359.0	102.2
49.1	195.7	160.3	3.9	7.0	44.5/42.8	1.1/1.0	366.9/360.0	101.9

*COMPUTED USING THE N2 CAL. FACTOR AND
THE KNOWN IONIZATION PROBABILITY OF H2O.

MISSION TOTAL ELAPSED TIME 28 DAYS

CALIB. PERIOD 30 ELAPSED TIME BETWEEN CALIB. 46.53 HOURS

CALIBRATION FACTORS (SENSITIVITY, TORR/VOLT)

		355T	360T	370T
NITROGEN	BEGIN	.00	69.06	.00
OXYGEN	BEGIN	.00	79.87	.00
CO2	BEGIN	.00	5.54	.00

TWO GAS SENSOR COMPARATIVE DATA

TIME HR	N2 TOR	O2 TOR	CO2 TOR	H2O* TOR	O2-PCT MS/MDA	CO2-PCT MS/MDA	TOTAL-TOR MS/MDA	TOTAL-PCT MS
.7	191.3	157.4	3.9	6.9	43.8/43.4	1.1/1.1	359.5/359.4	100.0
3.3	190.6	155.0	4.0	7.2	43.2/43.0	1.1/1.1	356.8/358.9	99.4
5.8	190.6	155.0	4.4	7.1	43.2/43.5	1.2/1.0	357.0/359.0	99.5
8.1	192.0	156.6	4.3	7.0	43.6/42.8	1.2/1.2	359.9/358.8	100.3
10.5	192.7	156.6	4.3	7.0	43.9/43.0	1.2/1.1	360.6/357.0	101.0
12.5	192.7	157.4	4.2	6.9	44.1/43.0	1.2/1.1	361.1/356.8	101.2
14.8	192.7	158.2	4.2	6.9	44.2/43.5	1.2/1.1	361.9/358.0	101.1
16.8	192.7	159.0	4.0	7.0	44.4/43.5	1.1/1.1	362.7/358.0	101.3
18.3	192.7	159.0	3.9	6.9	44.4/43.5	1.1/1.1	362.5/357.7	101.3
19.6	193.4	159.7	3.9	7.0	44.7/43.5	1.1/1.1	364.1/357.5	101.8
22.3	190.6	157.4	4.0	7.1	44.1/43.5	1.1/1.1	359.1/356.9	100.6
24.0	189.2	155.8	4.0	7.0	43.7/43.0	1.1/1.1	356.0/356.5	99.9
26.3	187.8	156.6	3.9	6.8	43.7/43.5	1.1/1.1	355.1/358.3	99.1
28.3	189.9	159.7	4.4	7.4	44.3/43.5	1.2/1.2	361.4/360.4	100.3
30.3	191.3	159.0	4.0	6.7	44.2/43.7	1.1/1.1	361.0/360.0	100.3
32.6	191.3	159.0	4.2	7.6	44.2/43.5	1.2/1.2	362.1/359.8	100.6
33.8	191.3	159.0	4.0	7.4	44.3/43.5	1.1/1.1	361.7/359.2	100.7
36.0	191.3	159.7	4.0	7.5	44.5/43.3	1.1/1.1	362.6/359.0	101.0
37.8	192.0	159.7	4.0	7.4	44.5/43.0	1.1/1.1	363.1/358.7	101.2
39.7	192.0	159.7	3.9	7.4	44.6/43.0	1.1/1.1	363.1/357.9	101.4
41.5	192.0	159.0	3.9	7.8	44.4/43.0	1.1/1.1	362.6/357.6	101.4
43.4	192.7	159.0	4.2	8.4	44.4/43.0	1.2/1.1	364.2/358.1	101.7
46.1	182.3	153.4	3.8	7.7	42.4/43.5	1.0/1.1	347.1/361.9	95.9

*COMPUTED USING THE N2 CAL. FACTOR AND
THE KNOWN IONIZATION PROBABILITY OF H2O.

MISSION TOTAL ELAPSED TIME 40 DAYS

CALIB. PERIOD 31 ELAPSED TIME BETWEEN CALIB. 23.90 HOURS

CALIBRATION FACTORS (SENSITIVITY, TORR/VOLT)

		355T	360T	370T
NITROGEN	BEGIN	.00	73.34	.00
OXYGEN	BEGIN	.00	84.80	.00
CO2	BEGIN	.00	5.90	.00

TWO GAS SENSOR COMPARATIVE DATA

TIME HR	N2 TOR	O2 TOR	CO2 TOR	H2O* TOR	O2-PCT MS/MDA	CO2-PCT MS/MDA	TOTAL-TOR MS/MDA	TOTAL-PCT MS
.4	194.3	162.8	4.4	1.9	45.0/43.2	1.2/1.2	363.4/361.5	100.5
1.7	189.9	159.4	4.4	7.4	44.1/44.2	1.2/1.2	361.2/361.5	99.9
2.3	188.5	160.3	4.6	7.3	44.4/43.8	1.3/1.2	360.7/361.0	99.9
3.8	189.2	159.4	4.7	7.3	44.3/43.0	1.3/1.3	360.6/360.0	100.2
5.4	189.9	159.4	4.6	7.3	44.4/43.7	1.3/1.3	361.3/359.0	100.6
6.4	189.9	158.6	4.7	8.5	44.1/43.5	1.3/1.3	361.7/359.9	100.5
7.4	190.7	159.4	4.7	7.7	44.4/43.5	1.3/1.3	362.5/359.0	101.0
9.8	190.7	158.6	4.6	7.6	44.4/43.5	1.3/1.3	361.4/357.4	101.1
10.4	190.7	158.6	4.5	7.3	44.4/43.5	1.3/1.3	361.1/357.0	101.2
11.4	190.7	158.6	4.8	7.8	44.4/43.3	1.3/1.4	361.8/357.2	101.3
12.4	190.7	157.7	4.8	8.0	44.2/43.2	1.3/1.4	361.2/357.1	101.1
13.4	190.7	157.7	4.7	7.2	44.2/43.2	1.3/1.3	360.3/356.8	101.0
14.4	191.4	158.6	4.7	7.2	44.5/43.2	1.3/1.3	361.9/356.2	101.6
16.9	191.4	158.6	4.5	7.1	44.6/43.2	1.3/1.3	361.7/355.5	101.7
18.9	191.4	158.6	4.2	6.8	44.6/43.2	1.2/1.2	361.0/355.2	101.6
21.5	191.4	160.3	4.1	7.2	45.1/43.5	1.1/1.1	363.0/355.5	102.1
23.4	190.7	157.7	4.0	7.7	44.3/43.4	1.1/1.1	360.1/355.8	101.2

*COMPUTED USING THE N2 CAL. FACTOR AND
THE KNOWN IONIZATION PROBABILITY OF H2O.

MISSION TOTAL ELAPSED TIME 41 DAYS

CALIB. PERIOD 32 ELAPSED TIME BETWEEN CALIB. 25.08 HOURS

CALIBRATION FACTORS (SENSITIVITY, TORR/VOLT)

		355T	360T	370T
NITROGEN	BEGIN	.00	65.25	.00
OXYGEN	BEGIN	.00	75.18	.00
CO2	BEGIN	.00	5.14	.00

TWO GAS SENSOR COMPARATIVE DATA

TIME HR	N2 TOR	O2 TOR	CO2 TOR	H2O* TOR	O2-PCT MS/MDA	CO2-PCT MS/MDA	TOTAL-TOR MS/MDA	TOTAL-PCT MS
.3	193.1	157.9	4.1	2.8	44.3/43.4	1.2/1.2	357.9/356.0	100.5
.5	189.9	156.4	4.1	7.0	43.9/43.2	1.2/1.2	357.4/356.0	100.4
1.5	189.2	156.4	4.2	7.6	43.9/43.5	1.2/1.1	357.3/356.0	100.4
3.5	191.2	151.9	4.1	7.0	42.7/42.2	1.2/1.1	354.2/356.0	99.5
5.5	192.5	151.9	4.1	7.1	42.9/42.5	1.1/1.1	355.5/354.0	100.4
6.5	193.1	151.1	4.1	7.4	42.7/42.3	1.2/1.2	355.7/354.1	100.5
8.9	194.4	150.4	4.1	7.4	42.5/42.0	1.2/1.1	356.3/354.0	100.6
12.3	195.7	151.9	4.0	7.2	42.8/41.0	1.1/1.0	358.8/355.0	101.1
13.3	195.7	152.6	4.0	7.2	42.9/41.4	1.1/1.0	359.6/356.0	101.0
15.0	195.7	159.4	4.0	7.2	44.1/42.1	1.1/1.0	366.3/361.0	101.5
17.5	197.7	156.4	4.1	7.7	43.4/41.8	1.1/1.1	365.8/360.5	101.5
19.5	197.7	158.6	4.2	7.5	43.8/42.0	1.2/1.1	368.0/362.0	101.7
21.0	197.7	159.4	4.2	7.7	44.0/42.0	1.1/1.1	368.9/362.6	101.7
23.8	198.4	159.4	4.1	7.3	43.7/42.0	1.1/1.0	369.1/364.5	101.3
24.7	197.7	159.4	4.1	7.3	43.8/42.2	1.1/1.0	368.5/364.2	101.2

* COMPUTED USING THE N2 CAL. FACTOR AND THE KNOWN IONIZATION PROBABILITY OF H2O.

MISSION TOTAL ELAPSED TIME 42 DAYS

CALIB. PERIOD 33 ELAPSED TIME BETWEEN CALIB. 22.52 HOURS

CALIBRATION FACTORS (SENSITIVITY, TORR/VOLT)

		355T	360T	370T
NITROGEN	BEGIN	.00	65.01	.00
OXYGEN	BEGIN	.00	74.86	.00
CO2	BEGIN	.00	5.14	.00

TWO GAS SENSOR COMPARATIVE DATA

TIME HR	N2 TOR	O2 TOR	CO2 TOR	H2O* TOR	O2-PCT MS/MDA	CO2-PCT MS/MDA	TOTAL-TOR MS/MDA	TOTAL-PCT MS
.2	198.9	160.2	4.2	3.3	44.0/42.1	1.1/1.0	366.6/364.1	100.7
2.1	195.0	158.7	4.2	7.3	43.5/42.0	1.1/1.1	365.2/365.1	100.0
6.3	193.1	158.7	4.6	7.4	43.2/42.0	1.2/1.1	363.8/367.2	99.1
8.6	195.7	158.7	4.6	7.6	43.2/42.0	1.2/1.1	366.6/367.2	99.8
11.7	196.3	160.2	4.6	6.8	43.8/42.2	1.3/1.1	367.9/366.0	100.5
13.7	197.6	160.2	4.4	7.0	43.8/42.2	1.2/1.1	369.2/365.5	101.0
16.2	197.6	160.2	4.4	6.8	44.0/42.1	1.2/1.1	369.0/364.5	101.2
18.2	197.6	160.2	4.2	6.8	44.0/42.2	1.2/1.1	368.8/363.8	101.4
20.0	198.3	160.2	4.1	6.9	44.0/42.7	1.1/1.0	369.4/363.7	101.6
20.5	197.6	159.5	4.1	7.2	43.9/42.5	1.1/1.1	368.4/363.4	101.4
22.4	197.0	159.5	4.2	7.3	43.8/43.2	1.2/1.1	367.9/364.0	101.1

*COMPUTED USING THE N2 CAL. FACTOR AND
THE KNOWN IONIZATION PROBABILITY OF H2O.

MISSION TOTAL ELAPSED TIME 43 DAYS

CALIB. PERIOD 34 ELAPSED TIME BETWEEN CALIB. 45.97 HOURS

CALIBRATION FACTORS (SENSITIVITY, TORR/VOLT)

		355T	360T	370T
NITROGEN	BEGIN	.00	64.77	.00
OXYGEN	BEGIN	.00	74.86	.00
CO2	BEGIN	.00	5.07	.00

TWO GAS SENSOR COMPARATIVE DATA

TIME HR	N2 TOR	O2 TOR	CO2 TOR	H2O* TOR	O2-PCT MS/MDA	CO2-PCT MS/MDA	TOTAL-TOR MS/MDA	TOTAL-PCT MS
.5	195.0	158.0	4.2	7.2	43.4/42.6	1.2/1.2	364.4/363.8	100.2
1.2	194.3	158.0	4.4	7.2	43.5/42.3	1.2/1.2	363.9/363.5	100.1
2.7	195.6	159.5	4.8	7.7	43.7/42.0	1.3/1.3	367.5/364.7	100.8
9.0	193.0	158.0	4.8	7.2	43.3/42.0	1.3/1.3	363.0/365.0	99.5
12.5	193.7	159.5	4.5	6.9	43.8/42.5	1.2/1.2	364.5/364.2	100.1
15.4	193.7	162.5	4.3	6.9	44.5/43.0	1.2/1.1	367.4/365.2	100.6
17.2	193.7	161.7	4.4	6.9	44.2/42.8	1.2/1.2	366.7/365.5	100.3
19.2	193.7	161.0	4.5	7.1	44.3/42.5	1.2/1.2	366.2/363.0	100.9
21.6	193.0	159.5	4.4	6.9	44.0/42.8	1.2/1.2	363.8/362.4	100.4
26.0	189.8	159.5	4.6	7.1	44.0/44.0	1.3/1.3	360.9/362.8	99.5
28.2	190.4	159.5	5.1	8.2	43.8/43.5	1.4/1.4	363.2/364.3	99.7
31.5	191.1	159.5	4.7	7.1	44.0/43.5	1.3/1.3	362.3/362.2	100.0
33.2	191.7	159.5	4.5	7.0	44.1/43.5	1.2/1.3	362.7/361.6	100.3
34.7	191.7	161.0	4.3	6.9	44.6/43.5	1.2/1.2	363.9/360.8	100.9
37.2	191.7	161.0	4.4	6.9	44.6/43.5	1.2/1.3	363.9/360.7	100.9
39.2	191.7	161.0	4.2	6.8	44.8/43.5	1.2/1.2	363.7/359.0	101.3
41.5	192.4	161.0	4.0	6.8	44.9/43.5	1.1/1.1	364.0/358.2	101.6
44.0	191.7	158.7	4.1	7.2	44.3/43.5	1.1/1.2	361.7/358.0	101.0
45.5	190.4	158.0	4.1	7.1	44.1/43.5	1.1/1.2	359.6/358.3	100.4

*COMPUTED USING THE N2 CAL. FACTOR AND
THE KNOWN IONIZATION PROBABILITY OF H2O.

MISSION TOTAL ELAPSED TIME 45 DAYS

CALIB. PERIOD 35 ELAPSED TIME BETWEEN CALIB. 43.65 HOURS

CALIBRATION FACTORS (SENSITIVITY, TORR/VOLT)

		355T	360T	370T
NITROGEN	BEGIN	.00	65.25	.00
OXYGEN	BEGIN	.00	75.18	.00
CO2	BEGIN	.00	5.14	.00

	TWO GAS SENSOR				COMPARATIVE DATA			
TIME HR	N2 TOR	O2 TOR	CO2 TOR	H2O* TOR	O2-PCT MS/MDA	CO2-PCT MS/MDA	TOTAL-TOR MS/MDA	TOTAL-PCT MS
.2	191.8	160.1	4.6	2.9	44.7/43.7	1.3/1.3	359.4/357.9	100.4
3.7	193.8	160.1	4.5	7.1	44.5/43.5	1.3/1.3	365.5/359.5	101.7
7.6	193.8	160.1	4.5	6.8	44.7/43.3	1.2/1.2	365.2/358.6	101.8
8.7	194.4	160.1	4.6	7.2	44.7/43.3	1.3/1.3	366.3/358.4	102.2
11.1	195.7	161.6	4.6	7.0	45.2/43.4	1.3/1.3	369.0/357.5	103.2
13.6	196.4	160.1	4.9	7.7	44.9/43.2	1.4/1.4	369.1/356.9	103.4
15.7	196.4	160.1	4.7	8.0	45.0/43.2	1.3/1.3	369.2/355.5	103.9
17.1	195.7	159.4	4.6	7.0	44.9/43.3	1.3/1.3	366.7/355.0	103.3
19.0	193.1	160.1	4.5	7.1	44.7/43.7	1.2/1.3	364.8/358.0	101.9
20.1	191.2	158.6	4.6	6.8	44.3/43.7	1.3/1.3	361.2/358.0	100.9
21.3	190.5	159.4	4.5	6.9	44.4/ .0	1.3/ .0	361.3/359.0	100.7
24.2	189.2	159.4	4.7	6.6	44.1/43.7	1.3/1.3	360.0/361.0	99.7
25.2	190.5	160.1	4.8	7.1	44.3/43.8	1.3/1.4	362.5/361.1	100.4
27.1	192.5	160.1	4.9	7.2	44.3/43.7	1.4/1.3	364.7/361.2	101.0
29.1	193.1	160.9	5.0	7.4	44.6/43.9	1.4/1.4	366.4/360.7	101.6
31.1	193.1	161.6	4.9	7.1	45.0/43.9	1.4/1.4	366.7/359.1	102.1
33.1	193.8	161.6	4.7	7.0	45.2/44.0	1.3/1.3	367.2/357.9	102.6
35.4	193.8	160.1	4.7	6.7	44.8/43.2	1.3/1.3	365.3/357.2	102.3
37.6	193.8	160.1	4.6	6.8	44.9/42.8	1.3/1.3	365.3/356.9	102.4
39.8	193.8	160.1	4.6	7.0	45.0/43.0	1.3/1.2	365.5/356.2	102.6
41.8	194.4	160.1	4.2	6.8	45.0/43.3	1.2/1.2	365.6/356.0	102.7
42.8	193.8	161.6	4.2	6.9	45.2/ .0	1.2/ .0	366.5/357.8	102.4

*COMPUTED USING THE N2 CAL. FACTOR AND
THE KNOWN IONIZATION PROBABILITY OF H2O.

MISSION TOTAL ELAPSED TIME 47 DAYS

CALIB. PERIOD 36 ELAPSED TIME BETWEEN CALIB. 70.33 HOURS

CALIBRATION FACTORS (SENSITIVITY, TORR/VOLT)

		355T	360T	370T
NITROGEN	BEGIN	.00	63.84	.00
OXYGEN	BEGIN	.00	73.63	.00
CO2	BEGIN	.00	4.93	.00

	TWO GAS SENSOR				COMPARATIVE DATA			
TIME HR	N2 TOR	O2 TOR	CO2 TOR	H2O* TOR	O2-PCT MS/MDA	CO2-PCT MS/MDA	TOTAL-TOR MS/MDA	TOTAL-PCT MS
.9	186.4	154.6	4.1	6.6	43.3/ .0	1.1/ .0	351.7/357.5	98.4
2.2	185.1	156.1	4.3	6.7	43.6/43.5	1.2/1.2	352.2/358.0	98.4
3.2	184.5	155.4	4.3	6.6	43.4/43.3	1.2/1.2	350.8/358.0	98.0
5.2	184.5	156.1	4.4	6.7	43.5/43.5	1.2/1.3	351.7/358.9	98.0
7.4	187.7	157.6	4.4	6.7	44.1/43.3	1.2/1.2	356.3/357.0	99.8
9.9	187.1	157.6	4.3	6.7	44.3/43.5	1.2/1.1	355.6/356.0	99.9
11.7	187.7	157.6	4.2	6.7	44.4/43.5	1.2/1.1	356.1/355.0	100.3
12.8	189.0	158.3	4.1	6.7	44.6/43.5	1.2/1.1	358.1/355.0	100.9
14.7	189.0	162.0	4.2	7.1	45.2/44.0	1.2/1.2	362.3/358.0	101.2
15.8	189.6	161.2	4.2	7.2	45.1/43.8	1.2/1.2	362.3/357.9	101.2
17.1	189.0	160.5	4.5	7.6	44.9/43.5	1.3/1.3	361.5/357.3	101.2
19.2	189.6	159.8	4.4	7.1	45.0/43.2	1.3/1.3	360.9/355.0	101.7
20.6	189.6	157.6	4.3	6.9	44.3/43.0	1.2/1.2	358.5/355.4	100.9
22.5	188.3	156.1	4.3	7.2	44.0/44.0	1.2/1.2	355.9/355.0	100.3
23.9	186.4	155.4	4.4	7.4	43.6/43.8	1.2/1.3	353.6/356.2	99.3
25.6	185.8	156.1	4.4	7.1	43.7/44.0	1.2/1.2	353.4/357.1	99.0
26.7	185.1	156.1	4.3	6.8	43.6/44.0	1.2/1.2	352.3/357.8	98.5
28.7	185.8	156.8	4.5	7.4	43.7/44.0	1.3/1.3	354.5/359.0	98.7
31.1	188.3	158.3	4.4	7.1	44.2/44.0	1.2/1.2	358.2/358.0	100.1
33.2	189.0	160.5	4.5	7.3	44.6/44.3	1.2/1.3	361.3/359.7	100.4
36.2	192.2	160.5	4.5	8.0	44.3/44.0	1.3/1.2	365.2/362.2	100.8
38.6	194.7	160.5	4.4	7.9	44.6/43.7	1.2/1.2	367.6/360.2	102.1
41.4	195.4	158.3	4.8	6.9	44.1/43.3	1.3/1.3	365.4/358.9	101.8
43.8	196.0	157.6	4.2	6.8	44.1/43.3	1.2/1.2	364.6/357.3	102.1
45.7	193.4	156.1	4.0	6.7	43.7/43.0	1.1/1.1	360.2/357.0	100.9
47.7	189.0	154.6	3.9	7.0	43.2/43.0	1.1/1.1	354.6/358.2	99.0
52.3	189.0	158.3	3.9	7.0	43.7/43.7	1.1/1.0	358.3/362.5	98.8
54.3	190.2	159.0	4.0	7.3	43.9/43.7	1.1/1.1	360.6/362.6	99.5
56.2	192.8	159.0	3.9	7.3	44.1/43.5	1.1/1.1	363.1/361.0	100.6
58.6	193.4	158.3	3.9	9.1	43.9/43.2	1.1/1.1	364.8/360.3	101.2
60.5	193.4	157.6	3.9	7.0	43.9/43.0	1.1/1.1	361.9/358.9	100.8
62.7	192.8	157.6	3.9	7.1	44.1/43.0	1.1/1.1	361.4/357.1	101.2
65.3	193.4	156.8	4.1	7.0	43.9/43.2	1.1/1.2	361.4/357.1	101.2
67.2	194.1	156.8	4.1	7.2	43.9/43.2	1.1/1.2	362.2/357.0	101.5
69.2	192.2	156.8	3.9	7.2	44.0/43.0	1.1/1.1	360.2/356.5	101.0
69.9	190.9	155.4	4.0	7.4	43.5/43.3	1.1/1.1	357.6/357.0	100.2

*COMPUTED USING THE N2 CAL. FACTOR AND
THE KNOWN IONIZATION PROBABILITY OF H2O.

MISSION TOTAL ELAPSED TIME 50 DAYS

CALIB. PERIOD 37 ELAPSED TIME BETWEEN CALIB. 47.95 HOURS

CALIBRATION FACTORS (SENSITIVITY, TORR/VOLT)

		355T	360T	370T
NITROGEN	BEGIN	.00	64.07	.00
OXYGEN	BEGIN	.00	74.86	.00
CO2	BEGIN	.00	5.14	.00

TWO GAS SENSOR COMPARATIVE DATA

TIME HR	N2 TOR	O2 TOR	CO2 TOR	H2O* TOR	O2-PCT MS/MDA	CO2-PCT MS/MDA	TOTAL-TOR MS/MDA	TOTAL-PCT MS
.4	183.2	157.2	4.1	7.8	44.0/43.0	1.2/1.1	352.4/357.3	98.6
.6	187.7	155.0	4.1	9.0	43.4/43.0	1.2/1.1	355.8/357.4	99.5
3.6	189.0	158.7	4.3	8.4	43.1/44.2	1.2/1.3	360.4/368.0	97.9
5.3	188.4	158.7	4.2	10.8	42.8/43.5	1.1/1.1	362.1/370.8	97.6
9.5	189.0	158.7	4.3	9.3	43.6/43.0	1.2/1.1	361.2/364.0	99.2
11.1	189.7	157.2	4.5	9.6	43.5/42.8	1.2/1.2	361.0/361.7	99.8
12.8	189.0	155.7	4.3	8.7	43.4/42.8	1.2/1.1	357.7/358.8	99.7
14.6	190.3	156.5	4.3	8.2	43.9/42.5	1.2/1.1	359.2/356.8	100.7
15.7	190.3	157.2	4.3	8.1	44.2/42.7	1.2/1.1	359.8/356.0	101.1
17.6	190.3	162.5	4.1	7.6	45.3/43.5	1.1/1.0	364.5/358.4	101.7
18.7	189.7	161.7	4.0	7.5	45.2/43.5	1.1/1.0	362.9/357.4	101.5
20.5	189.7	163.2	3.9	7.6	45.5/44.0	1.1/ .9	364.3/358.8	101.5
22.2	187.1	163.2	3.9	7.6	45.5/44.5	1.1/ .9	361.8/359.0	100.8
25.1	182.0	161.7	4.0	7.4	44.7/45.0	1.1/1.1	355.1/362.0	98.1
27.1	179.4	159.5	4.1	7.4	44.2/45.0	1.1/1.2	350.4/360.8	97.1
29.1	179.4	158.7	4.2	7.4	44.0/44.8	1.2/1.3	349.7/360.5	97.0
31.2	182.0	160.2	4.1	7.5	44.6/44.0	1.1/1.2	353.8/359.0	98.6
34.5	178.8	160.2	4.0	7.3	45.0/44.0	1.1/1.1	350.3/356.2	98.3
35.8	188.4	160.2	4.0	7.2	45.0/43.8	1.1/1.1	359.8/356.0	101.1
37.7	190.9	159.5	4.0	7.5	44.7/73.5	1.1/1.1	361.9/357.0	101.4
38.8	191.6	158.7	4.1	7.5	44.4/42.8	1.2/1.2	361.9/357.3	101.3
40.8	194.8	161.7	4.2	7.2	44.8/42.8	1.2/1.2	367.9/361.0	101.9
42.8	196.1	163.2	4.5	8.1	45.1/43.0	1.3/1.3	371.8/362.0	102.7
44.7	194.8	162.5	4.3	7.6	45.0/42.8	1.2/1.2	369.1/361.1	102.2
46.8	190.9	159.5	4.2	7.8	44.0/43.5	1.2/1.1	362.4/362.3	100.0
47.3	189.7	159.5	4.2	7.6	44.0/ .0	1.2/ .0	360.9/362.8	99.5

*COMPUTED USING THE N2 CAL. FACTOR AND
THE KNOWN IONIZATION PROBABILITY OF H2O.

MISSION TOTAL ELAPSED TIME 52 DAYS

CALIB. PERIOD 38 ELAPSED TIME BETWEEN CALIB. 73.60 HOURS

CALIBRATION FACTORS (SENSITIVITY, TORR/VOLT)

		355T	360T	370T
NITROGEN	BEGIN	.00	65.01	.00
OXYGEN	BEGIN	.00	75.49	.00
CO2	BEGIN	.00	5.00	.00

TWO GAS SENSOR COMPARATIVE DATA

TIME HR	N2 TOR	O2 TOR	CO2 TOR	H2O* TOR	O2-PCT MS/MDA	CO2-PCT MS/MDA	TOTAL-TOR MS/MDA	TOTAL-PCT MS
.6	192.4	160.8	4.2	2.5	44.4/43.2	1.2/1.1	360.0/362.5	99.3
3.7	184.6	160.0	4.1	7.3	43.6/44.5	1.1/ .0	356.1/367.5	96.9
5.4	184.6	160.0	4.4	7.9	43.3/44.3	1.2/1.0	357.0/369.5	96.6
8.2	185.9	160.0	4.4	7.6	43.6/43.9	1.2/1.3	358.1/367.5	97.4
10.9	189.8	160.0	4.4	7.6	43.8/43.9	1.2/1.3	362.0/365.8	98.9
13.7	192.4	160.8	4.3	7.6	44.3/43.5	1.2/1.3	365.2/363.2	100.5
14.8	193.1	160.0	4.2	7.7	44.2/43.0	1.2/1.2	365.1/362.4	100.7
16.9	194.4	161.6	4.1	7.3	44.8/43.0	1.2/1.2	367.4/360.8	101.8
19.1	197.6	164.6	4.0	7.4	45.6/43.0	1.1/1.2	373.6/360.8	103.6
20.6	198.3	164.6	4.0	8.1	45.7/43.0	1.1/1.2	375.0/360.5	104.0
22.9	195.7	162.3	4.0	8.2	45.1/43.0	1.1/1.2	370.2/360.0	102.8
25.0	191.1	160.8	4.2	8.5	44.4/ .0	1.2/ .0	364.6/361.8	100.8
26.7	191.1	160.8	4.3	8.2	44.5/43.0	1.2/1.2	364.5/361.7	100.8
28.4	191.1	158.5	4.5	8.5	43.9/43.0	1.2/1.2	362.6/360.9	100.5
32.2	192.4	159.3	4.4	8.2	44.4/42.5	1.2/1.2	364.4/359.0	101.5
34.4	192.4	158.5	4.2	7.9	44.3/42.2	1.2/1.1	363.1/358.0	101.4
36.5	193.1	158.5	4.0	7.6	44.4/42.3	1.1/1.1	363.3/357.1	101.7
38.8	193.7	160.8	4.1	7.8	44.9/42.7	1.2/1.2	366.5/358.0	102.4
41.8	194.4	164.6	4.0	7.5	45.8/43.0	1.1/1.1	370.5/359.0	103.2
44.7	195.0	165.3	4.4	8.3	45.8/43.2	1.2/1.2	373.1/360.8	103.4
46.7	194.4	164.6	4.3	7.9	45.7/43.2	1.2/1.2	371.2/360.2	103.0
50.1	192.4	164.6	4.3	8.4	45.5/43.4	1.2/1.2	369.7/362.0	102.1
52.1	193.1	165.3	4.2	7.6	45.7/43.5	1.2/1.2	370.3/362.0	102.3
54.2	193.1	166.1	4.5	8.5	45.9/43.5	1.3/1.2	372.2/362.2	102.8
56.3	193.7	166.1	4.5	8.4	45.8/43.7	1.2/1.2	372.7/362.3	102.9
60.2	193.7	166.1	4.4	8.4	46.0/43.8	1.2/1.2	372.6/361.2	103.2
62.6	194.4	165.3	4.4	8.2	45.9/43.7	1.2/1.2	372.3/360.5	103.3
64.6	193.7	165.3	4.4	8.5	45.8/43.3	1.2/1.2	372.0/360.8	103.1
66.7	193.7	165.3	4.2	7.8	45.9/43.7	1.2/1.2	371.1/359.9	103.1
68.7	193.7	165.3	4.1	7.6	46.0/44.0	1.1/1.1	370.8/359.5	103.1
70.8	193.7	165.3	4.1	8.0	45.9/44.1	1.1/1.1	371.2/360.3	103.0
73.0	191.8	165.3	4.1	8.4	45.7/44.1	1.1/1.1	369.6/362.0	102.1

*COMPUTED USING THE N2 CAL. FACTOR AND
THE KNOWN IONIZATION PROBABILITY OF H2O.

MISSION TOTAL ELAPSED TIME 55 DAYS

CALIB. PERIOD 39 ELAPSED TIME BETWEEN CALIB. 48.48 HOURS

CALIBRATION FACTORS (SENSITIVITY, TORR/VOLT)

		355T	360T	370T
NITROGEN	BEGIN	.00	63.39	.00
OXYGEN	BEGIN	.00	73.33	.00
CO2	BEGIN	.00	4.93	.00

	TWO GAS SENSOR				COMPARATIVE DATA			
TIME HR	N2 TOR	O2 TOR	CO2 TOR	H2O* TOR	O2-PCT MS/MDA	CO2-PCT MS/MDA	TOTAL-TOR MS/MDA	TOTAL-PCT MS
.1	189.5	162.8	4.0	3.2	45.0/44.1	1.1/1.1	359.5/361.5	99.5
1.8	186.4	159.9	4.0	7.5	44.1/44.2	1.1/1.1	357.8/362.2	98.8
3.5	187.6	161.3	4.1	7.8	44.5/44.2	1.1/1.2	360.8/362.3	99.6
5.7	190.2	162.1	4.2	8.2	44.8/44.2	1.2/1.1	364.6/362.0	100.7
7.6	192.1	161.3	4.0	7.9	44.8/44.0	1.1/1.1	365.3/360.0	101.5
9.6	192.7	161.3	4.0	7.4	44.9/43.6	1.1/1.0	365.4/359.1	101.8
12.6	192.1	161.3	3.9	7.8	44.9/43.5	1.1/1.1	365.1/359.0	101.7
14.6	192.1	161.3	4.0	8.0	45.0/43.5	1.1/1.1	365.4/358.6	101.9
16.6	192.7	161.3	4.0	7.7	45.1/43.5	1.1/1.1	365.7/358.0	102.2
18.6	192.7	161.3	3.9	7.6	45.1/43.5	1.1/1.1	365.6/357.5	102.3
20.6	190.2	159.9	3.8	7.8	44.7/43.5	1.1/1.0	361.7/357.5	101.2
23.4	187.6	159.1	3.9	7.9	44.2/43.5	1.1/1.0	358.5/360.0	99.6
25.4	186.4	159.1	4.0	7.9	44.0/43.5	1.1/1.0	357.4/361.5	98.9
27.5	186.4	159.9	4.1	7.7	44.1/43.8	1.1/1.1	358.0/362.1	98.9
29.9	188.3	161.3	4.0	8.0	44.6/43.9	1.1/1.1	361.6/361.9	99.9
31.6	188.3	160.6	4.3	8.4	44.5/43.9	1.2/1.1	361.6/360.6	100.3
33.7	188.9	159.9	4.4	8.1	44.5/43.5	1.2/1.2	361.2/359.3	100.5
35.9	188.3	160.6	4.4	8.1	44.8/43.5	1.2/1.2	361.3/358.8	100.7
38.0	190.8	159.9	4.4	8.2	44.8/43.1	1.2/1.1	363.2/357.2	101.7
40.1	190.8	159.9	4.2	7.7	44.9/43.2	1.2/1.1	362.6/356.0	101.9
42.2	190.8	159.9	4.7	8.2	44.9/43.1	1.3/1.3	363.5/356.1	102.1
45.5	190.8	159.1	4.4	7.7	44.6/43.2	1.2/1.2	362.1/356.8	101.5
47.6	189.5	157.7	4.5	8.0	44.2/43.0	1.3/1.2	359.7/356.5	100.9
47.8	188.9	156.9	4.5	7.9	44.0/ .0	1.3/ .0	358.2/356.4	100.5

*COMPUTED USING THE N2 CAL. FACTOR AND
THE KNOWN IONIZATION PROBABILITY OF H2O.

MISSION TOTAL ELAPSED TIME 57 DAYS

CALIB. PERIOD 40 ELAPSED TIME BETWEEN CALIB. 47.58 HOURS.

CALIBRATION FACTORS (SENSITIVITY, TORR/VOLT)

		355T	360T	370T
NITROGEN	BEGIN	.00	62.94	.00
OXYGEN	BEGIN	.00	72.44	.00
CO2	BEGIN	.00	4.86	.00

	TWO GAS SENSOR				COMPARATIVE DATA			
TIME HR	N2 TOR	O2 TOR	CO2 TOR	H2O* TOR	O2-PCT MS/MDA	CO2-PCT MS/MDA	TOTAL-TOR MS/MDA	TOTAL-PCT MS
.2	189.4	158.6	4.5	2.9	44.5/ .0	1.3/ .0	355.5/356.2	99.8
3.2	185.7	155.0	4.5	7.6	43.2/44.0	1.2/1.3	352.8/358.5	98.4
5.0	185.0	156.5	.0	7.7	43.6/43.2	.0/1.2	349.2/359.0	97.3
7.0	185.7	157.9	4.4	7.9	44.0/43.7	1.2/1.2	355.9/359.0	99.1
9.0	185.7	157.9	4.2	7.4	44.1/43.8	1.2/1.1	355.2/358.0	99.2
11.0	186.3	157.9	4.0	7.3	44.2/43.5	1.1/1.1	355.5/357.0	99.6
12.8	185.7	158.6	4.1	7.6	44.3/43.5	1.1/1.1	355.9/357.9	99.5
15.0	186.3	159.4	4.1	7.2	44.6/43.5	1.1/1.1	356.9/357.2	99.9
17.0	186.3	159.4	4.4	7.8	44.6/43.5	1.2/1.2	357.9/357.0	100.2
19.0	186.3	159.4	4.1	7.4	44.7/44.0	1.2/1.1	357.2/356.5	100.2
21.0	185.7	158.6	4.0	7.4	44.6/44.0	1.1/1.1	355.7/356.0	99.9
23.3	185.0	157.9	4.1	8.1	43.9/43.6	1.1/1.1	355.2/359.8	98.7
25.1	184.4	157.2	4.3	7.8	43.4/43.8	1.2/1.2	353.7/362.2	97.7
27.1	185.7	157.2	4.3	7.6	43.5/43.5	1.2/1.2	354.7/361.0	98.3
29.2	185.7	156.5	4.3	7.4	43.5/43.7	1.2/1.2	353.8/359.6	98.4
31.8	186.9	156.5	4.4	7.5	43.7/43.7	1.2/1.2	355.2/357.8	99.3
33.8	187.5	156.5	4.4	7.3	43.8/43.1	1.2/1.3	355.7/357.0	99.6
35.8	188.2	157.9	4.5	7.4	44.2/42.7	1.3/1.3	357.9/357.0	100.3
38.0	189.4	157.9	4.4	7.6	44.2/42.7	1.2/1.3	359.4/357.1	100.7
40.0	189.4	160.8	4.4	7.6	44.8/43.2	1.2/1.2	362.3/358.8	101.0
41.8	189.4	161.5	4.3	7.9	44.9/43.2	1.2/1.2	363.2/359.5	101.0
43.7	188.2	161.5	4.3	7.6	44.9/43.4	1.2/1.2	361.6/360.0	100.5
46.4	185.7	160.1	4.1	7.7	44.2/43.8	1.1/ .0	357.6/362.0	98.8
47.0	183.8	158.6	4.2	7.6	43.9/ .0	1.2/ .0	354.2/361.1	98.1

*COMPUTED USING THE N2 CAL. FACTOR AND
THE KNOWN IONIZATION PROBABILITY OF H2O.

MISSION TOTAL ELAPSED TIME 59 DAYS

CALIB. PERIOD 41 ELAPSED TIME BETWEEN CALIB. 42.93 HOURS

CALIBRATION FACTORS (SENSITIVITY, TORR/VOLT)

		355T	360T	370T
NITROGEN	BEGIN	.00	63.39	.00
OXYGEN	BEGIN	.00	73.33	.00
CO2	BEGIN	.00	4.80	.00

TWO GAS SENSOR COMPARATIVE DATA

TIME HR	N2 TOR	O2 TOR	CO2 TOR	H2O* TOR	O2-PCT MS/MDA	CO2-PCT MS/MDA	TOTAL-TOR MS/MDA	TOTAL-PCT MS
.2	187.6	162.1	4.2	2.4	44.9/43.6	1.2/1.2	356.3/361.0	98.7
3.3	183.2	159.9	4.2	7.5	44.2/44.2	1.2/1.2	354.8/361.8	98.1
5.2	185.1	159.1	4.3	7.6	44.2/44.6	1.2/1.2	356.1/359.8	99.0
7.3	186.4	158.4	4.2	7.5	44.2/44.5	1.2/1.2	356.4/358.0	99.6
9.5	187.6	159.9	4.0	7.9	44.6/43.6	1.1/1.1	359.3/358.4	100.3
11.6	188.3	159.9	3.9	8.1	44.7/43.5	1.1/1.1	360.1/358.0	100.6
13.1	188.3	159.9	3.9	8.1	44.7/43.3	1.1/1.1	360.1/357.4	100.8
15.3	188.3	159.9	3.9	8.2	44.6/43.1	1.1/1.1	360.3/358.5	100.5
17.3	189.5	161.3	3.8	8.2	45.0/43.1	1.1/1.1	362.8/358.8	101.1
19.3	188.9	161.3	3.9	8.2	44.9/43.2	1.1/1.1	362.3/359.2	100.9
21.8	188.3	160.6	3.9	8.2	44.6/ .0	1.1/ .0	361.0/360.0	100.3
23.5	186.4	157.7	4.1	8.1	43.8/43.5	1.1/1.1	356.2/359.8	99.0
27.6	186.4	157.7	4.6	8.1	43.6/43.0	1.3/1.2	356.6/361.5	98.7
29.3	187.0	159.1	4.8	8.3	44.0/43.5	1.3/1.3	359.2/362.0	99.2
31.4	187.6	159.9	4.7	8.1	44.2/43.5	1.3/1.3	360.2/361.8	99.6
33.5	188.3	159.9	4.7	8.3	44.3/43.6	1.3/1.3	361.1/361.0	100.0
35.5	188.9	160.6	4.5	7.6	44.6/43.6	1.2/ .0	361.6/359.9	100.5
37.2	189.5	159.9	4.6	7.9	44.5/43.0	1.3/1.2	361.8/359.0	100.8
39.4	189.5	159.1	4.4	7.7	44.3/43.0	1.2/1.2	360.8/359.0	100.5
40.8	190.8	159.1	4.3	7.5	44.4/42.8	1.2/1.2	361.8/358.2	101.0
41.9	190.2	158.4	4.2	7.5	44.3/43.8	1.2/1.1	360.2/357.2	100.9
42.7	190.2	158.4	4.2	7.4	44.3/43.2	1.2/1.1	360.2/357.3	100.8

*COMPUTED USING THE N2 CAL. FACTOR AND
THE KNOWN IONIZATION PROBABILITY OF H2O.